Technical University of Denmark

DTU

Verification of long-term load measurement technique

Work Package 1B.2 under the European Commission, Integrated Wind Turbine Design (UPWIND)

Schmidt Paulsen, Uwe

Publication date:
2011

Document Version
Publisher's PDF, also known as Version of record

[Link back to DTU Orbit](#)

Citation (APA):
Schmidt Paulsen, U. (2011). *Verification of long-term load measurement technique: Work Package 1B.2 under the European Commission, Integrated Wind Turbine Design (UPWIND)*. Danmarks Tekniske Universitet, Risø Nationallaboratoriet for Bæredygtig Energi. (Denmark. Forskningscenter Risoe. Risoe-R; No. 1782(EN)).

DTU Library
Technical Information Center of Denmark

Work Package 1B.2 under the European Commission, Integrated Wind Turbine Design (UPWIND): Verification of long-term load measurement technique

Uwe Schmidt Paulsen
Risø-R-1782
February 2011

Author: Uwe Schmidt Paulsen
Title: Work Package 1B.2 under the European Commission, Integrated Wind Turbine Design (UPWIND): Verification of long-term load measurement technique
Division: Wind Energy Division
Abstract (max. 2000 char.):

The present report is the final effort of tasks carried out under UPWIND WP1B2 transmission and conversion, which describes:

1) results and recommendations developed in the course of developing the long-term load measurement technique

2) the hardware details, type of sensors and location, data storage and

3) data analysis technique to verify design load assumptions.

The work is carried out under Contract no 019945 (SES6) "UPWIND" within the European Commission

The interaction between the mechanical and electrical generator subsystems is described rudimentarily, based primarily on HAWC2 simulations below stall of the mechanical system with simple generator and gearbox systems. The electrical system simulations were not carried out as intended in DOW[2], but indications of the conditions for establishing the interaction have been described by measurements and by argument, that this might have an effect as indicated.

The hypothesis stating, that the power signal can be utilized as a basic signal for extended analysis of mechanical as well as electrical power signal with static and dynamic features, has been demonstrated on performance and dynamic bandwidth capability. It is however from present analysis obvious that improved signal conditions could be achieved with other mechanical joint solutions than with the present torque signal as measured with the cardan joint. For the reasons mentioned, the comparison with a signal showing the mechanical properties could be improved, with a likely gain on the accuracy as a result.

Contents

Verification of long-term load measurement technique

Preface

This work is part of the sixths framework programme on the integrated design for wind turbines within transmission/conversion with the acronym UPWIND[1], which in particular for the work package WP 1B2 transmission and conversion deals with "..the entire drive train including mechanical and electrical components. The overall purpose is to develop the technology necessary to overcome the present limitations in turbine size, power, and effectiveness and to increase predictability and reliability."[2]. The members of the working group under WP 1B2 are:

WP Member	Country	Name
Risoe National Laboratory	Denmark	RISOE
GE Global Research, a registered branch office of General Electric Deutschland Holding GmbH	Germany	GE
WZL der RWTH Aachen	Germany	WZL
Samtech s.a.	Belgium	SAMT
Lohmann und Stolterfoht GmbH	Germany	REXR
Aalborg University	Denmark	AAU
Delft University of Technology	Netherland	DUWIND
University of Edinburgh	UK	EDIN
ISET	Germany	ISET
Fundacion ROBOTIKER	Spain	ROBOT

Acknowledgements

1 Introduction

It is further stated in the DOW[2] of the project, that the drive train in terms of reliability today is the most critical component of modern wind turbines, a statement which might be enhanced by looking at the picture provided in the front page, demonstrating *gear wheel pitting* observed on a Flender PEAC gearbox .

The typical drive train of modern wind turbines consists of an integrated serial approach where rotor shaft, main bearing, gearbox and generator are as close together as possible with the aim of compactness and mass reduction. Field experiences throughout the entire wind industry show that this construction approach results in many types of failures (especially gearbox failures) of drive train components, although the components are well designed according to contemporary design methods and all known loads. It is assumed that the basic problem of all these unexpected failures is based on a principal misunderstanding of the dynamic behaviour of the complete system "wind turbine" due to the lack of an integral approach ready to use which at the same time integrates the structural nonlinear elastic behaviour with the coupled dynamic behaviour of multi body systems together with the properties of electrical components. The following different system parts need to be addressed within one coupled "integral" model: Wind field simulation; Aero-elastic interaction at blades; Nonlinear flexibilities of fibre blades; Linear flexibilities of metal components of e.g. drive train; Nonlinear behaviour of drive train components e.g. gears, bearings, bushings; Electro-mechanic behaviour of generator; Electrical behaviour of power electronic converter and grid.

Depending on the specific location of a wind turbine the actual loads on the components are quite different from the design loads, which for the reasons of the component level needs verification on a real wind turbine. The objective of this work is to participate within the work package with a set of specific information, which validates the design assumptions. Therefore a long-term measurement technique is the necessary tool to provide load cycle analysis for all turbine conditions. As a secondary effort on a technology driven approach, the same technology will be used for development of a low-cost drive train load monitoring system, which enables to

down-count the proposed and designed lifetime according to the actual measured load cycles. The measured load cycles for specific conditions will be compared to simulation results performed within task 1B.2a.1. Thus the commonly used assumptions for component design can be verified and enhanced towards future large-scale wind turbines. Electromechanical models for wind turbines usually include the drive train components of the wind turbine, while aeroelastic models apply simplified generator models. However, preliminary simulations and measurements have indicated that there is a significant dynamic coupling between the generator and the wind turbine structure beyond the drive train, and that this coupling can cause oscillations in the drive train and tower. The interaction between the mechanical system and the generator will be studied further as explained in 4 Design tools.

Risø DTU elaborates in the project on a drive train measurement system for long-time measurements, in particular generator power P and angular rotor speed Ω with high accuracy both in time resolution and with appropriate dynamical performance as in

Extended experimental approach: The aim is to demonstrate that the drive train conditions can be measured in a simple and robust way. In order to ensure sufficient bandwidth, the generator power is derived by measured 3-phase generator AC current I and –voltage V according to:

$$P(t) = \sum_{i=1}^{3} U_i(t) \cdot I_i(t)$$

The measurements are expected to be carried out on the 500 kWwind turbine online measurement laboratory (WTMLAB) facilities at the Risø Campus (http://www.winddata.com/nordtank/). Analysis of indicated electromagnetic generator torque (equal to $P \cdot \Omega^{-1}$) is provided with subsequent emphasis on describing the interaction between the mechanical and the electrical system under wind turbine operation. The method is tested for robustness by comparing with results of measured mechanical torque Q. Based on this comparison done in the time domain as well as frequency domain, the bandwidth with which the mechanical torque is close to the electrical is determined and compared to the free-free eigenfrequency for oscillation between generator and wind turbine rotor inertias. The possible benefit of including the generator inertia in a dynamic conversion of power and speed to mechanical torque is also investigated. The probability distribution of the indicated torque is calculated for the complete measurement period. Load cycles under specific wind turbine and - conditions are investigated. The measured load spectrum is compared to the compound design load spectrum. Elaboration on higher order excitations from primarily the indicated torque is performed. Simulations with and without interaction between the mechanical and electrical system and comparison with measurements are carried out.

Risø's aeroelastic model HawC2 is used for analysis of the interaction between the mechanical- and electrical system. This issue will be studied further, applying HawC2 model with generator dynamics and/or a Power Factory model with extended structural model beyond the drive train. The plan to use DigSilent has been skipped because of extra capability built into HAWC2. The measurements will be applied to validate the simulations. The report briefly describes DigSilent and Powerfactory tools for complementary purpose.

2 Description of the experimental facility

2.1 Site

The Wind turbine is geographically located at the Risø Campus, about 6 km North of Roskilde as shown on Figure 1. The wind turbine is placed on the foundation no 4, in a rather gentle sloping terrain towards the area 'Bløden' on the west side of the Roskilde firth. The free undisturbed inflow is from the dominant western wind sector.
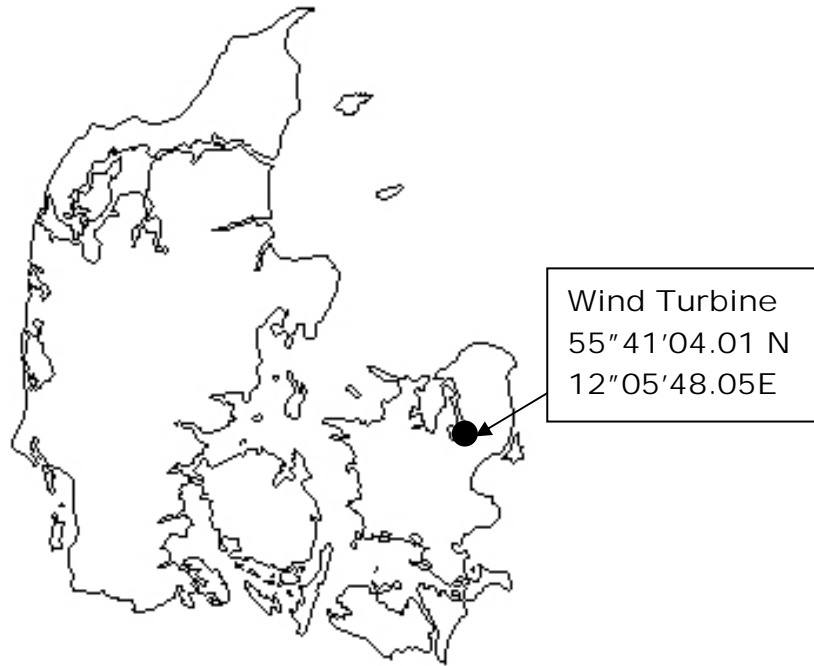

**Wind Turbine
55″41′04.01 N
12″05′48.05E**

Figure 1: Location of turbine

2.2 Wind Turbine Description

The test wind turbine, which is located at Risø Campus, Roskilde, is a traditional Danish three-bladed stall regulated Nordtank, NTK 500/41 wind turbine – see specifications in Table 1. Figures in brackets reflect results from post survey on turbine specs. The turbine is primarily used for energy production and tests and it is serviced on commercial conditions.

Figure 2 Photo of NTK500/41 wind turbine

Table 1: Nordtank NTK 500/41 specifications.

Identification No.	92-500
Rotor	
Rotor Diameter	41.1m
Swept area	1320 m²
Rotational Speed:	27.1 rpm
Measured tip angle:	-0.2º±0.2º

Tilt	2º
Coning	0º
Blades	
Blade type:	LM 19.1
Blade profile[s]	NACA 63-4xx & NACA FF-W3, equipped with vortex generators.
Blade length:	19.04 m
Blade chord:	0.265 – 1.630 m
Blade twist:	0.02 – 20.00 degrees
Air brakes	Pivotal blade tips, operated in FS-mode
Drivetrain	
Mechanical brake	High speed shaft, operated in FS-mode
Power regulation	Passive aerodynamic stall
Gearbox	Flender; ratio 1:55.35
Generator	Siemens 500 kW, 4 poles, 690 V
Tower	
Type	Conical steel tube, h=33.8 m
Hub height	36.0 m
Masses:	
Blade weight:	1960 kg (2249 kg incl. Extender and bolts)
Rotor incl. hub	9030 kg (9846 kg)
Tower head mass	24430 kg (25246kg)
Tower mass	22500 kg

The turbine was installed in 1992 with a 37 m diameter rotor, which in 1994 was substituted with a 41 m diameter rotor in combination with a rotor speed reduction to limit the power output. The wind turbine has been subjected to tests, modifications and investigations during 1992- 1999 according to references [3, 4, 5, 6, 7, 8, 9]. There have been load measurements on the wind turbine drive train [16], and load simulations on a 600 kW gearbox design similar to the present wind turbine gearbox [17].

2.3   Grid connection
The wind turbine is connected to a local 400 V grid, designed for test of smaller wind turbines. The 400 V is supplied from the public 10 kV grid through a 1000 kVA, 10/ 0.4 kV transformer that is presently shared between the 500 kW Nordtank wind turbine and a 100 kW Tellus wind turbine.
The Nordtank wind turbine is rated to 690 V, and therefore an additional 800 kVA, 0.4 / 0.69 kV transformer is installed to increase the voltage. The principal electric connection diagram is shown in Figure 3.
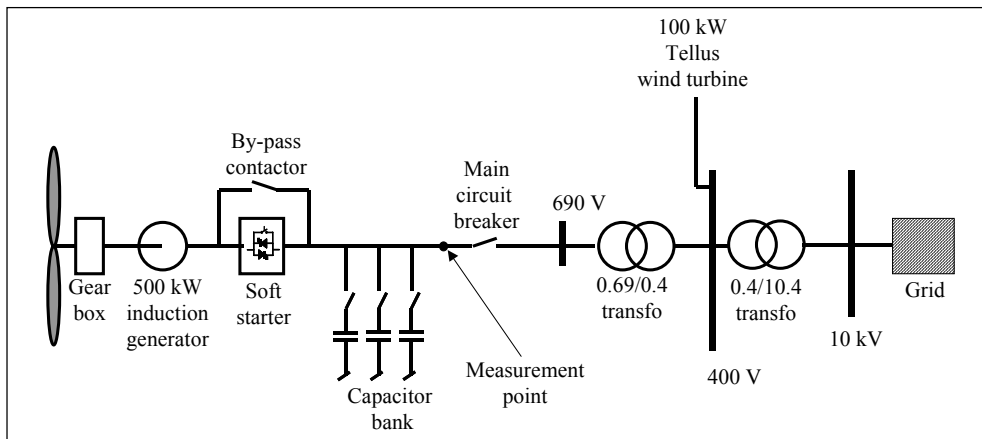
Figure 3: Connection diagram of 500 kW Nordtank in Risø.

A frequency converter system has been designed and implemented allowing the wind turbine to operate at variable grid frequency. This wind turbine operation mode can be switched to from stall regulated mode by means of a by-pass contactor as seen on Figure 3.

2.4 Instrumentation

Presently the experimental facility is instrumented as described in the following:

A meteorological mast is placed 2½ rotor diameters in westerly direction from the wind turbine. The mast is equipped for measurement of wind speed at hub height, wind direction, air temperature, air barometric pressure and air humidity. The installation is made in accordance with the recent IEC recommendations for both power performance [10] and structural load measurements [11] and [15].

The structural loads are monitored by strain gauges mounted at the blade root, on the main shaft, at the tower top and at the tower bottom. The instrumented locations are detailed below:

2.4.1 Blades

The load signals from the reference blade includes bending moments at the blade root, measured by strain gauges mounted on the blade root steel extenders, as shown on Figure 4. The gauge installation enables measurements of both flap-wise and edge-wise bending moments in a rotating reference system.

During autumn 2005 the strain gauges installation at the radius 1.24m has been abandoned and the instrumentation has been extended with strain gauges on all three blades, both for measuring flap-wise and edge-wise bending moments in the blade root at radii of 2.1 m from the rotor centre.
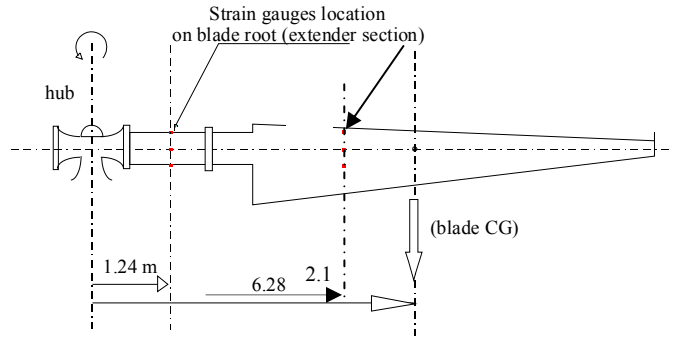
Figure 4: Structural load measurements in the blade root at radius 2.1 m.

2.4.2   Rotor and drivetrain

The load measurement on the main shaft includes a torque sensor in front and right after the main bearings, and two bending moments at a position behind the hub/main shaft flange – in a rotating reference system, as shown on Figure 5 . The gauge location enables measurements of bending moments in two directions, perpendicular to each other in a rotating reference system. The two bending moments combined with the rotor position are used to determine the rotor bending moments in yaw and tilt direction - in a nacelle reference system.
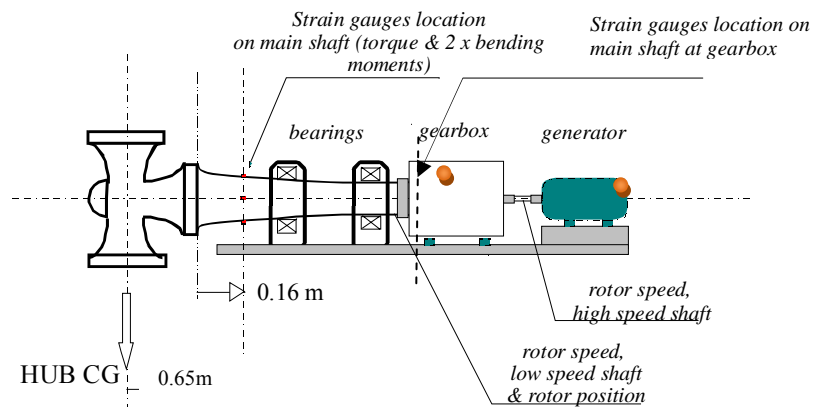
Figure 5: Structural load measurements on the main shaft.

Additionally accelerometers are positioned on the gearbox, see Figure 6 and on the rear of the nacelle, see in Figure 7 .
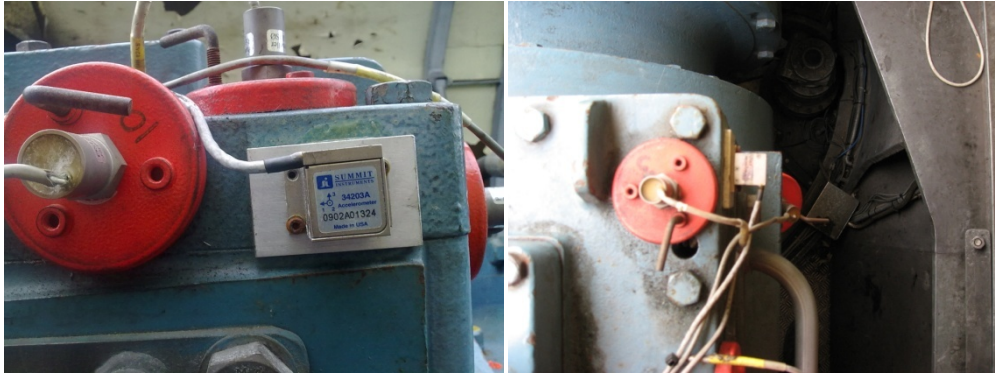
Figure 6: DanControl VS3 accelerometers on gearbox corner

Figure 7: DanControl VC3 accelerometers in the rear of the nacelle

2.4.3   Spinner

A spinner anemometer has been installed in order to get detailed information about the interaction between of wind flow towards the turbine, and the turbine yaw response. The instrument is a prototype and is not working properly.

2.4.4   Tower

The tower loads includes torque at the tower top and bending moments in two directions at the tower bottom, as shown on Figure 8 in a (fixed) tower reference system.

Strain gauges location (torsion)

Accelerometers in direction: turbine-met mast and in transverse direction

Strain gauges location
2 x bending moments

3.5 m

Online View
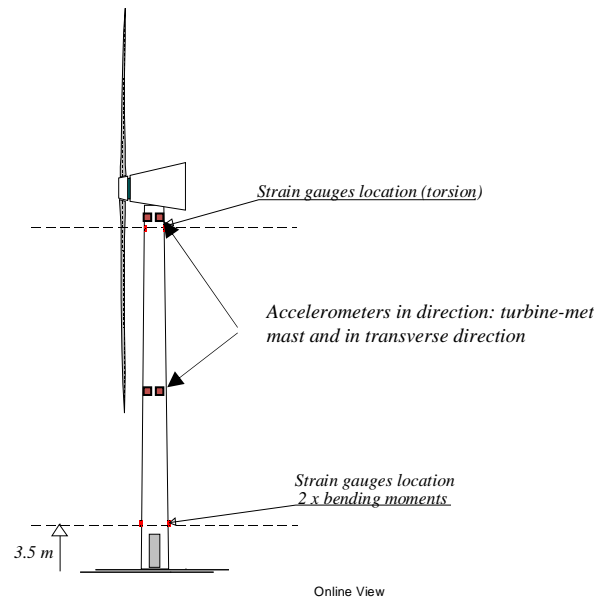
Figure 8: Structural load measurements on the welded tubular steel tower.

Various sensors are installed to measure the operational conditions of the wind turbine. The position of the nacelle, the wind direction and the wind speed on top of the nacelle are measured. Pulses from sensors placed on the fast rotating generator shaft and on the slow rotating main shaft are used to determine the rotational speeds. Status information on tip position, grid connection and shaft brake are registered. Finally, the electric power production is derived by integrating measurements of the 690 V line voltages and currents in the time domain using the Time Division Multiplication Principle.

An overview of the signals, the type and sensor conversion principle is given in Overview **of sensor and transmitter**

Table 7, see appendix.

Conventional measurement transformers are used to measure at the 690 V level at the common point. Three current transformers (ratio 500:1) followed by Hall elements convert the phase currents to voltage signals in the ratio 5A to 1A. Table 8 provides the sensor and transmitter details for the data acquisition system carrying out high speed sampling.

2.5 Data Acquisition

A PC-based data acquisition system has been designed to monitor and collect data from the wind turbine sensors – see *Figure 9*.
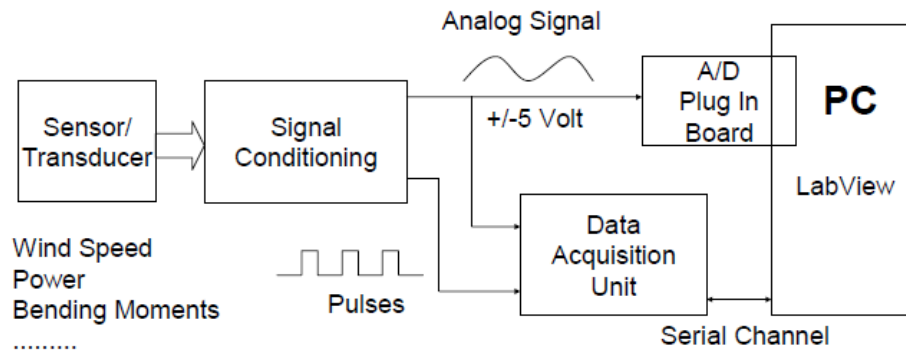
Figure 9: Overall load monitoring data acquisition system (35 Hz)

The output signals from all sensors are conditioned to the +/- 5 V range. Analogue signals are either continuously varying (strain gauges, temperature…), digital types such as train of pulses (rotational speed, anemometer…) or on/off levels (status signals for brake, blade tips and generator modes). All signals - except outputs from voltage and current transformers - are connected to one of three RISØ P2558A data acquisition units (DAU), each of which provides 16 analogue input channels and 6 general-purpose digital input channels [14]. The analogue inputs are converted into 16-bit quantities. Data from all channels are assembled in a binary telegram, each data occupying 16 bits. The telegram is preceded by two synchronization bytes and it is succeeded by two check-sum bytes. The whole telegram is transmitted to the PC over a RS232 serial channel at a rate of 38400 Baud. The sampling rate at the DAUs is set to 35 Hz so new telegrams are created and send 35 times per second per channel.

One DAU is installed in the bottom of the wind turbine tower, another in the nacelle and the last one is mounted on the hub – it is rotating and transmitting data over a RF-link. The serial channel from each DAU is connected to the PC over a multi-port serial plug-in board.

The 35 Hz scan rate is high when considering meteorological conditions, appropriate for mechanical phenomena, but it is far too slow when studying the impact of the wind turbine on the power grid or mechanical loading in the drive train. Thus, another part of the acquisition system works at a much higher sampling rate (12.8 kHz) on transducer signals originating from the 3 phase voltages and currents at the 690 V generator terminals – see Figure 1. The signals are fed to a signal-conditioning interface that performs sample and hold operation, scales down the signals to the ±5 V level and delivers the conditioned signals to a 12-bit multi-channel ADC plug-in board in the PC.

The data acquisition system is build up around a standard desktop PC. The PC is connected to the Internet and thereby to DTU from where it can be operated remotely.

An important aspect of WTMLAB is instant access to a real wind turbine, which are well documented at all possible operational situations. Besides being a test facility the wind turbine works as production unit creating revenue for Risø DTU, so most of the time it is running on normal, commercial basis.

To build up complete documentation of the wind turbine behaviour, data acquisition is carried out constantly. Dedicated measurement software has been developed under LabVIEW©. The data streams received on the serial channels from the DAUs are read, error checked and the measured values are derived from the data telegrams. Data are assembled in 10-minutes time series and statistics such as mean, standard deviation, maximum and minimum values are calculated. The whole time series and the statistics – with a time stamp added – are stored on disk in ASCII-format.

The electric power signals are treated differently due to the fast sampling rate. The idea is to aggregate power quality parameters over 10 minutes' intervals – synchronous with the DAU intervals - so atmospheric, mechanical and electrical behaviour directly can be correlated. To diminish the amount of data, on-line data reduction is compulsory.

Another benefit of WTMLAB is that the students are able to develop data acquisition programs of their own, upload the programs to the PC at Risø and perform test directly on an operating wind turbine. In addition, due to the built-in server in LabVIEW©, the measurement application can be monitored and controlled across the Web.

The extension of data acquisition capacity in excess of that for statistical reference of load conditions as indicated in Figure 9 is shown in Figure 21. The figure shows a data acquisition system capable of fast sampling (50 kHz).

2.6   Calibration and measured signals

The signals are calibrated in comparison with known sources. The strain gauge signals are calibrated by applying known loads on the structure schematically as shown in Figure 10. This is carried out on regular intervals. Details in the calibration procedure are shown in [Fisher, Shawn].

There are regularly checks carried out on these signals; these are categorized as to idling at constant rotational speed at low wind speed as in Figure 11 and in Figure 12, and as yawing of the turbine 360 Deg around the horizon with results as in Figure 13 and with applied scaling the result shown in Figure 14.
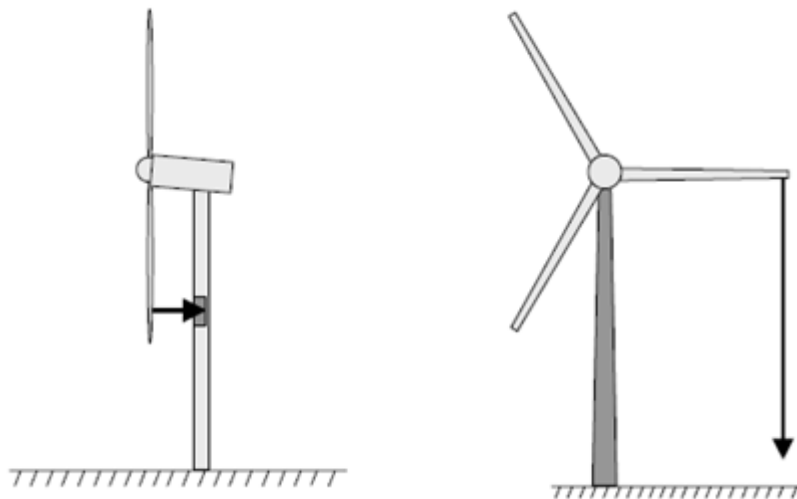
Figure 10 Rotor load calibration: Flapwise loads(left), Edgewise loads(right)[]
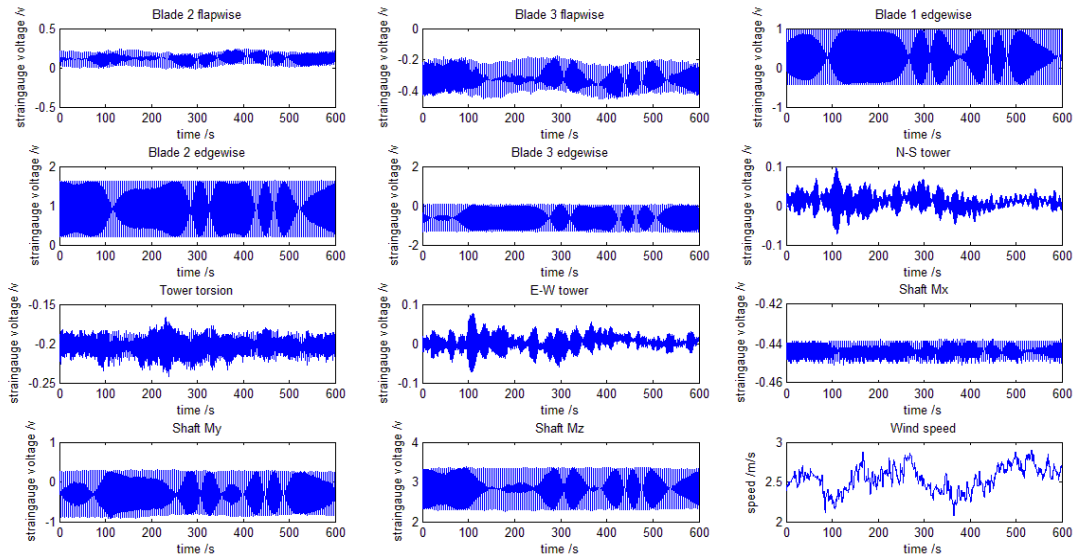
Figure 11 Idling of rotor at low wind speeds
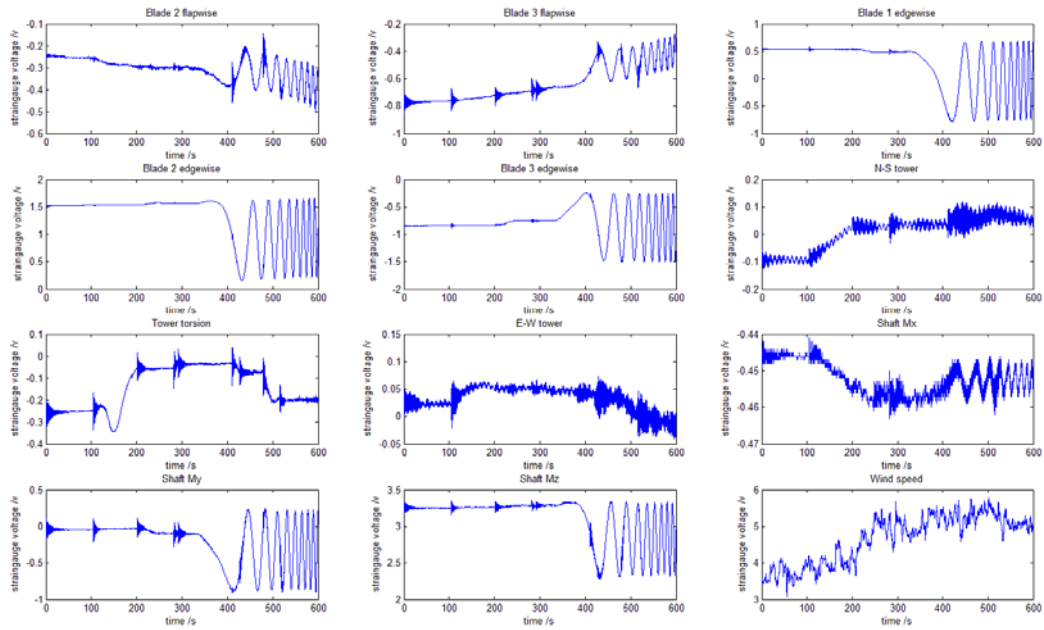
Figure 12: Wind turbine start sequence at low to medium wind speed
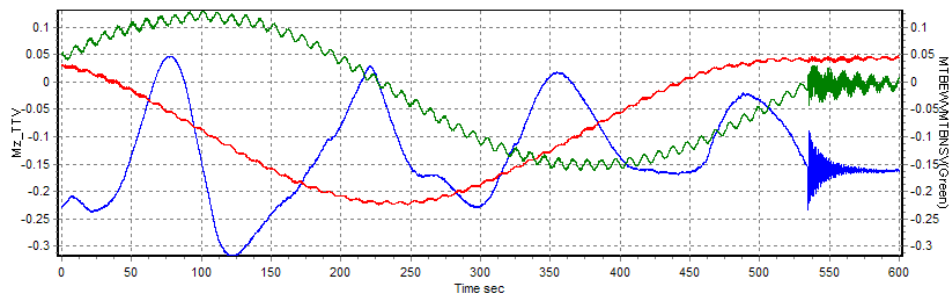
Figure 13: Mz_TT (Blue),MTBEW(Red) and MTBNS(Green) during 360° yaw test performed 28-07-2010

16   Risø-R-1782(EN)
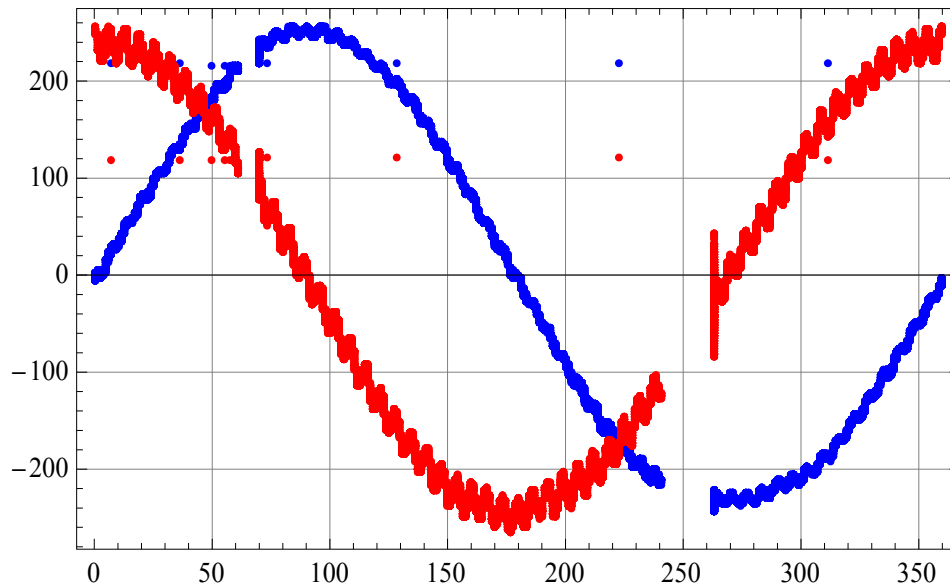
Figure 14MTBNS (Red), MTBEW (Blue) with scaling in kNm vs nacelle position, in Deg. From yaw test 28-07-2010

The measurement signals with the complete gain and offset values are listed in Table 2.

Table 2 Signals with Gain and offset values for scaling

Ind	Signal	Description	Gain	Offset	Units
1	WS_hh	WS_hh	1	0	[m/s]
2	T_Air	T_Air	1	0	DegC
3	B_Air	B_Air	1	0	hPa
4	Mz_TT	Mz_TT	-272.087	121.0785	kNm
5	MTBEW	MTBEW	1841.92	155.7	kNm
6	MTBNS	MTBNS	1782.25	31.4	kNm
7	Pe	Pe	1	0	kW
8	TBAcc_x1	TBAcc_x1	2.212389	-4.77655	g
9	TBAcc_y1	TBAcc_y1	2.227171	-7.34967	g
10	TBAcc_x2	TBAcc_x2	2.207506	-5.85872	g
11	TBAcc_y2	TBAcc_y2	2.325581	-5.97674	g
12	IO_tip	IO_tip	1	0	[-]
13	IO_brk	IO_brk	1	0	[-]
14	IO_gen	IO_gen	1	0	[-]
15	IO_stl	IO_stl	1	0	[-]
16	Precip	Precip	1	0	[-]
17	DAU_STATUS#0	DAU_STATUS#0	1	0	[-]
18	WDMet_cos	WD_Met_cos	1	0	V
19	WDMet_sin	WD_Met_sin	1	0	V
20	WDMet	WD_Met	1	0	Deg
21	Yaw	Yaw	1	0	Deg
22	RotAzi	Rot_Azi_Pos	1	0	Deg
23	Rot_Sp_L	Rot_Speed_slow	1	0	RPM

24	Rot_Sp_H	Rot_Speed_fast	1	0	RPM
25	WS_Nac	WS_Nac	1	0	m/s
26	Acc_Gearx	Acc_Gearx	2.212389	-4.86062	g
27	Acc_Geary	Acc_Geary	2.267574	-5.38549	g
28	Acc_Gearz	Acc_Gearz	2.257336	-5.17381	g
29	Acc_Nacx	Acc_Nacx	2.227171	-4.70379	g
30	Acc_Nacy	Acc_Nacy	2.217295	-4.19734	g
31	Acc_Nacz	Acc_Nacz	2.309469	-4.65127	g
32	Shaft_tors2	Shaft_tors2	-505.786	1487.863	kNm
33	Shaft_tors3	Shaft_tors3	13.1032	4.895	kNm
34	DAU_STATUS#14	DAU_STATUS#14	1	0	[-]
35	WD_Nac_ref	WD_Nac_ref	1	0	V
36	WD_Nac_sig	WD_Nac_sig	1	0	V
37	WD_Nac	WD_Nac	1	0	Deg
38	MxNR	ShaftQx	193.2	-84.8548	kNm
39	MyNR	ShaftBy	108.2142	28.84643	kNm
40	MzNR	ShaftBz	-117.738	331.7142	kNm
41	Mx11	MxBlade1	-169.865	139.2525	kNm
42	My11	MyBlade1	-142.72	-84.0623	kNm
43	Mx31	MxB2(3)	-164.488	-107.937	kNm
44	My31	MyB2(3)	-143.756	45.85806	kNm
45	Mx21	MxB3(2)	157.7466	-78.9389	kNm
46	My21	MyB3(2)	109.27	80.85978	kNm
47	DAU_STATUS#07	DAU_STATUS#07	1	0	[-]
48	S_stat	Sstat	1	0	[-]
49	S_heat	Sheat	1	0	[-]
50	SX	SX	1	0	[m/s]
51	SY	SY	1	0	[m/s]
52	SZ	SZ	1	0	[m/s]
53	ST	ST	1	0	Deg C
54	Sdir	Sdir	1	0	[-]
55	S_speed	Sspeed	1	0	[m/s]
56	S_tilt	Stilt	1	0	[-]
57	Spsp_Av	Spsp_Av	1	0	[m/s]
58	Spyw_Av	Spyw_Av	1	0	[-]
59	Spin_Av	Spin_Av	1	0	[-]
60	Sp_sped	Spspd	1	0	[m/s]
61	Sp_yaw	Spyaw	1	0	Deg
62	Sp_incl	Spincl	1	0	[-]
63	Sp_temp	Sptemp	1	0	Deg C
64	Spspd_Q	Spspd_Q	1	0	[-]
65	Spacc_Q	Spacc_Q	1	0	[-]
66	Spcal_Q	Spcal_Q	1	0	[-]
67	Sp_Stat	Spstat	1	0	[-]

2.7 Field experiences

The instrumentation was designed and partially carried out during 2006, and finished by 2007. Although testing in the laboratory showed satisfactory and expected results, we experienced 50 Hz noise and spikes in the signals from the fast measurement tests on the turbine. To solve noise and spikes emission caused a 3 months of time delay in the project. The long–term measurements were initiated with tests on the system, with efforts a) to improve noise reduction in recorded signals from the electrical system, and to improve the data acquisition system performance capability; b) to carry out regular campaigns of 10 sec data sets every 10 minutes, synchronized with load measurements. An upgrade of the data logger and a powerful PC has been installed to accomplish operations involved with calibration, synchronization and speed when accessing data.

Breakdown of equipment (sensors and pc) has resulted in considerable time delays, which has caused the long-term measurements campaign to be improved further.

The measurements have been subject to several outages because of different reasons: the wind turbine was stopped due to machine overhaul and sensor failure especially in strain gauges after initial test late 2007. In 2008 there was a special experimental loads investigation on the turbine. The Nordtank turbine was then under repair from 2008 to 2009. Here the rotor was taken down for rotor blade repairs: refurbishment of tips, repair of surface cracks, and renewing the blade vortex generators which where broken. During spring the rotor was installed without blade strain gauges. During summer the strain gauges on the blades were installed. Still measurement performance is low, and not fully complying and performing synchronously with the fast sampled measurements. Improvement of synchronicity with Frankfurt clocking is made by installing dedicated software together with a precision GPS signal in excess of windows timeserver. In July 2010 the system was ready for loads calibration, and a fault in blade No 1flapwise was discovered. In connection with the re-establishment of blade 1 strain gauges, the installations on the blade have shown drifting problems due to water ingress. Even after during 2010 and onwards, blade strain gauges are prone to drifting-even when considering that mounting are executed with the same quality procedures 'as usual'. In late 2010 the channels setup worked nicely when the incident with clipping the signal cables to the met mast occurred. It was decided to use the nacelle wind speed cup anemometer (signal *WS_nac*) as the reference instrument for wind speed measurements.

3   Extended experimental approach

3.1   Methodology

The intended DOW of WP 1B2[2] provides a road map to issues on mechanical transmission systems which to be covered, and has been mentioned in the introduction to this report:

Firstly, a novel method of gathering an estimate for the mechanical torque is presented. The suggested method originates from using the AC measured power and converting this into a torque. The method is applicable to systems with a well defined power-outlet, which simply states that the energy produced or dissipated can be experimentally measured. For the actual wind turbine the asynchronous generator directly driven via the gearbox high speed shaft outlet and the power is easily measured at the nodal point within the controller shown in Figure 3. For the turbine there is additionally a practical point that the gearbox losses are quite moderate and constant and mostly concerned with friction in bearings and thermal influences on lubrication. To verify the method an independent measure of mechanical torque is necessary along with rotor shaft speed.

Secondly, the interaction is investigated between the impacts from mechanical substructures-primarily originating from the 1´st modal shape of the tower movement and the rotor stator relative movement in the generator, by monitoring the angular deflection of the tower and comparing this against the electrical power.

The signals are basis for statistical treatment in terms of parametric dependency rain flow counting and for test of robustness in a broader perspective in the wind energy industry. The signals of mechanical based torque and virtual torque derived from power and rotational speed are represented as an ensemble. The ensemble is processed according to standard time series analysis techniques. Analysis of data is carried out on duty cycles according to recommendations of IEC 61400-13[11] with respect to categorized conditions defining a capture matrix and recommended practices[14] with respect to load cycles and counting techniques.:

- normal power production
- normal power production plus occurrences of faults
- parked conditions
- normal transients events and
- other than normal transients events

The above conditions has to be adjusted for real conditions, which limits the load cases to normal power production, parked conditions and production at very high wind speeds.

In the analysis of gear loads [16] the components on the high speed section are primarily reported to deflect and independent observations as shown on the cover proof for faults. The gearbox analysis will be used as a basis of 'possible problem' for a state space analysis. Previous measurements on the wind turbine [17] conclude that much of the gearbox load is transferred in the lower frequency range up to 10 Hz. This will be emphasized further.

Elaboration on higher order excitations from primarily the indicated torque is performed. The signals are monitored and conditioned on events determined by operational -and meteorological conditions in a standardized hierarchy developed at Risø DTU. The measured load spectrum is compared to the compound design load spectrum for these load cycles. The data are stored as time series for analysis with Mathematica™ or similar products.

3.2   Supplemental equipment

The derived torque mentioned previously is provided by means of mounting a torque sensor along with a high precision counter for gathering rotational revolutions and variations, on the high speed shaft located between the gearbox and the generator. An experimental setup of a torque transducer is provided in Figure 15, showing the central part of the shaft suitable for the installation along with an adequately rpm sensor. The strain gauge mounting is in shown in Figure 16. The counterpart is sled into the top opening.

It is by far not the best technical solution to place the strain gauge as shown in Figure 16. Excessive axial deflections in the 2 cardan peaces relative to each other and electrical soldering problems due to grease and centrifugal loads are potential sources for errors. Another source for misinterpreting the torque signal is the non-horizontal positioning of the flexible joint end nodes. Even a small offset angle introduces a sinusoidal signal and harmonic distortion. Therefore we investigated the cardan joint with FEM analysis in order to find out if the torsion transducer can be placed in an area of the cardan joint protecting the strain gauge(cavity behind the buckle head indicated in Figure 15). It was possible to detect a suitable area, but

with relatively small strain exposure. The idea was abandoned in favour of the placement shown in Figure 16.

The torque transducer conditions and digitizes the strain gage signal within a miniature transmitter module right on the rotor. With precision signal conditioning circuitry, 16-bit digital resolution, and digital data transmission off of the rotor, the torque transducer provides extremely high precision torque measurement capability. This single-channel telemetry system is inductively powered, allowing long-term monitoring without the need for batteries. A built-in shunt calibration function insures the highest levels of accuracy and integrity. Analogue output as well as Queued Serial Peripheral Interface (QSPI) high speed streaming digital data output are available. The signals are fed into the high-speed acquisition system as indicated-see *Figure 21*.
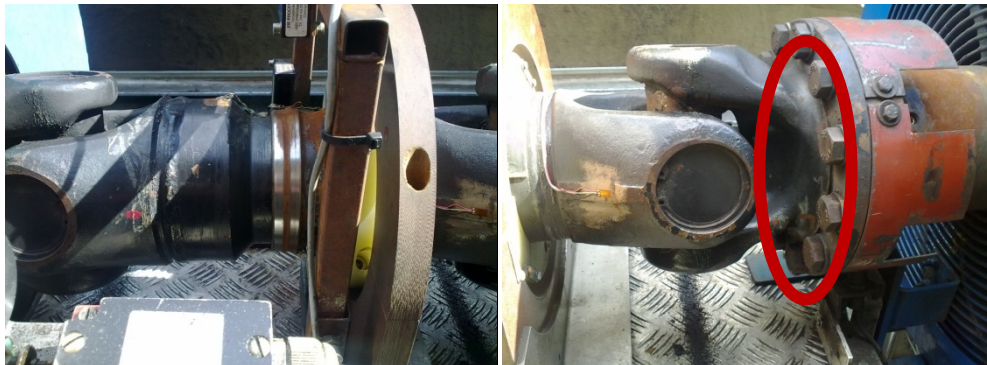
Figure 15: Left: Drive train detail (cover of disk brake, flexible cardan joint knuckle head, optic transducer for HSS shaft deflection measurement and Accumetrix torque transducer and pickup for strain gauge data measurement transmission.. Right: Same HSS shaft with cardan joint knuckle head and generator

Figure 16: Details of the torque sensor installation (left) on the cardan joint (right)

Figure 17: Summit 3-axial accelerometer at generator corner at different viewpoints

AC 3-phase power is measured; to study these phenomena, voltage and current transformers have been installed at the common point of connection and directly at the generator terminals – see *Figure 18*. It is a 690 V 3-phase electrical power system. Measurements are taken in each of the three phases resulting in 3 phase voltages (V_R, V_S and V_T) and 3 phase currents (I_R, I_S and I_T) – see *Figure 18* and *Figure 19*.
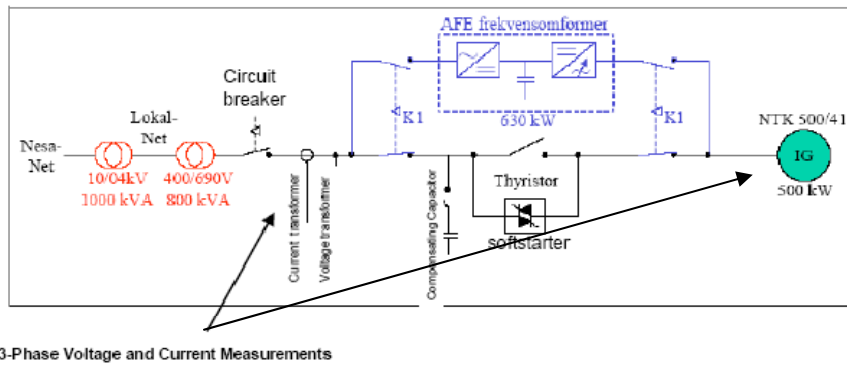
Figure 18: Electrical connection of Nordtank 500 kW induction generator - one phase representation.
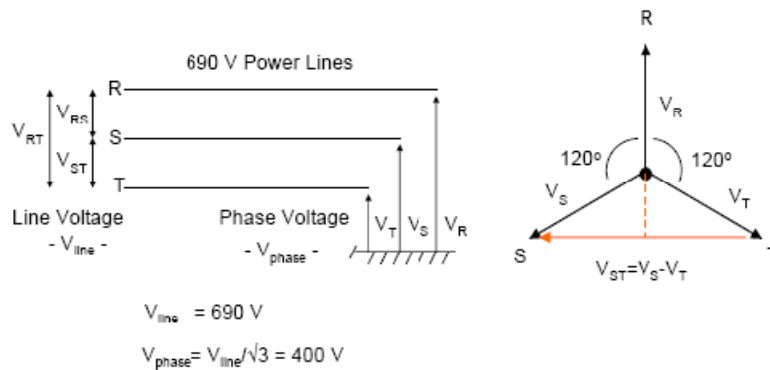
Figure 19: The 3-phase system
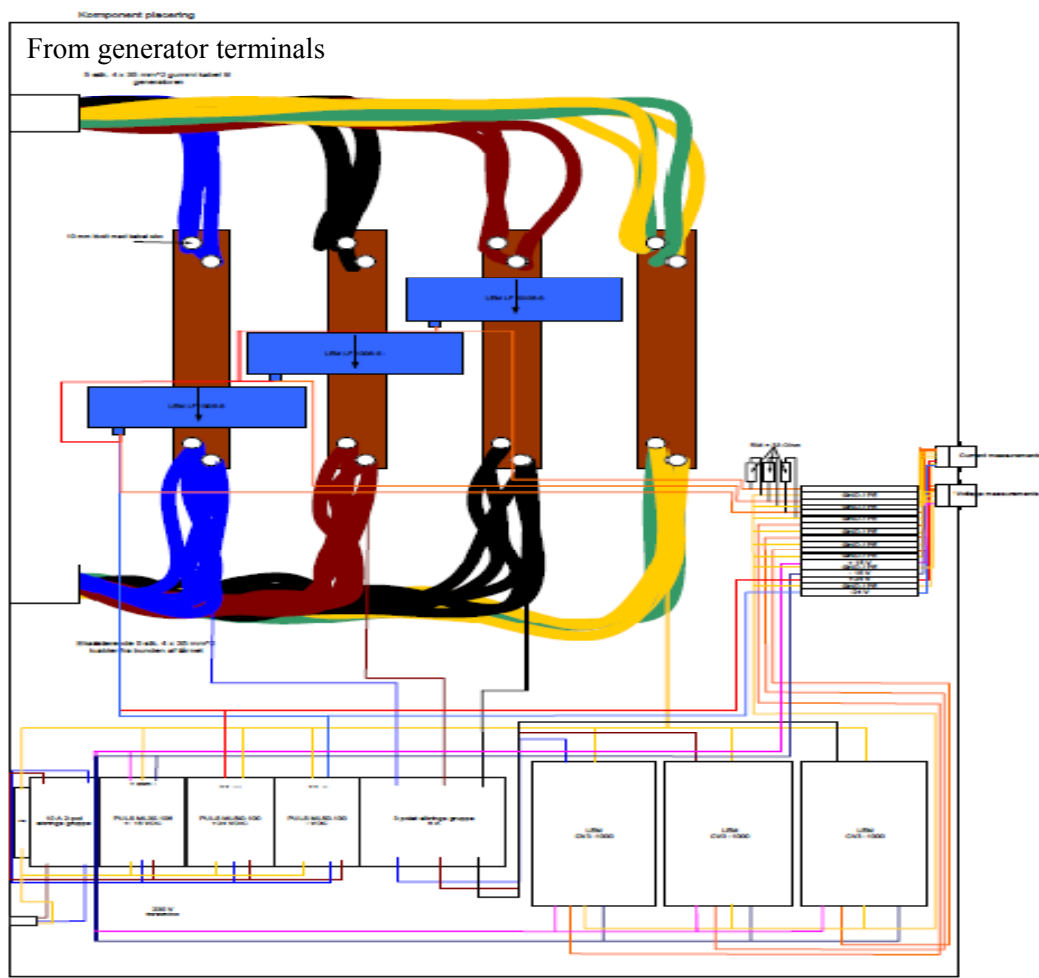
Figure 20: Overview diagram of current and voltage measurement

The signal path from the voltage and current transformers, as shown in *Figure 20* to the PC includes signal-conditioning equipment and a ADC-system (National Instruments CRIO) -see *Figure 21* .

The NI CompactRIO programmable automation controller is a low-cost reconfigurable control and acquisition system designed for applications that require high performance and reliability. The system combines an open embedded architecture with small size, extreme ruggedness, and hot-swappable industrial I/O modules. CRIO is powered by reconfigurable I/O (RIO) field-programmable gate array (FPGA) technology. The modules for analogue voltage measurements are: 7 NI 9239 4-Ch ±10 V, 50 kS/s/Ch, 24-bit, Ch-Ch Isolated AI Module. For digital measurements on the rpm transducer, one NI 9401 8-Channel, 100 ns, TTL Digital Input/Output Module is used.
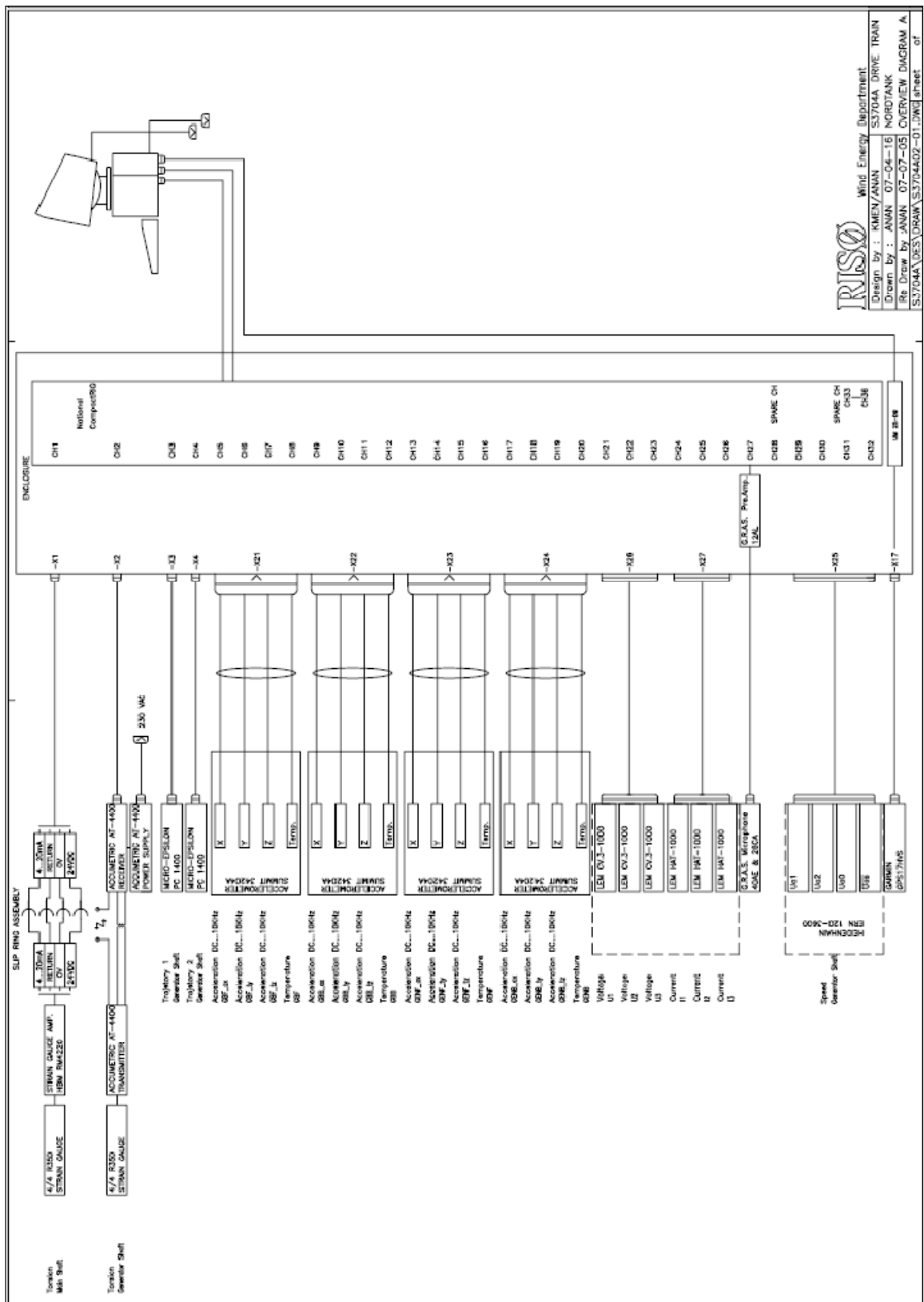
Figure 21: Overview of the high speed data acquisition system

Inside the CRIO, the signal conditioning unit performs 3 main functions:

1) Fitting the voltage to the CRIO level.
   The transformer signal are adjusted within the voltage range +/- 10 V
2) Anti-aliasing filtering.

The signals are filtered internally by a low-pass filtered according to a Nyquist frequency match of 0.25 the sampling frequency. The cut-off frequency has been selected so that systems dynamics up to 50 kHz can be detected. This fulfils requirements set by the IEEE Electric Power Quality Standards [13].

3) Simultaneous sample and hold of the signal levels.
   Internally in the CRIO, when receiving a trigger pulse from the outside the level of all 36 signals are kept at their present value until the value changes at receiving the next trigger pulse. This ensures simultaneous values of all the signals at the subsequent A/D conversion, carried out in a sequence channel by channel.

The CRIO-board contains a multi-channel 24-bit A/D-converter, that translates the +/- 10V input signals into integer values in the range 0-16777216. Further facilitations can be carried out by means of the FPGA features inherently in the CRIO board; they could be used to obtain e.g. frequency analysis using FFT algorithms if this number is a power of 2, which leaves (128 or) 256 samples per period as good choices.

Details on scaling of the physical voltage and power signals to the +/- 10 V CRIO DAQ system and computer are shown in *Figure 20*. The phase-to-ground voltage and the phase current in the 3 phases are measured.

The power supply is 690 V phase-phase or 400 V phase-ground (note, it is RMS-values). Thus, the instantaneous voltage will cover the range +/- $\sqrt{2}\cdot400$ V or +/- 566 V. The measurement range has been increased 180% i.e. +/- 1000 V, to allow for spikes in the voltage.

The range of the current is determined by the power system voltage and by the production capacity of the generator, which is specified to a rated power of 500 kW. The relation between power, voltage and current is:

$$\text{Active Power: } P = 3\cdot V_{Phase}\cdot I_{Phase} \text{ (W)}$$

This yields - at rated power 500 kW and at 400 V phase voltage - a phase current of about 400 A RMS or a current span of +/- 566 A. To take inrush currents at start-up into account this span is increased by a factor of 1.8 - as seen in *Figure 22*. In each current line, a voltage drop over a $33\pm5\%$ Ω resistor is measured and indicating the instantaneous current. In uncertainty terms, each of the resistivity has a equal uncertainty $\cong5\%$; the aggregated influence is interpreted to be $3/\sqrt{3}\cdot 5\%$ for the active power.

The ADC-board can be governed from software through an instrument driver installed on the PC. Special LabVIEW VIs [©]are meant for that purpose. One VI initialises the board and sets up sampling rate, number of channels etc. Another VI starts the measurements and writes the data into an internal buffer. A third VI reads a specified number of data from the buffer and delivers them in an array - the VI waits until the wanted number of data has arrived. In that way, it is possible - in one go - to read all samples covering one period of the 50 Hz power signal - as illustrated in *Figure 22* .

However, a real-time requirement to the measurement program is that the buffer is emptied faster then it is filled up, otherwise buffer overflow occurs.
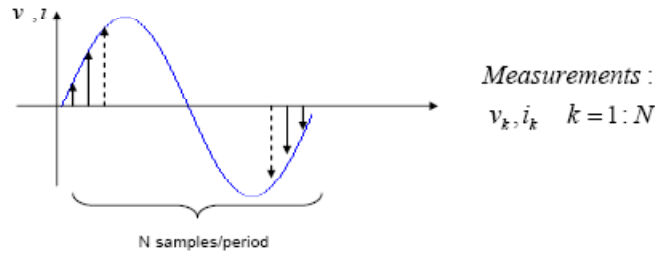
Figure 22: One period of samples[20]

From the sampled values the following power signal parameters are calculated:
1) RMS values

$$V_{RMS} = \sqrt{\frac{\sum_{k=1}^{N} v_k^2}{N}} \qquad I_{RMS} = \sqrt{\frac{\sum_{k=1}^{N} i_k^2}{N}}$$

2) Active, Reactive and Apparent Power in one phase

Active Power P in W:

$$P = \frac{\sum_{k=1}^{N} v_k \cdot i_k}{N}$$

3) Active and Reactive Power in 3 phases R-S-T – given as the sum of powers in each phase

$$P = \frac{1}{N} \sum_{k=1}^{N} (v_{R,k} \cdot i_{R,k} + v_{S,k} \cdot i_{S,k} + v_{T,k} \cdot i_{T,k})$$

$$Q = \frac{1}{\sqrt{3} \cdot N} \sum_{k=1}^{N} ((v_{S,k} - v_{T,k}) \cdot i_{R,k} + (v_{T,k} - v_{R,k}) \cdot i_{S,k} + (v_{R,k} - v_{S,k}) \cdot i_{T,k})$$

4) Harmonics

Typically the 50 Hz voltage is superimposed with uneven harmonics of rather low order, such as 3rd (150 Hz), 5th (250 Hz), 7th (350 Hz) etc, but power electronic equipment can introduce harmonics of higher order - and even inter- harmonics are created. However, in all parts of the grid the voltage will be dominated by a clear 50 Hz component and harmonics just account for a minor part - less than 10% of the total signal energy. It is otherwise for the current that can appear in the most peculiar forms.

If the time series covers exactly one period of the fundamental 50 Hz then the frequency resolution in the spectral analysis is also 50 Hz and the output from the VI contains RMS-values at DC, 50 Hz, 100 Hz, 150 Hz,.... up to N/2*50 Hz, where N is the number of samples in the time series.

5) Torque

The torque is represented as a 16-Bit signal for comparison with the derived (virtual) torque. The signal is treated like the other signals by means of simultaneous sample and hold triggering-with shaft rotational power it is a basis for loads during one revolution, which can be analyzed further on harmonics.

6) Seismic accelerometers

Angular accelerometers provide signals for estimation of the rotational influence on the generator during operation. These signals are designated "Adpgbx_?" and Adpgen_? for the gearbox and generator respectively, where ? symbolizes either X, Y, Z coordinate and the result is expressed in Radians.

7) Load spectra :

A statistical description of the torque width is described in a frequency distribution diagram for long term operation with emphasis on start/stop normal operation and shut down sequences.

8) Calibration

Careful calibration is carried out on transducers where accurate performance is expected down to DC-level. In general for AC signals, this is carried out.
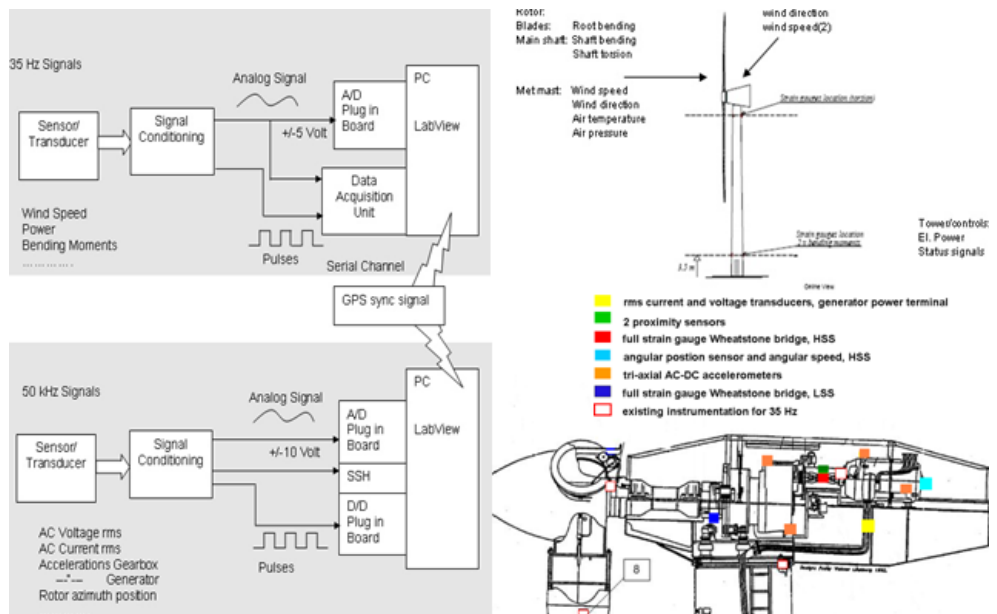
Figure 23 Overview of data acquisition systems for data capture of drivetrain loads
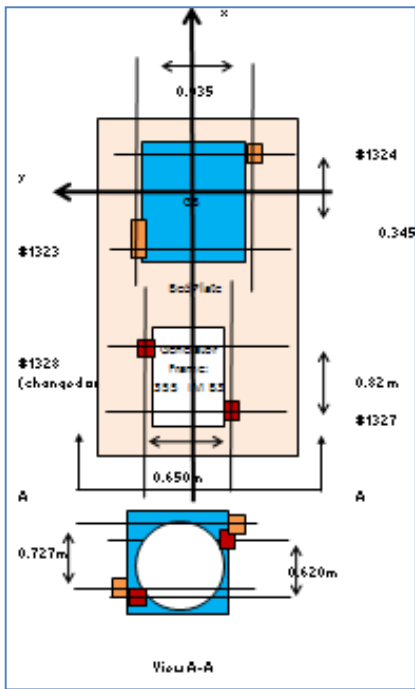
Figure 24: Placement of accelerometers. Gearbox (blue), Generator (white)

In addition to the details for the use of the cardan joint equipped with strain gauges, an analysis of the structure for alternative placement of strain gauge foils was conducted. This exercise should show placements which are more tolerant to external impacts harming the strain gauge signal. The area of interest is shown in
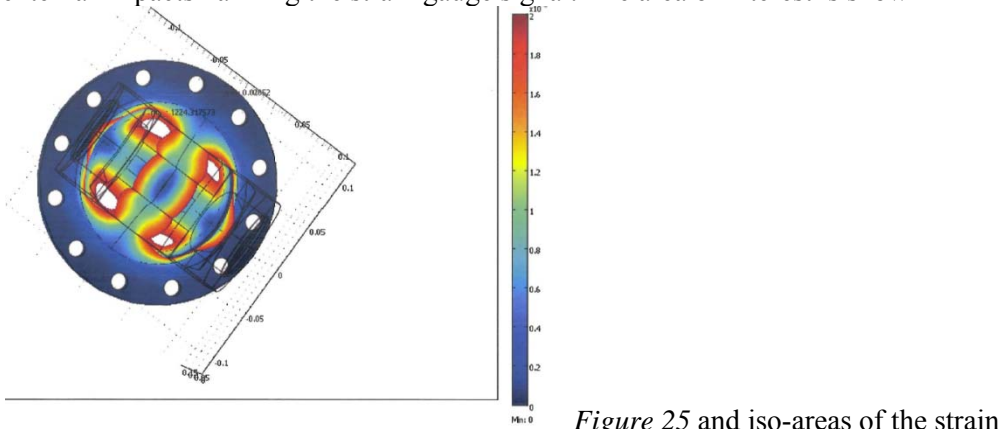
Figure 25 and iso-areas of the strain level is show (red most significant). A strain gauge installation in a shear bridge constellation would provide a signal which is protected by the curved area above the gauges, and the back plate to be mounted against. Unfortunately, the installation was not completed out.
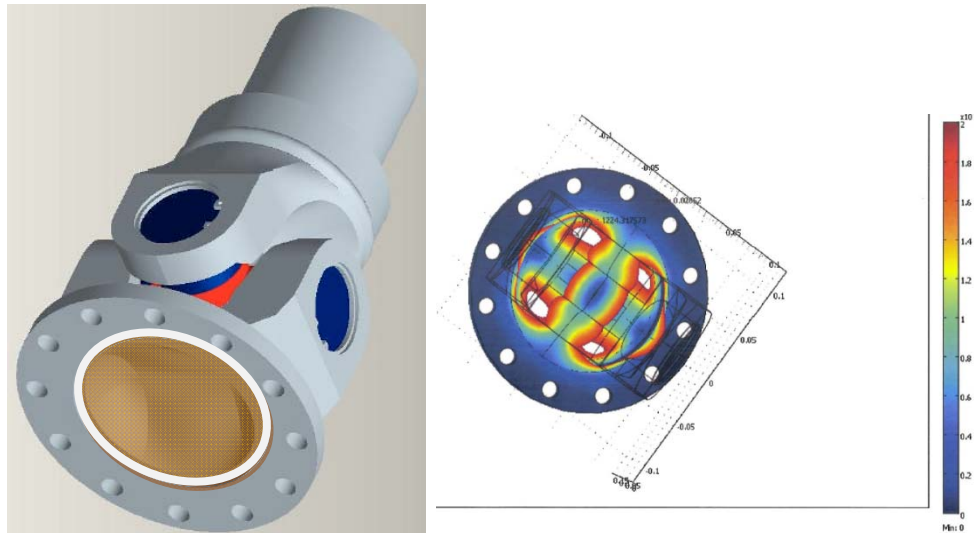
Figure 25: Left: Universal joint details for alternative strain gauge instrumentation in the coloured area. Right: FEM strain analysis result for torsion load input. Red colour: most favourable area for sg placement.

3.3 Calibration and signal overview, extended measurements

The fast sampled data are collected as signals shown in Table 3.

Table 3 Overview of gain and offset factors for fast sampled signals

Ind	P	Description	Gain	Offset	Units
1	Sht_SSP	Torsion_LSS	-625.921	1843.041	kNm
2	Sht_HSP	Torsion_HSS	10.07151	4.079968	kNm
3	Sht_dplX	Trajectory_X	1	0	mm
4	Sht_dplY	Trajectory_Y	1	0	mm
5	GbxF_aX	Gbx_F_aX	1.359693	-3.32934	g
6	GbxF_aY	Gbx_F_aY	1.354114	-3.51149	g
7	GbxF_aZ	Gbx_F_aZ	1.370952	-3.51348	g
8	GbxF_aT	Gbx_F_aT	112.3269	-253.554	Deg C
9	GbxB_aX	Gbx_B_aX	1.355234	-3.46994	g
10	GbxB_aY	Gbx_B_aY	1.367222	-3.55587	g
11	GbxB_aZ	Gbx_B_aZ	1.356521	-3.38384	g
12	GbxB_aT	Gbx_B_aT	112.191	-253.554	Deg C
13	GenF_aX	Gen_F_aX	1.476887	-3.75676	g
14	GenF_aY	Gen_F_aY	1.469983	-4.07053	g
15	GenF_aZ	Gen_F_aZ	1.398425	-3.80344	g
16	GenF_aT	Gen_F_aT	112.2893	-253.636	Deg C
17	GenB_aX	Gen_B_aX	1.363494	-3.44473	g
18	GenB_aY	Gen_B_aY	1.350603	-3.47672	g
19	GenB_aZ	Gen_B_aZ	1.358936	-3.70283	g
20	GenB_aT	Gen_B_aT	112.8482	-253.554	Deg C
21	U1N	Phase Voltage	100	0	V
22	U2N	Phase Voltage	100	0	V
23	U3N	Phase Voltage	100	0	V
24	I1	Phase Current	151.5152	0	A
25	I2	Phase Current	151.5152	0	A

26	I3	Phase Current	151.5152	0	A
27	Sound	SoundPressure	20	0	Pa
28	Dummy1	Dummy	1	0	[-]
29	Rotor_Azi	Angular_position	1	0	Deg
30	Ang_Speed	Angular_speed	1	0	1/s
31	Status	Status	1	0	[-]
32	Dummy2	Dummy	1	0	[-]

Signal 31and 32 are signals which potentially can be used for quality controls. The accelerometers signals 5-20 are as per manufacturer calibration compensated for temperature effects according to a polynomial regression with the coefficients:

GbxF_aX	75.5854	-161.273	135.519	-56.291	11.5866	-0.94666	0	0
GbxF_aY	-108.239	234.53	-202.481	86.6418	-18.334	1.53421	0	0
GbxF_aZ	-2.13418	1.07551	0.022328	-0.04405	0	0	0	0
GbxB_aX	-17.4105	29.3506	-18.0429	4.83354	-0.47934	0	0	0
GbxB_aY	-5.5548	10.8989	-7.62592	2.29182	-0.25191	0	0	0
GbxB_aZ	35.1758	-61.8425	39.3541	-10.8643	1.10662	0	0	0
GenF_aX	-58.0093	133.669	-122.651	55.5524	-12.3818	1.08609	0	0
GenF_aY	-13.4515	24.0517	-15.4437	4.28591	-0.43834	0	0	0
GenF_aZ	-163.588	356.005	-308.287	132.467	-28.2026	2.37817	0	0
GenB_aX	35.171	-60.4864	37.5496	-10.0824	0.995757	0	0	0
GenB_aY	271.406	-566.251	468.724	-192.441	39.2004	-3.17107	0	0
GenB_aZ	-6.77934	10.9055	-6.47273	1.69339	-0.16612	0	0	0

The temperature signals are input to the corrections performed. Derivate signals such as angular displacement[1] is calculated from the appropriate signals, i.e $XXX(d^2x/dt^2 ,F- d^2x/dt^2 ,B)/\frac{1}{2}(x,F-x,B)$, where F means front and B back of the XXX part, gearbox or generator, respectively. As indicated it still needs double integration to provide true inclination.
The reactive power is here concerted into positive values.

3.4 Analysis

The mechanical drive train loads are compared with the virtual torque with the basis of statistical methods and time series analysis methods. Within statistical methods are parametric fit of data, load cycle analysis, peak detection and for frequency analysis processing of load cycle dependent time series. Literature dealing with machine vibration is reviewed for potential use within analysis of higher order frequency dynamics.

The fatigue loads are evaluated using the Rainflow counting method (RFC). The RFC results in a load spectrum with information regarding the number of load cycles with a certain magnitude. The load spectrum was calculated for every 10-minute period. This procedure took place immediately after the end of each 10-minute sampling period (as a background operation) and simultaneously with the sampling of the next data set. The original result is a two dimensional vector consisting of the magnitudes of loads and the number of times these magnitudes appeared during those ten minutes. From these numbers the equivalent load corresponding to an equivalent predefined number of load cycles was calculated.

---

1 Angular displacement signal is here angular acceleration, without double integration

The RFC method is described in detail in Ref. [1] and the fundamental assumption is that the Palmgren-Miner damage rule applies. This rule states that, it is possible to accumulate the fatigue damage experienced by a component with the use of a simple linear method and thus obtain information on the total fatigue damage in a certain time period. The RFC is here performed using 50 range levels between minimum and maximum of the signals and a jitter filter size of one range level After the RFC load spectrum is established for an average of ten-minutes it is converted into an equivalent load range L_{eq} , and an equivalent number of load cycles N_{eq} , which together should have the same damaging effect as the original RFC load spectrum for the time period of the 10 minutes. Thus two numbers Leq and Neq can express the fatigue damage in a ten-minute period finally. N_{eq} has in this case, been selected arbitrarily equal to 600 in order to match one second. With N_{eq} selected as constant all information on the fatigue damage is expressed as L_{eq}, defined as:

$$L_{eq} = \left[\frac{\sum_i R_i^{\,m} \cdot n_i}{N_{eq}} \right]^{1/m}$$

where R_i is the magnitude of the range level (i) and n_i the number of times this range level appeared.

The exponent (1/m) is the slope of the material Wöhler curve and the summation is carried out over the total number of ranges (i=50) in the Rainflow spectrum. L_{eq} is in the present case calculated for m=12 for strain gauges on the blades, m=8 for strain gauges on the shaft and m=4 for strain gauges on the tower.

The method has been performed on 35 Hz sampled data sets.

3.5 Selection of data

While the 35 hz data acquisition system runs on an automatic mode, regular data collections are provided. The 50 kHz data acquisition system has been operated manually and some preferred statistics have been made at particular high wind speeds. The data presented here are chosen with filtering and test conditions as follows:

- The measurement period is: January 5. to February 18 2011

- All westerly wind direction sectors within the measurement period, i.e. between 180° to 360°.

- Run duration equal to 600 sec. For 50 kHz measurements the run duration is 10 sec initiated every minute within the above 600 seconds or for every 10 minutes. Therefore there is no full coverage of 50 kHz and 35 Hz data possible.

- Wind turbine available (production=1)

- No failure on the test equipment, except for the met mast signals

- No turbulence selection/specification

- No fault, maintenance or manual shut down on the wind turbine(failfree=0)

- No still stand data

4 Design tools

4.1 General

The purpose of the planned analyses is to study the interaction between the mechanical system and the electric system of a wind turbine, to provide a better understanding of the mutual influence of those systems on the design. It has been common practice to analyse and design those systems independently, but lately studies have indicated that the dynamic coupling between the mechanical and electrical systems interferes more than it is expected in the design of wind turbines.

Aeroelastic codes like HAWC [18] or Flex are applied to simulate the structural design loads on a wind turbine. It is common practice to use very simple, steady state models of the wind turbine generator systems to define the link to the grid in these codes. HAWC2 is nowadays used instead of HAWC. The chapter highlights initial plans and providing a survey on how to conduct analyses, but the extent of analyses had to be reduced due to practical limitations.

4.2 Aeroelastic design – HAWC

The aero elastic simulation tool HAWC (*Horizontal Axis Wind turbine simulation Code*) is a code designed for calculating wind turbine response in time domain. It has been developed at the aeroelastic design research programme in the Wind Energy Department of the Risø National Laboratory.

Larsen et. al. [21] extended the HAWC code with generator dynamics including stator as well as rotor flux transients. The new code can also simulate with the traditional steady state generator model, and with rotor flux transients only. Larsen's simulations with the complete structural model combined with full generator dynamics of a SCIG indicate that there is a risk for coupling between the generator eigenfrequency and structural modes of the wind turbine. Thus, it is confirmed that generator dynamics can be essential, even in normal operation of the wind turbine, assuming an ideal power system with constant grid voltage on the generator terminals.

Currently, a new version of HAWC, namely HAWC2 has been developed. The new HAWC2 code is based on a multibody formulation where the turbine is subdivided into to a number of bodies interconnected by constraint equations. Within a body the calculations are linear, which is valid as long as deflections and rotations are small, whereas large deflections and rotations are accounted for through the coupling of bodies. Using too few bodies will therefore result in a reduction of non-linear problems into a linear.

The coordinate system used in HAWC2 is shown in Figure 26.
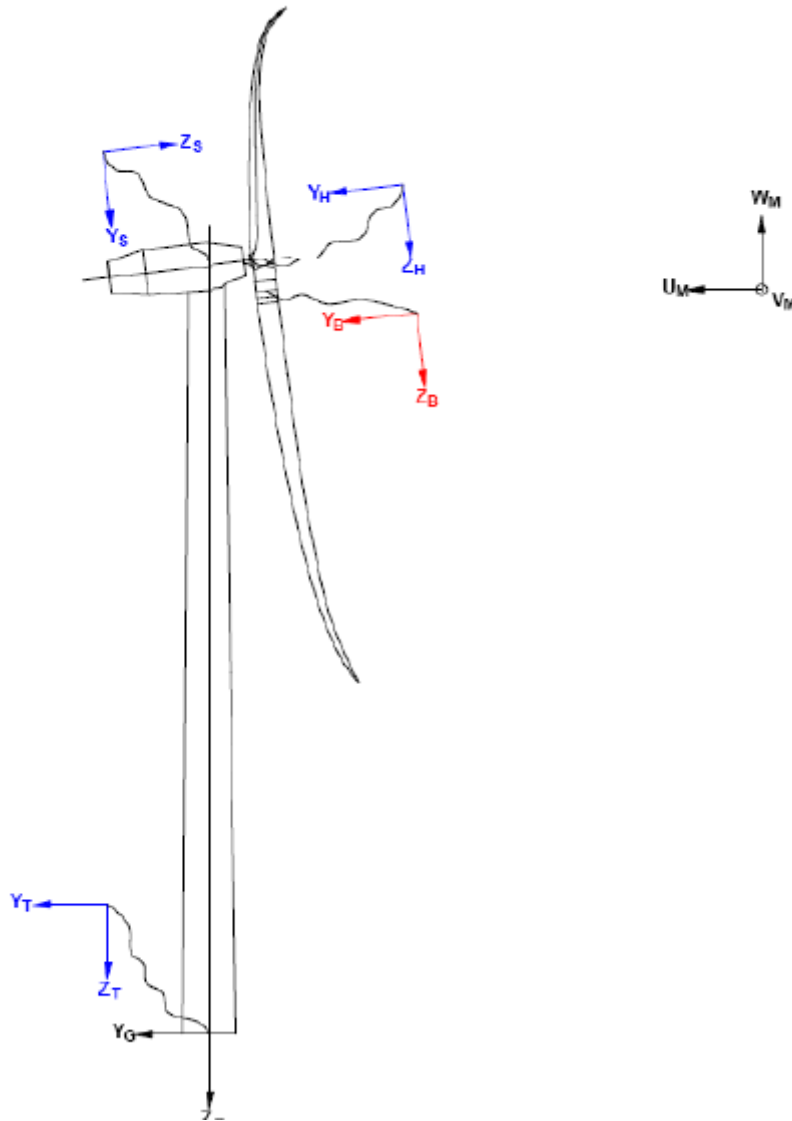
Figure 26 Illustration of coordinate system as result of user input[18]. There are two coordinate systems in black which are the default coordinate systems of global reference and default wind direction. The blue coordinate systems are main body coordinate systems attached to node 1 of the substructure, the orientation of these are fully determined by the user. The red coordinate systems are also defined by the user, but in order to make the linkage between aerodynamic forces and structure work these have to have the z from root to tip, x in chordwise direction and y towards the suction side.

The main parts of HAWC2 are the structural part, the external loading part, and the control part. The structural model of HAWC2 is based on flexible multibody dynamics. The wind turbine structure is modelled by a number of bodies, e.g. a tower or a blade, and these bodies are then connected by a set of constraint equations. Normally, the tower and shaft are modelled by a single body each, while the blades are divided into several bodies in order to capture geometric non-linear effects. Further, all inertia forces and external loading are based on the deformed shape of the structure.

The aerodynamic part is based on the blade element momentum (BEM) principle with input data from 2D lift, drag and moment table values. The aerodynamic calculation points on the blades are positioned independently of the structural

node/element discretization to provide an optimal distribution of these points, which normally differs from the optimal structural discretization. The spacing between aerodynamic calculation points are closest at the tip and root where the largest aerodynamic force gradients normally occur. The BEM method used for calculation of the induced velocities is modified to handle dynamic inflow, large yaw errors and dynamic stall effects. Since the code is especially intended to handle large deflections also influences in the BEM due to large deflections e.g. reduction in the effective rotor area is considered.

In HAWC2 the electrical components (generator) and the control are implemented as external DLL (*Dynamic Link Library*) [22]. Thus, the induction generator coupled to a fixed speed wind turbine will be implemented as a DLL, as presented in Figure 27.
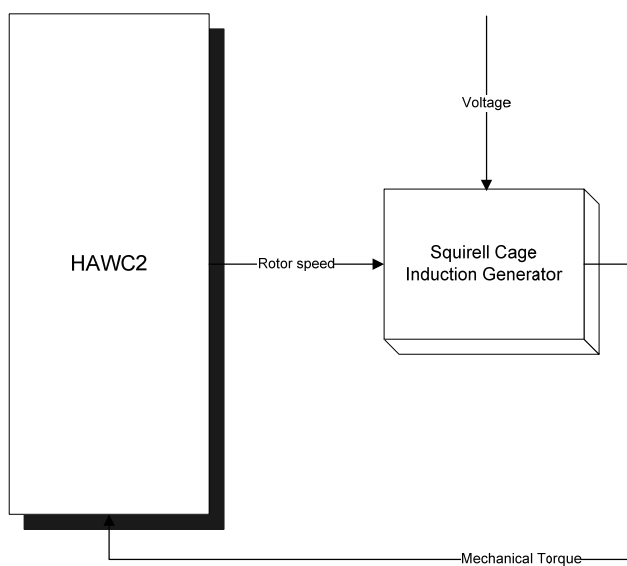
Figure 27 Fixed speed wind turbine with SCIG block diagram

Cutululis[23] extended HAWC2 with SCIG dynamics including the rotor flux transients only. The simulations conducted so far aimed at validating the SCIG model and its operation with the complete structural model of the wind turbine.

4.3   Electric design - Power Factory

In studies of power system stability and power quality, wind turbines and other generators are normally represented by the dynamics of the rotating system, i.e. the drive train.

The simplest representation of the drive train is by a lumped inertia, representing the wind turbine rotor, hub, shaft, gearbox and generator inertias as it appears from the generator shaft if this structure was stiff and the gearbox was ideal. Akhmatov [24] showed that the shaft flexibility of wind turbines has a significant influence in dynamic power system stability studies with wind power.

The most commonly used mechanical model for wind turbine drive trains in power system studies is the two-mass model shown in Figure 28. It lumps the inertias on the generator on one side and on wind turbine rotor on the other side. Between those two inertias, the flexibility is represented by stiffness and damper. The gear box is assumed ideal.
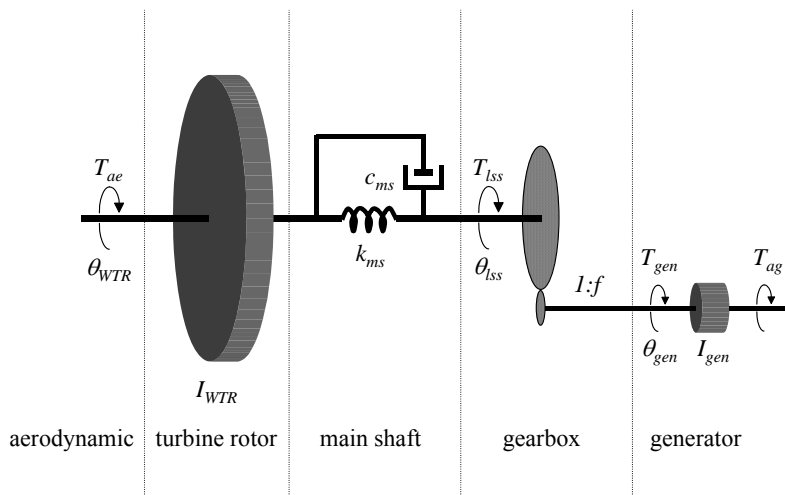
Figure 28: Two mass model of wind turbine drive train.

A significant advantage of the two-mass model is that the stiffness and damping parameters can be estimated by a torque measurement on the shaft. Normally, the inertias are known relatively well from the component data, but the stiffness and damping can vary significantly from values obtained by calculations based on data for material. The torque is measured right after the generator is disconnected from the grid. In that case, the torque will start oscillating because the generator air gab torque T_{ag} becomes zero, and the generator inertia I_{gen} can oscillate freely over spring and damper with the rotor inertia I_{WTR}. Then the stiffness is given by the frequency of the measured torque oscillation and the damping is given by the logarithmic decrement from one oscillation period to the next.

Sørensen et.al.[25] have used the two-mass model to simulate power output fluctuations from a wind turbine during normal operation. This model was implemented in Power Factory, and included the dynamics of the generator corresponding to rotor flux transients, which is the standard in power system stability studies. Comparisons of simulations to measurements showed a distinct fluctuation around 5 Hz on the simulations, which was not present in the simulations.

The 5 Hz component corresponds to the generator frequency described by Thiringer [26]. It surprised in the first place that this frequency did not appear in the Power Factory simulations, because the generator dynamic is represented in Power Factory's standard model for the induction generator. The correct representation of the generator dynamics in Power Factory has also been confirmed by simulations of transients by Sørensen et.al. [27], where the response to short circuits in the grid has been simulated. When the voltage returns after a short circuit is cleared, the generator oscillates with 5 Hz corresponding to the generator frequency, see Figure 29.
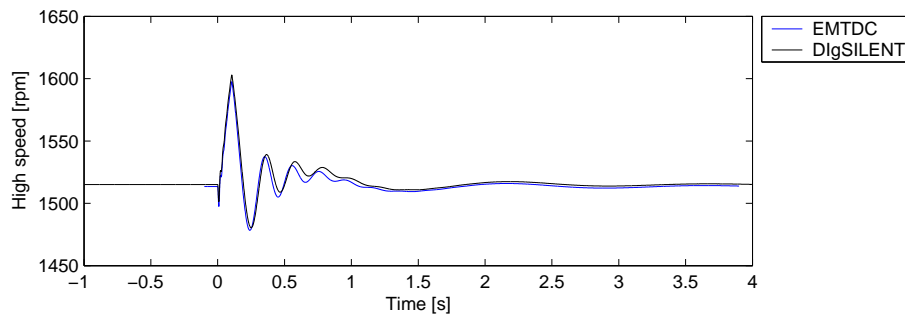
Figure 29: Generator rotor speed response to a short circuit from t=0 tot t=0.1 s.

The reason why the generator frequency then does not appear in the simulations of normal operation, i.e. without grid disturbances, is still not clear. However, HAWC simulations indicate that it could be due to the dynamic interaction with the remaining wind turbine structure, particularly the tower. This interaction is not included in the Power Factory simulations, since it is assumed that the generator stator is fixed.

We will limit the analysis to study the angular deflection of the generator in connection with tower deformation.

4.4 Analyses

The analysis will be based on the measurements on the 500 kW Nordtank wind turbine. Since the scope is to analyse the impact of electrical system on structural design as well as the impact of structural system on electrical design, the analysis will be performed in HAWC2 with a simplified gearbox model.

The planned analyses will require models for the structural components as well as the electrical (read generator) in the Nordtank wind turbines. The models are not available in HAWC2.

HAWC2 simulations was initially planned to be performed with three different assumptions:

1. The traditional structural design approach: a detailed representation of the structural flexibility combined with a simple steady state model of the generator.
2. The extended structural design approach: a detailed representation of the structural flexibility combined with a standard dynamic model of the generator representing the rotor flux transients.
3. The equivalent electric design approach: a stiff structure combined with the standard dynamic model of the generator representing the rotor flux transients.

This selection corresponded to the studies done by Larsen et.al. [20], but in the planned analyses, only the 1st simulation assumption will be derived and compared to measurements. A paper on the turbine drive train simulation [30] will be consulted to illustrate on the inner gear dynamics in the drive train.

The model will be extended to include tower top rotation as well. The comparison of the simulations will mainly be done on power spectral densities,
 i.e. statistically in the frequency domain, because different time series are expected in measurements, HAWC2 and Power Factory due to the stochastic wind input. Thus it will be possible to compare aeroelastic design simulations and electric design simulations to each other and to measurements. In the time domain, it will also be

possible to compare the three HAWC2 simulations to each other and the two Power Factory simulations to each other, because the same random seeds will be used. We have been limited to rather rudimentary approach with modelling the turbine in HAWC2 code and providing just a few results.

4.4.1   Aero elastic results, previous work

A collection of data [29], which are necessary for numerical calculations on the NTK500 wind turbine, gives a summary of modal information as shown in Table 4 and compared with calculated modal frequencies[30]. The calculations are based on input from a 600 kW wind turbine rather than the present 500 kW wind turbine. In addition the drive train is consisting of a more components modelled more complex than normal.

The gearbox consists in this case of the drivetrain as shown in Figure 30. In this model the main components in the drive train was modelled using a lumped spring/mass approach coupled to a 2D spring mass model of the planetary stage. The tooth contact in the planetary stage illustrated in Figure 31 is modelled using linear springs for the tooth flexibility and lumped inertia for the wheel bodies.
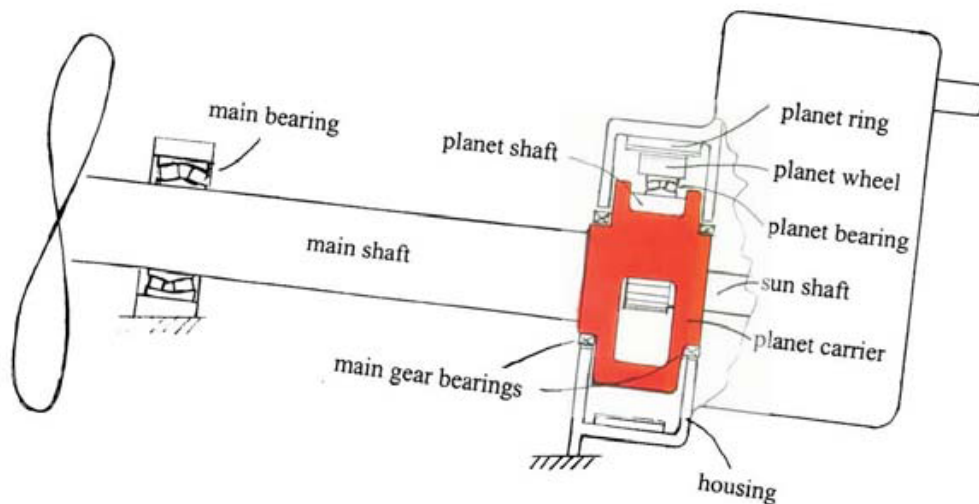
*Figure 30 Drivetrain model of 600 kW turbine used in the modelling [29]. The present 500 kW turbine has **two** main bearings in front of the gearbox. They are connected with the gearbox(see Figure 5).*
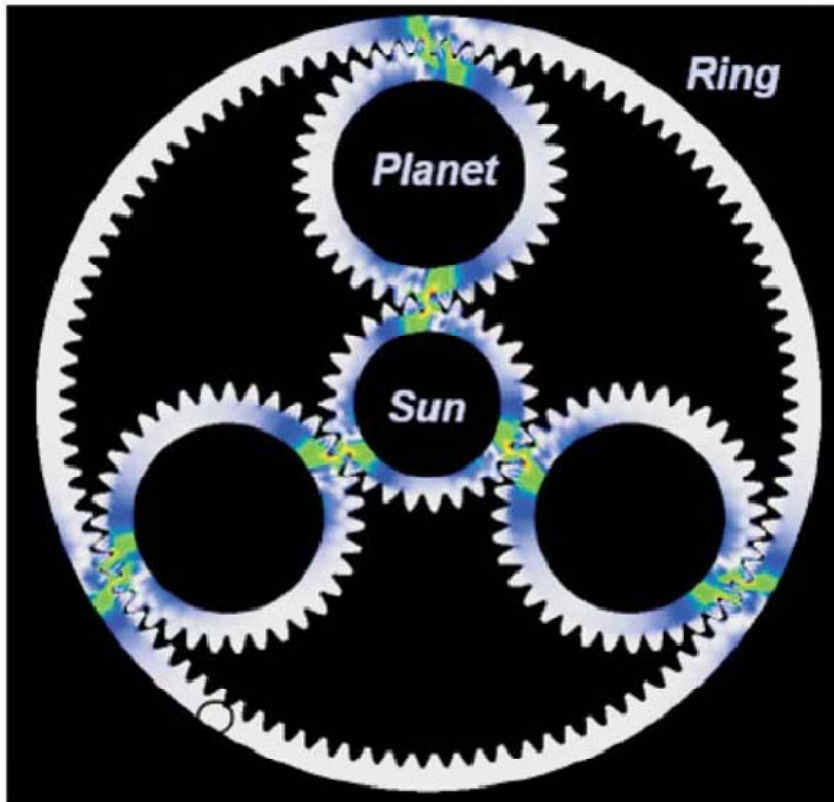
Figure 31 Sectional view of a planetary gear stage

Table 4Modal frequencies and damping extracted from standstill measurements [29], and from calculations on a 600 kW wind turbine [30]

Mode	Frequency [Hz]	Damping ratio [%] Structural + some aerodynamical	Frequency [Hz]
1. lateral tower bending	0.75	0.9	0.76
1. longitudinal tower bending	0.79	1.6	0.80
1. fixed-free drivetrain torsion	0.94	1.4	0.94
1. yawing flapwise rotor bending	1.31	4.9	1.31
1. tilting flapwise rotor bending	1.38	3.7	1.38
1. symmetric flapwise rotor bending	1.71	2.9	1.71
1. horizontal edgewise rotor bending	2.81	0.4	2.81
1. vertical edgewise rotor bending	2.90	0.4	2.90

An eigenvalue analysis of the models have been carried out and the natural frequencies and mode shapes have been determined [16]. The input data to the drive train model is linearized stiffness data around the static load situation, which is mainly nominal driving torque and gravity load. The frequencies are given in Table 5.

Table 5 Natural frequencies of the planetary stage

no.	Mode shape	Frequency [Hz]	Damping [log. decr. %]
1	Shaft and gear lateral	9.7	15.02
2	Shaft and gear vertical	18.4	7.93
3	Shaft and gear lateral, opposite	57.7	2.53
4	All rotation	79.4	0.006
5	Shaft and gear vertical, opposite	85.1	1.71
6	Planets translation, sun rotation	325.3	4.48
7	Planets, sun and carrier translation	326.6	0.43
8	Planets and sun translation	382.9	0.38
9	Planets translation	601.1	0.24
10	Planets and sun translation	718.0	0.23
11	Planets translation	1018.9	0.24
12	Planets and sun translation	1129.4	0.19
13	Planets and sun translation	1136.1	0.18
14	Planets and sun rotation	1259.8	0.09
15	Planets and sun translation	1813.9	0.08
16	Planets and sun translation	1828.9	0.08
17	Planets rotation	1966.3	0.05
18	Planets and sun translation	2497.3	0.06
19	Planets and sun translation	2524.9	0.06
20	Planets and sun rotation	2876.0	0.07

5   Results

5.1   Aero elastic results, with simplified gearbox simulations

The wind turbine has been modelled with a simple gearbox for studies mostly accurate in the 0-20 Hz frequency domain. For this configuration the signals calculated are listed in *Figure 32* .

Figure 32: Channel List for calculated signals in HAWC2.

5.1.1 Statistics

The calculations presented in the following figures are statistics of a single seed from simulating the turbine at uniform wind and 10 % turbulence intensity with wind speeds between 4 and 12 m/s. Ideally the calculation are carried out with more seeds and at different turbulence with a more realistic wind shear for the complete wind range from below cut-in (approximately 3 m/s) to stop wind speed (25 m/s).
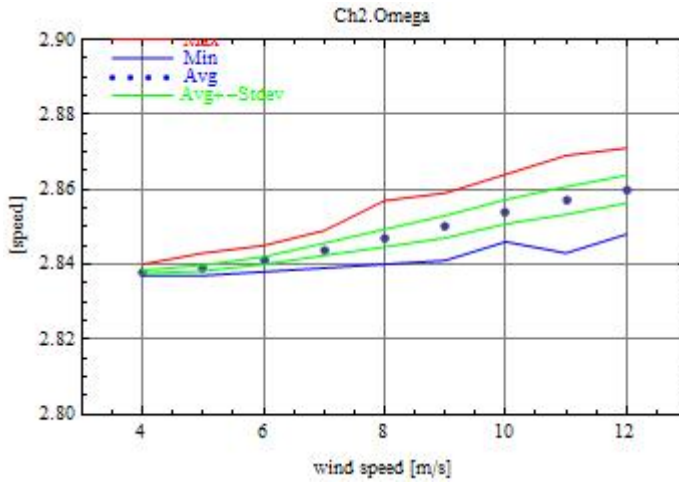
Figure 33 Calculated rotor main shaft speed vs wind speed
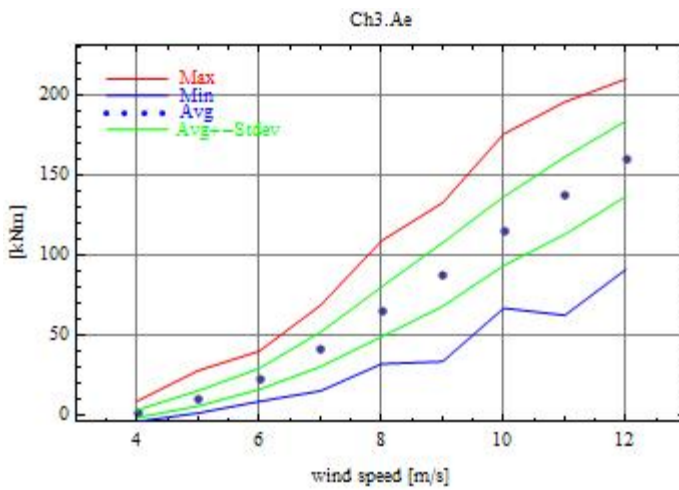
Figure 34Calculated rotor main shaft torque vs wind speed
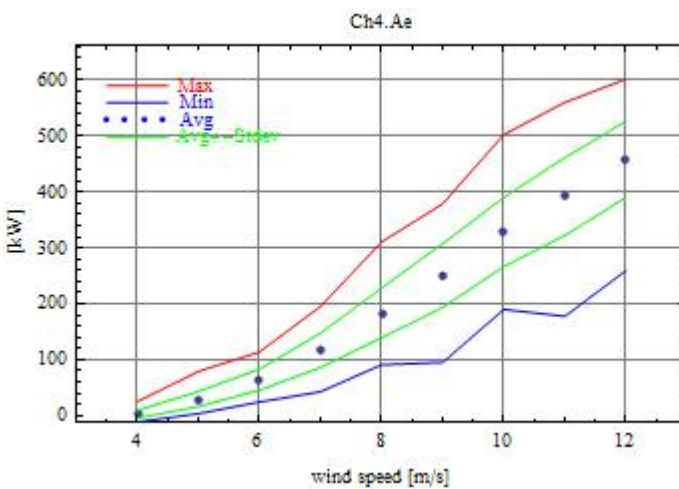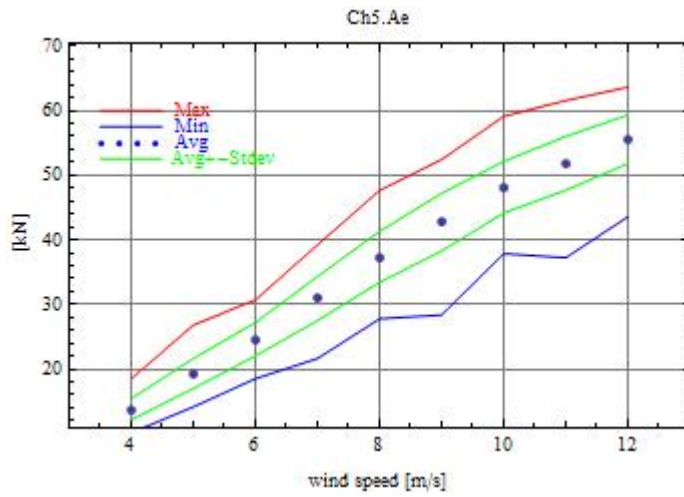
Figure 35 Calculated thrust vs wind speed
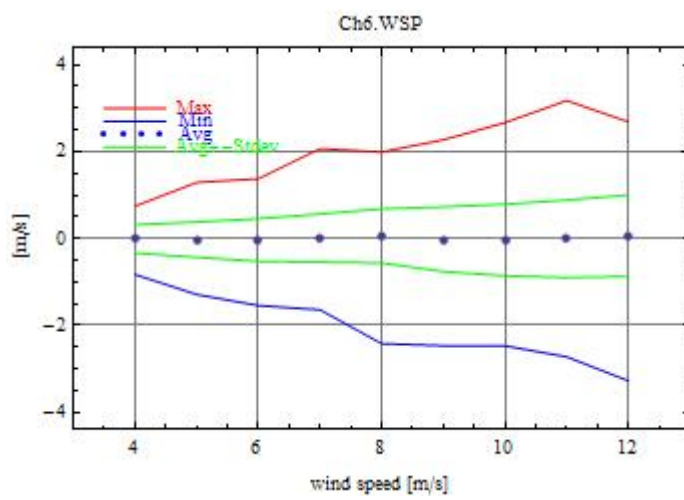
Figure 36 Calculated wind speed vx vs wind speed
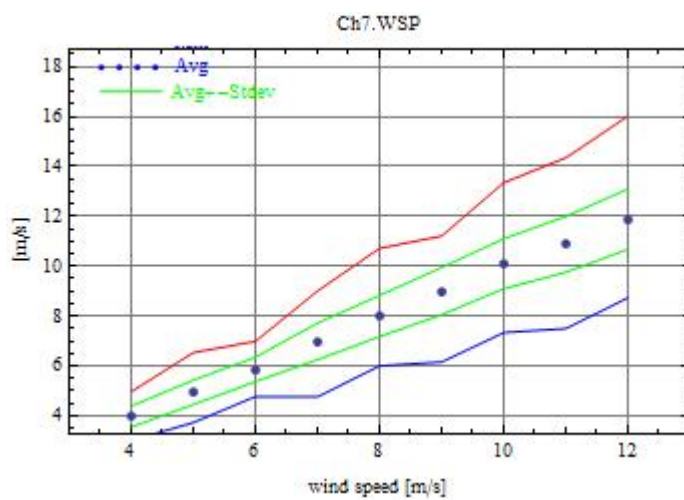
Figure 37 Calculated wind speed vy vs wind speed
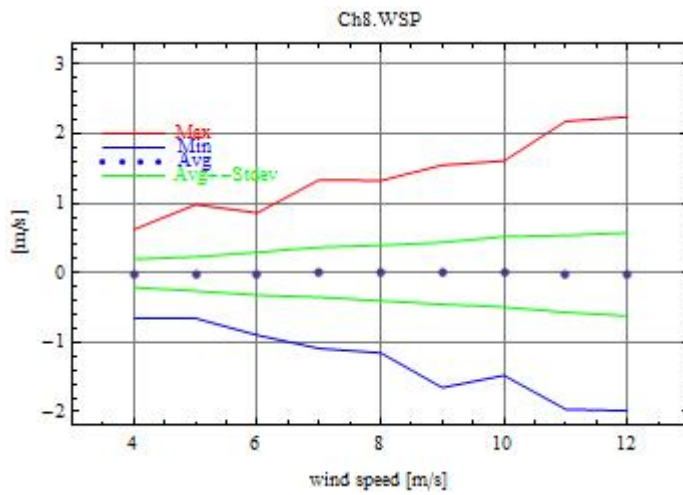
Figure 38 Calculated wind speed vz vs wind speed
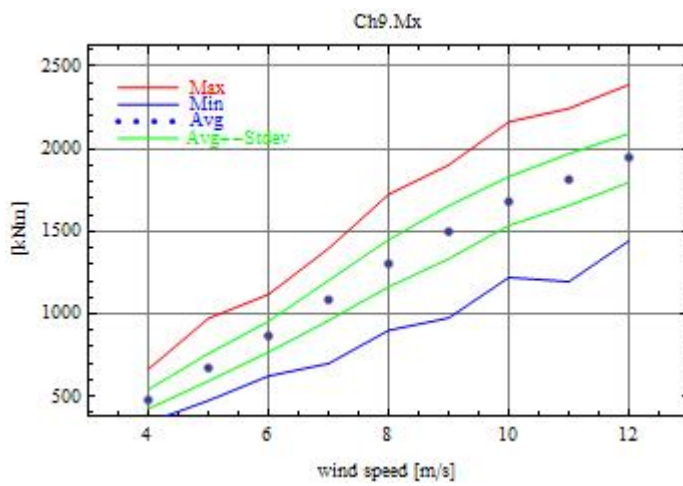
Figure 39 Calculated Mx, tower bottom vs wind speed
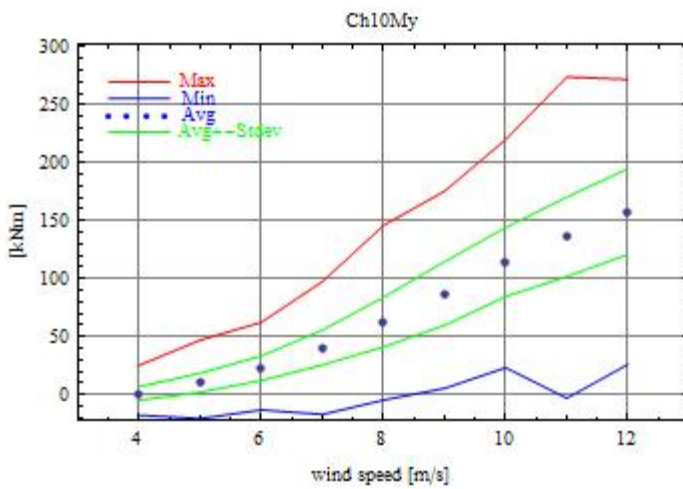
Figure 40 Calculated My, tower bottom vs wind speed

Risø-R-1782(EN)
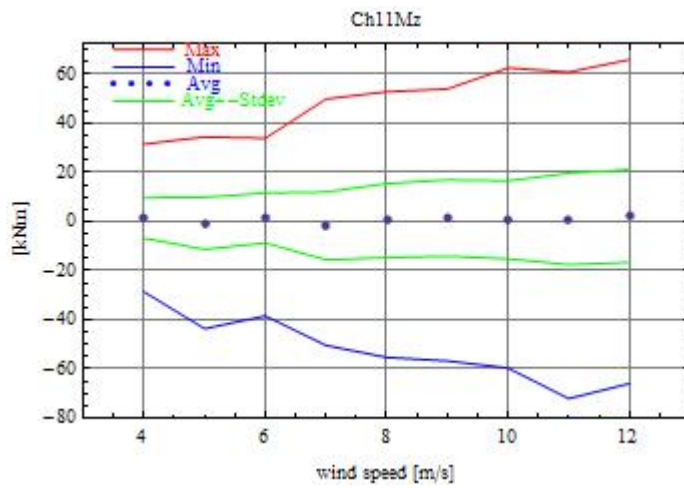
Figure 41 Calculated Mz, tower bottom vs wind speed
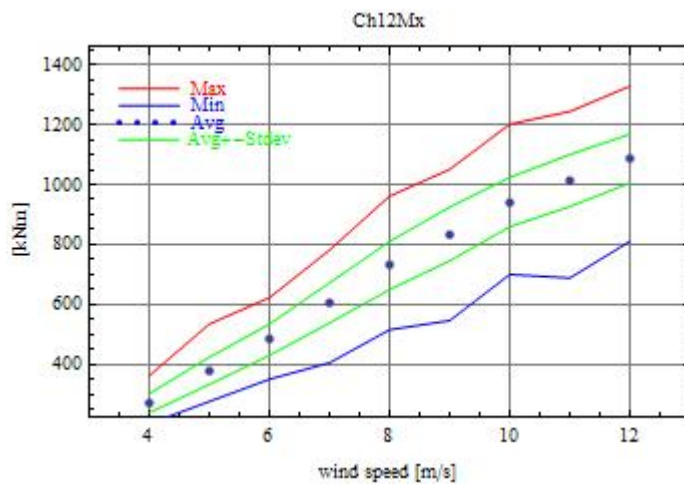
Figure 42 Calculated Mx, tower mid vs wind speed
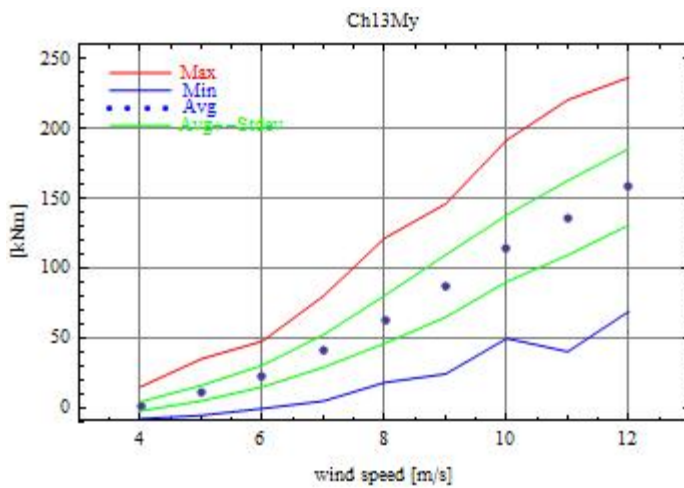
Figure 43 Calculated My, tower mid vs wind speed
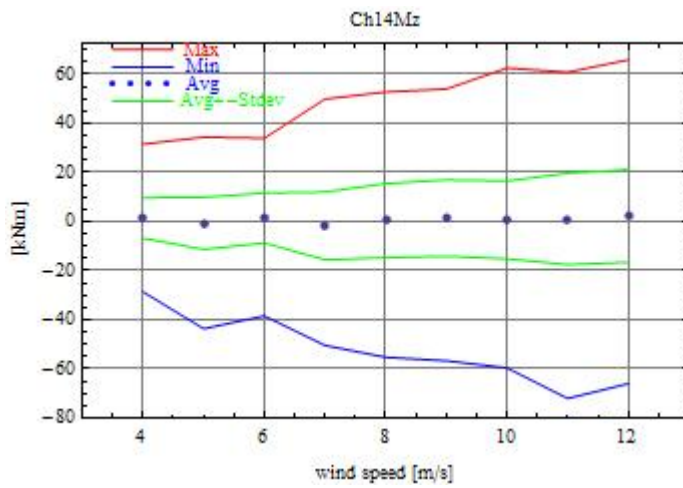
Figure 44 Calculated Mz, tower mid vs wind speed
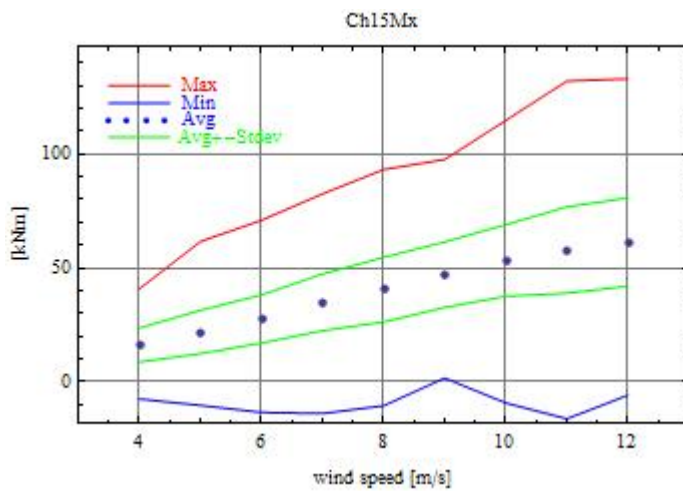
Figure 45 Calculated Mx, tower top vs wind speed
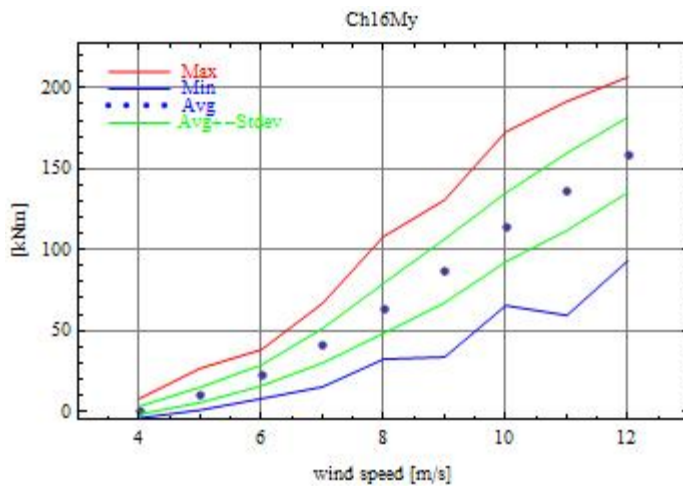
Figure 46 Calculated My, tower top vs wind speed
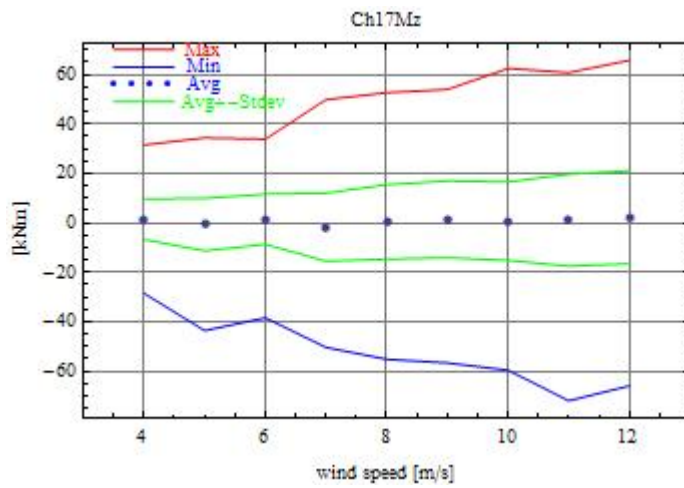
Figure 47 Calculated Mz, tower top vs wind speed
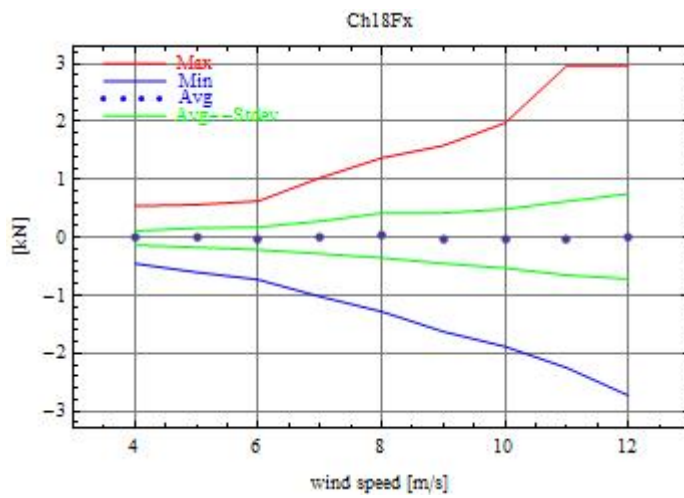
Figure 48 Calculated force Fx, tower top vs wind speed
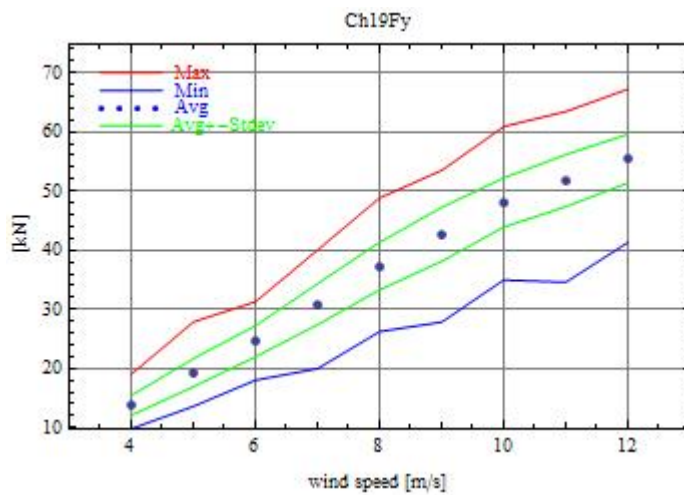
Figure 49 Calculated force Fy, tower top vs wind speed
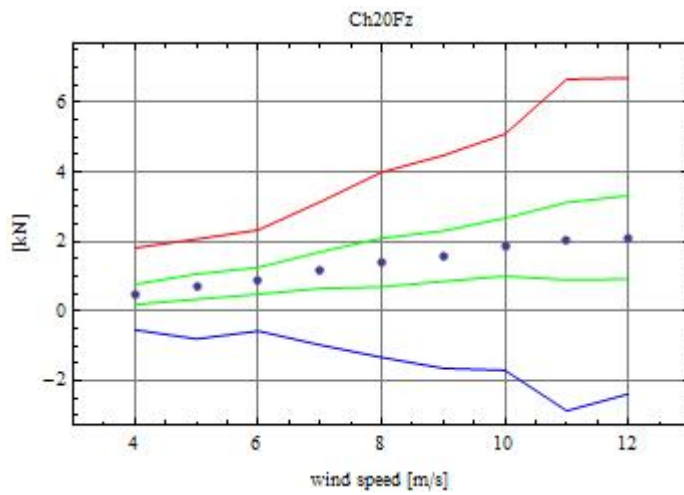
Figure 50 Calculated force Fz, tower top vs wind speed
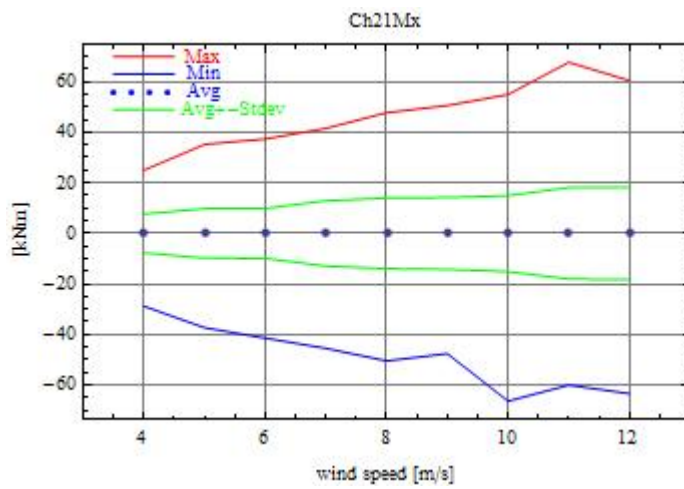
Figure 51 Calculated rotor main shaft moment Mx vs wind speed
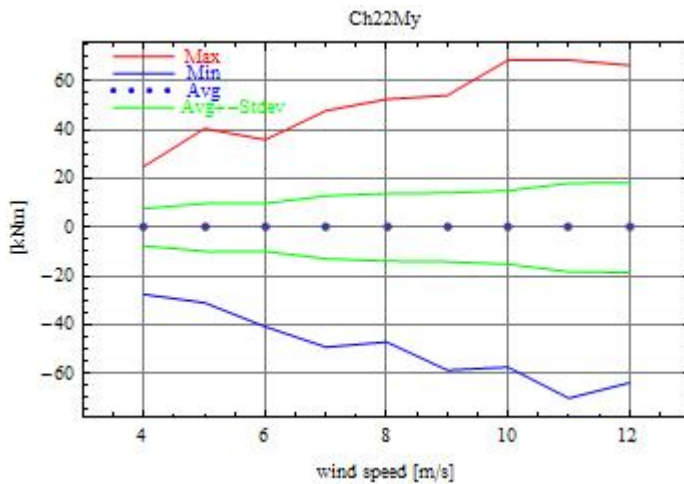
Figure 52 Calculated rotor main shaft moment My vs wind speed
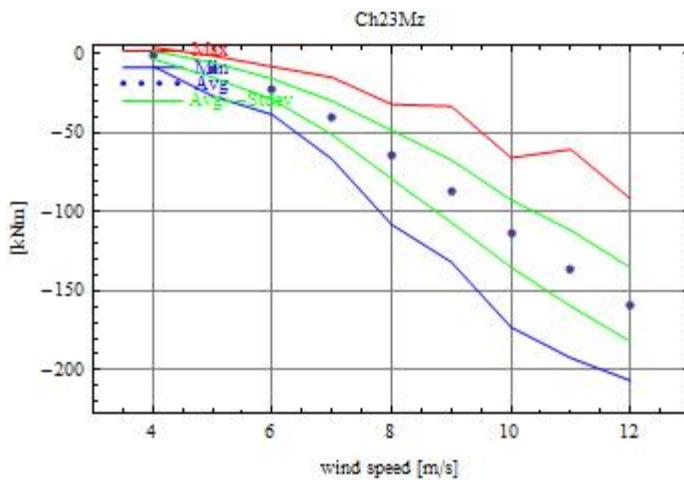
Figure 53 Calculated rotor main shaft moment Mz vs wind speed
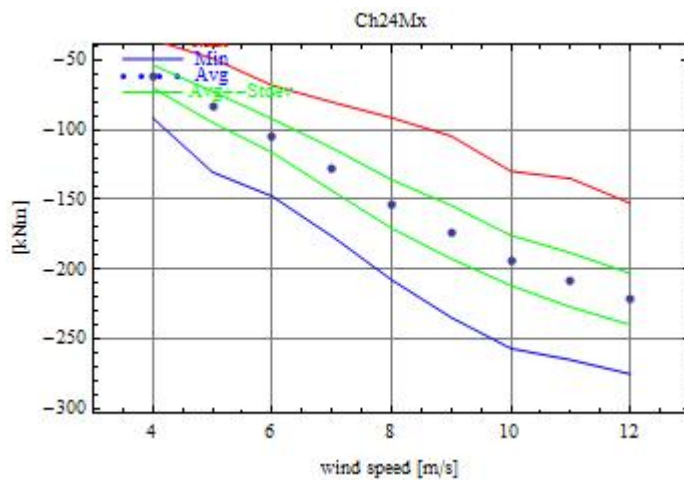
Figure 54 Calculated rotor blade 1 moment Mx vs wind speed
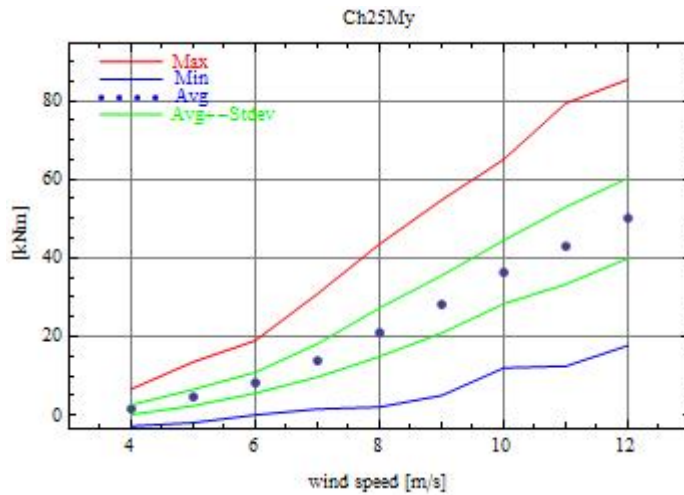
Figure 55 Calculated rotor blade 1 moment My vs wind speed
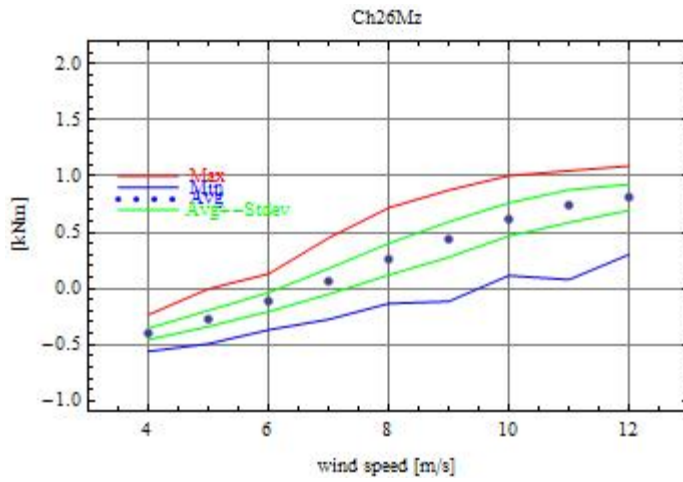
Figure 56 Calculated rotor blade 1 moment Mz vs wind speed
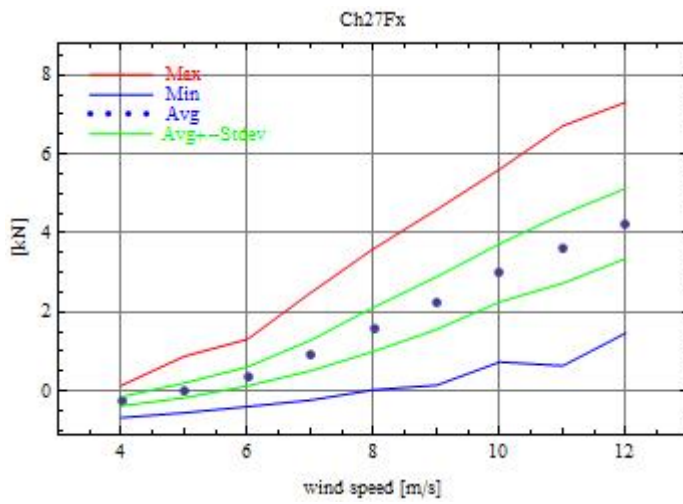
Figure 57 Calculated rotor blade 1 force Fx vs wind speed
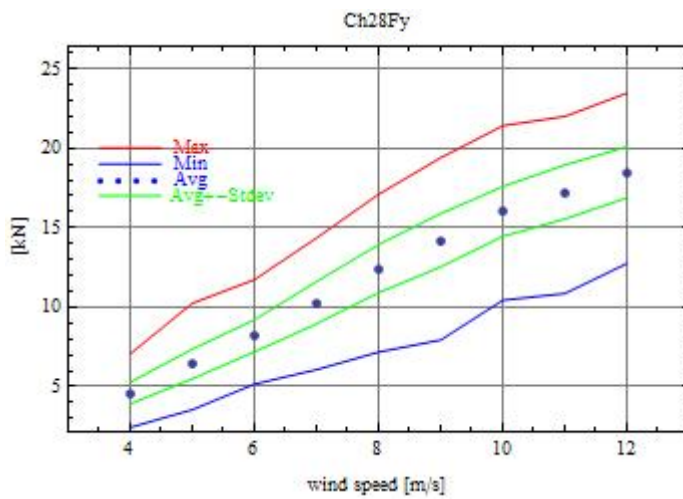
Figure 58 Calculated rotor blade 1 force Fy vs wind speed
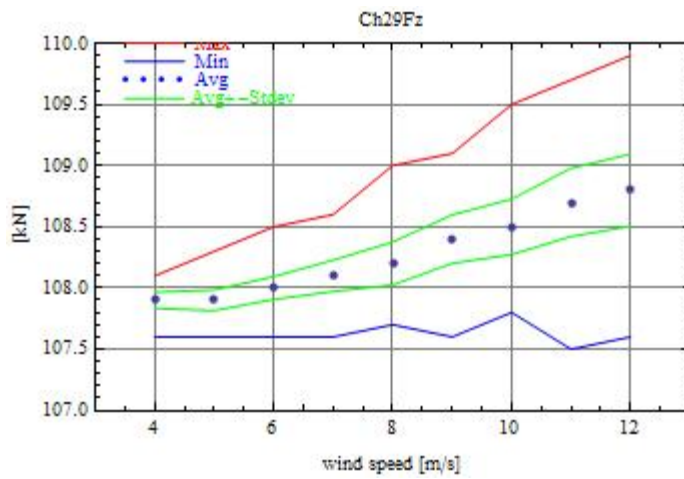
Figure 59 Calculated rotor blade 1 force Fz vs wind speed
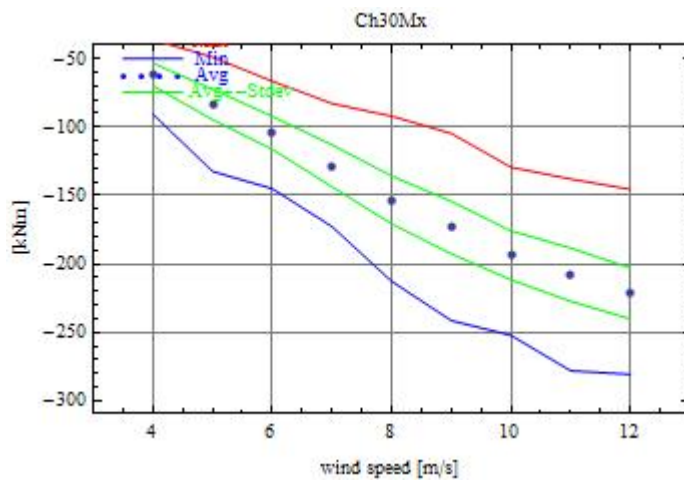
Figure 60 Calculated rotor blade 2 moment Mx vs wind speed
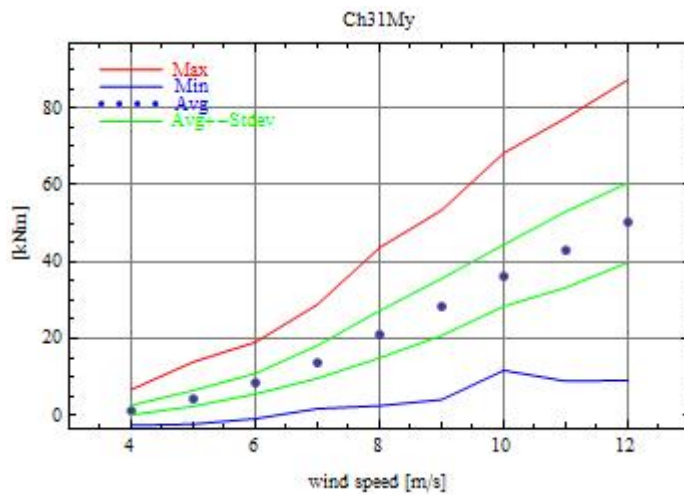
Figure 61 Calculated rotor blade 2 moment My vs wind speed
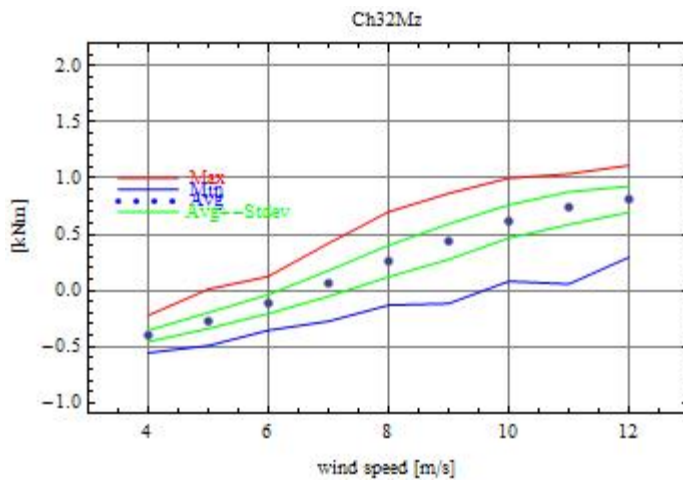
Figure 62 Calculated rotor blade 2 moment Mz vs wind speed
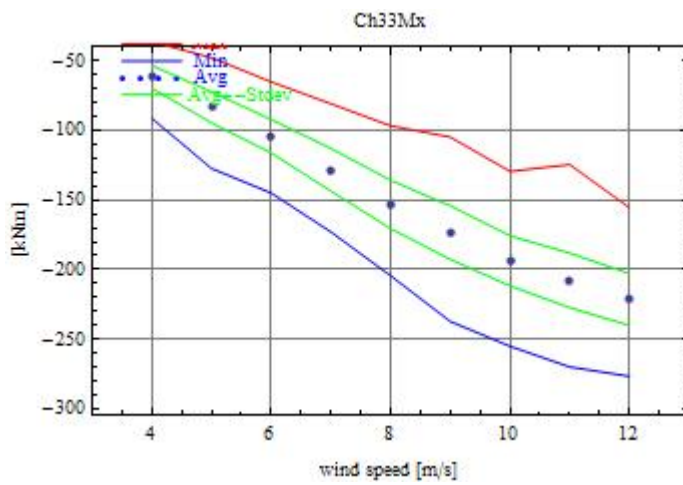
Figure 63 Calculated rotor blade 3 moment Mx vs wind speed
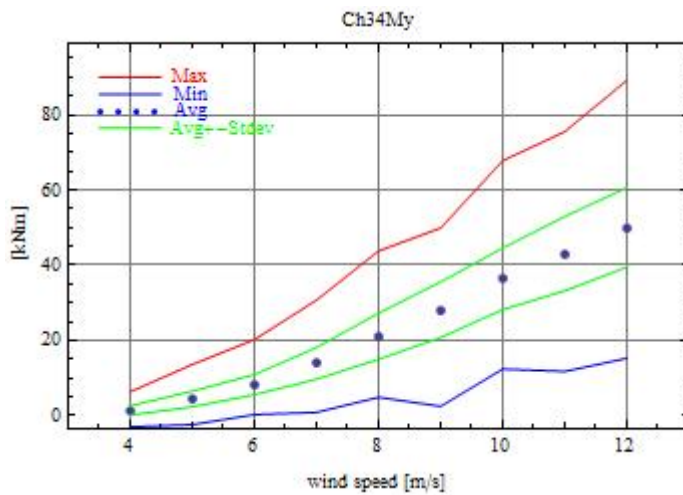
Figure 64 Calculated rotor blade 3 moment My vs wind speed
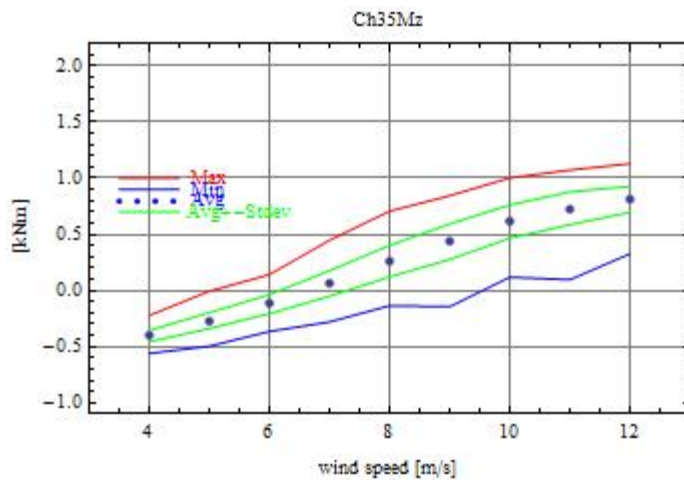
Figure 65 Calculated rotor blade 3 moment Mz vs wind speed
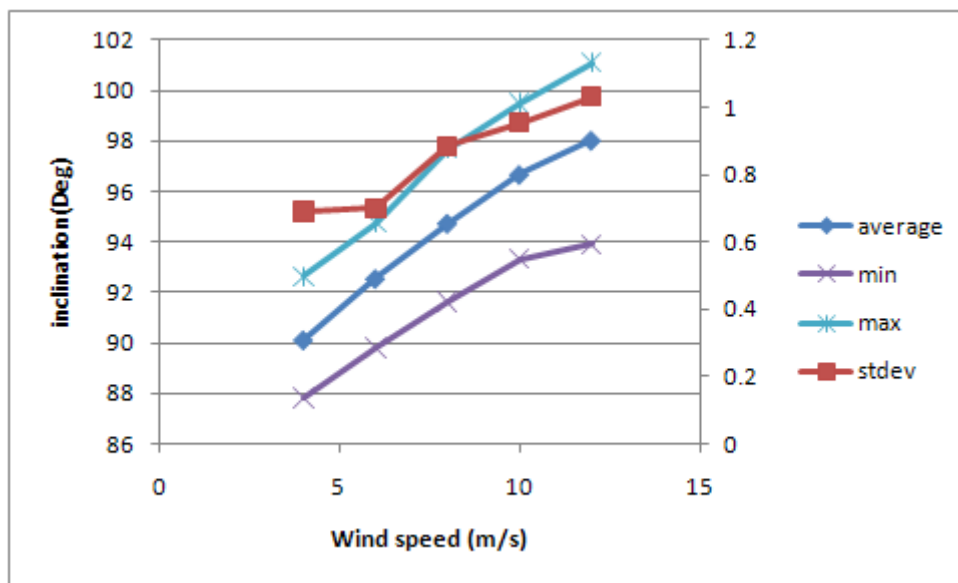
Figure 66 Calculated statistics of tower top inclination

Although not shown here, the standard deviation of the acceleration signal at the tower top is increasing with the wind. The setup for the simulations contains the calculated deflections at the tower top position, and the calculated inclination of the tower with respect to the tower centre line is computed for steps of 2 m/s and the result is shown in Figure 66. From the plots it is plausible, that a normalisation of force with a mass, and a following double integration will reflect a deflection which also is increasing standard deviation with wind speed, as indicated by simulation. An argument similar can be concluded on the vertical force component, and these two legs form an angle which is correlated with the rotational deflection of the tower top. In this way the standard deviation of this derived sensor is increasing with wind speed, as shown in Figure 66. It is however shown in the measurements chapter 5.2.1, that the acceleration at the generator housing increases with wind speed.
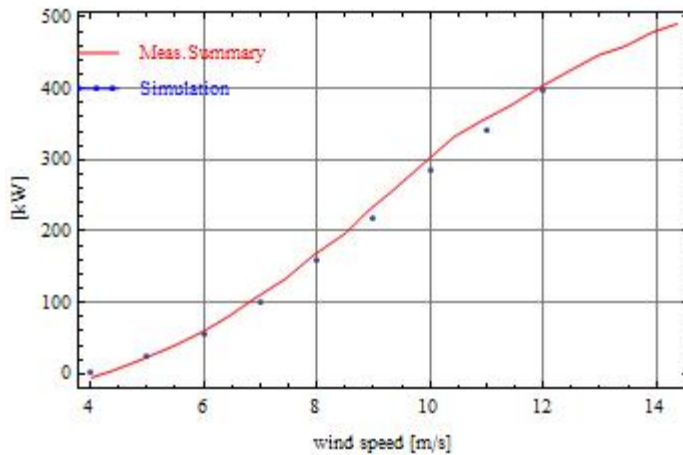
Figure 67 Comparison of calculated and measured power curve

A comparison of the calculated power curve against the measured, 'official' power curve form the measurement summary is shown in Figure 67. In the plot it is assumed to transform mechanical rotor power into electrical power with an efficiency of 87%.

The results of statistics of selected parameters agree qualitatively with the measurements in a 4-12 m/s wind speed range. However, the power performance is not calculated for stall, and a comparison of calculated and measured power curve show minor differences. A fit of calculated power data seems to over-power for wind speeds higher than 12 m/s.

5.1.2 Dynamics

Selected signals are shown in this chapter, with dynamics typically ranging up to 10 Hz. Figure 68 shows the spectral components of the tower force signal. For the electrical power, the most clear frequency components are derived from the rotational speed signal. The electrical power is clearly influenced by the 3P dominance at 1.37 Hz, and their harmonics at 2.7 Hz, 4, and 6.5 Hz.
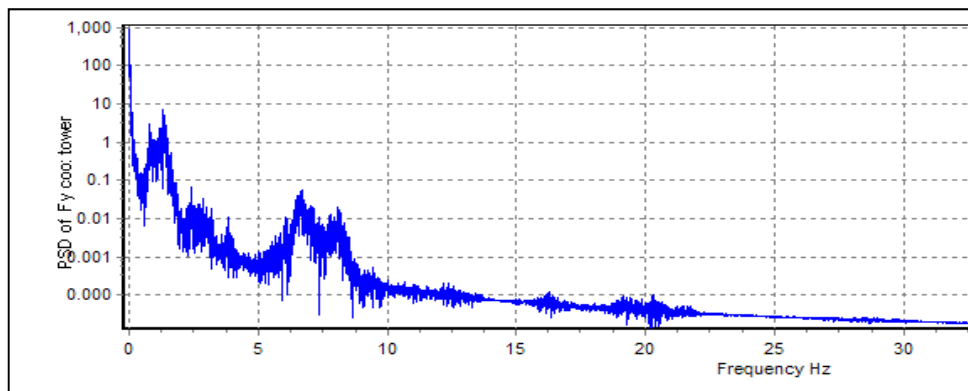
Figure 68 PSD of tower force Fy
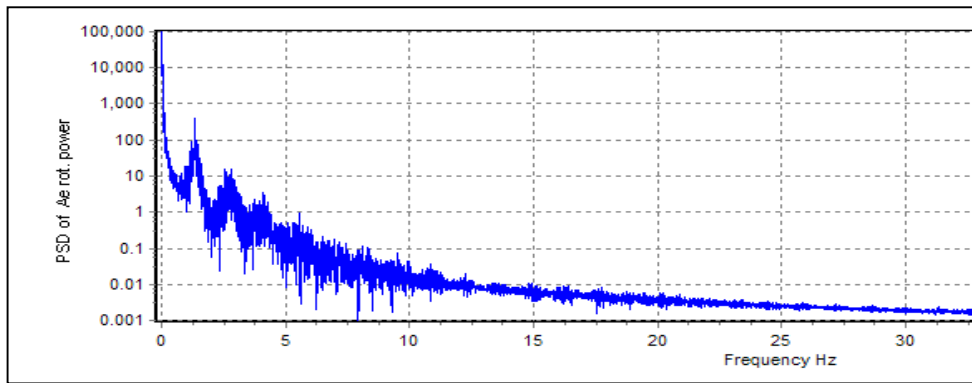
Figure 69 PSD of mech. Power
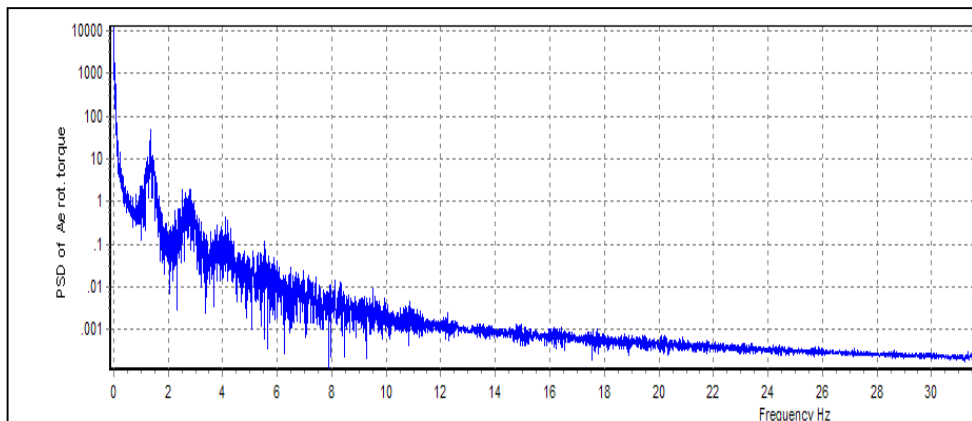
Figure 70 PSD of Rotor main shaft torque
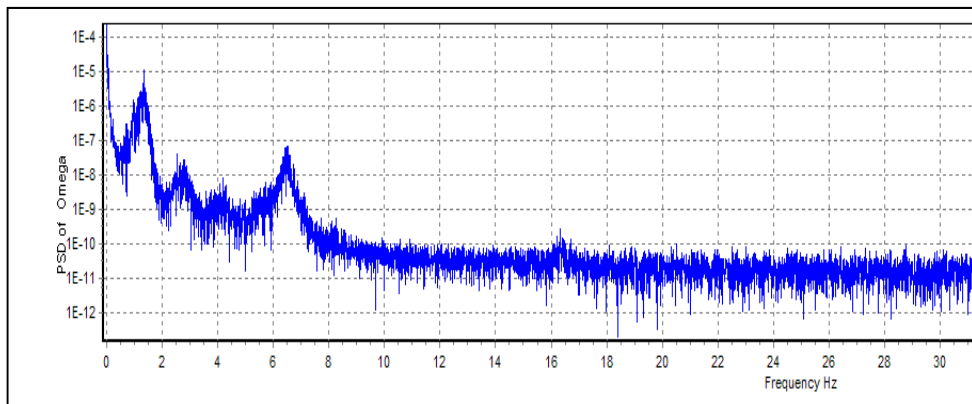
Figure 71 PSD of Rotor main shaft speed

5.2 Statistics, based on 35 Hz samples

The chapter contains the results derived from time traces built over 35 Hz samples and contain statistics over the measurement period chosen. The graphs are shown in the appendix. Results of fatigue analysis based on the distribution of the torque are provided.

5.2.1 Statistics

The graphs show the signals from Table 2 with variation of wind speed. Also 120 seconds duration time traces at 6, 16 and 23 m/s are shown with spectral density

figures for relevant conditions. Structural signals are extended with graphs showing rainflow counting results derived as described previously in 3.4.

From the statistics, a selection of sensor output is shown in Figure 72. A double integration of the angular acceleration for selected time traces results into approximately 5 Deg inclinations for a 150 kNm torque change. This angular rotation is a first order estimate of the interaction between the mechanical and electrical system, where the static moment of the generator weight may play a role in the dynamics. In comparison with the remarks based on the HAWC2 simulations the standard deviation increases with wind speed at a comparable rate. Figure 72 indicates, that stall provides a quite complex interaction and that this should be investigated further in detail.
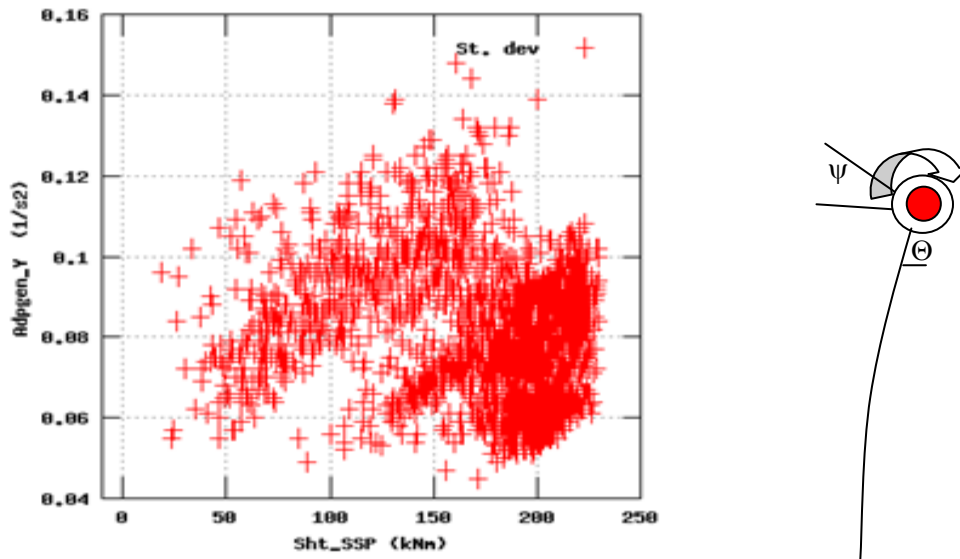
Figure 72 (Left) Generator angular acceleration vs. rotor main shaft torque .
(Right) Indication of tower inclination with relative angle between rotor and stator of generator

It is however not clear how this moment- induced by the weight in the distorted 'equilibrium', is balanced by a reaction force. Obviously, by looking at the possible dynamical couplings, it cannot origin from a gyroscopic moment. The gyroscopic moments work on the main shaft under certain conditions. These are present if the wind turbine is operating, and it is subject to yaw or to tower bending originated from thrust. These contributions are out of the plane relative to Figure 72.

From the statistics, the torque measured in front and after the gearbox is derived; in Figure 73 a comparison of Electrical Power 'Pel_net', the rotor shaft power and the shaft power developed in the flexible cardan joint is shown. Ideally the re-sampled 35 Hz signal from the 50 kHz sampled generator power signal would facilitate the interpretation of the dependency between the signals.

Conclusively it is recommended for future research to establish a re-sampling of this fast-sampled signal to provide a better comparison with the robust mechanical measured signals discussed in this chapter.
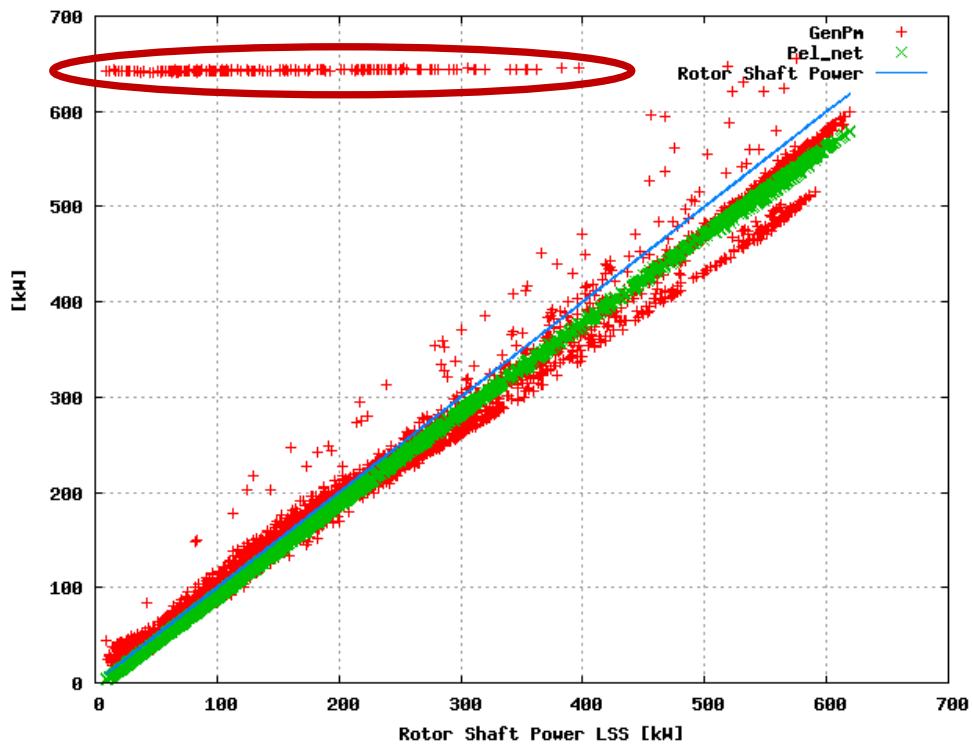
Figure 73: Comparison of static performance of "power meter", marked data according to wireless transmission loss.

The graph shows de-trended curves of different sensor outputs. The changes are probably caused by means of a development of the history of the flexible joint, where the calibration most likely changes due to changes of length and inclination of the cardan joint. Another issue is the mechanical complexity of a flexible joint to transfer torque but with uncounted bending moment components.

The points with constant values represent conditions due to loss of signal in the wireless transmission. They will not be considered in the following analysis.

In conclusion the GENPM sensor is not an ideal transducer to capture drivetrain loads, considering the difficulties in accessing the dynamics of the flexible cardan joint. The linearity between the rotor shaft in front of the gear box and the cardan joint is ´lost' at wind speeds, where idling occurs probably due to non-linearity in the flexible joint and relative deflections between gearbox and generator. An answer could be facilitated with Newton's second law; the inertial forces are dynamically outbalanced more or less by friction forces at the generator's end (free-free condition) with boundary conditions that are subject to change. Statistically this results in correlated with the no twist condition in the cardan shaft. In Figure 73 it is interesting to see what happens to a distribution of loads on the low speed shaft, correlated with the distribution measured on the high speed drive. It is however not obvious that these are equal. Conclusively the complexity of a cardan joint makes it difficult to be used as a sensor and should not be applied in real applications. A better measuring spot would be to place the sensor on the generator shaft or as suggested in the cavity of the hull-like base of the flexible joint.

The power signal Pel_net is in comparison more robust and more countable than measuring mechanically strain. In the next chapter a comparison of the 3 phase derived power signal with mechanical power is shown. If this signal would be represented as a re-sampled signal at 35 hz, this signal would be representative as the Pel_net signal, and comparable to the load measuring transducer, but with linear performance.

In addition to the descriptive found in the appendix, the distribution of the wind speed (measured at the nacelle) is shown in Figure 74 . The Turbulence intensity is shown in Figure 75. The turbulence data ranges between 8.0% and 29.7%.
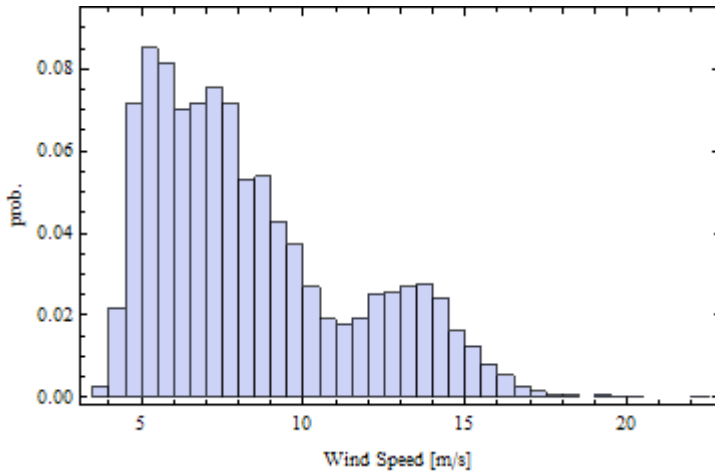
Figure 74 Histogram of measured data from nacelle cup anemometer

Based on the measured distributions, data have been selected to fit a Weibull PDF of the wind speed distribution, see *Figure 76*. The basic distribution shown in the figure as red is fitted with Wei(8.44011, 2.92233). Excursions from the fitted to the measured is originating from lacking a sufficient amount of data, as explained by the relative short duration of measurement period. Another difference is that the fit is not considering the characteristics of the circumstances behind the high wind speeds. To compensate for this, a joint distribution of two Weibull distributions is needed, with peak roughly at 7 m/s and at 14 m/s. Another complexity is the offset wind speed*(roughly 3.7 m/s)* which distorts the distribution into a more steep curve. Apparently there is a tradeof between fitting the CDF and the PDF of the wind speeed data. Here we have ommitted further complexity, by only considering the above, basic Weibull distribution.
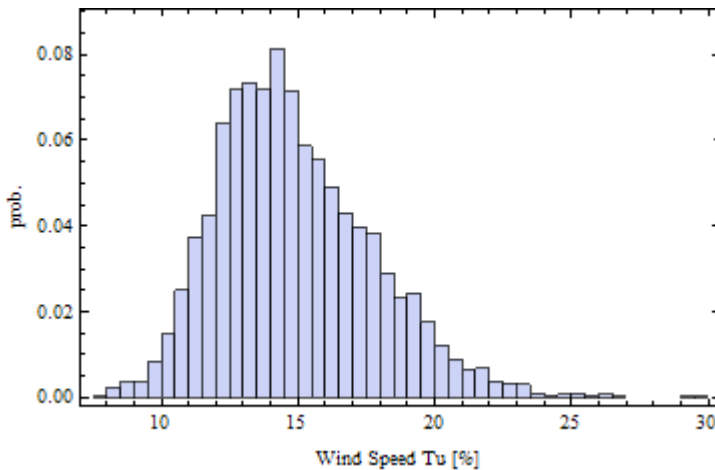
Figure 75 PDF of Turbulence intensity, nacelle anemometer
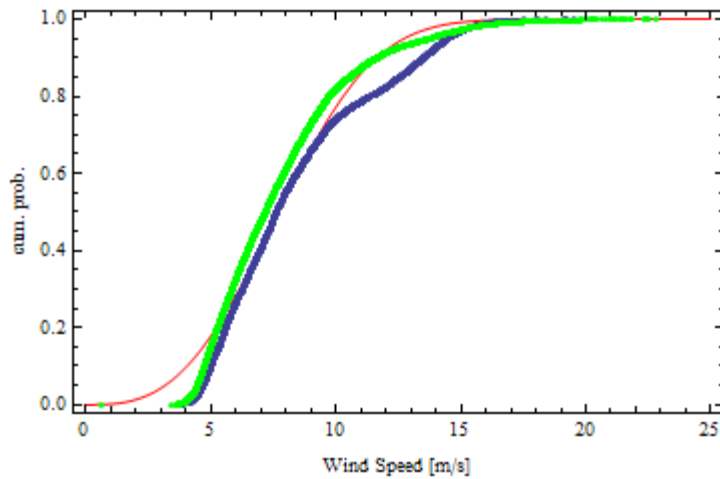
Figure 76 CDF of measured wind speed (blue) in comparison with fitted (red) and synthesis of data from a longer database (green)

The distribution of torque width is shown in Figure 77 and Figure 78. The bin size is 5 kNm. An atypical 'bump' at the high torque region is found, which is due to manual collection of particular data at high wind speeds as commented earlier. The main shaft rotor torque curve is shown in Figure 79.
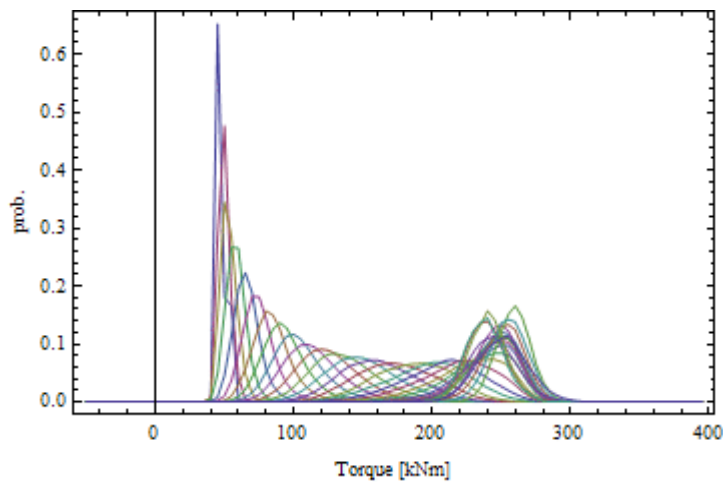
Figure 77 PDF of rotor main shaft torque
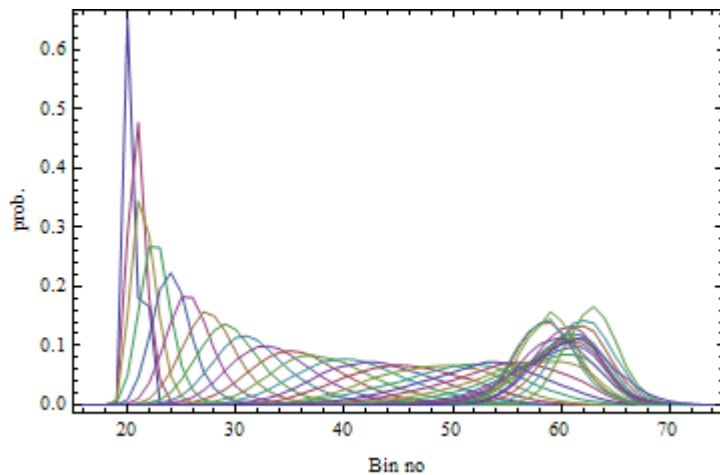
Figure 78 PDF of main shaft torque vs. 0.5 m/s Bin size no,
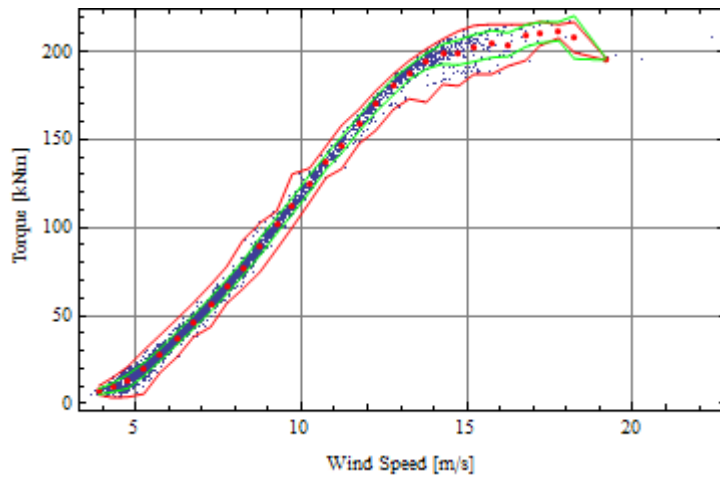
Figure 79 Main rotor shaft torque curve. Red dots are bin averages and lines average+-1 standard deviation(as per definition for larger population than1)

5.2.2 Equivalent moment calculation over 20 years

In principle the task has been to feature the quality of the power signal derived from integration of the 3 phase voltage and current. As seen later on the 50 ksamples allow only 10 sec duration due to limitations in computing memory and storage. If this signal would have been sampled at 35 Hz, it could be interpreted as the main shaft torque to evaluate fatigue issues. Because this has not been implemented, we will consider the main shaft as the signal with likewise properties and conduct an analysis of the equivalent moment over 20 years lifetime at different climatic conditions.

The main shaft torque probability distribution given in Figure 77 PDF of rotor main shaft torqueFigure 77 is calculated at wind conditions with the wind speed probability function of Figure 74, despite of the rough fit of wind data to derive at a conditional distribution as shown in Figure 80.
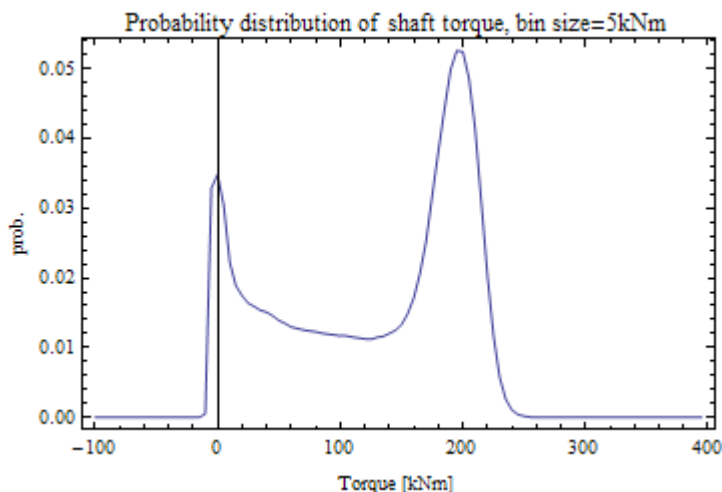
Figure 80 Conditional PDF of main shaft torque

To evaluate the equivalent moment at other wind speed distributions over a lifetime of 20 years, Weibull fits with scale parameter C at 1.75, 2.00 and 2.25, and annual wind speed at 4, 6, 8 and 12 m/s have been calculated. The results are shown in *Figure 81*.
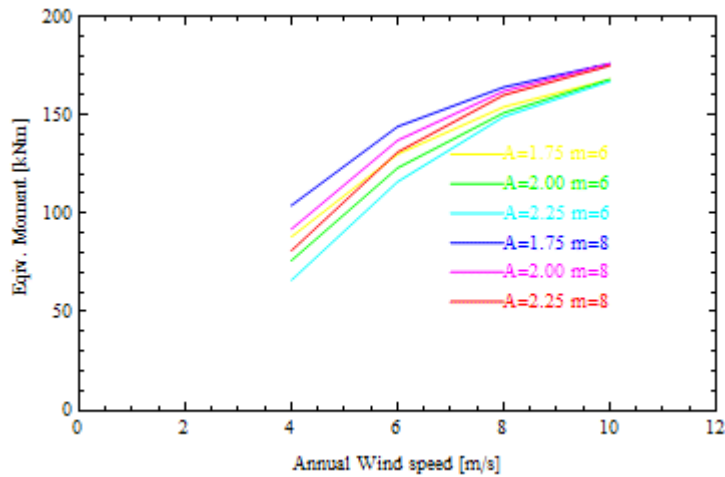
Figure 81 Equivalent moment of main shaft moment over 20 years for Wöhler exponents 6 and 8

Conclusively the method can be developed further to monitor the heath of the drivetrain system, given a proper signal. This signal could be the signal which is re-sampled at 35 Hz from 50 kHz electrical power, derived at the generator and modified with angular shaft speed into torque.

5.3   Results, based on 50 kHz samples

5.3.1   Statistics
The results are derived through analysis of about 1 month of data which is shown in the appendixes.

5.3.2   Time series
Representative time series at three different wind speeds are shown, supplementing the statistical information as shown in appendixes.

Additionally, to assist in comparison of the quality of the derived power signal, a close up picture of a 10 second time series 20110402233332 is provided in this chapter.

Following frequencies are obtained, by manually reading the spectral peaks:

Table 6 Frequency identification of power signal

Primary mode	Frequency [Hz]
1st	1.9
2nd	7.2
3rd	8.4
4th	10
5th	17.2
6th	25.5
7th	33.8
8th	41.1
9th	50
10th	67.4
11th	93.3
12th	100.2

13th	134.0
14th	150.5
15th	200.4
16th	299.6
17th	349.3
18th	400.3
19th	432.2
20th	451
21st	466.7
22nd	499.6
23rd	548.8
24th	602.7
25th	650.8
26th	702.7
27th	733.3
28th	752.3
29th	798.5
30th	847.6
31st	899.7
32nd	946.6
33rd	1000
34th	1100
35th	1200
36th	1213.2
37th	1220.3
38th	1226.6
39th	1250.1
40th	1300
41st	1313.5
42nd	1400
43th	1413
44th	1500
45th	1513
46th	1526
47th	1600
48th	1626
49th	1700
50th	1712
51st	1800
52nd	1817
53rd	1827
..	..

In comparison with the simulations there is a reasonable overlap with the measured frequencies. However, the measured frequencies are rather uncertain at the very low and high frequency range. Improvements could be achieved by averaging 10-second spectra consecutively. Conclusively the signal is a powerful signal for drivetrain analysis.
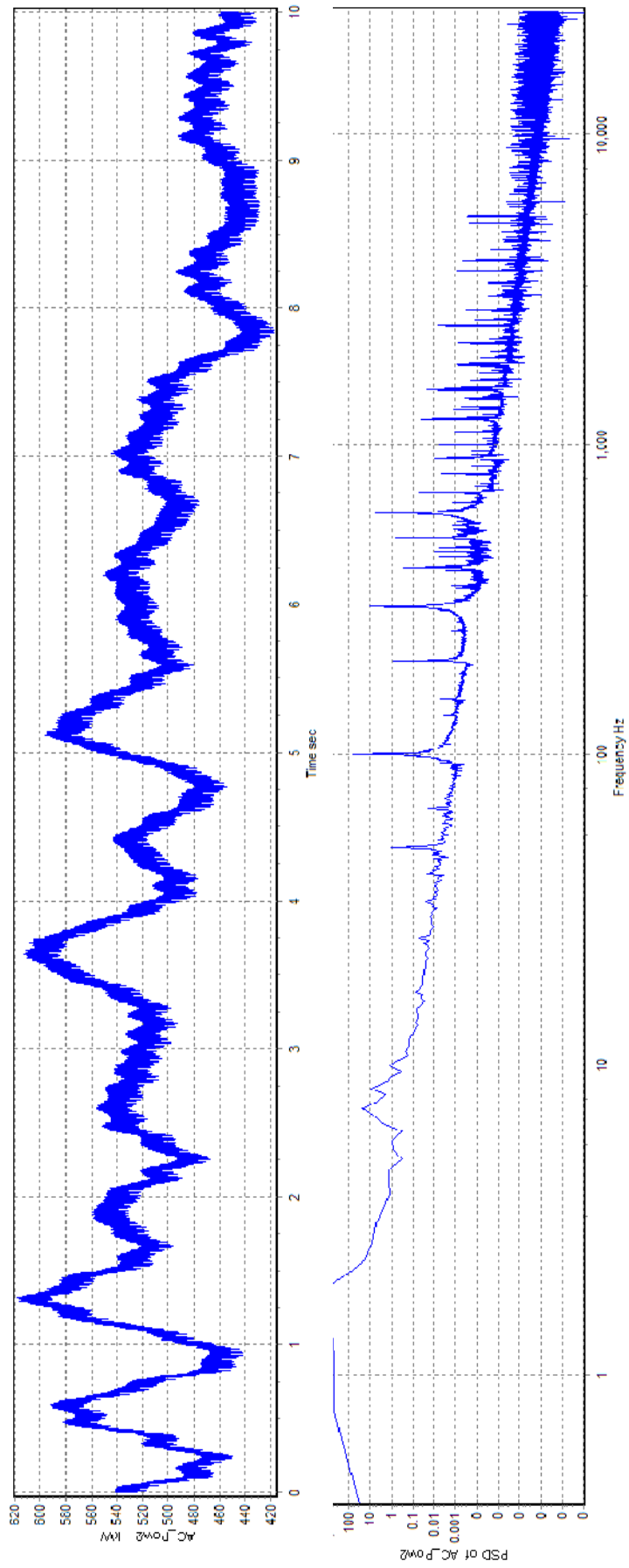
Figure 82 Left: timeseries. Right: PSD

To illustrate the quality of the derived power signal, the signal has been converted into a torque at the high speed shaft end, and compared with the mechanical signal derived from strain measurements. This comparison is performed in Figure 83.
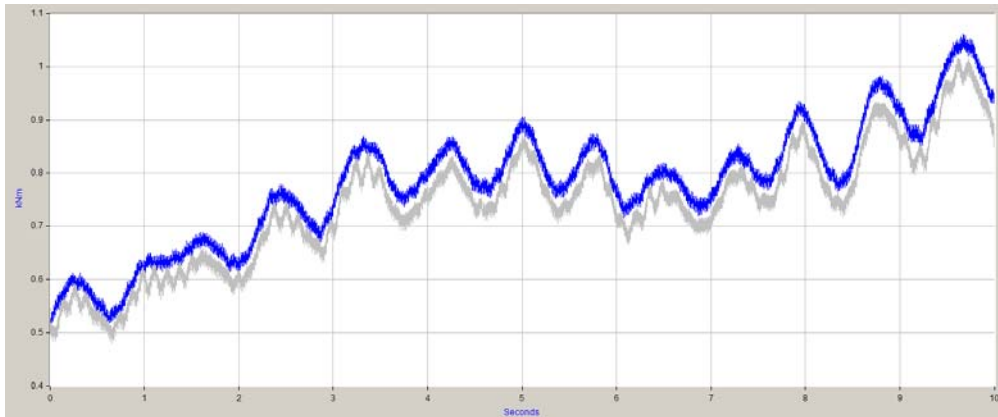
Figure 83 Comparison of torque(HSS) from mechanical strain (gray) and derived signal from electrical measurement (blue)

There is a good transparency between the two signals from the figure. Additionally by observing periodicity also dynamics at lower frequencies are possible to detect. However, due to lack of a model- explaining the mechanical complexity of the flexible joint, this mechanical transfer function is not further explored.

In frequency domain, the comparison for power derived at the generator outlets, the HSS and the LSS is shown in Figure 84.
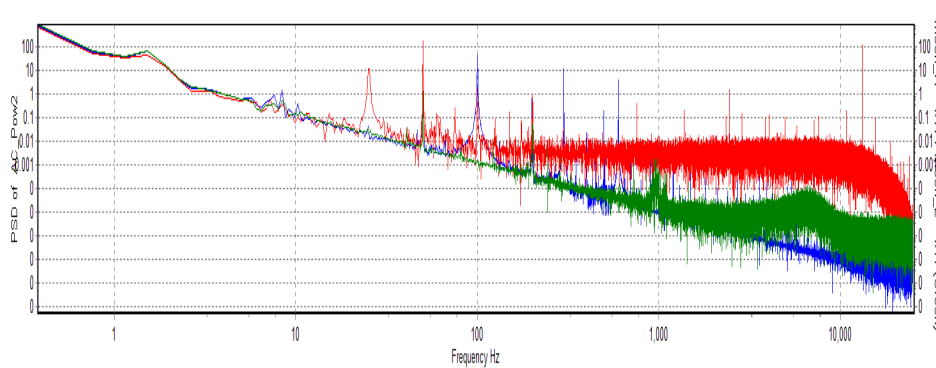
Figure 84 Comparison of PSDs: power from generator outlet(blue),HSS cardan joint power(red) and LSS main shaft power(green)

Figure 84 shows that the cardan joint is performing dynamically different than obtained from the generator outlet or the main shaft. The bandwidth for the generator signal is fully covered, and for the main shaft it is up to approximately 7kHz before a 2 decade drop.
In comparison this figure show a lot of frequencies as mentioned before and it will need additional analysis methods to 'filter' out noise from accentuated modes.
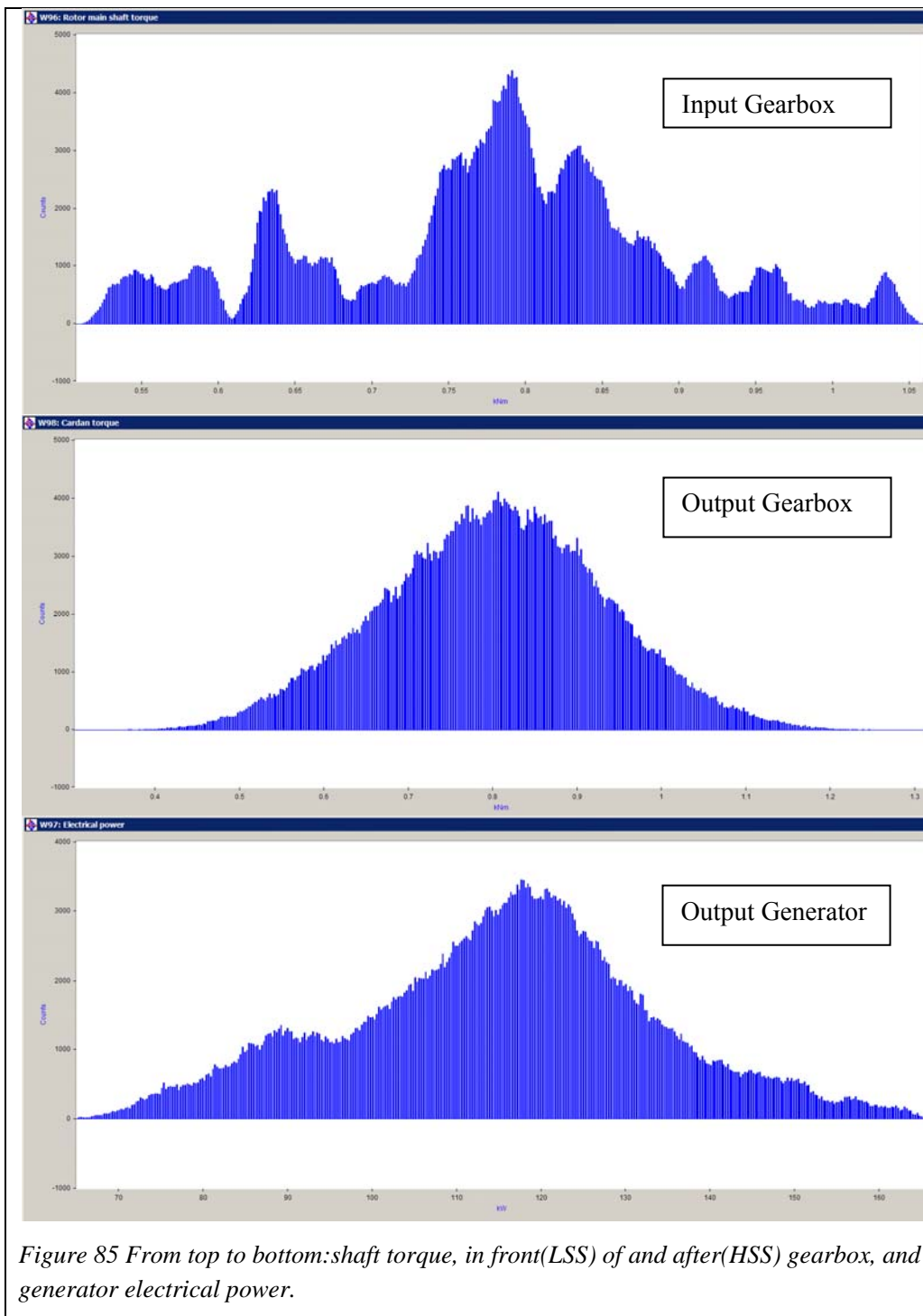
Figure 85 From top to bottom:shaft torque, in front(LSS) of and after(HSS) gearbox, and generator electrical power.

The distribution of signals from main shaft torque, the cardan joint torque and the derived electrical power is shown in Figure 85.

There is a clear indication that the signal in front of and after the gearbox is substantially different with the gearbox as 'modifier' for reasons, which has been discussed earlier. The electrical power signal seems for the 'eye' to provide information biased with what is going on upfront in the drivetrain.

6 Conclusion

The present report describes the deliverable within "Drive train load analysis and lifetime prediction" the verification of long-term load measurement technique under the sixth framework programme on the integrated design for wind turbines UPWIND (SES6) within WP 1B2, transmission and conversion.

The report describes the developed measurement technique, presents the hardware details, type of sensors and location, data types, data analysis technique for verifying design load assumptions, and finally the report describes the obtained results from data analysis performed on measurements on the wind turbine of approximately one month duration.

The interaction between the mechanical and electrical generator subsystems is described rudimentarily, based primarily on HAWC2 simulations below stall of the mechanical system with simple generator and gearbox systems. The electrical system simulations were not carried out as intended in DOW[2], but indications of the conditions for establishing the interaction have been described by measurements and by argument, that this might have an effect as indicated.

The hypothesis stating, that the power signal can be utilized as a basic signal for extended analysis of mechanical as well as electrical power signal with static and dynamic features, has been demonstrated on performance and dynamic bandwidth capability. It is however from present analysis obvious that improved signal conditions are more suitable with other mechanical joint solutions than with a present torque signal as measured with the cardan joint. For the reasons mentioned, the comparison with a signal showing the mechanical properties could be improved, with a likely gain on the accuracy as a result.

References

[1] Sixth framework programme priority 6 Sustainable development, global change and ecosystems, Call ID: FP6-2004-Energy-3, October 2006.

[2] Workpackage 1B2: Transmission and conversion (month 13 - 30) Work document WP 1B2 January 2007

[3] *K.O. Helgesen, LabVIEW Data Acquisition exercise from 500 kW Wind Turbine*, DTU-Oersted 2005

[4] Vindmølleafprøvning Nordtank *NTK 500/37,* Måling af Effektkurve, Risø-I-731, September 1993.

[5] Wind turbine Test, *NORDTANK NTK 500/37, Risø-R-714*, December 1994

[6] Vindmølleafprøvning Nordtank NTK 500/41, Måling af Effektkurve, Risø-I-889, Maj 1995.

[7] Power curve measurements, Measurement Summary, No. 12.2, June 1995, NTK 500/41

[8] Validation of Aeroelastic Model of Nordtank 500/37, Risø-R-1006, November 1997

[9] Accelerated Fatigue Testing of LM 19.1 Blades, Risø-R-1358, May 2003

[10] INTERNATIONAL STANDARD IEC 61400-12, Wind turbine generator systems – Part 12: Wind turbine power performance testing

[11] Technical specification IEC TS 61400-13, Wind turbine generator systems – Part 13: Measurements of mechanical loads.

[12] INTERNATIONAL STANDARD IEC 61400-21, Wind turbine generator systems – Part 21: Measurement and assessment of power quality characteristics of grid connected wind turbines

[13] INTERNATIONAL STANDARD IEC 61000-4-7, Testing and measurement techniques –General guide on harmonics and interharmonics measurements and instrumentation, for power supply systems and equipment connected thereto

[14] IEA Recommended Practices for wind turbine testing and evaluation; 3. FATIGUE CHARACTERISTICS.

[15] *DAU P2858 Data Acquisition Unit description, User manual*. Risø 17-12-2001

[16] *Larsen, T.J et al,* Dynamics of a Wind Turbine Planetary Gear Stage. Paper presented at the European Wind Energy Conference EWEC 2003, Madrid 16-19 June 2003

[17] *Thomsen, K. et al,* Experimental investigation of wind turbine- and gear dynamics for Nordtank 550 kW, Risø-I-2123(DA), December 2003

[18] *Larsen TJ.* How 2 HAWC2, the user manual – version 1.4 Risø-R-report(EN), Risø National Laboratory, April 2006.

[19] *Iov, F.; Timbus, A.V.; Hansen, A.D.; Sørensen, P.; Blaabjerg, F.*, Wind turbine blockset in Saber. General overview and description of the models. (2004) 41 p.

[20] Course notes in s31784. DTU autumn 2009

[21] *Larsen T.J.; Hansen, M.H.; Iov, F.*, Generator dynamics in aeroelastic analysis and simulations. Risø-R-1395(EN) (2003) 45 p.

[22] *Larsen T.J.*, Description of the DLL regulation interface in HAWC. Risø-R-1290(EN), Risø National Laboratory, 2001.

[23] *Cutululis, N.A.; Larsen, T.J., Sørensen, P.; Iov, F.; Hansen, A.D.; Blaabjerg, F.*, Electrical Components Library for HAWC2. Risø-R-1587(EN), Risø National Laboratory, 2007.

[24] *V. Akhmatov.* Analysis of Dynamic Behaviour of Electric Power System with Large Amount of Wind Power, PhD Thesis. Technical University of Denmark.2003

[25] *Sørensen, P.; Hansen, A.D.; Janosi, L.; Bech, J.; Bak-Jensen, B.*, Simulation of interaction between wind farm and power system. Risø-R-1281(EN) (2001) 65 p

[26] *T. Thiringer*, Measurement and modeling of low-frequency disturbances in induction machines, Ph.D. dissertation, Chalmers University of Technology, Göteborg, Sweden, 1996.

[27] *Sørensen, P.; Hansen, A.D.; Christensen, P.; Mieritz, M.; Bech, J.; Bak-Jensen, B.; Nielsen, H.*, Simulation and verification of transient events in large wind power installations. Risø-R-1331(EN) (2003) 80 p.

[28] IEA Recommended Practices for Wind Turbine Testing and Evaluation, 3 Fatigue Characteristics, 2 editions. 1990

[29] *Morten Hansen.* Data for aeroelastic modelling of the Nordtank 500 kW turbine with LM19.1 blades 2010 Risø report to be published

[30] *Torben Juul et al.* Dynamics of a Wind Turbine Planetary Gear Stage. In Proceedings CD-ROM. CD 2. European wind energy conference and exhibition 2003 (EWEC 2003). EWEA, 2003.

7 Appendixes

- Power curve summary NTK500/41 June 1995 (without vortex generators)

- Table view of sensor and transmitter for 35Hz measurements

- Table view of sensor and transmitter parts for 50 kHz measurements

- 35 hz signal graphs

- 50 kHz signal graphs

RISØ
Risø National Laboratory

**Meteorology and
Wind Energy Department**
P.O. Box 49
DK-4000 Roskilde, Denmark
Phone +45 46 77 46 77, Telex 43 116
Fax +45 42 37 29 65
The Test Station for Wind Turbines

Measurement Summary No. 12.2, June 1995
NTK 500/41

Power Curve Measurement

Wind Turbine Identification:

Danish System Approval :	A-1002-2
Turbine Identification No:	92-500
Rotor Diameter:	41.1 m
Rotational Speed:	27.1 rpm
Measured tip angle:	-0.2°±0.2°

Test Site:

The test was performed at Test Pad 4, The Test Station for Wind Turbines, Risø.

Reference Measurement Procedure:

The Danish Recommendation for Wind Turbine Power Curve Measurements, 18 September 1992. The measurement sector was 262°-328°. Anemometer calibrated traceable with traceability through NLR wind tunnel. A WASP-analysis of the site shows an average speed-up of 2% from the meteorology mast to the wind turbine in the measurement sector.

Measured Power Curve:

Documentation for measurements reported in: "Vindmølleafprøvning Nordtank NTK 500/41, Måling af Effektkurve", Risø-I-889, Maj 1995. Measurement period was March 1995 to May 1995. The measured power curve was adjusted to a reference air density of 1.225 kg/m³. The measured power curve is shown on the opposite side of this summary. The power curve is corrected for speed-up effects due to site topography.

Annual Energy Production:

Annual Energy Production is calculated under the assumption of 100% availability and a stop wind speed of 25 m/s. The Annual Energy Production is estimated assuming Weibull distributed wind conditions for Danish applications and assuming Rayleigh distributions with annual average wind speeds from 5 to 11 m/s, at hub height for general applications.

Danish applications (Weibull distribution):

European Wind Atlas, Beldringe, hub height 35 m

Rough. Class [ ]	Weibull Par. A [m/s]	C [ ]	Annual Energy Production [MWh]	Uncertainty of Measurement [MWh]	[%]
0	9.14	2.09	1681	87	5
1	7.19	1.94	1056	77	7
2	6.59	1.91	865	71	8
3	5.59	1.89	559	59	11
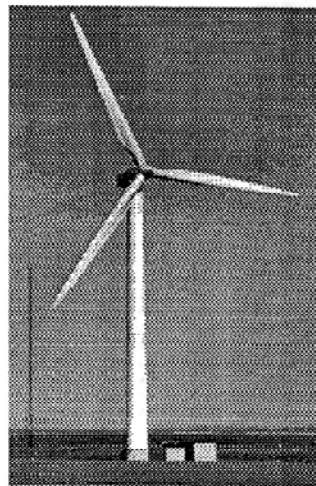
Photo of NTK500

The uncertainties of the measured wind speed, electrical power, air temperature and air pressure are tabulated below. The uncertainties are described as absolute and relative standard deviations. The relative uncertainty due to site topography(2%), speed-up effect (1%), and of cup-anemometer uncertainty (0.1 m/s) is included in the analysis.

	Wind speed	Power	Air Temp.	Air Press.
absolute	0.25 m/s	1.55 kW	0.6 °C	0.6 hPa
relative	0.0224	0.00087	0	0

General applications (Rayleigh distribution):

Annual Avg. Wind Speed [m/s]	Annual Energy Production [MWh]	Uncertainty of Measurement [MWh]	[%]
5	552	59	(11)
6	910	73	(8)
7	1288	82	(6)
8	1652	87	(5)
9	1980	88	(4)
10	2257	88	(4)
11	2474	86	(3)

262-328 Deg, 27.1 rpm, no rain

Wind Speed [m/s]

262-328 Deg, 27.1 rpm, no rain

Wind Speed [m/s]

Bin nr	Wind speed	#data	Avg	Stdev	Min	Max	
8	4.02	18	-5.22	3.57	-11.00	4.04	-0.
9	4.42	14	5.10	8.48	-2.70	28.90	0.
10	4.96	18	21.84	8.33	7.86	44.07	0.
11	5.49	23	39.83	5.91	26.22	48.87	0.
12	5.99	26	59.18	7.52	45.85	70.18	0.
13	6.43	42	79.85	9.08	58.22	95.96	0.
14	6.91	43	106.12	9.70	91.13	131.94	0.
15	7.44	43	132.87	12.48	108.50	155.67	0.
16	7.94	36	166.07	12.07	143.94	193.92	0.
17	8.50	24	198.75	17.96	159.49	221.79	0.
18	8.92	21	229.33	16.74	189.21	256.29	0.
19	9.39	21	260.21	18.10	216.80	289.77	0.
20	9.93	18	298.04	16.98	262.94	316.03	0.
21	10.42	25	331.92	10.92	312.58	351.67	0.
22	10.90	28	354.21	18.83	301.64	379.90	0.
23	11.43	27	376.39	19.08	324.59	405.72	0.
24	11.96	23	402.60	18.35	349.15	433.83	0.
25	12.44	15	423.79	17.53	377.50	455.03	0.
26	12.97	14	446.62	17.93	396.33	467.41	0.
27	13.44	18	459.12	17.41	422.50	483.10	0.
28	13.92	24	478.71	14.08	443.25	501.50	0.
29	14.36	14	490.53	9.85	467.06	505.08	0.
30	14.88	7	498.88	15.91	472.34	513.17	0.1
31	15.46	5	501.63	15.64	474.09	520.56	0.1
32	15.89	5	515.84	16.99	492.18	530.60	0.1
33	16.49	7	531.52	6.08	520.24	540.45	0.1
34	16.85	6	528.43	12.52	502.45	540.43	0.1
35	17.30	5	538.20	2.37	534.71	540.64	0.1
36	17.85	3	534.07	5.31	526.81	539.38	0.1
37	18.35	3	532.71	7.47	522.30	539.45	0.1
38	18.71	2	525.90	6.74	519.16	532.64	0.0
39	19.35	1	521.85	0.00	521.85	521.85	0.0
40	19.81	3	514.84	1.09	513.89	516.37	0.0
41	20.30	2	487.39	4.09	483.30	491.48	0.0
43	21.15	2	504.61	0.31	504.30	504.92	0.0

Overview of sensor and transmitter

Table 7: Sensor and transmitter description 35 Hz sampling

Measurement description	Sensor	Signal type	Conversion principle	Transmitter
Wind speed at hub height	Risø cup anemometer P2546A with Reed relay	Digital	Direct counting of pulses and pulse pr rpm	Risø P2858A DAU Configured to periodic time measurement
Wind Direction at hub height-1.5m	Wind vane P2021A with Cosine/Sine resolver	Analogue	2-phase transformer w. rotor mounted directly on turning shaft, attached to vane	Risø P2420 (DC to AC supply, 2 separate channels sin and cos)
Air temperature at hub height – 1.5m	Pt 100 thermistor and radiation shielding	Analogue	Metal Resistor response to heat	Risø P1867a (Wheatstone Bridge)
Air barometric pressure 1 m..a.g.l	Vaisala PTB100B Pressure sensitive vessel with position gauge	Analogue	Measuring of gauge position	
Precipitation	LED Light array	Digital	Blockage of light array path	LED circuit
Position of nacelle	Resistor with gearbox attached to yaw drive	Analogue	Measuring on resistive path	Voltage divider
Position of rotor	Inductive sensor on low speed shaft together with inductive sensor on high speed shaft with 6 holes	Digital	Dampening of transistor oscillations due to presence of metal provides pulse	Risø P2858A DAU Configured to position measurement
Rotor shaft speed low speed	Inductive sensor one pulse/rev	Digital	Dampening of transistor oscillations due to presence of metal provides pulse	Risø P2858A DAU Configured to periodic time measurement
Rotor shaft speed high speed	Inductive sensor with 6 pulses/rev	Digital	Dampening of transistor oscillations due to presence of metal provides pulse	Risø P2858A DAU Configured to periodic time measurement
Wind speed nacelle	Risø cup anemometer P2546A with Reed relay	Digital	2 magnets on turning shaft controls the contact closure timings of the relay per revolution	Risø P2858A DAU Configured to periodic time measurement
Wind Direction nacelle	Vector Wind vane F2819A	Analogue	Measuring on resistive viper path relative to one full turn	Voltage divider
Flap-wise bending root moment #1	Micro Measurement Strain Gauge CEA-06-250A-350	Analogue	Semiconductor foil subjected to resistive change due to bending	RisøP2912B SG amplifier
Edge-wise bending root moment #1	Micro Measurement Strain Gauge CEA-06-250A-350	Analogue	Semiconductor foil subjected to resistive change due to bending	Risø P2912B SG amplifier
Rotor shaft torque	Micro Measurement Strain Gauge CEA-06-W250C-350	Analogue	Semiconductor foil subjected to resistive change due to twisting	Risø P2912B SG amplifier
Main shaft bending moment X,	Micro Measurement Strain Gauge CEA-06-250A-350	Analogue	Semiconductor foil subjected to resistive change due to bending	Risø P2912B SG amplifier
Main shaft bending moment Y	Micro Measurement Strain Gauge CEA-06-250A-350	Analogue	Semiconductor foil subjected to resistive change due to bending	Risø P2912B SG amplifier
Tower top torsion,	Micro Measurement Strain Gauge CEA-06-W250C-350	Analogue	Semiconductor foil subjected to resistive change due to twisting	Risø P2912B SG amplifier
Tower bottom bending moment X	Micro Measurement Strain Gauge CEA-06-250C-350	Analogue	Semiconductor foil subjected to resistive change due to bending	Risø P2912B SG amplifier
Tower bottom bending moment Y	Micro Measurement Strain Gauge CEA-06-250UW-350	Analogue	Semiconductor foil subjected to resistive change due to bending	Risø P2912B SG amplifier
Electrical Power	Camille Bauer 502-34F1 Z291 0090 61 Watt converter, cl 05	Analogue	Time division multiplier principle of 3 voltage and 3 current signals	3 Garre G30/20 cl. 01 Current transformers 500/1
Tip deployment indicator	Via Controller electronics	Digital	Non-potential hazardous NPN signal amplifier	Risø P2858A DAU Configured to status measurement
Brake	Via Controller electronics	Digital	Non-potential hazardous NPN	Risø P2858A DAU

Measurement description	Sensor	Signal type	Conversion principle	Transmitter
activation indicator			signal amplifier	Configured to status measurement
Generator mode indicator	Via Controller electronics	Digital	Non-potential hazardous NPN signal amplifier	Risø P2858A DAU Configured to status measurement
Operations mode indicator	Via Controller electronics	Digital	Non-potential hazardous NPN signal amplifier	Risø P2858A DAU Configured to status measurement

Table 8: Sensor and transmitter description high speed sampling.

Measurement description	Sensor	Signal type	Conversion principle	Transmitter
Rotor shaft torque low speed shaft(LSS)	Micro Measurements Strain Gauge CEA-06-W250C-350	Analogue	Semiconductor foil subjected to resistive change due to torsion	HBM RM4220 over slipring,converted into current and via 250±0.05Ω resistor into 1-5 V
Rotor shaft torque high speed	Micro Measurements Strain Gauge CEA-06-W250C-350	Analogue	Semiconductor foil subjected to resistive change due to torsion in the cardan joint	Accumetrix AT4400 completion circuit
Proximity sensor x	Laser beam	Digital		Micro Epsilon PC 140
Proximity sensor y	Laser beam	Digital		Micro Epsilon PC 140
Phase-Neutral Voltage L1	LEM CV 3-1000 E -1000V..+1000V, 0-500 kHz	Analogue	Hall element	
Phase-Neutral Voltage L2	LEM CV 3-1000 E -1000V..+1000V, 0-500 kHz	Analogue	Hall element	
Phase-Neutral Voltage L3	LEM CV 3-1000 E -1000V..+1000V, 0-500 kHz	Analogue	Hall element	
Phase Current I1	LEM LF-1005-S -1500A..+1500A,0-150 kHz	Analogue	Hall element 1000 A rms:200mA rms	33±5% Ω resistor
Phase Current I2	LEM LF-1005-S -1500A..+1500A,0-150 kHz	Analogue	Hall element 1000 A rms:200mA rms	33±5% Ω resistor
Phase Current I3	LEM LF-1005-S -1500A..+1500A,0-150 kHz	Analogue	Hall element 1000 A rms:200mA rms	33±5% Ω resistor
Active Power	3-phase voltage and current signals	Derived	Integration of signals in CRIO system	
Reactive Power	3-phase voltage and current signals	Derived	Integration of signals in CRIO system	
Azimuth position of rotor shaft at generator	HeidenHein ERN 120 3600 27S12-03	Digital	Counting of light pulses over gate time and per revolution	
Angular speed	HeidenHein ERN 120 3600 27S12-03	Digital	Counting of light pulses over gate time and per revolution	
Angular acceleration	HeidenHein ERN 120 3600 27S12-03	Digital	Counting of light pulses over gate time and per revolution	
Sound pressure	G:R:A:S 40AE ½" pre-polarised microphone 3.15 Hz - 20 kHz	Analogue		26CA ½" CCP preamplifier
Acceleration gearbox front	Summit 34204A 0-10 kHz	Analogue	Tri-axial MEMS including temperature sensor	
Acceleration gearbox back	Summit 34204A 0-10 kHz	Analogue	Tri-axial MEMS including temperature sensor	
Acceleration generator front	Summit 34204A 0-10 kHz	Analogue	Tri-axial MEMS including temperature sensor	
Acceleration generator back	Summit 34204A 0-10 kHz	Analogue	Tri-axial MEMS including temperature sensor	
Angular rotation of gearbox x,y,z	Distance between front and back: (0.345m, 0.935m, 0.727m)	Derived		
Angular rotation of generator x,y,z	Distance between front and back: (0.82m, 0.65m, 0.62m)	Derived		

½-inch Prepolarized, Free-field Microphone Type 40AE

Product Data and Specifications

Typical applications

- *Precision acoustic measurements*
- *Type 0 and 1 SPL measurements*
- *Free-field measurements*
- *Use with G.R.A.S. CCP[1] preamplifiers*

The G.R.A.S. Microphone Type 40AE is a ½-inch precision condenser microphone for general purpose measurements in open acoustic fields. It is a prepolarized free-field microphone with a large dynamic range and a wide frequency response.

As a free-field microphone, the Type 40AE is for measuring the sound pressure which existed before it was placed in the sound field pointing towards the sound source.

The disturbing effects of its presence in the sound field are minimal at low frequencies (large wavelengths compared with microphone size). At higher frequencies, the effects of reflections and diffractions generally lead to an increase in the measured sound pressure levels.

Fig. 3 shows what these are in a free-field for various angles of incidence. The Type 40AE compensates for this to provide a flat frequency response at an angle of 0° incidence in a free-field (see Fig. 2).

Fig. 1   ½-inch Prepolarized Free-field Microphone Type 40AE

G.R.A.S. CCP[1] preamplifiers are also available for use with the Type 40AE, these are:

½-inch Preamplifier Type 26CA
¼-inch Preamplifier Type 26CB with adaptor RA0003
(see separate data sheets)

All G.R.A.S. microphones comply with the specifications of IEC 61094: *Measurement Microphones, Part 4: Specifications for working standard microphones.*

Non-corrosive, stainless materials are used in manufacturing these microphones to enable them to withstand rough handling and corrosive environments.

All G.R.A.S. microphones are guaranteed for 5 years and are individually checked and calibrated before leaving the factory. An individual calibration chart is supplied with each microphone.

[1]   Constant Current Power

Specifications

Frequency response:		Microphone thermal noise:	
3.15 Hz - 20 kHz ....±2.0 dB			15 dBA re. 20 µPa
5 Hz - 10 kHz ....±1.0 dB		Capacitance:	
Nominal sensitivity:			14.1 pF
	50 mV/Pa	Effective front volume:	
Polarization voltage:		Nominal at 250 Hz:.....................50 mm³	
	0 V	Temperature range:	
Upper limit (3 % distortion):			-40 °C to +150 °C
	146 dB re. 20 µPa		...continued overleaf

Statistics, 35 hz
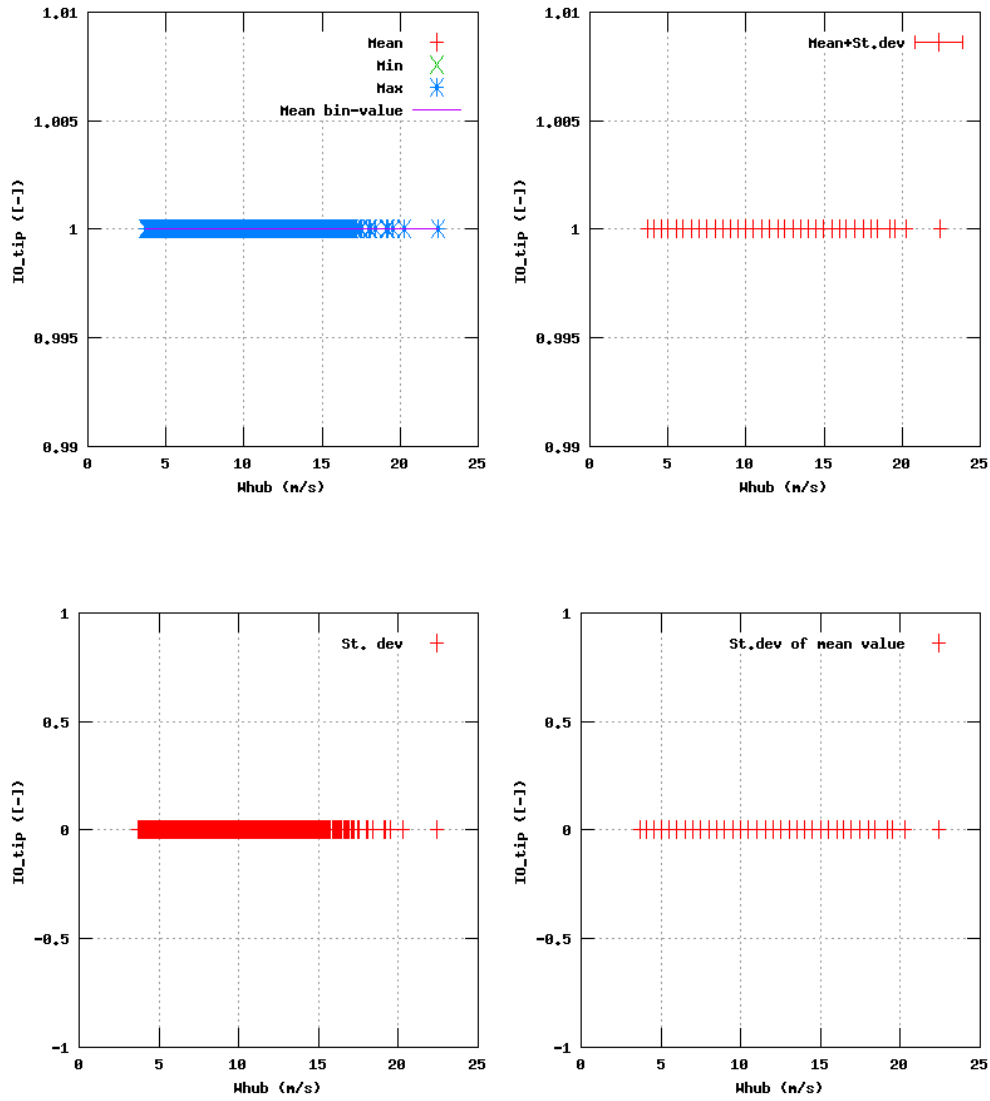
Figure 12a, Sensor 47: Controls:tip on/off IO_tip versus wind speed
Input files: ntk500res.dat, stat_47.dat
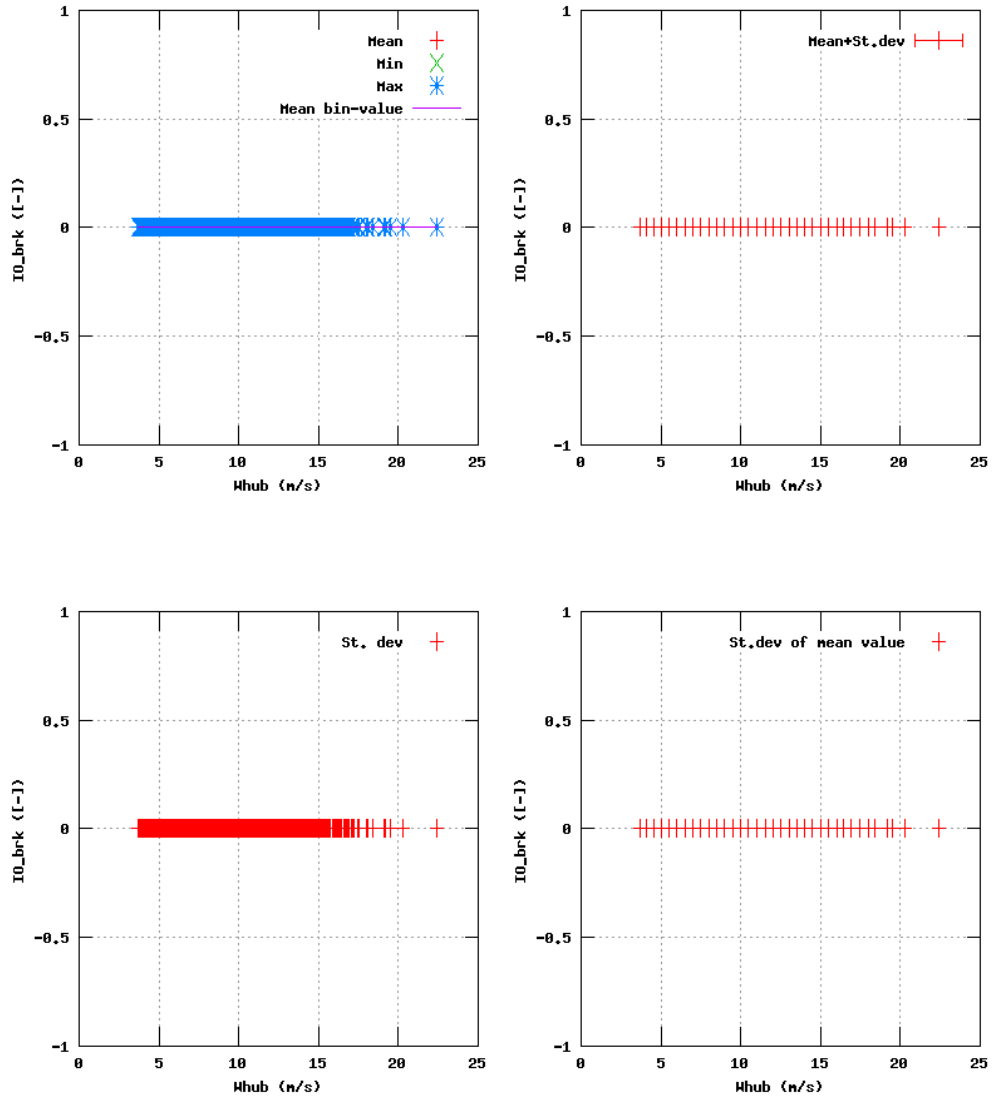
Figure 13a, Sensor 51: Controls;brake on/off IO_brk versus wind speed
Input files: ntk500res.dat, stat_51.dat
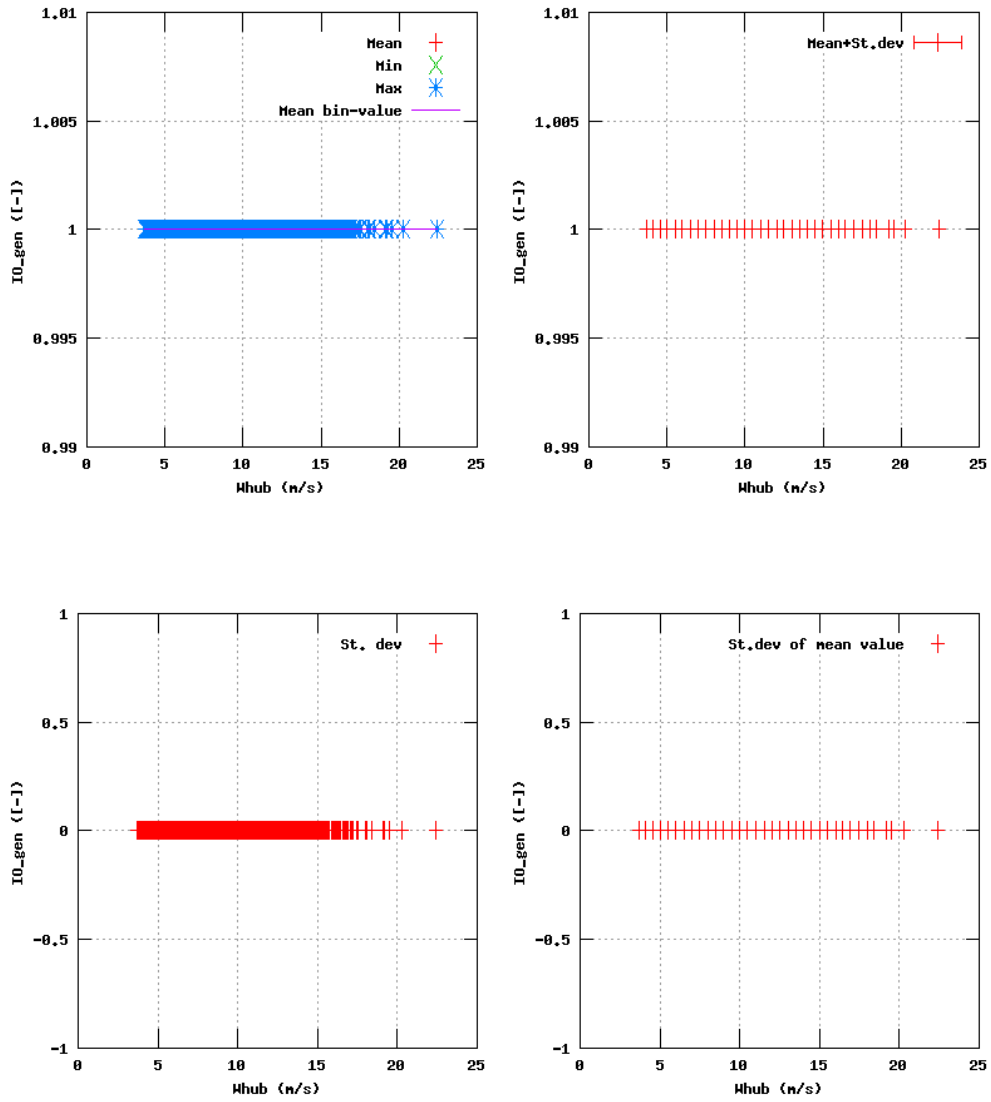
Figure 14a, Sensor 55: Controls:generator on/off IO_gen versus wind speed
Input files: ntk500res.dat, stat_55.dat
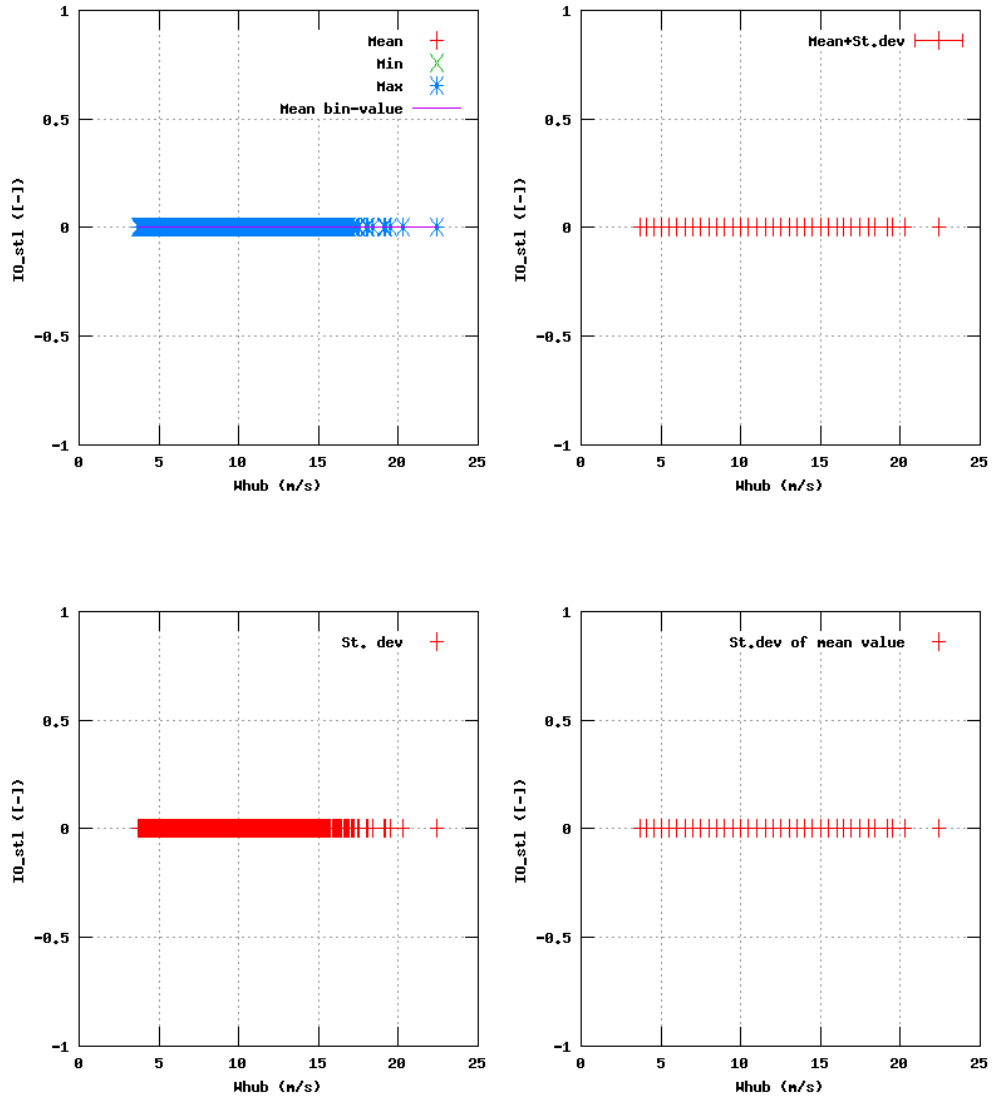
Figure 15a, Sensor 59: Controls:constant/variable speed on/off IO_stl versus wind speed
Input files: ntk500res.dat, stat_59.dat
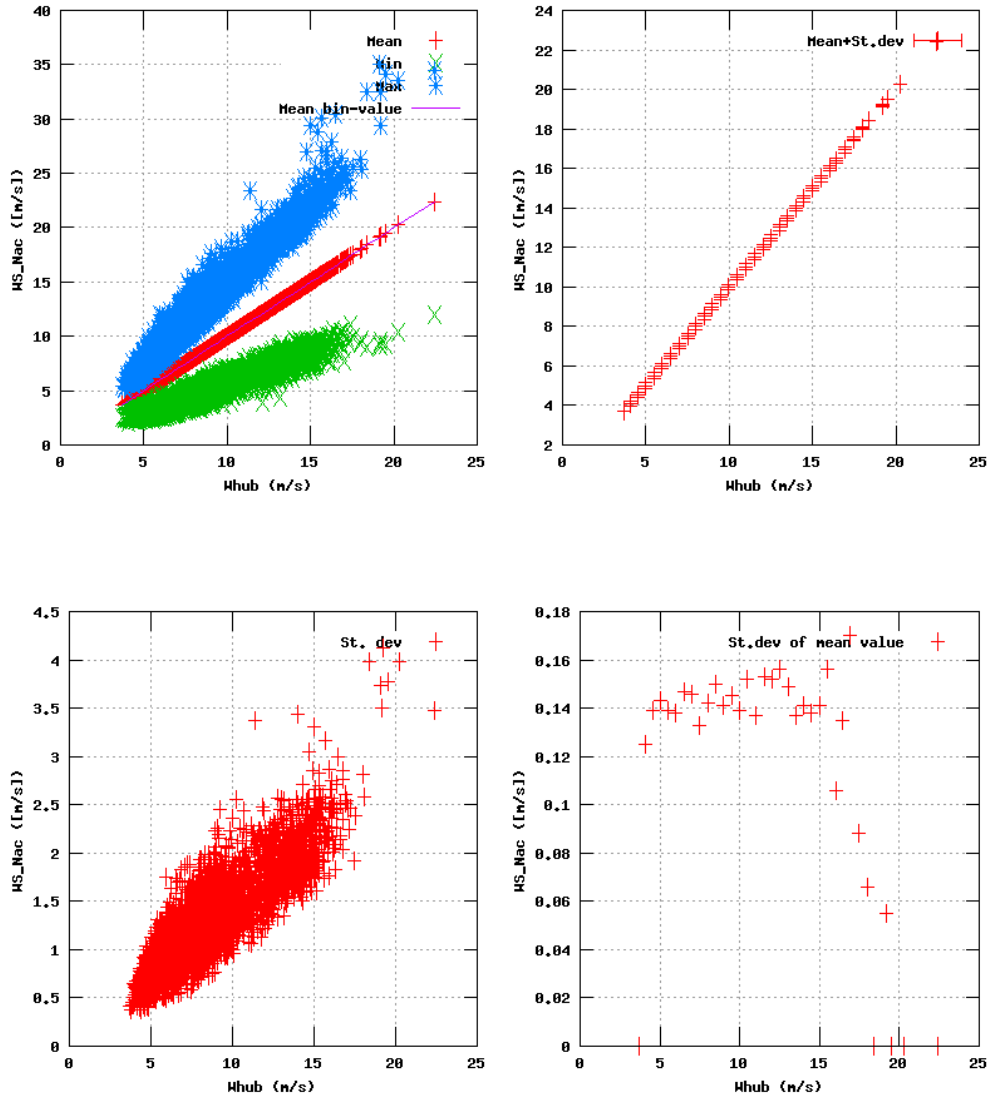
Figure 25a, Sensor 99: Wind speed WS_Nac versus wind speed
Input files: ntk500res.dat, stat_99.dat
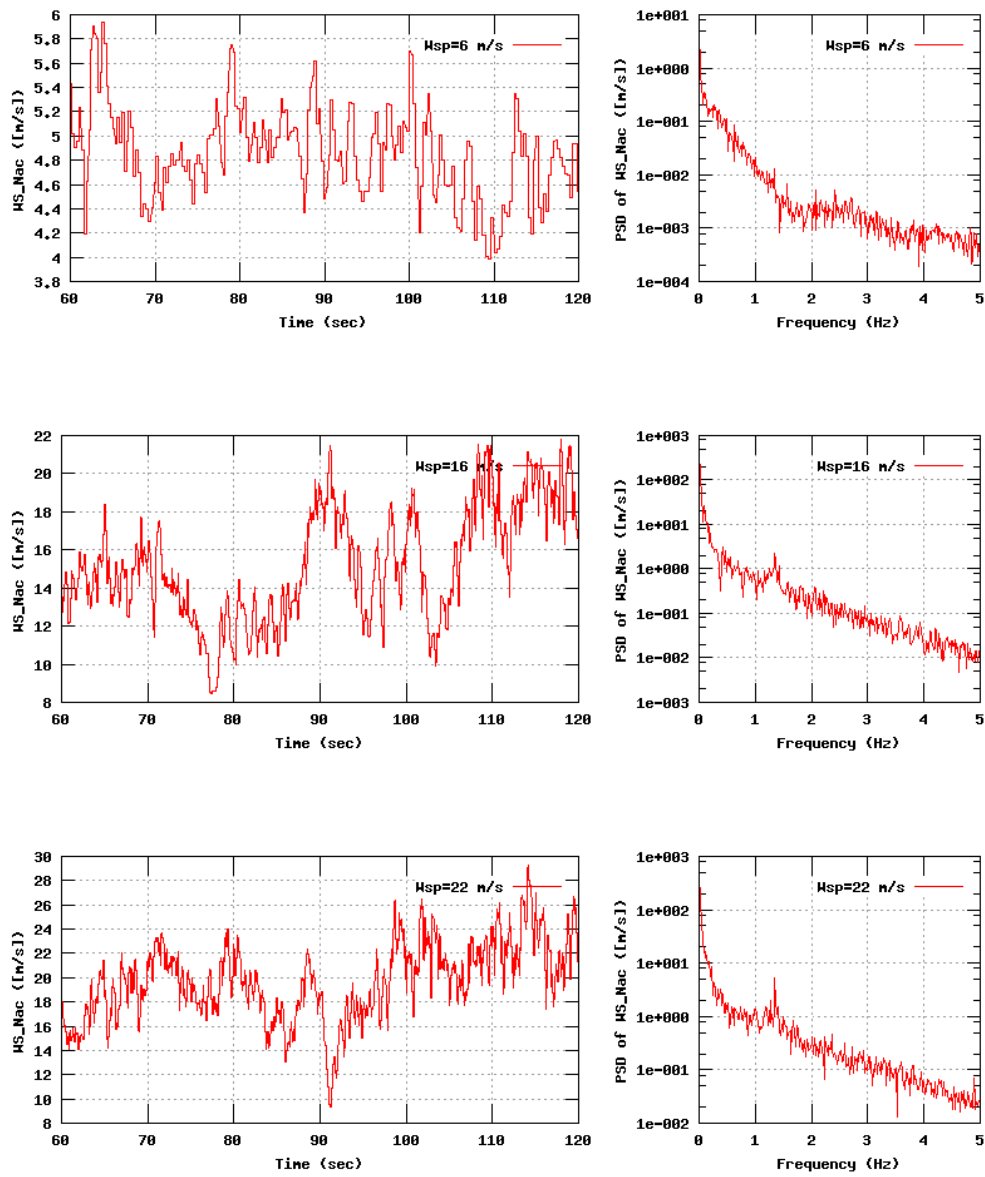
Figure 25b, Sensor 99: Wind speed WS_Nac versus time and frequency
Input files: m06.dat, m16.dat, m22.dat, m06.psd, m16.psd and m22.psd
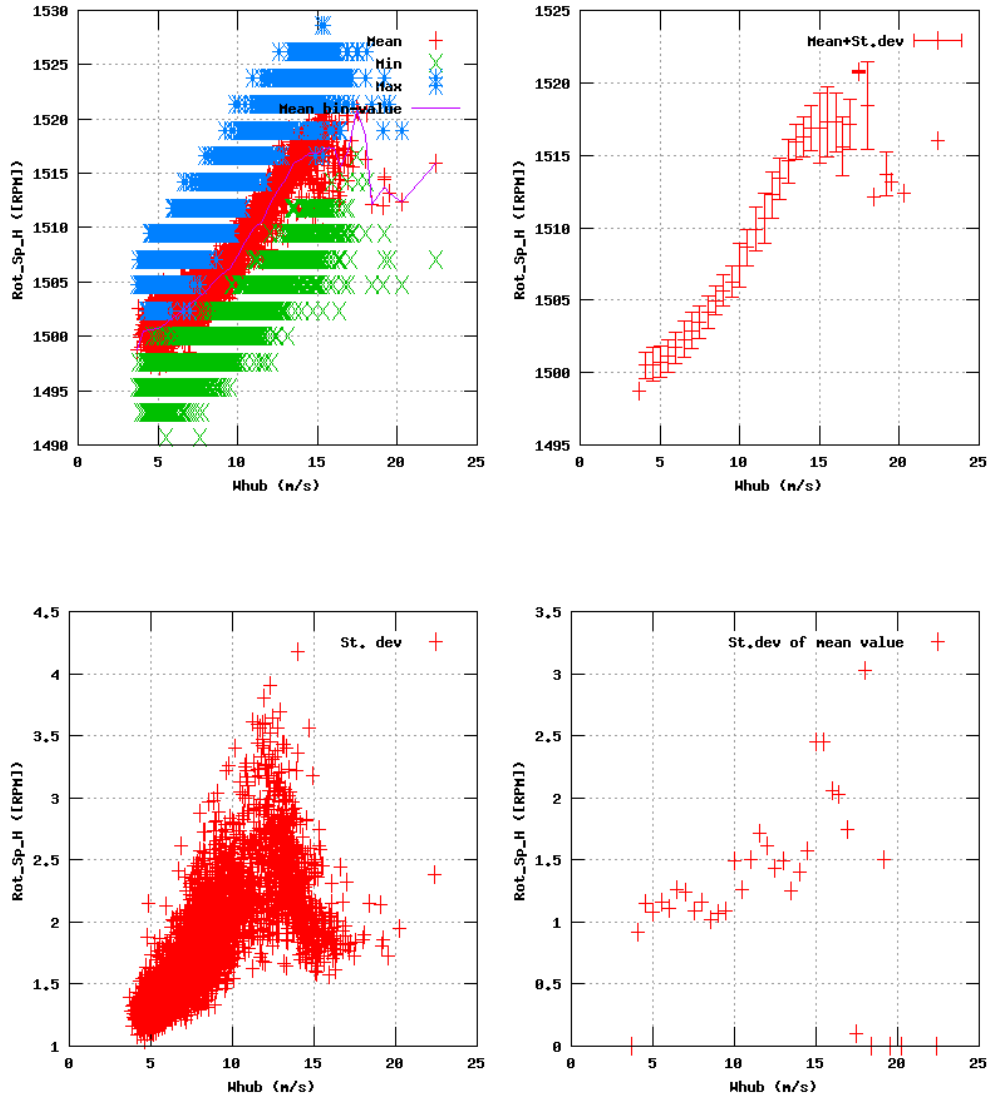
Figure 24a, Sensor 95: Rotor shaft speed HSS Rot_Sp_H versus wind speed
Input files: ntk500res.dat, stat_95.dat
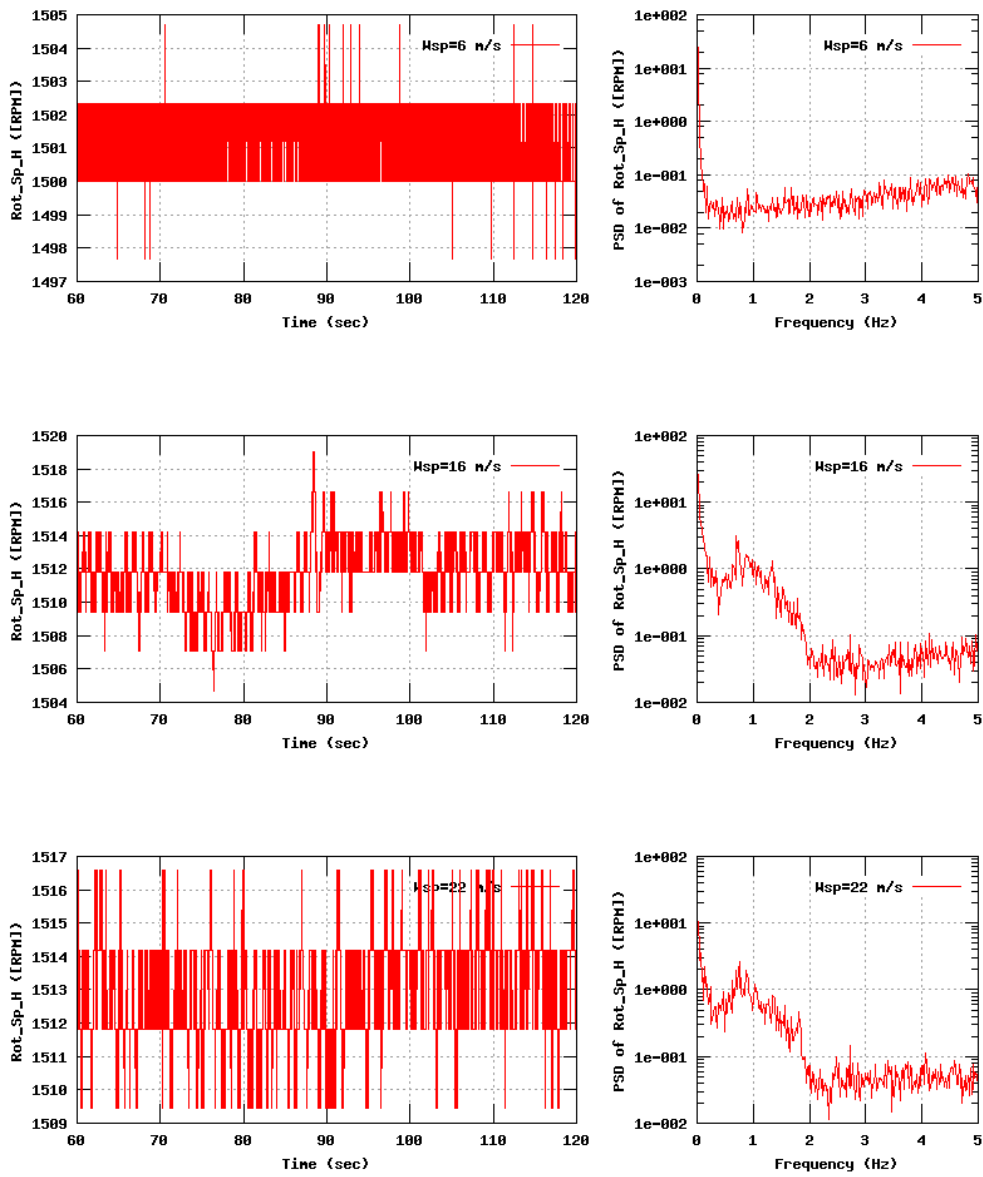
Figure 24b, Sensor 95: Rotor shaft speed HSS Rot_Sp_H versus time and frequency
Input files: m06.dat, m16.dat, m22.dat, m06.psd, m16.psd and m22.psd
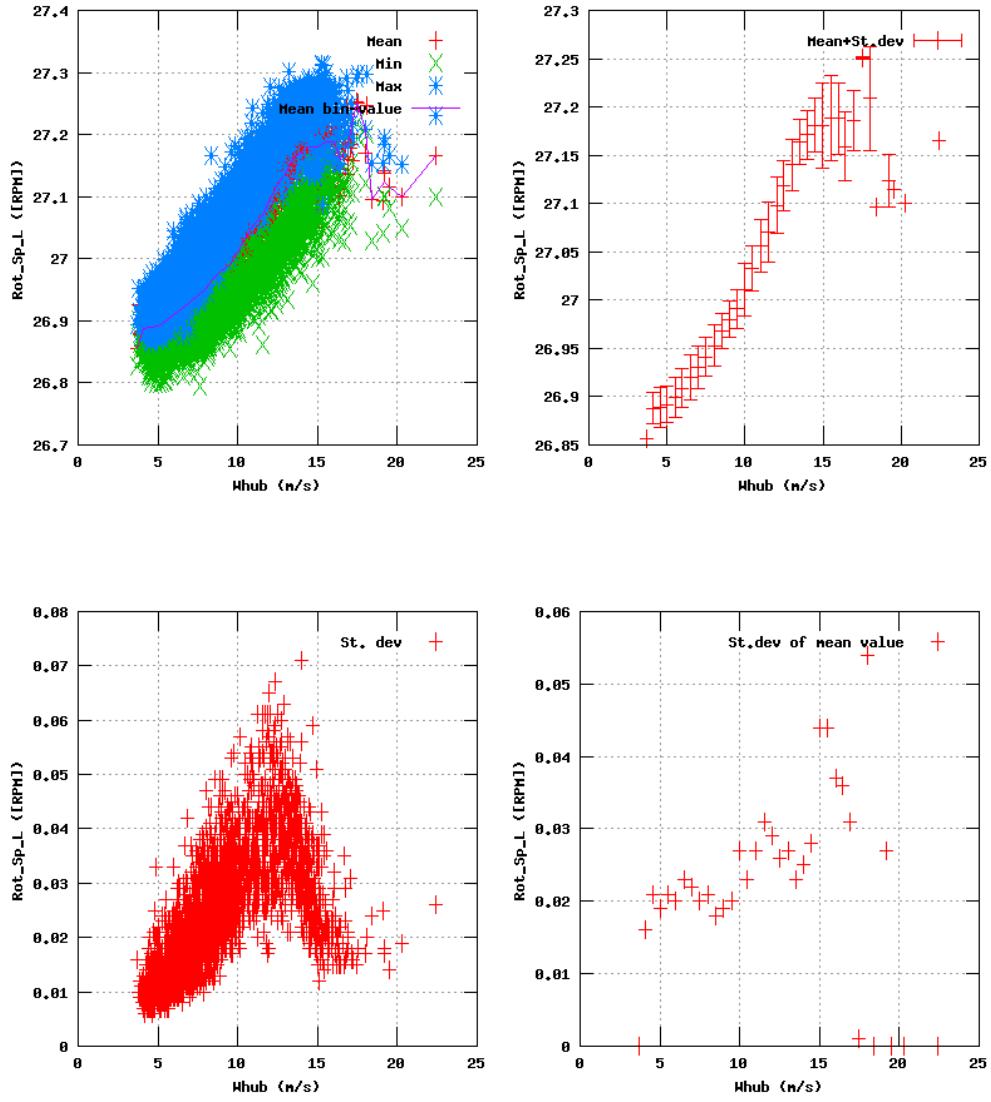
Figure 23a, Sensor 91: Rotor shaft speed LSS Rot_Sp_L versus wind speed
Input files: ntk500res.dat, stat_91.dat
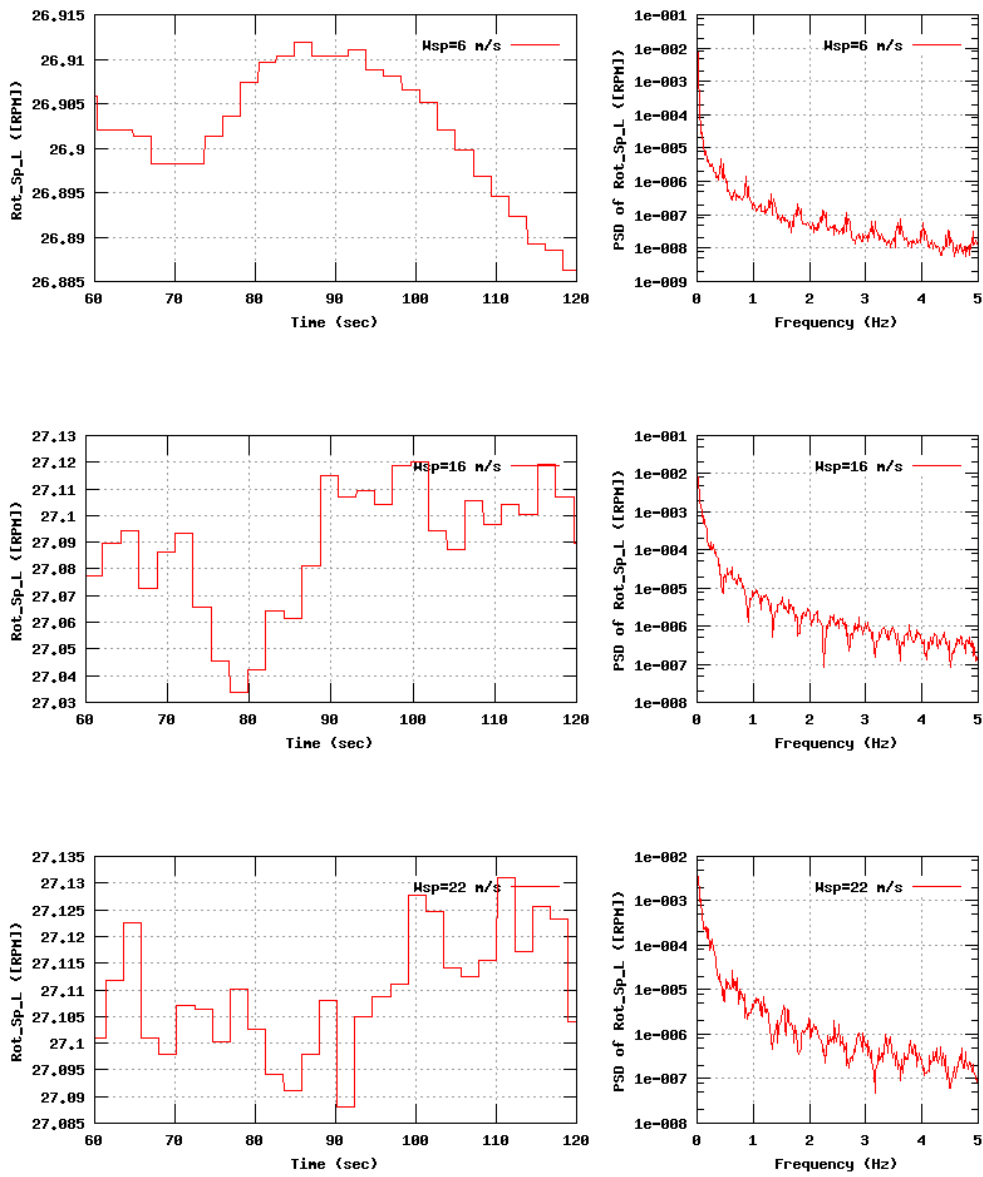
Figure 23b, Sensor 91: Rotor shaft speed LSS Rot_Sp_L versus time and frequency
Input files: m06.dat, m16.dat, m22.dat, m06.psd, m16.psd and m22.psd
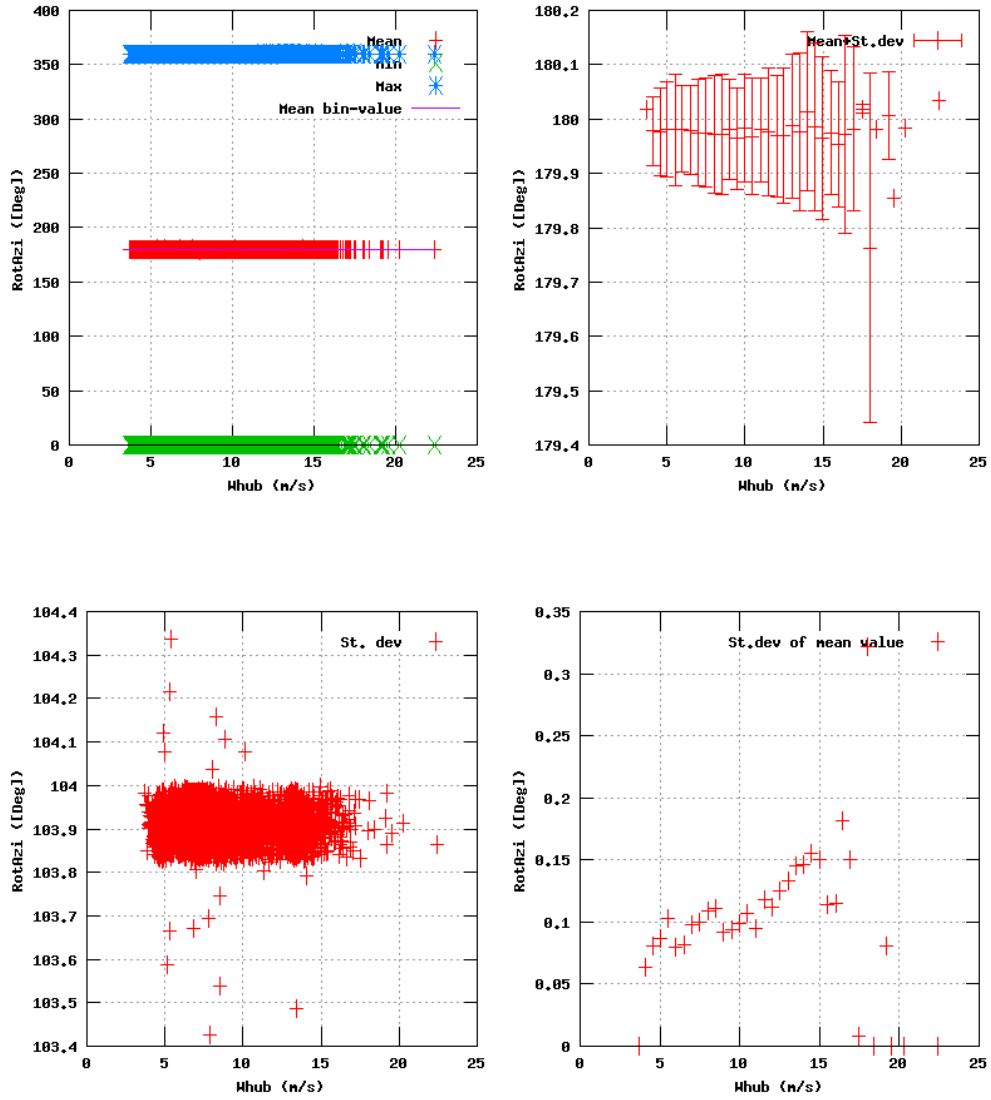
Figure 22a, Sensor 87: Rotor blade azimuth angle RotAzi versus wind speed
Input files: ntk500res.dat, stat_87.dat
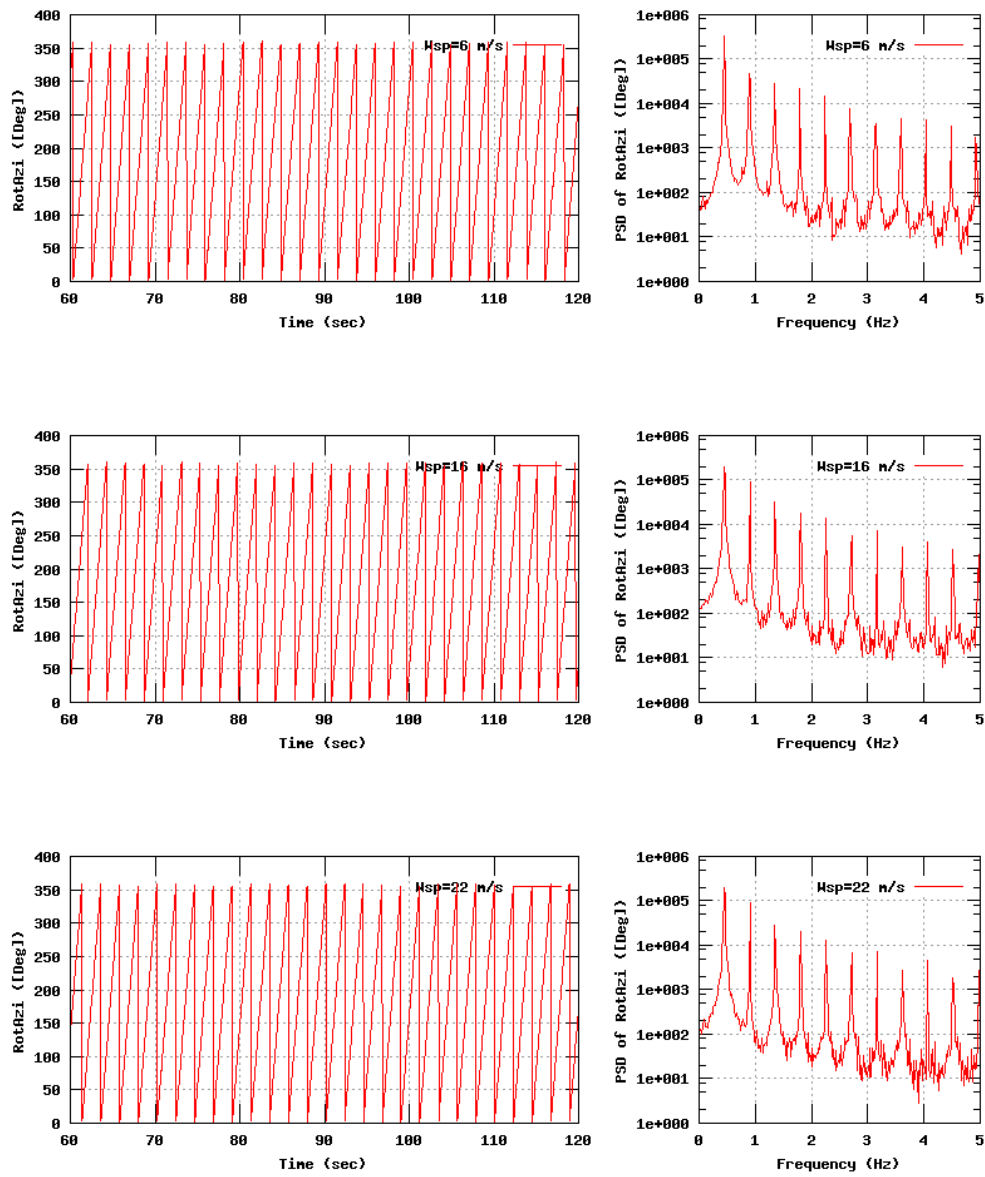
Figure 22b, Sensor 87: Rotor blade azimuth angle RotAzi versus time and frequency
Input files: m06.dat, m16.dat, m22.dat, m06.psd, m16.psd and m22.psd
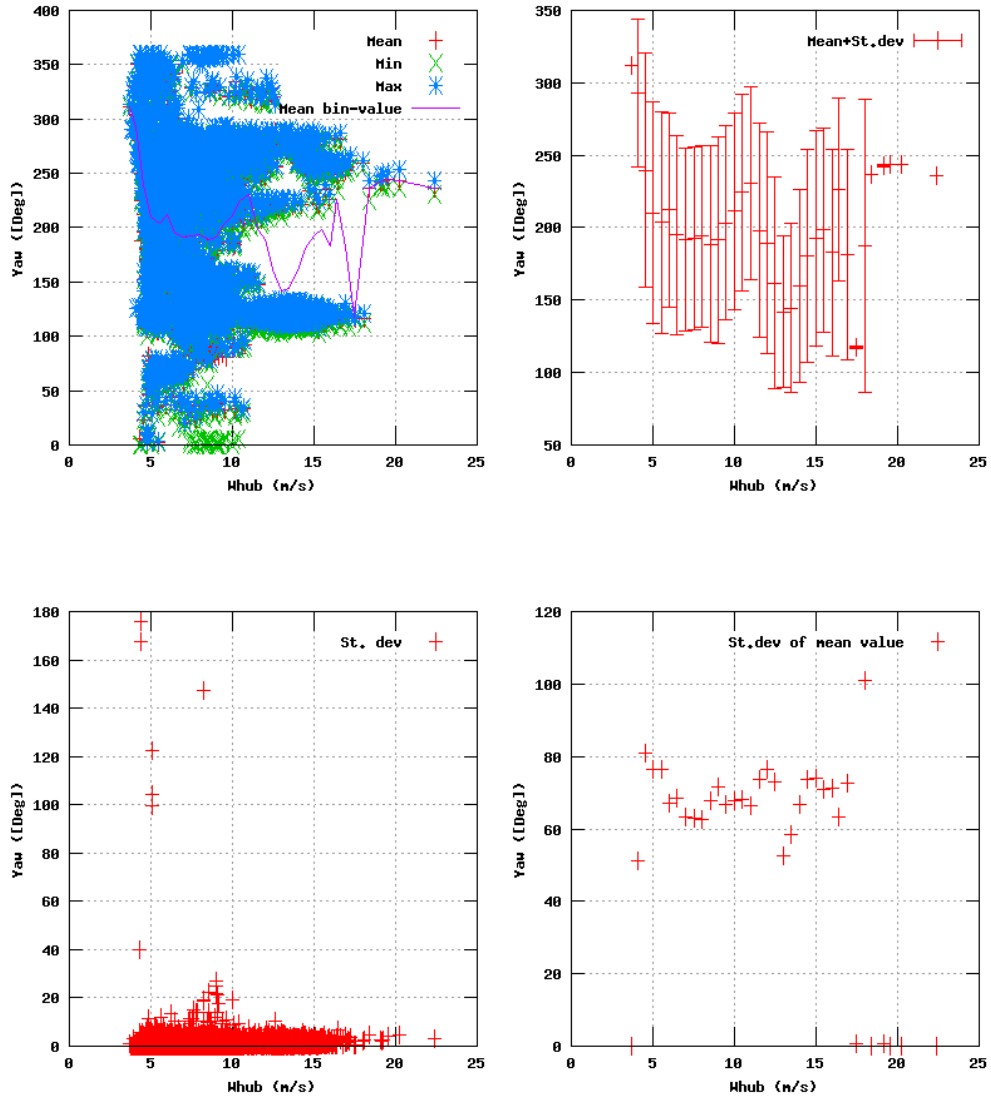
Figure 21a, Sensor 83: Wind turbine nacelle position Yaw versus wind speed
Input files: ntk500res.dat, stat_83.dat
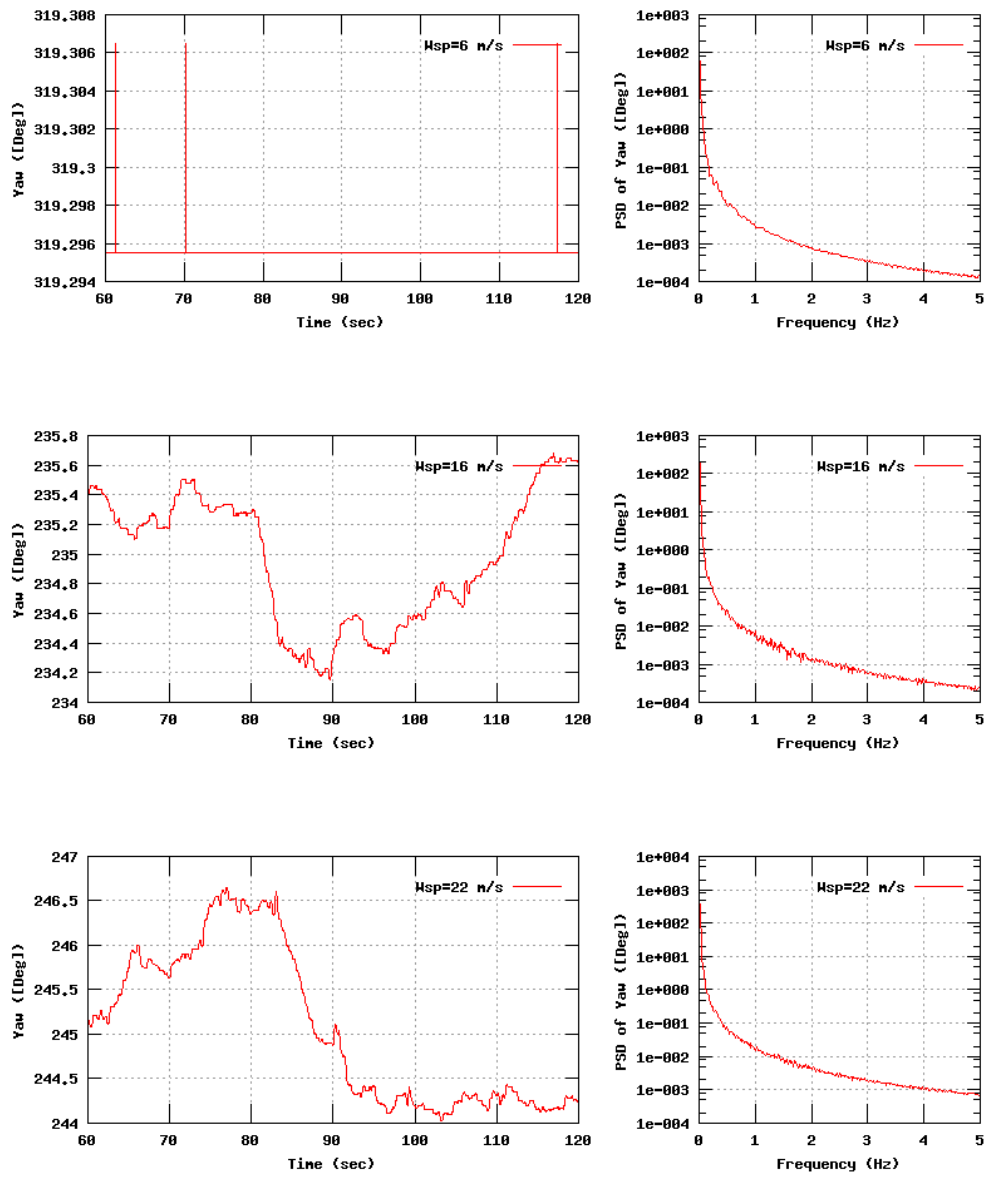
Figure 21b, Sensor 83: Wind turbine nacelle position Yaw versus time and frequency
Input files: m06.dat, m16.dat, m22.dat, m06.psd, m16.psd and m22.psd
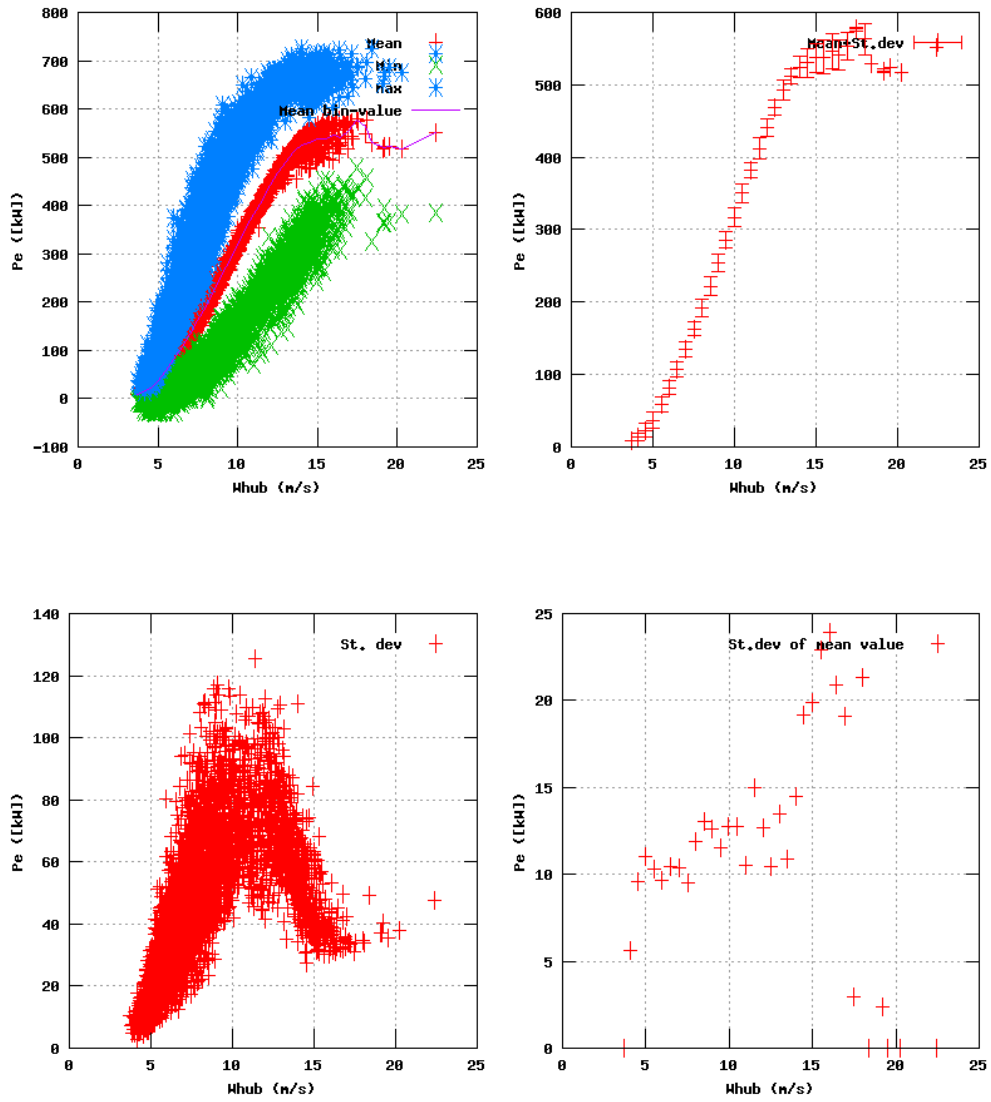
Figure 7a, Sensor 27: Electrical net power Pe versus wind speed
Input files: ntk500res.dat, stat_27.dat
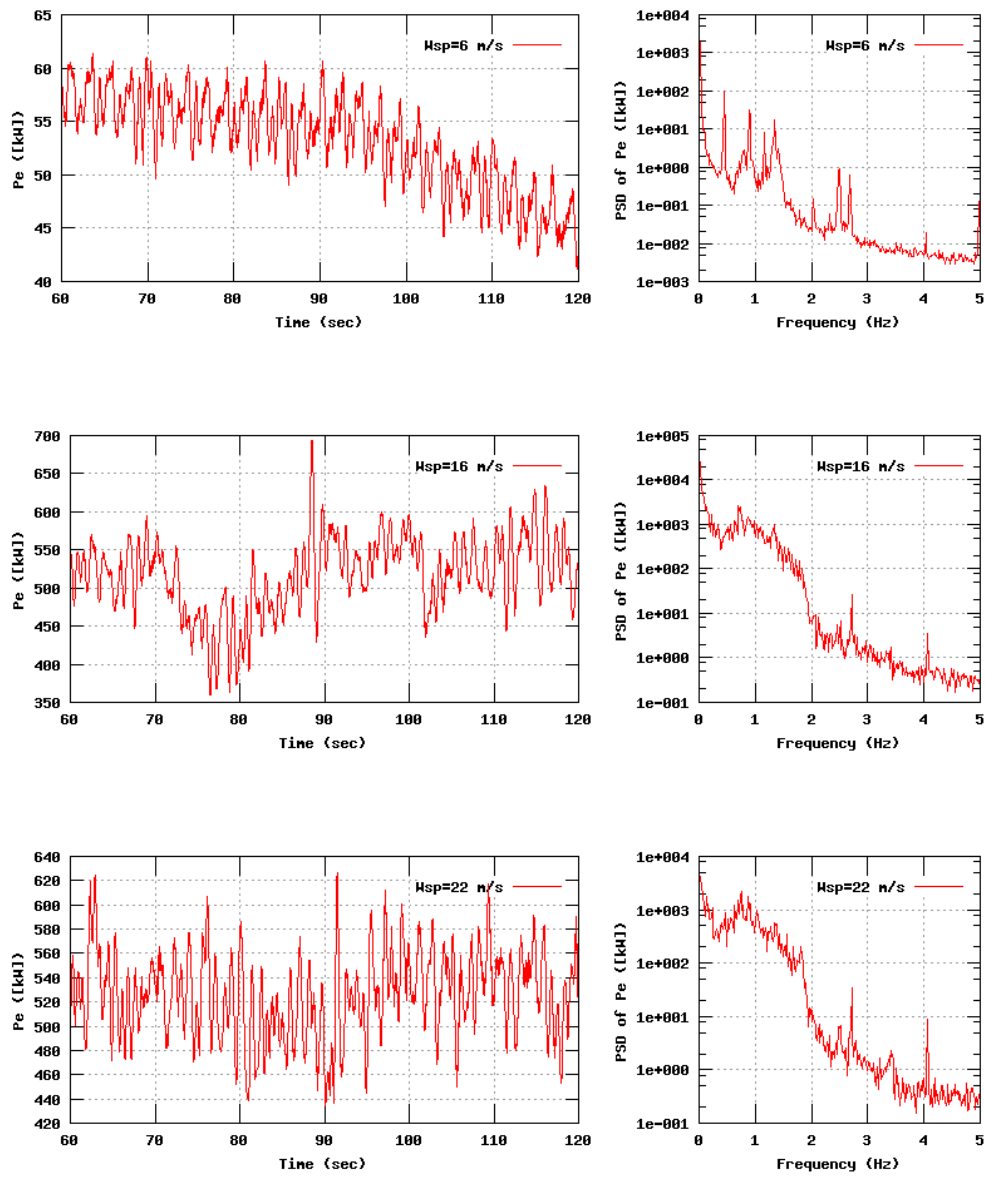
Figure 7b, Sensor 27: Electrical net power Pe versus time and frequency
Input files: m06.dat, m16.dat, m22.dat, m06.psd, m16.psd and m22.psd
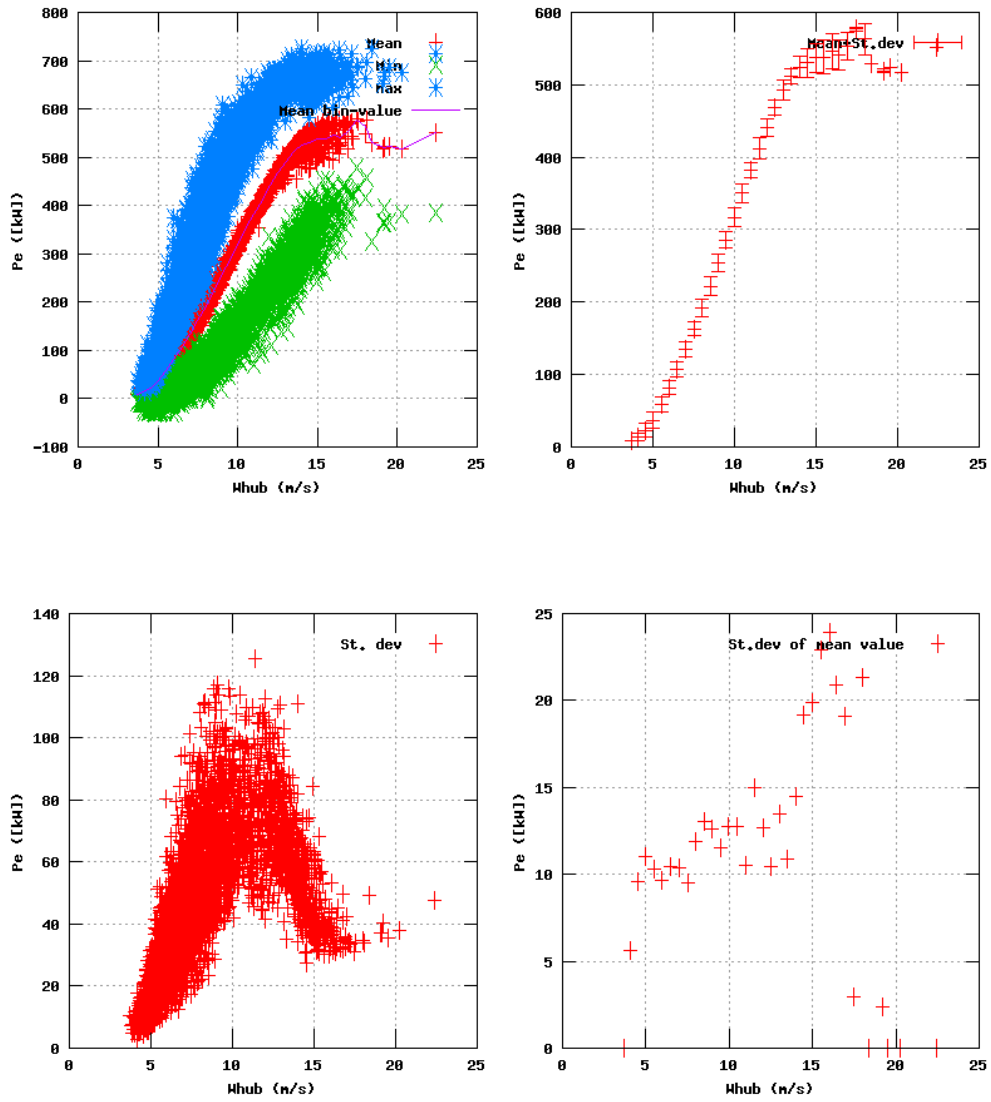
Figure 7a, Sensor 27: Electrical net power Pe versus wind speed
Input files: ntk500res.dat, stat_27.dat
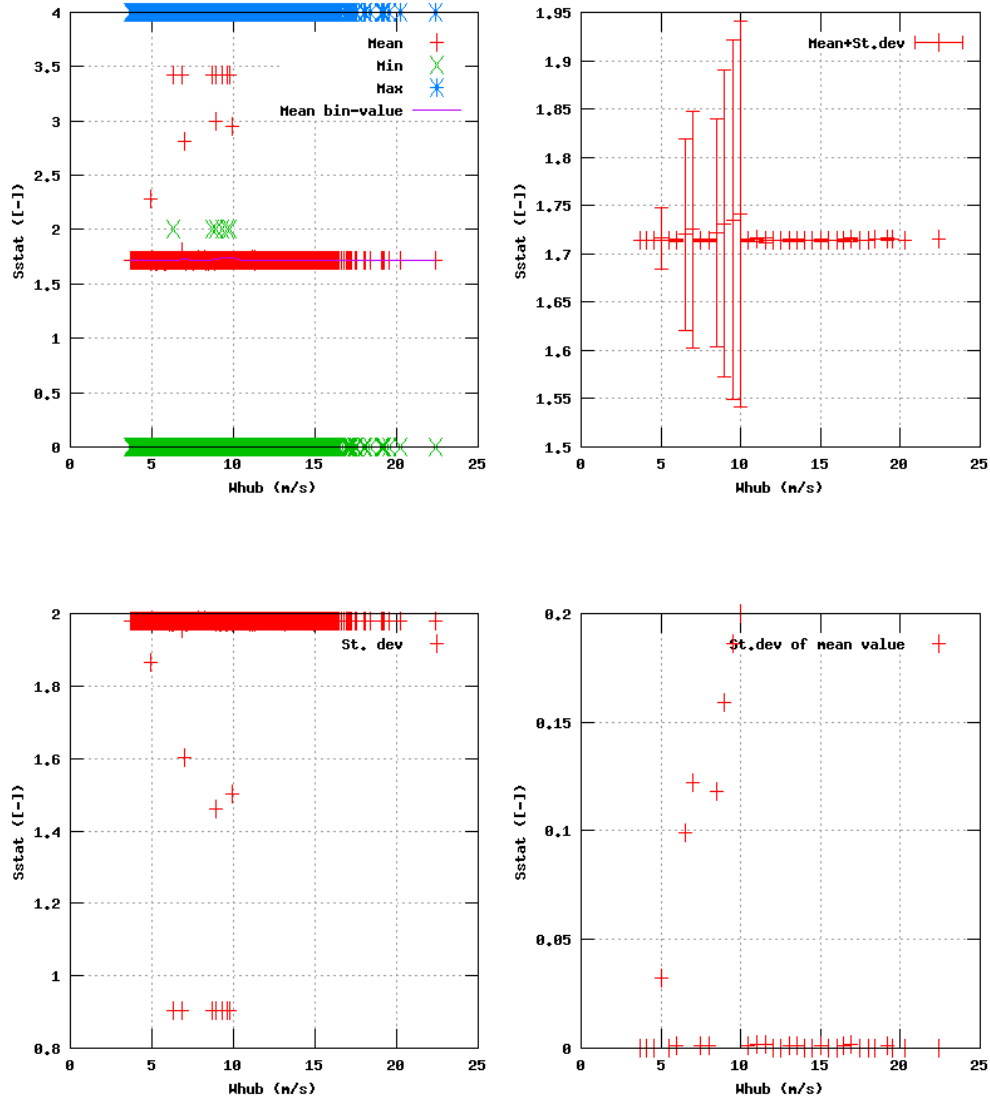
Figure 48a, Sensor 191: Sonic status Sstat versus wind speed
Input files: ntk500res.dat, stat_191.dat
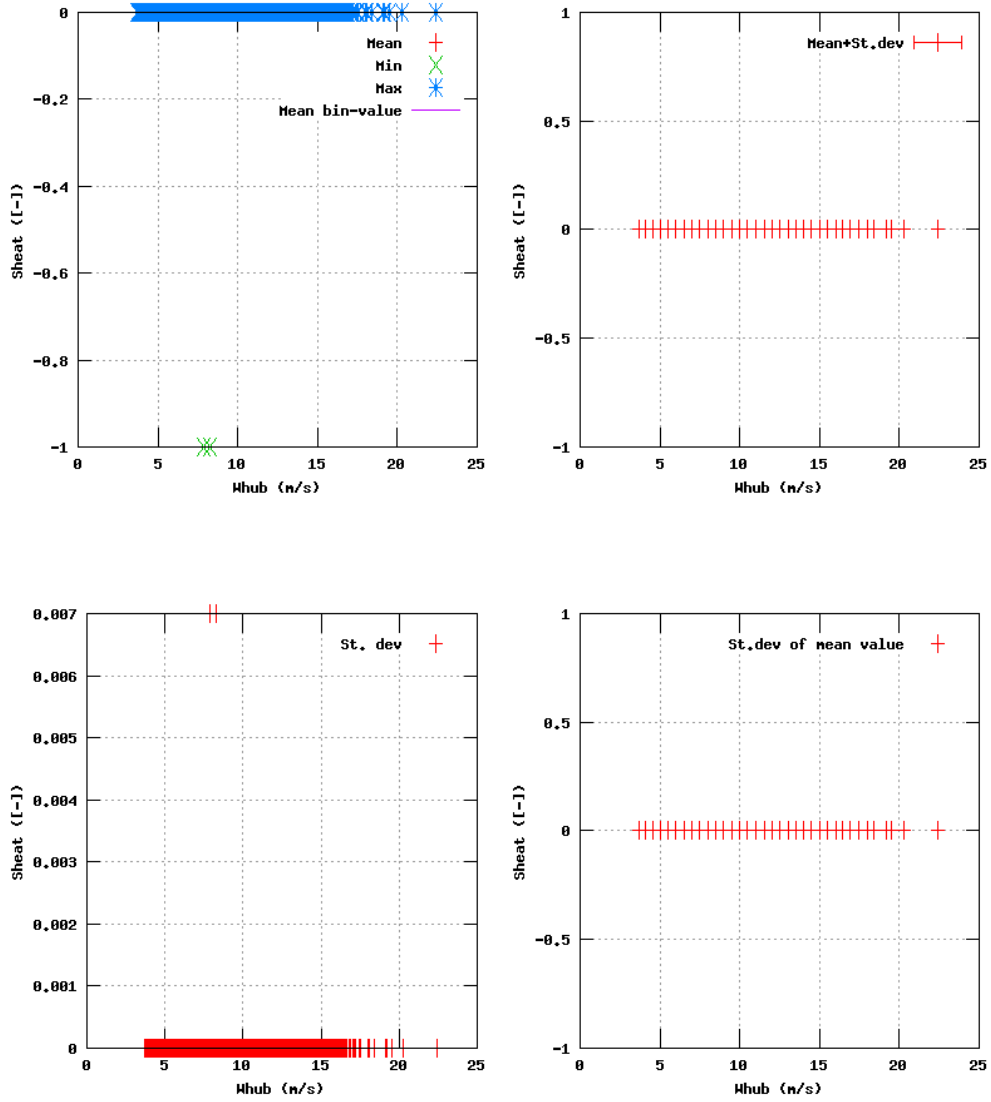
Figure 49a, Sensor 195: Sonic status Sheat versus wind speed
Input files: ntk500res.dat, stat_195.dat
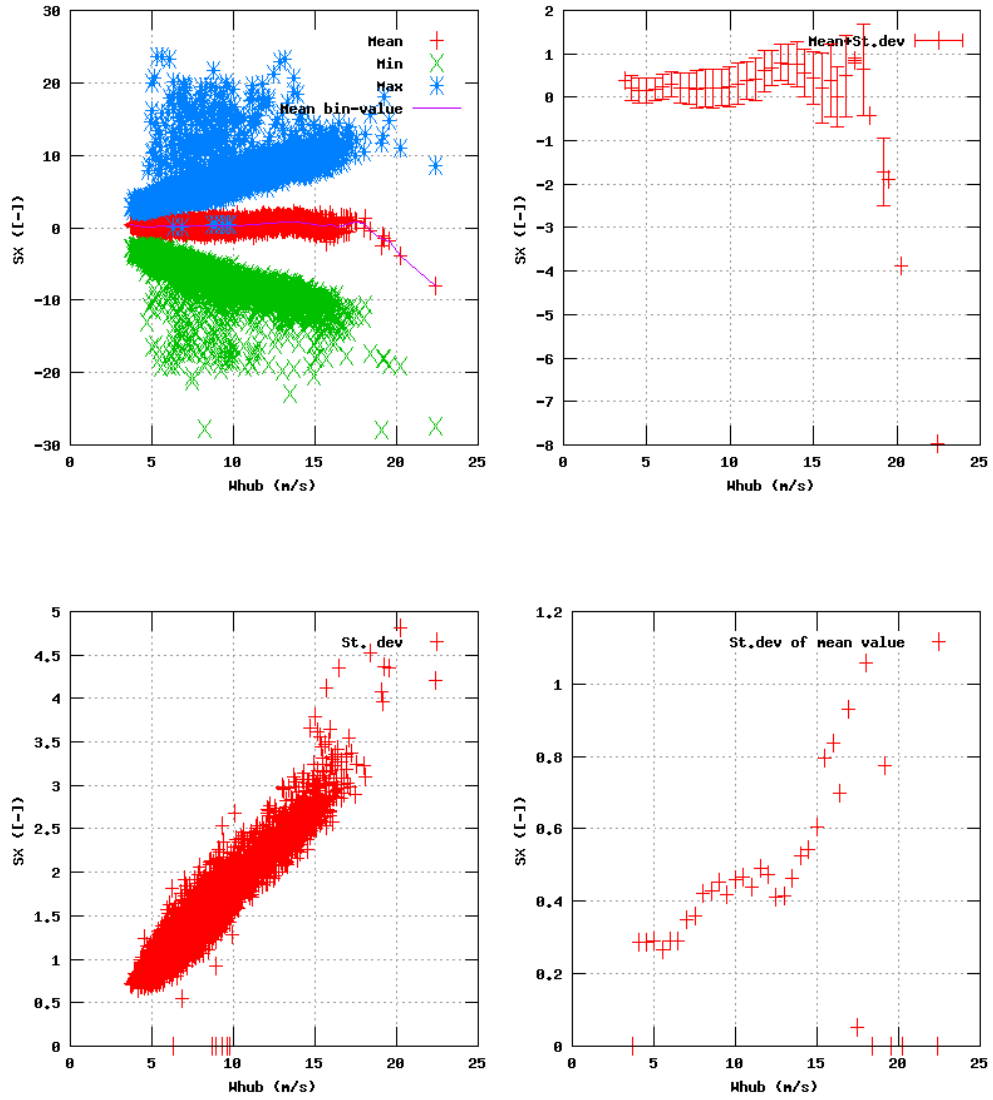
Figure 50a, Sensor 199: Sonic wind component SX versus wind speed
Input files: ntk500res.dat, stat_199.dat
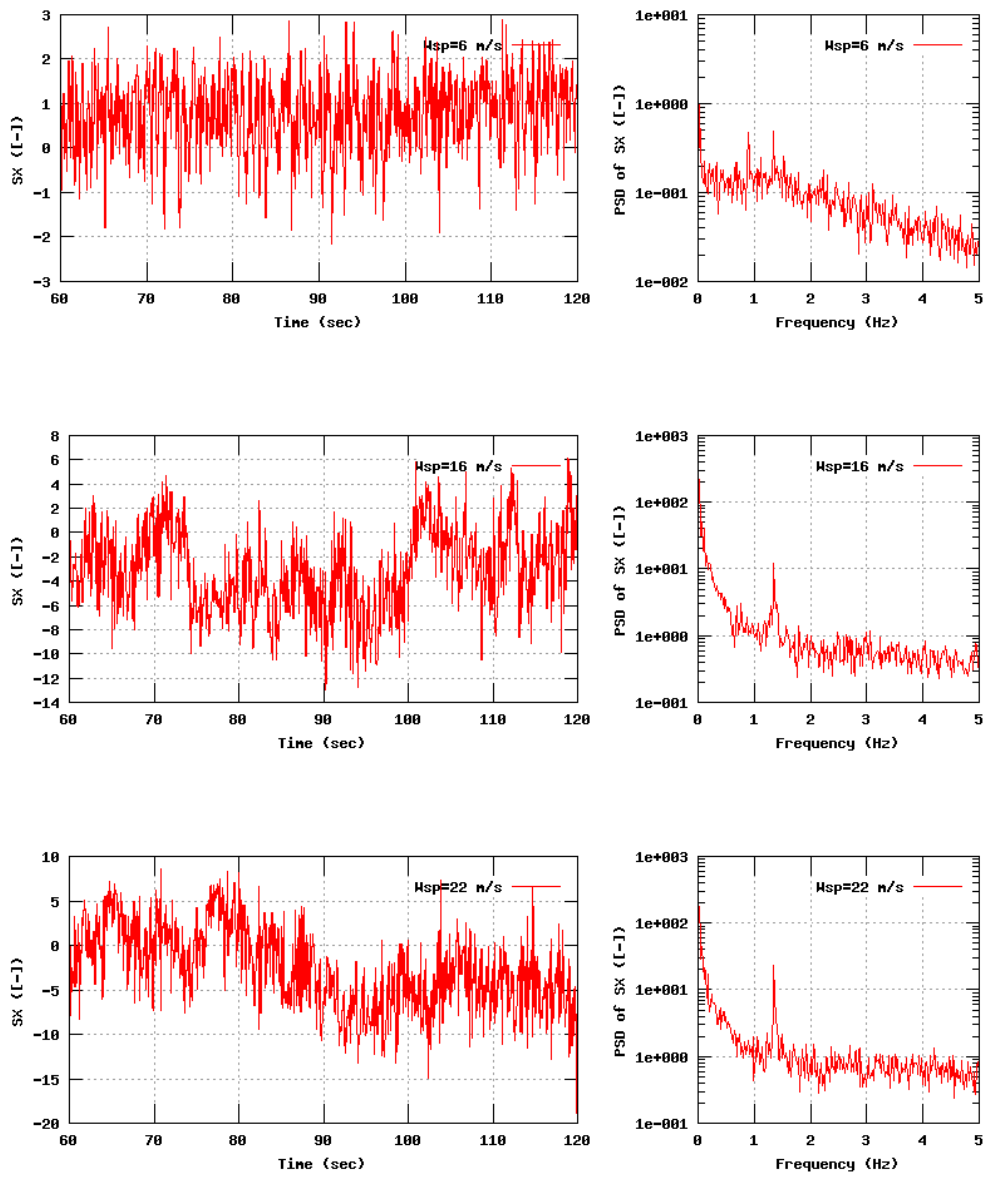
Figure 50b, Sensor 199: Sonic wind component SX versus time and frequency
Input files: m06.dat, m16.dat, m22.dat, m06.psd, m16.psd and m22.psd

Risø-R-1782(EN)
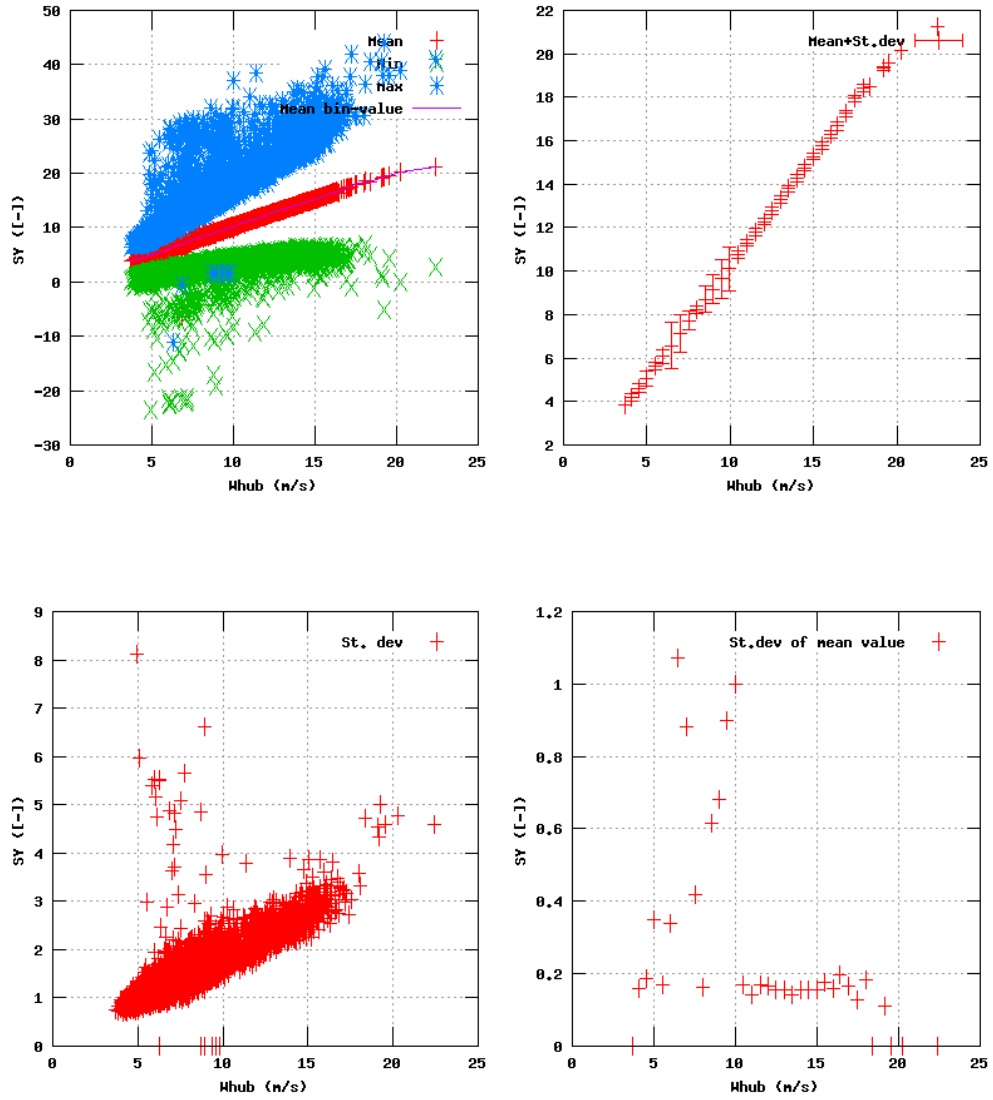
Figure 51a, Sensor 203: Sonic wind component SY versus wind speed
Input files: ntk500res.dat, stat_203.dat
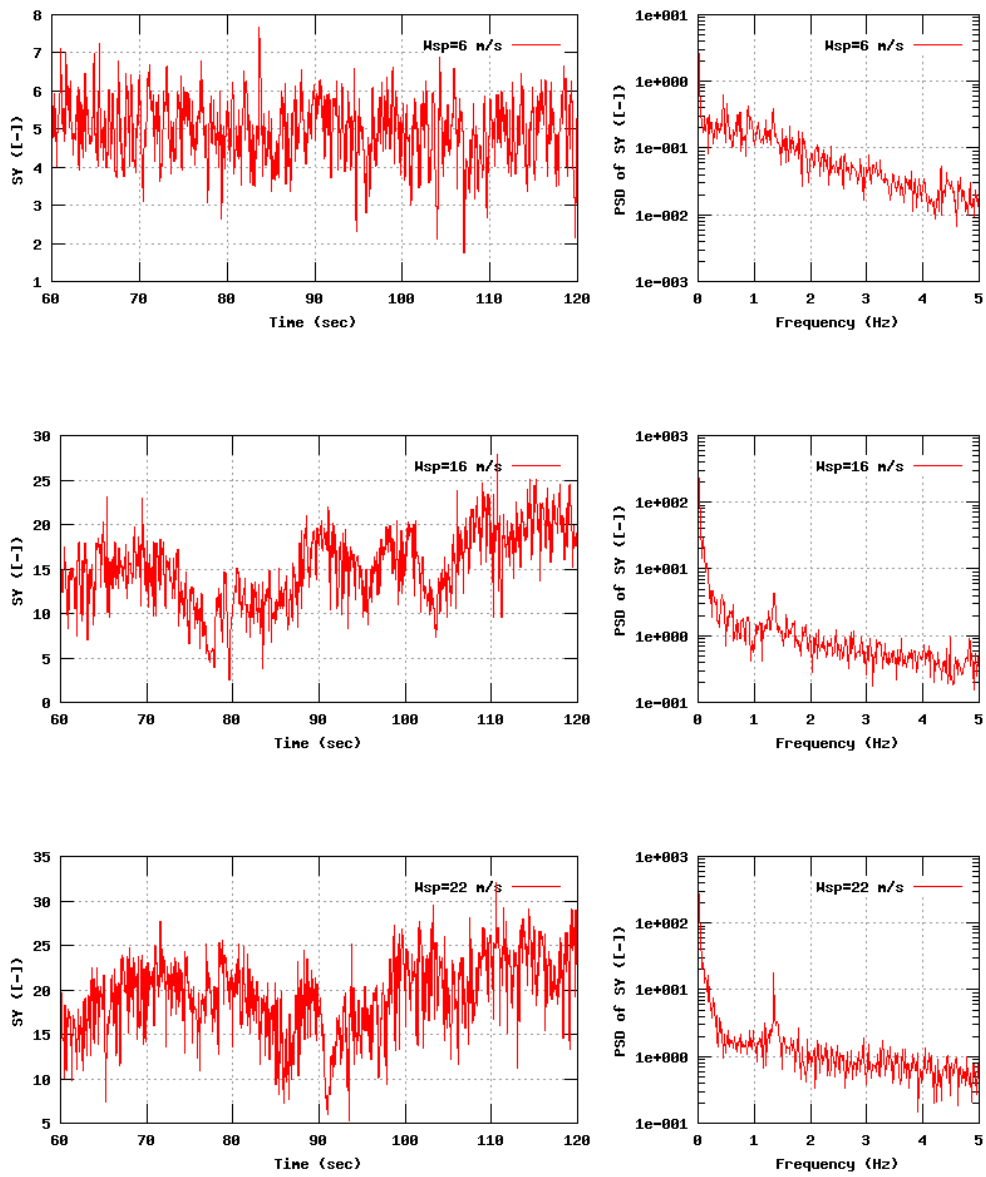
Figure 51b, Sensor 203: Sonic wind component SY versus time and frequency
Input files: m06.dat, m16.dat, m22.dat, m06.psd, m16.psd and m22.psd
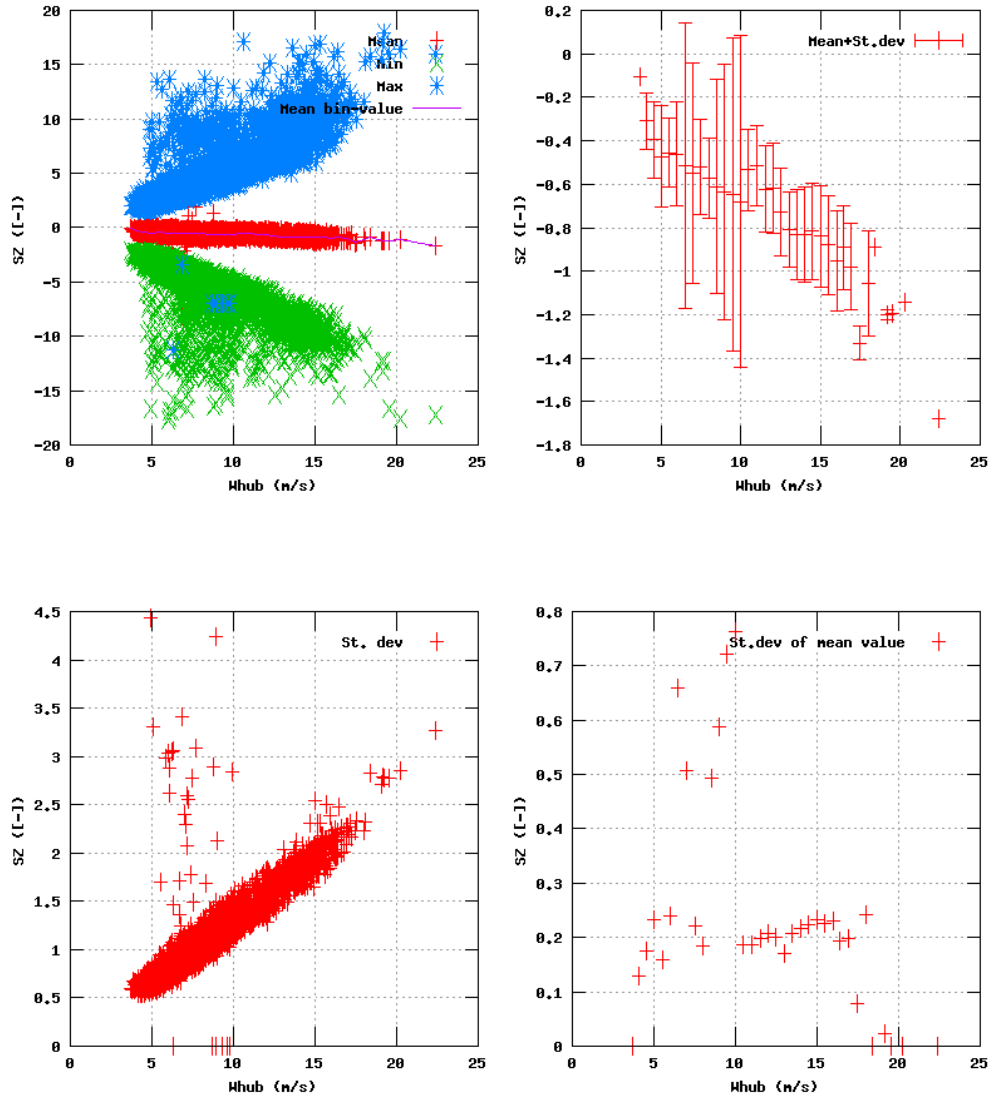
Figure 52a, Sensor 207: Sonic wind component SZ versus wind speed
Input files: ntk500res.dat, stat_207.dat
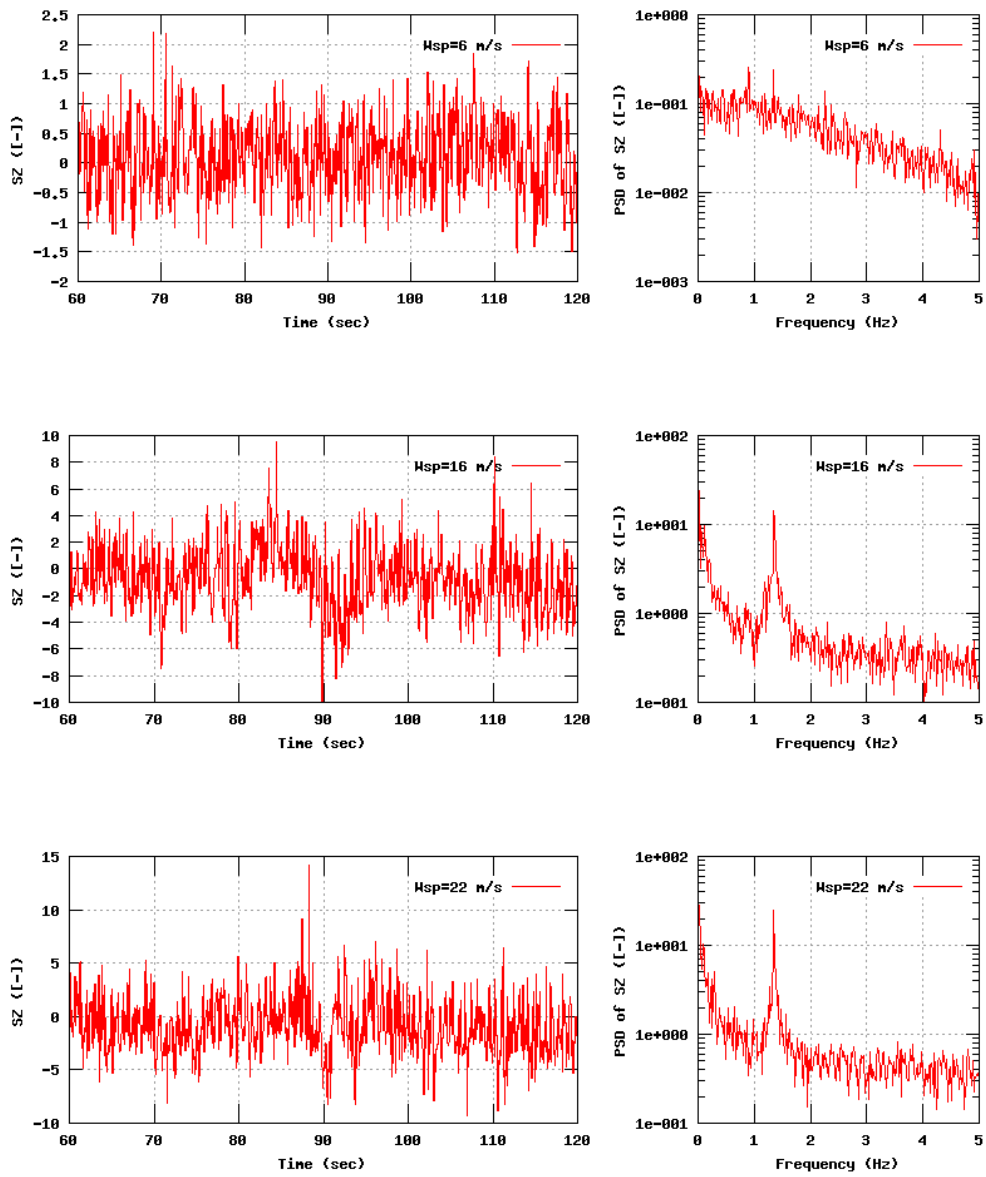
Figure 52b, Sensor 207: Sonic wind component SZ versus time and frequency
Input files: m06.dat, m16.dat, m22.dat, m06.psd, m16.psd and m22.psd
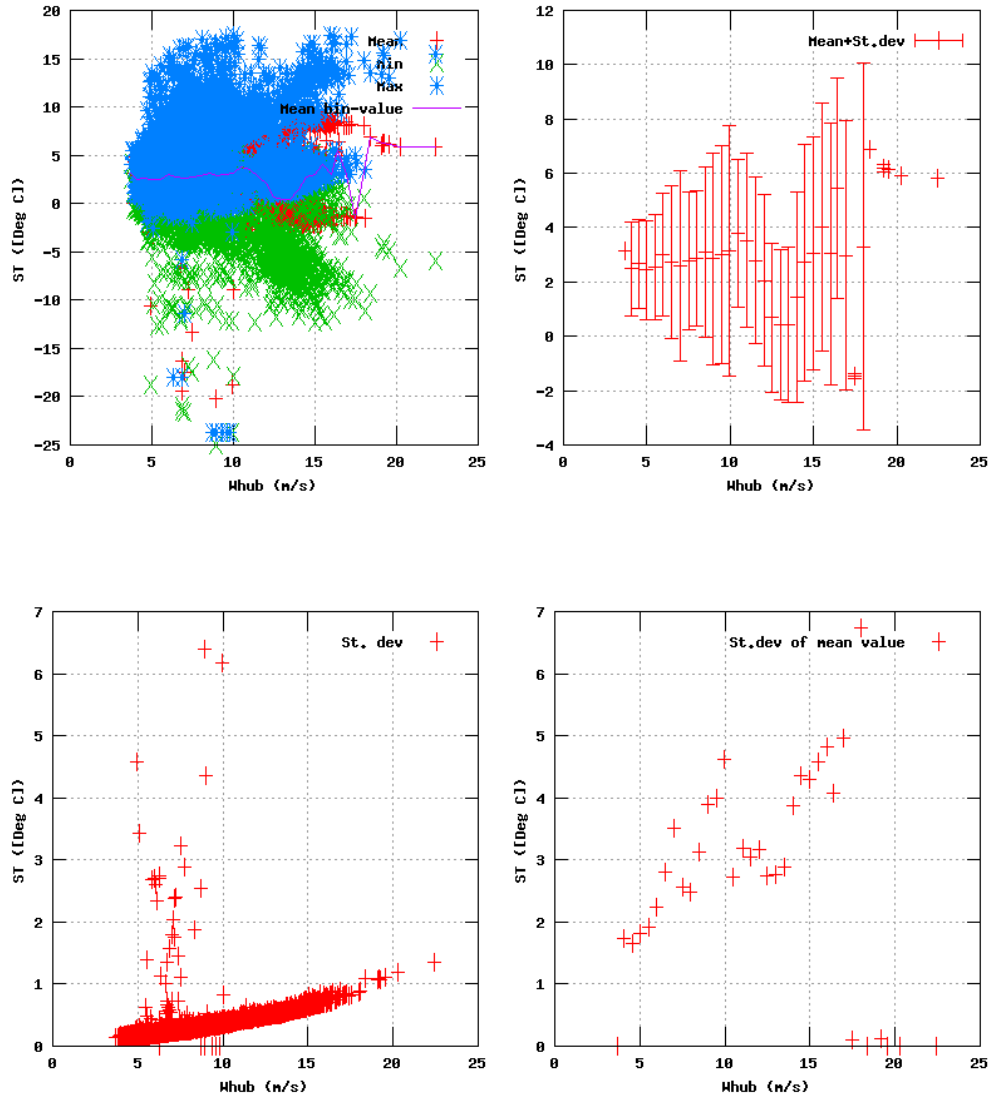
Figure 53a, Sensor 211: Sonic air temperature ST versus wind speed
Input files: ntk500res.dat, stat_211.dat
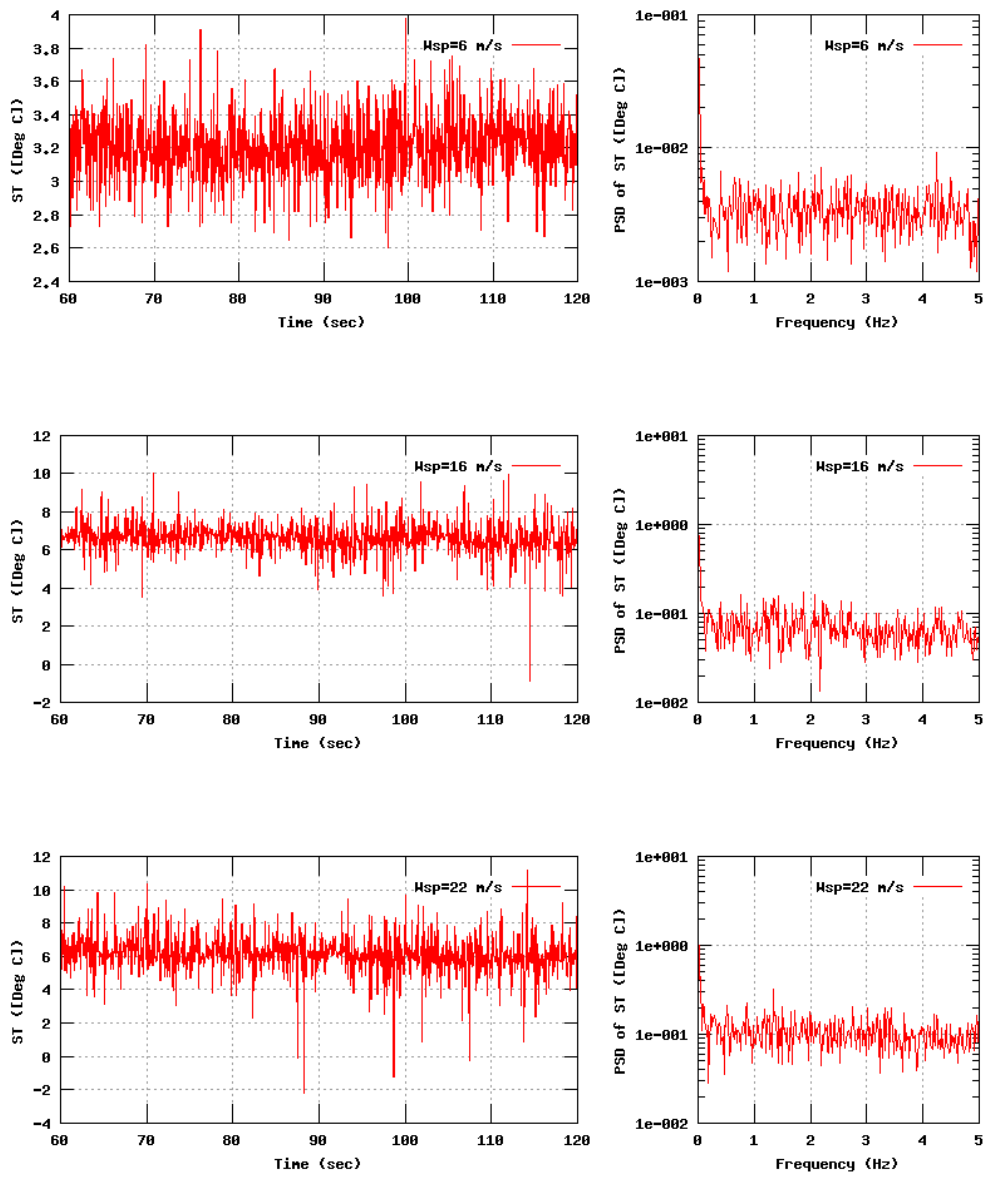
Figure 53b, Sensor 211: Sonic air temperature ST versus time and frequency
Input files: m06.dat, m16.dat, m22.dat, m06.psd, m16.psd and m22.psd
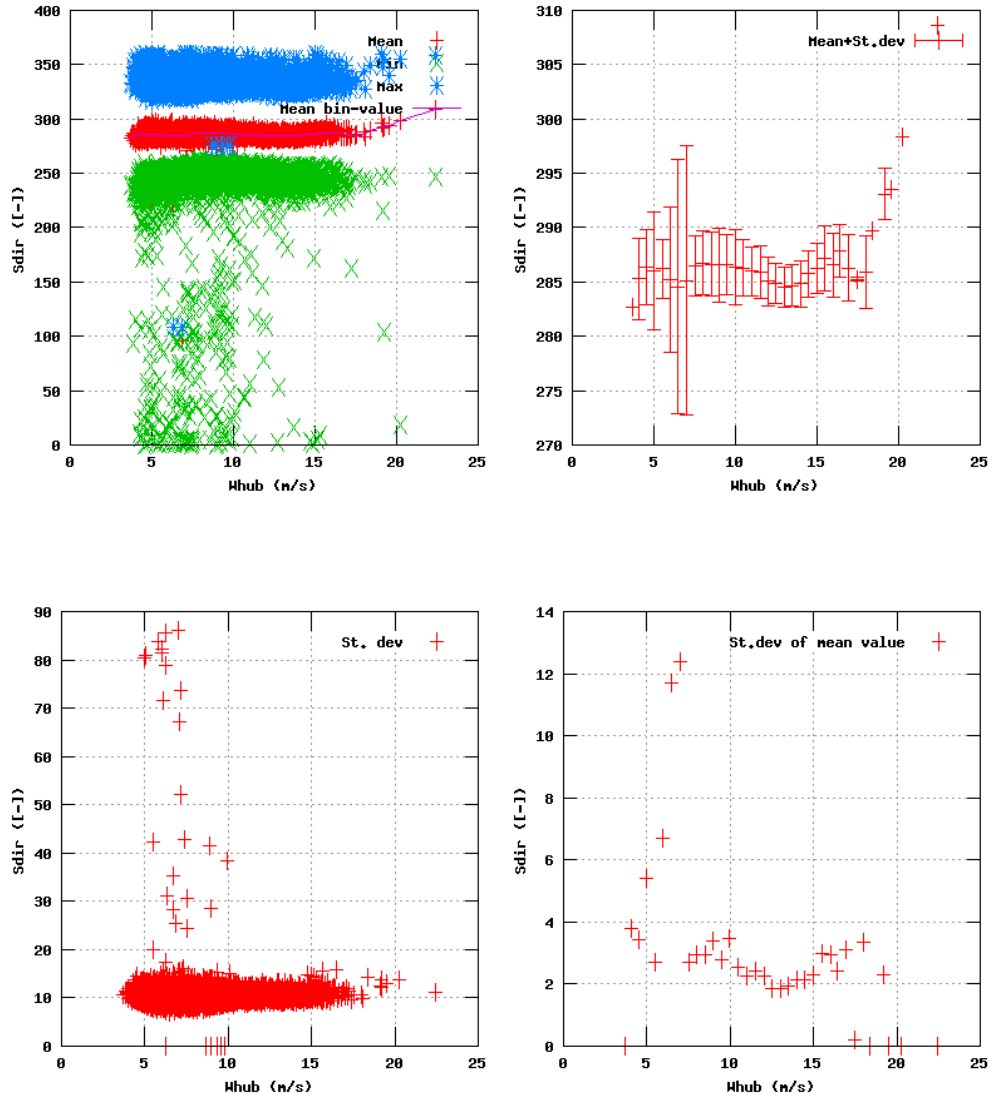
Figure 54a, Sensor 215: Sonic horisontal flow direction Sdir versus wind speed
Input files: ntk500res.dat, stat_215.dat
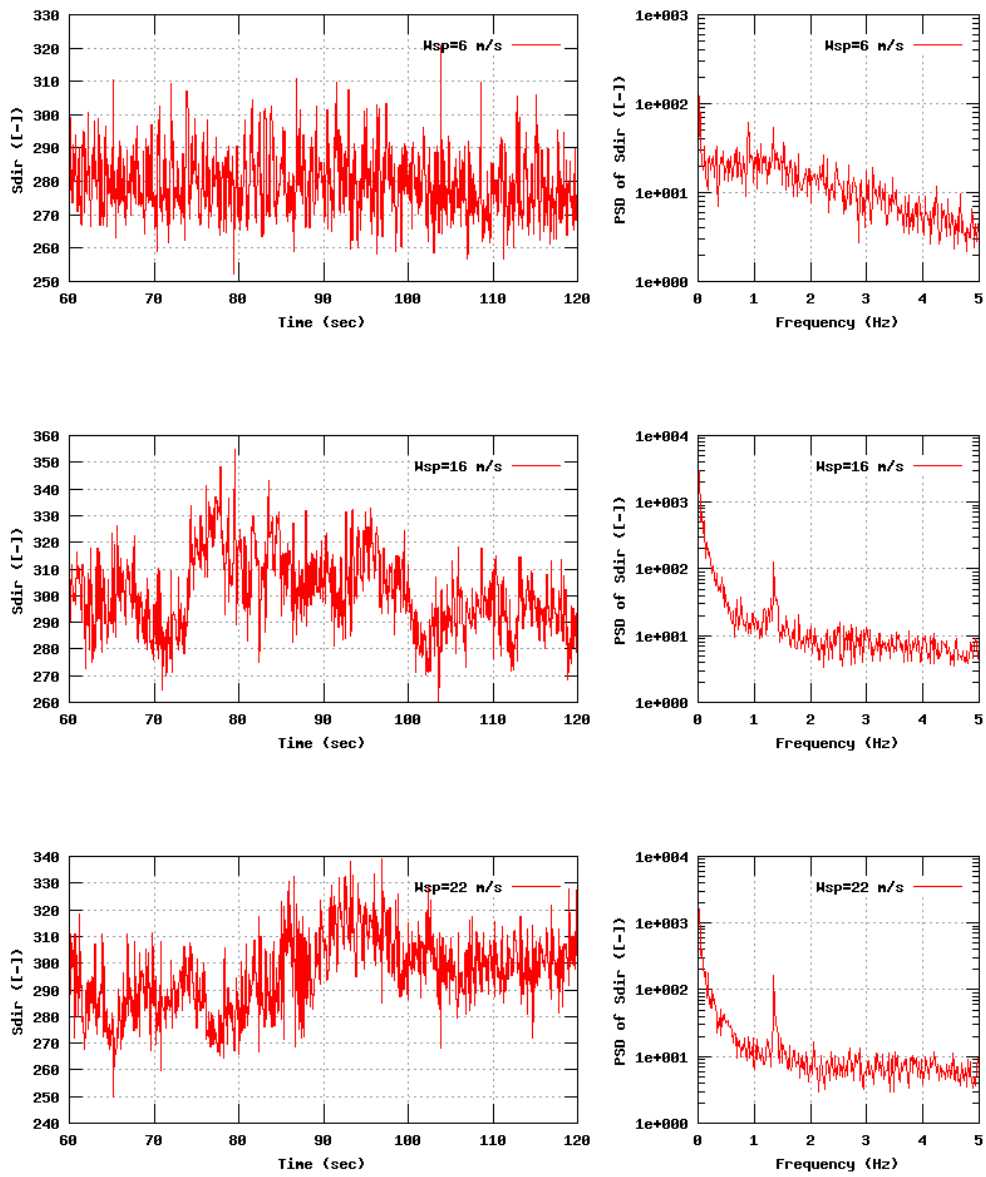
Figure 54b, Sensor 215: Sonic horisontal flow direction Sdir versus time and frequency
Input files: m06.dat, m16.dat, m22.dat, m06.psd, m16.psd and m22.psd
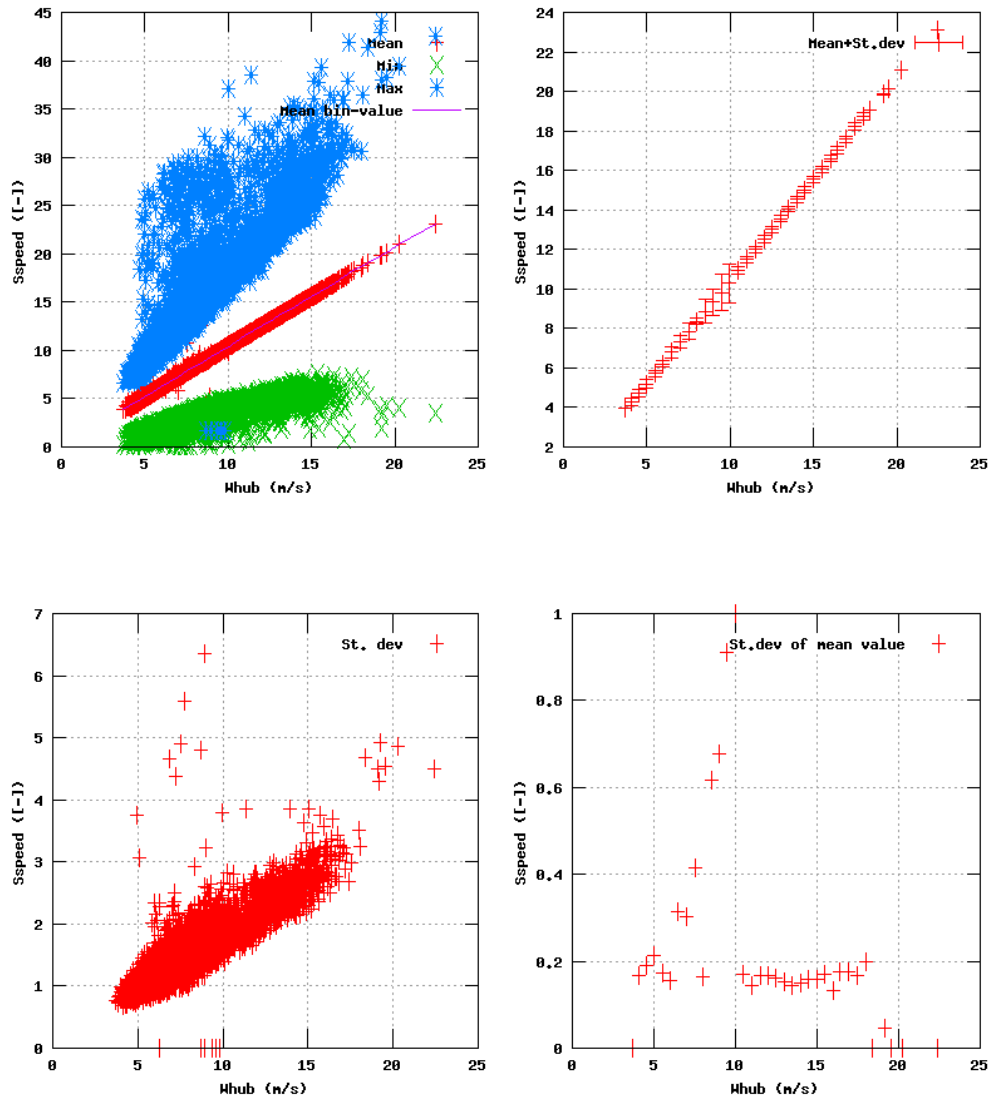
Figure 55a, Sensor 219: Sonic wind speed Sspeed versus wind speed
Input files: ntk500res.dat, stat_219.dat
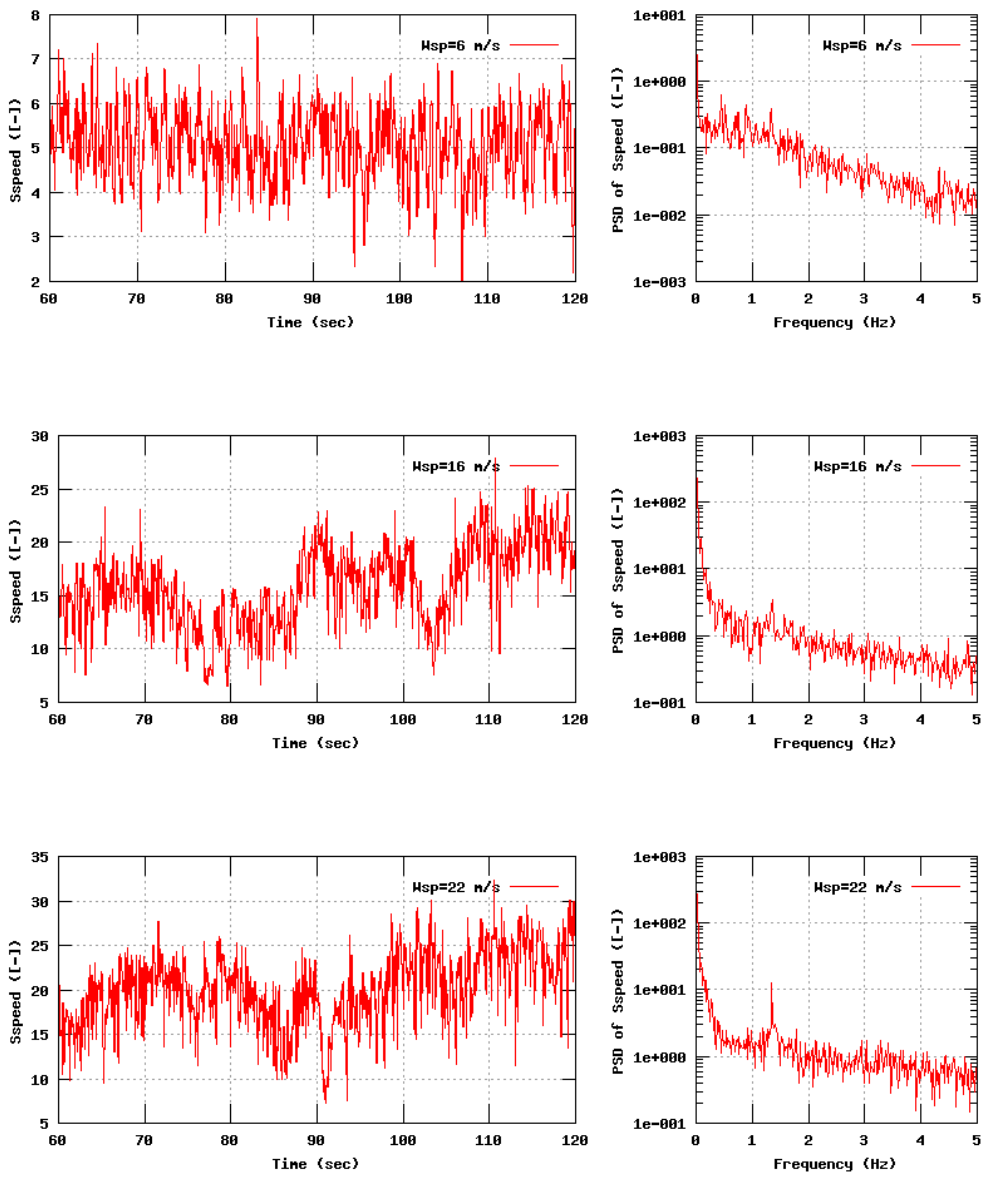
Figure 55b, Sensor 219: Sonic wind speed Sspeed versus time and frequency
Input files: m06.dat, m16.dat, m22.dat, m06.psd, m16.psd and m22.psd

Risø-R-1782(EN)
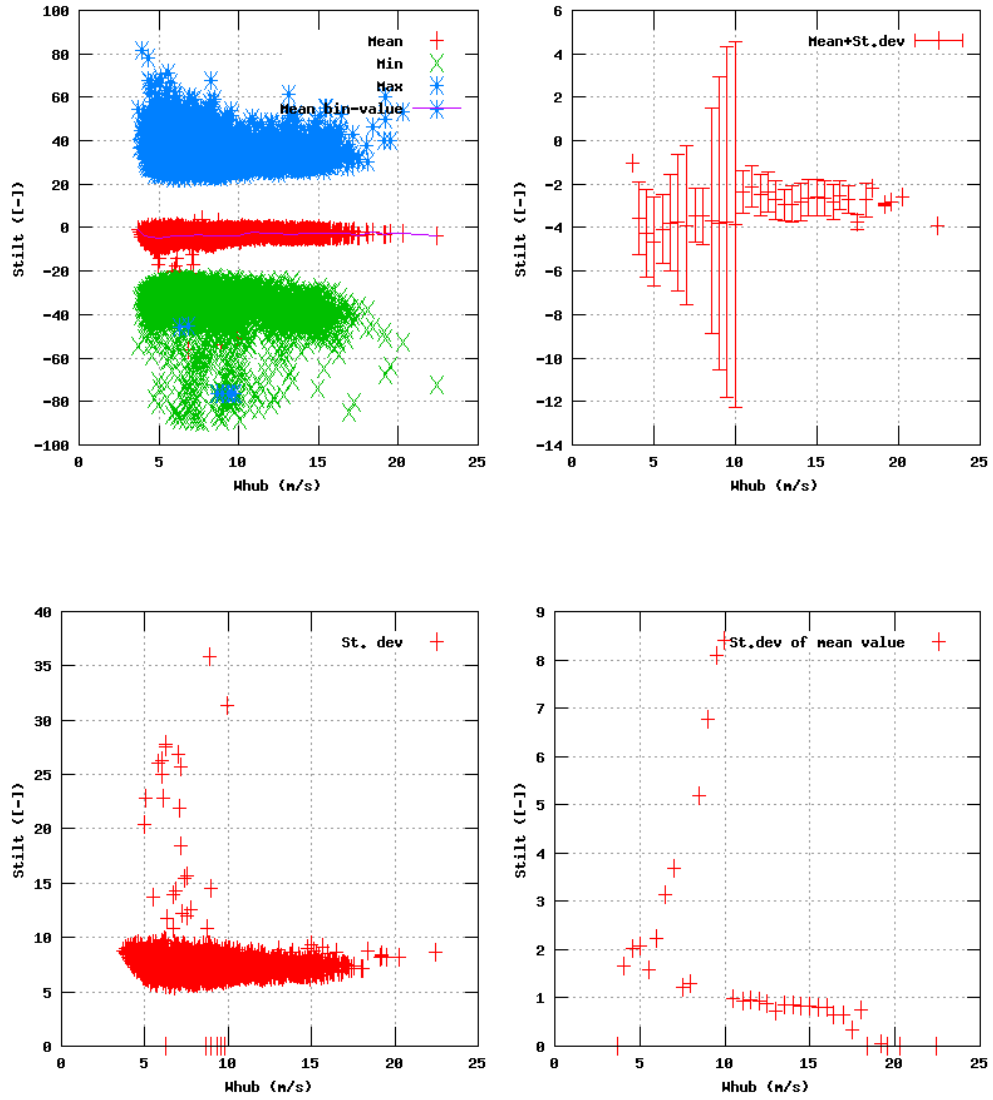
Figure 56a, Sensor 223: Sonic vertical flow angle Stilt versus wind speed
Input files: ntk500res.dat, stat_223.dat
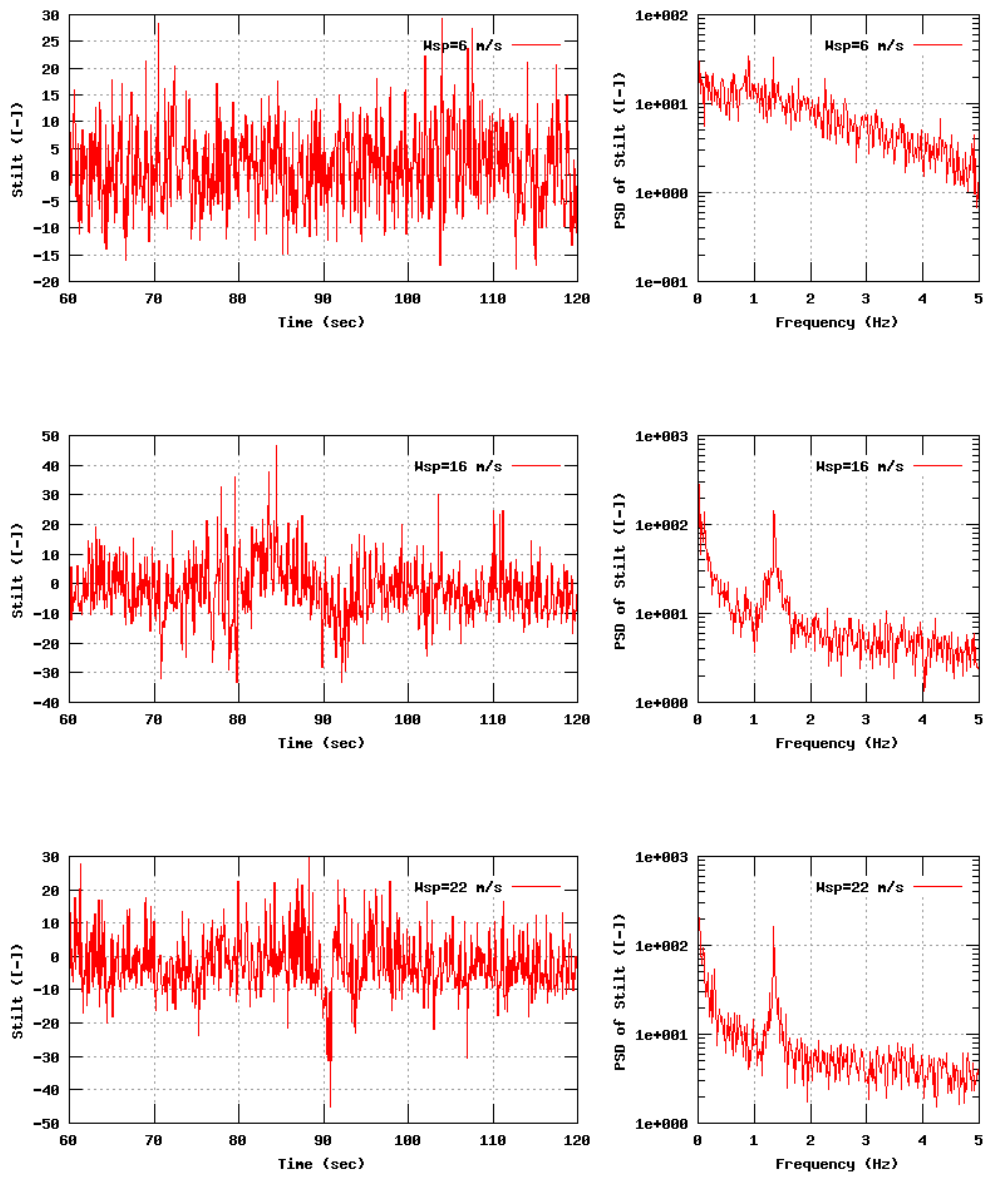
Figure 56b, Sensor 223: Sonic vertical flow angle Stilt versus time and frequency
Input files: m06.dat, m16.dat, m22.dat, m06.psd, m16.psd and m22.psd
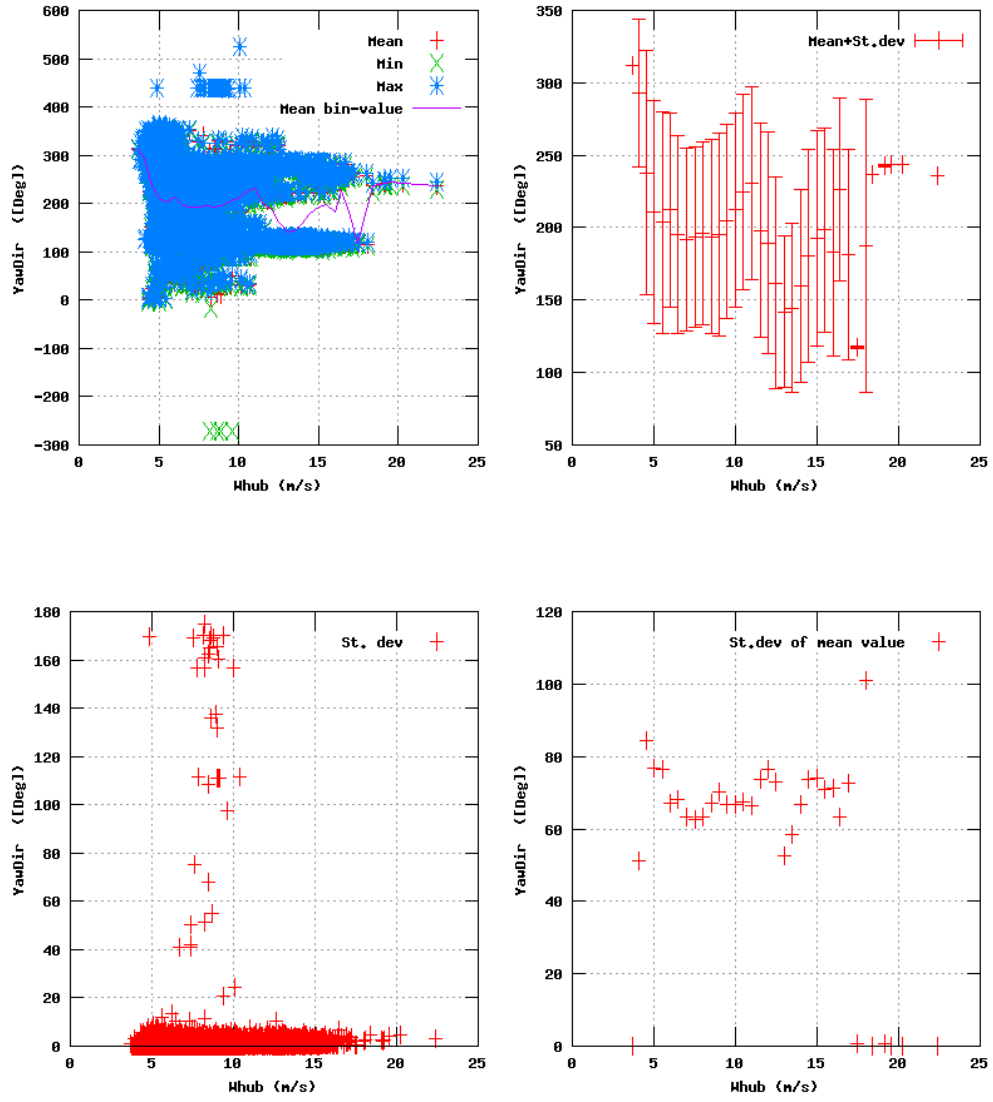
Figure 70a, Sensor 279: YawDir versus wind speed
Input files: ntk500res.dat, stat_279.dat
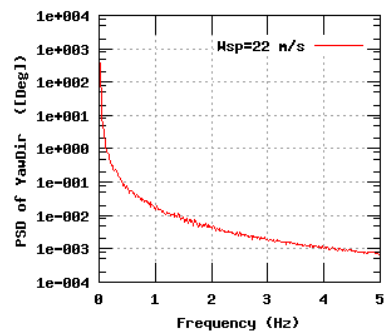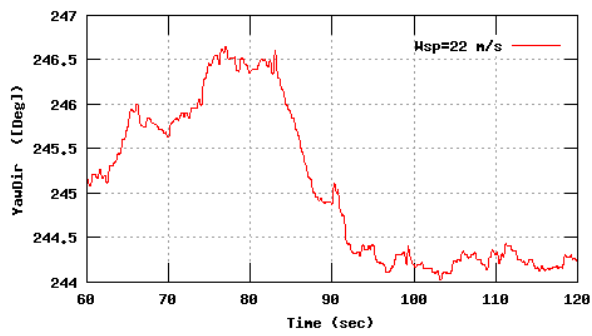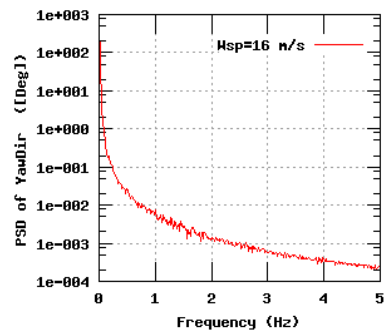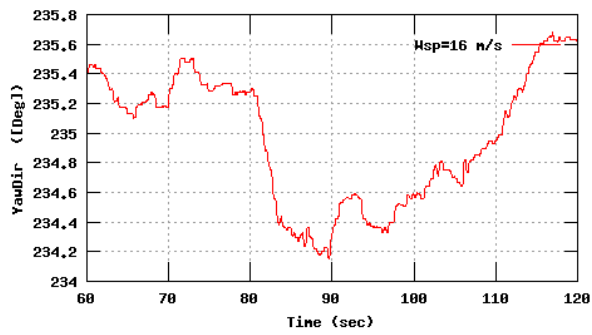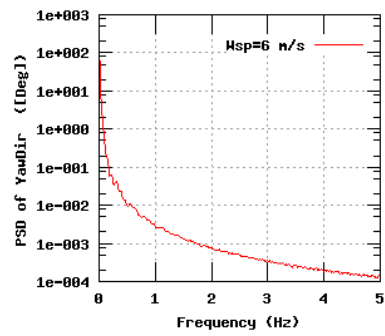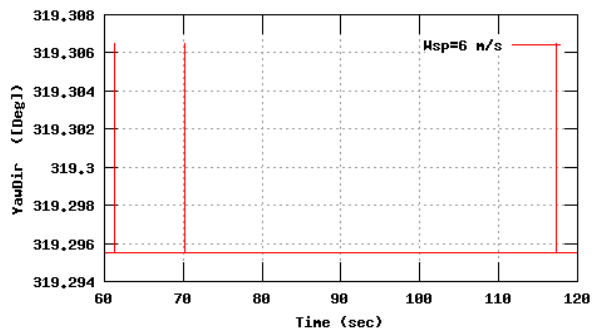
Figure 70b, Sensor 279: YawDir versus time and frequency
Input files: m06.dat, m16.dat, m22.dat, m06.psd, m16.psd and m22.psd
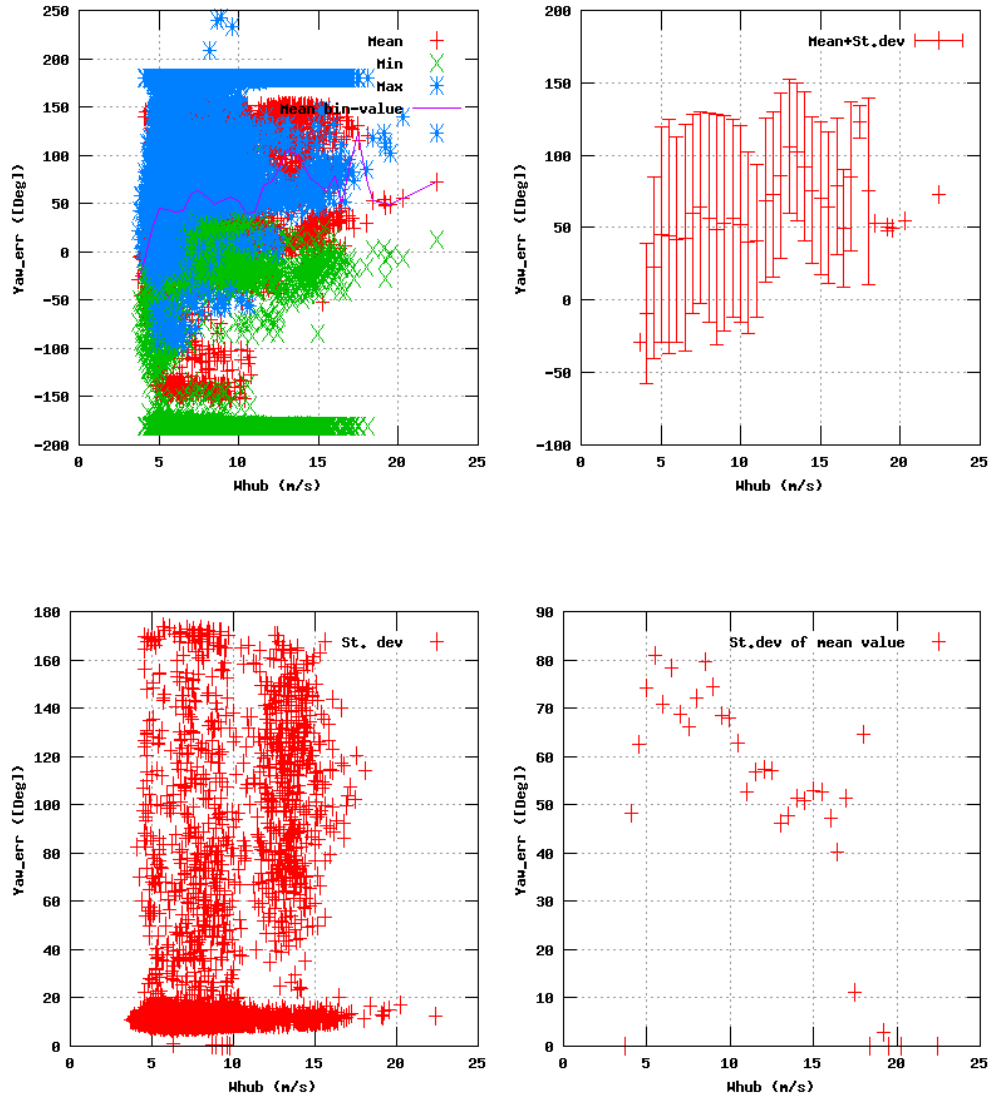
Figure 71a, Sensor 283: Yaw_err versus wind speed
Input files: ntk500res.dat, stat_283.dat
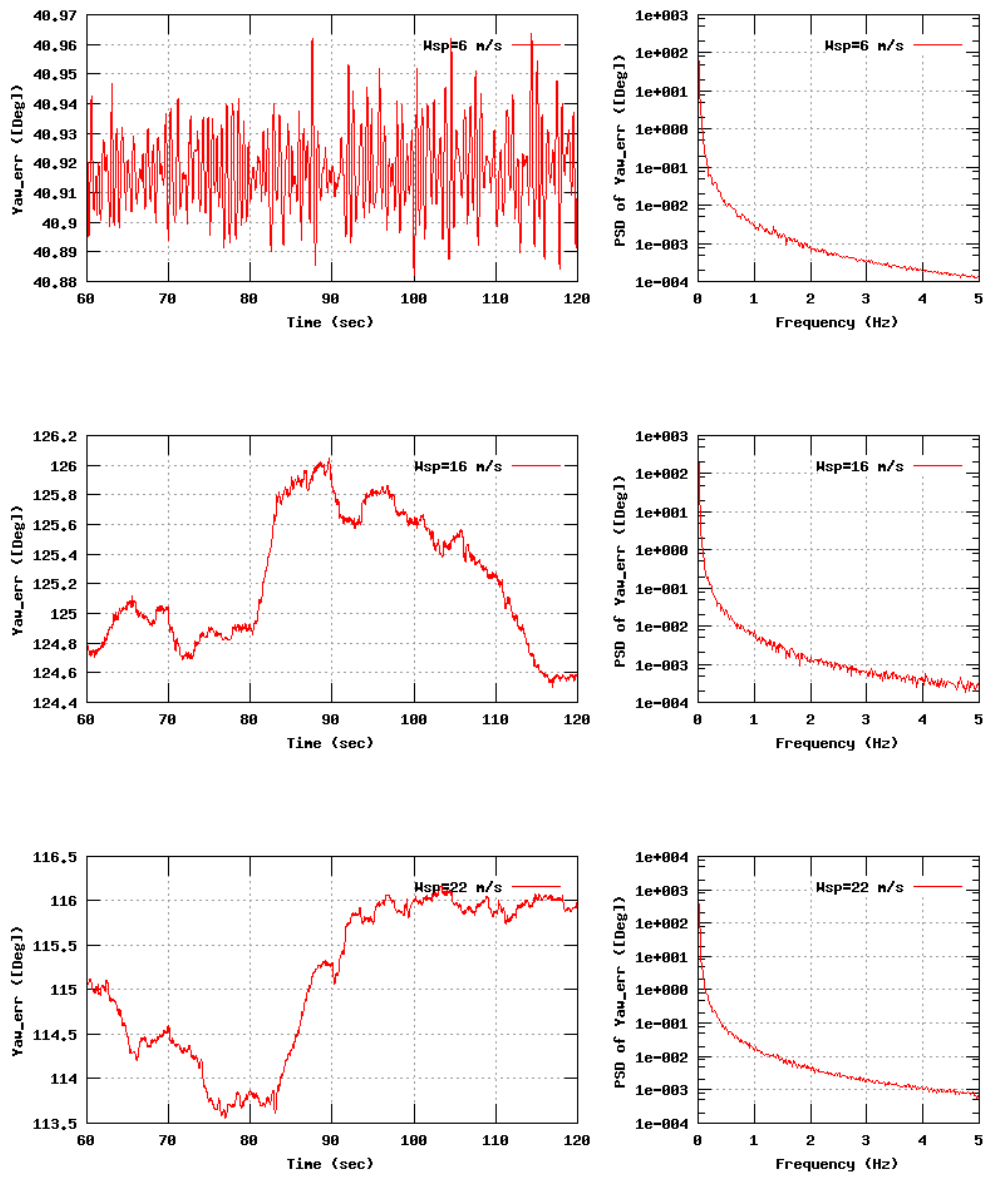
Figure 71b, Sensor 283: Yaw_err versus time and frequency
Input files: m06.dat, m16.dat, m22.dat, m06.psd, m16.psd and m22.psd
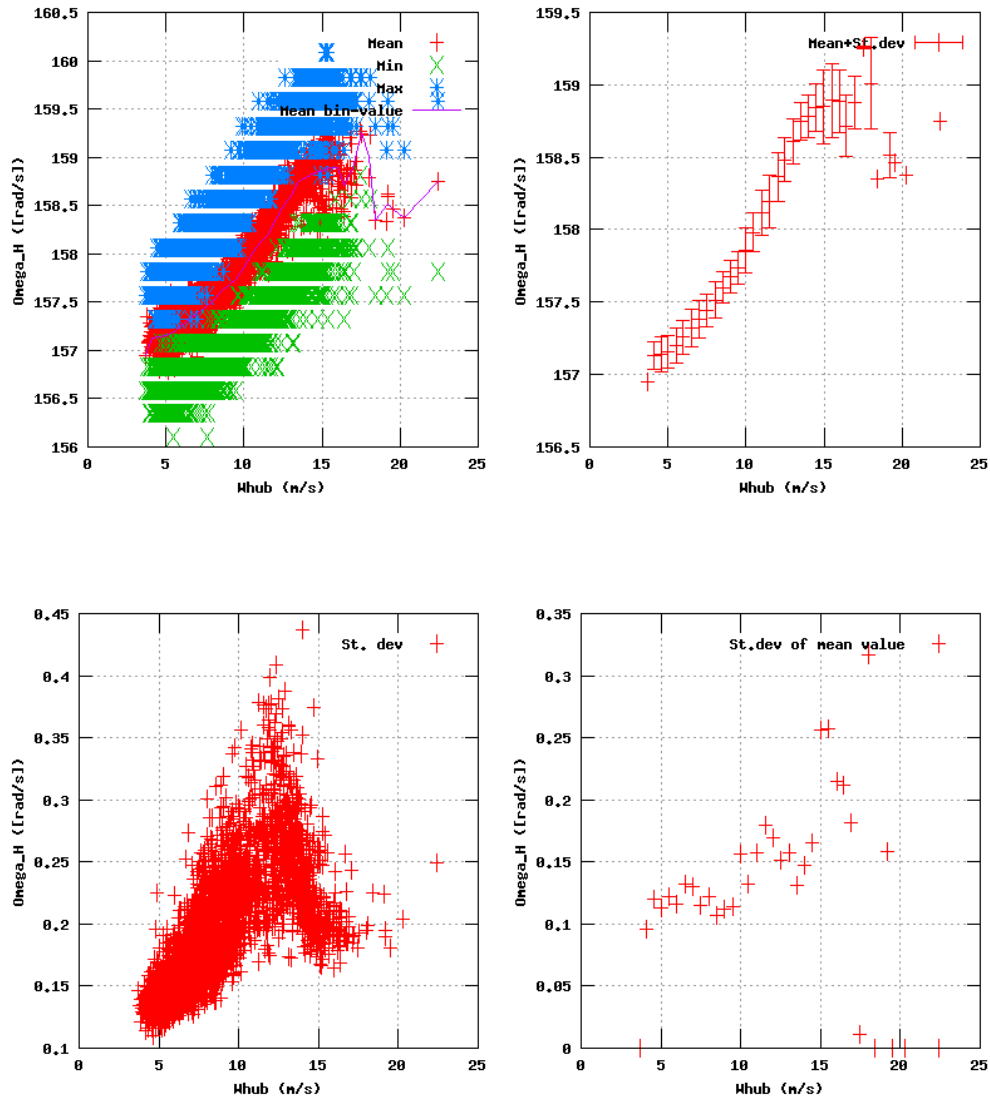
Figure 77a, Sensor 307: Rotor speed Omega_HSS versus wind speed
Input files: ntk500res.dat, stat_307.dat
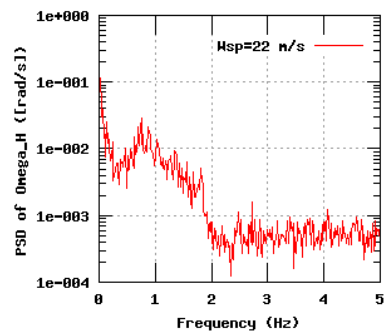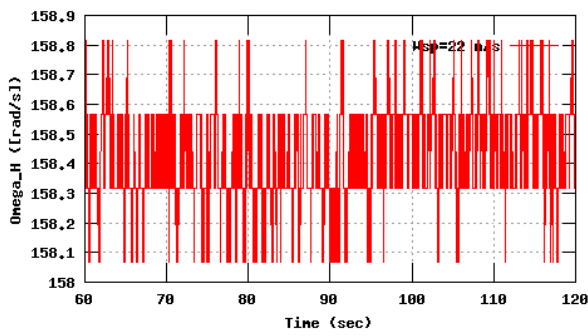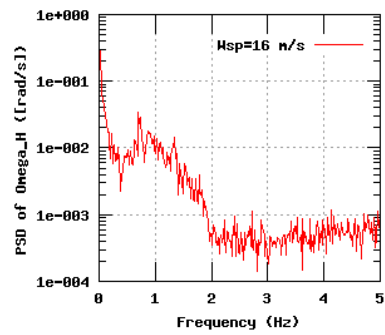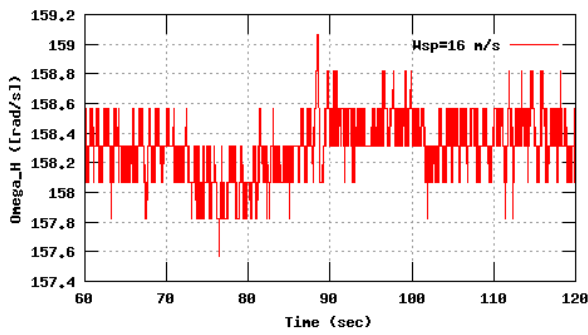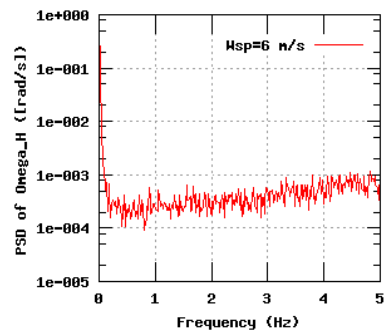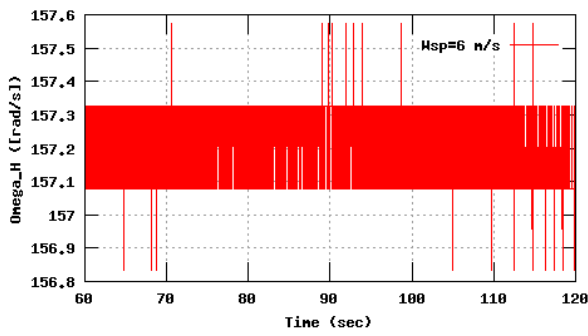
Figure 77b, Sensor 307: Rotor speed Omega_HSS versus time and frequency
Input files: m06.dat, m16.dat, m22.dat, m06.psd, m16.psd and m22.psd
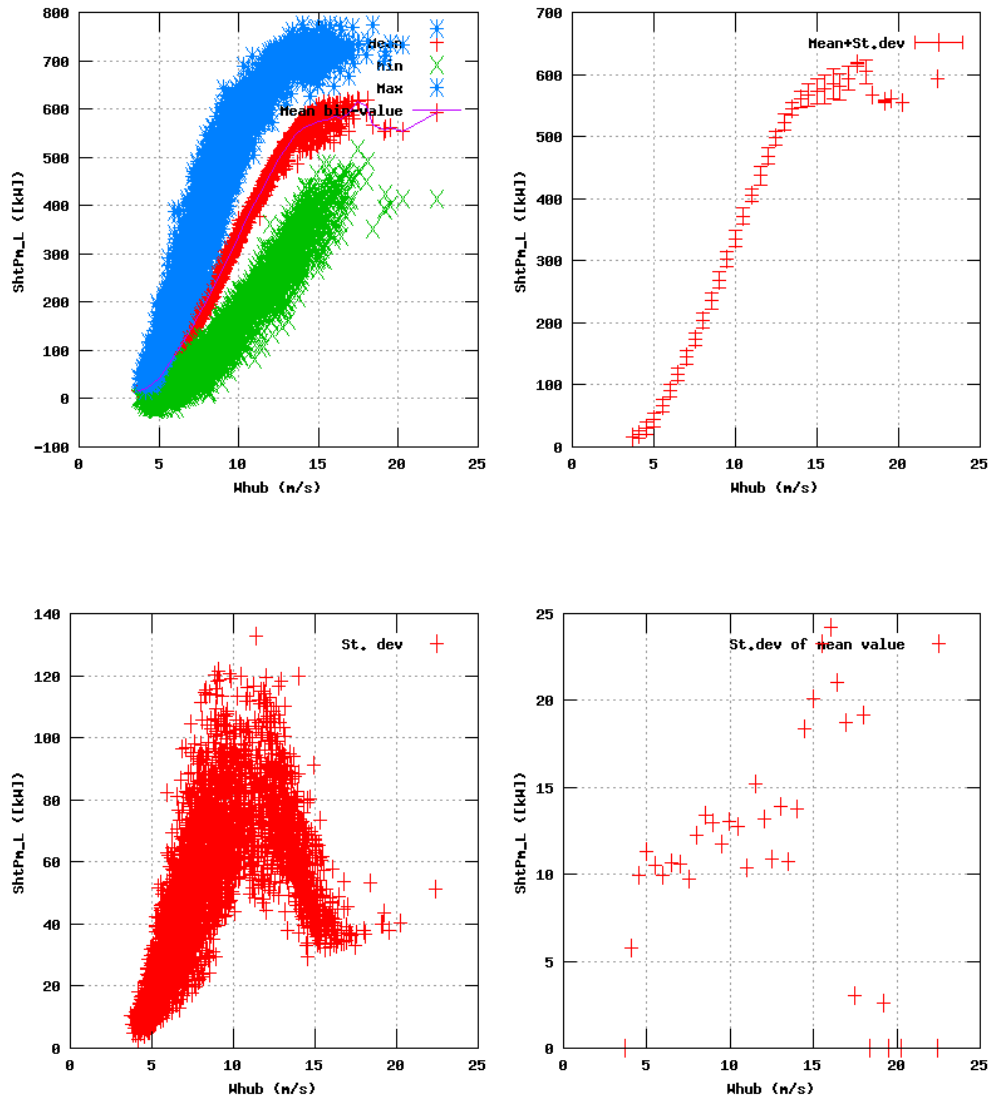
Figure 76a, Sensor 303: Mechanical shaft power LSS versus wind speed
Input files: ntk500res.dat, stat_303.dat
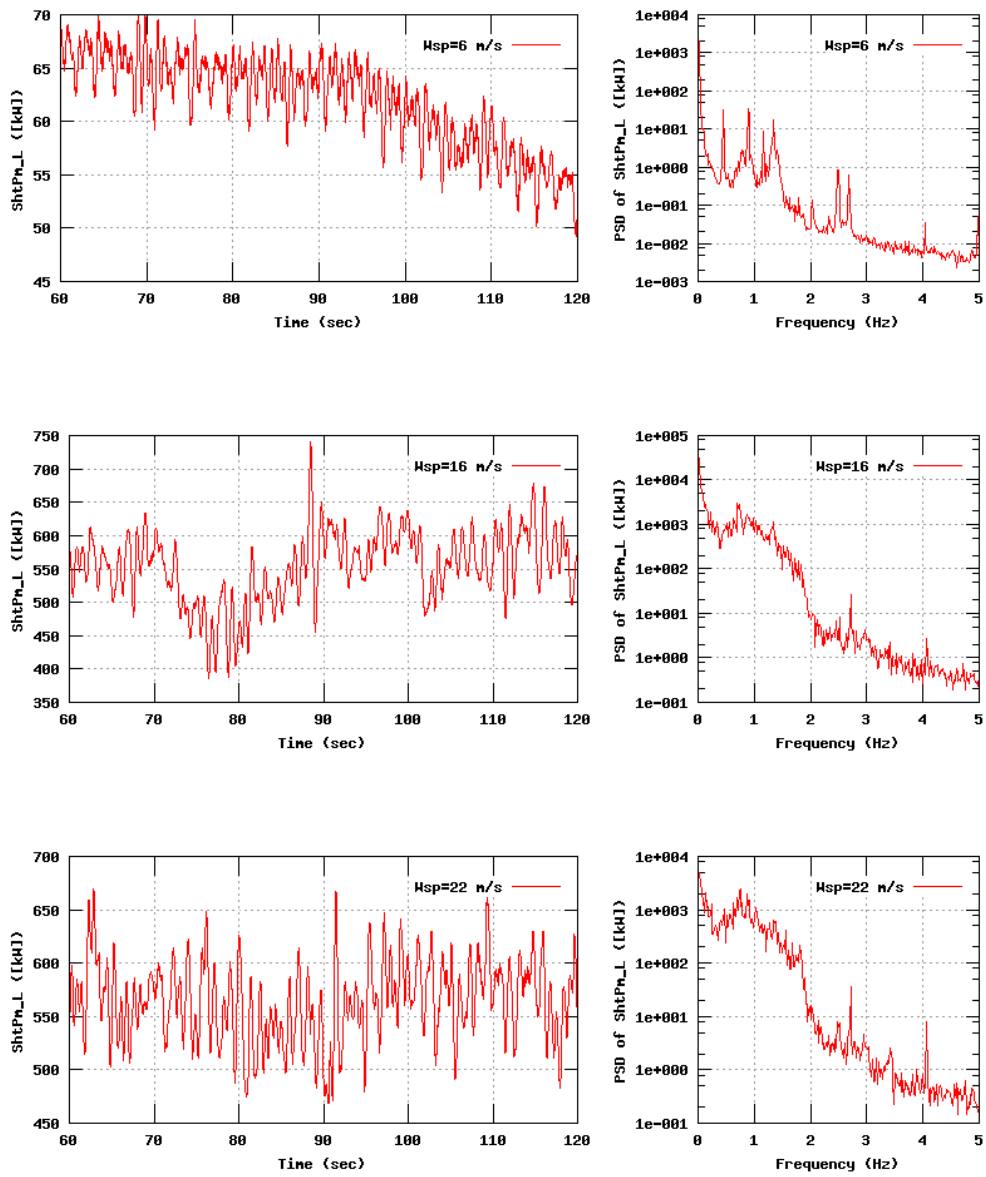
Figure 76b, Sensor 303: Mechanical shaft power LSS versus time and frequency
Input files: m06.dat, m16.dat, m22.dat, m06.psd, m16.psd and m22.psd
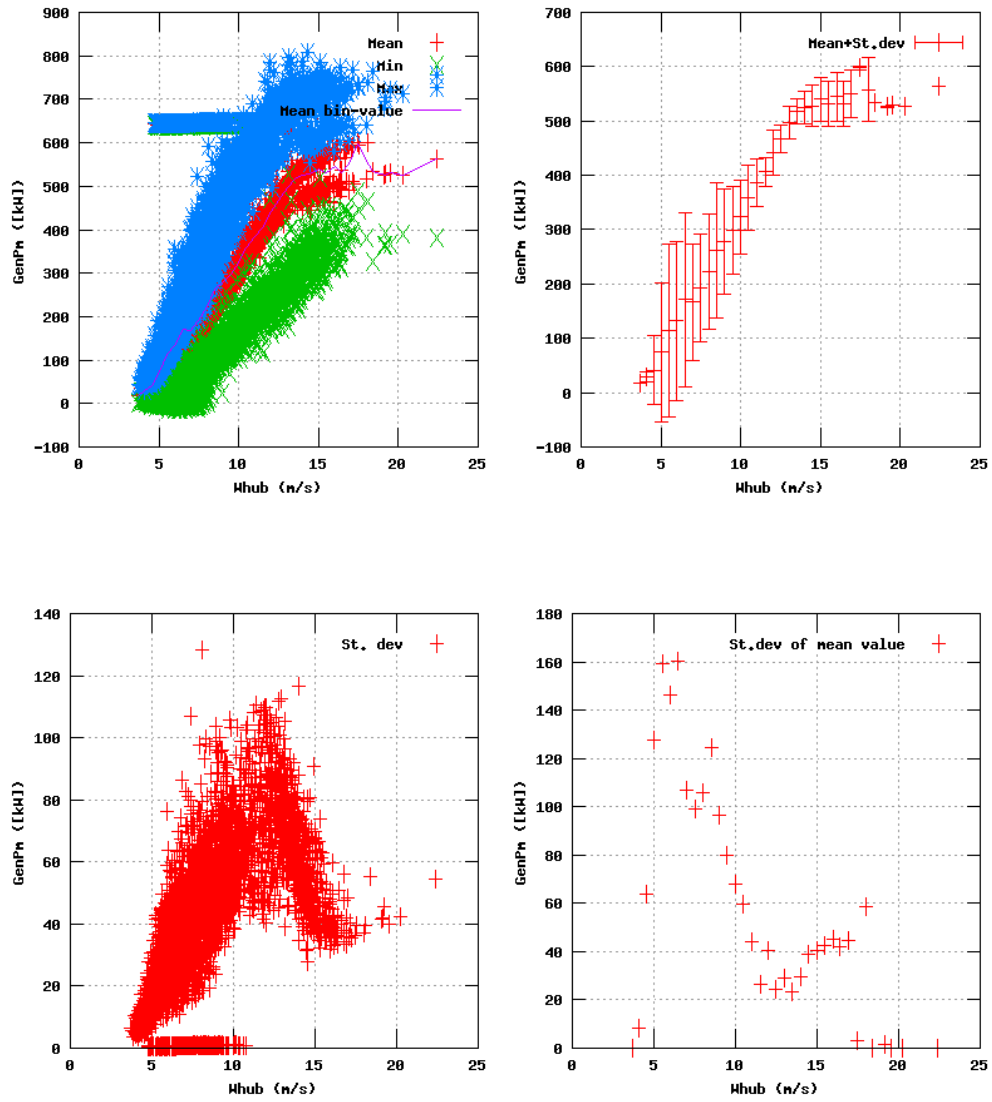
Figure 78a, Sensor 311: Mechanical shaft power Generator versus wind speed
Input files: ntk500res.dat, stat_311.dat
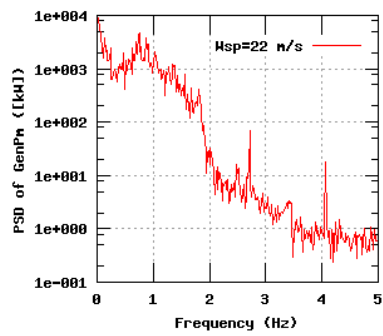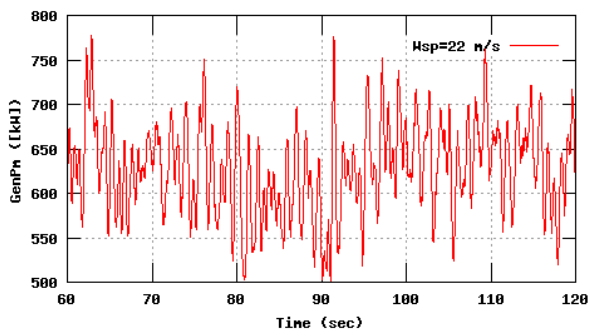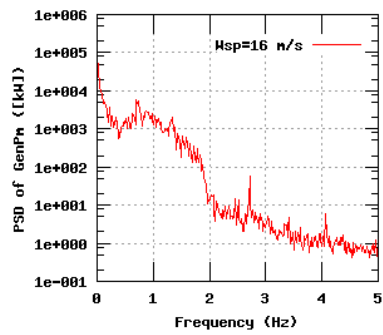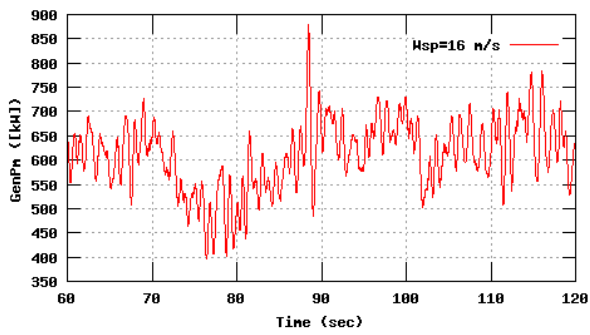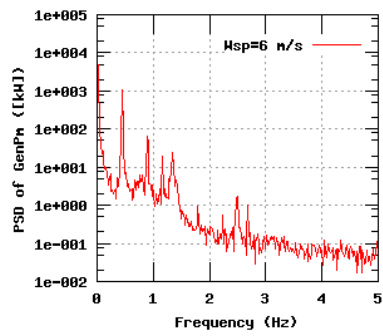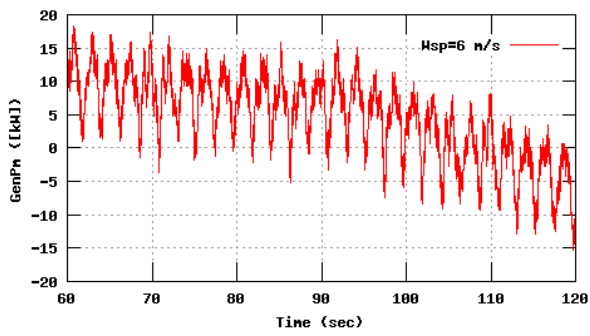
Figure 78b, Sensor 311: Mechanical shaft power Generator versus time and frequency
Input files: m06.dat, m16.dat, m22.dat, m06.psd, m16.psd and m22.psd
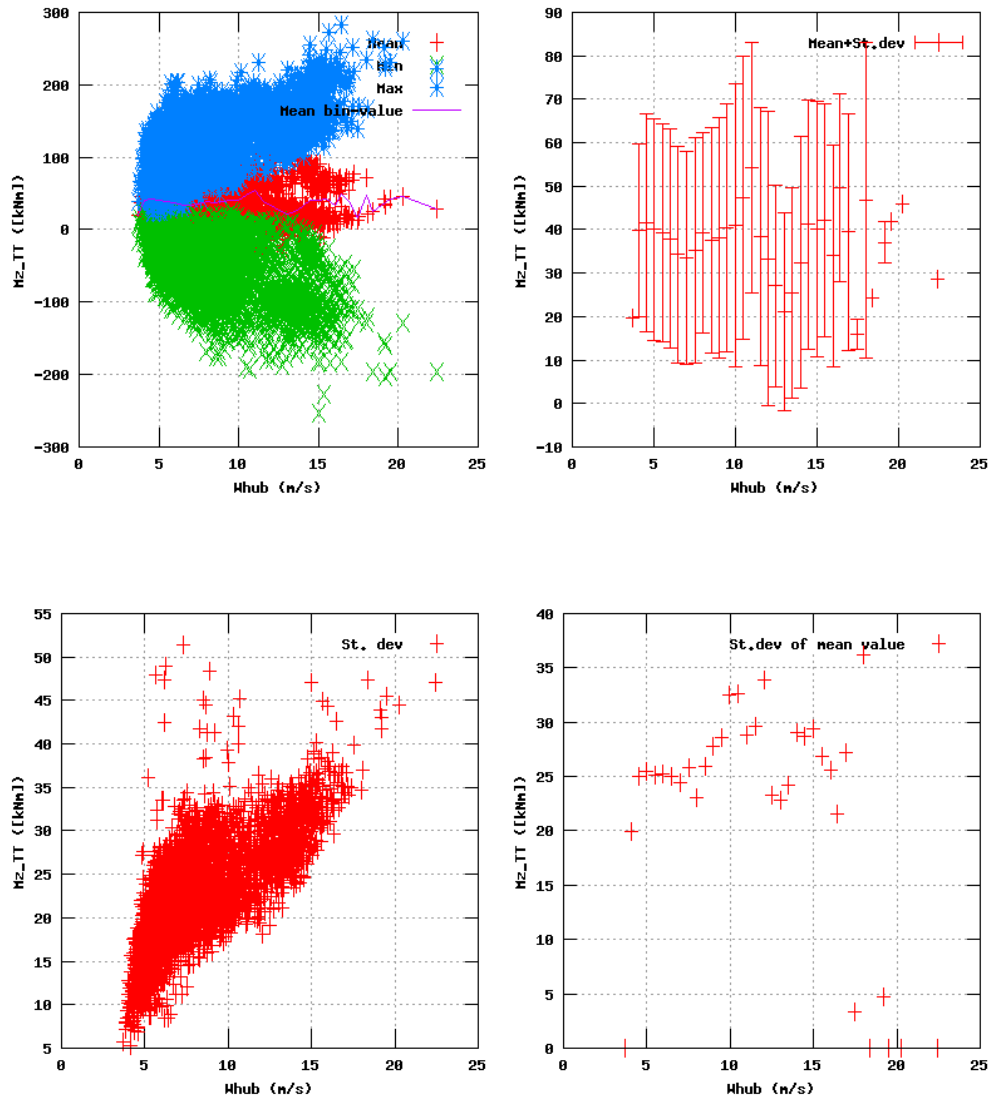
Figure 4a, Sensor 15: Tower torsion top Mz_TT versus wind speed
Input files: ntk500res.dat, stat_15.dat
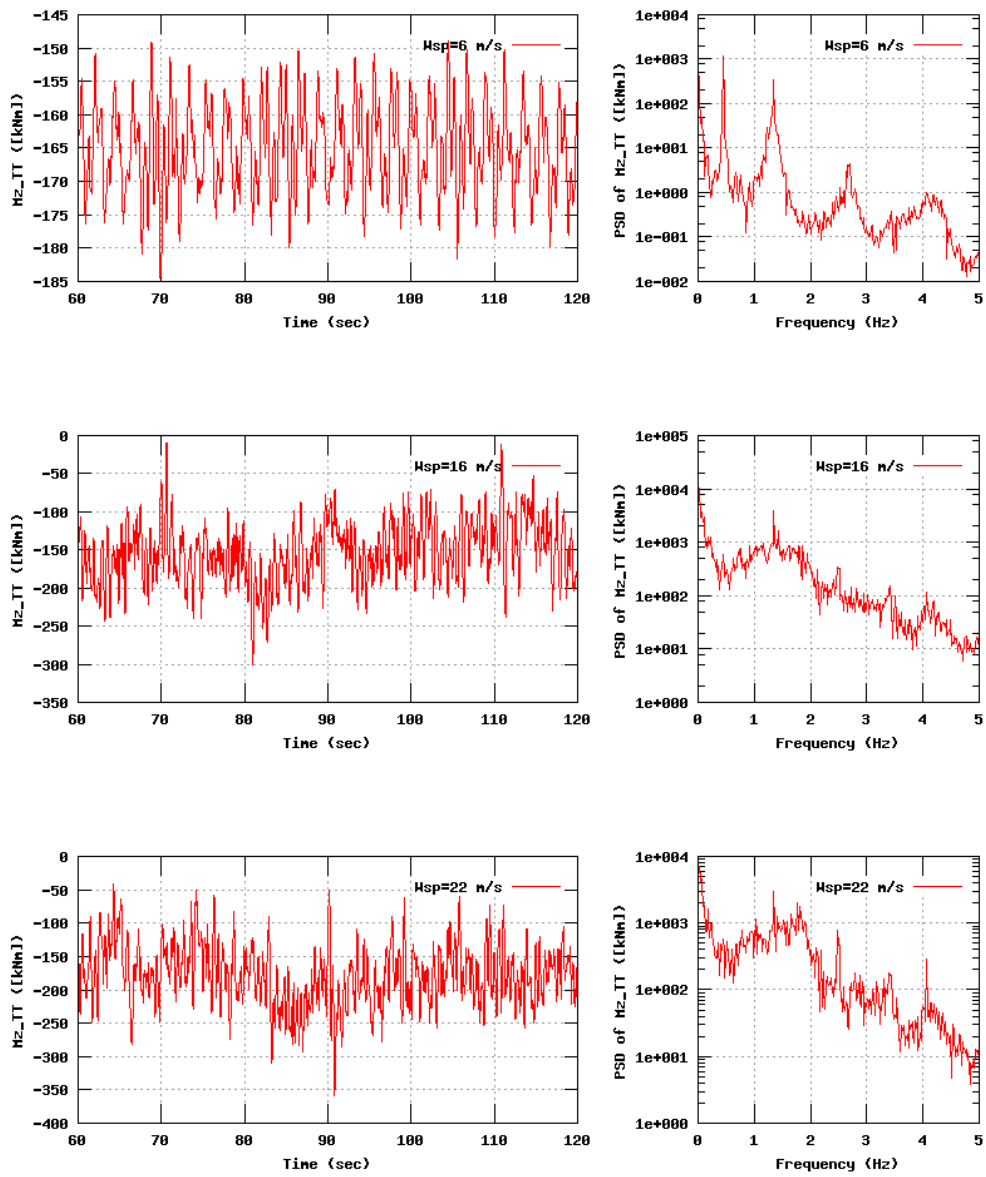
Figure 4b, Sensor 15: Tower torsion top Mz_TT versus time and frequency
Input files: m06.dat, m16.dat, m22.dat, m06.psd, m16.psd and m22.psd
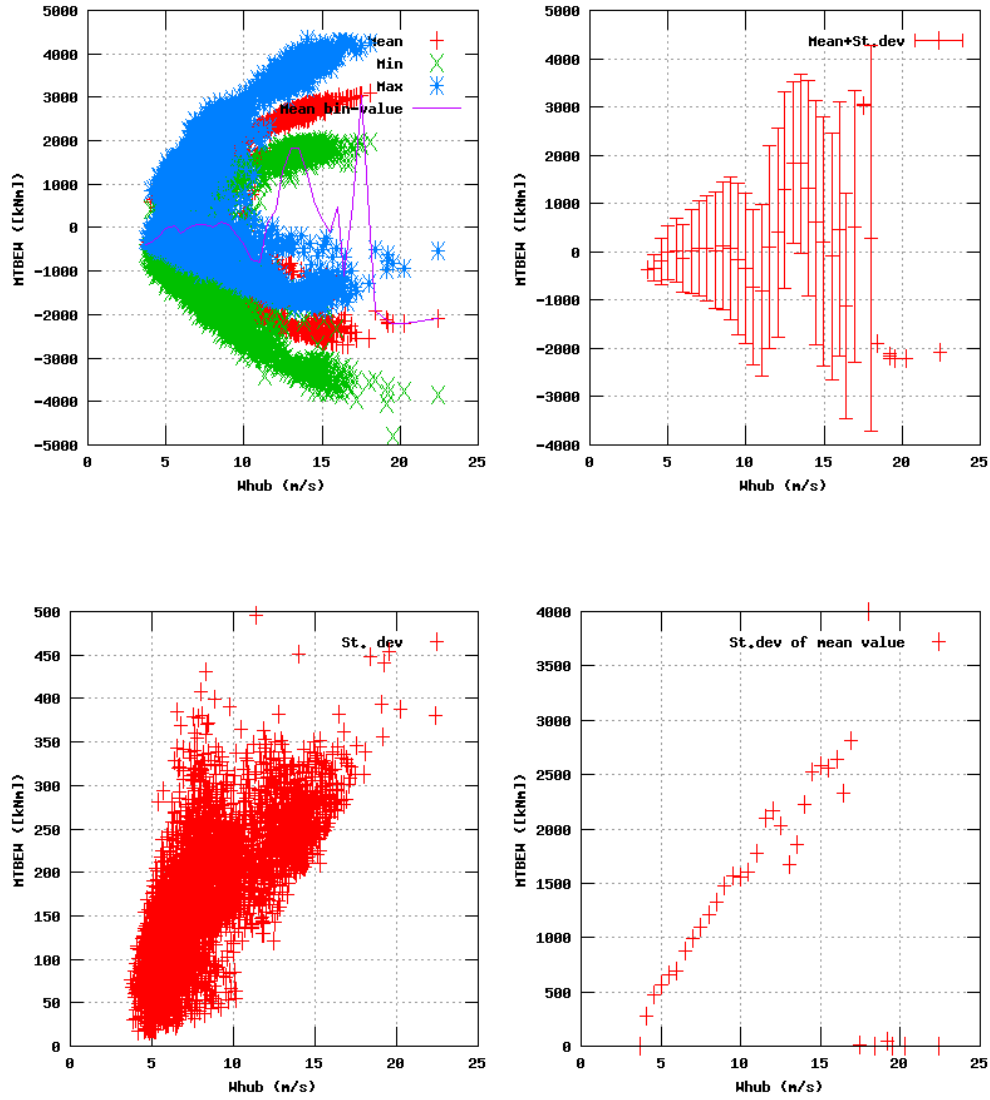
Figure 5a, Sensor 19: Tower bending bottom MTBEW versus wind speed
Input files: ntk500res.dat, stat_19.dat
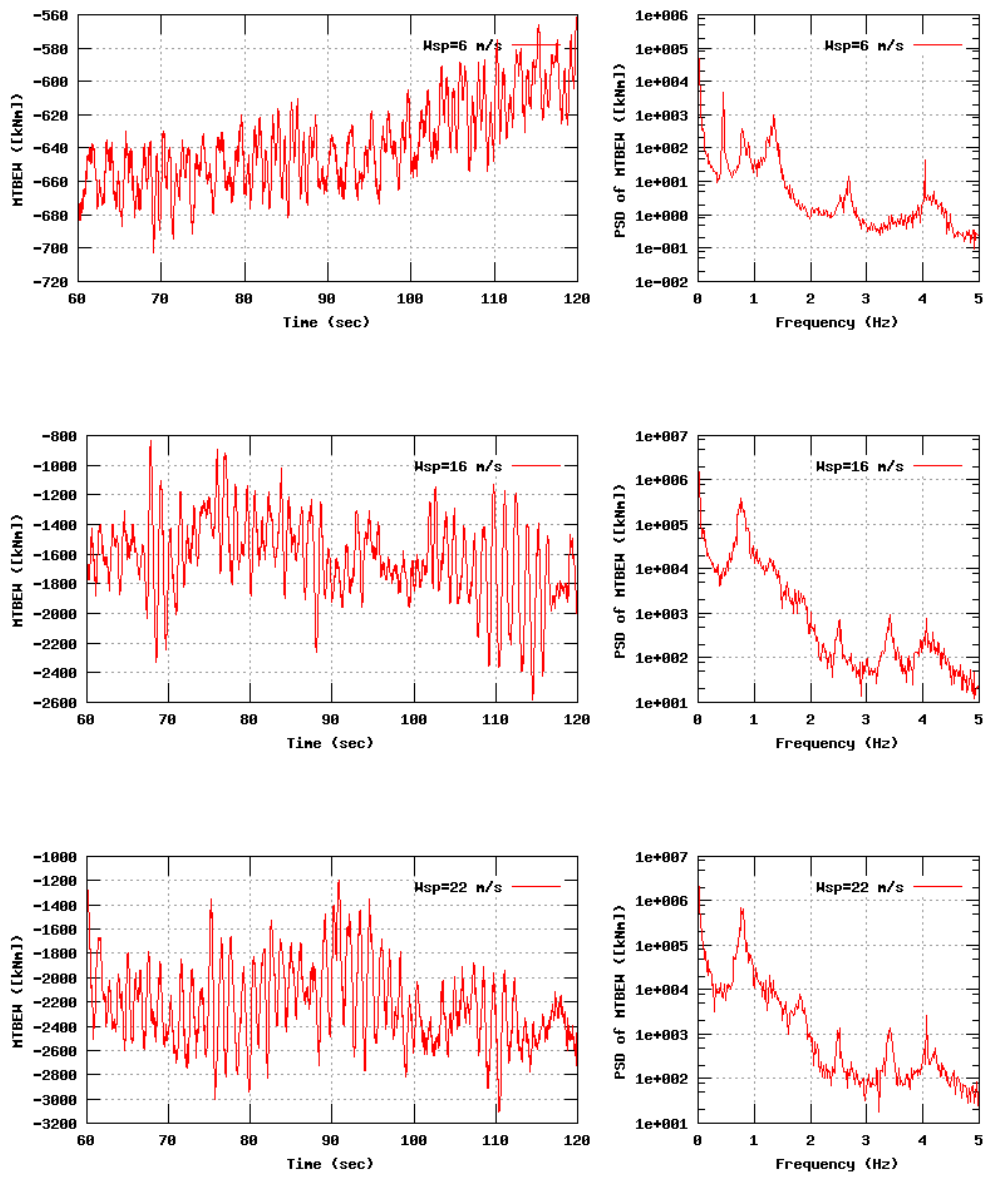
Figure 5b, Sensor 19: Tower bending bottom MTBEW versus time and frequency
Input files: m06.dat, m16.dat, m22.dat, m06.psd, m16.psd and m22.psd
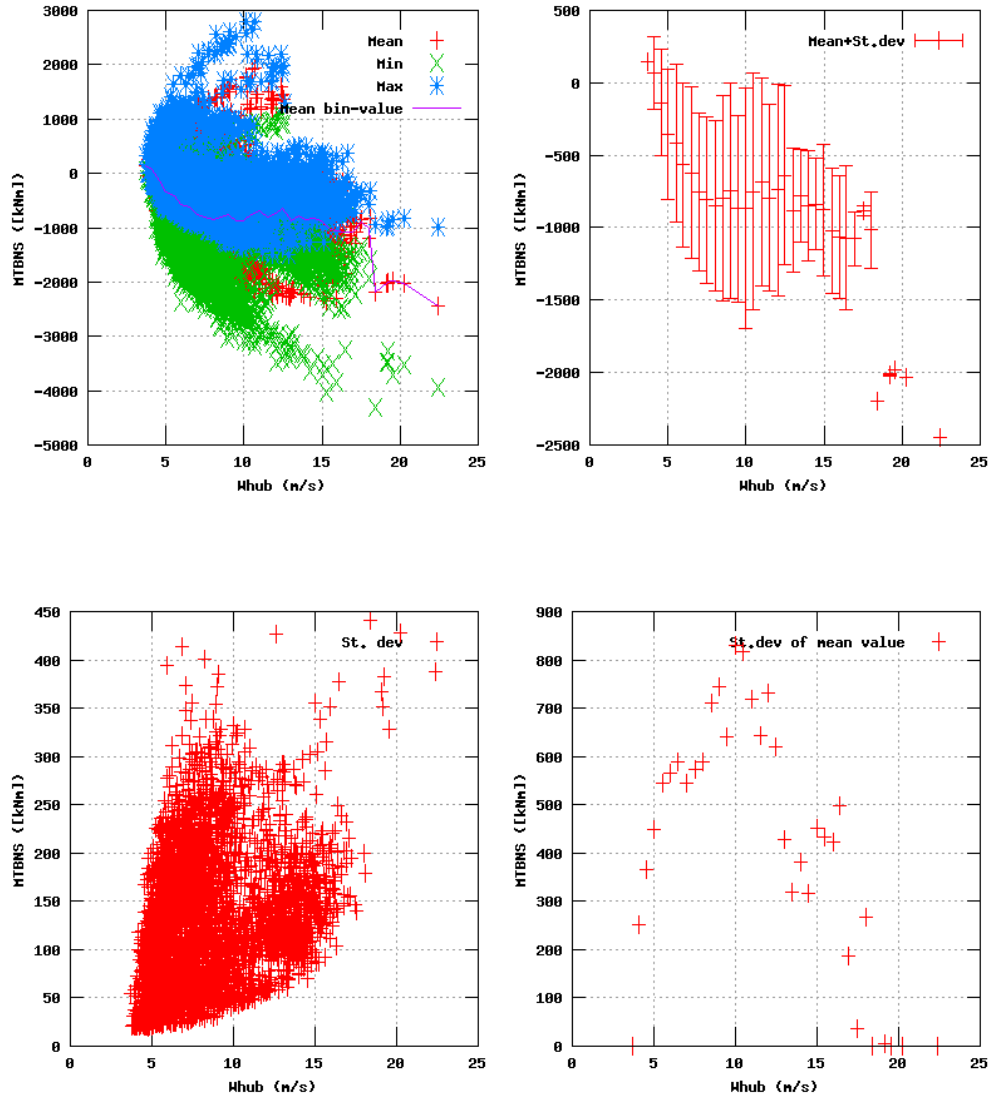
Figure 6a, Sensor 23: Tower bending bottom MTBNS versus wind speed
Input files: ntk500res.dat, stat_23.dat
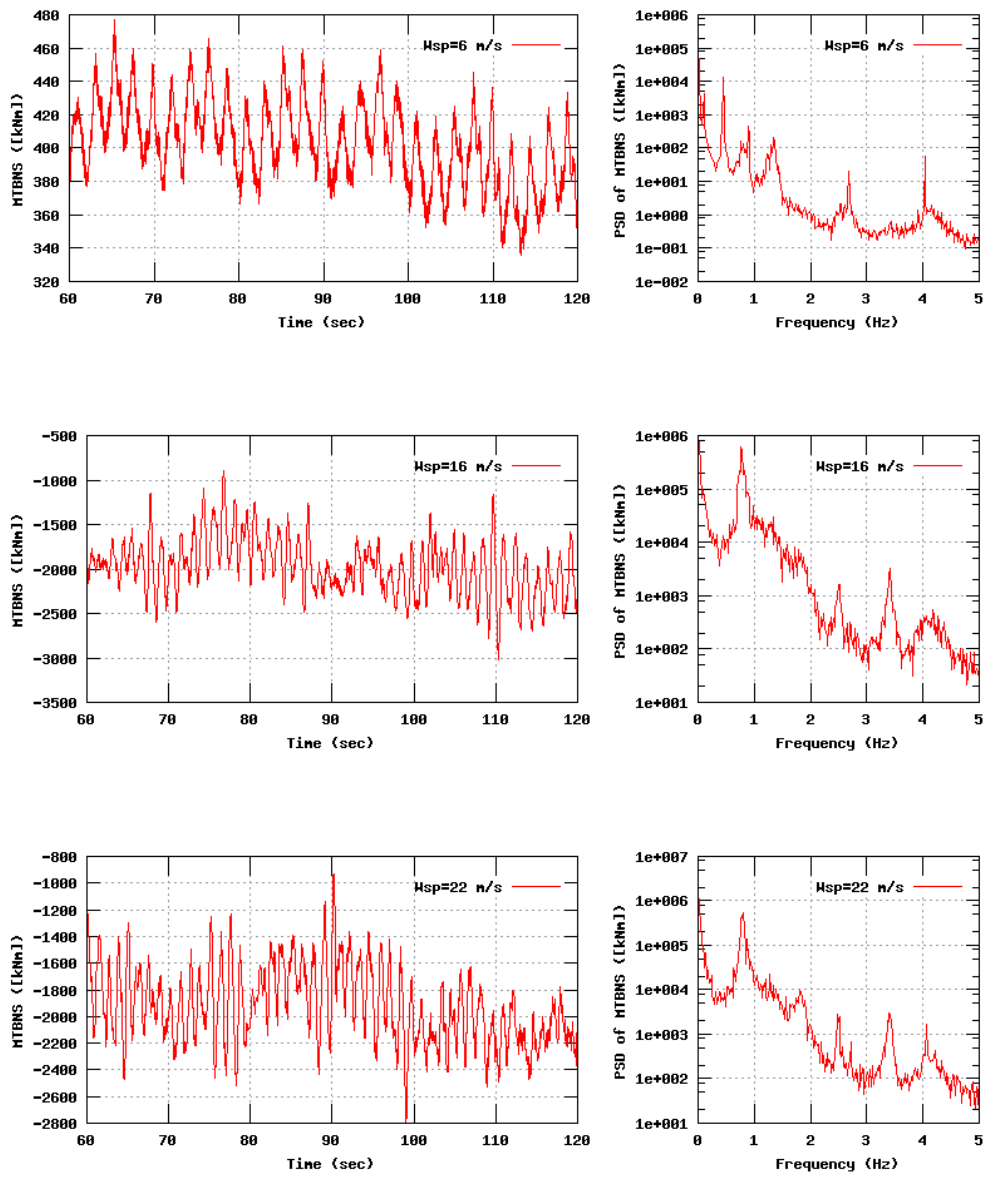
Figure 6b, Sensor 23: Tower bending bottom MTBNS versus time and frequency
Input files: m06.dat, m16.dat, m22.dat, m06.psd, m16.psd and m22.psd
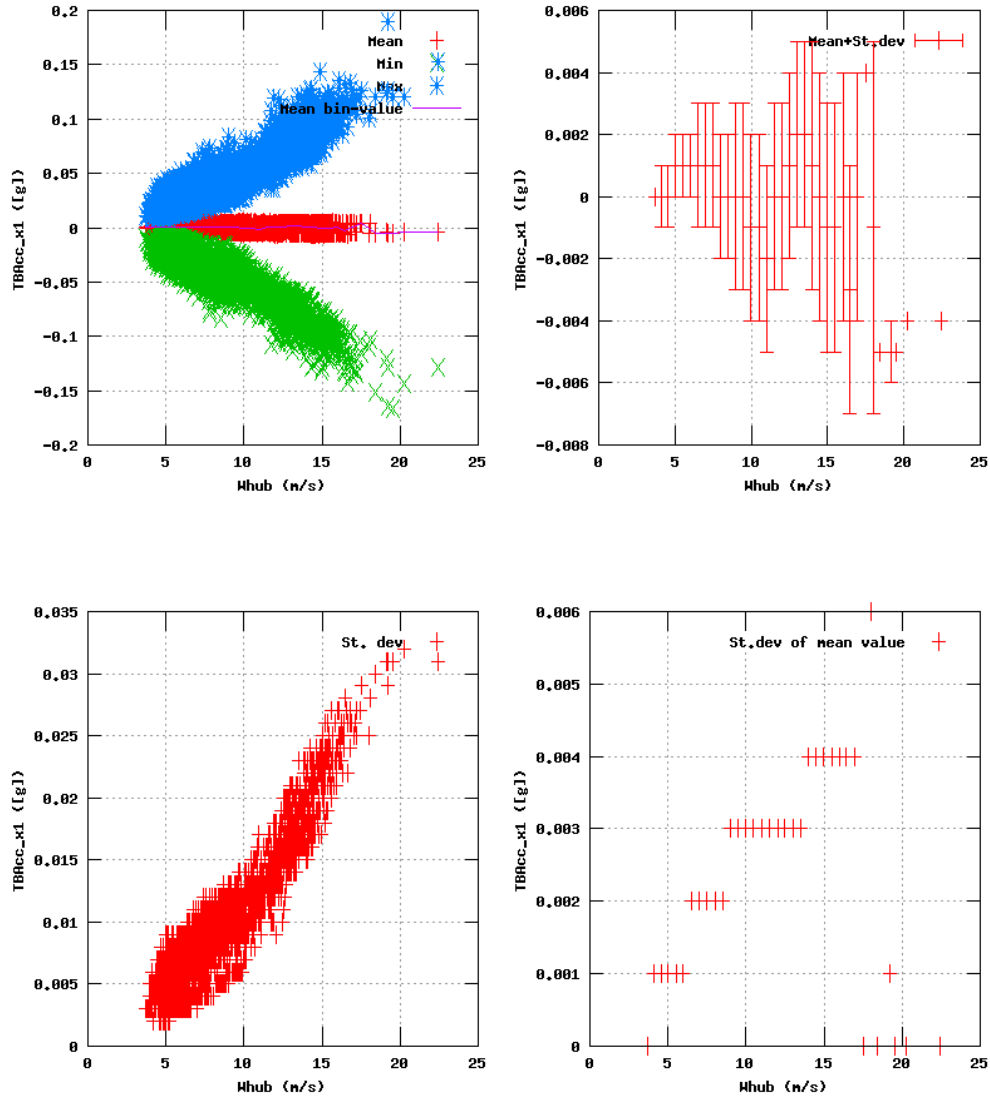
Figure 8a, Sensor 31: Tower accelleration 140 cm from top flange TBAcc_x1 versus wind speed
Input files: ntk500res.dat, stat_31.dat
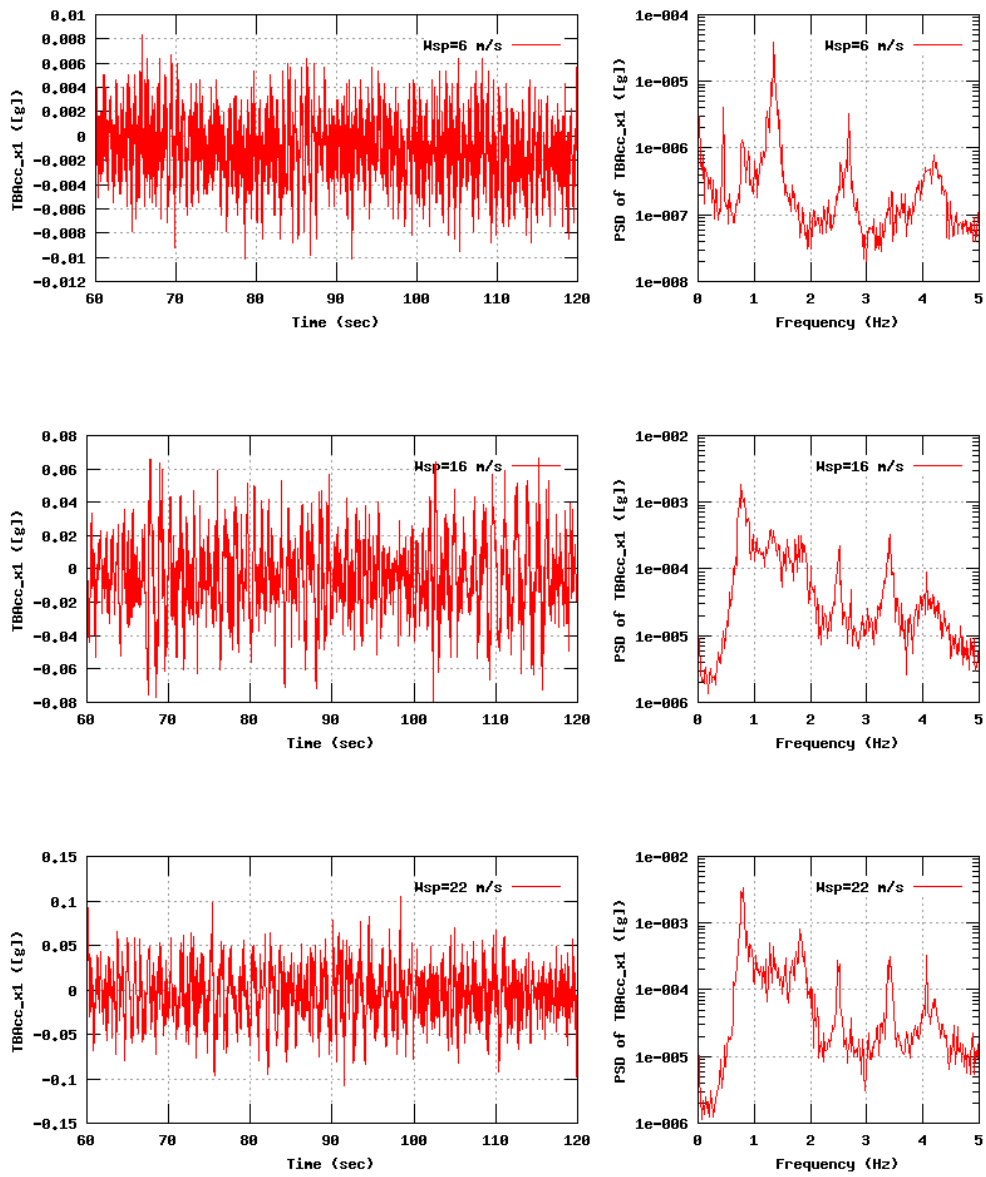
Figure 8b, Sensor 31: Tower accelleration 140 cm from top flange TBAcc_x1 versus time and frequency
Input files: m06.dat, m16.dat, m22.dat, m06.psd, m16.psd and m22.psd
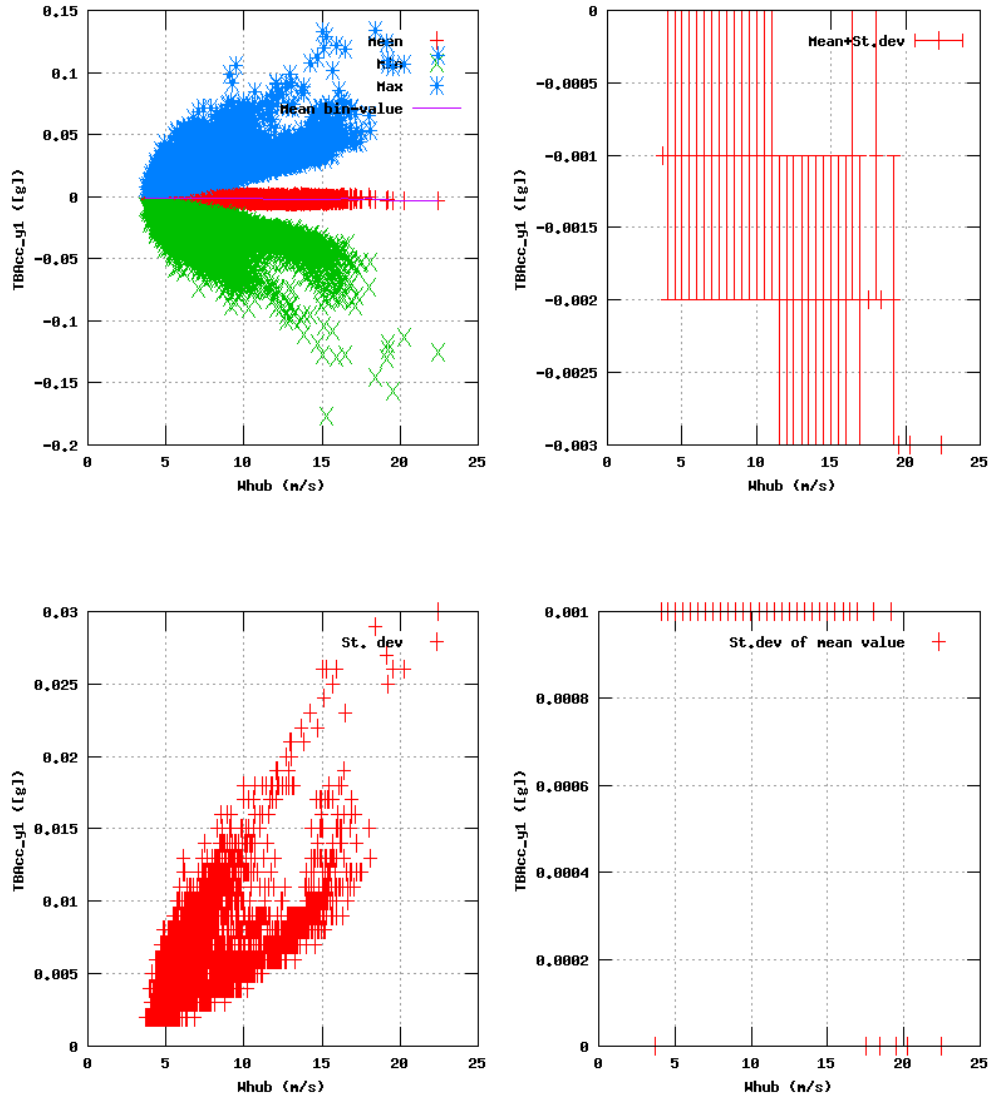
Figure 9a, Sensor 35: Tower accelleration 140 cm from top flange TBAcc_y1 versus wind speed
Input files: ntk500res.dat, stat_35.dat
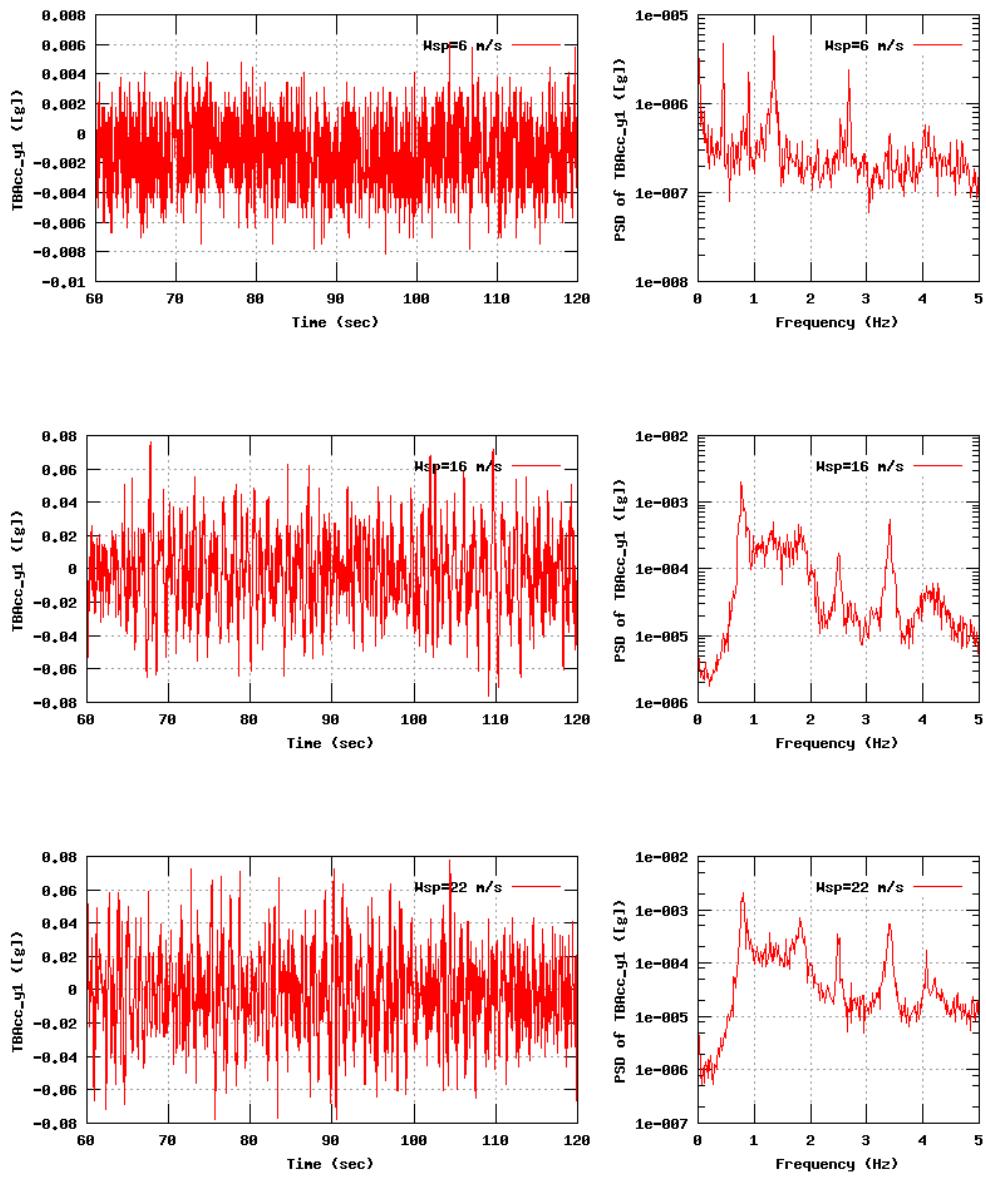
Figure 9b, Sensor 35: Tower accelleration 140 cm from top flange TBAcc_y1 versus time and frequency
Input files: m06.dat, m16.dat, m22.dat, m06.psd, m16.psd and m22.psd
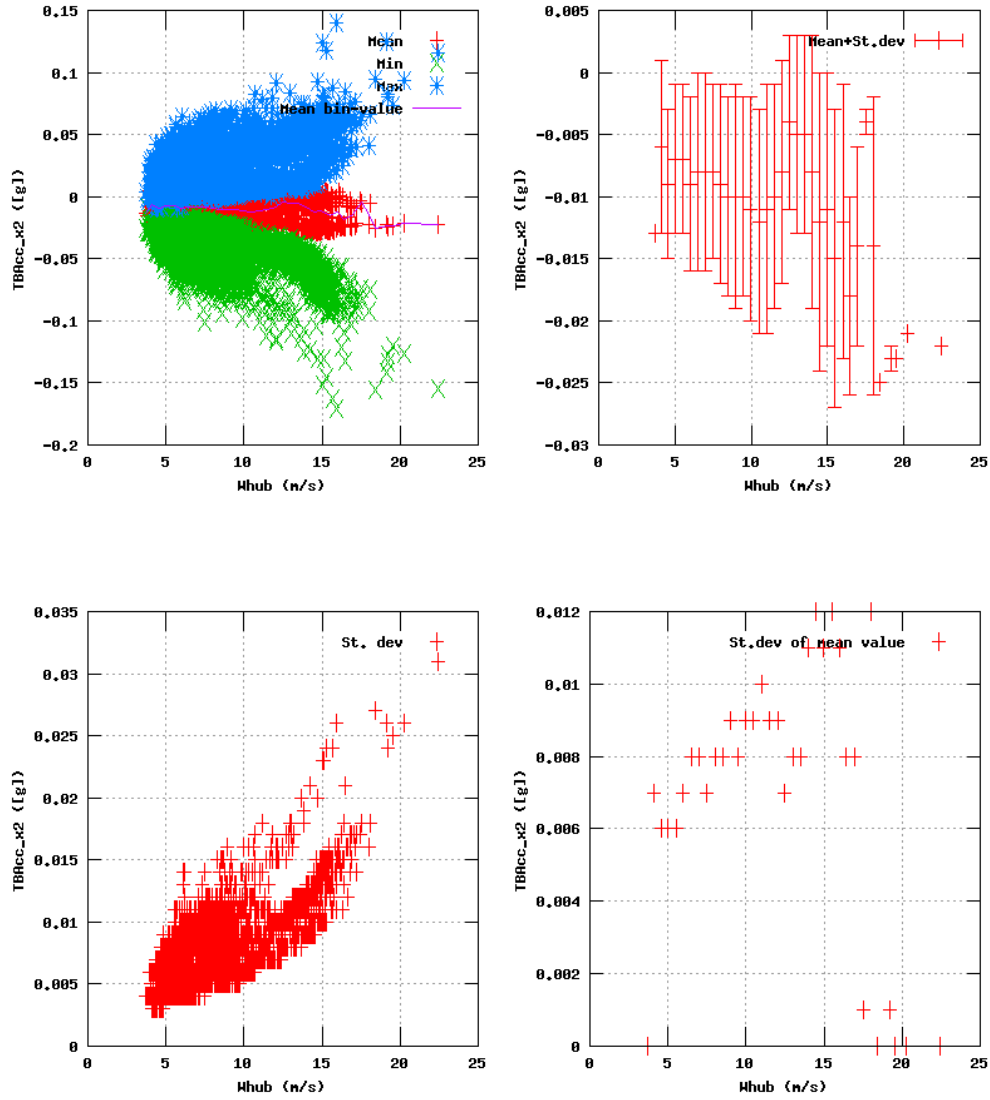
Figure 10a, Sensor 39: Tower accelleration 80 cm from flange and 1st repos TBAcc_x2 versus wind speed
Input files: ntk500res.dat, stat_39.dat
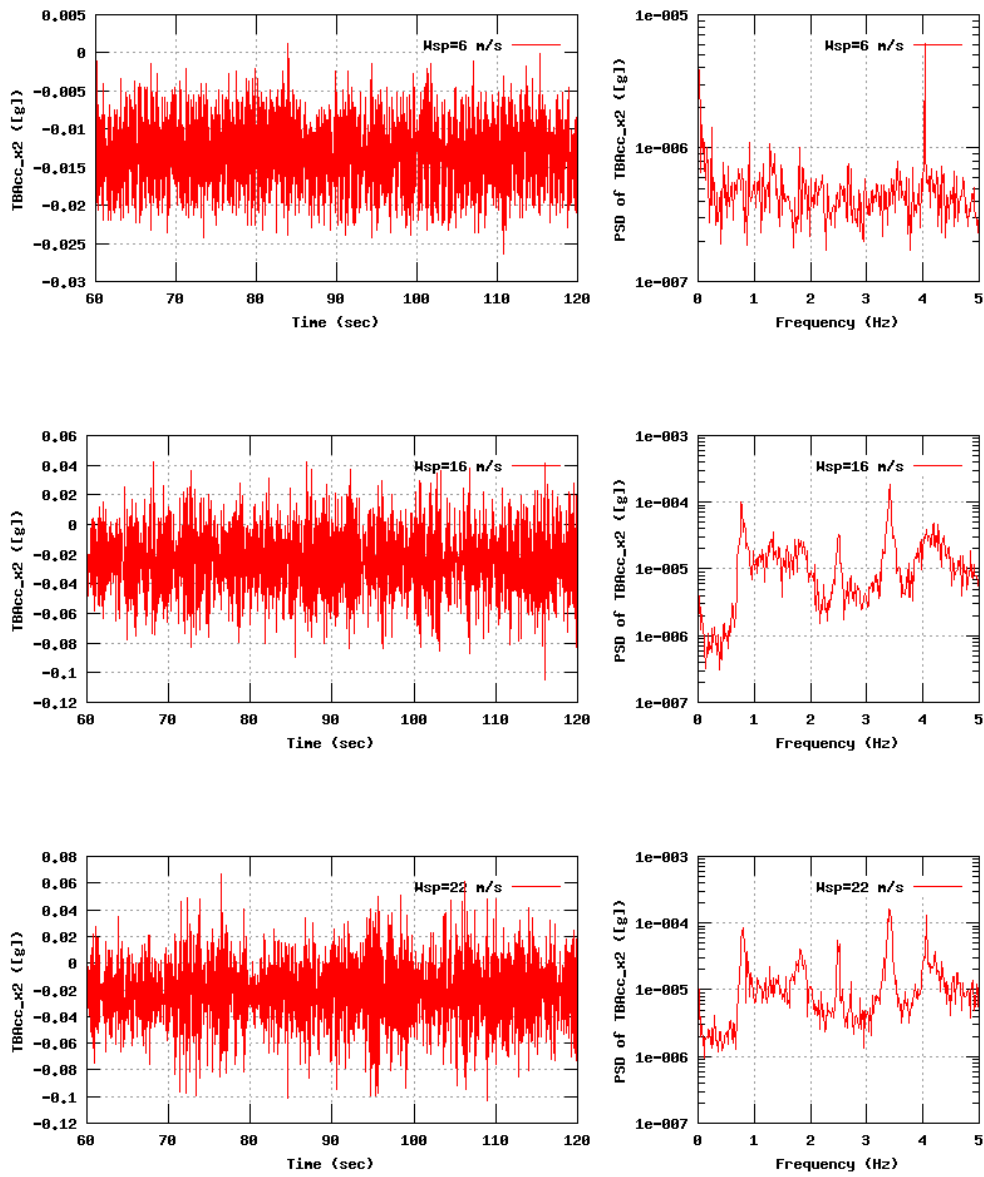
Figure 10b, Sensor 39: Tower accelleration 80 cm from flange and 1st repos TBAcc_x2 versus time and frequency
Input files: m06.dat, m16.dat, m22.dat, m06.psd, m16.psd and m22.psd
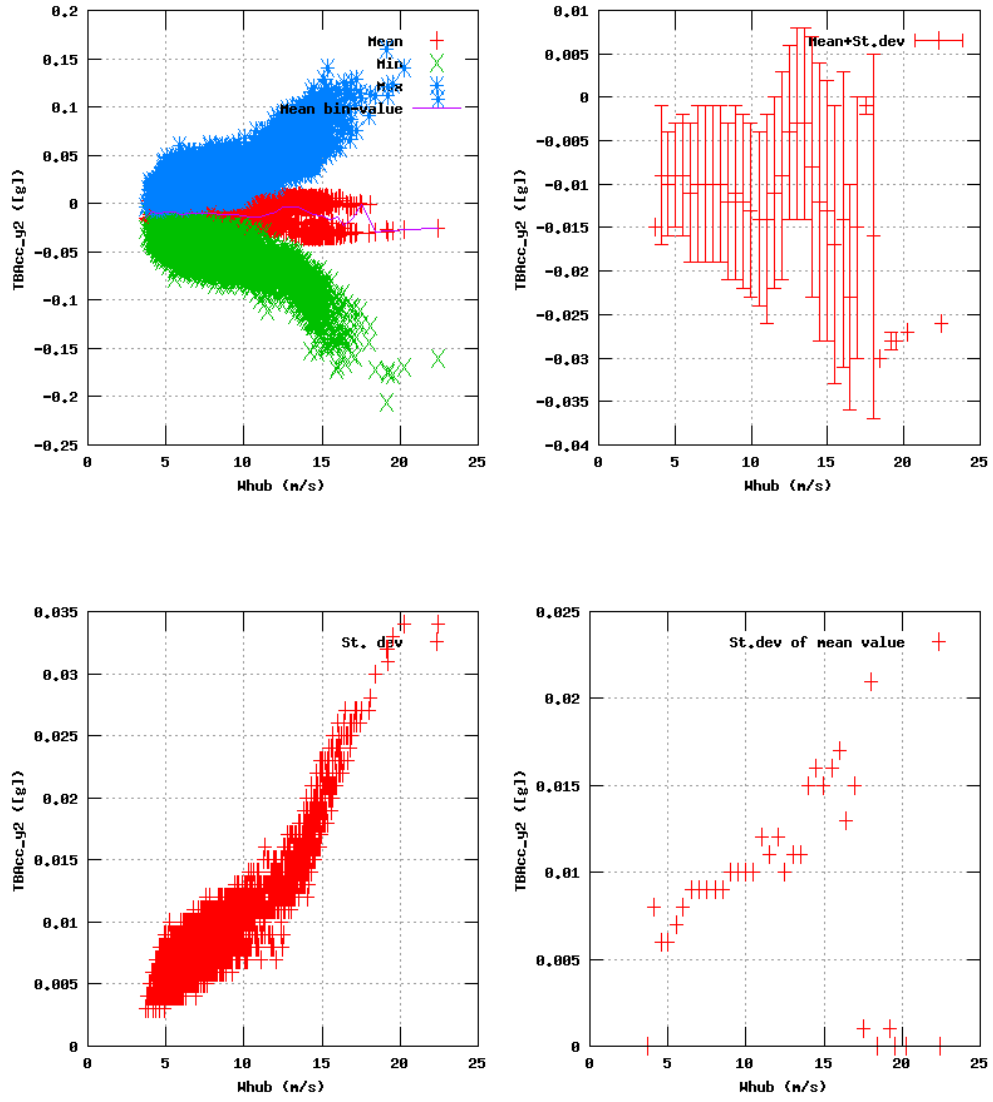
Figure 11a, Sensor 43: Tower accelleration 80 cm from flange and 1st repos TBAcc_y2 versus wind speed
Input files: ntk500res.dat, stat_43.dat
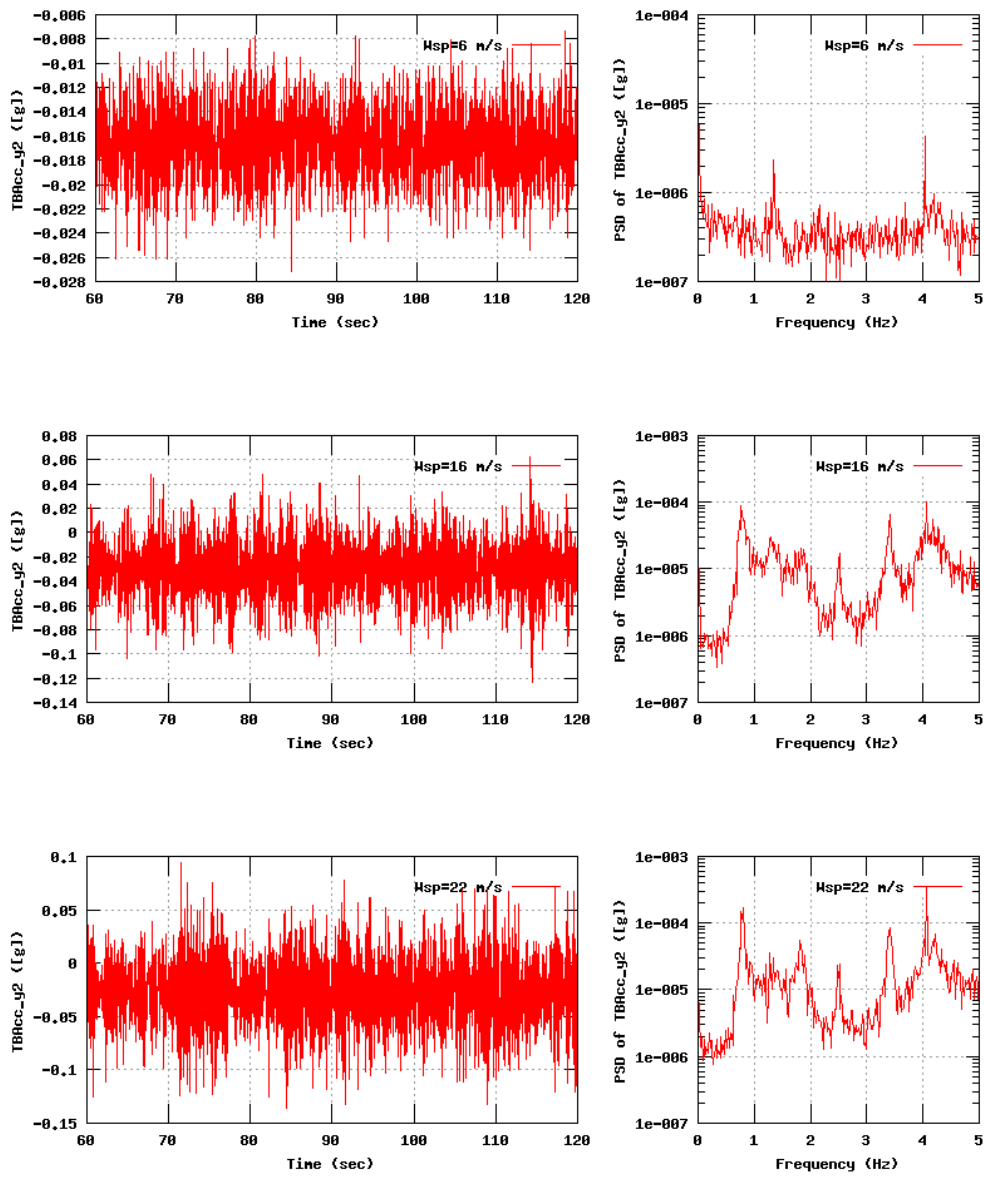
Figure 11b, Sensor 43: Tower accelleration 80 cm from flange and 1st repos TBAcc_y2 versus time and frequency
Input files: m06.dat, m16.dat, m22.dat, m06.psd, m16.psd and m22.psd
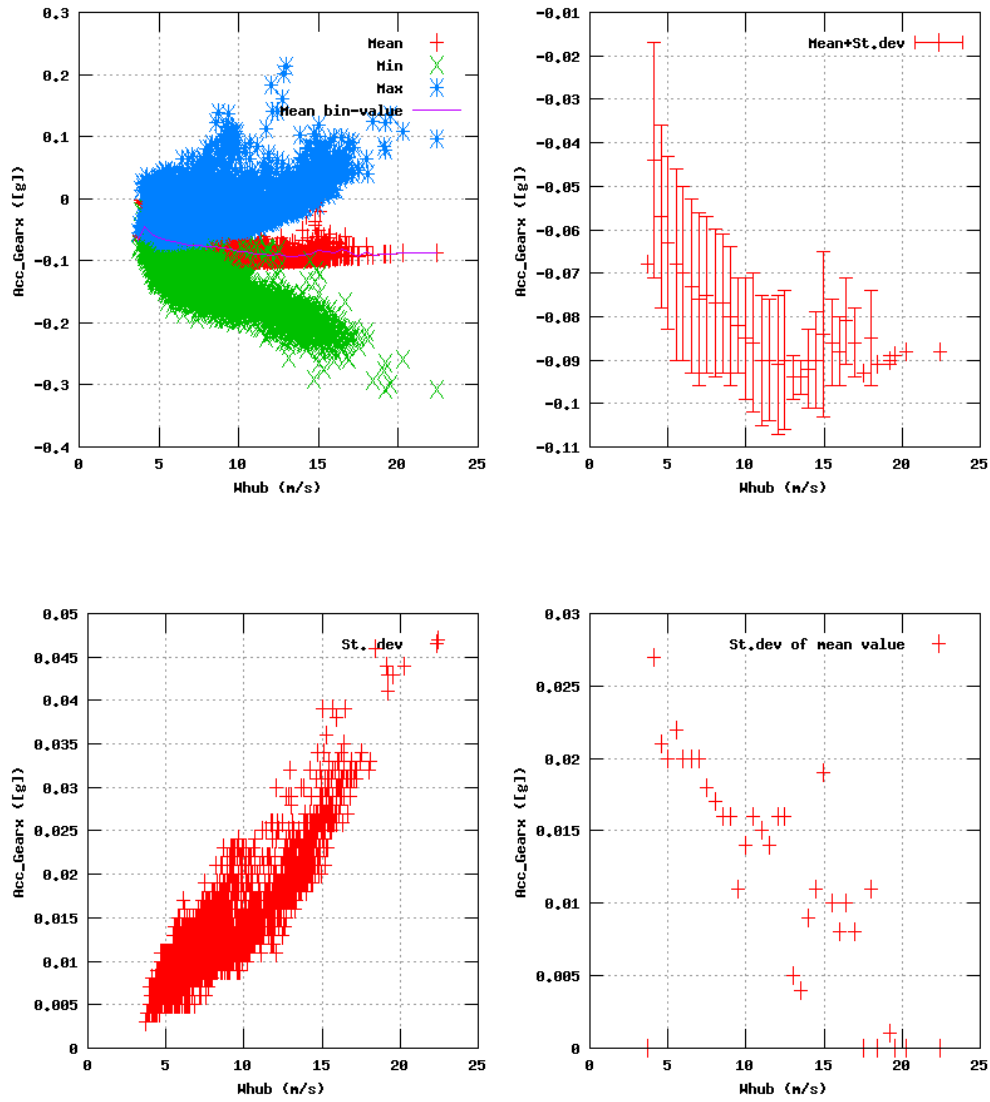
Figure 26a, Sensor 103: Acceleration gearbox Acc_Gearx versus wind speed
Input files: ntk500res.dat, stat_103.dat
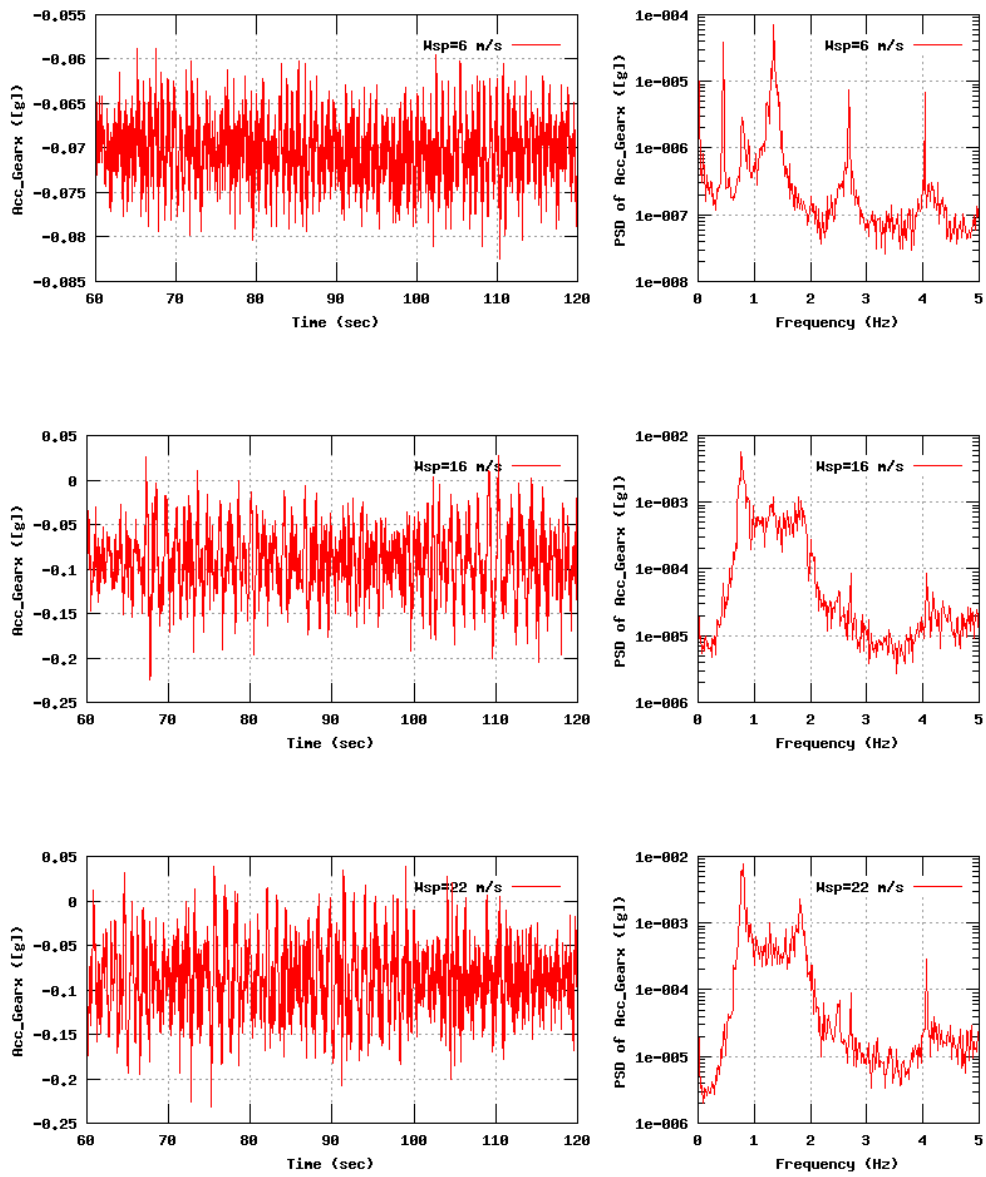
Figure 26b, Sensor 103: Acceleration gearbox Acc_Gearx versus time and frequency
Input files: m06.dat, m16.dat, m22.dat, m06.psd, m16.psd and m22.psd

Risø-R-1782(EN)
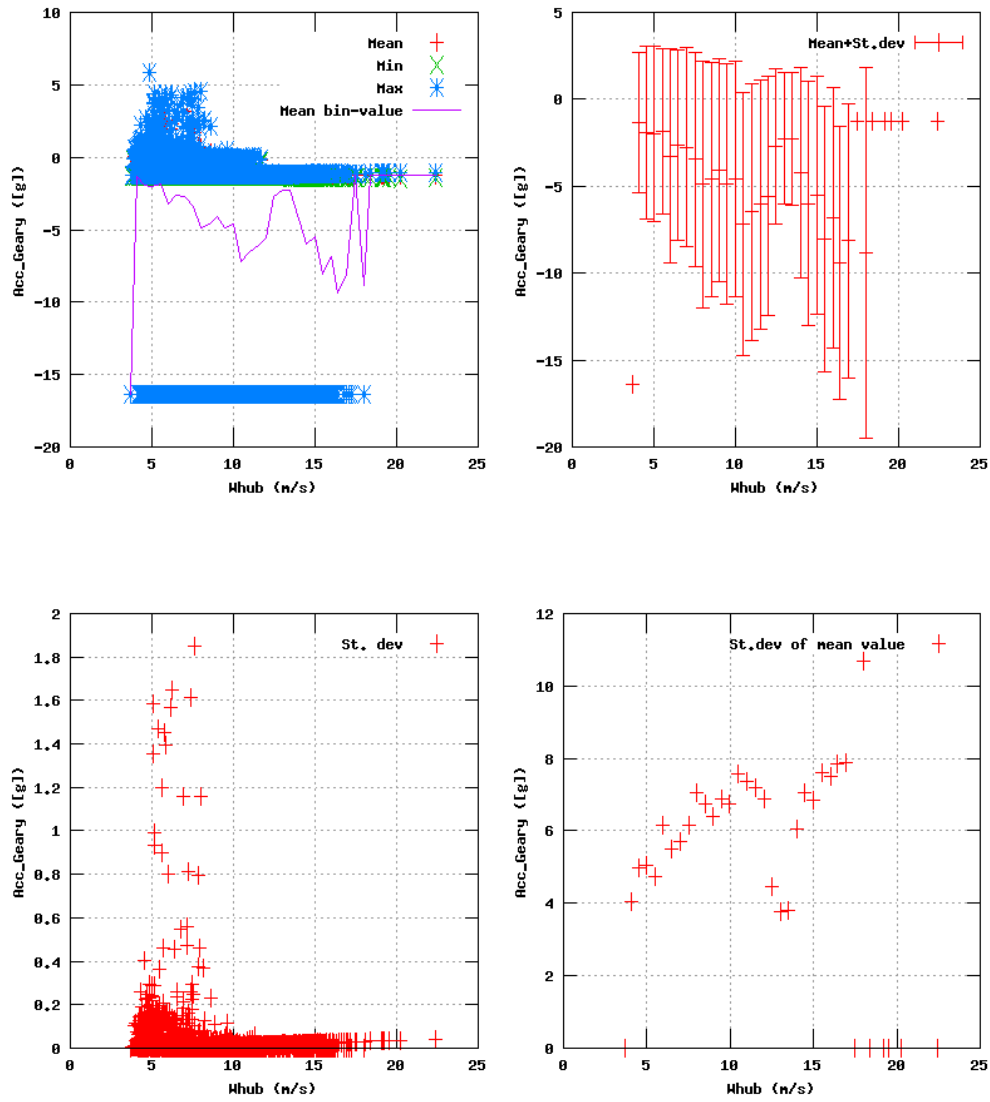
Figure 27a, Sensor 107: Acceleration gearbox Acc_Geary versus wind speed
Input files: ntk500res.dat, stat_107.dat
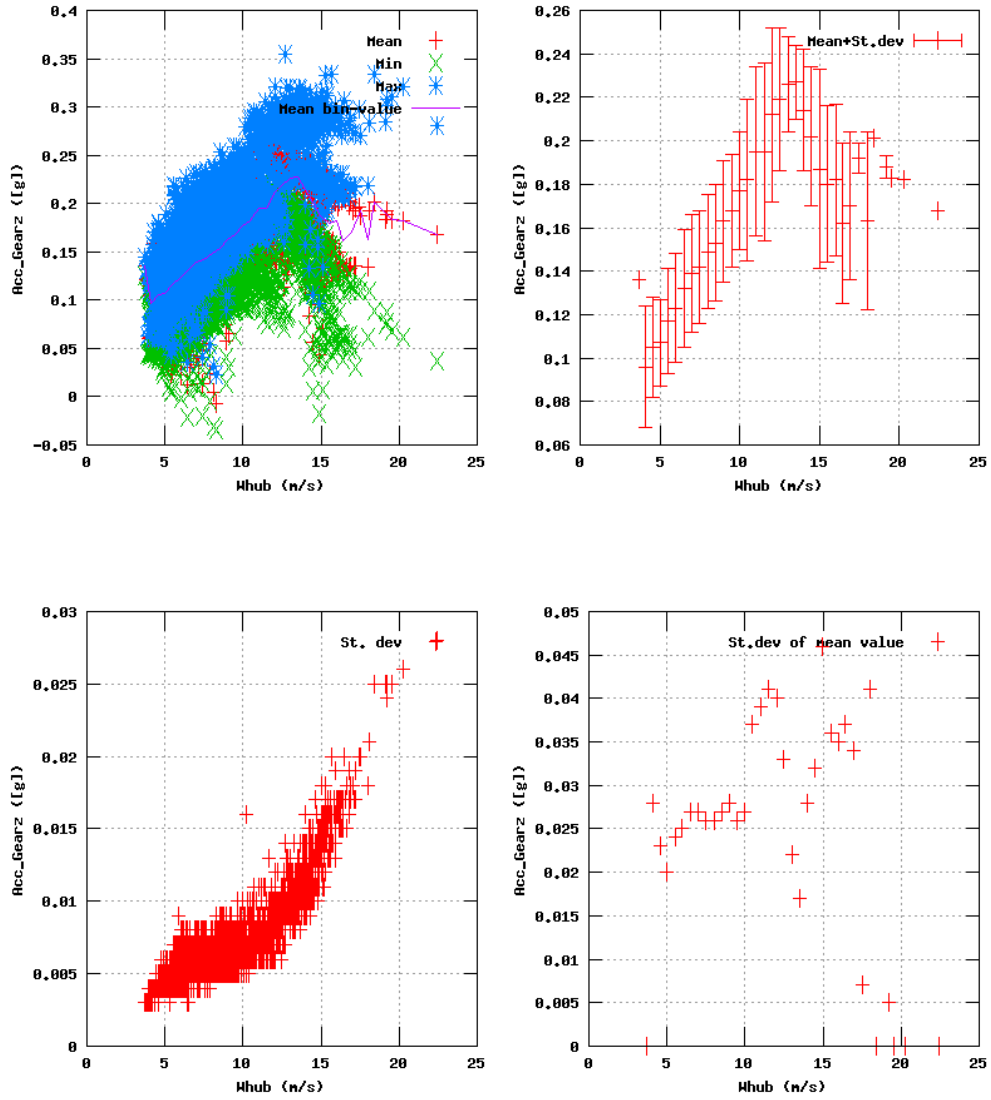
Figure 28a, Sensor 111: Acceleration gearbox Acc_Gearz versus wind speed
Input files: ntk500res.dat, stat_111.dat
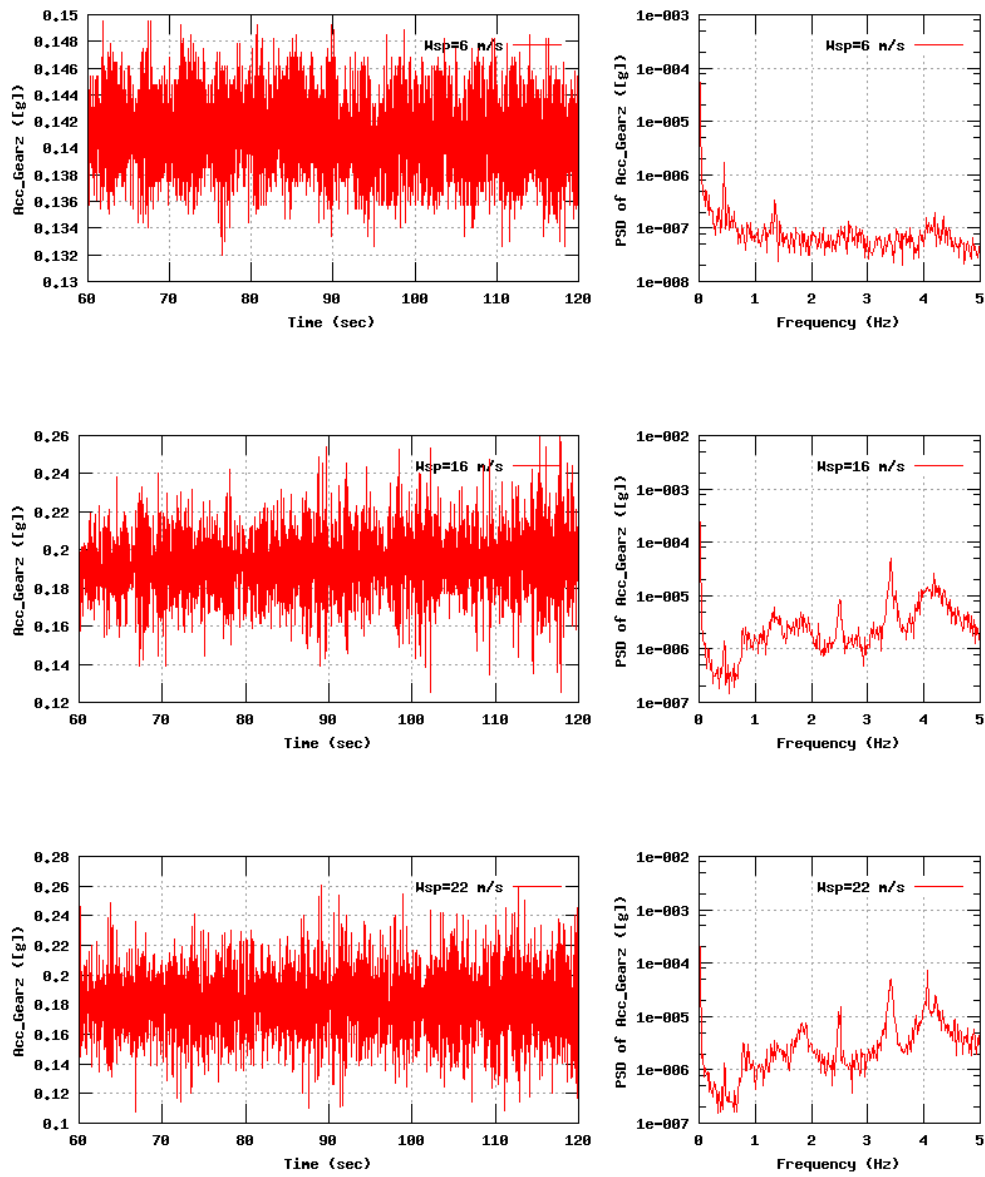
Figure 28b, Sensor 111: Acceleration gearbox Acc_Gearz versus time and frequency
Input files: m06.dat, m16.dat, m22.dat, m06.psd, m16.psd and m22.psd
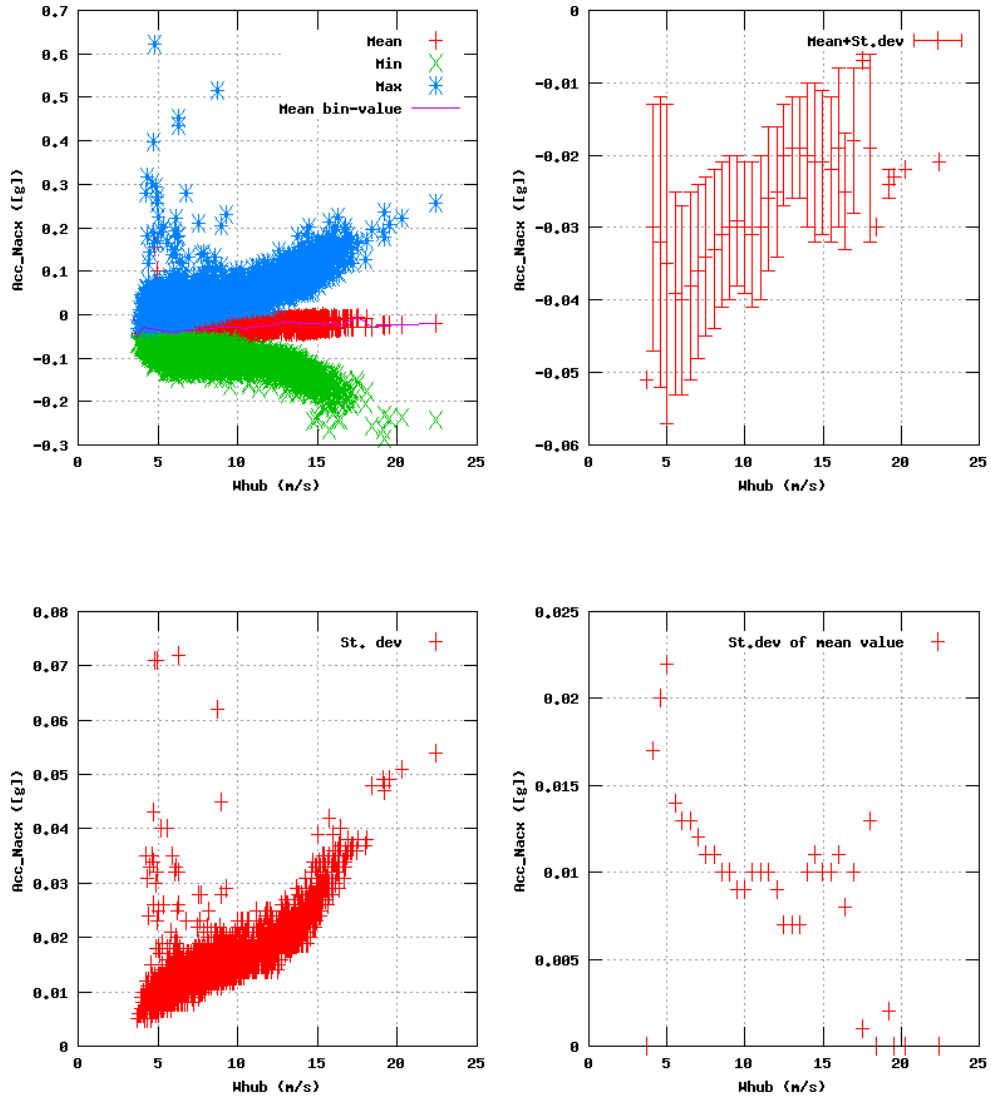
Figure 29a, Sensor 115: Acceleration nacelle leeward Acc_Nacx versus wind speed
Input files: ntk500res.dat, stat_115.dat
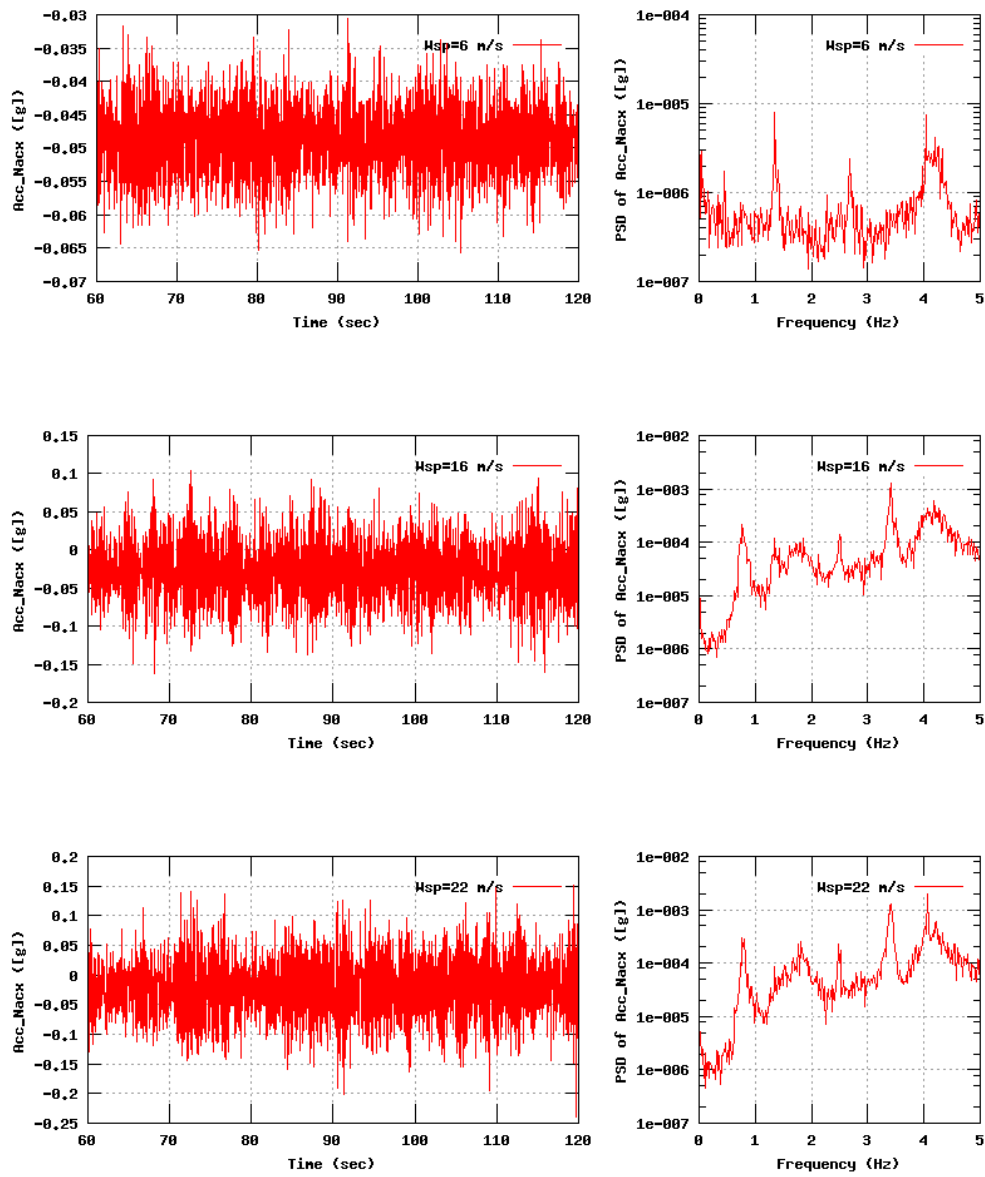
Figure 29b, Sensor 115: Acceleration nacelle leeward Acc_Nacx versus time and frequency
Input files: m06.dat, m16.dat, m22.dat, m06.psd, m16.psd and m22.psd
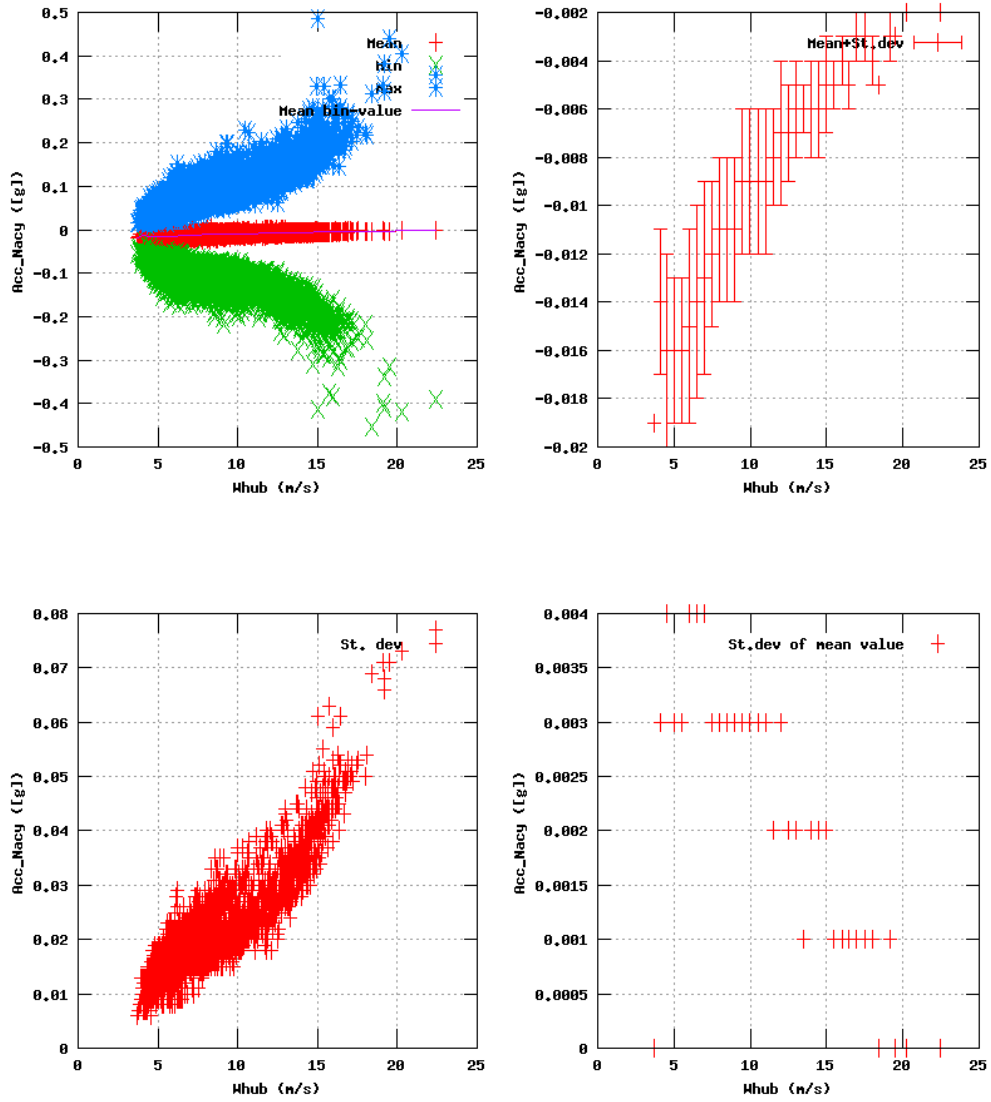
Figure 30a, Sensor 119: Acceleration nacelle leeward Acc_Nacy versus wind speed
Input files: ntk500res.dat, stat_119.dat
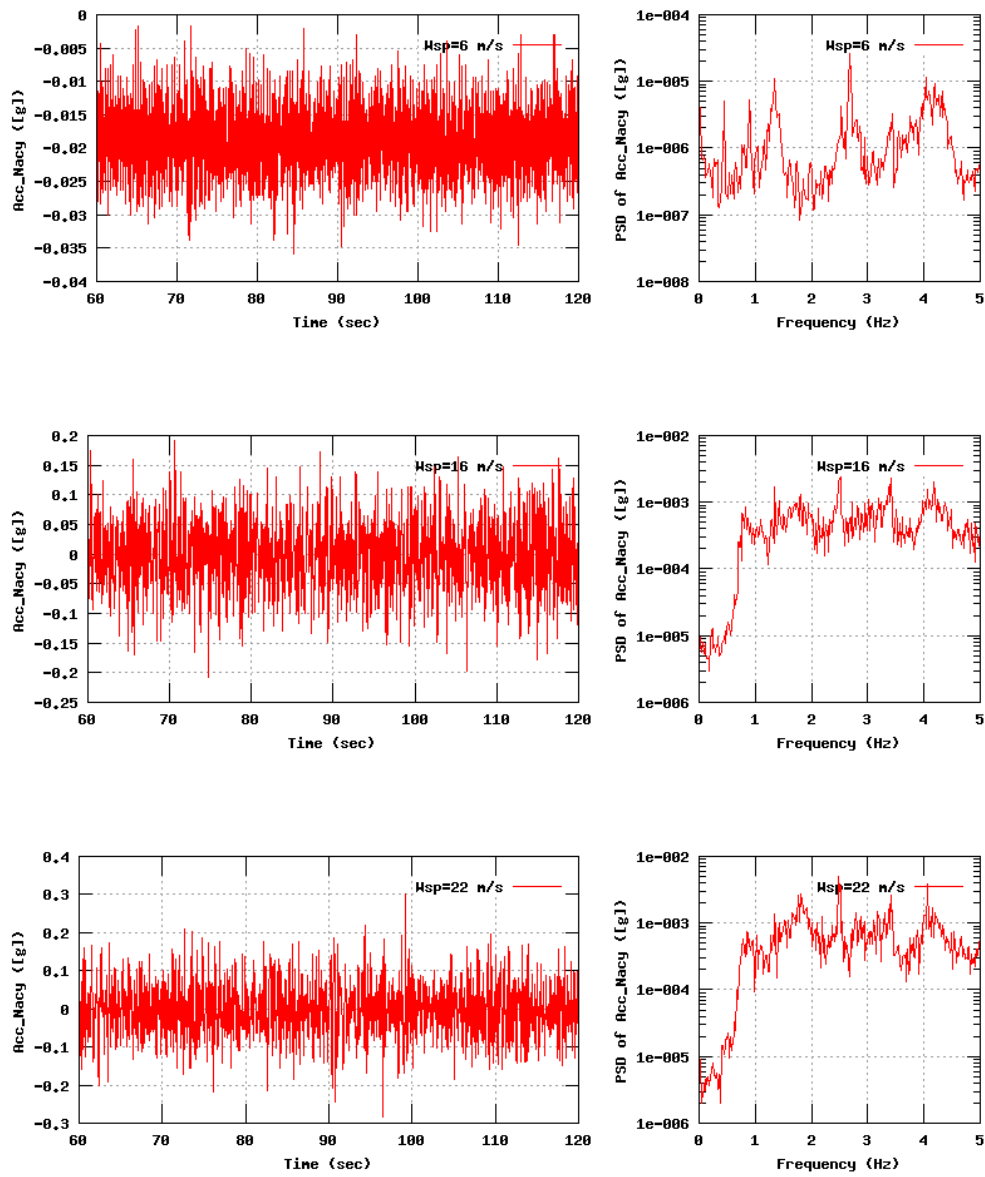
Figure 30b, Sensor 119: Acceleration nacelle leeward Acc_Nacy versus time and frequency
Input files: m06.dat, m16.dat, m22.dat, m06.psd, m16.psd and m22.psd
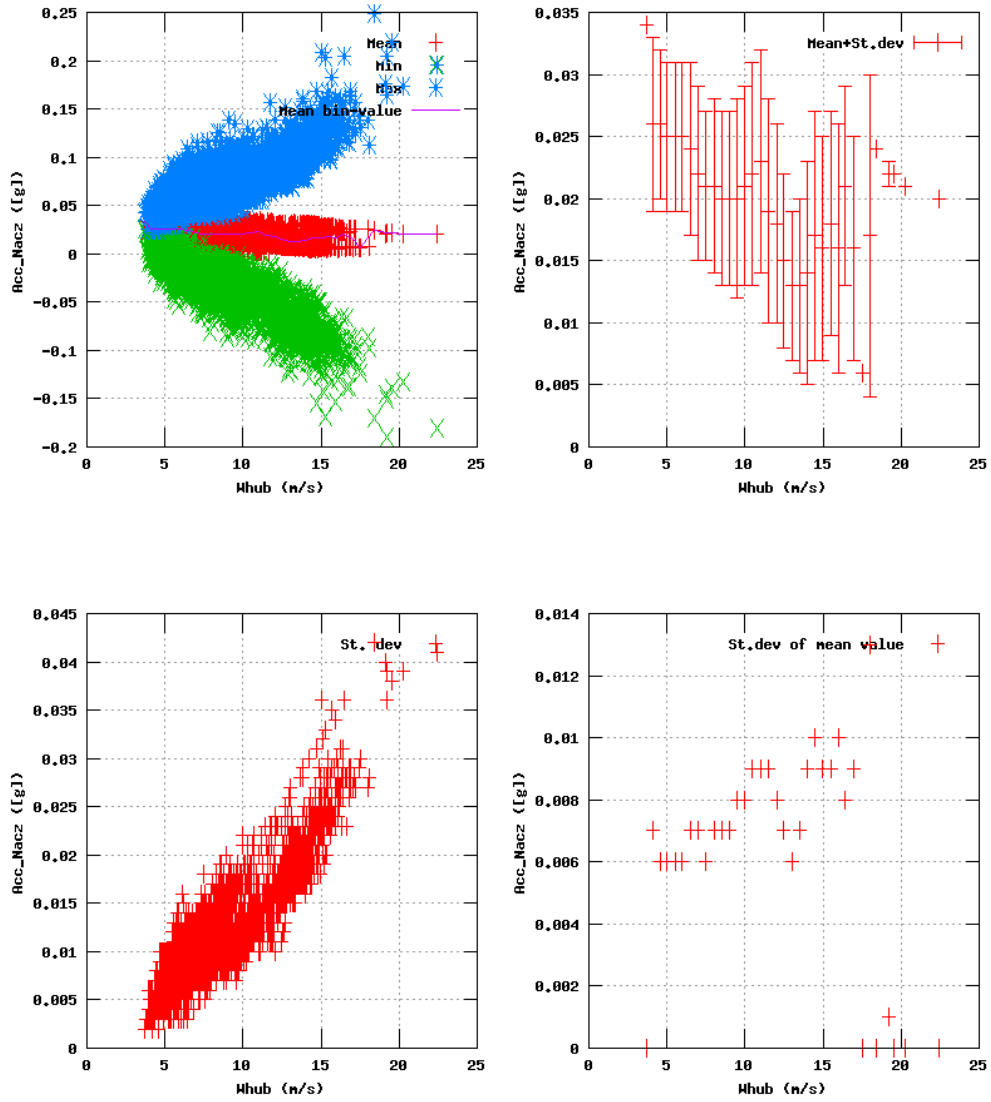
Figure 31a, Sensor 123: Acceleration nacelle leeward Acc_Nacz versus wind speed
Input files: ntk500res.dat, stat_123.dat
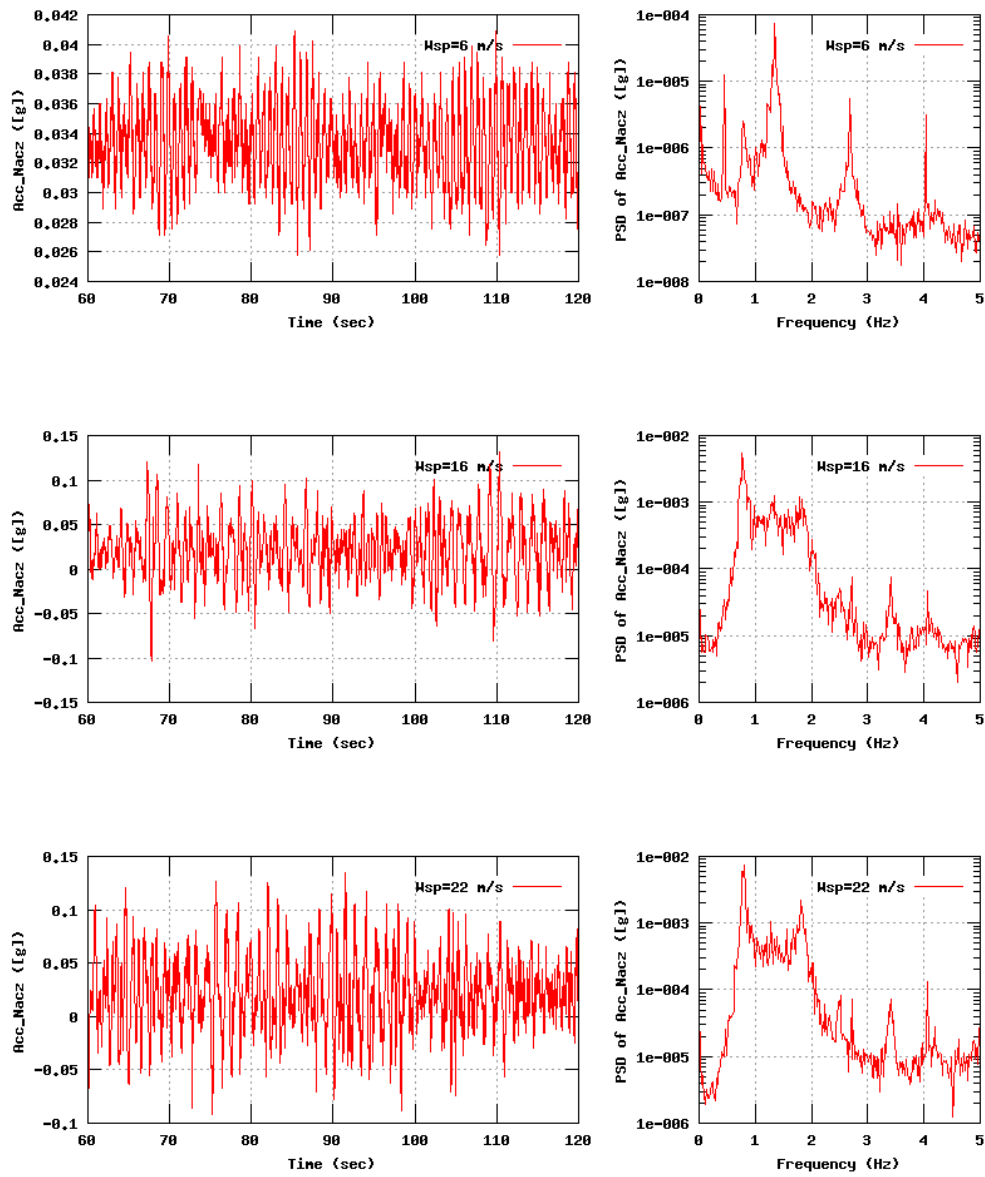
Figure 31b, Sensor 123: Acceleration nacelle leeward Acc_Nacz versus time and frequency
Input files: m06.dat, m16.dat, m22.dat, m06.psd, m16.psd and m22.psd
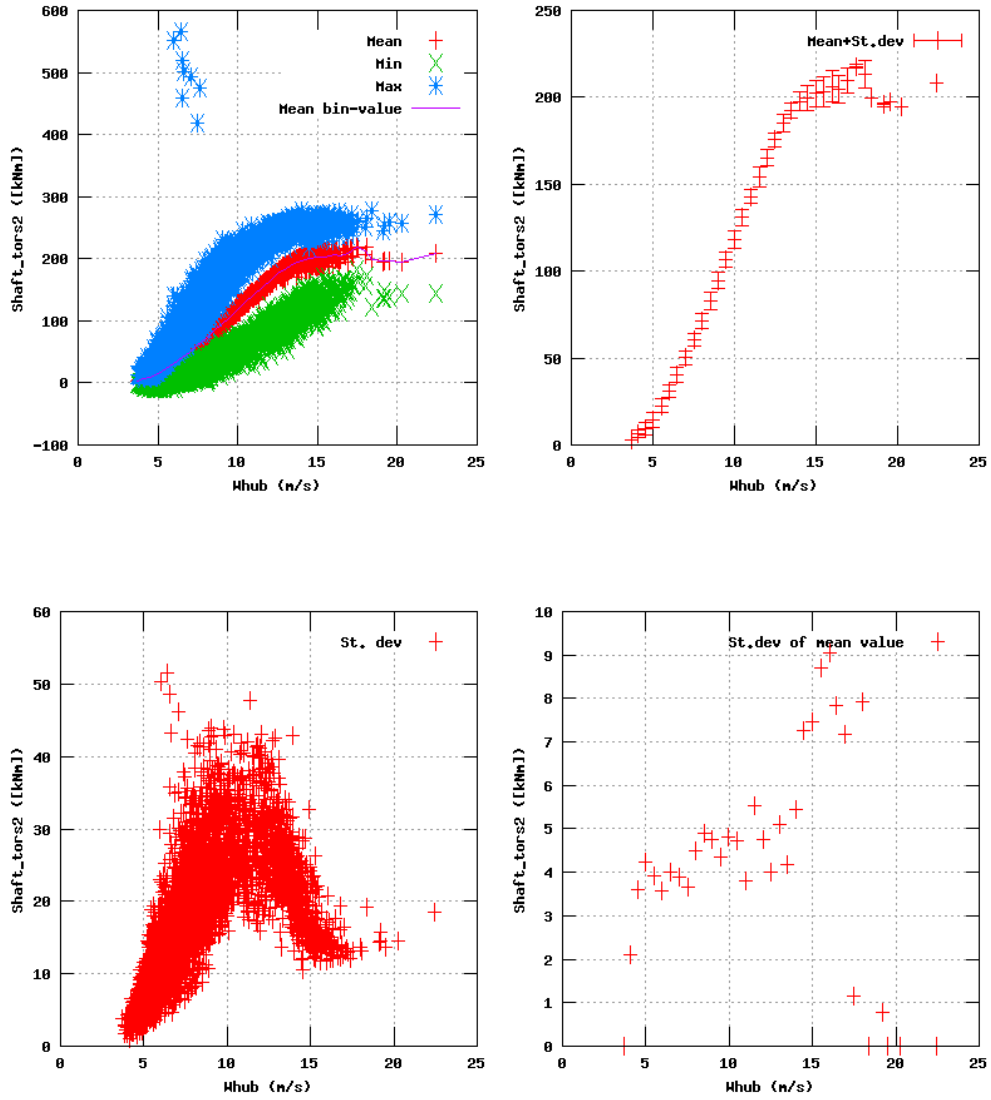
Figure 32a, Sensor 127: Rotor shaft torsion into gearbox Shaft_tors2 LSS versus wind speed
Input files: ntk500res.dat, stat_127.dat
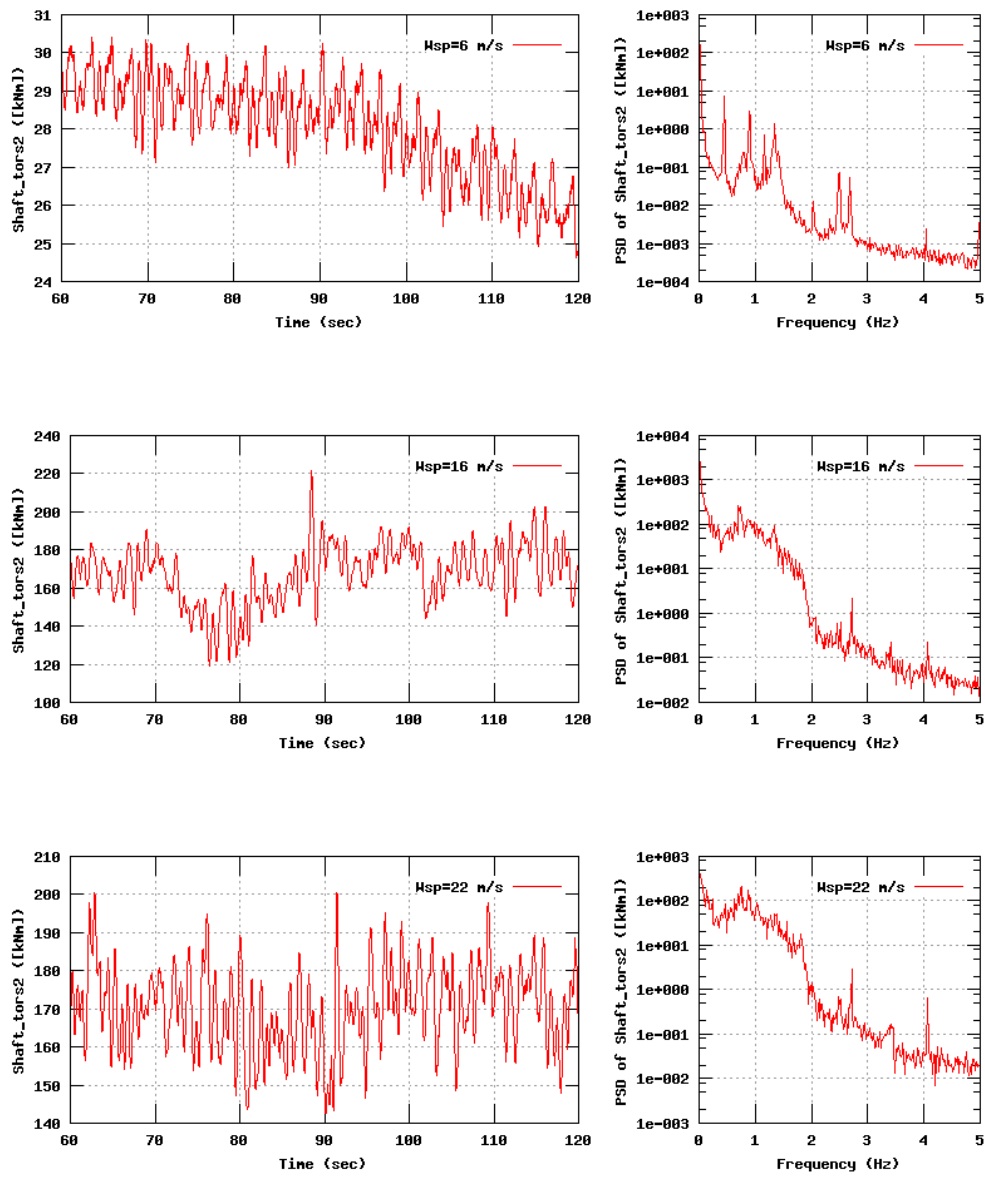
Figure 32b, Sensor 127: Rotor shaft torsion into gearbox Shaft_tors2 LSS versus time and frequency
Input files: m06.dat, m16.dat, m22.dat, m06.psd, m16.psd and m22.psd
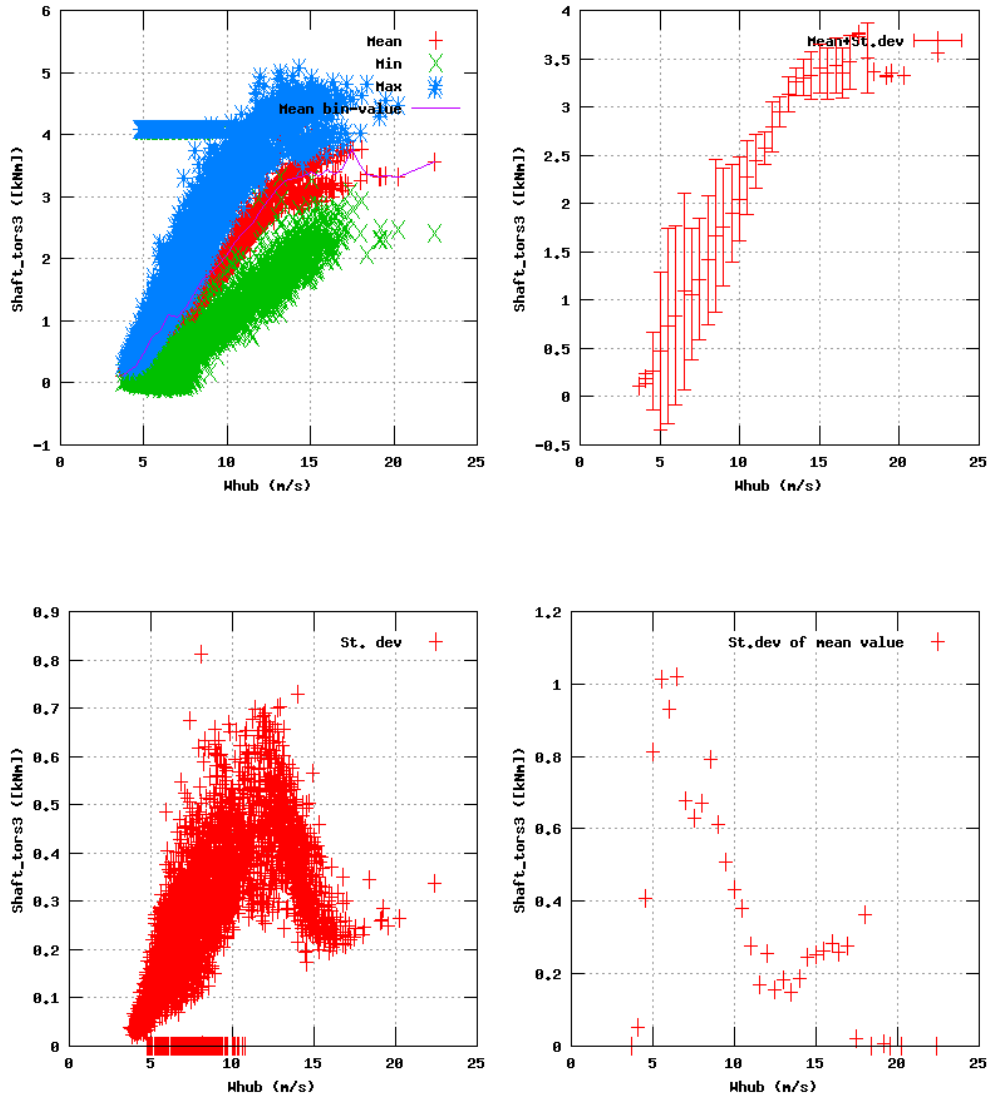
Figure 33a, Sensor 131: Rotor shaft torsion into generator Shaft_tors3 HSS versus wind speed
Input files: ntk500res.dat, stat_131.dat
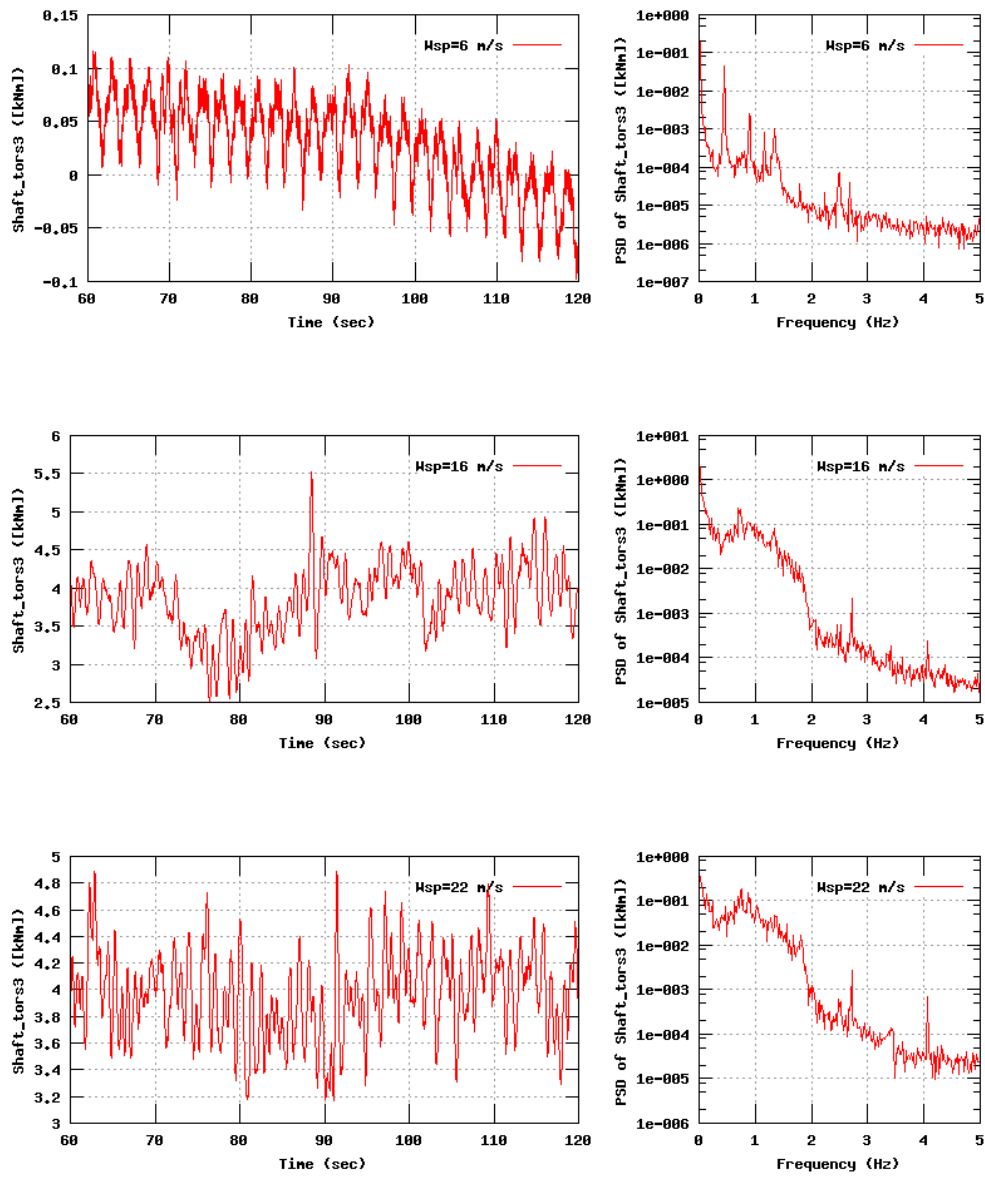
Figure 33b, Sensor 131: Rotor shaft torsion into generator Shaft_tors3 HSS versus time and frequency
Input files: m06.dat, m16.dat, m22.dat, m06.psd, m16.psd and m22.psd
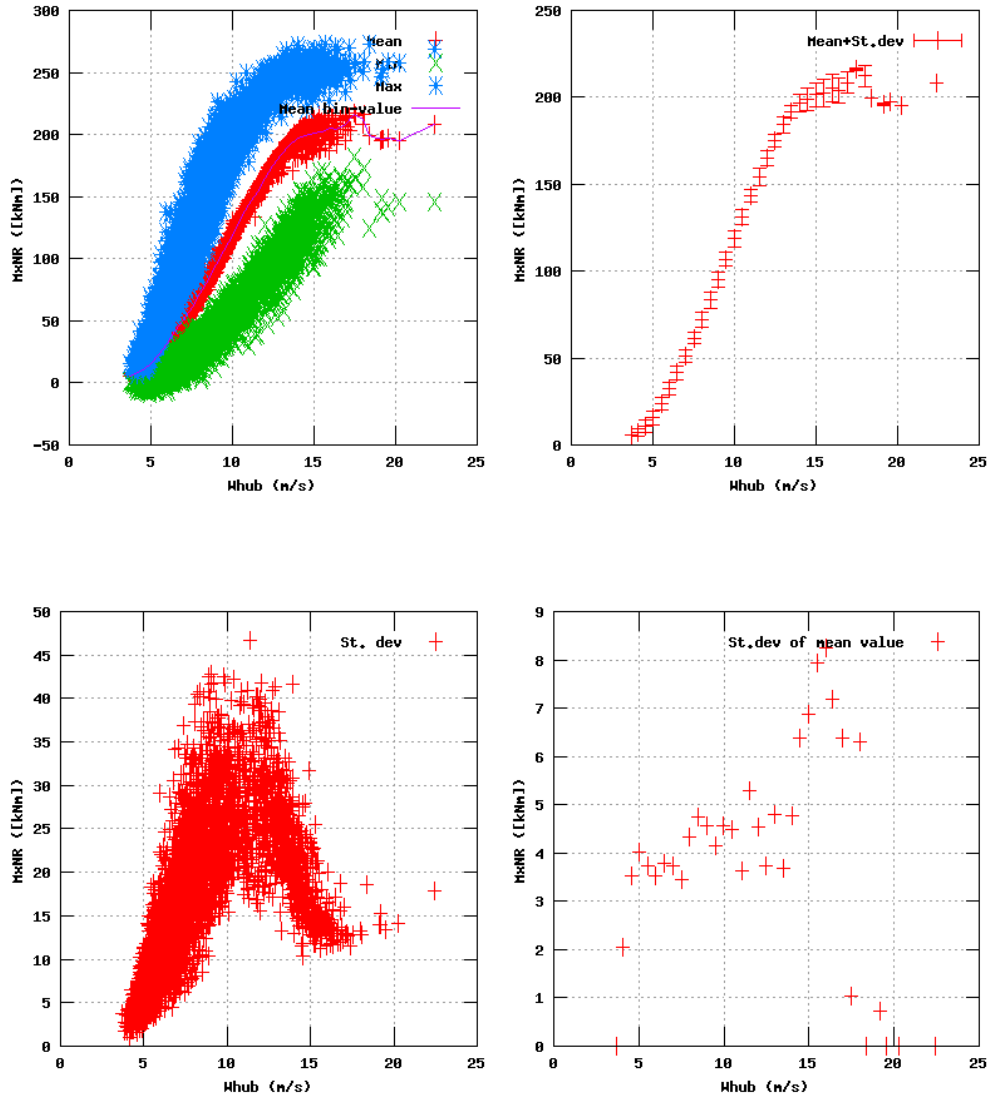
Figure 38a, Sensor 151: Rotor shaft torsion LSS versus wind speed
Input files: ntk500res.dat, stat_151.dat
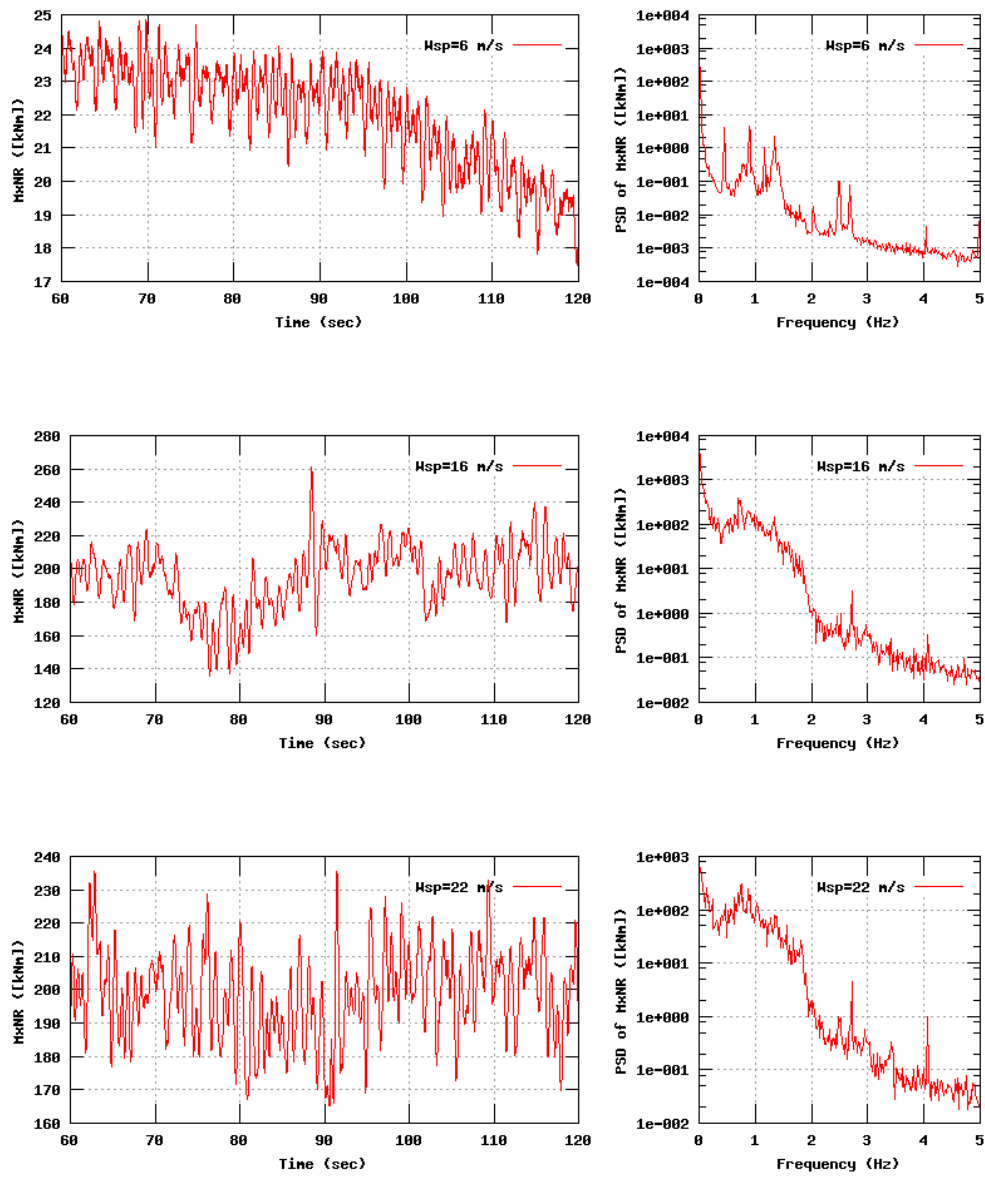
Figure 38b, Sensor 151: Rotor shaft torsion LSS versus time and frequency
Input files: m06.dat, m16.dat, m22.dat, m06.psd, m16.psd and m22.psd
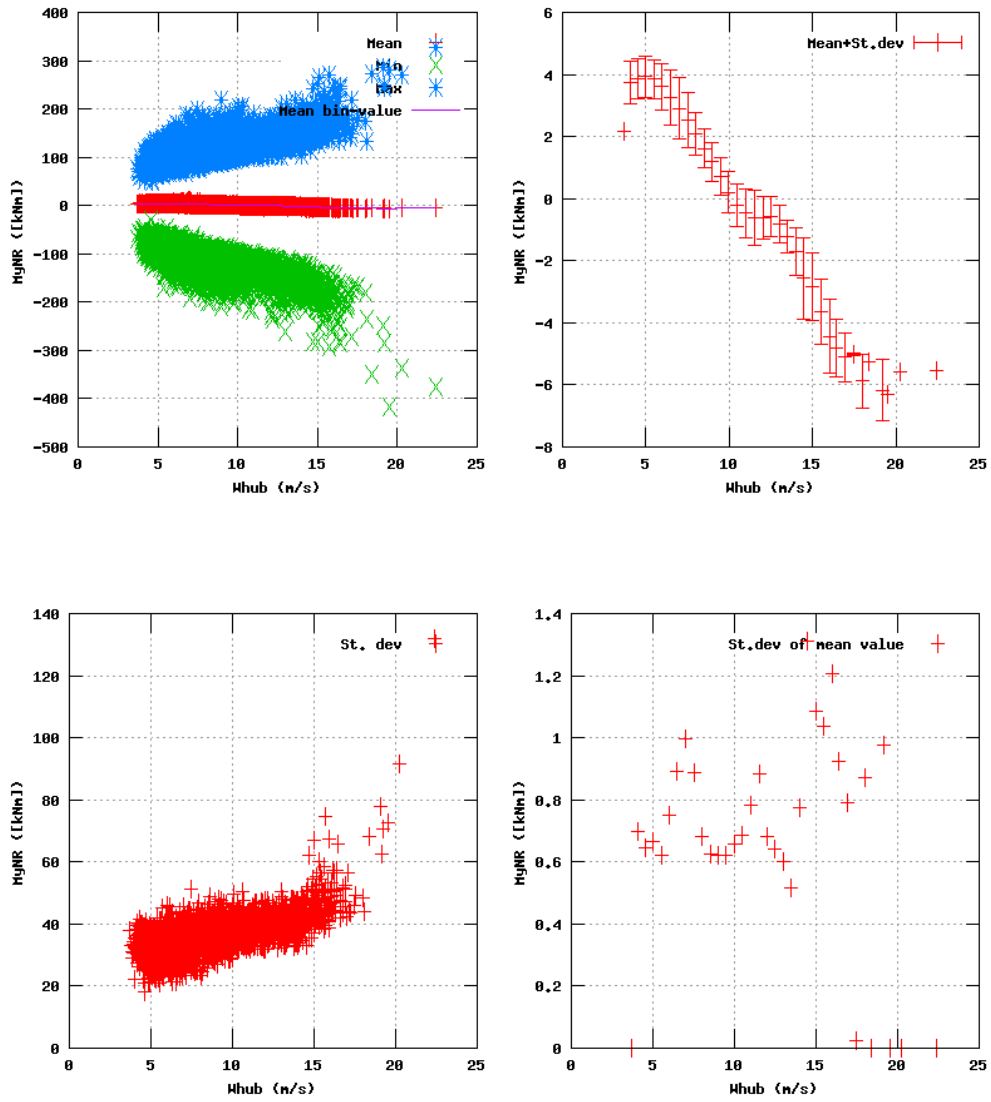
Figure 39a, Sensor 155: Rotor shaft bending moment y versus wind speed
Input files: ntk500res.dat, stat_155.dat
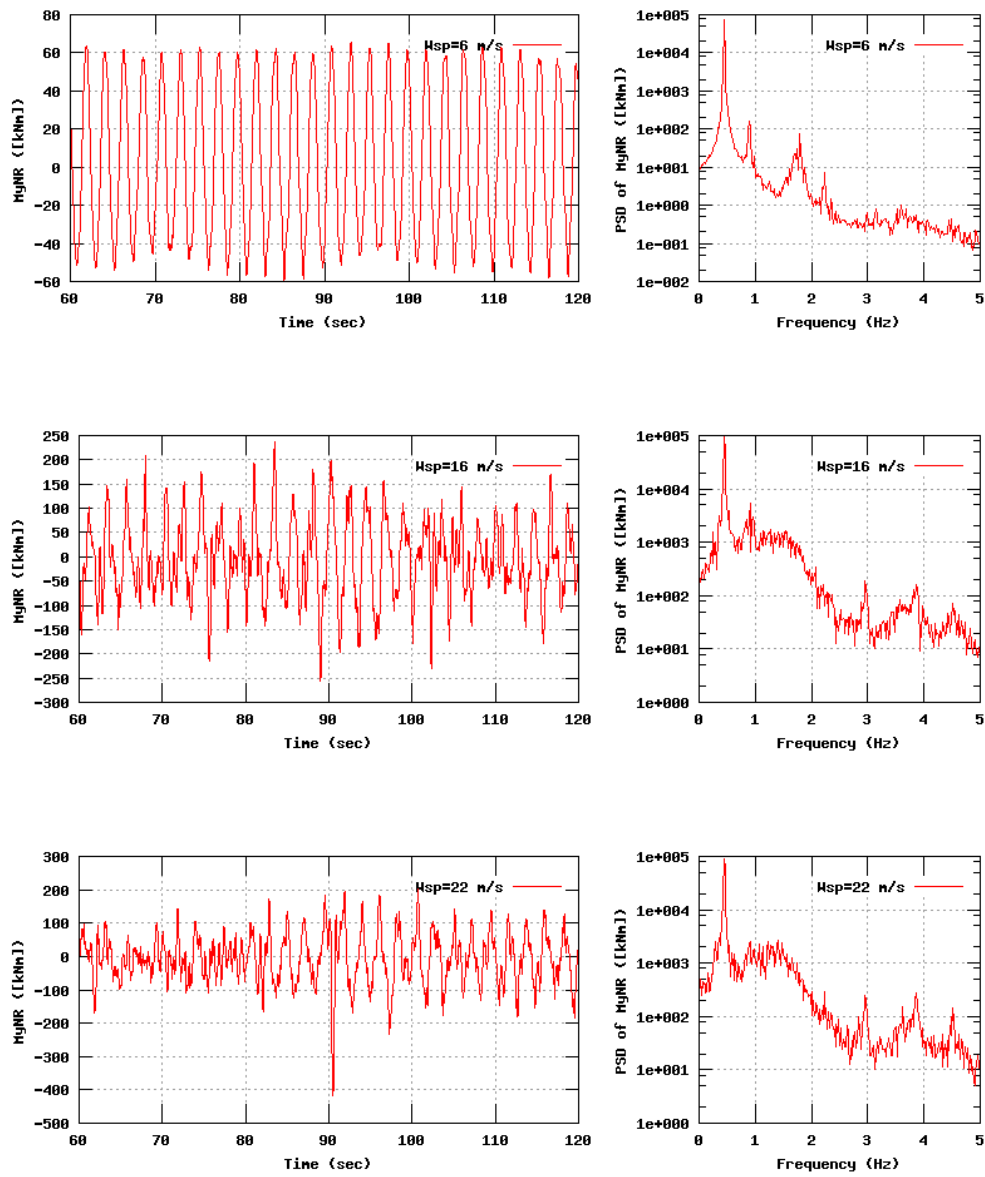
Figure 39b, Sensor 155: Rotor shaft bending moment y versus time and frequency
Input files: m06.dat, m16.dat, m22.dat, m06.psd, m16.psd and m22.psd
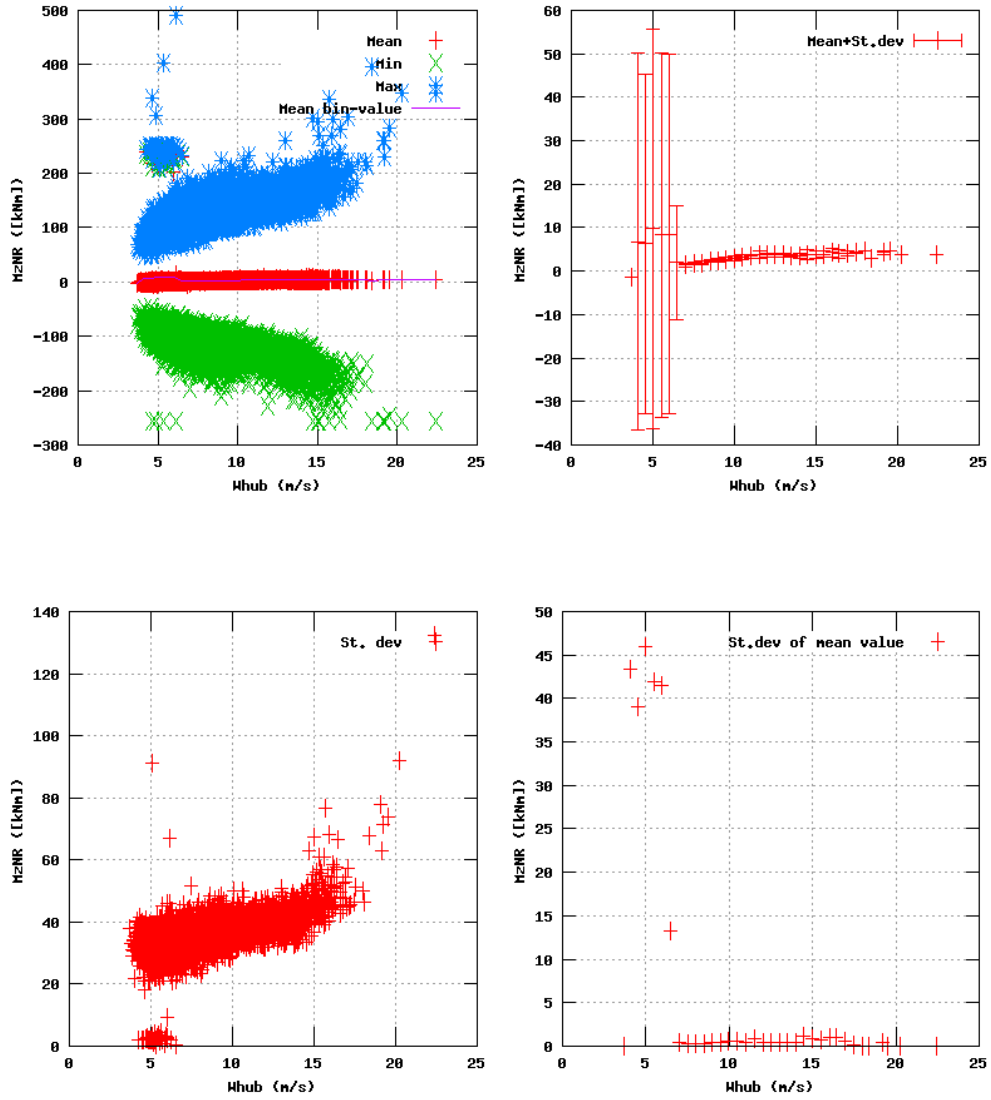
Figure 40a, Sensor 159: Rotor shaft bending moment z versus wind speed
Input files: ntk500res.dat, stat_159.dat
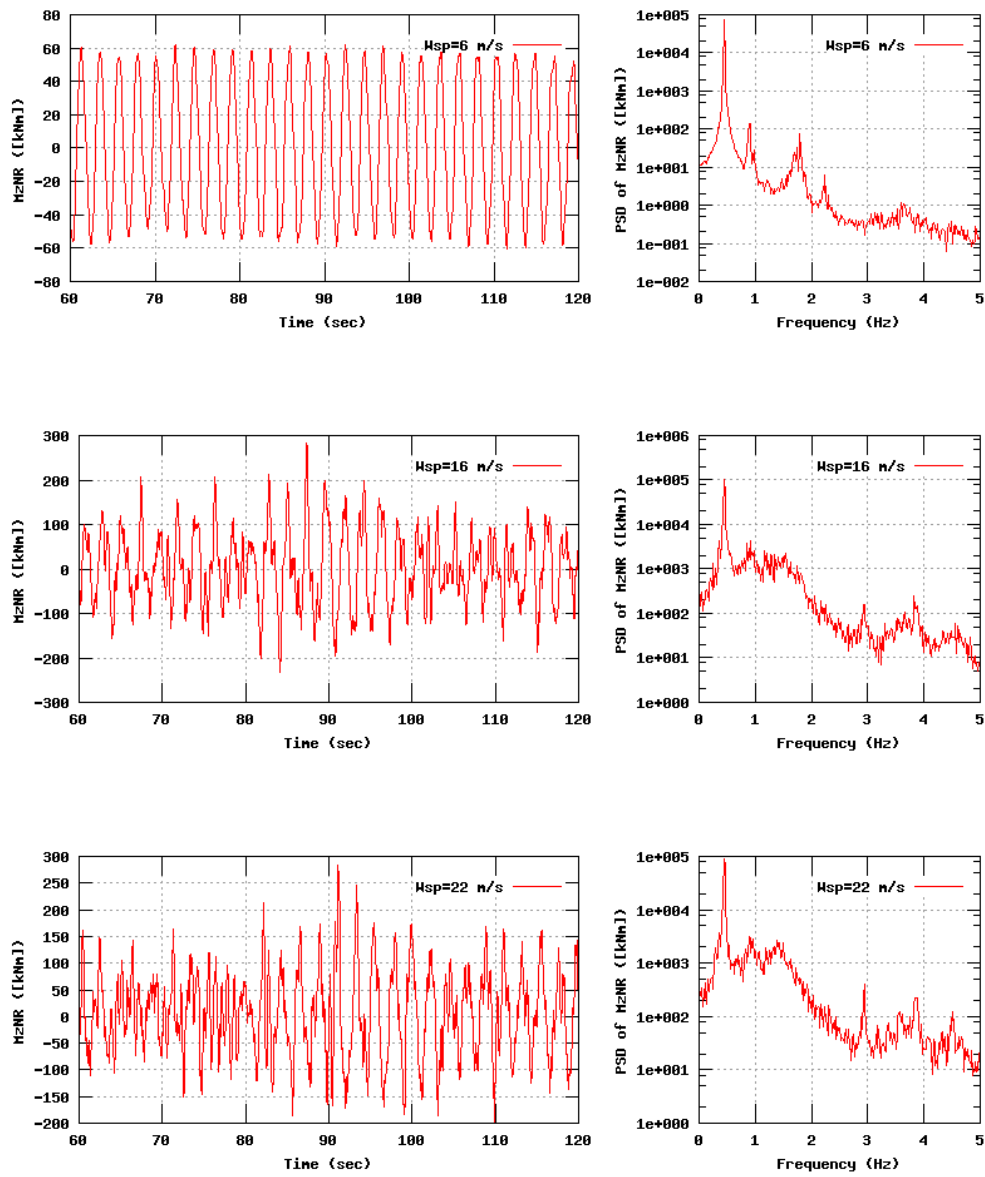
Figure 40b, Sensor 159: Rotor shaft bending moment z versus time and frequency
Input files: m06.dat, m16.dat, m22.dat, m06.psd, m16.psd and m22.psd
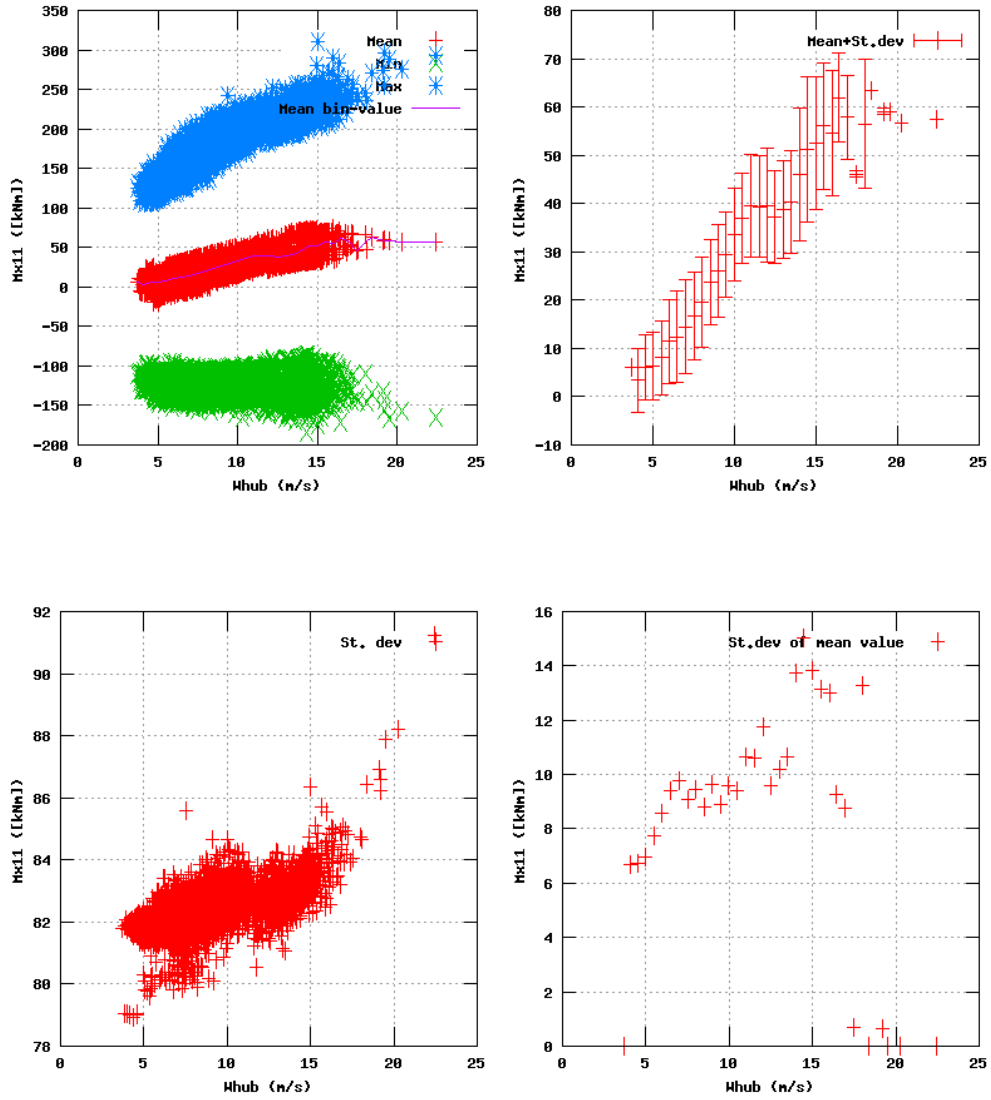
Figure 41a, Sensor 163: Edge bending moment B1 r=2.1m versus wind speed
Input files: ntk500res.dat, stat_163.dat
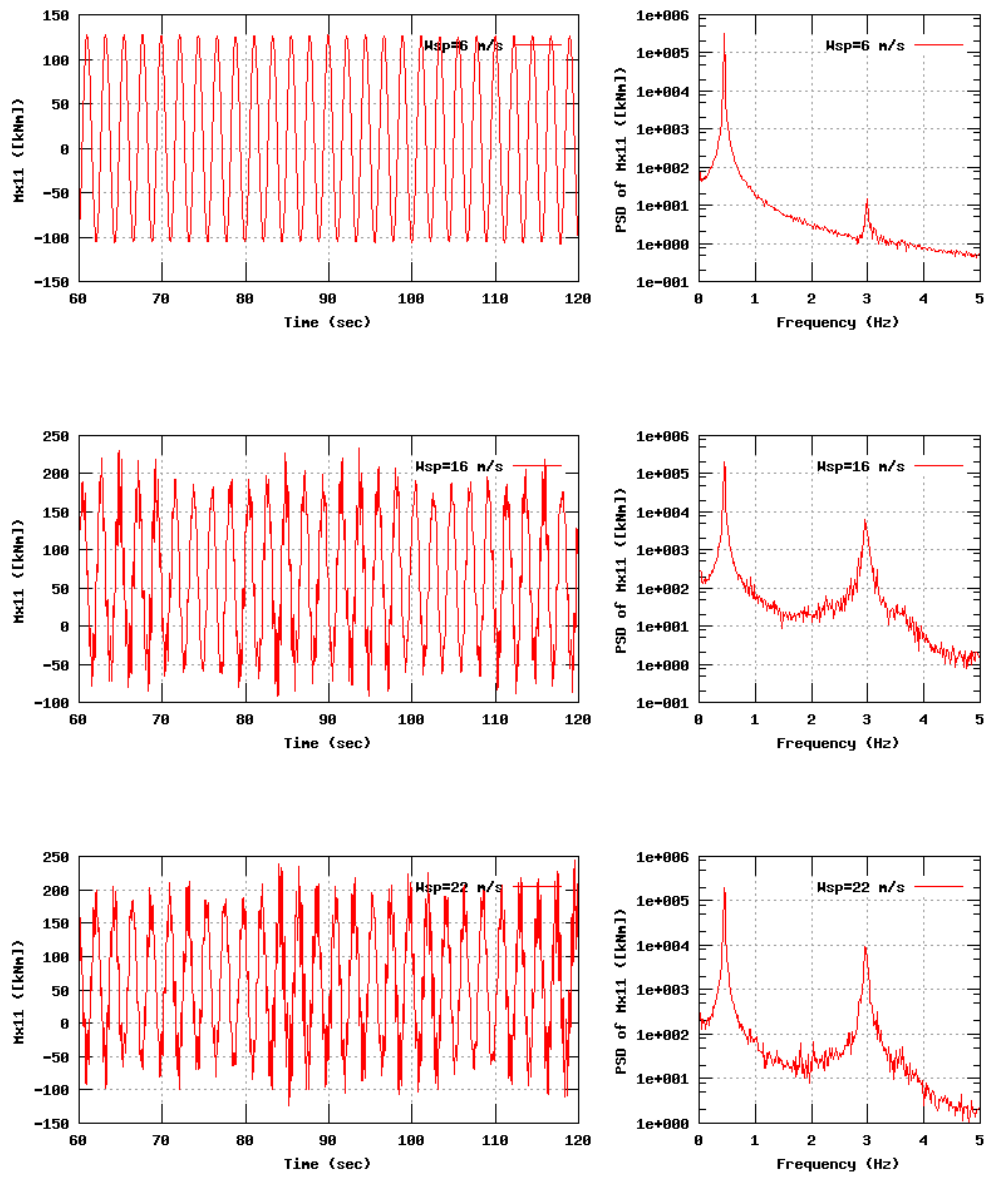
Figure 41b, Sensor 163: Edge bending moment B1 r=2.1m versus time and frequency
Input files: m06.dat, m16.dat, m22.dat, m06.psd, m16.psd and m22.psd
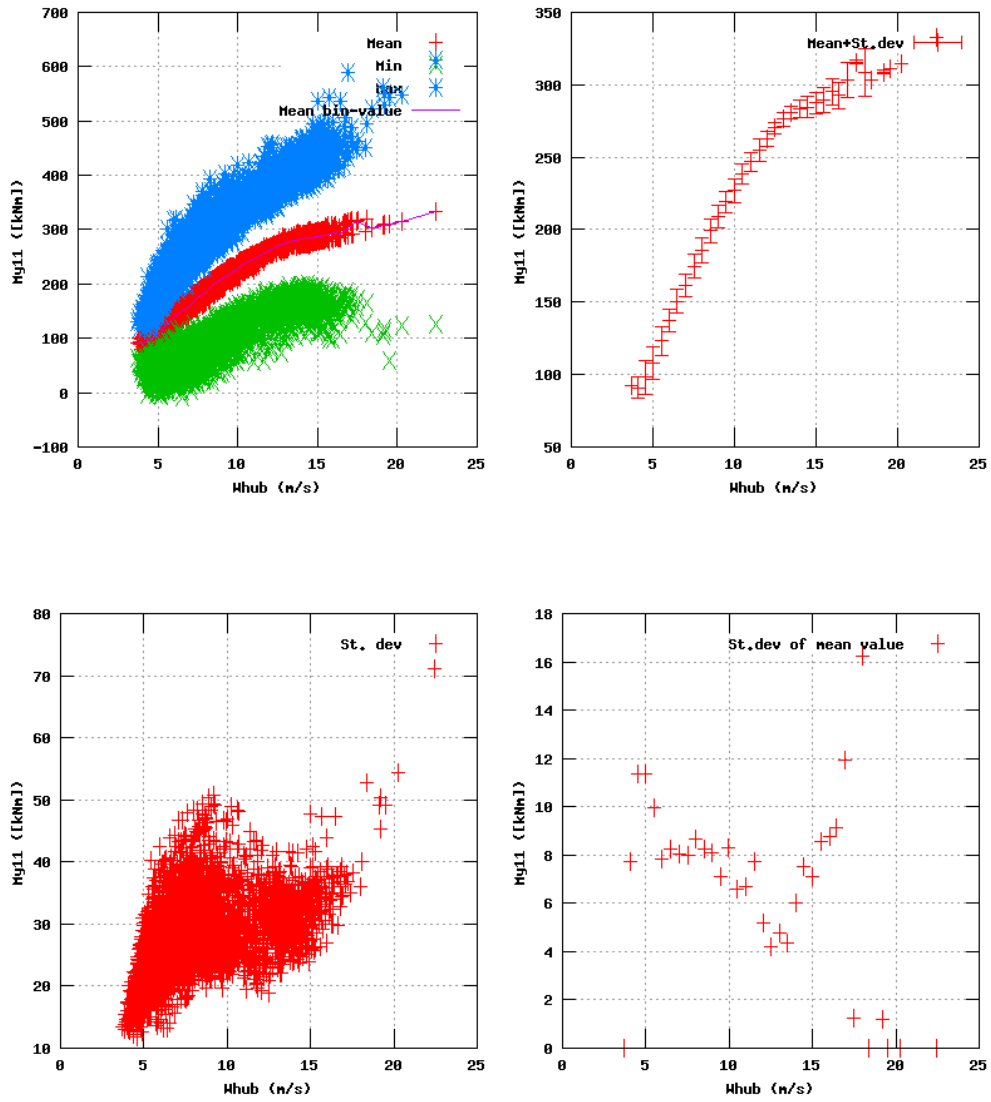
Figure 42a, Sensor 167: Flap bending moment B1 r=2.1m versus wind speed
Input files: ntk500res.dat, stat_167.dat
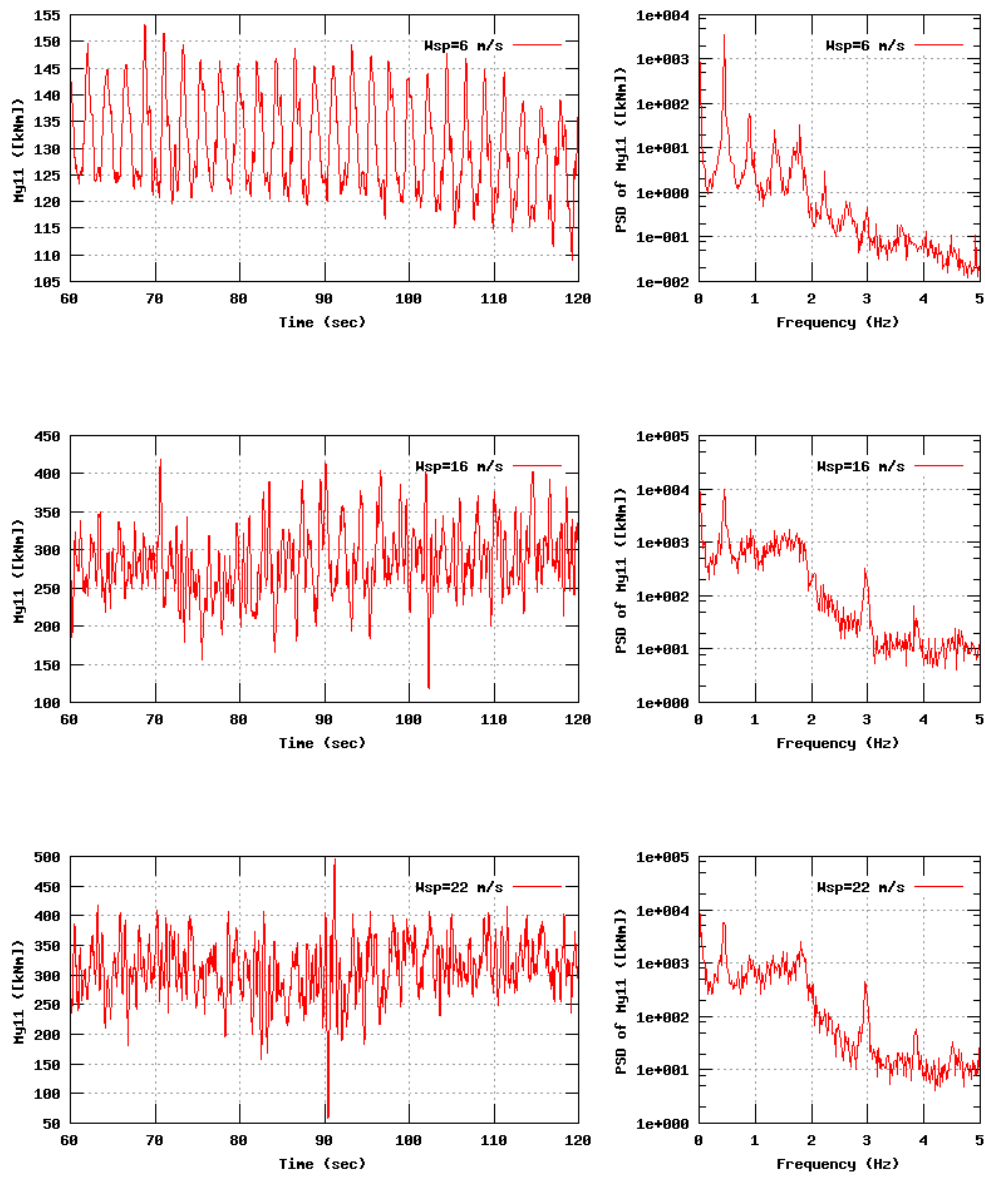
Figure 42b, Sensor 167: Flap bending moment B1 r=2.1m versus time and frequency
Input files: m06.dat, m16.dat, m22.dat, m06.psd, m16.psd and m22.psd
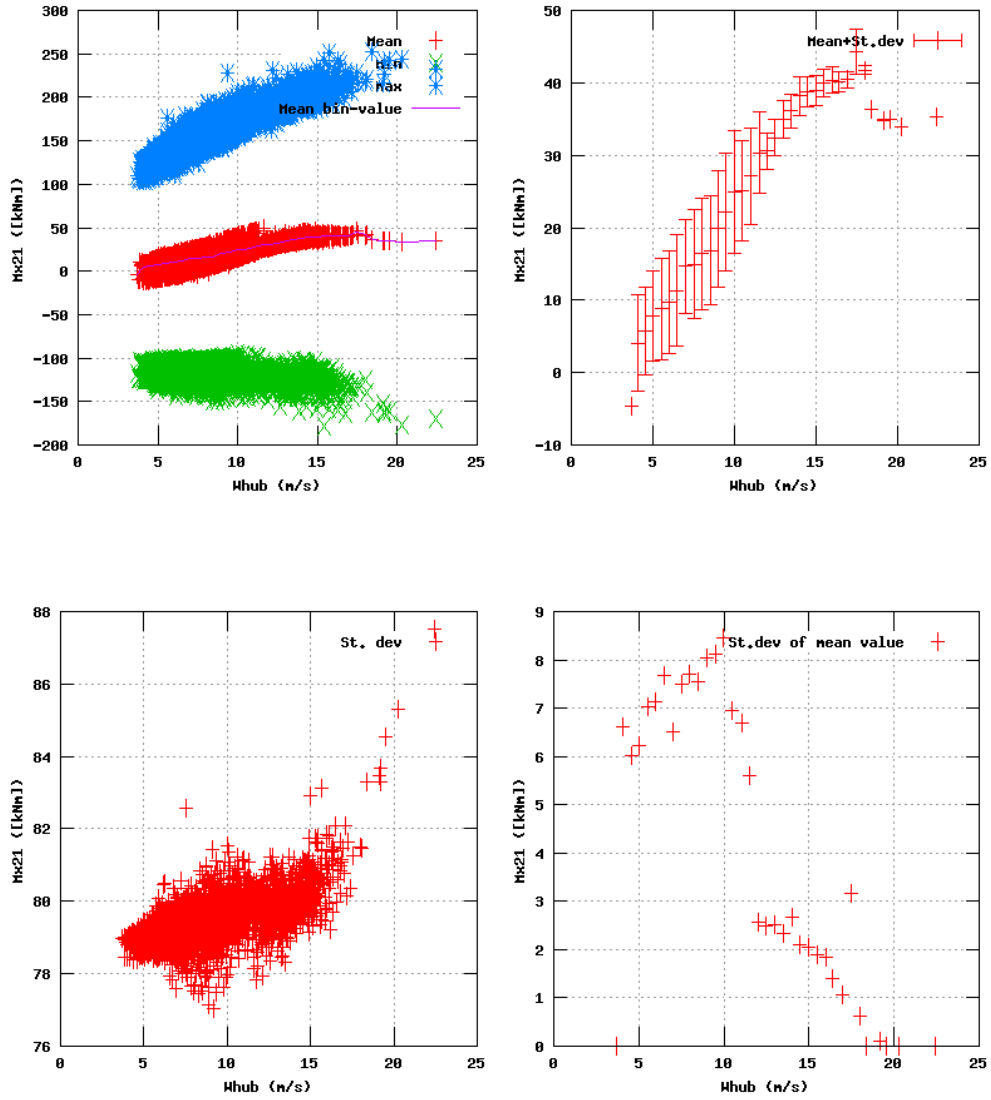
Figure 45a, Sensor 179: Edge bending moment B2 r=2.1m versus wind speed
Input files: ntk500res.dat, stat_179.dat
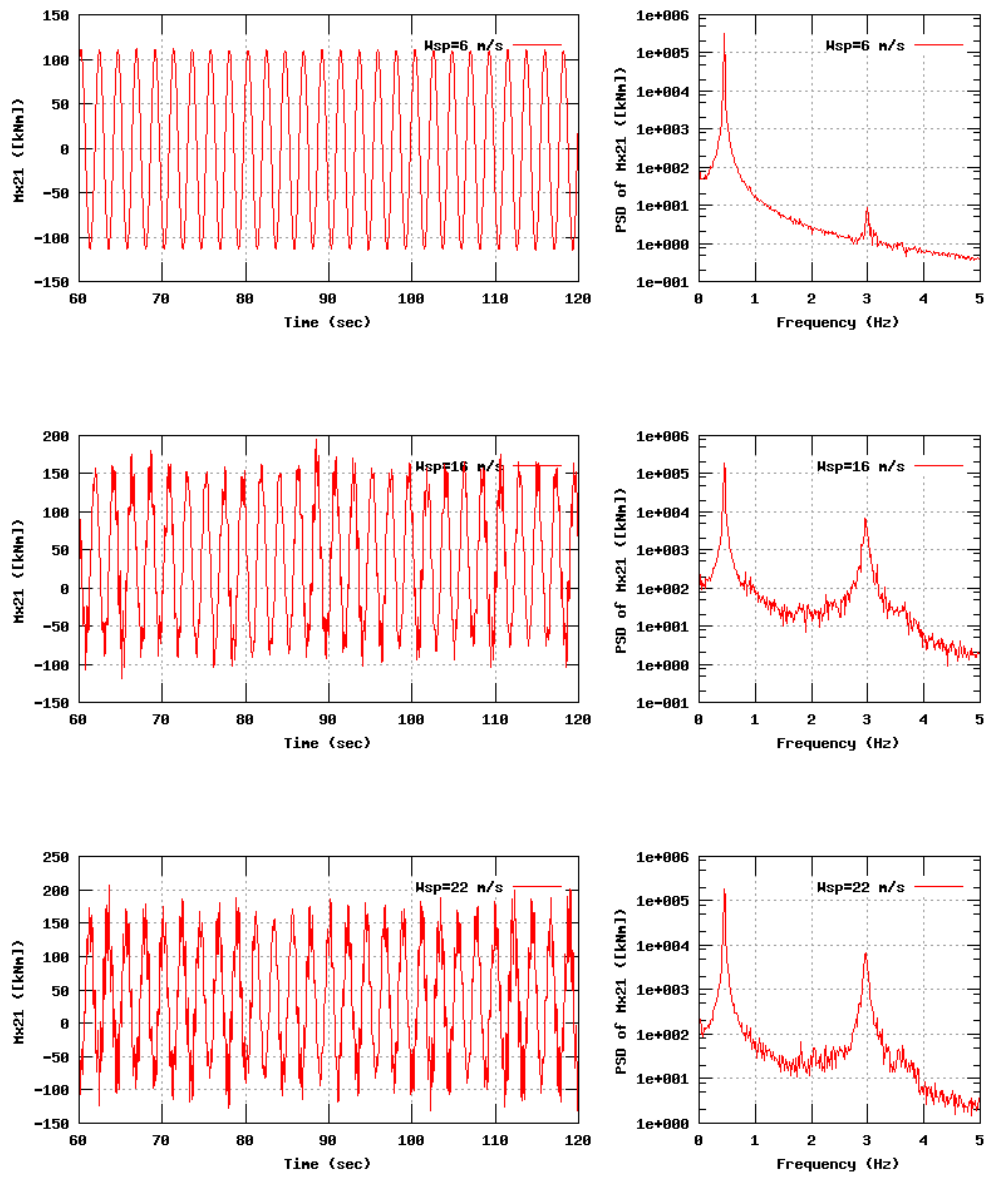
Figure 45b, Sensor 179: Edge bending moment B2 r=2.1m versus time and frequency
Input files: m06.dat, m16.dat, m22.dat, m06.psd, m16.psd and m22.psd
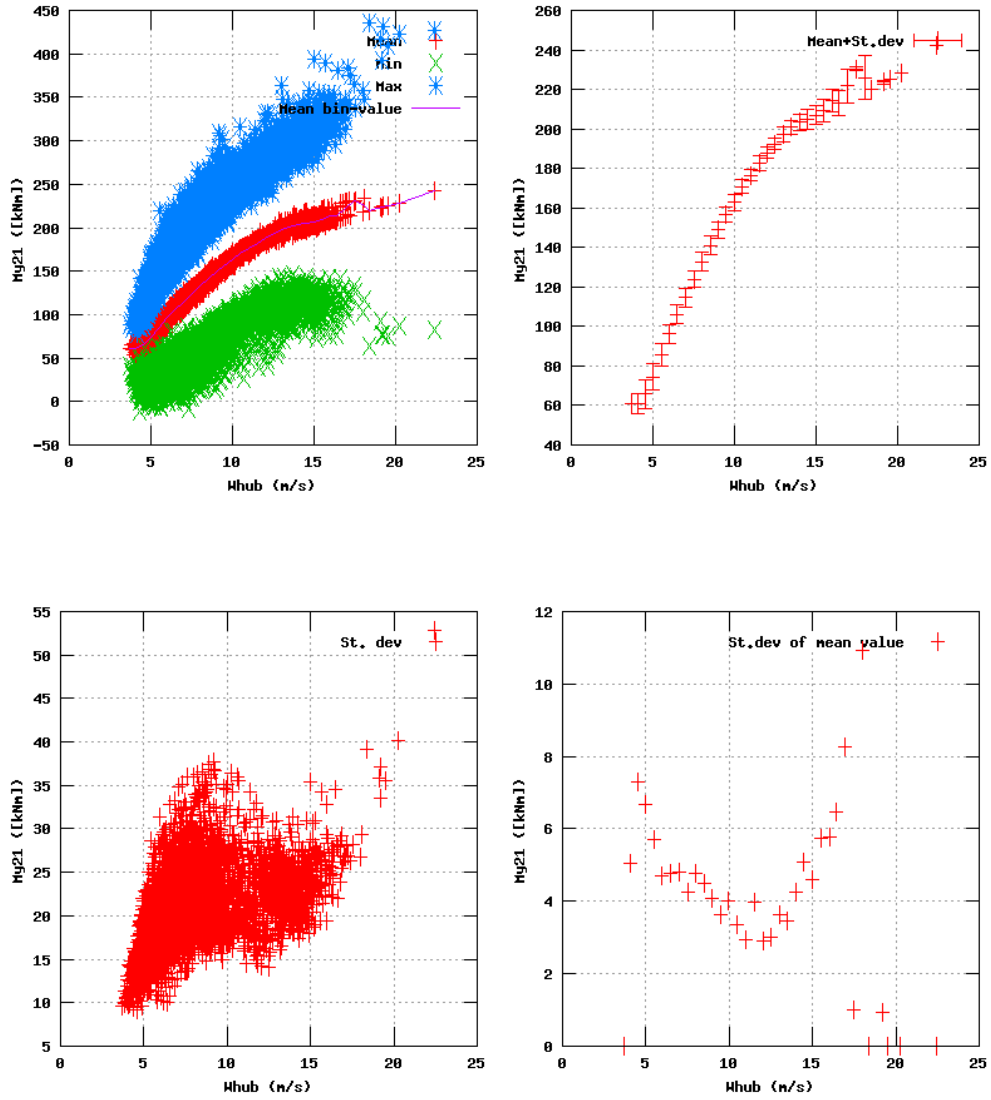
Figure 46a, Sensor 183: Flap bending moment B2 r=2.1m versus wind speed
Input files: ntk500res.dat, stat_183.dat
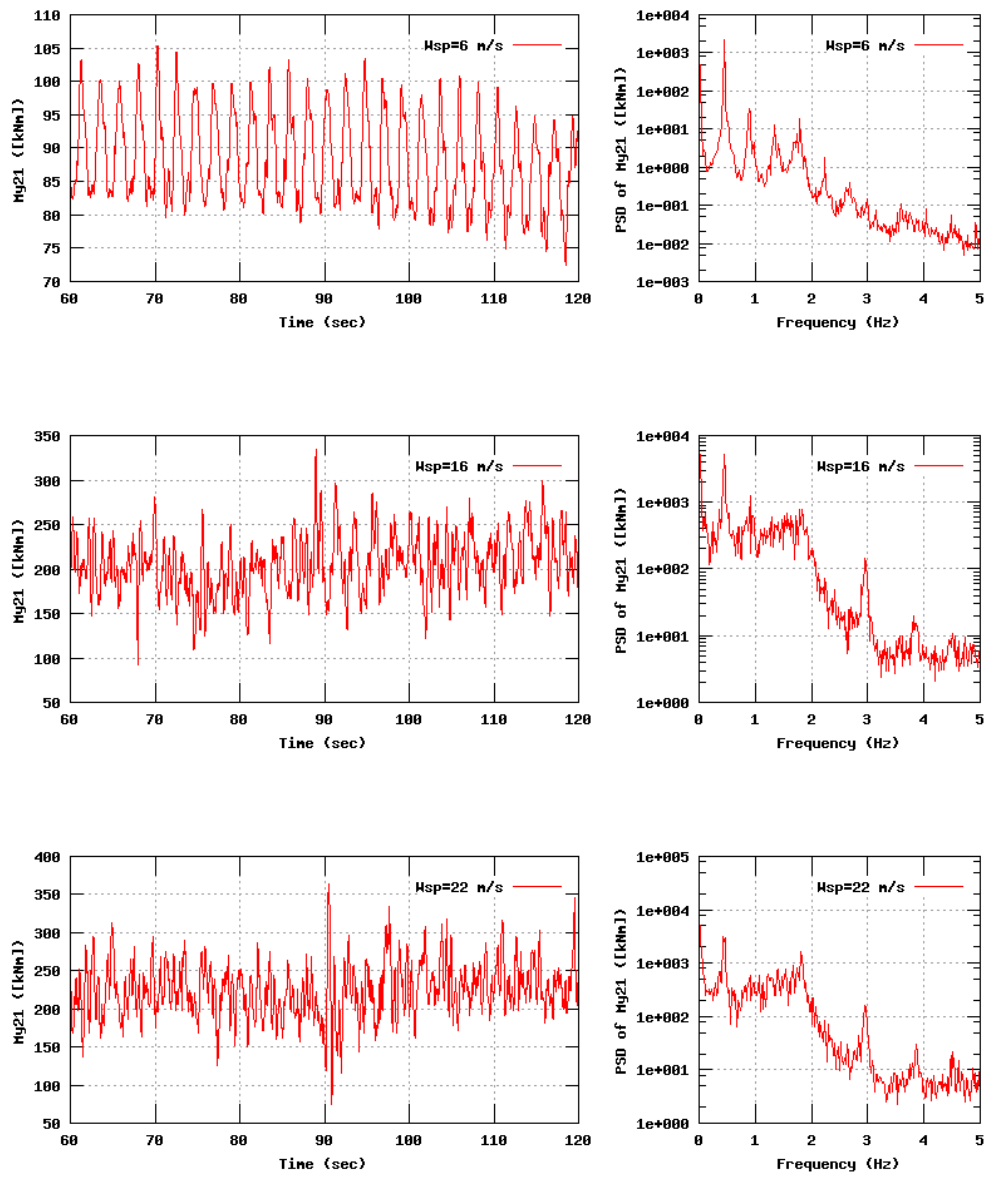
Figure 46b, Sensor 183: Flap bending moment B2 r=2.1m versus time and frequency
Input files: m06.dat, m16.dat, m22.dat, m06.psd, m16.psd and m22.psd
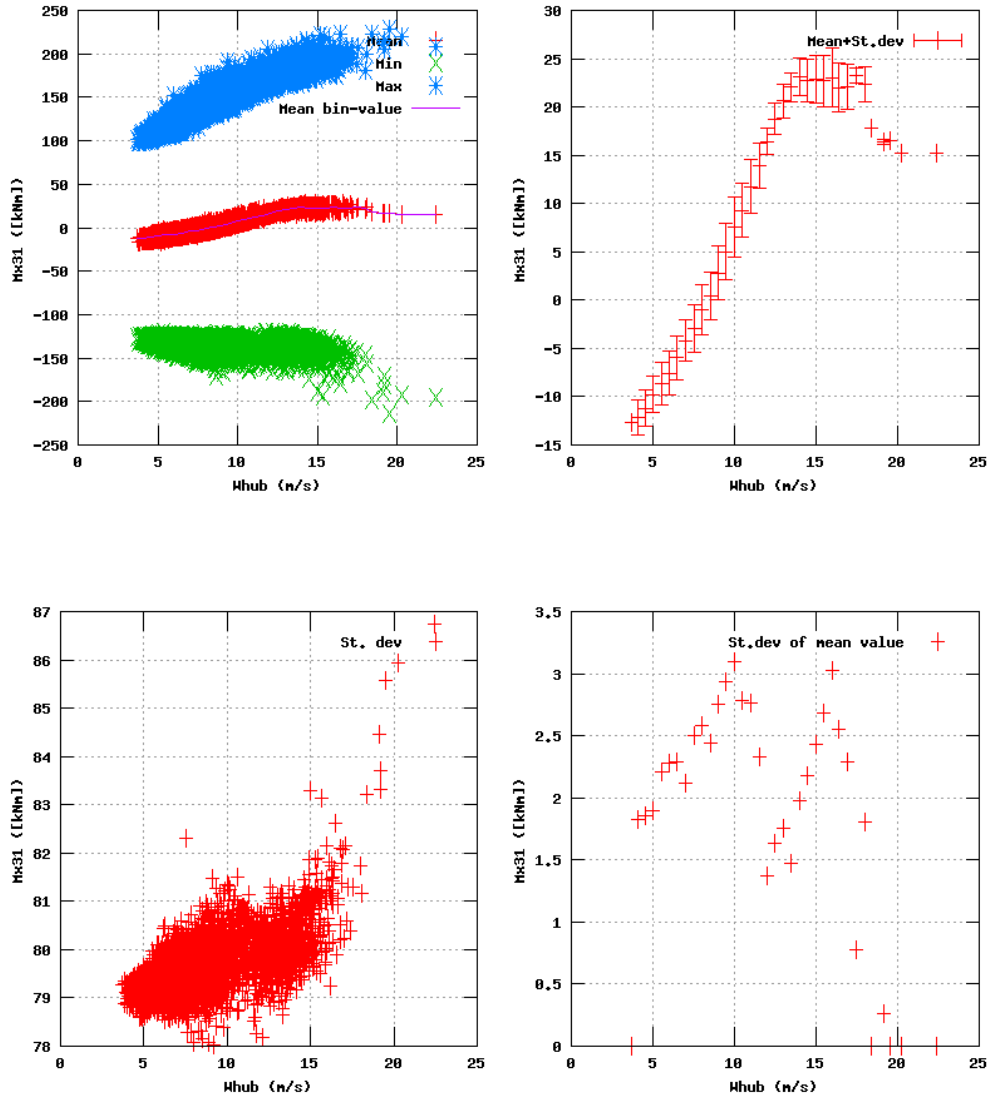
Figure 43a, Sensor 171: Edge bending moment B3 r=2.1m versus wind speed
Input files: ntk500res.dat, stat_171.dat
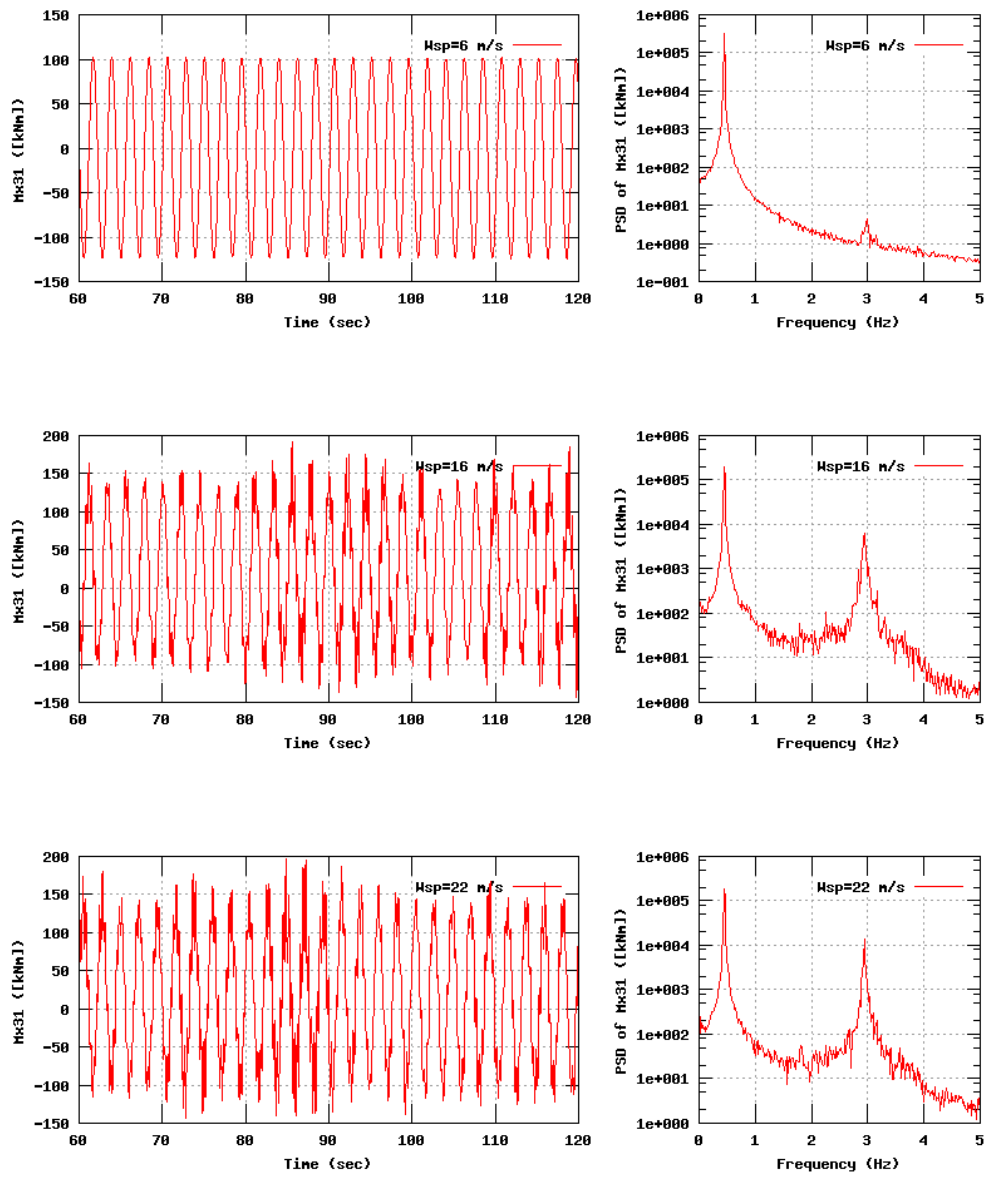
Figure 43b, Sensor 171: Edge bending moment B3 r=2.1m versus time and frequency
Input files: m06.dat, m16.dat, m22.dat, m06.psd, m16.psd and m22.psd
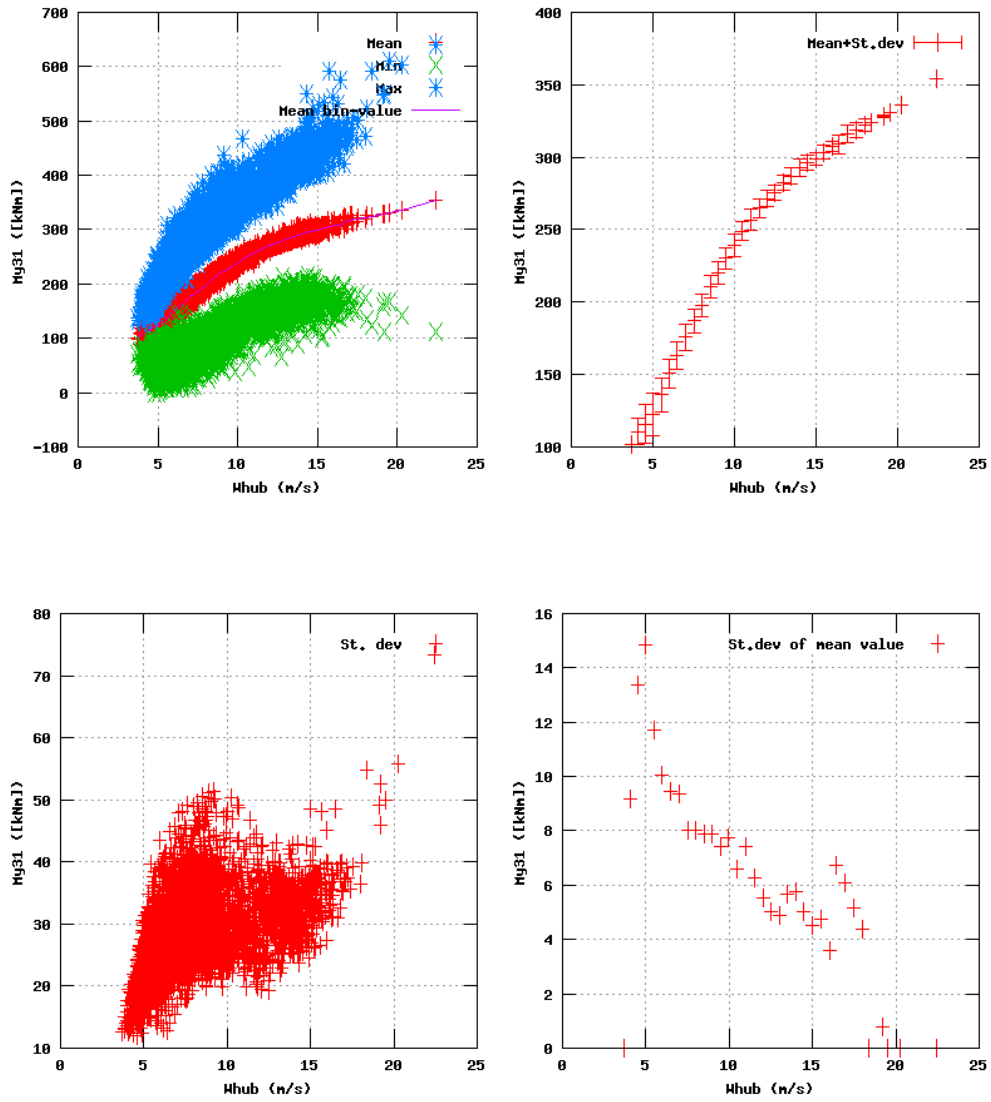
Figure 44a, Sensor 175: Flap bending moment B3 r=2.1m versus wind speed
Input files: ntk500res.dat, stat_175.dat
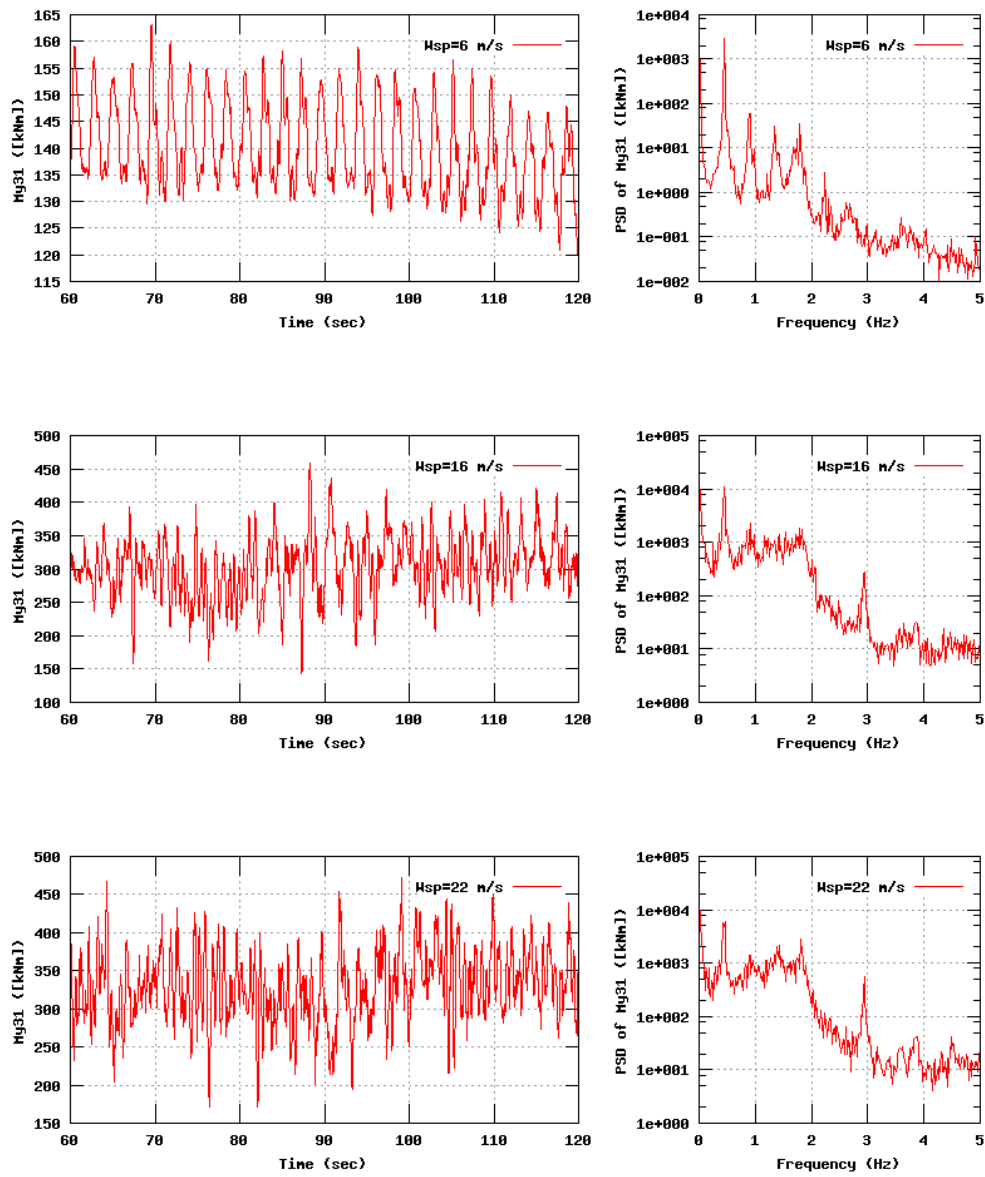
Figure 44b, Sensor 175: Flap bending moment B3 r=2.1m versus time and frequency
Input files: m06.dat, m16.dat, m22.dat, m06.psd, m16.psd and m22.psd
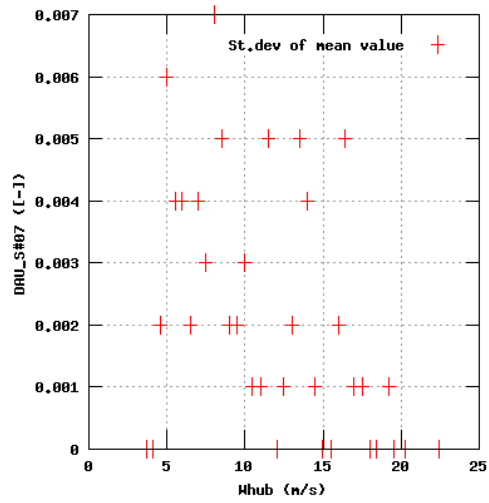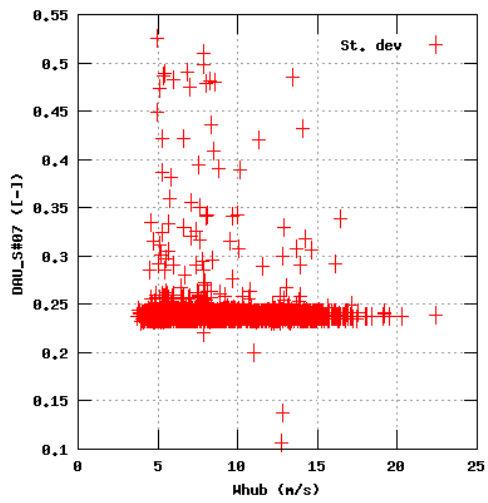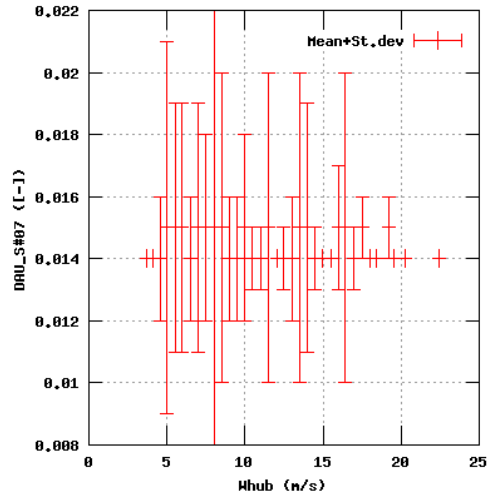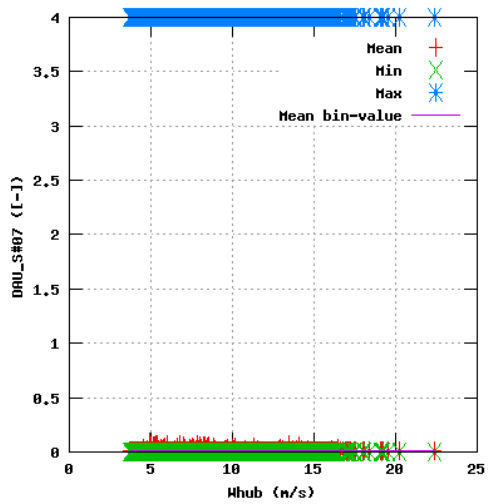
Figure 47a, Sensor 187: DAU_S#07 versus wind speed
Input files: ntk500res.dat, stat_187.dat
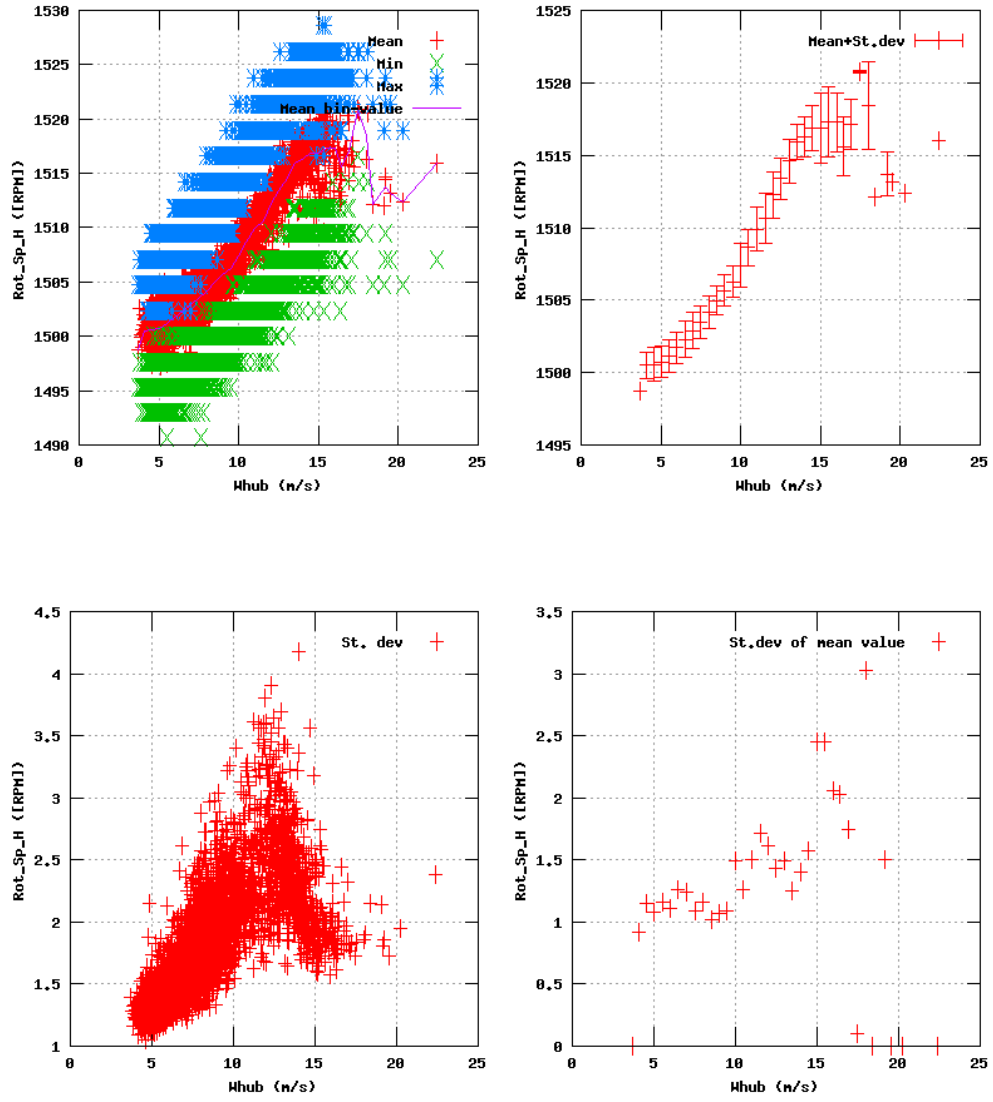
Figure 24a, Sensor 95: Rotor shaft speed HSS Rot_Sp_H versus wind speed
Input files: ntk500res.dat, stat_95.dat
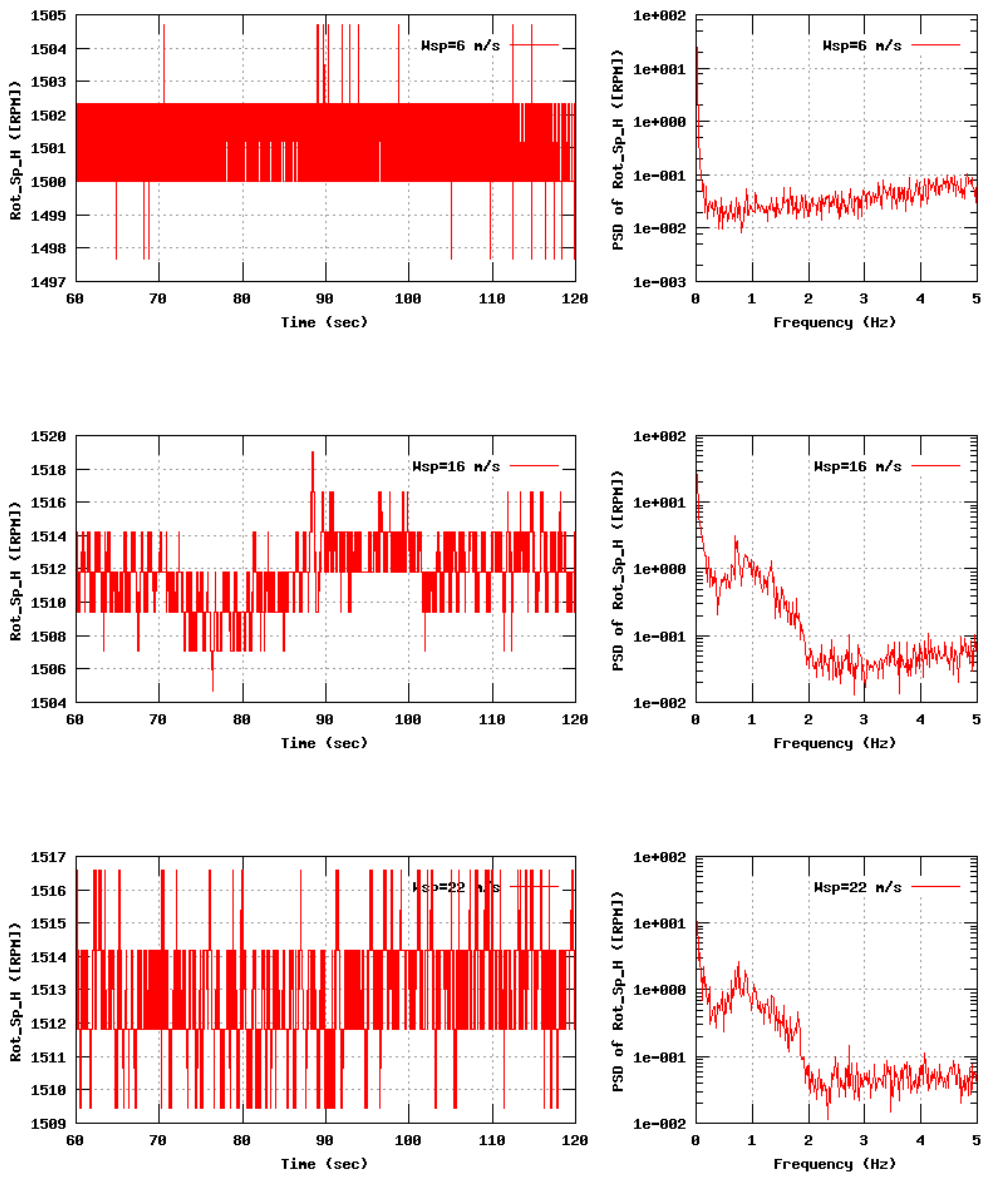
Figure 24b, Sensor 95: Rotor shaft speed HSS Rot_Sp_H versus time and frequency
Input files: m06.dat, m16.dat, m22.dat, m06.psd, m16.psd and m22.psd
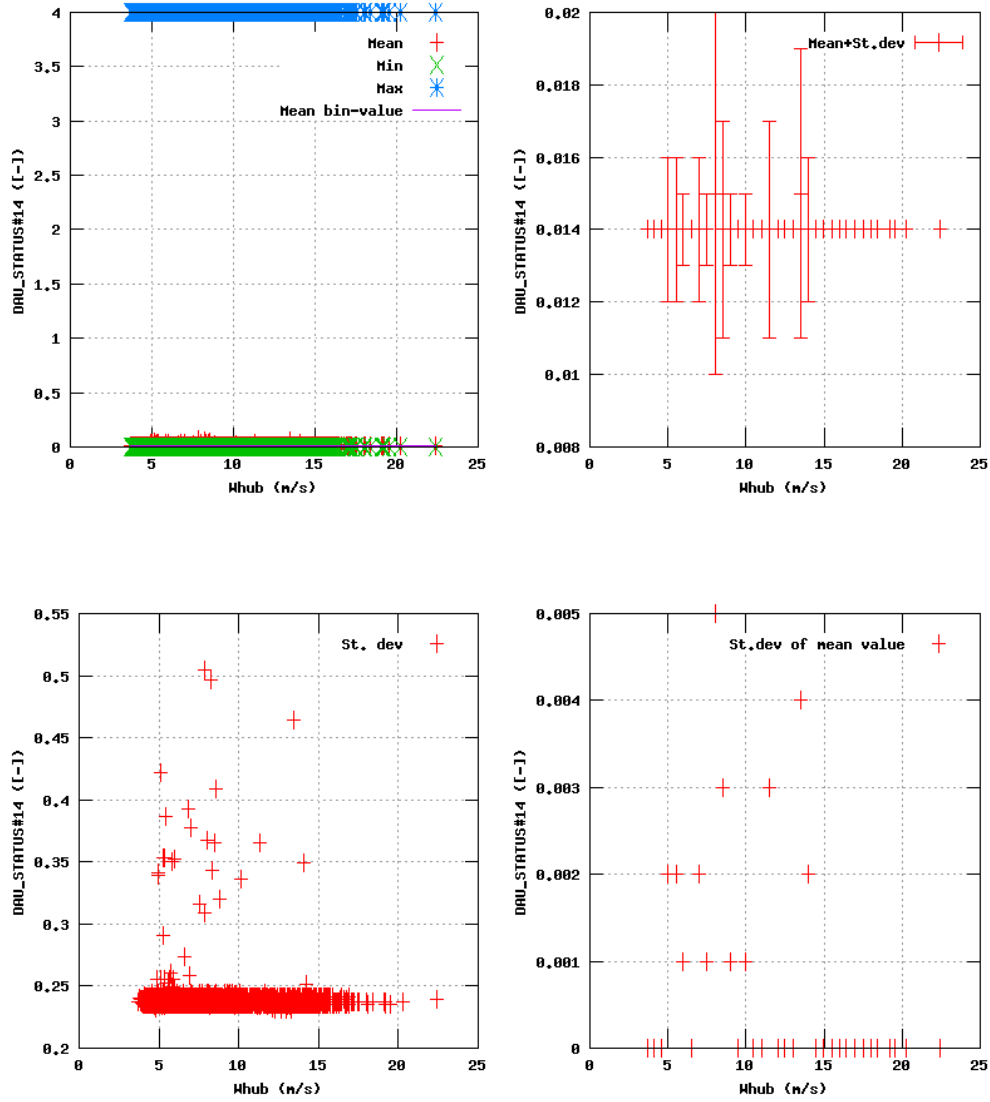
Figure 34a, Sensor 135: DAU_STATUS#14 versus wind speed
Input files: ntk500res.dat, stat_135.dat
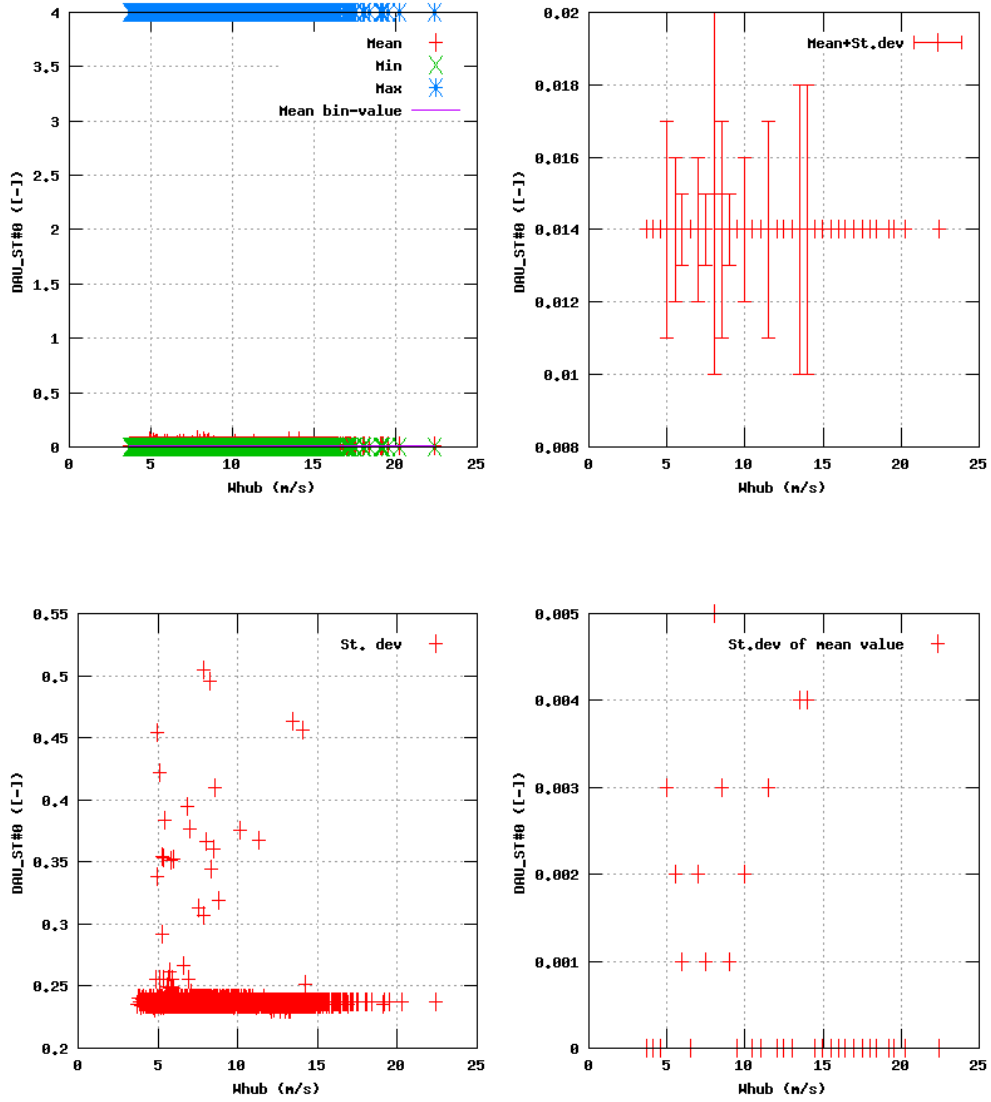
Figure 17a, Sensor 67: DAU_ST#0 versus wind speed
Input files: ntk500res.dat, stat_67.dat
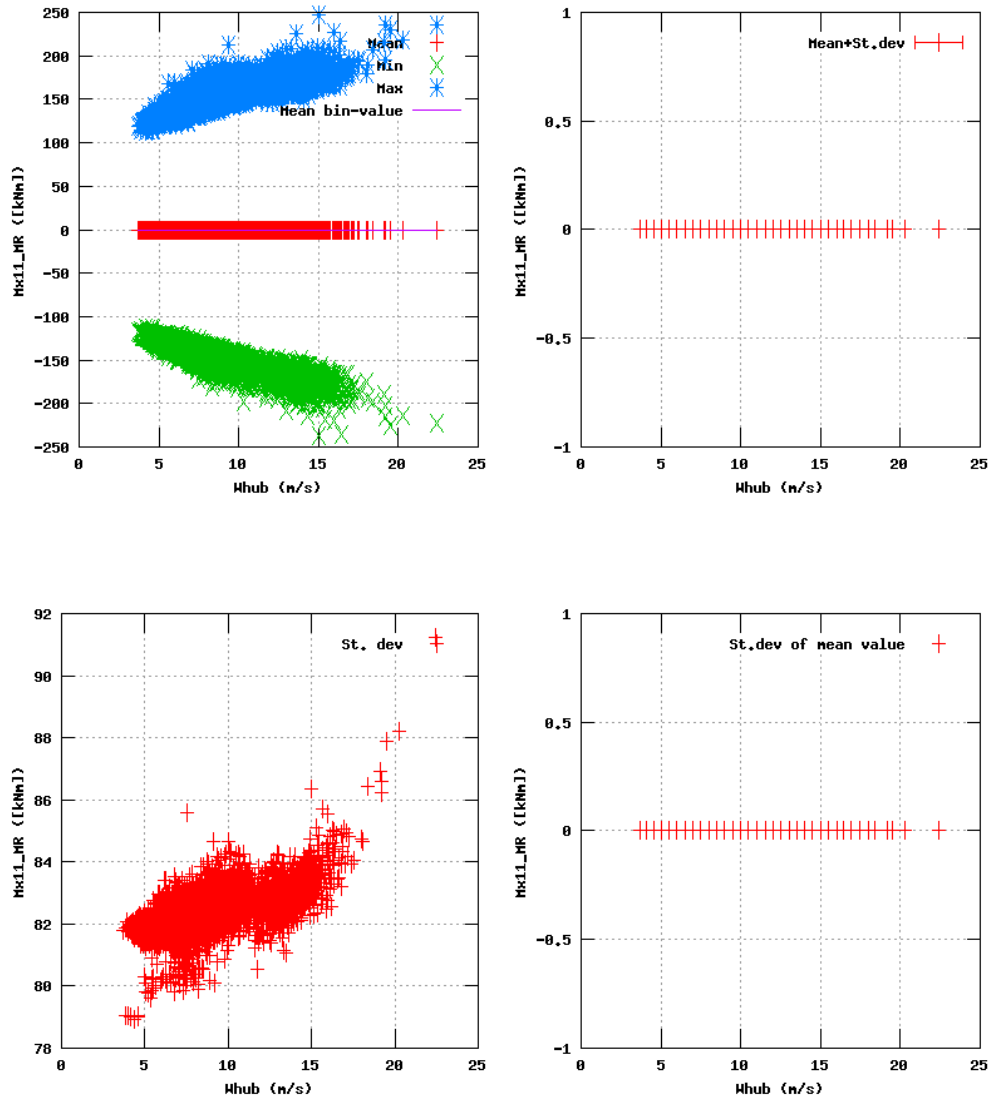
Figure 72a, Sensor 287: Edge bending mean removal Mx11_MR versus wind speed
Input files: ntk500res.dat, stat_287.dat
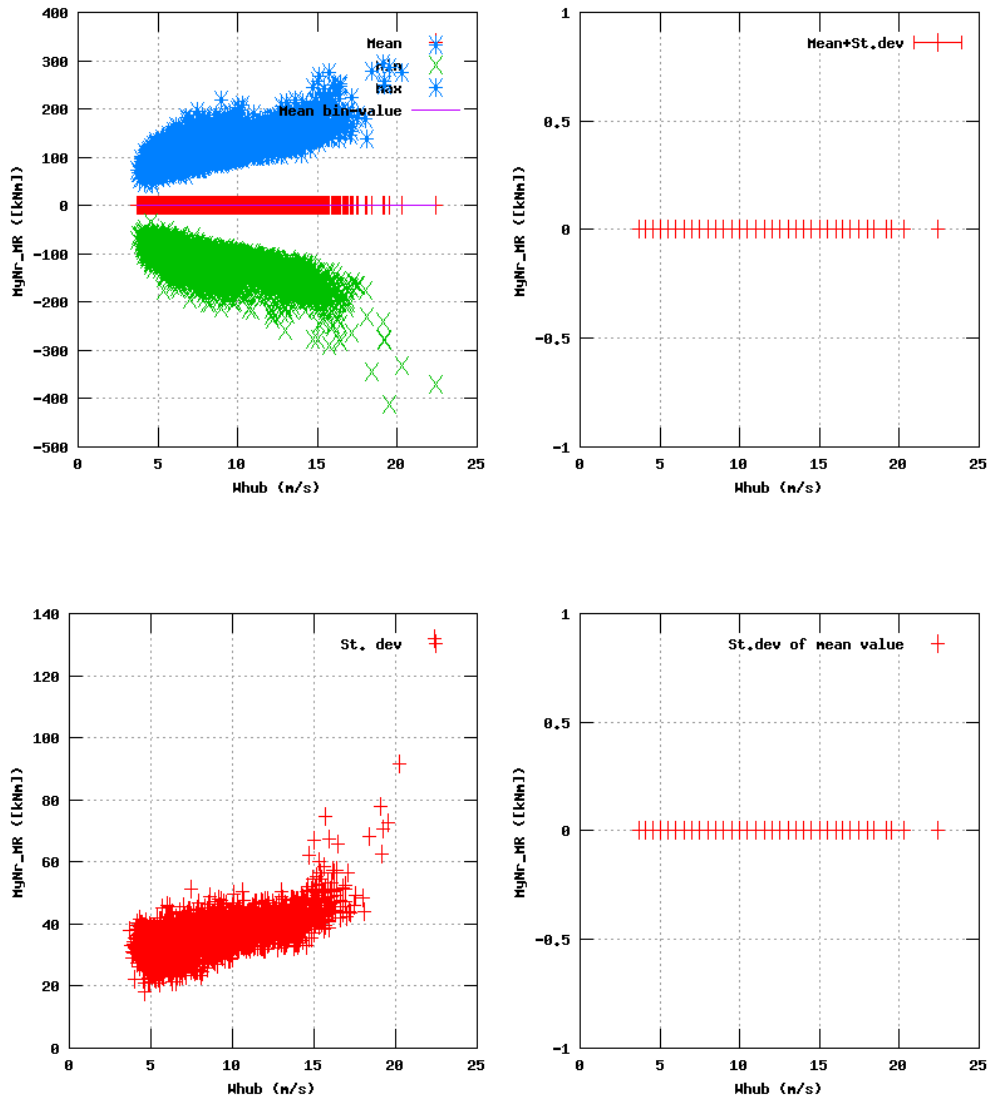
Figure 73a, Sensor 291: Rotor shaft moment mean removal MyNr_MR versus wind speed
Input files: ntk500res.dat, stat_291.dat
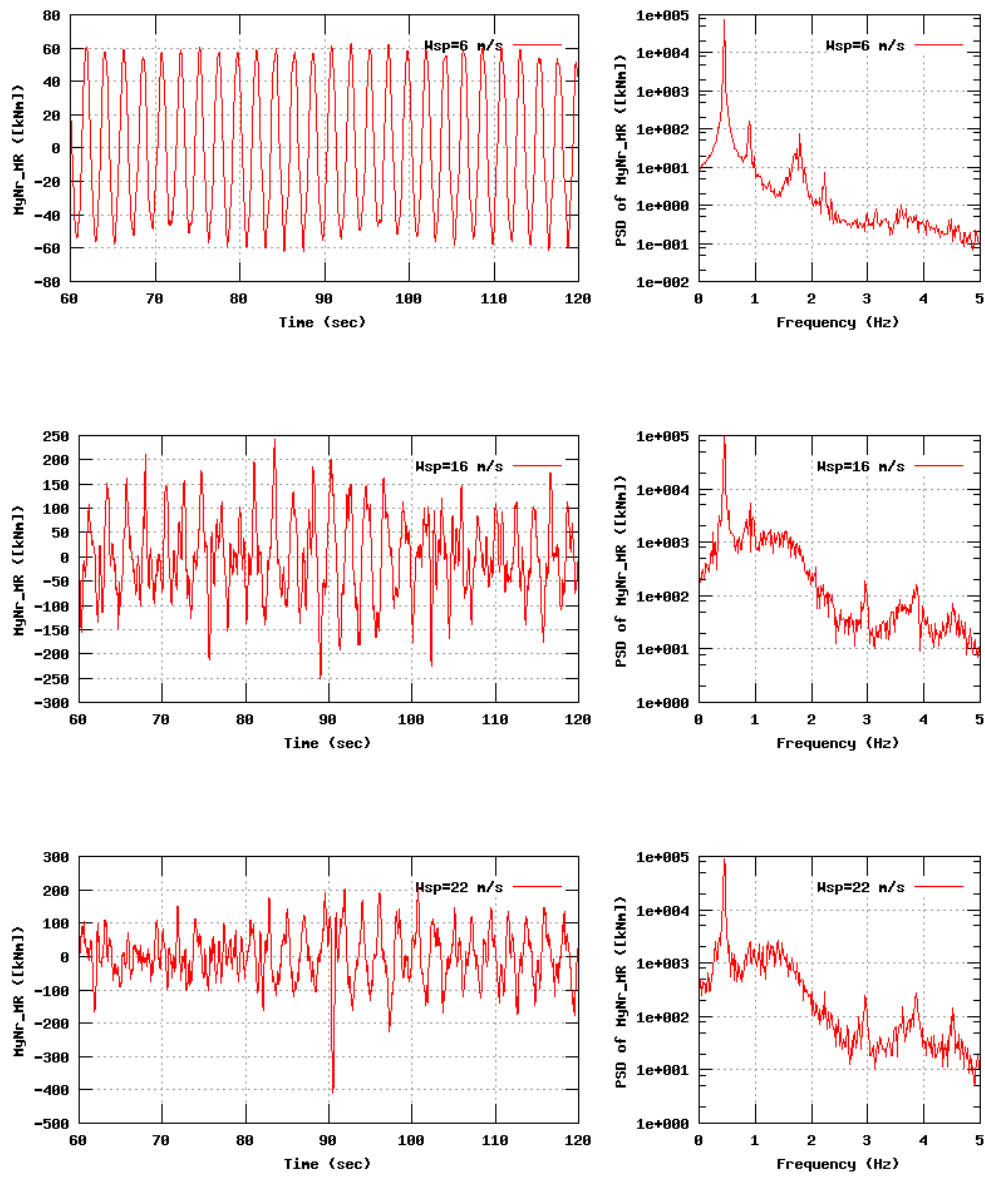
Figure 73b, Sensor 291: Rotor shaft moment mean removal MyNr_MR versus time and frequency
Input files: m06.dat, m16.dat, m22.dat, m06.psd, m16.psd and m22.psd
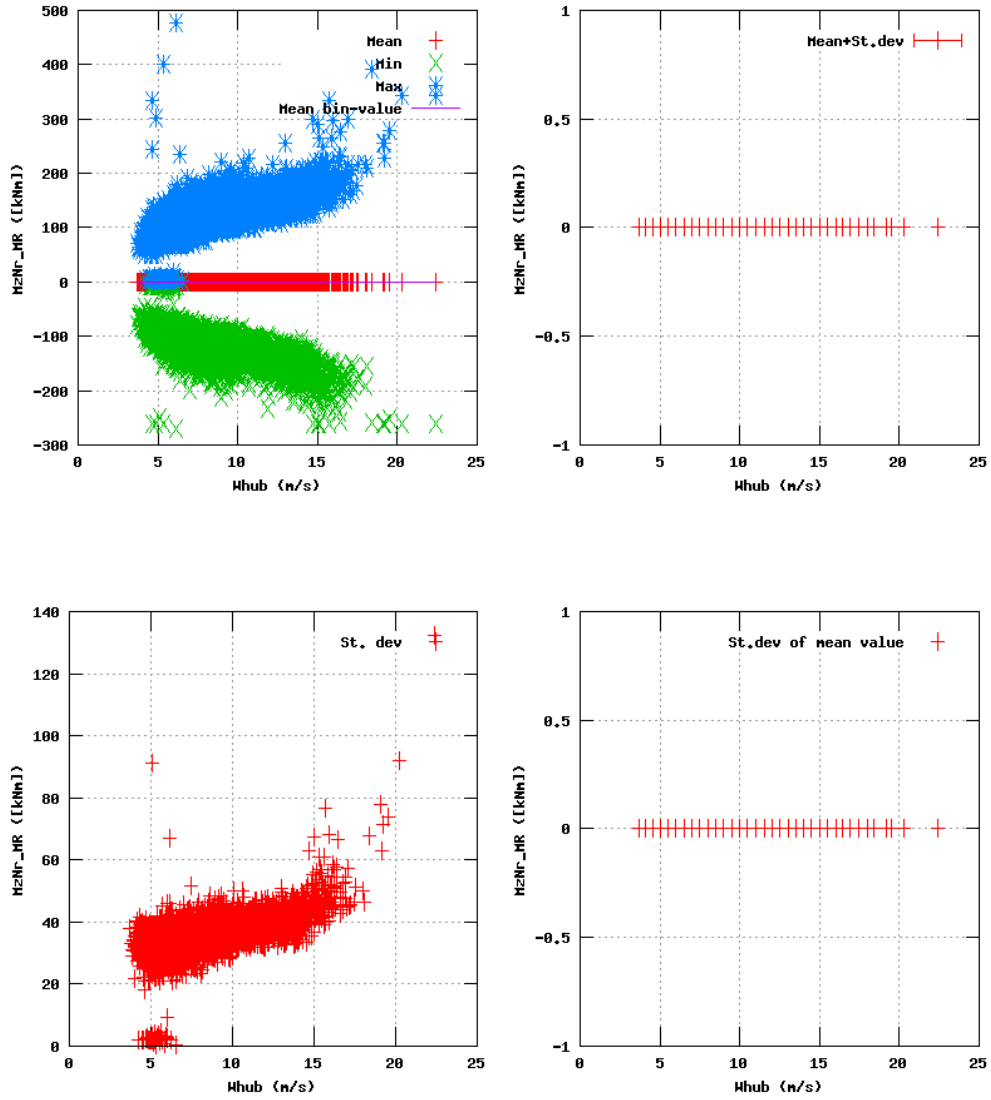
Figure 74a, Sensor 295: Rotor shaft moment mean removal MzNr_MR versus wind speed
Input files: ntk500res.dat, stat_295.dat
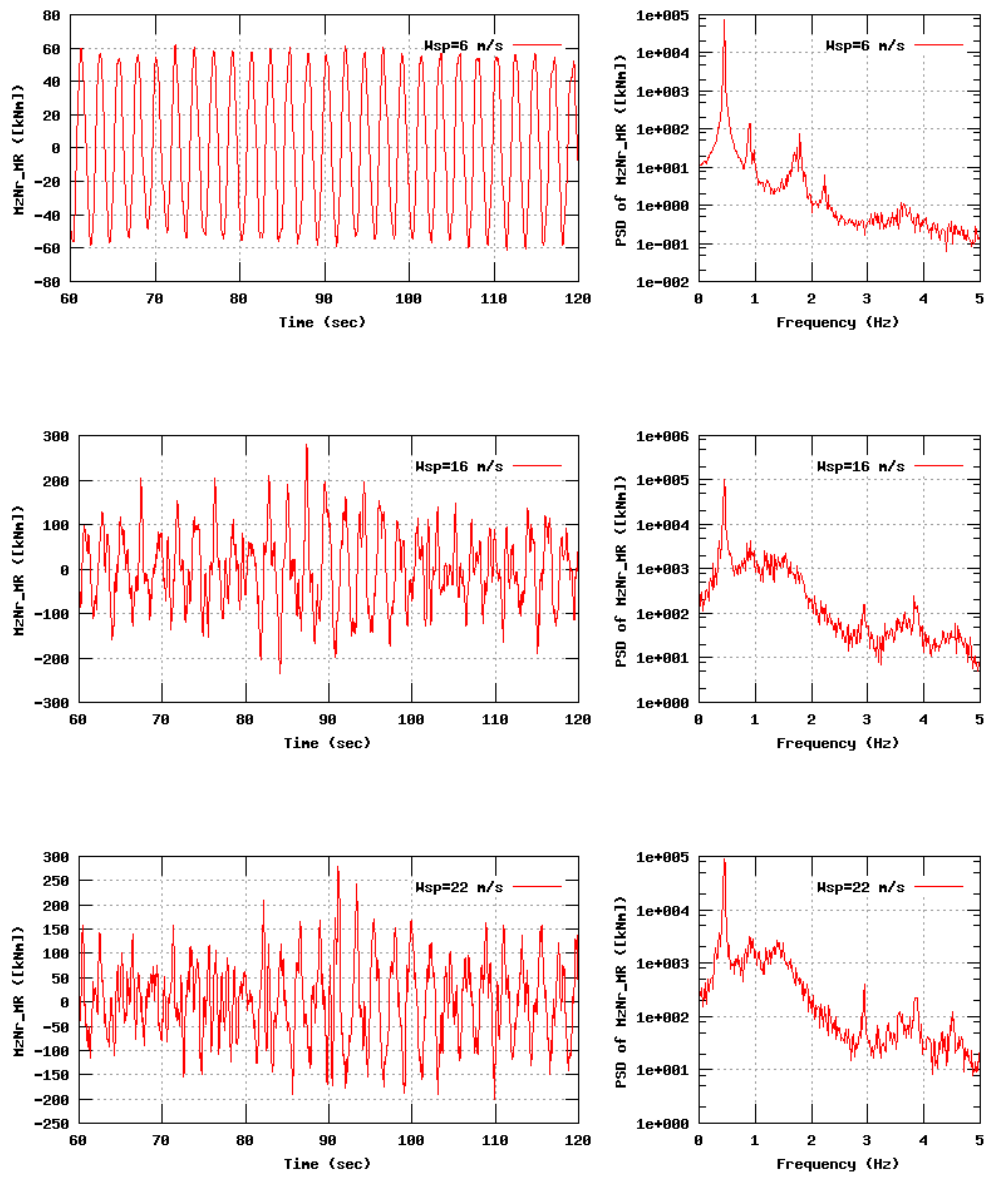
Figure 74b, Sensor 295: Rotor shaft moment mean removal M2Nr_MR versus time and frequency
Input files: m06.dat, m16.dat, m22.dat, m06.psd, m16.psd and m22.psd
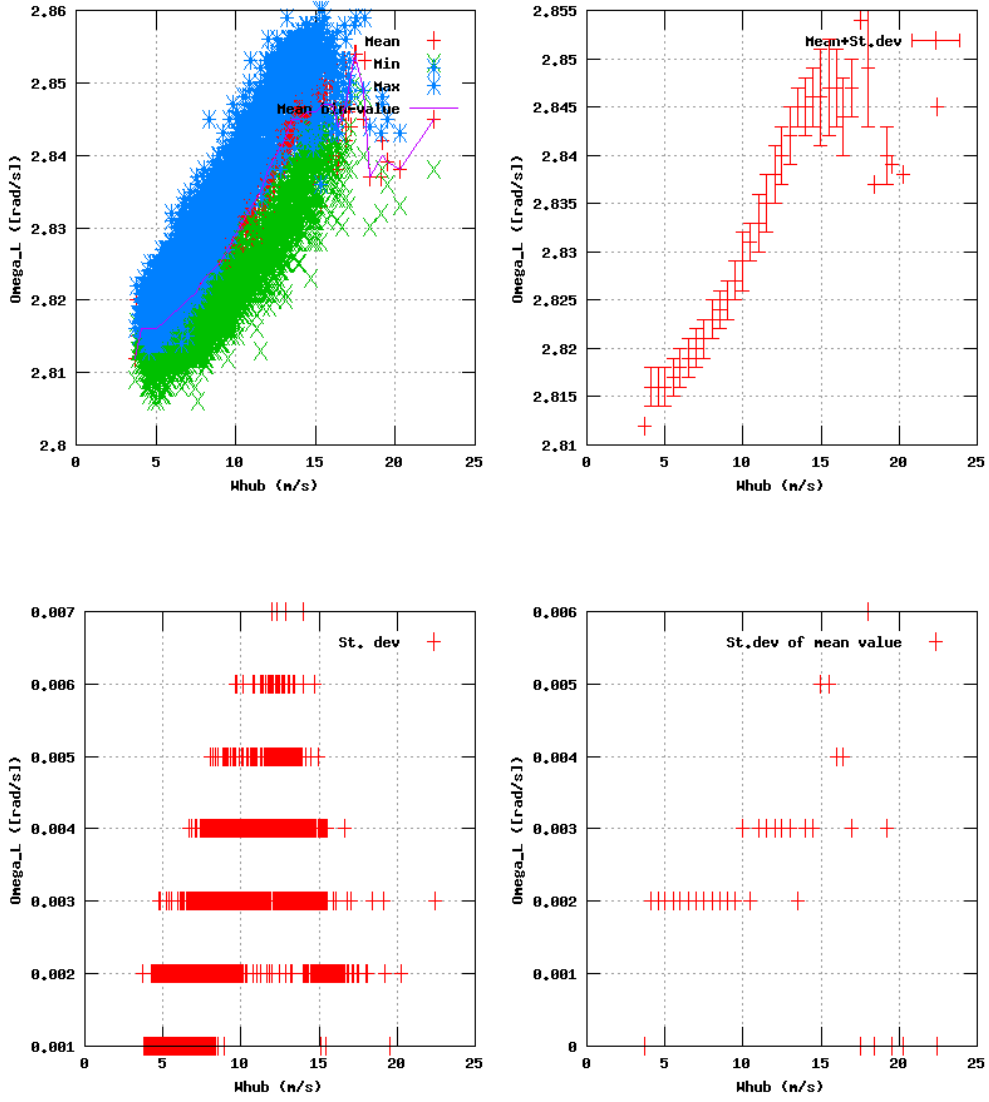
Figure 75a, Sensor 299: Rotor shaft speed LSS versus wind speed
Input files: ntk500res.dat, stat_299.dat
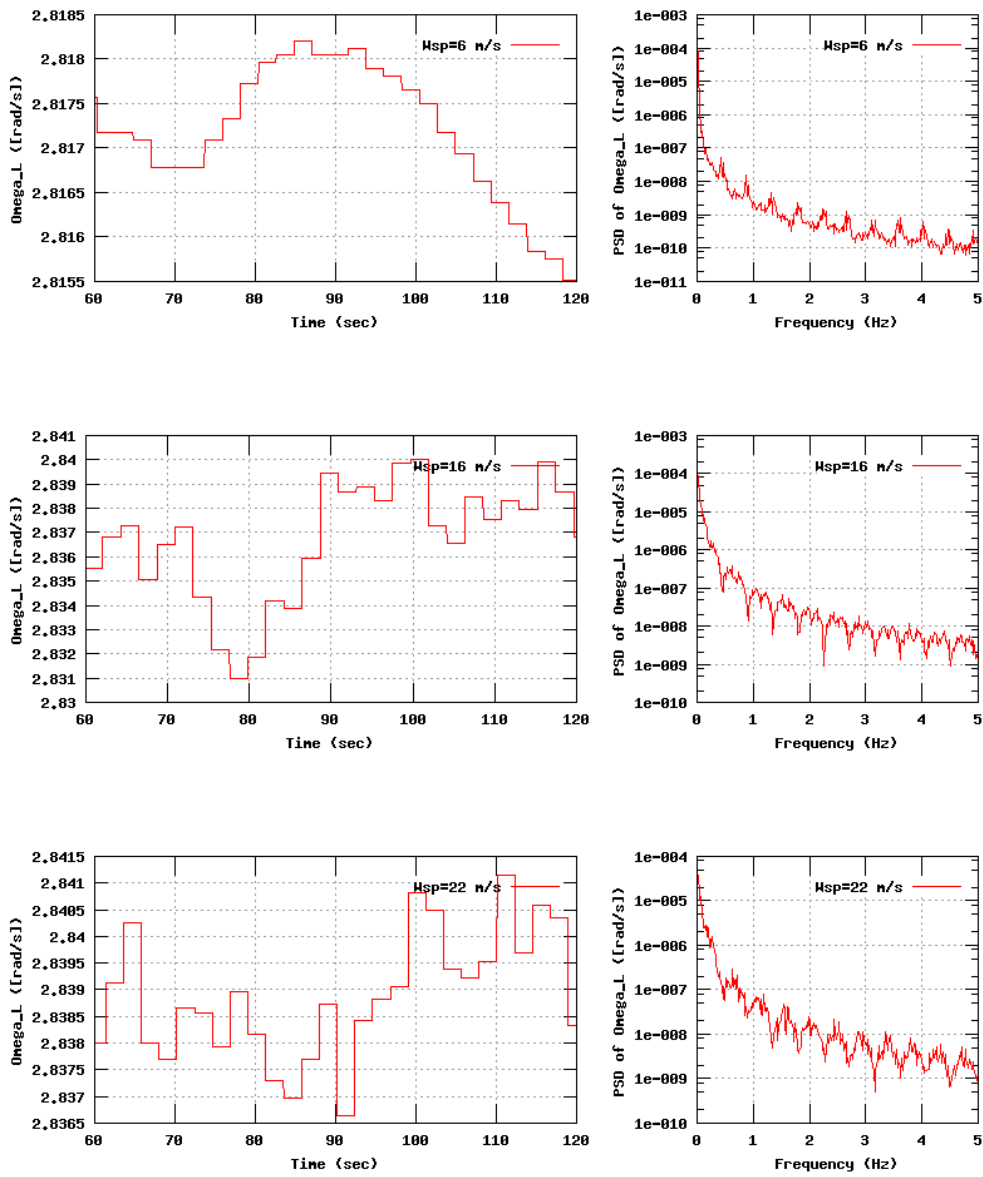
Figure 75b, Sensor 299: Rotor shaft speed LSS versus time and frequency
Input files: m06.dat, m16.dat, m22.dat, m06.psd, m16.psd and m22.psd
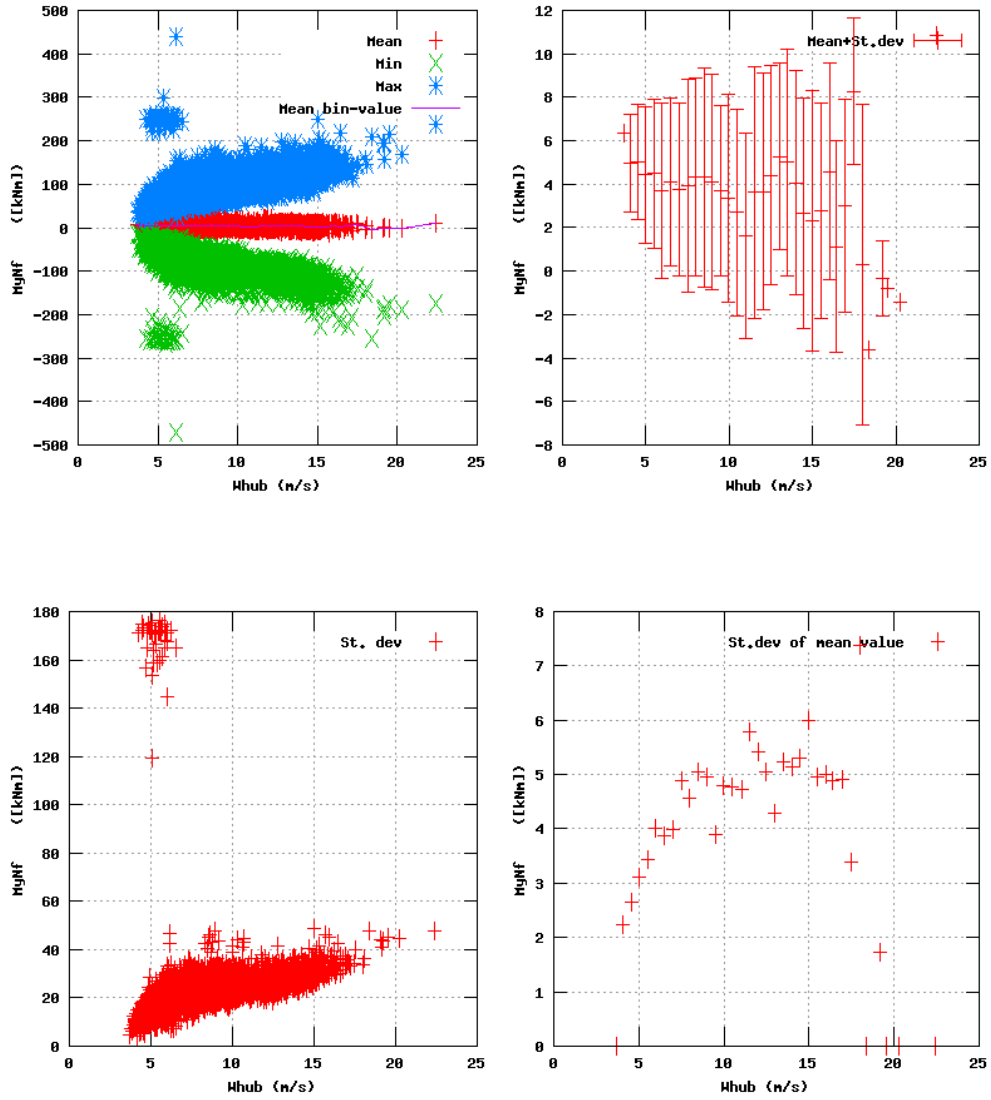
Figure 79a, Sensor 315: Rotor Tilt Moment versus wind speed
Input files: ntk500res.dat, stat_315.dat
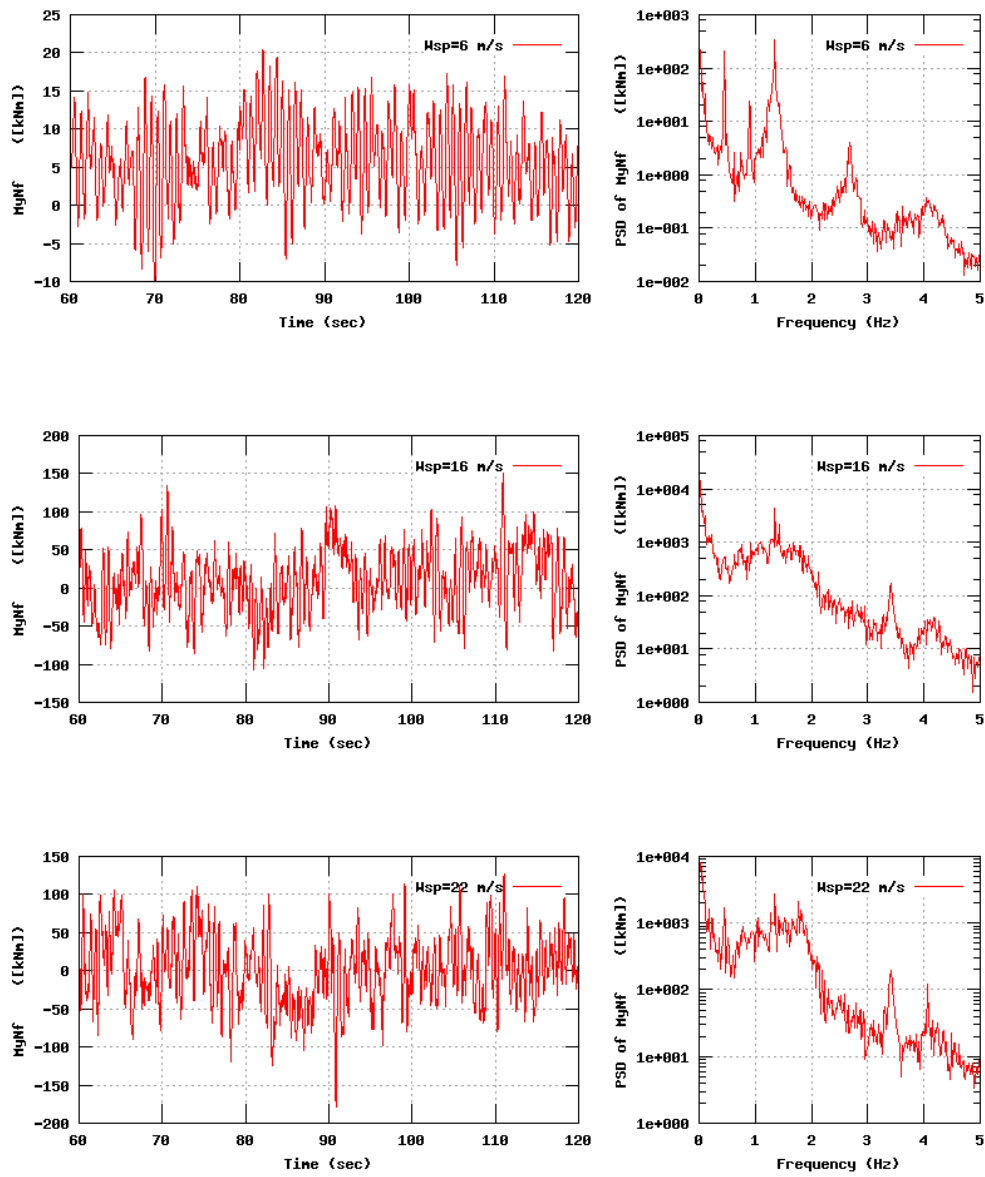
Figure 79b, Sensor 315: Rotor Tilt Moment versus time and frequency
Input files: m06.dat, m16.dat, m22.dat, m06.psd, m16.psd and m22.psd
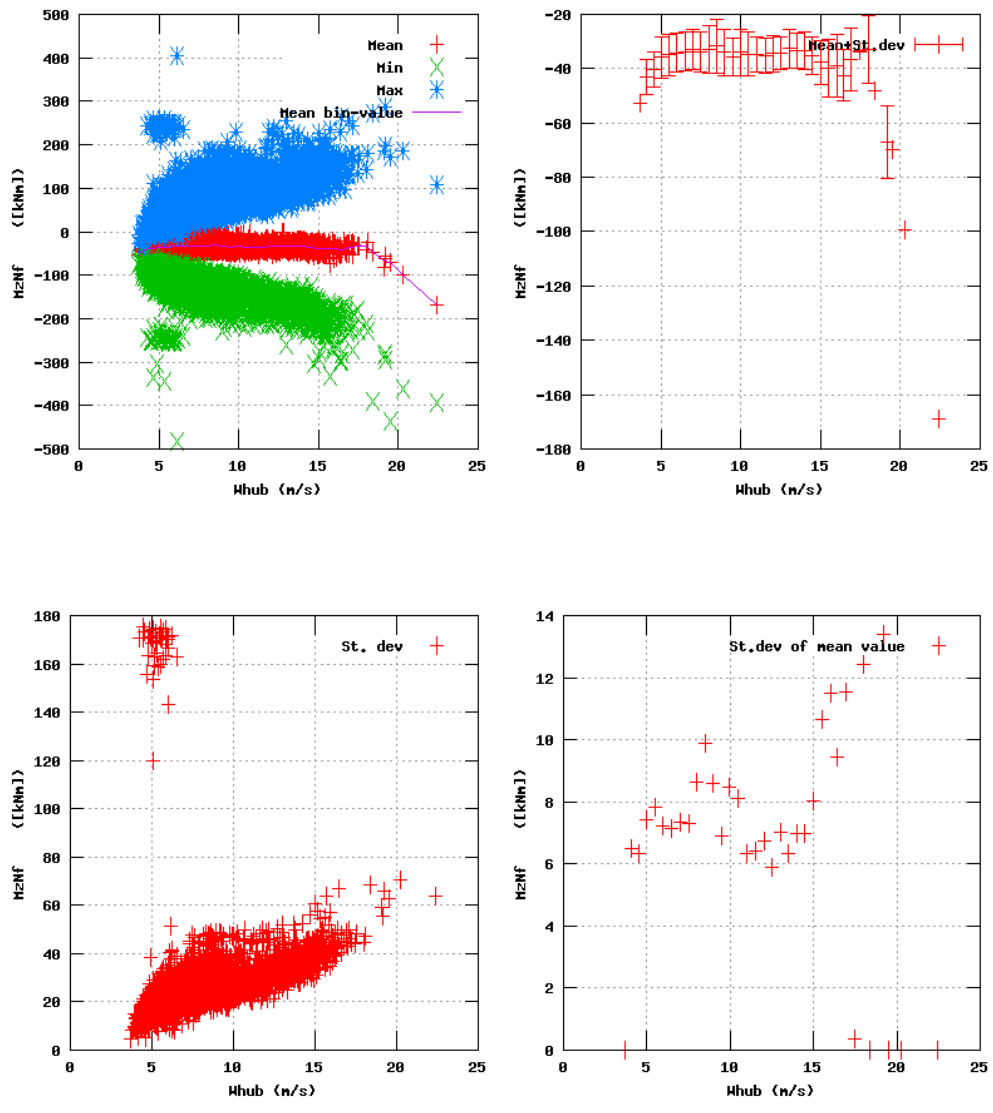
Figure 80a, Sensor 319: Rotor Yaw Moment versus wind speed
Input files: ntk500res.dat, stat_319.dat
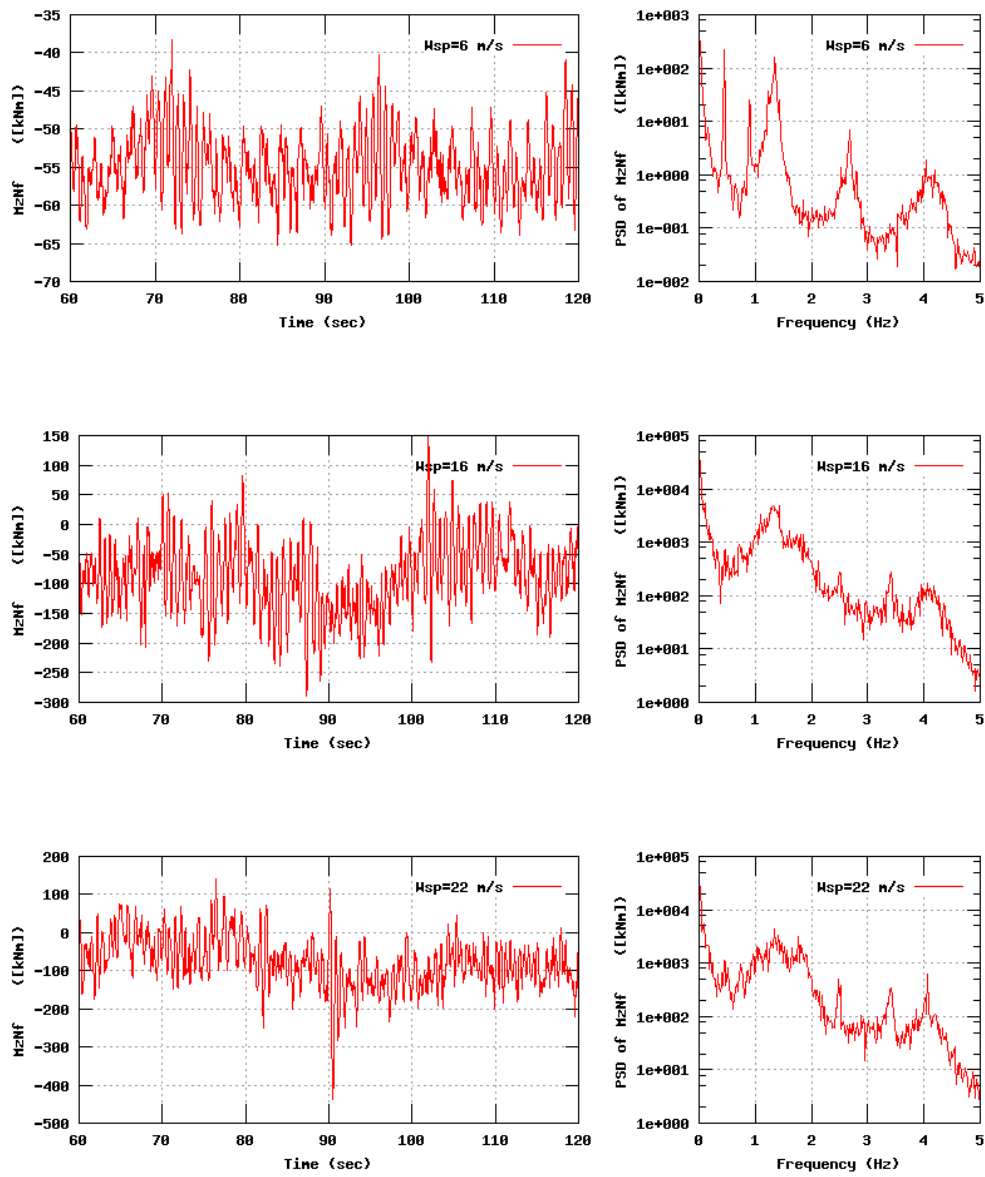
Figure 80b, Sensor 319: Rotor Yaw Moment versus time and frequency
Input files: m06.dat, m16.dat, m22.dat, m06.psd, m16.psd and m22.psd
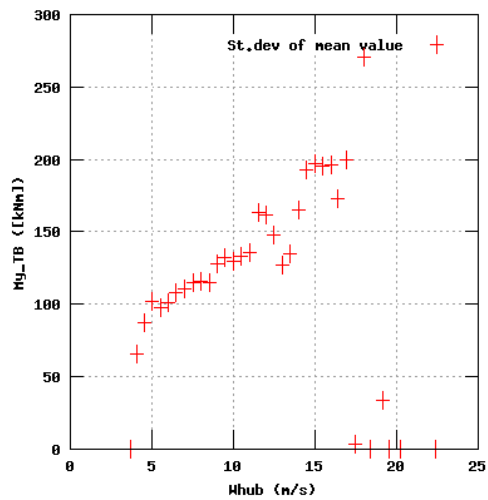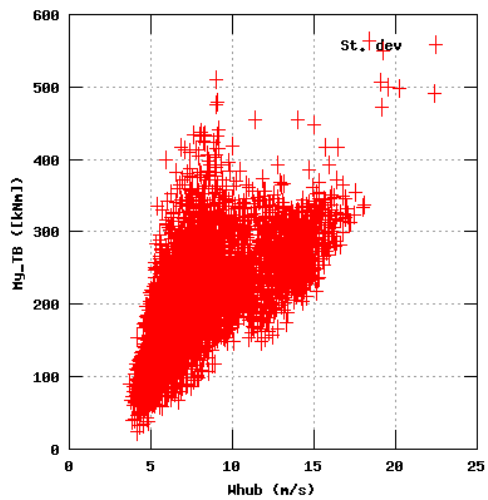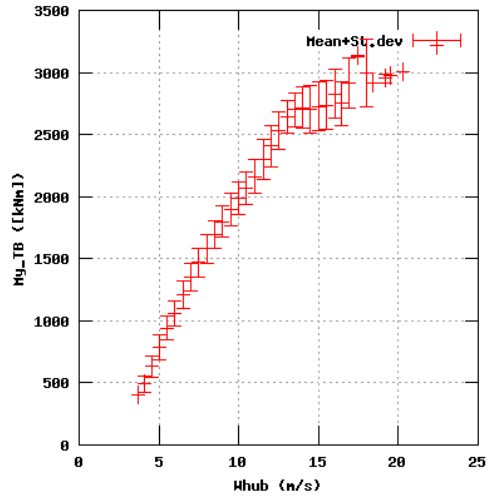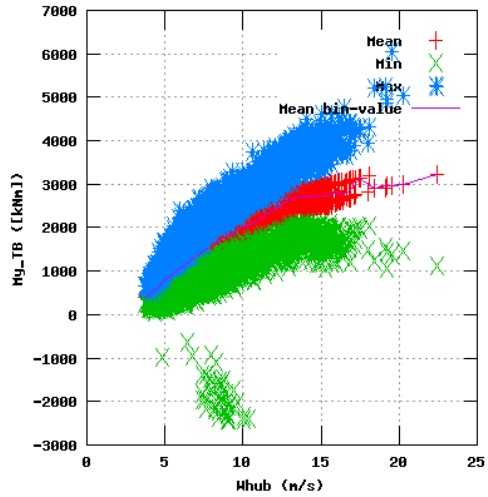
Figure 81a, Sensor 323: Tower Tilt bending moment versus wind speed
Input files: ntk500res.dat, stat_323.dat
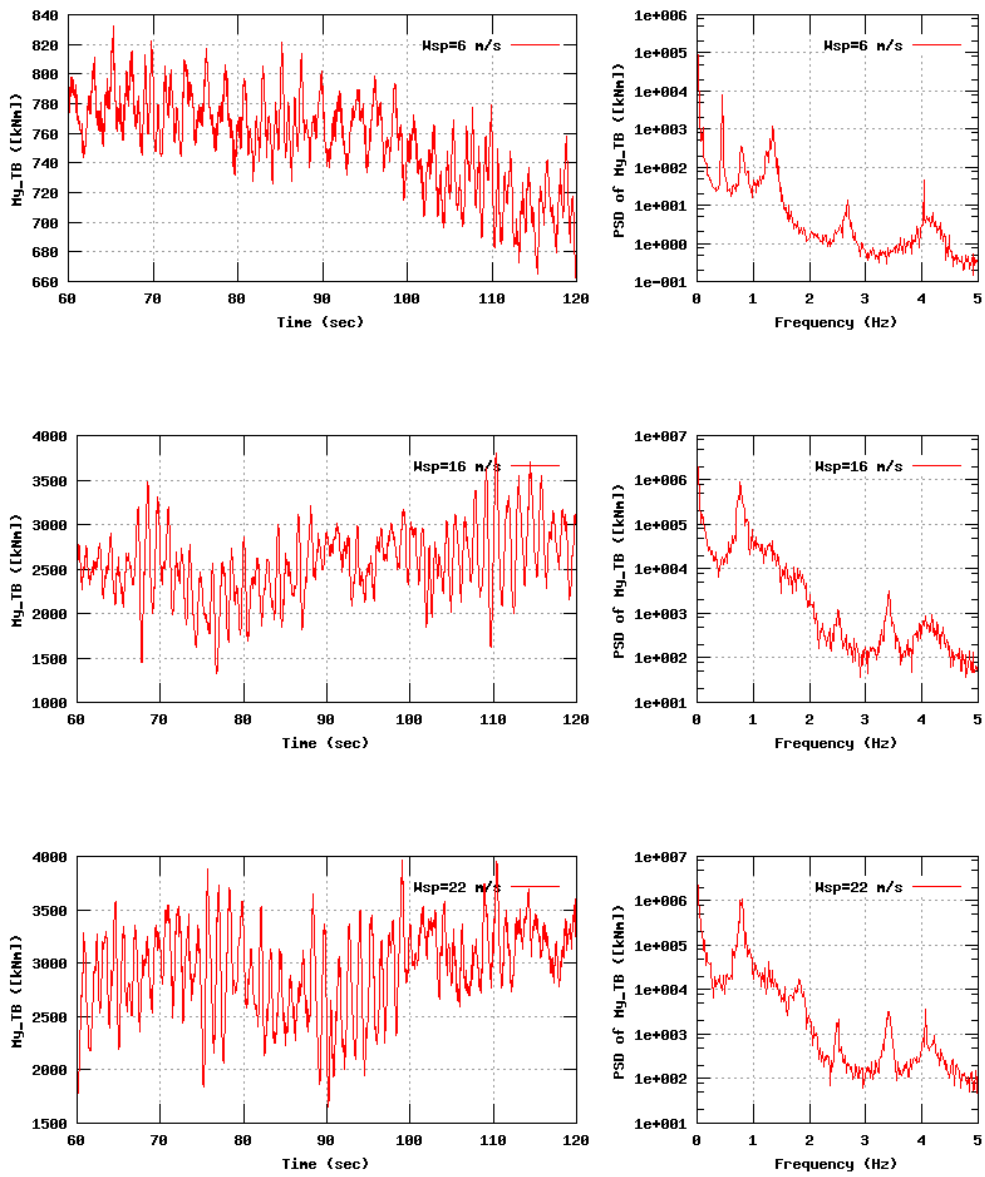
Figure 81b, Sensor 323: Tower Tilt bending moment versus time and frequency
Input files: m06.dat, m16.dat, m22.dat, m06.psd, m16.psd and m22.psd
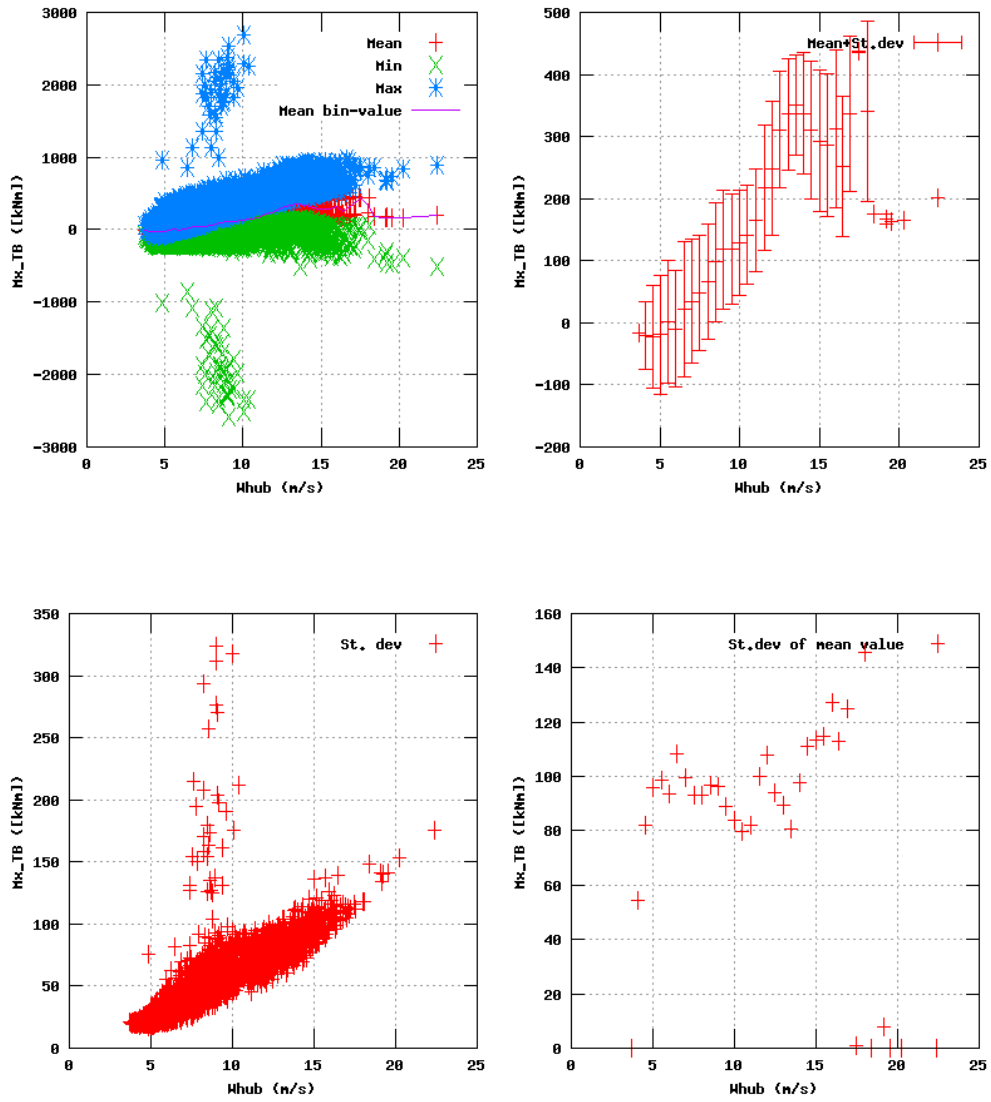
Figure 82a, Sensor 327: Tower Roll bending moment versus wind speed
Input files: ntk500res.dat, stat_327.dat
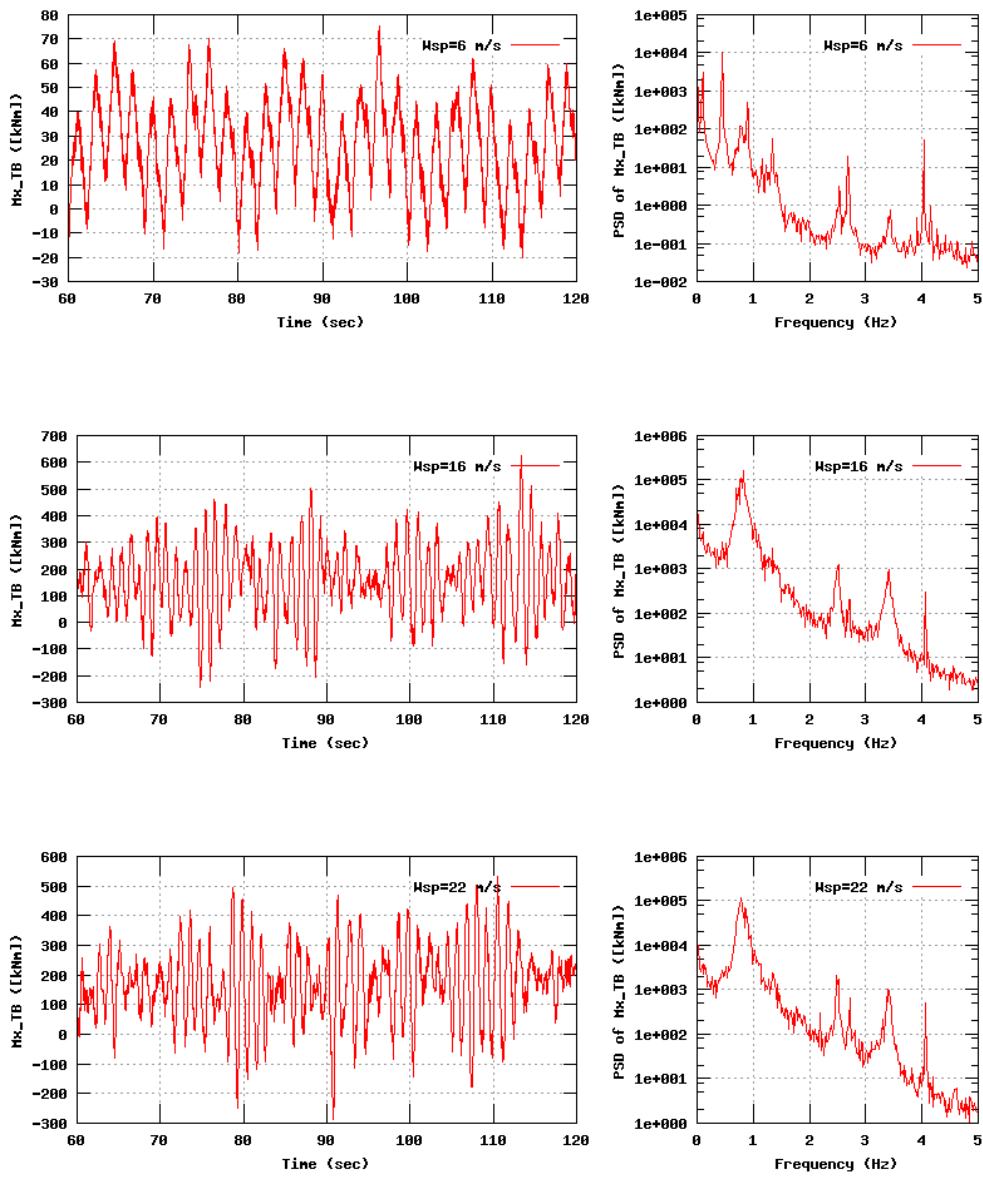
Figure 82b, Sensor 327: Tower Roll bending moment versus time and frequency
Input files: m06.dat, m16.dat, m22.dat, m06.psd, m16.psd and m22.psd
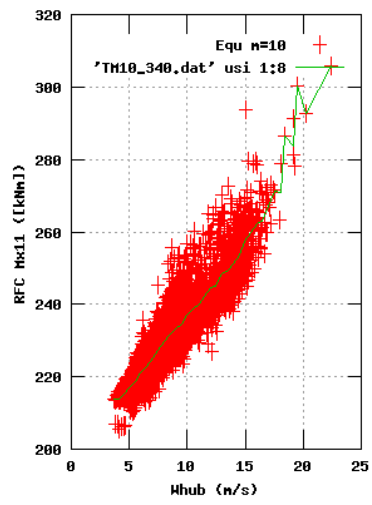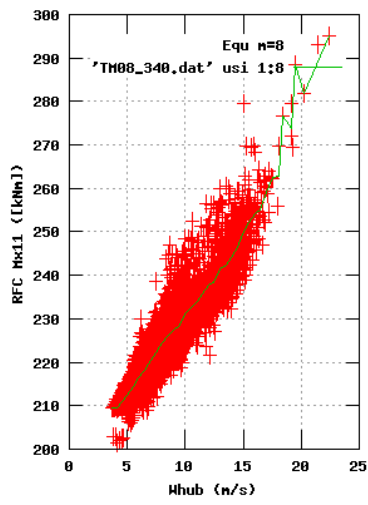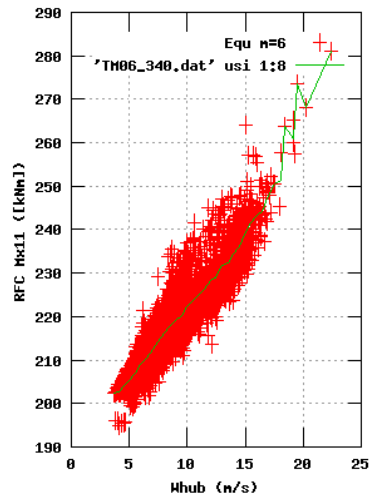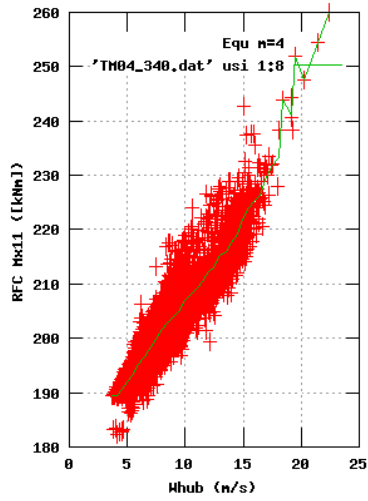
Figure 83a, Sensor 340: RFC Mx11 versus wind speed
Input files: ntk500res.dat, TM04_340.dat, TM06_340.dat,TM08_340.dat,TM10_340.dat

Risø-R-1782(EN)
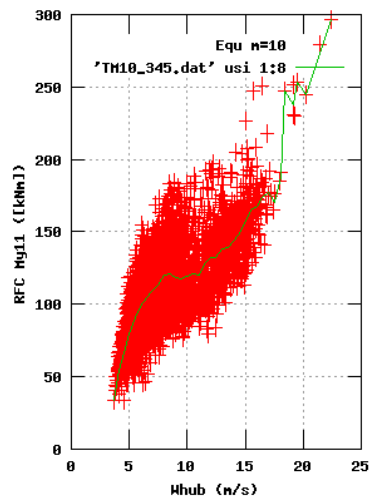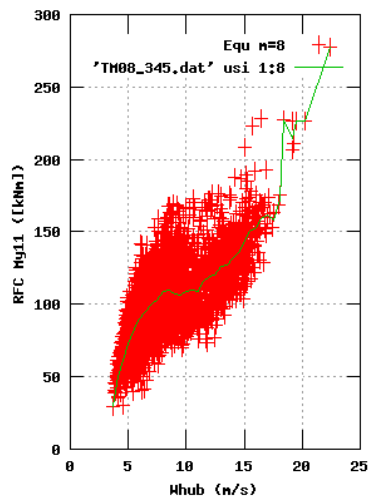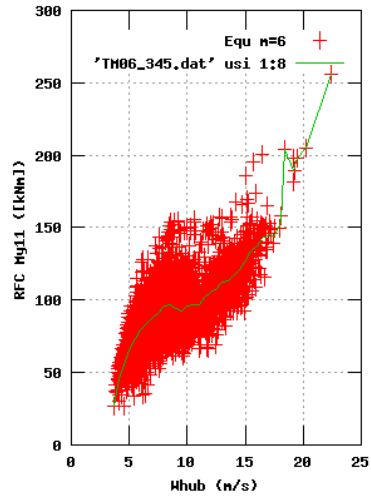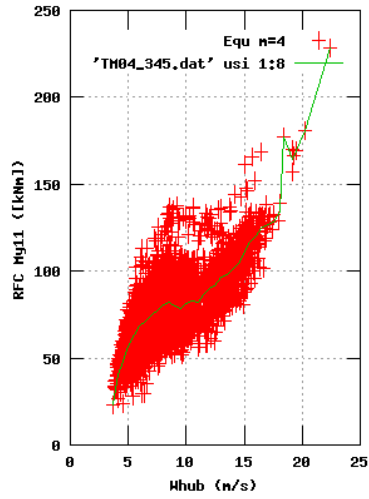
Figure 84a, Sensor 345: RFC My11 versus wind speed
Input files: ntk500res.dat, TM04_345.dat, TM06_345.dat,TM08_345.dat,TM10_345.dat
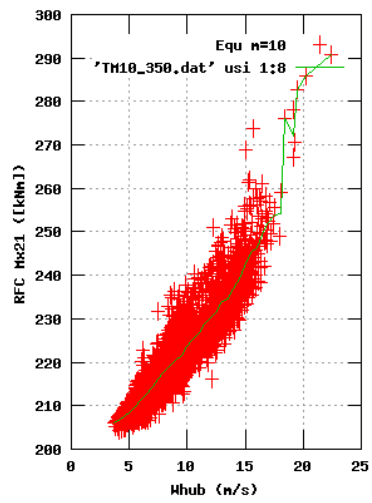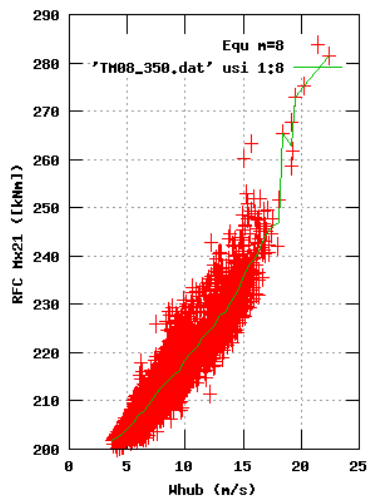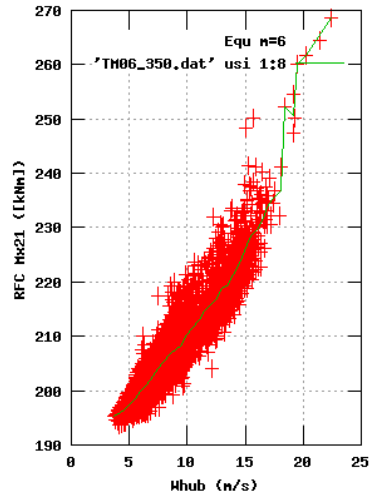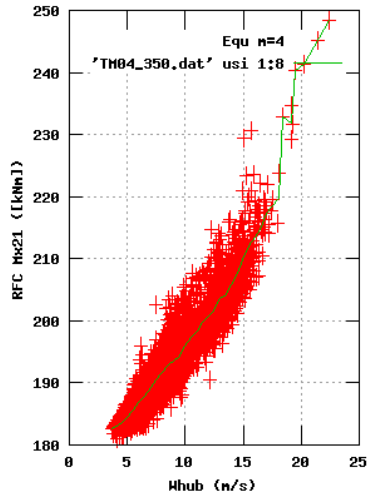
Figure 85a, Sensor 350: RFC Mx21 versus wind speed
Input files: ntk500res.dat, TM04_350.dat, TM06_350.dat,TM08_350.dat,TM10_350.dat
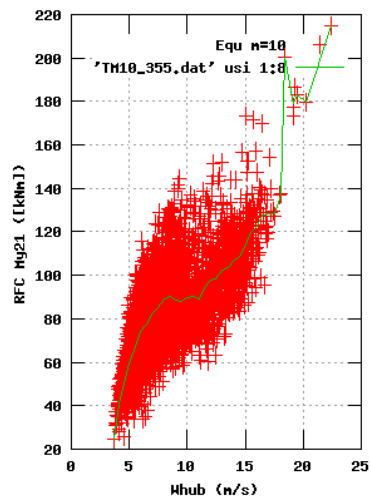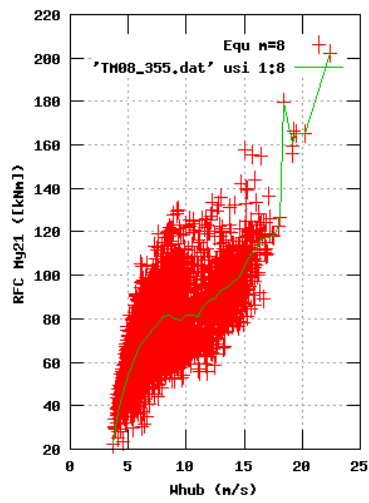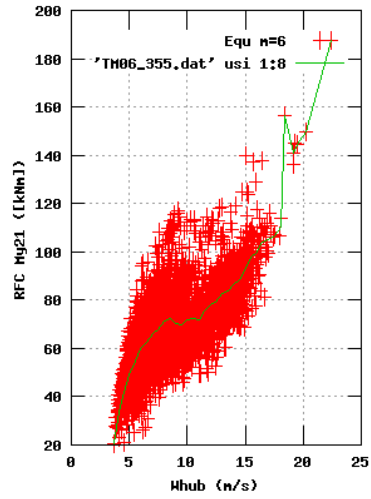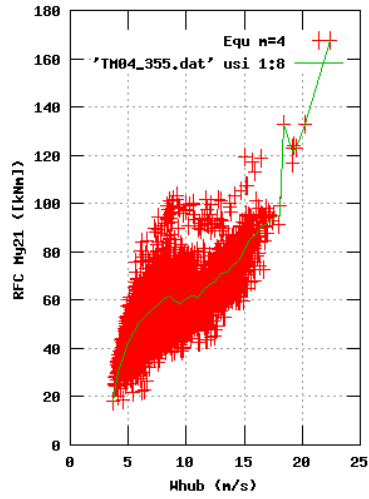
Figure 86a, Sensor 355: RFC My21 versus wind speed
Input files: ntk500res.dat, TM04_355.dat, TM06_355.dat,TM08_355.dat,TM10_355.dat
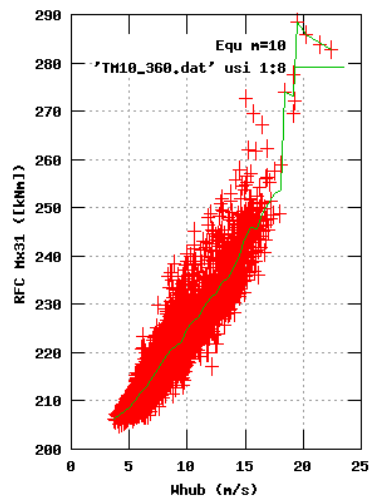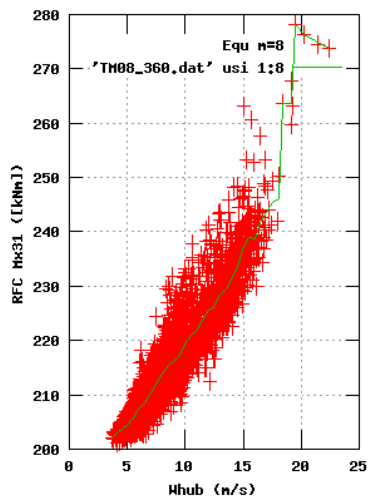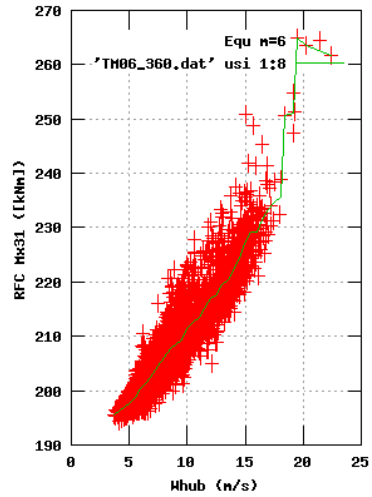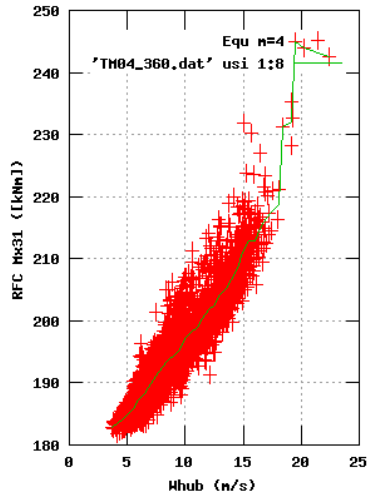
Figure 87a, Sensor 360: RFC Mx31 versus wind speed
Input files: ntk500res.dat, TM04_360.dat, TM06_360.dat,TM08_360.dat,TM10_360.dat
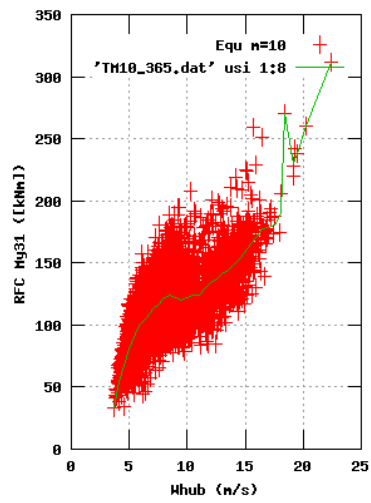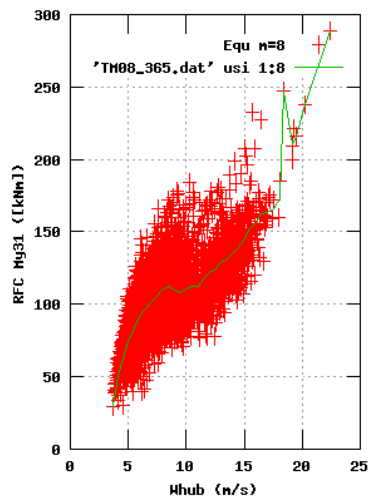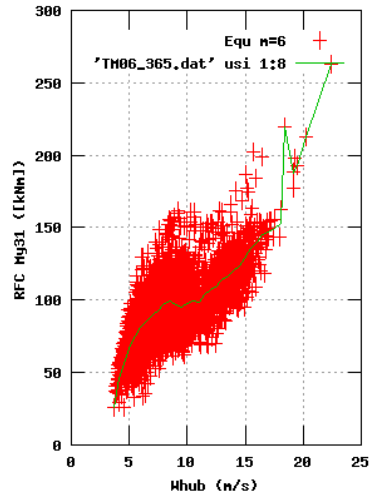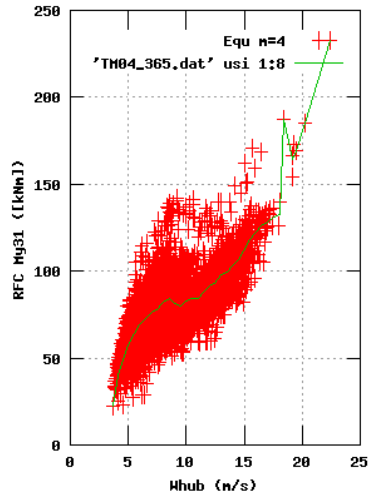
Figure 88a, Sensor 365: RFC My31 versus wind speed
Input files: ntk500res.dat, TM04_365.dat, TM06_365.dat,TM08_365.dat,TM10_365.dat
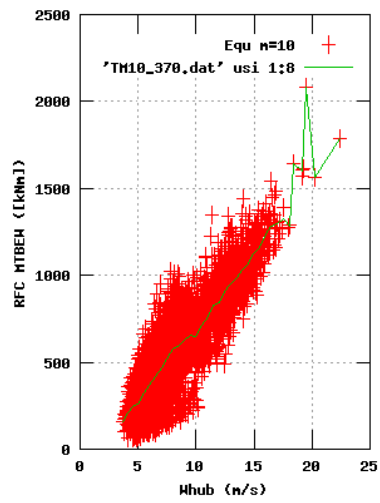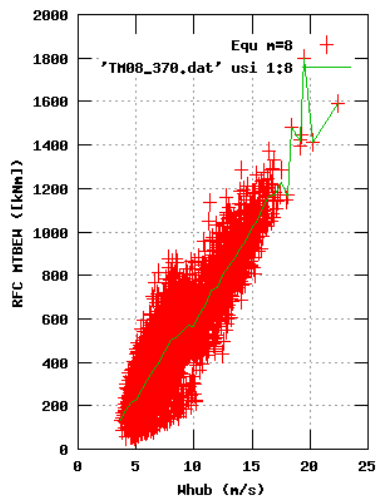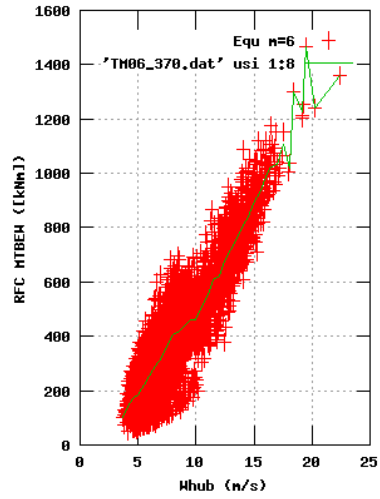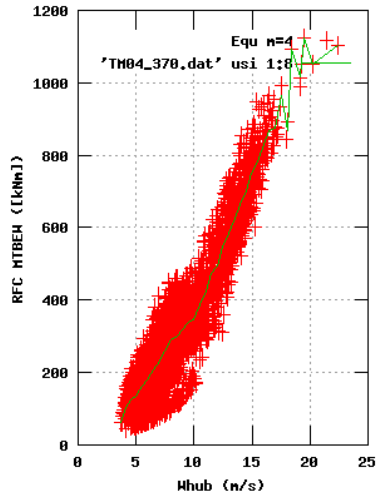
Figure 89a, Sensor 370: RFC MTBEH versus wind speed
Input files: ntk500res.dat, TM04_370.dat, TM06_370.dat,TM08_370.dat,TM10_370.dat
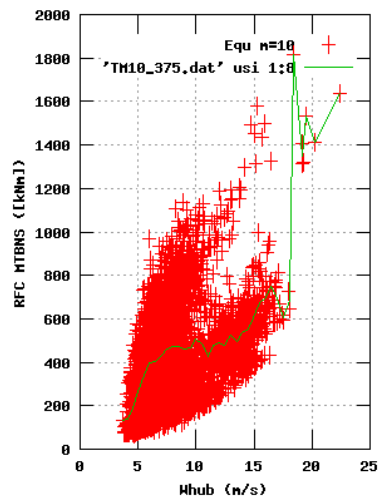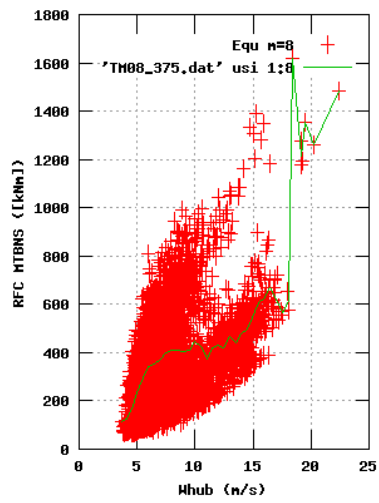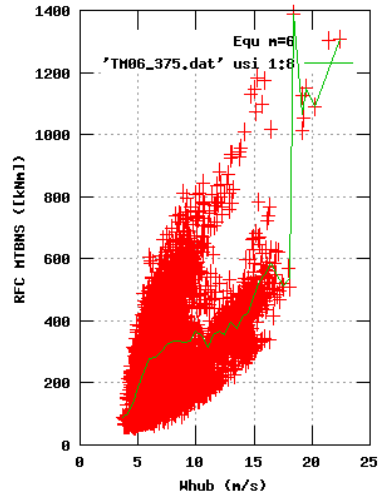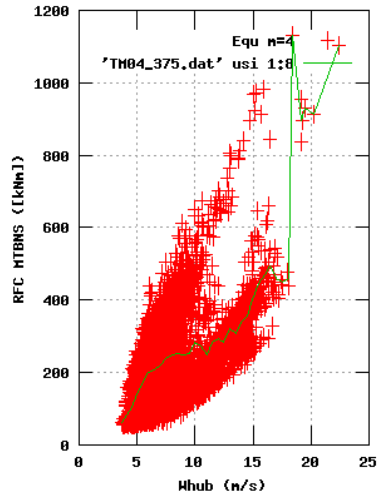
Figure 90a, Sensor 375: RFC MTBNS versus wind speed
Input files: ntk500res.dat, TM04_375.dat, TM06_375.dat,TM08_375.dat,TM10_375.dat
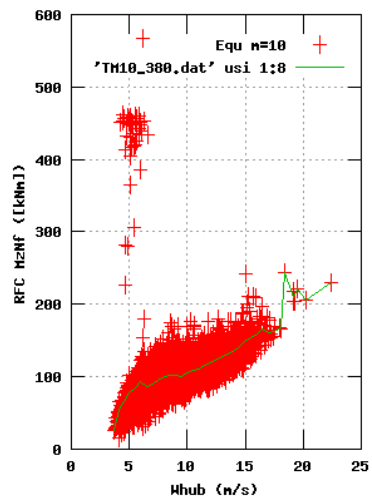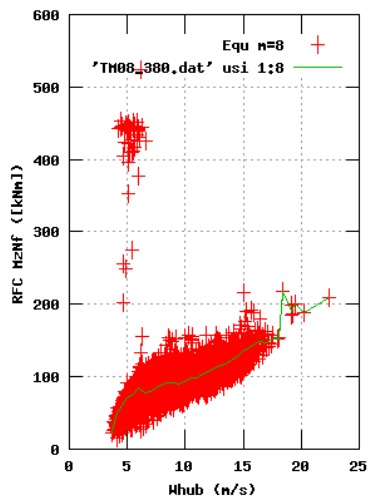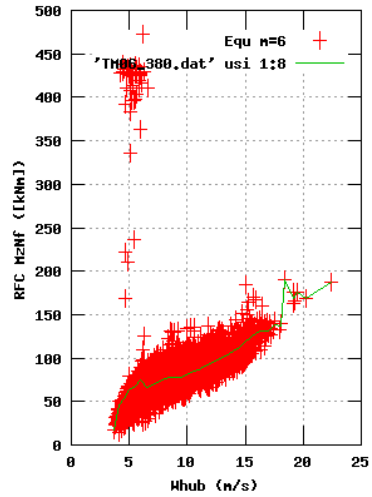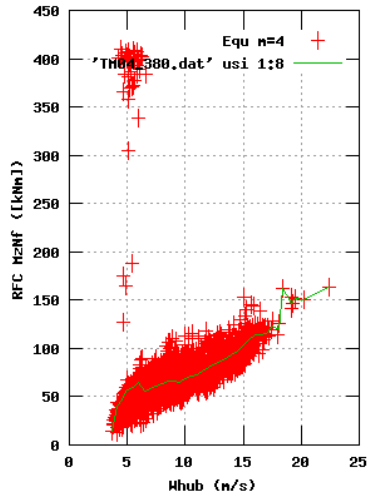
Figure 91a, Sensor 380: RFC M2Nf versus wind speed
Input files: ntk500res.dat, TM04_380.dat, TM06_380.dat,TM08_380.dat,TM10_380.dat
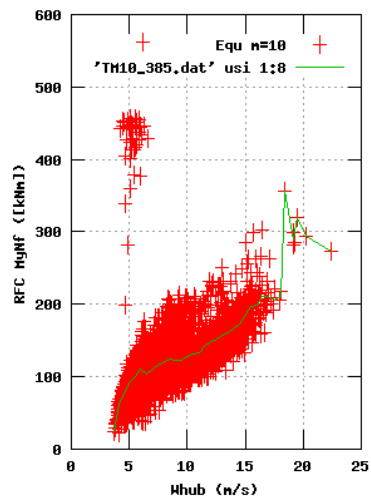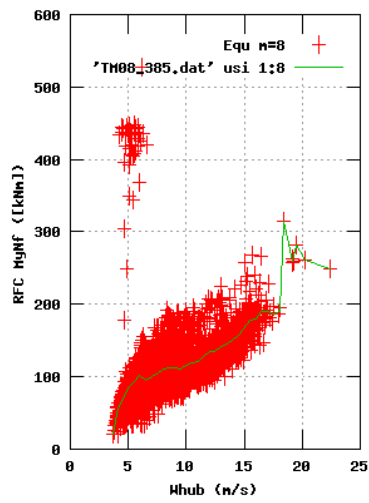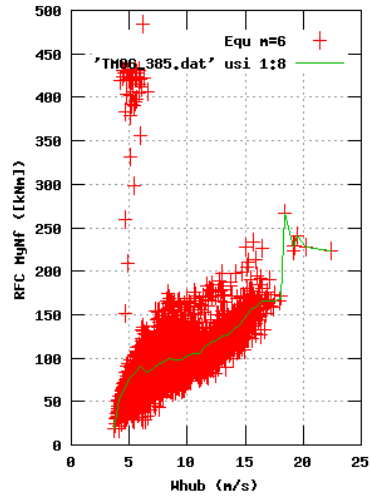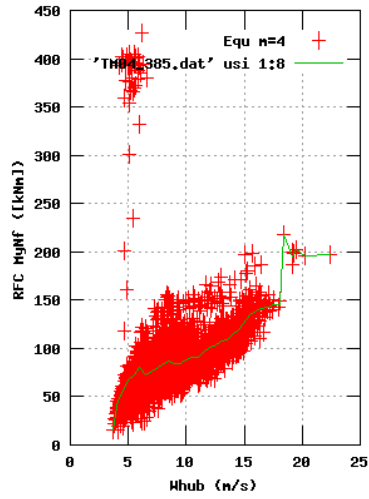
Figure 92a, Sensor 385: RFC MyNf versus wind speed
Input files: ntk500res.dat, TM04_385.dat, TM06_385.dat,TM08_385.dat,TM10_385.dat
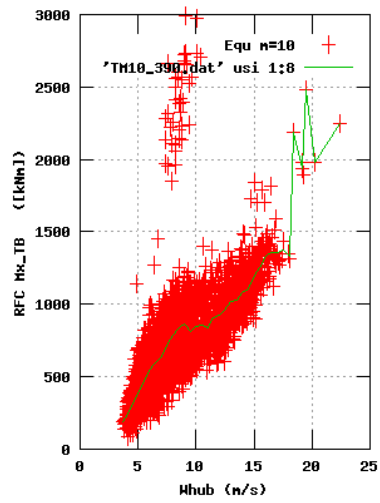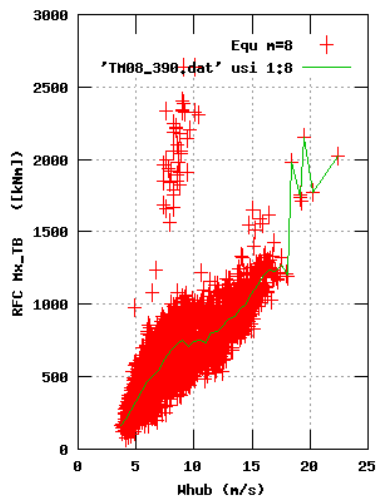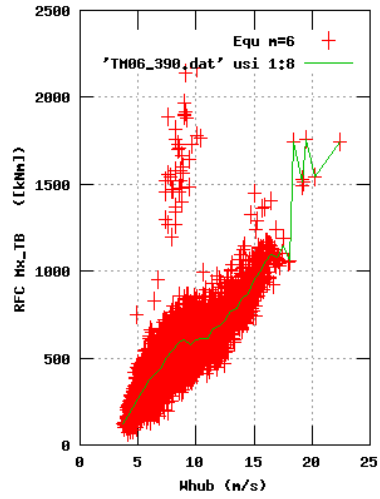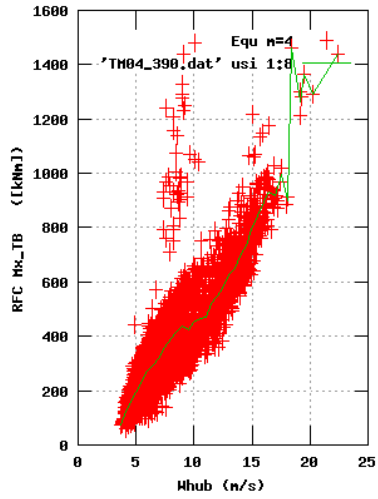
Figure 93a, Sensor 390: RFC Mx_TB   versus wind speed
Input files: ntk500res.dat, TM04_390.dat, TM06_390.dat,TM08_390.dat,TM10_390.dat
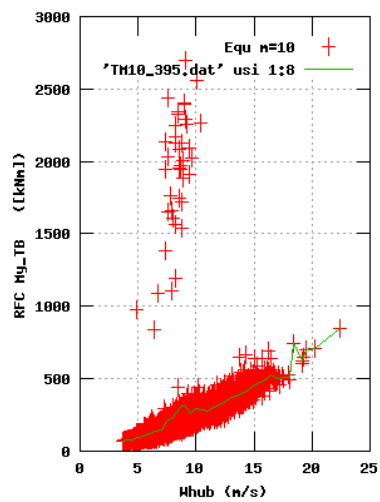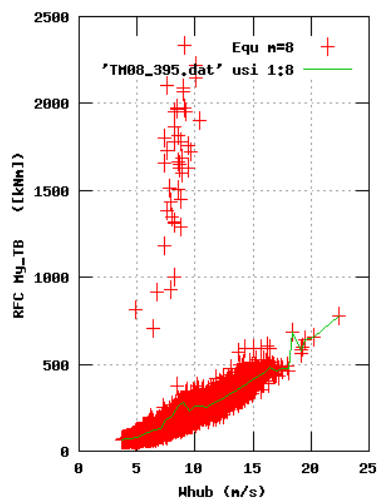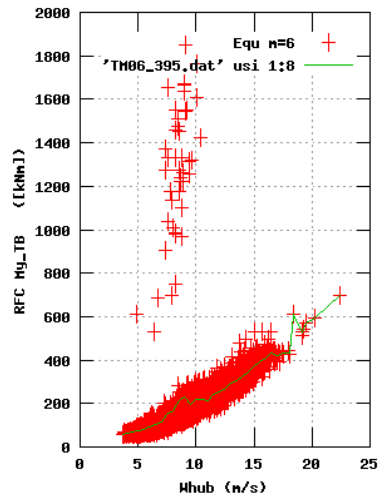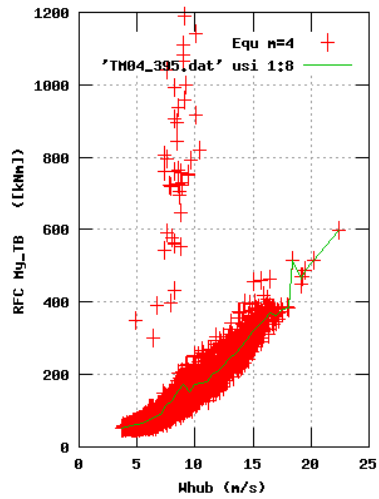
Figure 94a, Sensor 395: RFC My_TB   versus wind speed
Input files: ntk500res.dat, TM04_395.dat, TM06_395.dat,TM08_395.dat,TM10_395.dat

Time series, 50 kHz sampling

Fast sampling data set: run id 2011_0203_1940

C:/Program Files/Borland/Delphi7/Projects/Bpl/mplot_d/test_20110203_194000.int.dat   Channels: 39 42 43 44 45 58
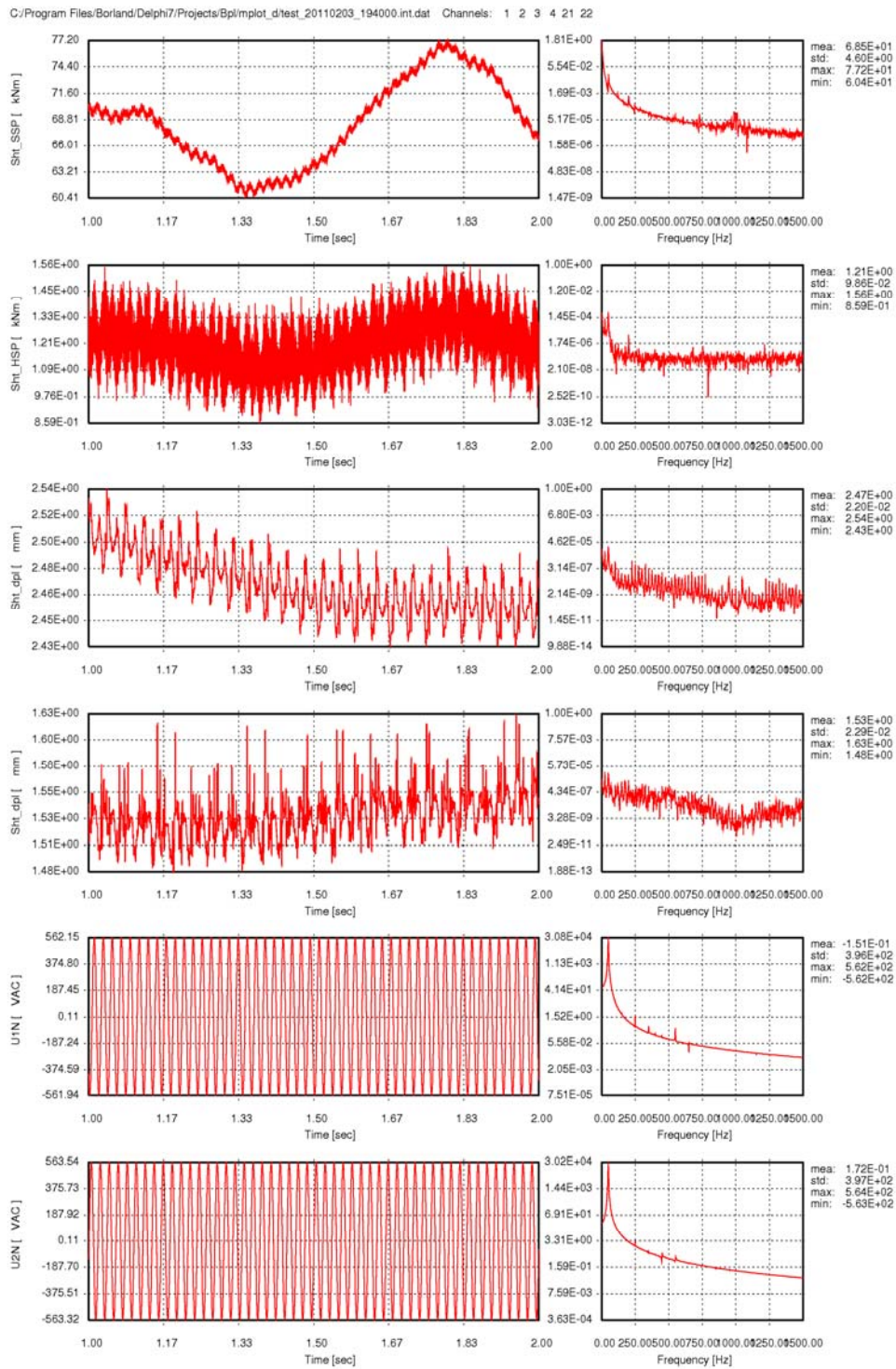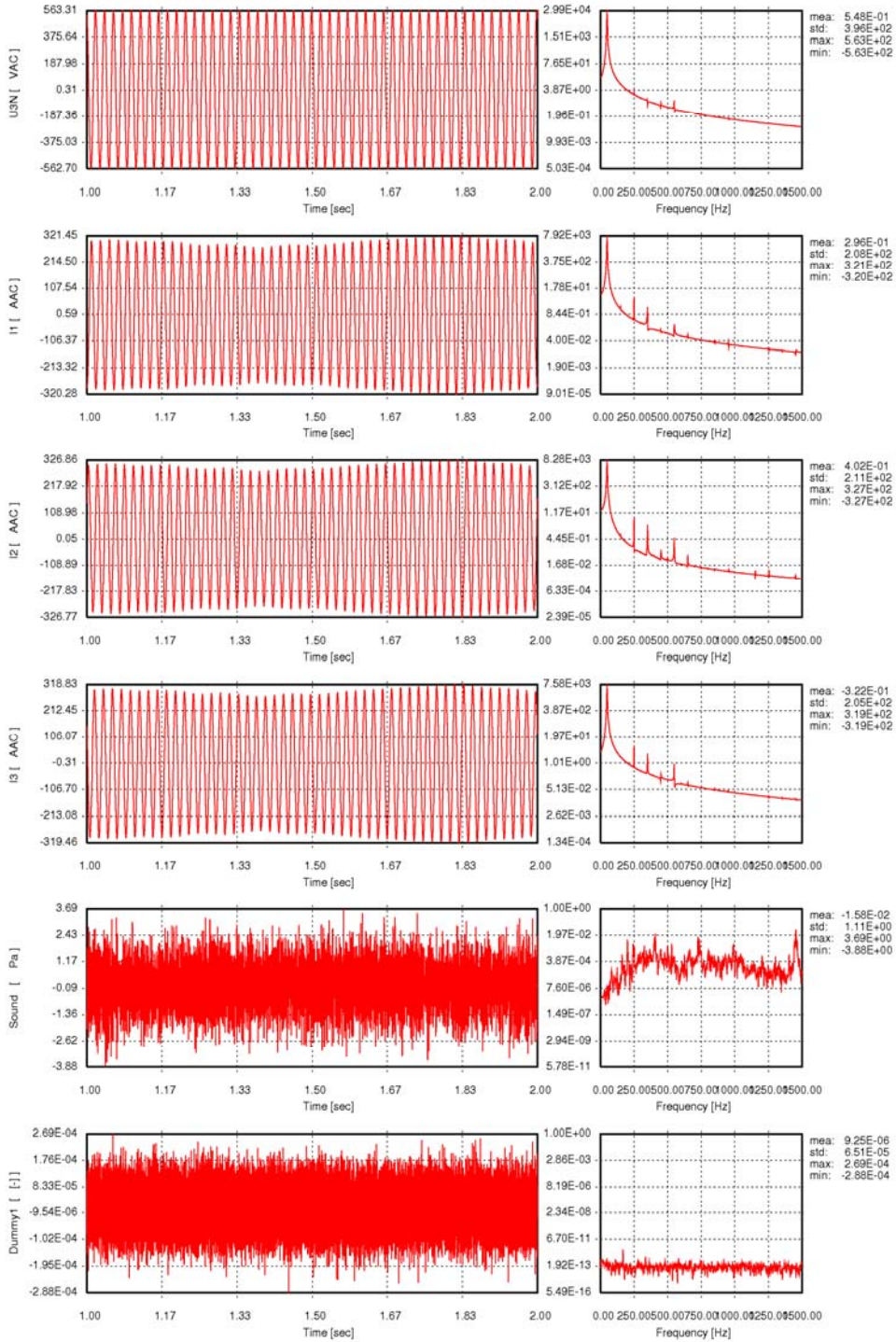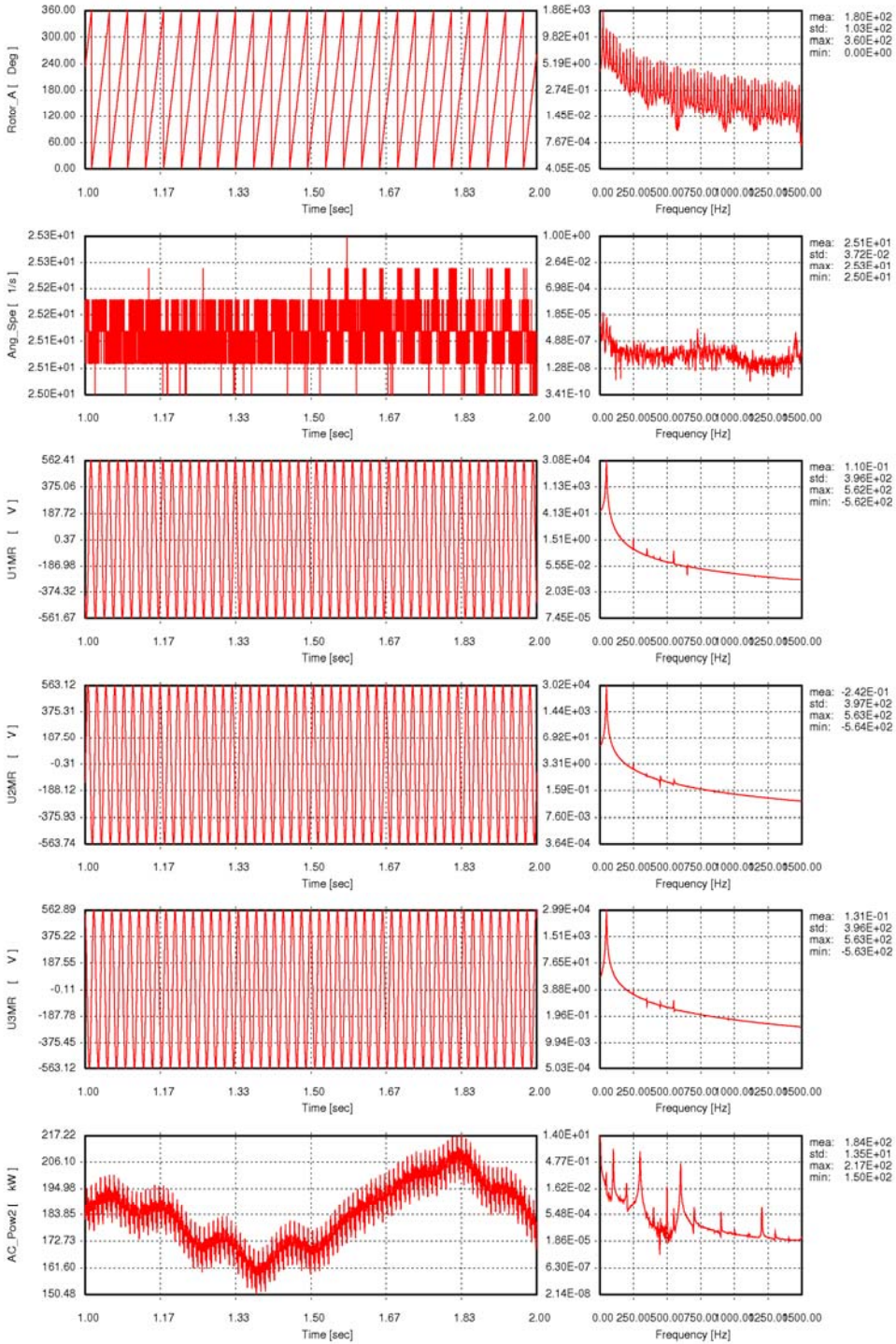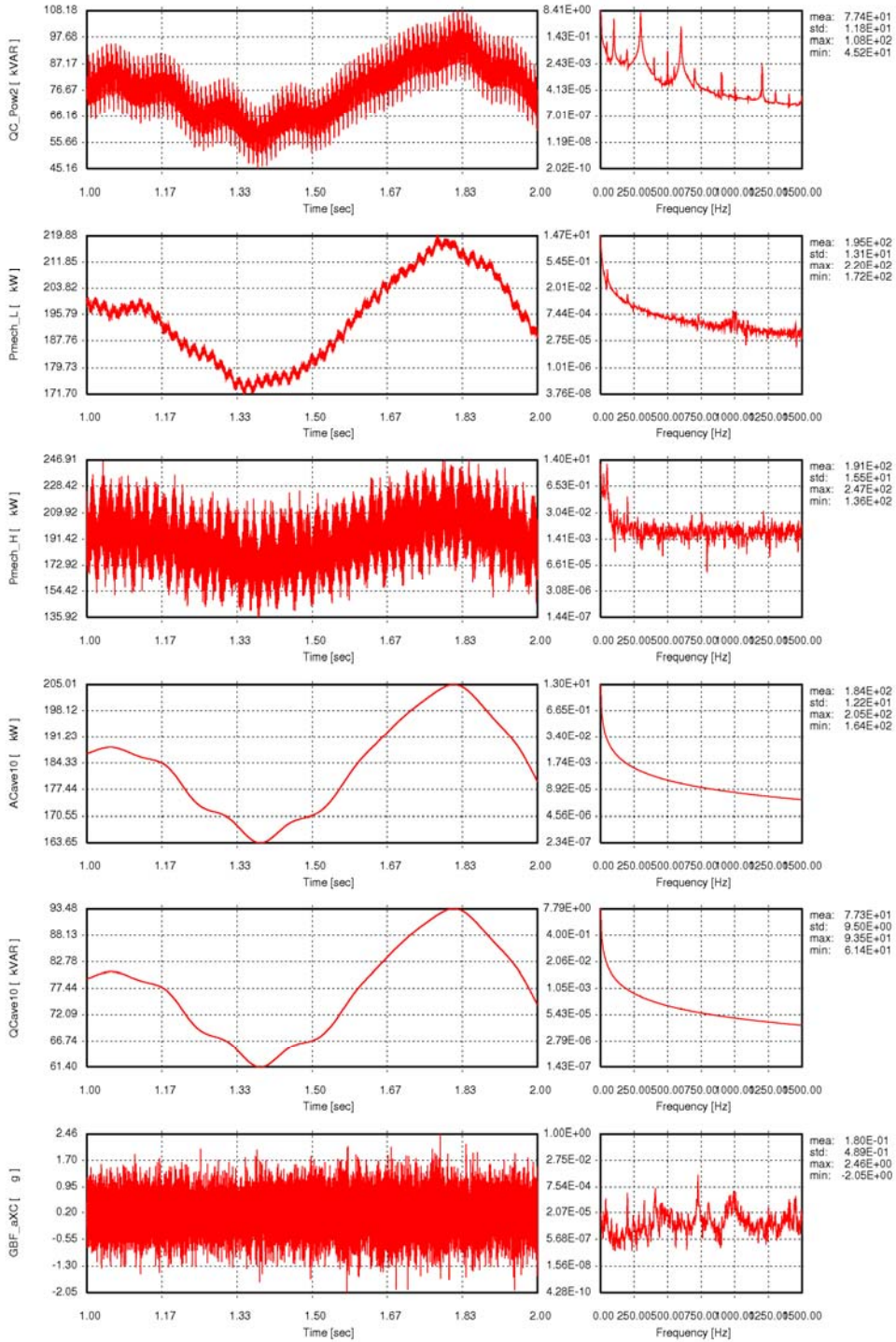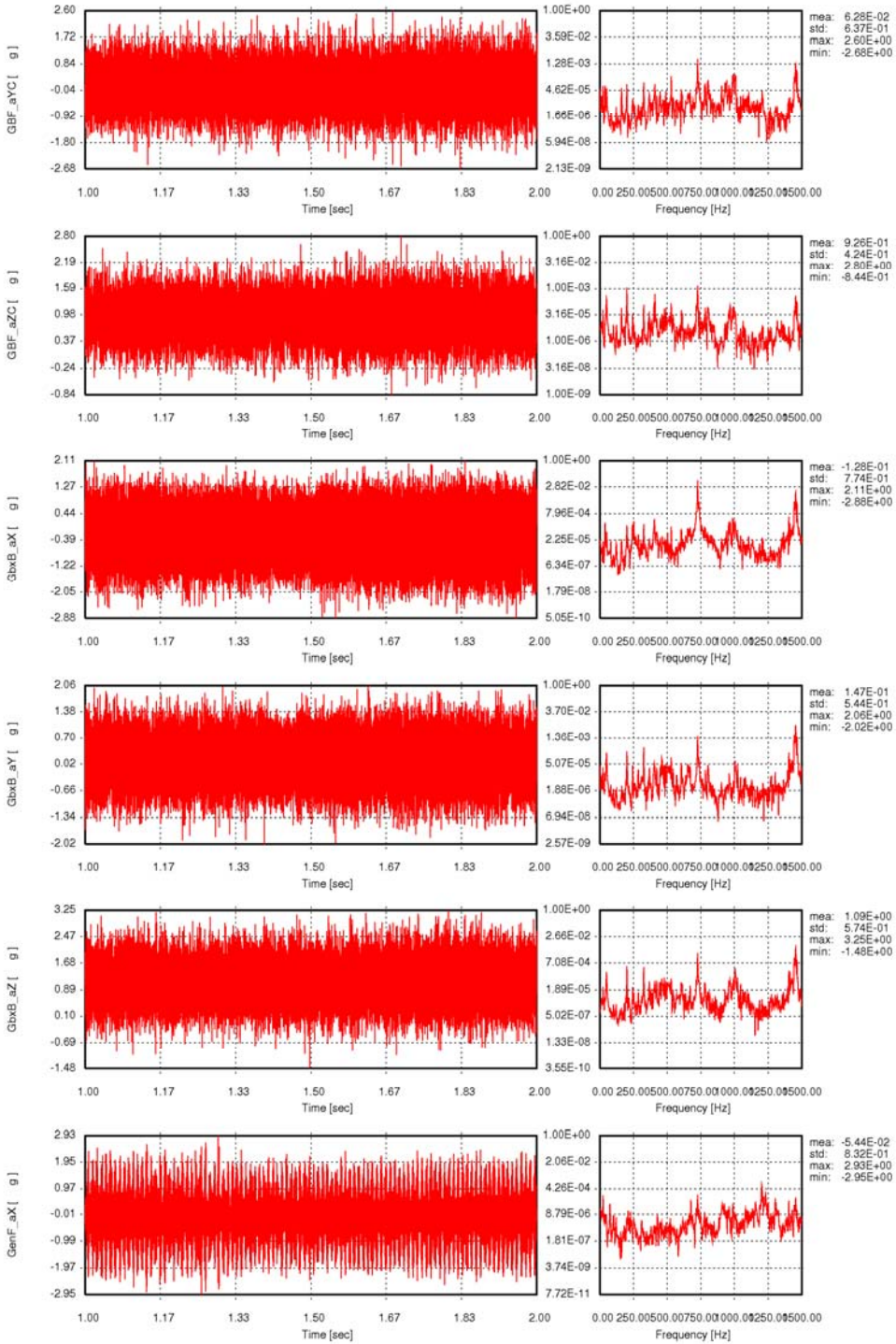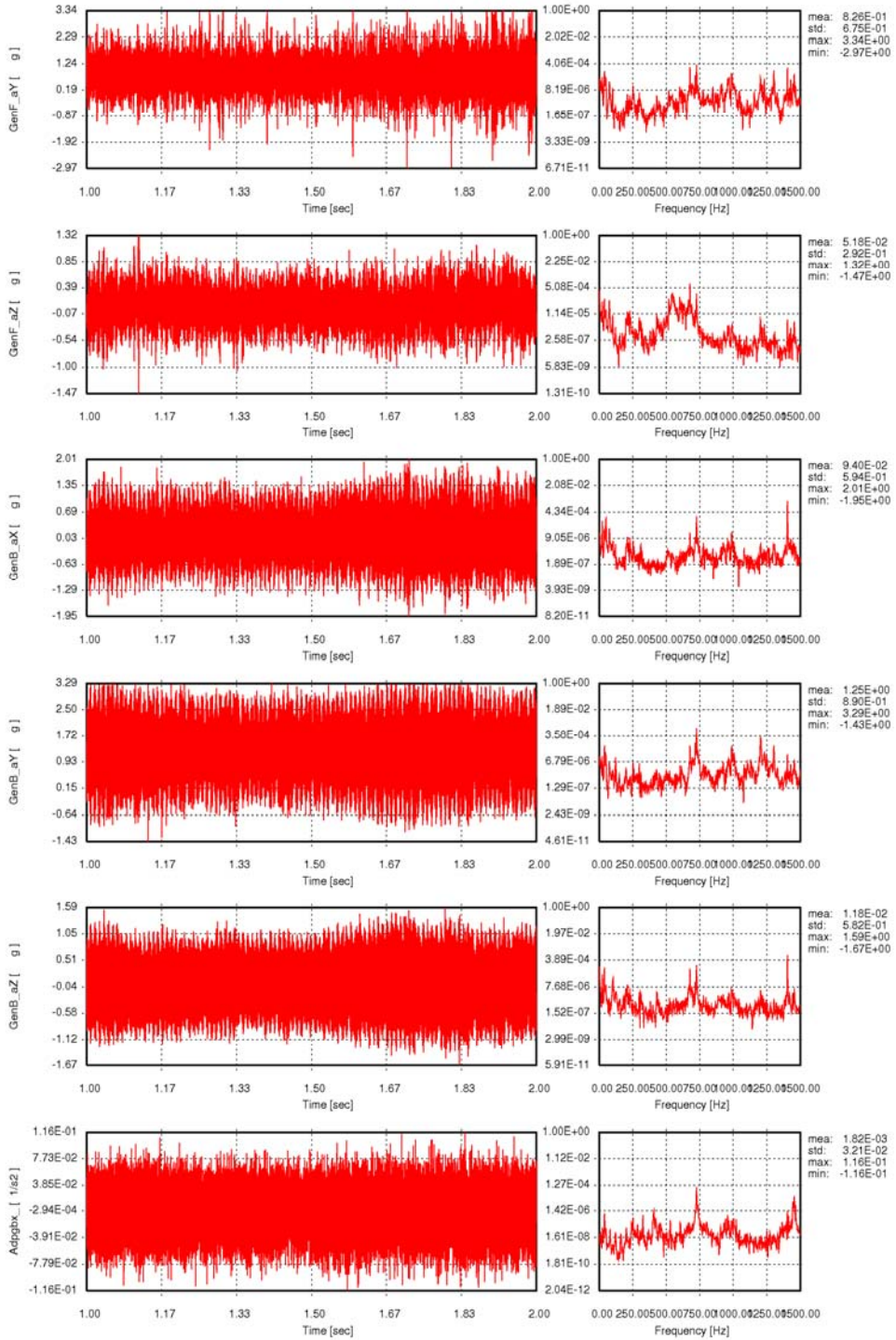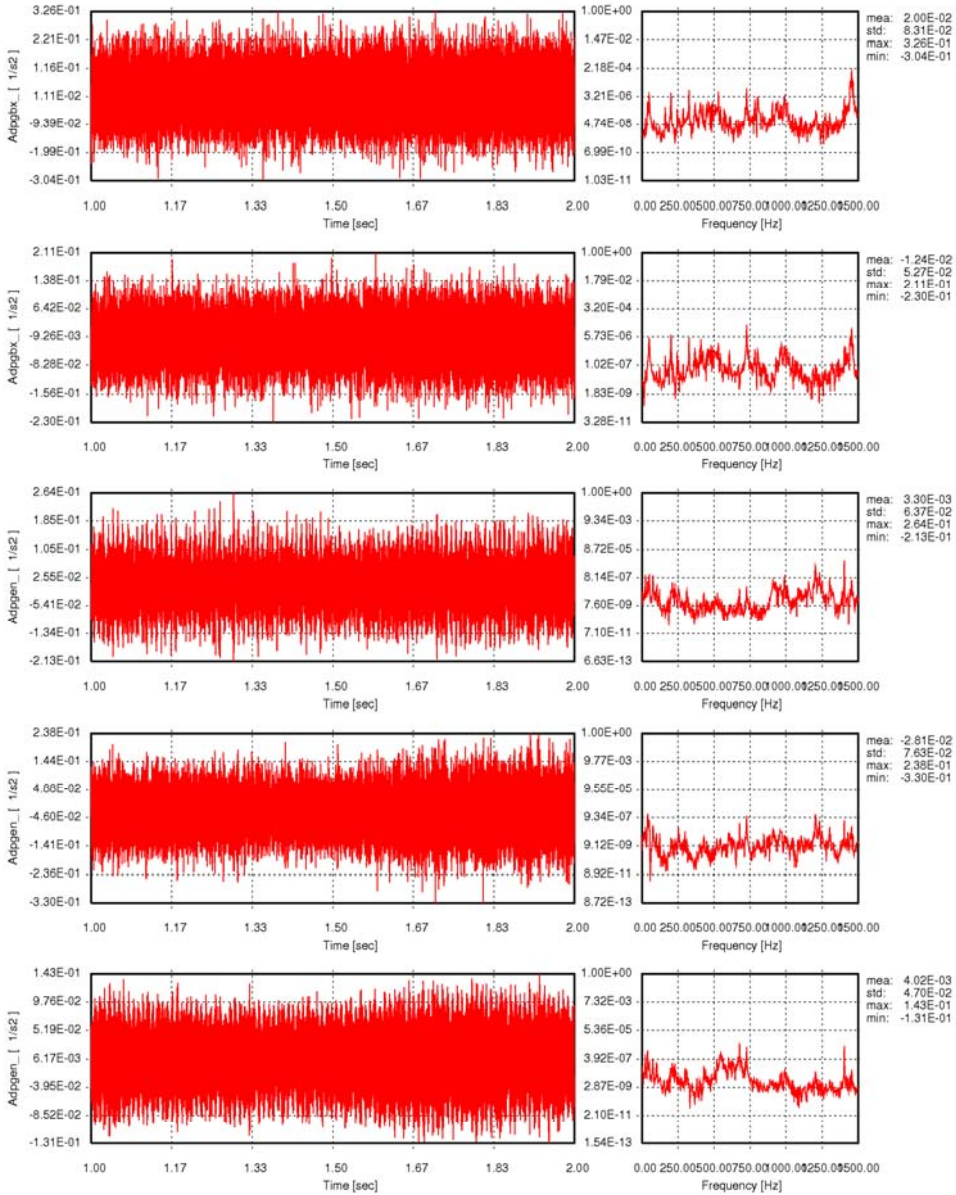
**Statistics, 50 kHz
sampling**
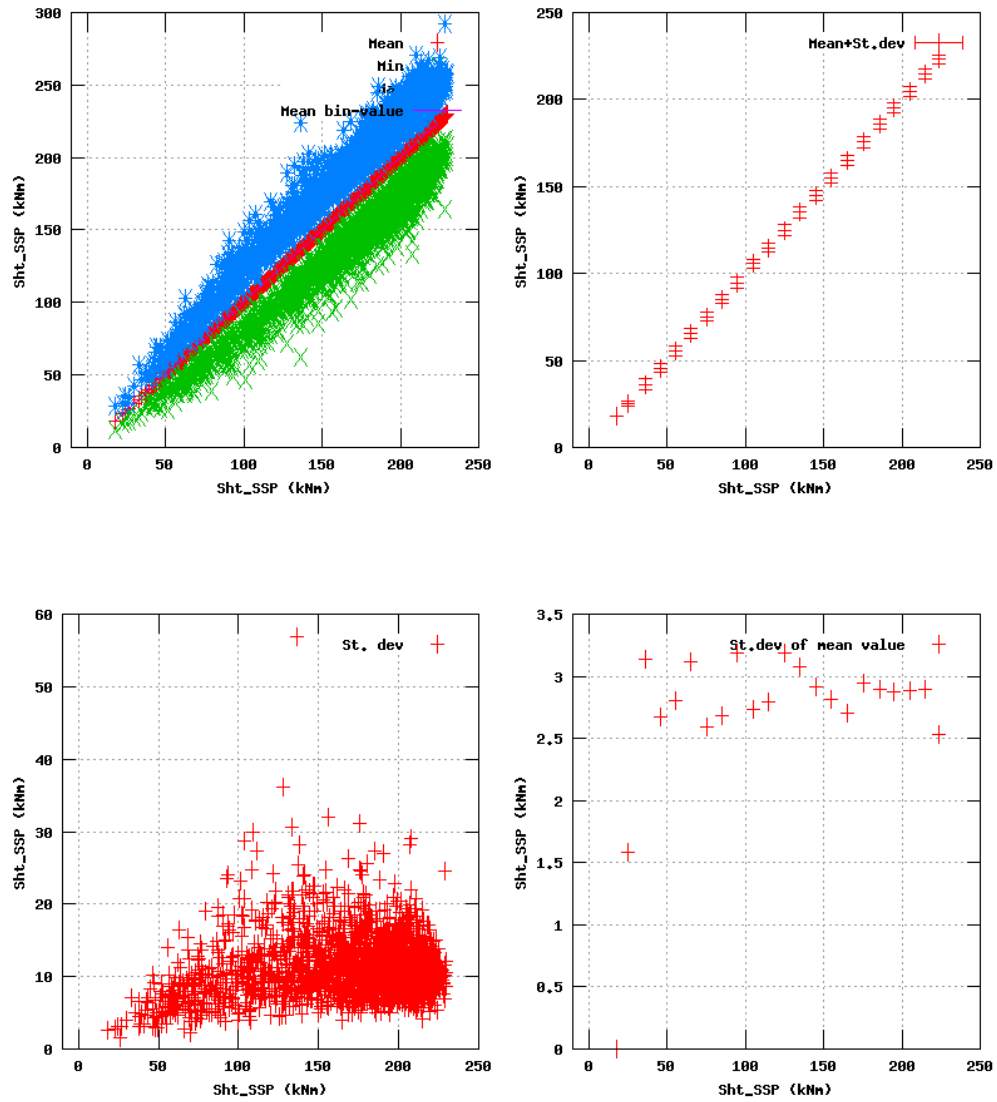
Figure 1a, Sensor 3: Torsion_LSS versus mainshaft torsion 'Sht_SSP'
Input files: NTK500fastres.dat, stat_3.dat
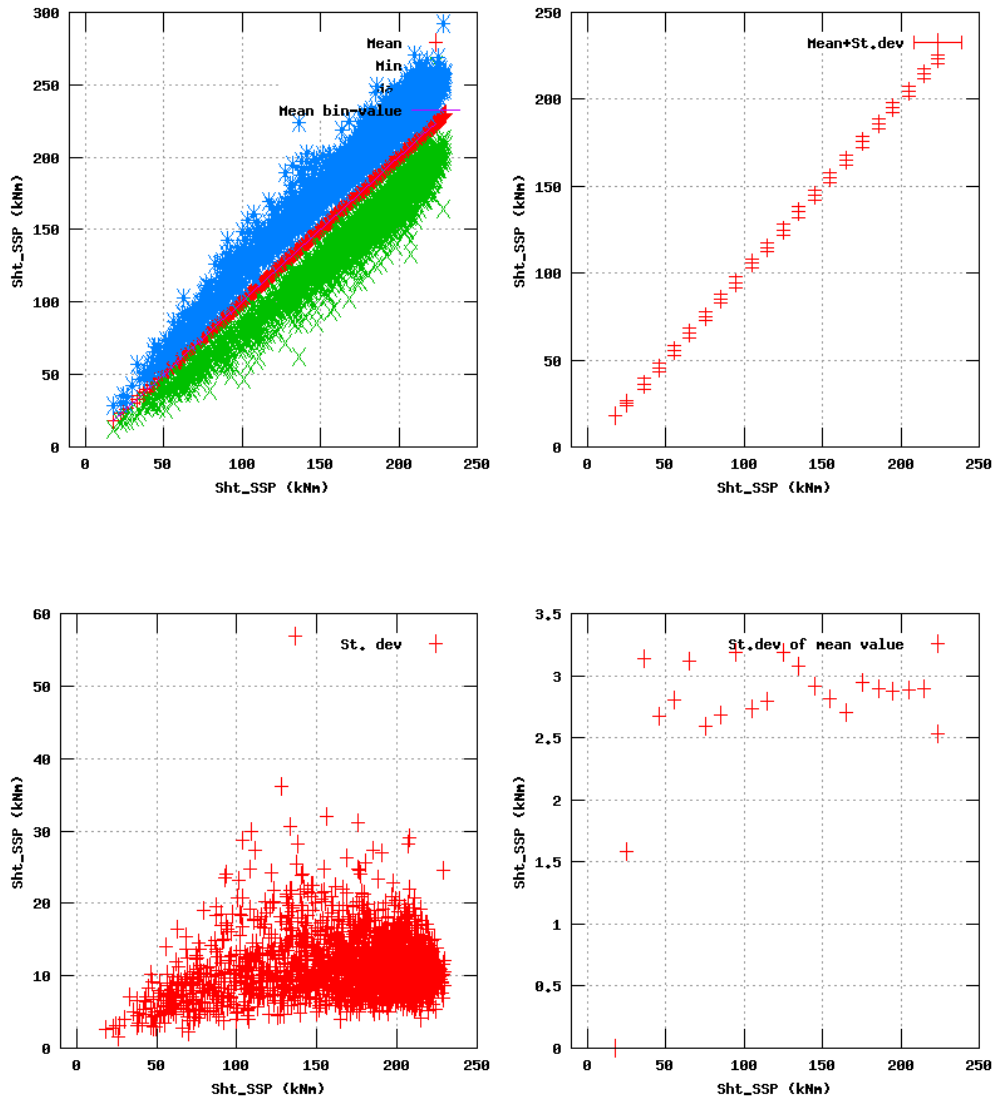
Figure 1a, Sensor 3: Torsion_LSS versus mainshaft torsion 'Sht_SSP'
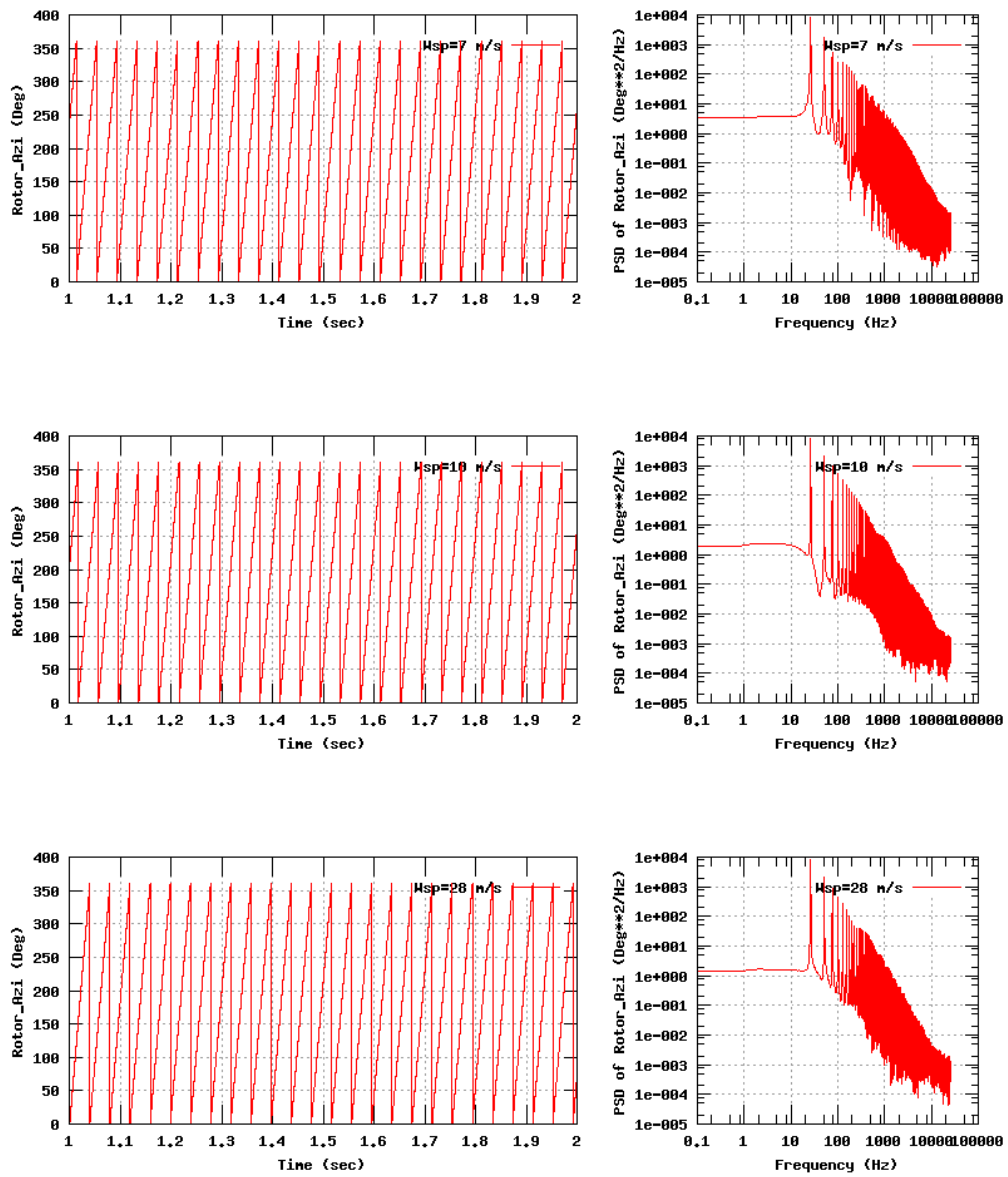Input files: NTK500fastres.dat, stat_3.dat
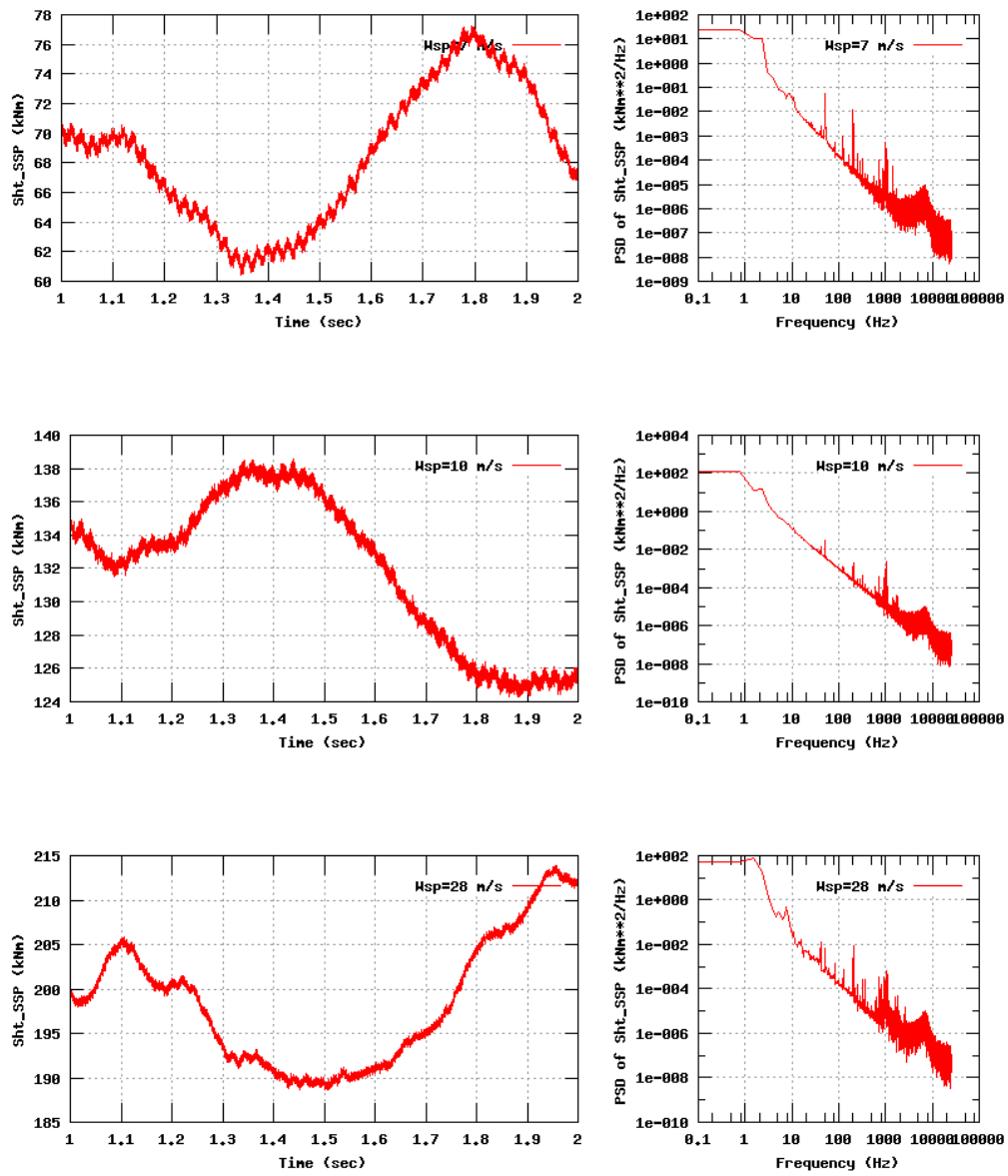
Figure 1b, Sensor 3: Torsion_LSS versus time and frequency
Input files: m07.dat, m10.dat, m28.dat, m07.psd, m10.psd and m28.psd
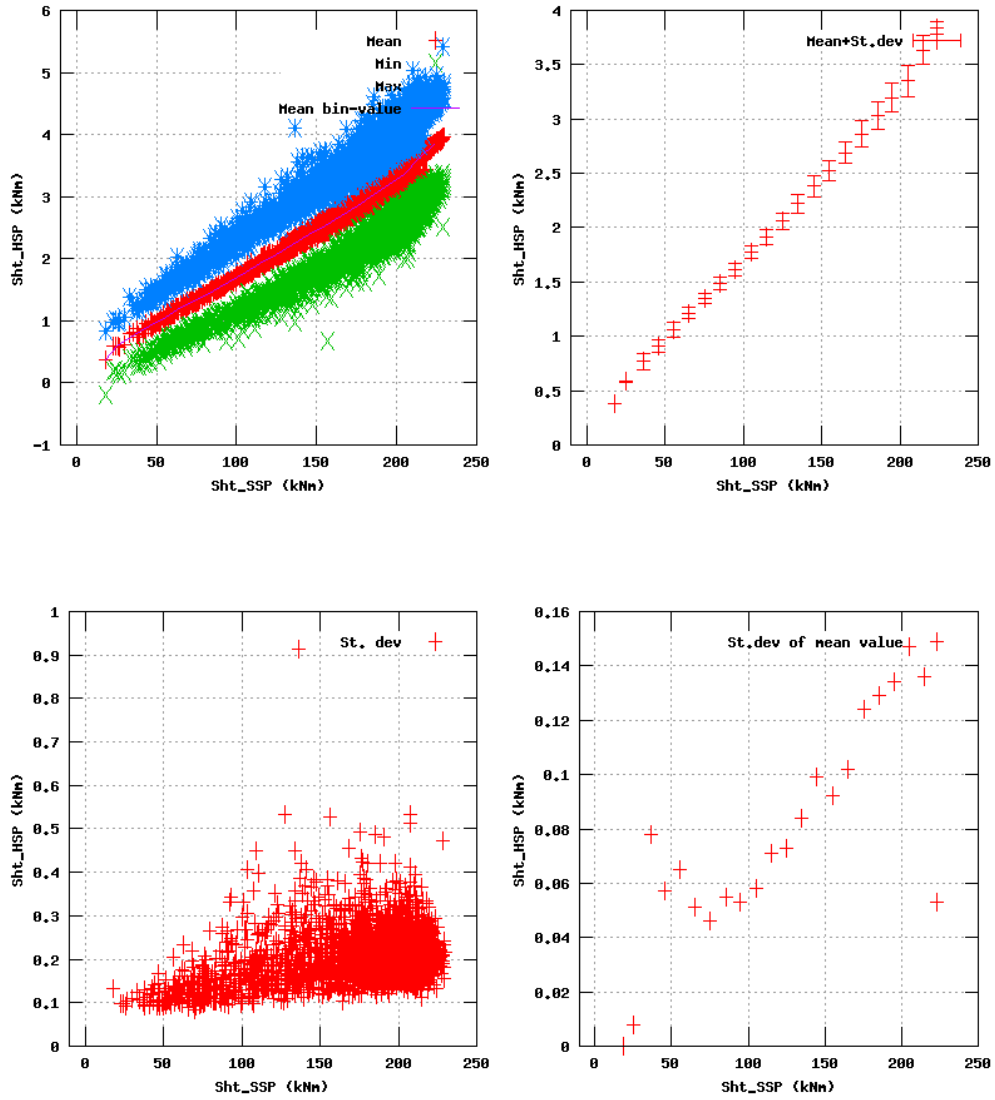
Figure 2a, Sensor 7: Torsion_HSS versus mainshaft torsion 'Sht_SSP'
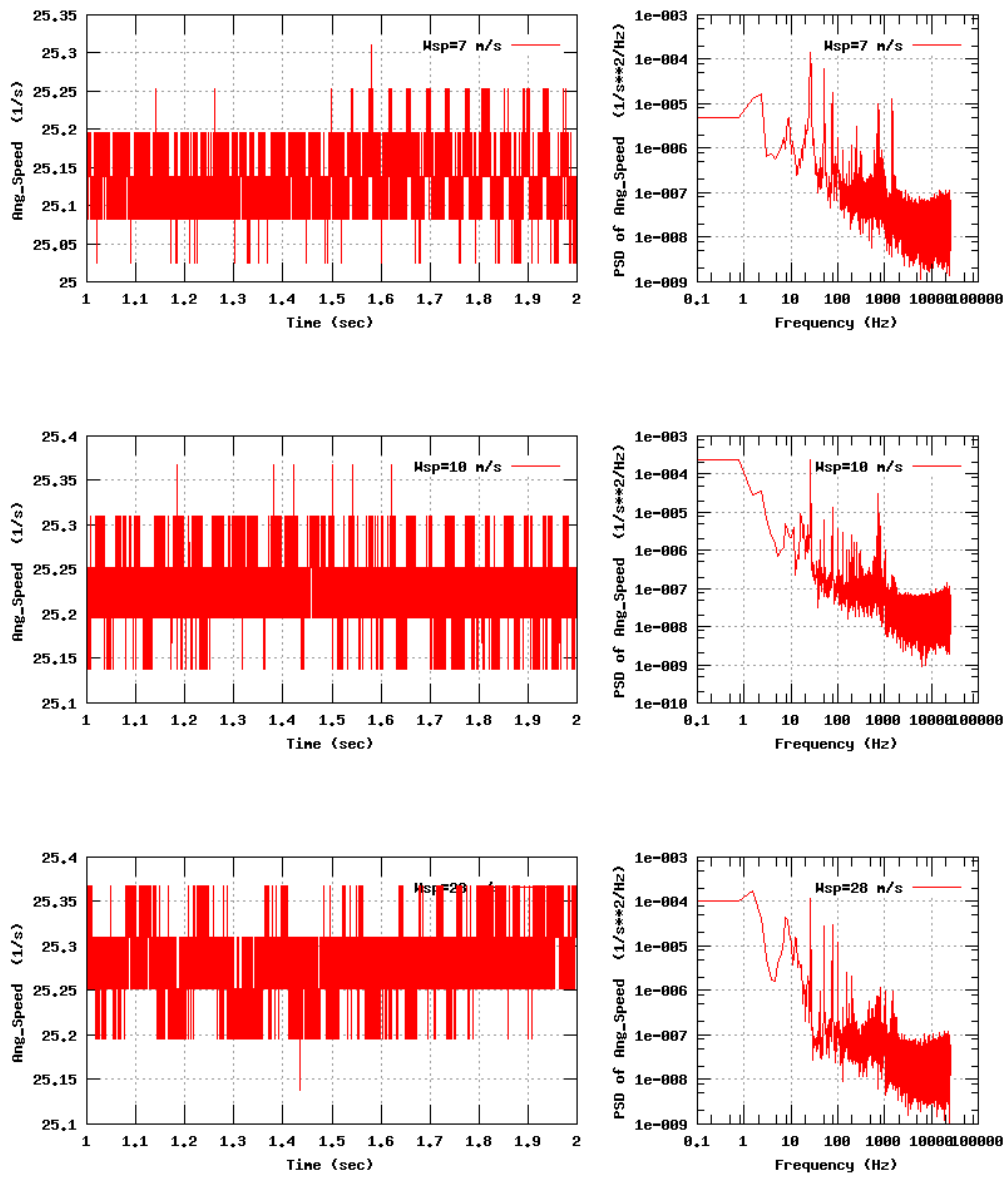Input files: NTK500fastres.dat, stat_7.dat
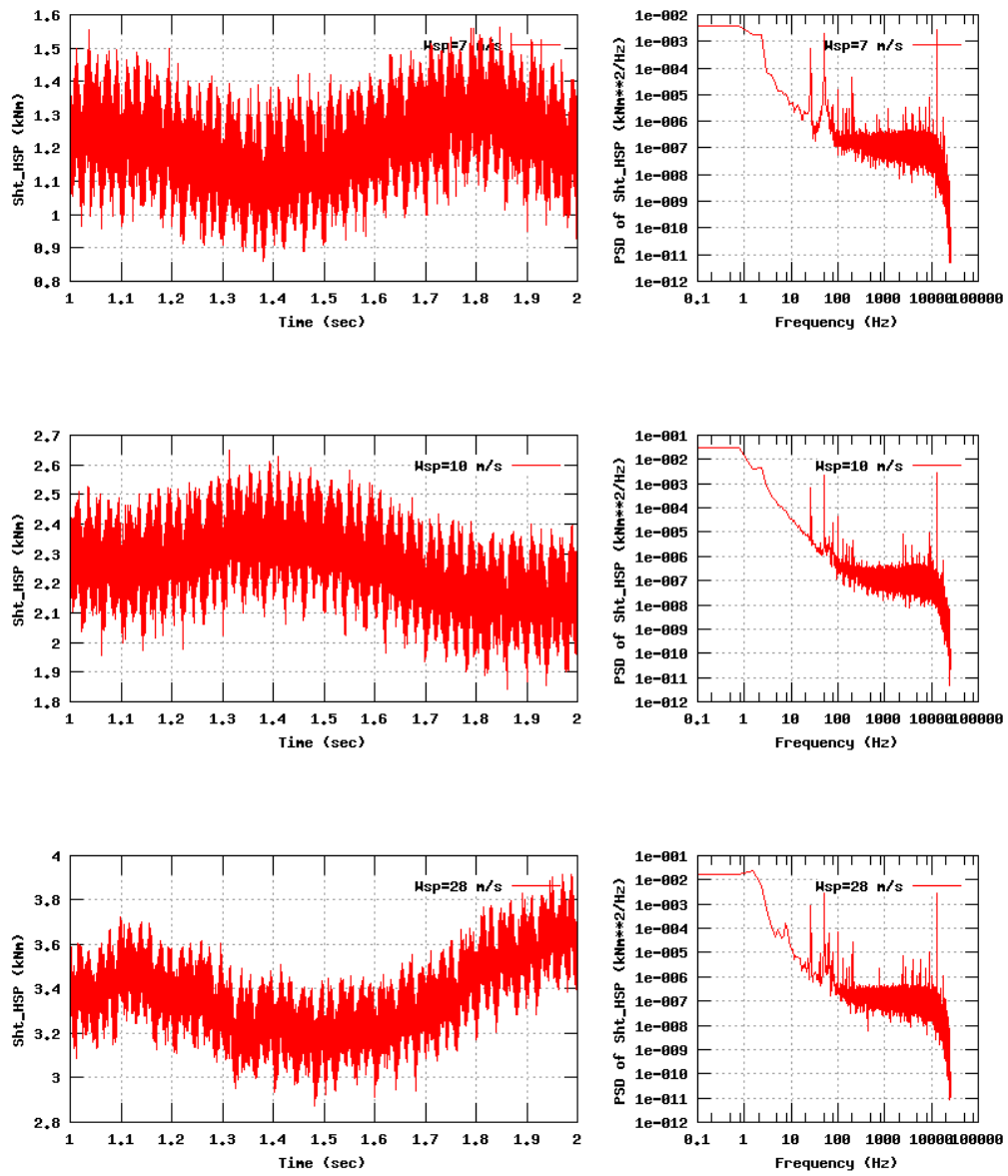
Figure 2b, Sensor 7: Torsion_HSS versus time and frequency
Input files: m07.dat, m10.dat, m28.dat, m07.psd, m10.psd and m28.psd
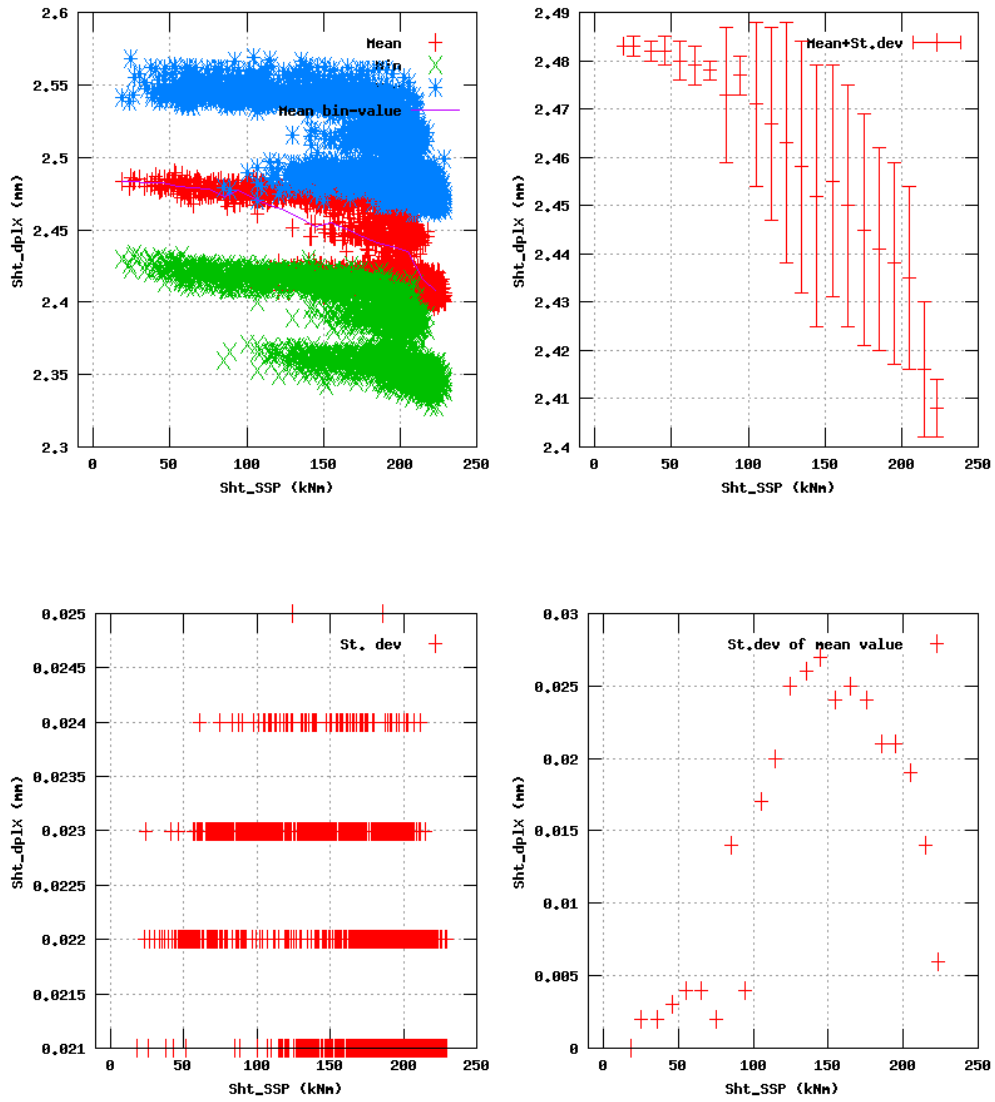
Figure 3a, Sensor 11: Trajectory_X versus mainshaft torsion 'Sht_SSP'
Input files: NTK500fastres.dat, stat_11.dat
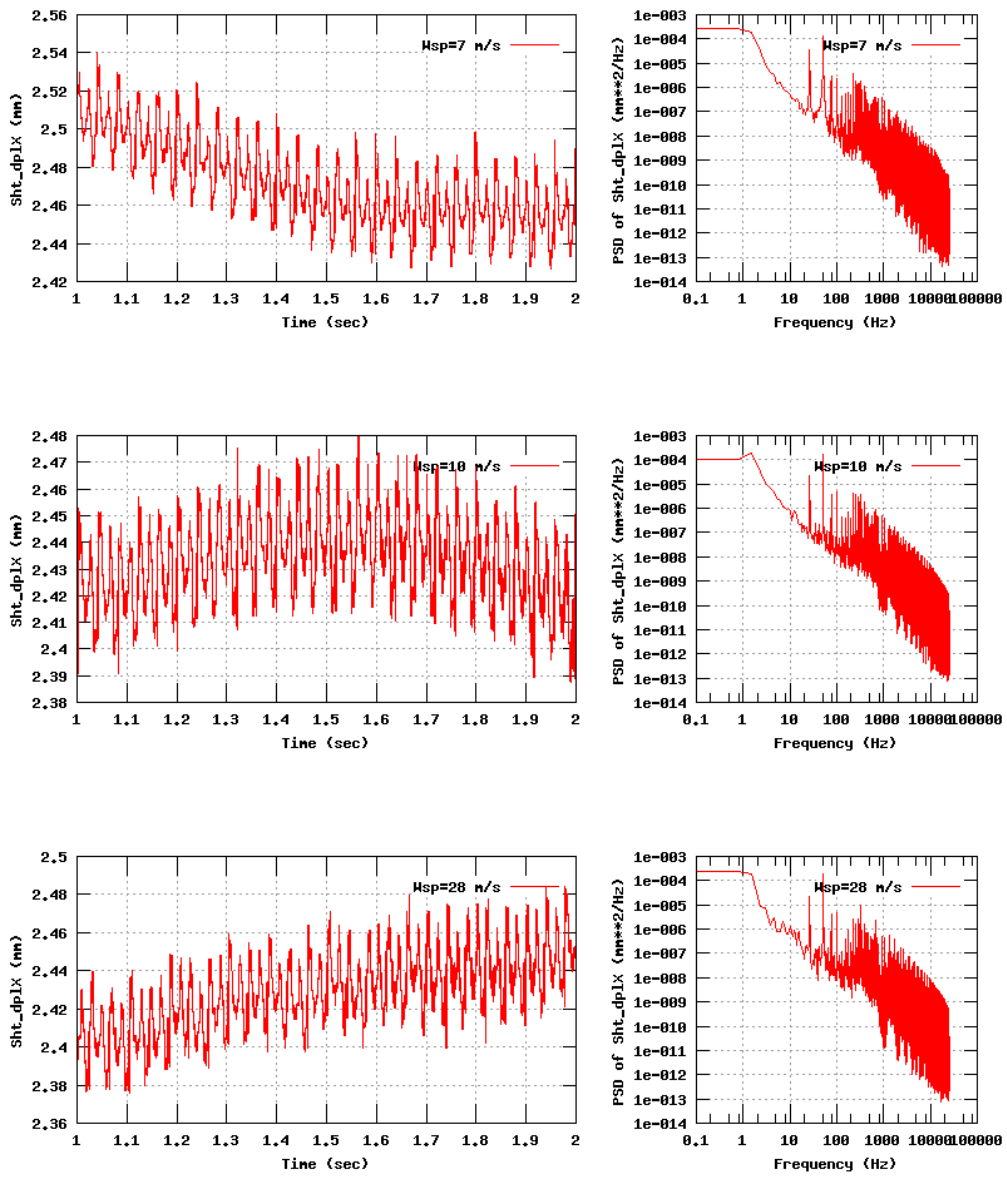
Figure 3b, Sensor 11: Trajectory_X versus time and frequency
Input files: m07.dat, m10.dat, m28.dat, m07.psd, m10.psd and m28.psd
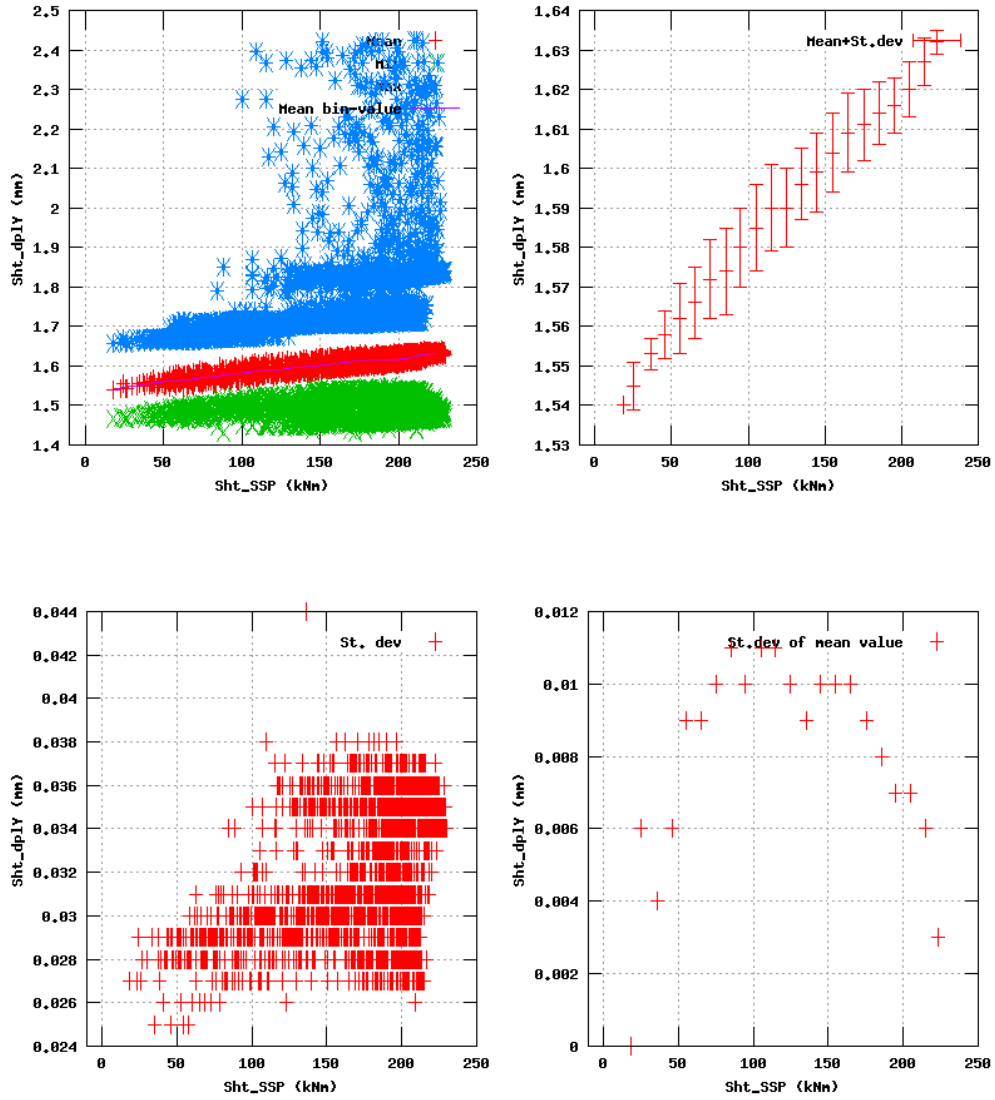
Figure 4a, Sensor 15: Trajectory_Y versus mainshaft torsion 'Sht_SSP'
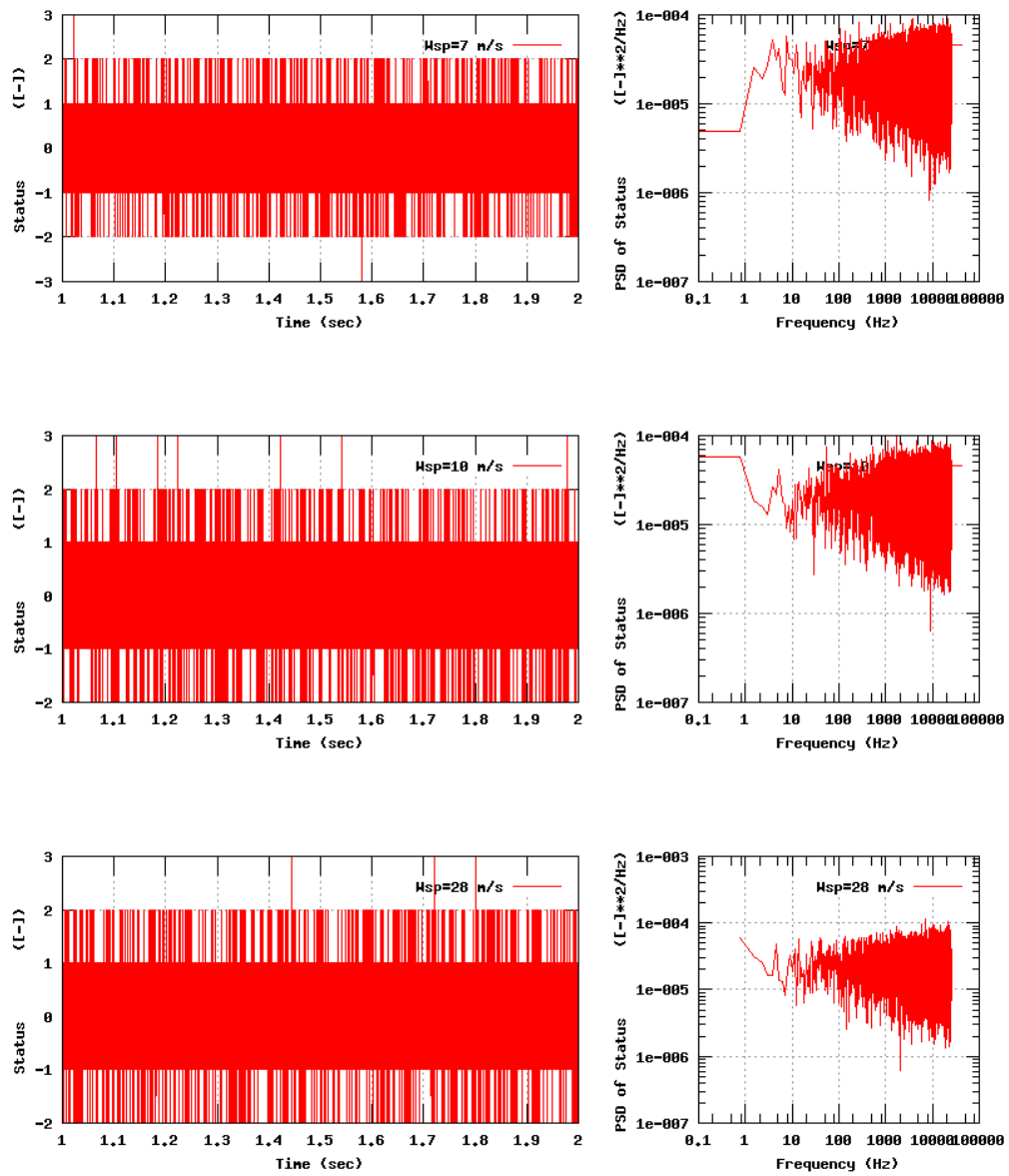Input files: NTK500fastres.dat, stat_15.dat
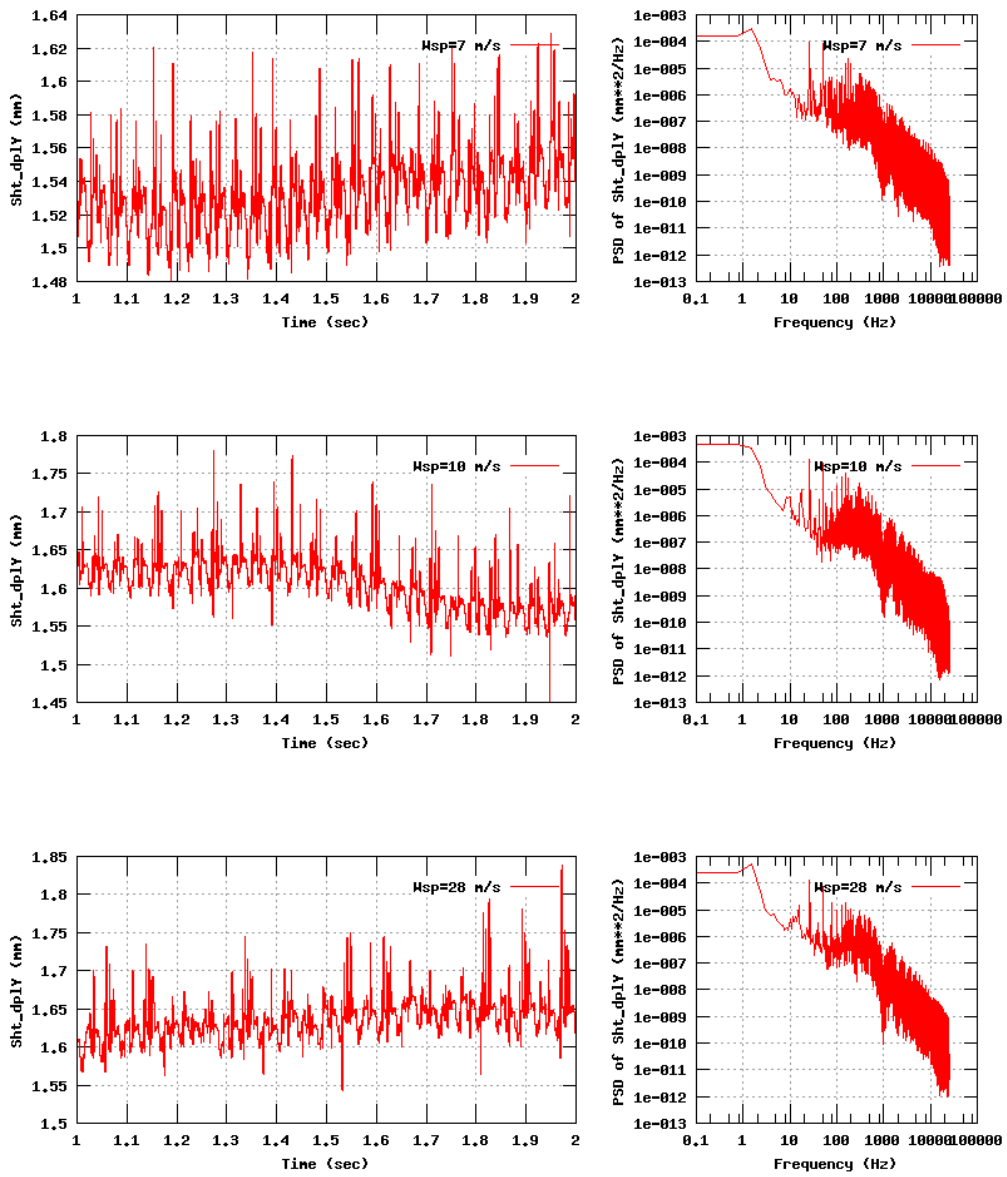
Figure 4b, Sensor 15: Trajectory_Y versus time and frequency
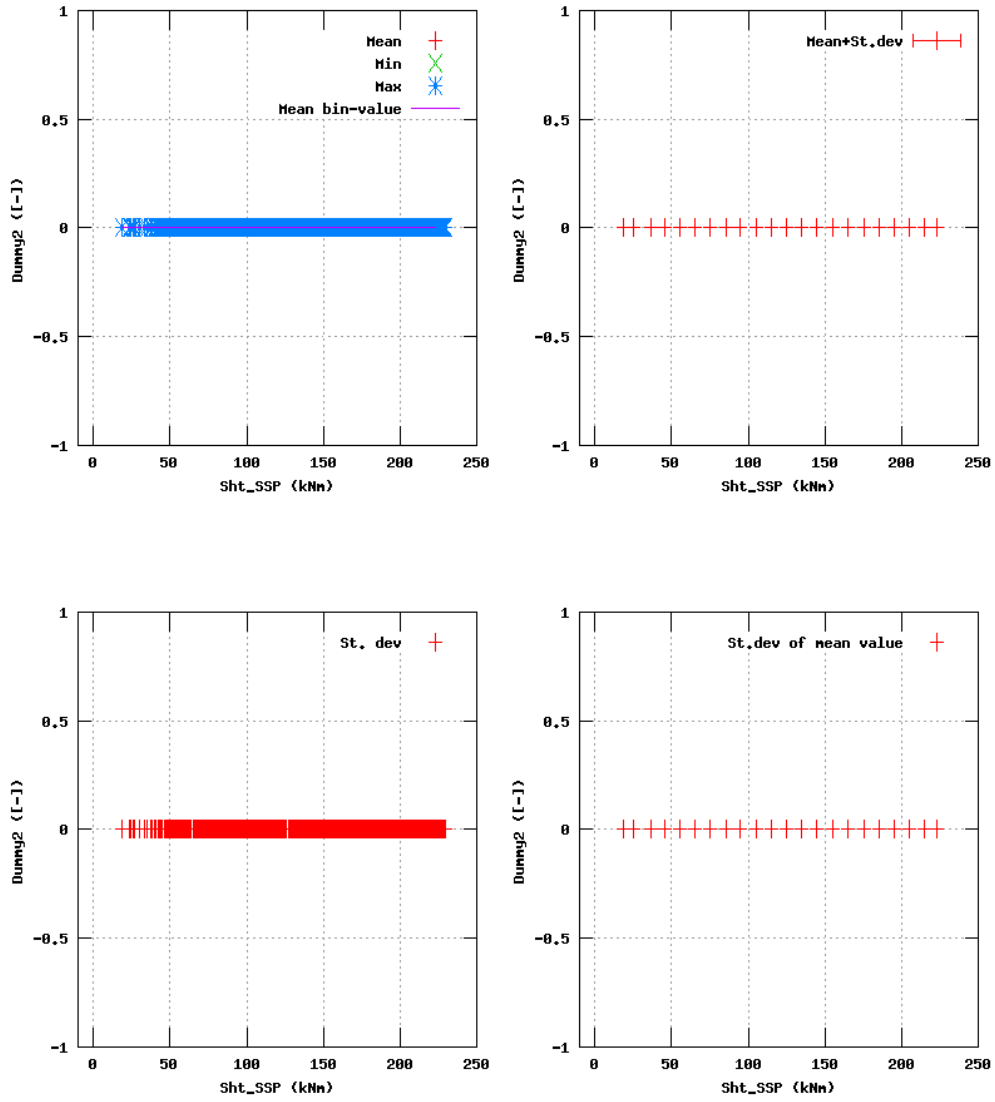Input files: m07.dat, m10.dat, m28.dat, m07.psd, m10.psd and m28.psd
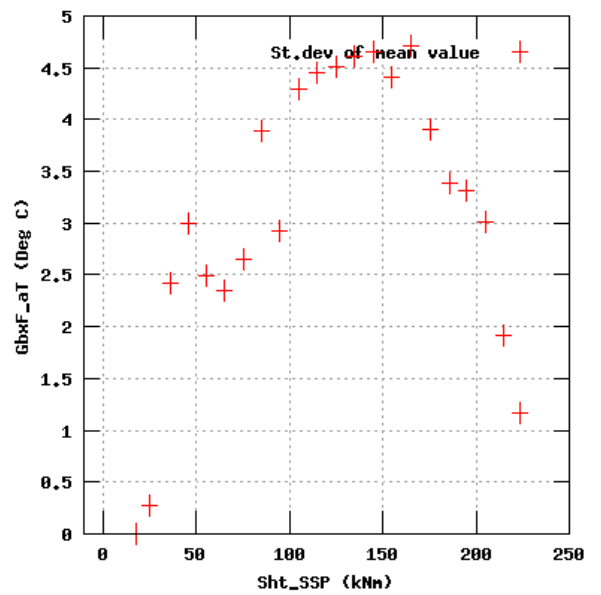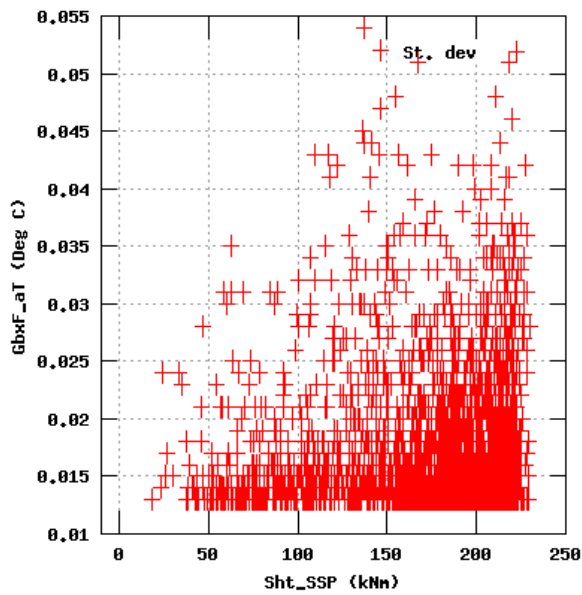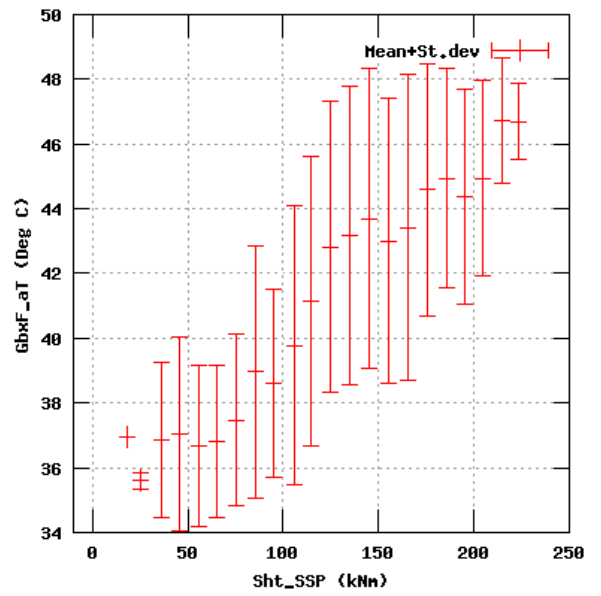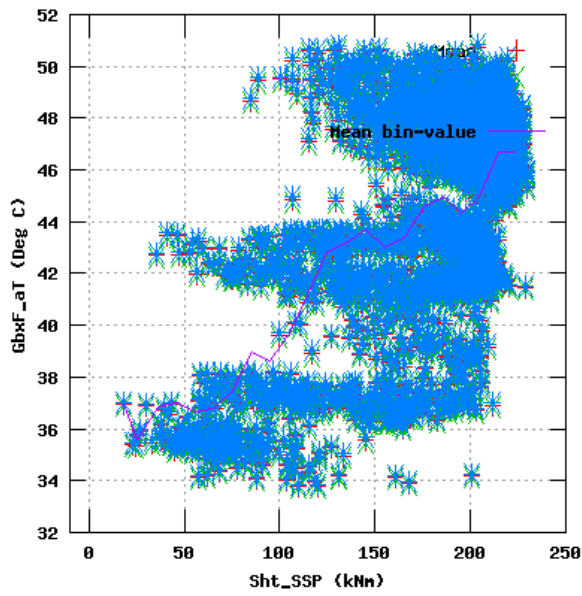
Figure 8a, Sensor 31: GearBoxF_aT versus mainshaft torsion 'Sht_SSP'
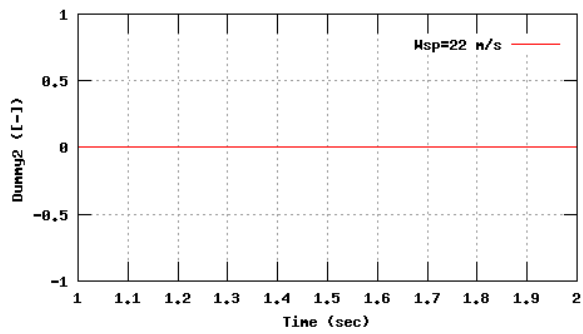Input files: NTK500fastres.dat, stat_31.dat
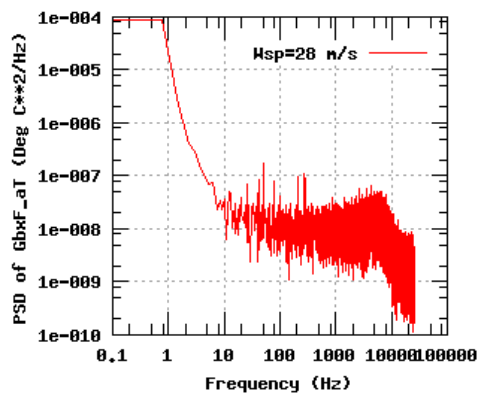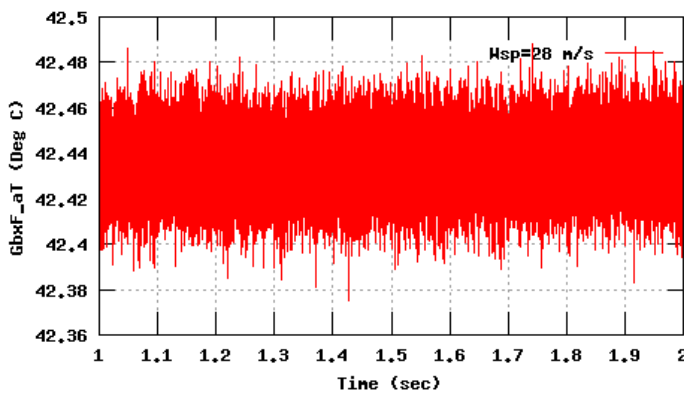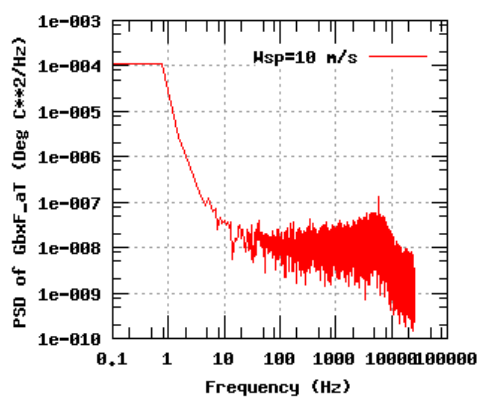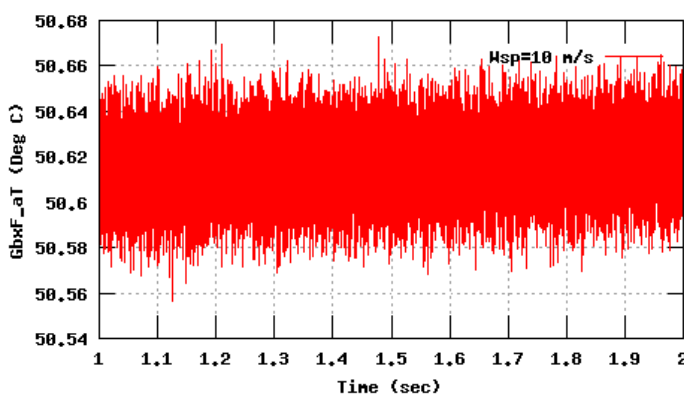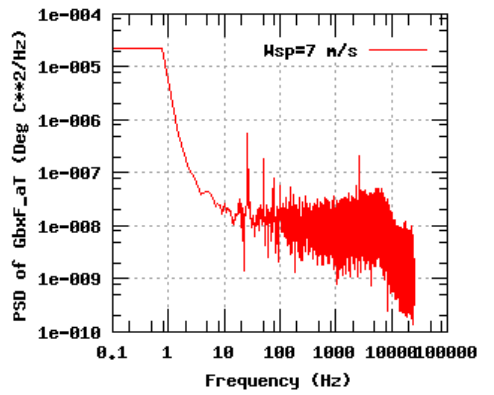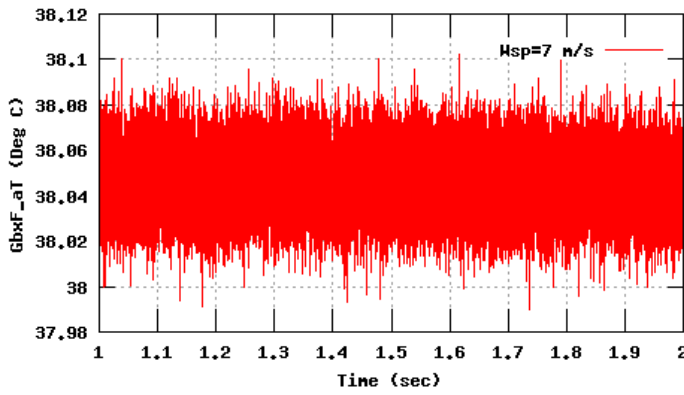
Figure 8b, Sensor 31: GearBoxF_aT versus time and frequency
Input files: m07.dat, m10.dat, m28.dat, m07.psd, m10.psd and m28.psd
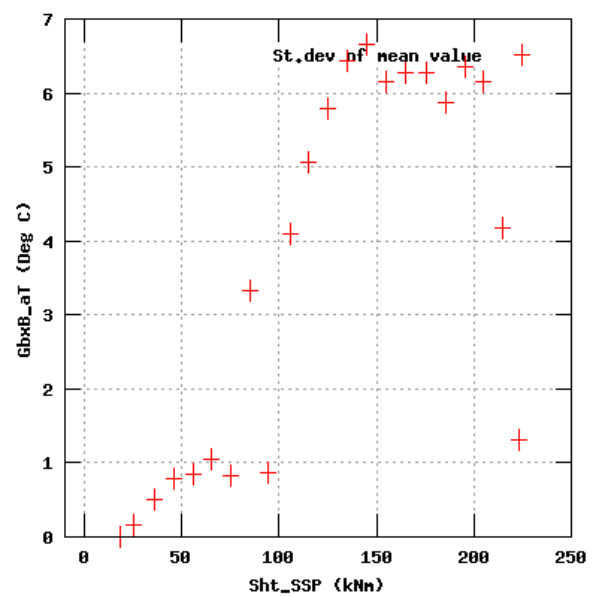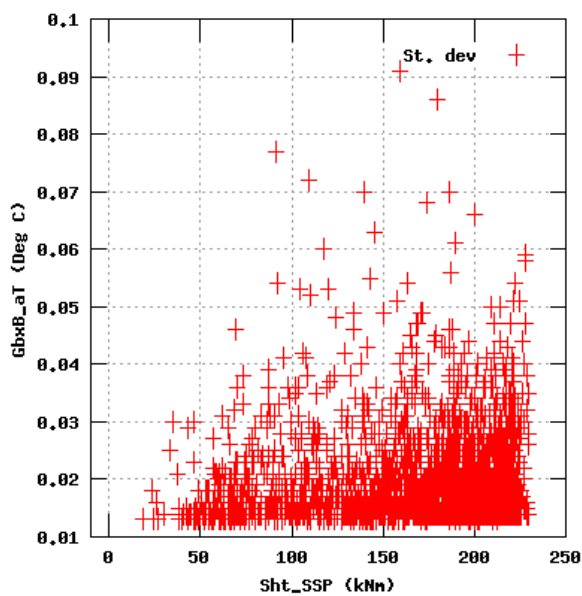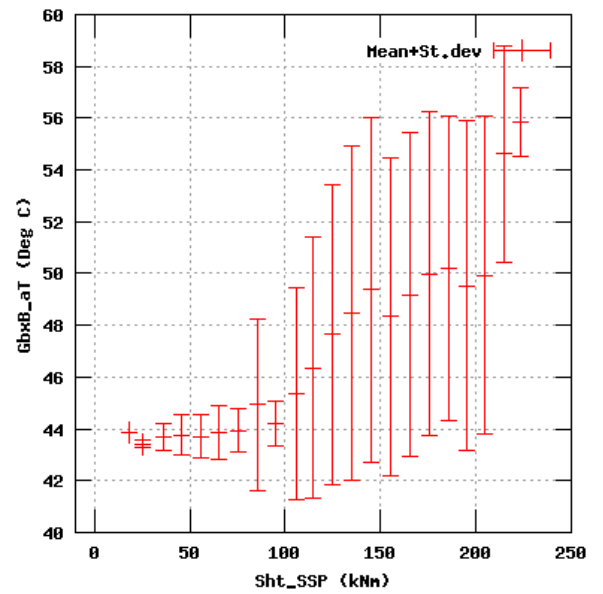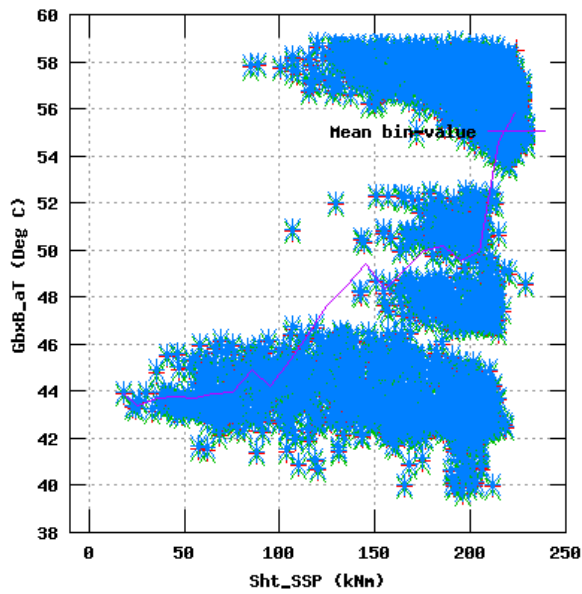
Figure 12a, Sensor 47: GearBoxB_aT versus mainshaft torsion 'Sht_SSP'
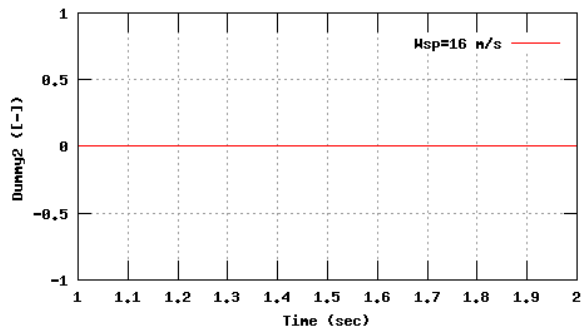Input files: NTK500fastres.dat, stat_47.dat
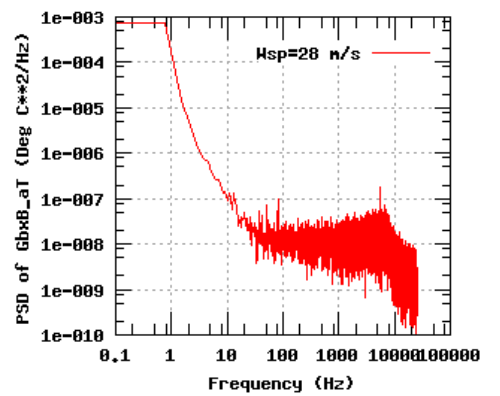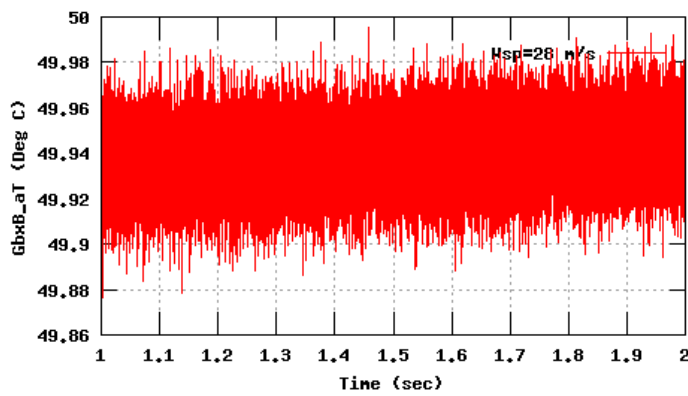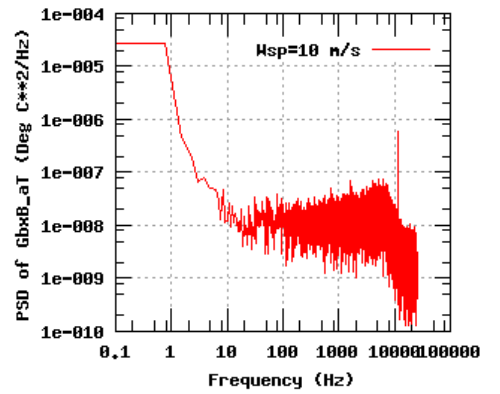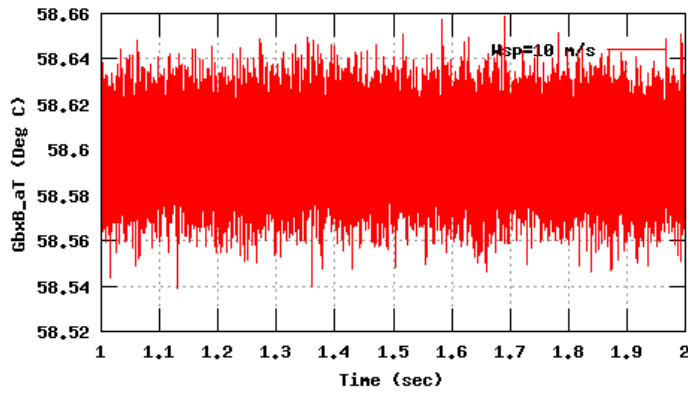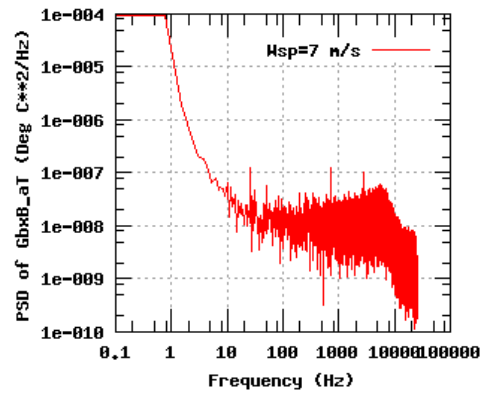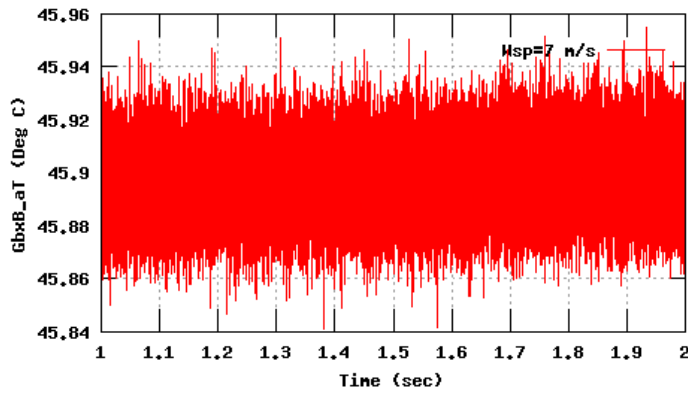
Figure 12b, Sensor 47: GearBoxB_aT versus time and frequency
Input files: m07.dat, m10.dat, m28.dat, m07.psd, m10.psd and m28.psd
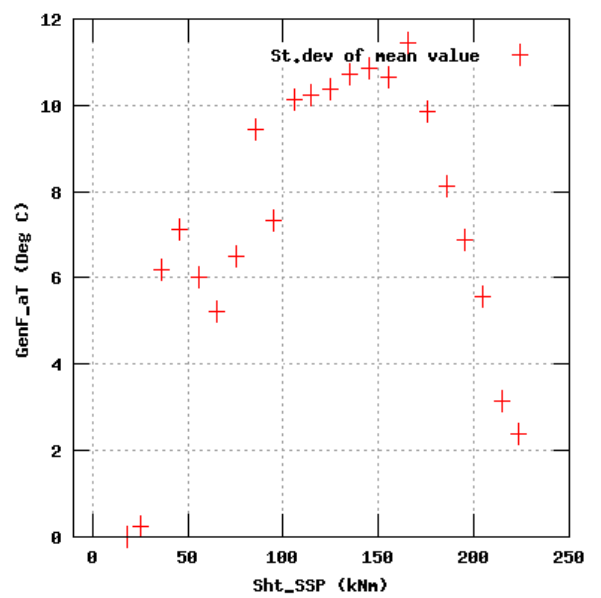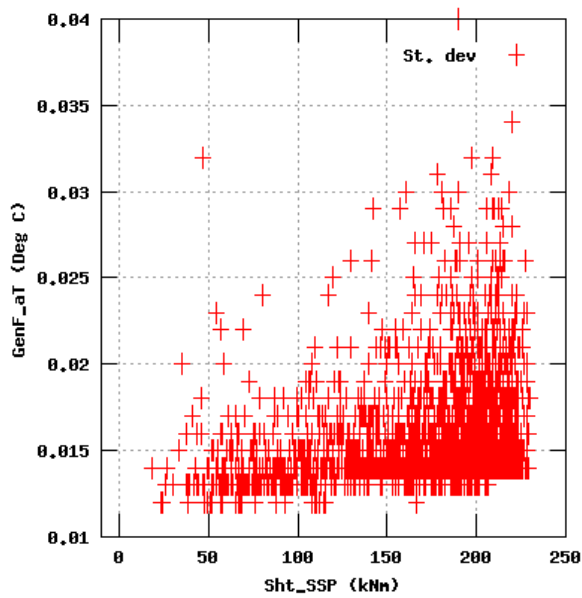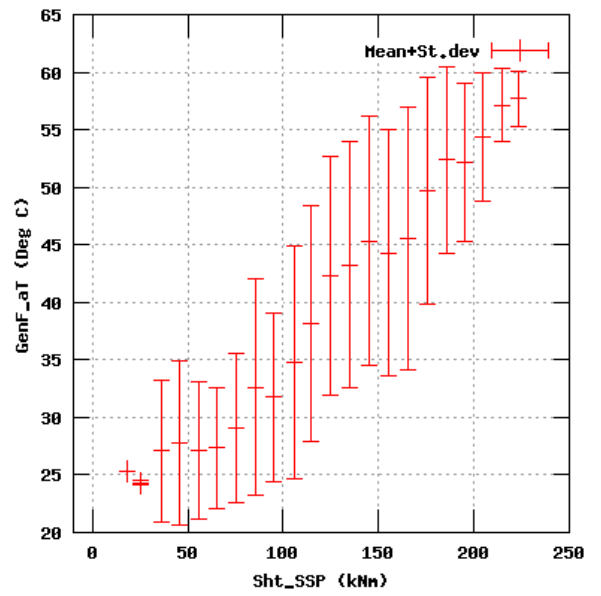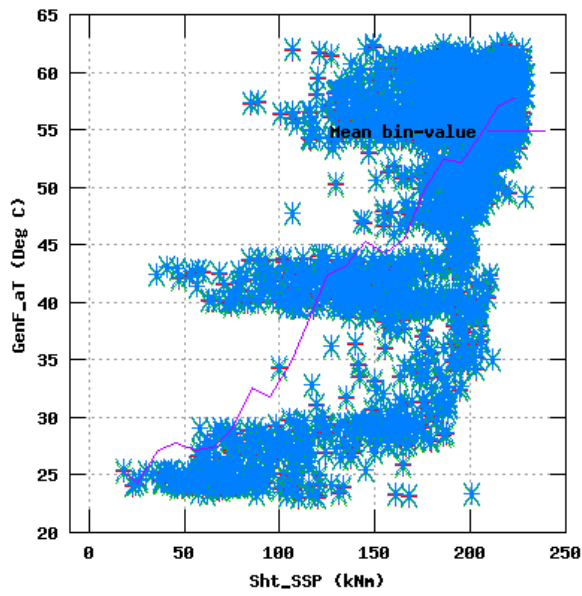
Figure 16a, Sensor 63: GeneratorF_aT versus mainshaft torsion 'Sht_SSP'
Input files: NTK500fastres.dat, stat_63.dat
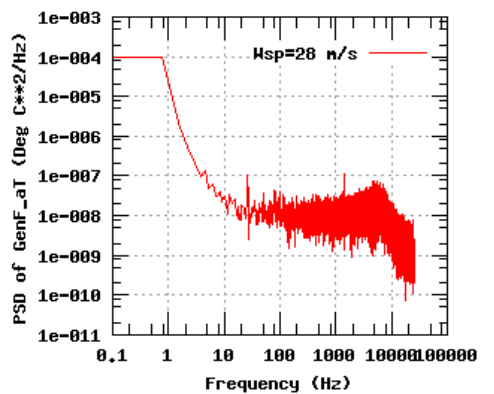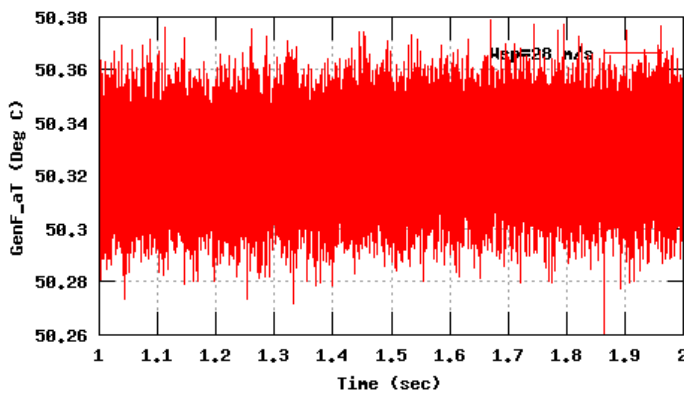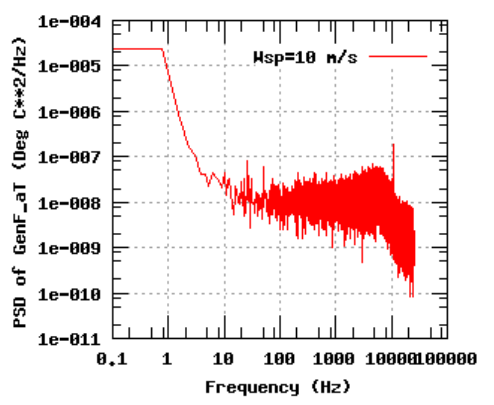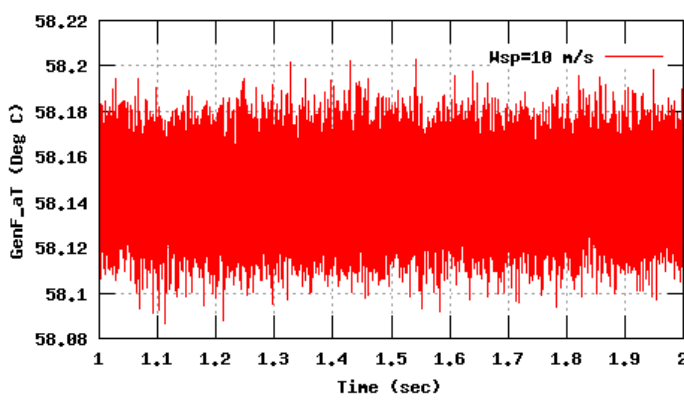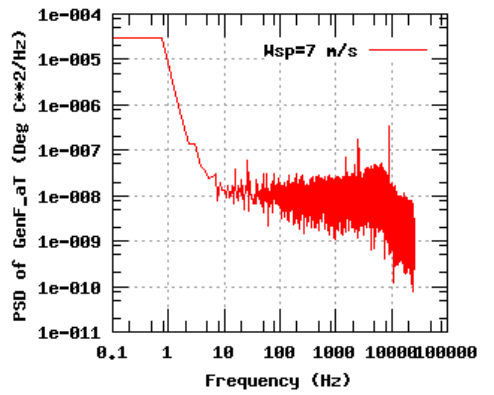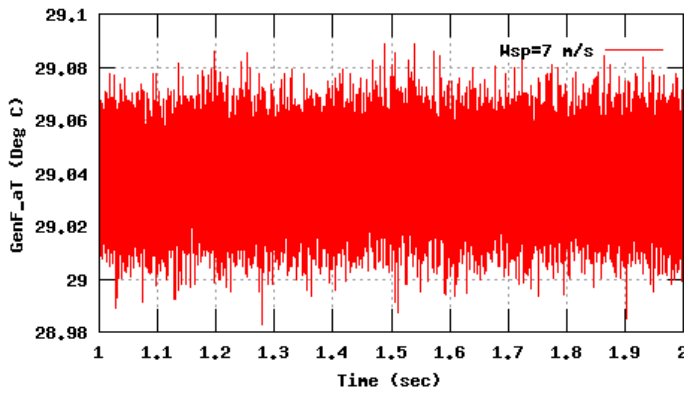
Figure 16b, Sensor 63: GeneratorF_aT versus time and frequency
Input files: m07.dat, m10.dat, m28.dat, m07.psd, m10.psd and m28.psd
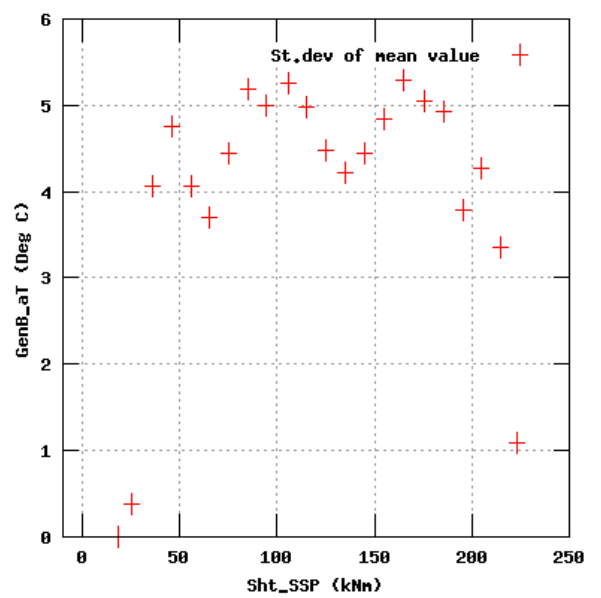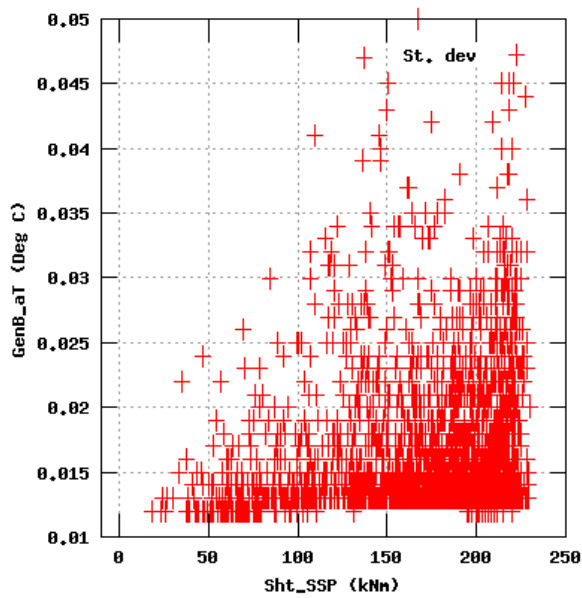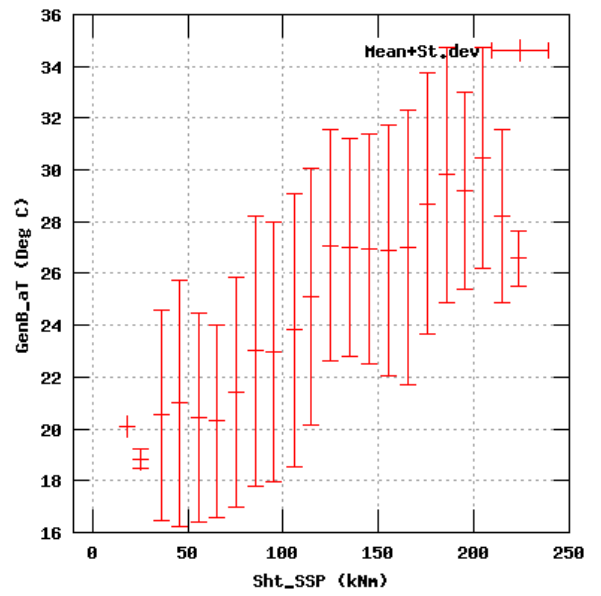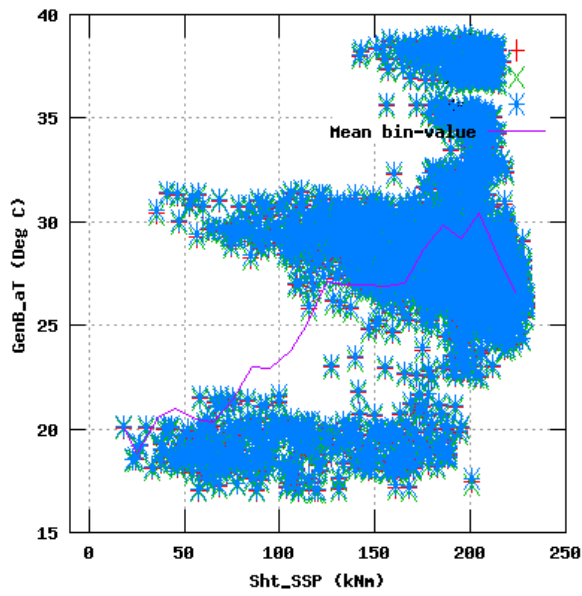
Figure 20a, Sensor 79: GeneratorB_aT versus mainshaft torsion 'Sht_SSP'
Input files: NTK500fastres.dat, stat_79.dat
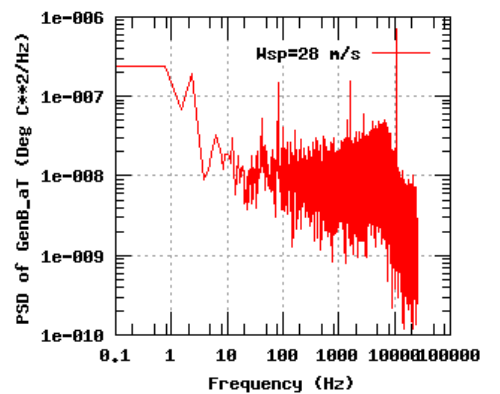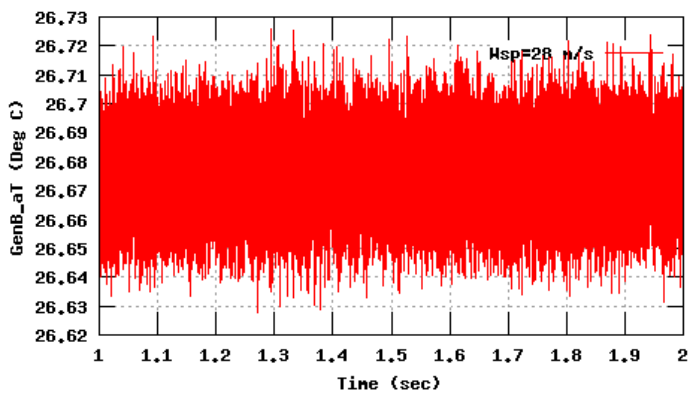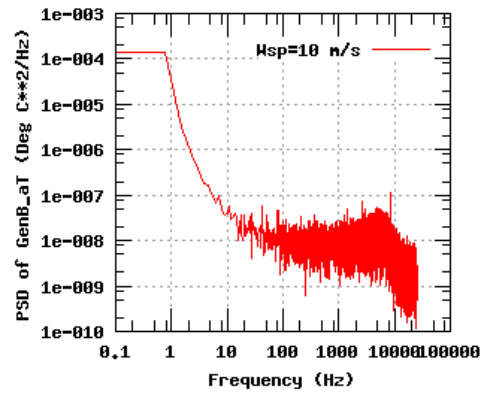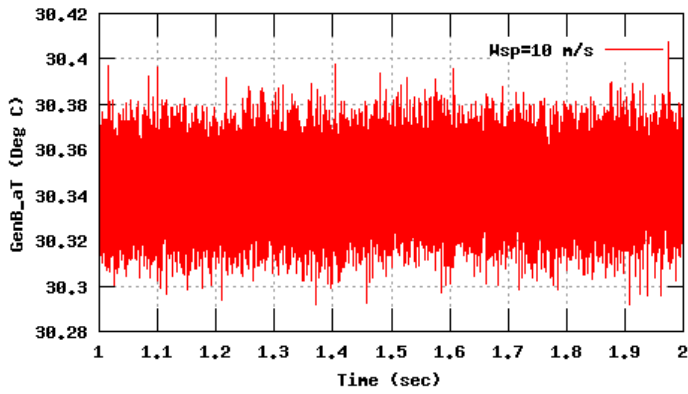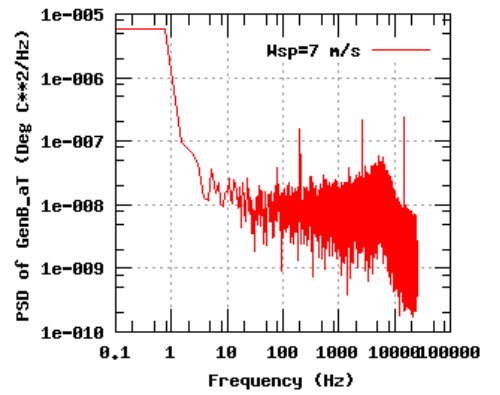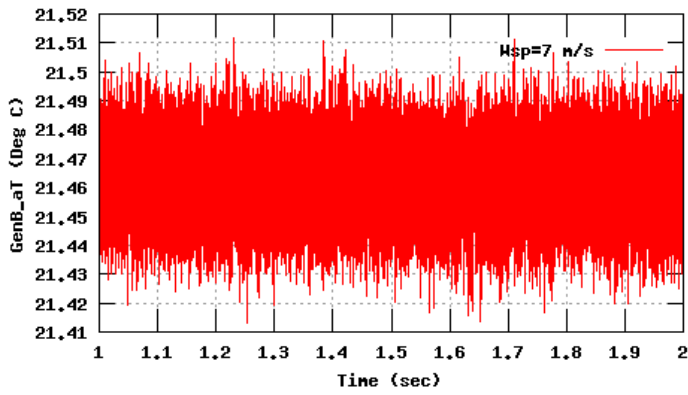
Figure 20b, Sensor 79: GeneratorB_aT versus time and frequency
Input files: m07.dat, m10.dat, m28.dat, m07.psd, m10.psd and m28.psd
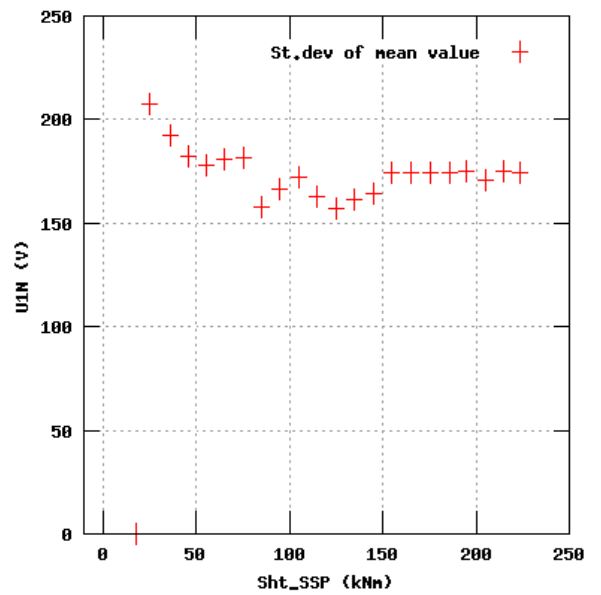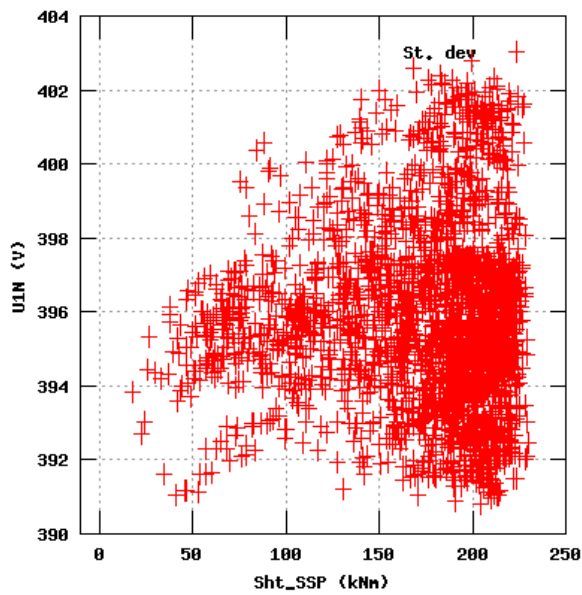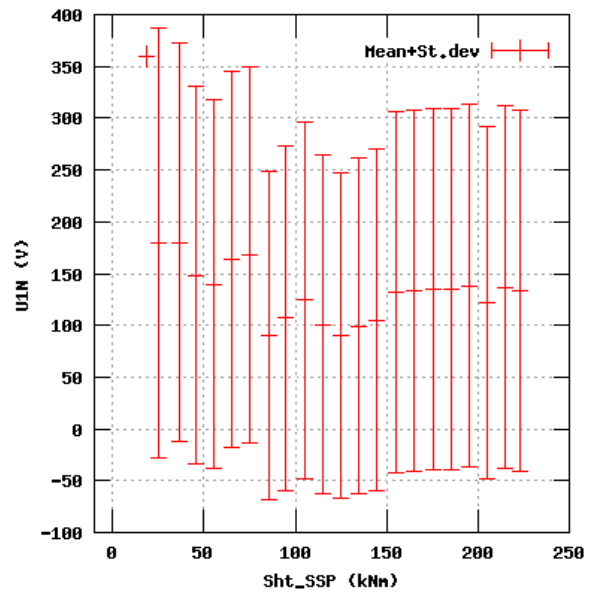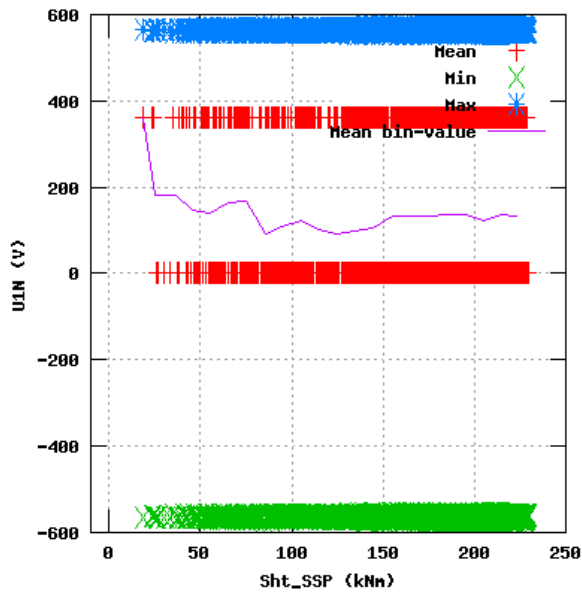
Figure 21a, Sensor 83: Phase Voltage versus mainshaft torsion 'Sht_SSP'
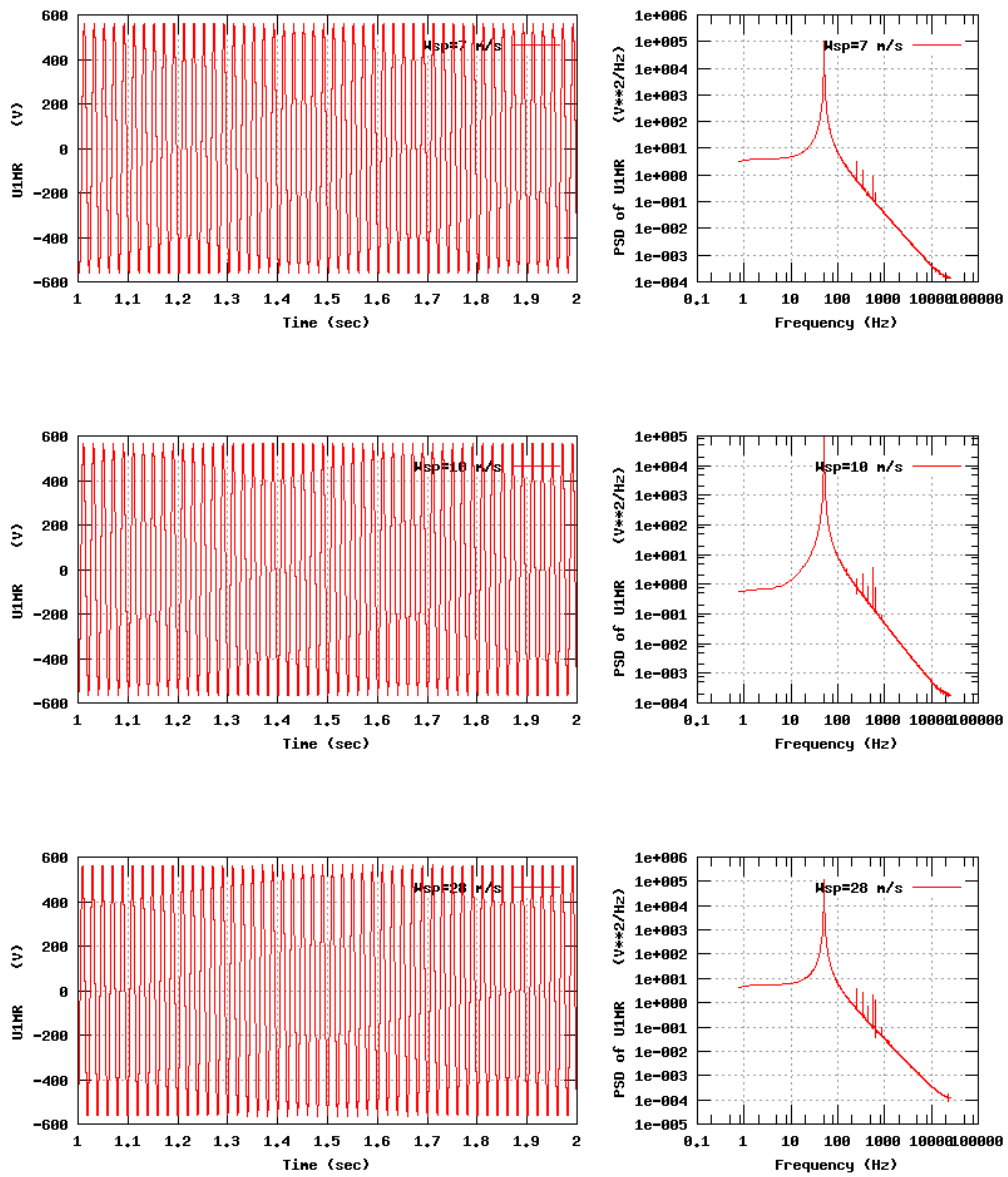Input files: NTK500fastres.dat, stat_83.dat
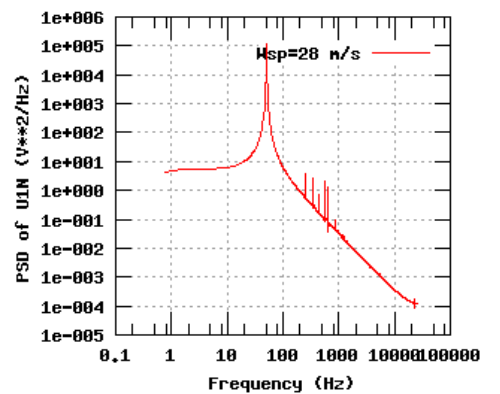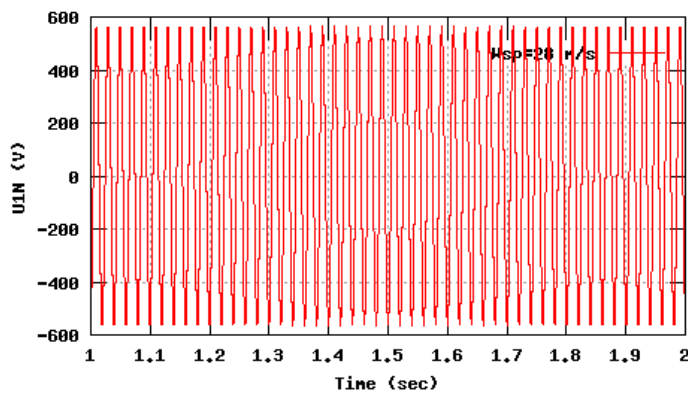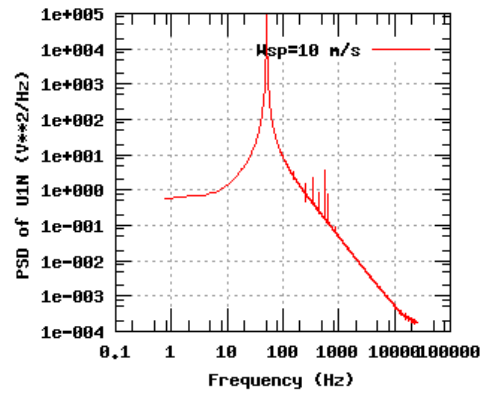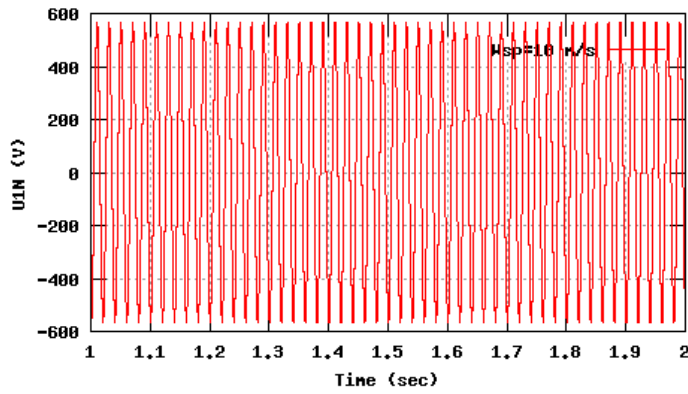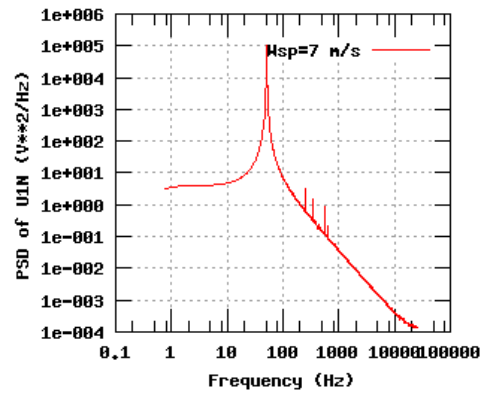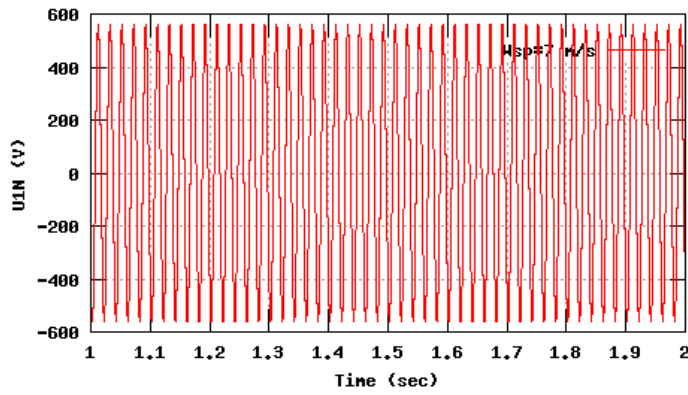
Figure 21b, Sensor 83: Phase Voltage versus time and frequency
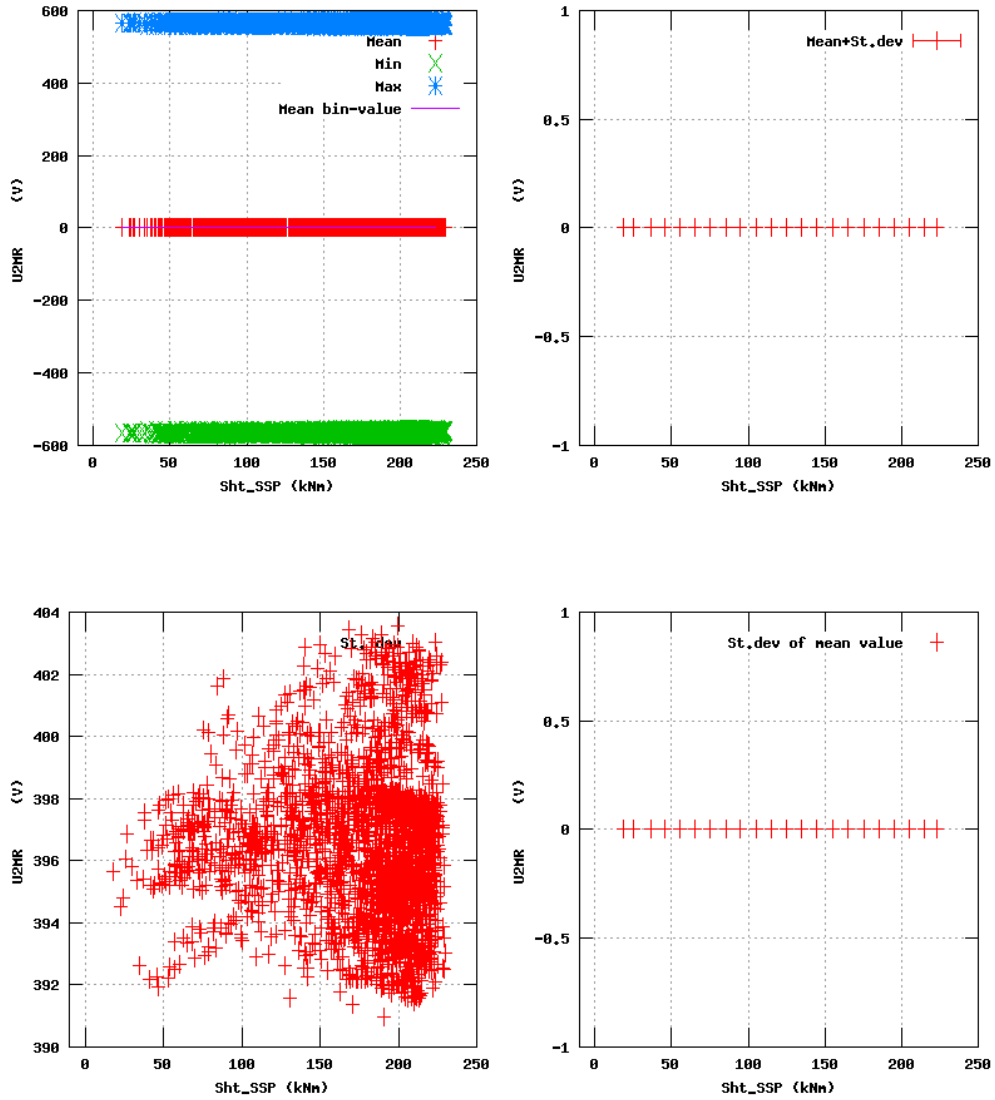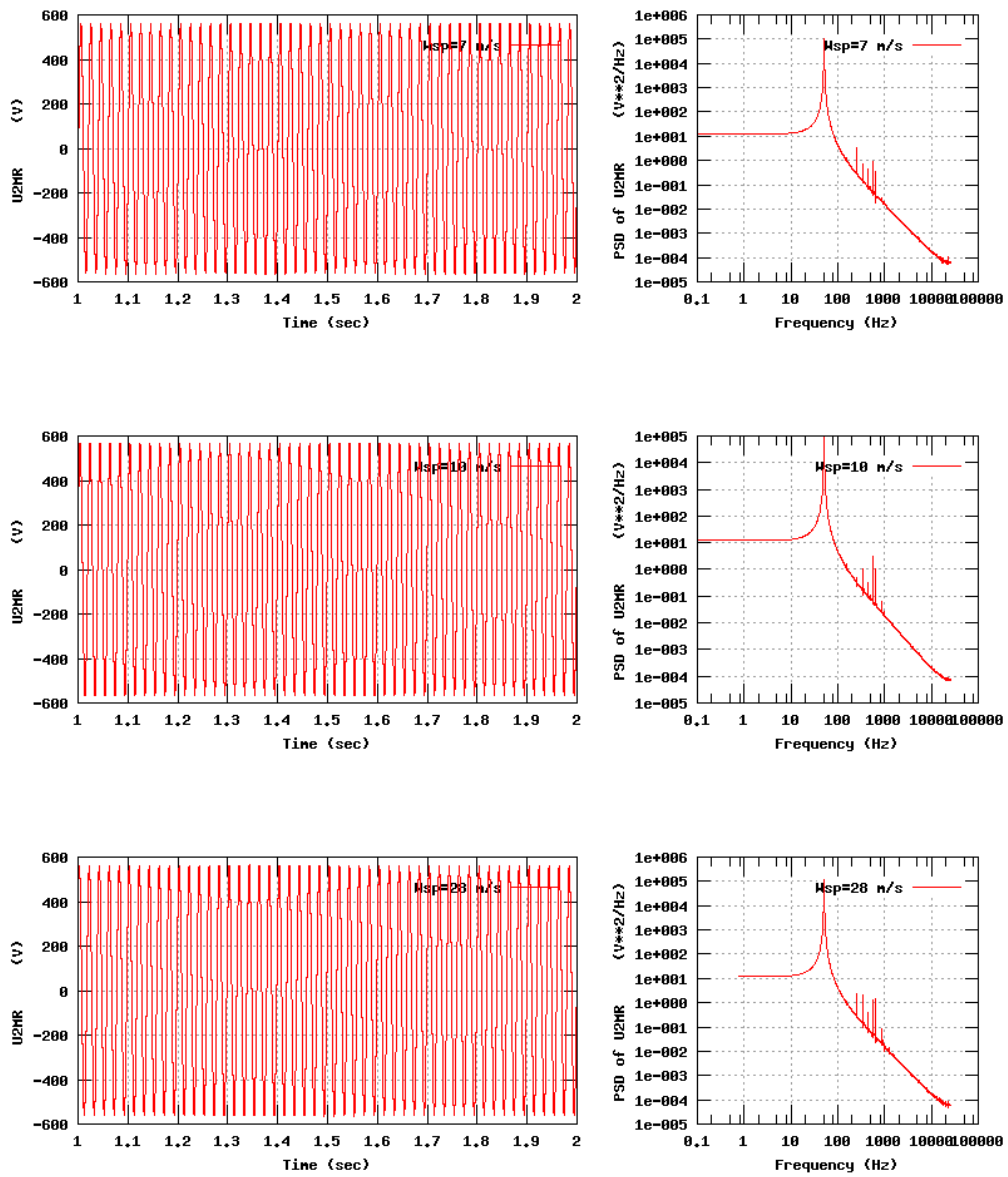Input files: m07.dat, m10.dat, m28.dat, m07.psd, m10.psd and m28.psd
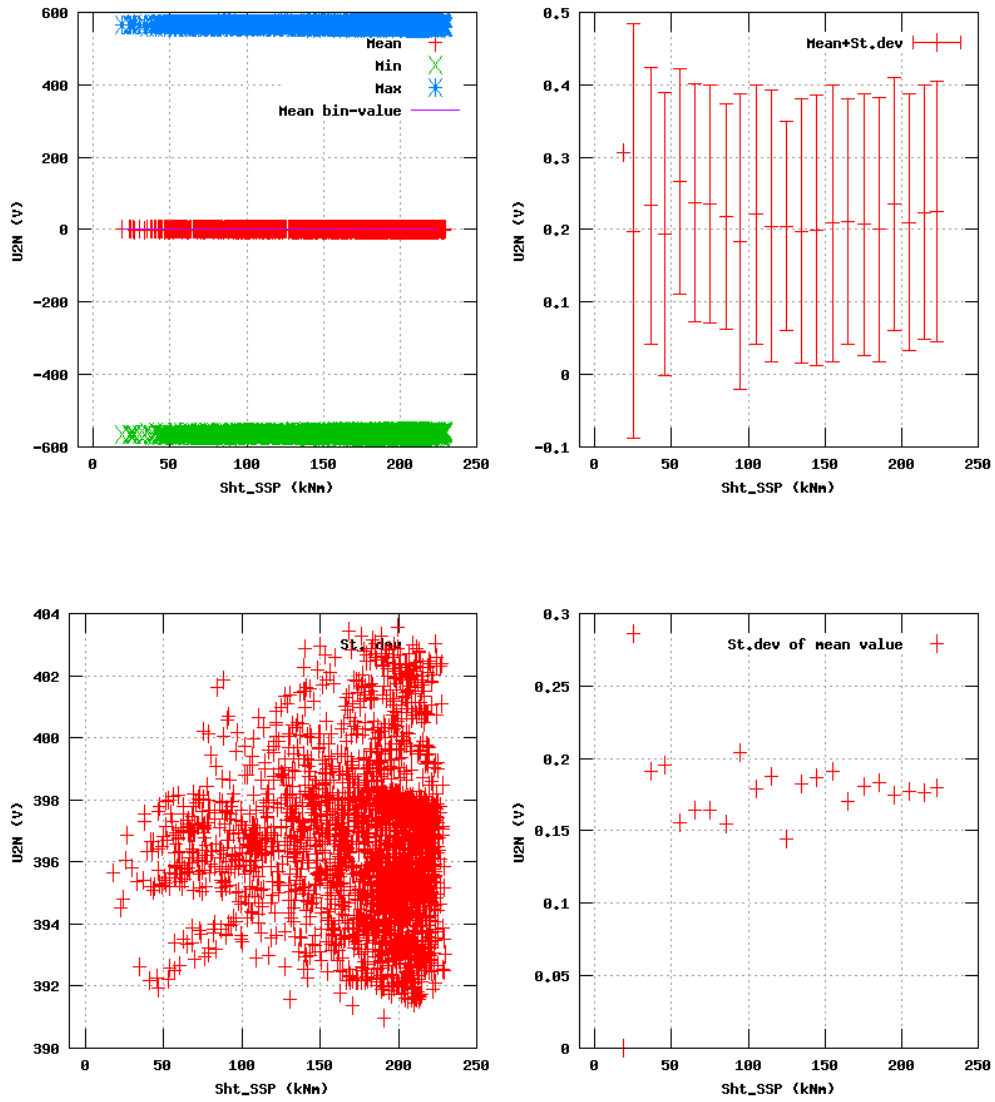
Figure 22a, Sensor 87: Phase Voltage versus mainshaft torsion 'Sht_SSP'
Input files: NTK500fastres.dat, stat_87.dat
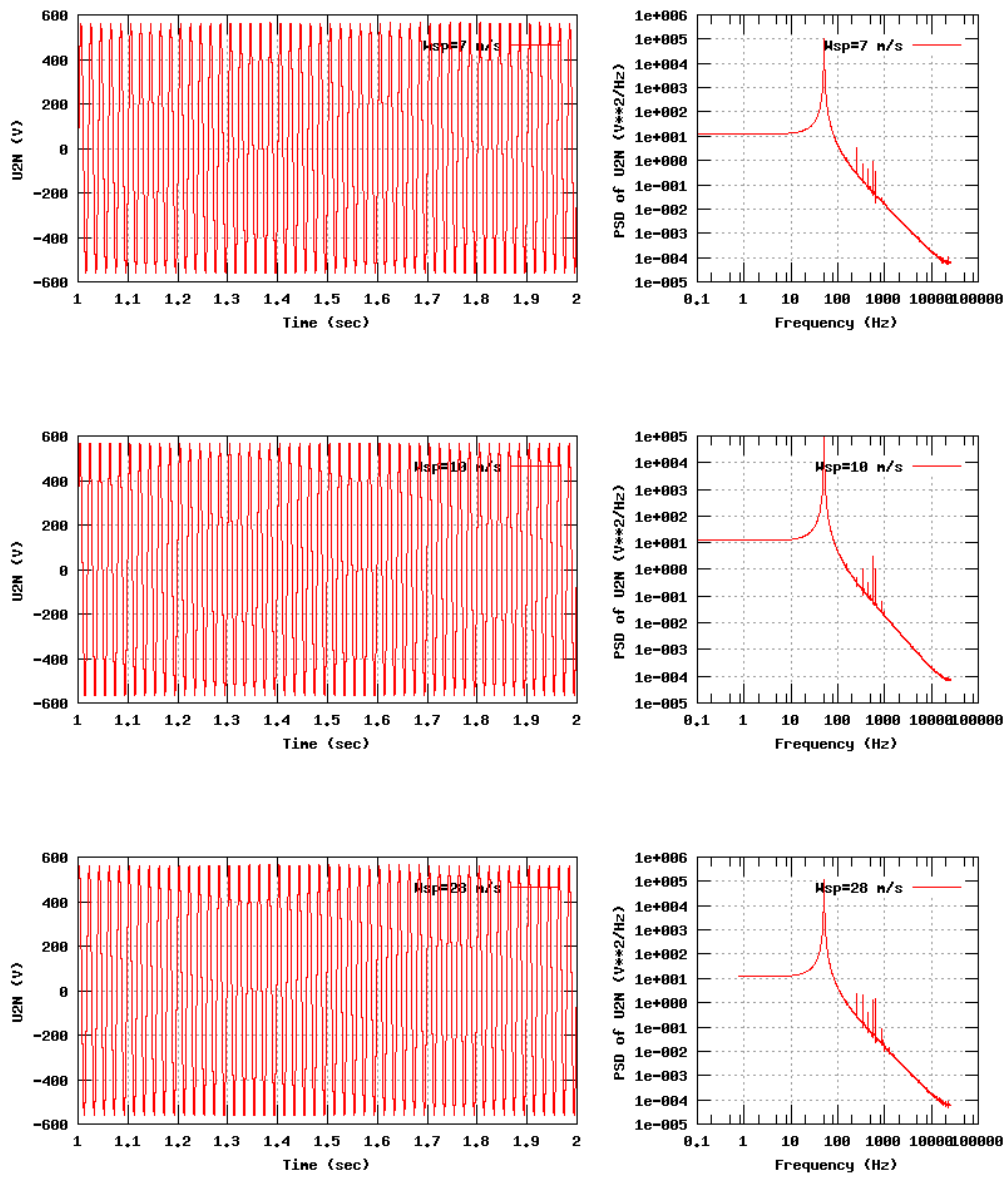
Figure 22b, Sensor 87: Phase Voltage versus time and frequency
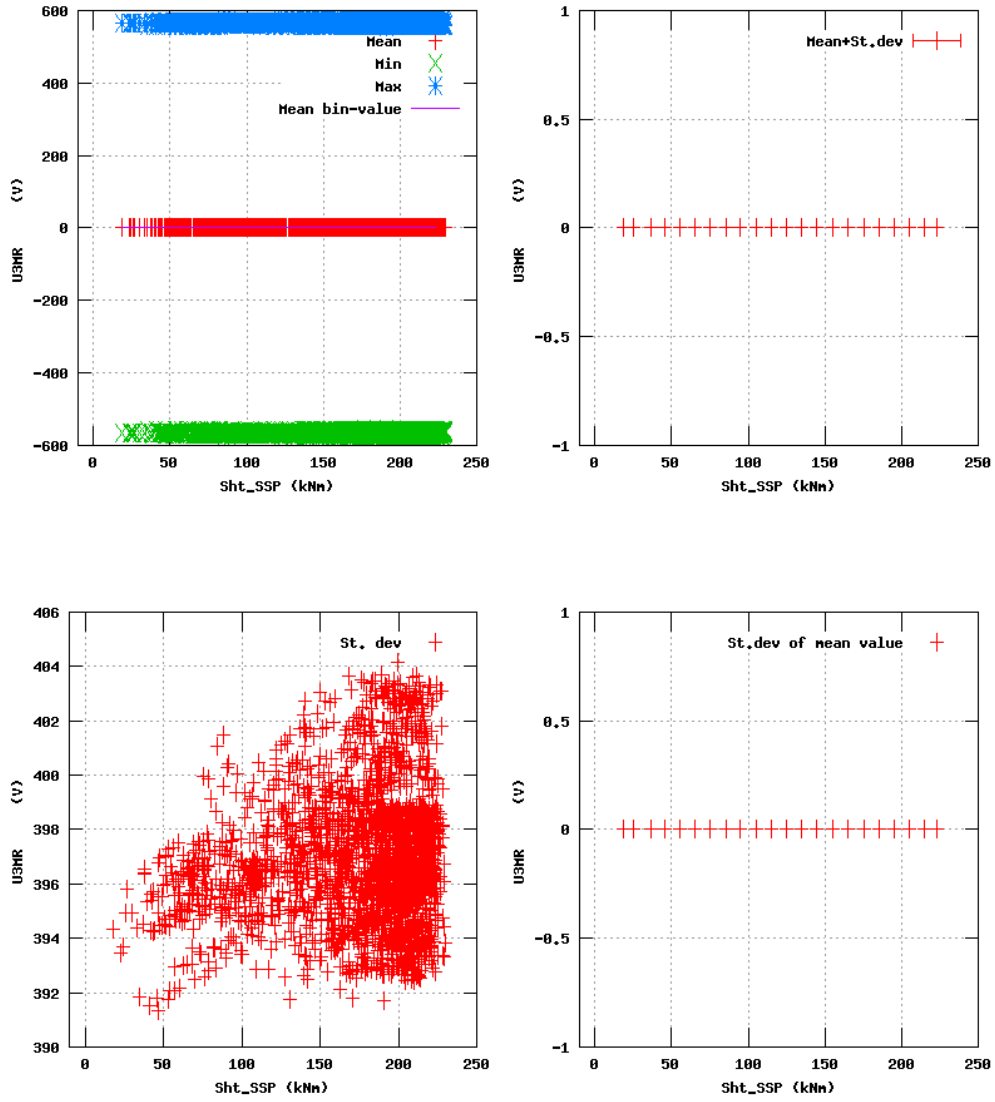Input files: m07.dat, m10.dat, m28.dat, m07.psd, m10.psd and m28.psd
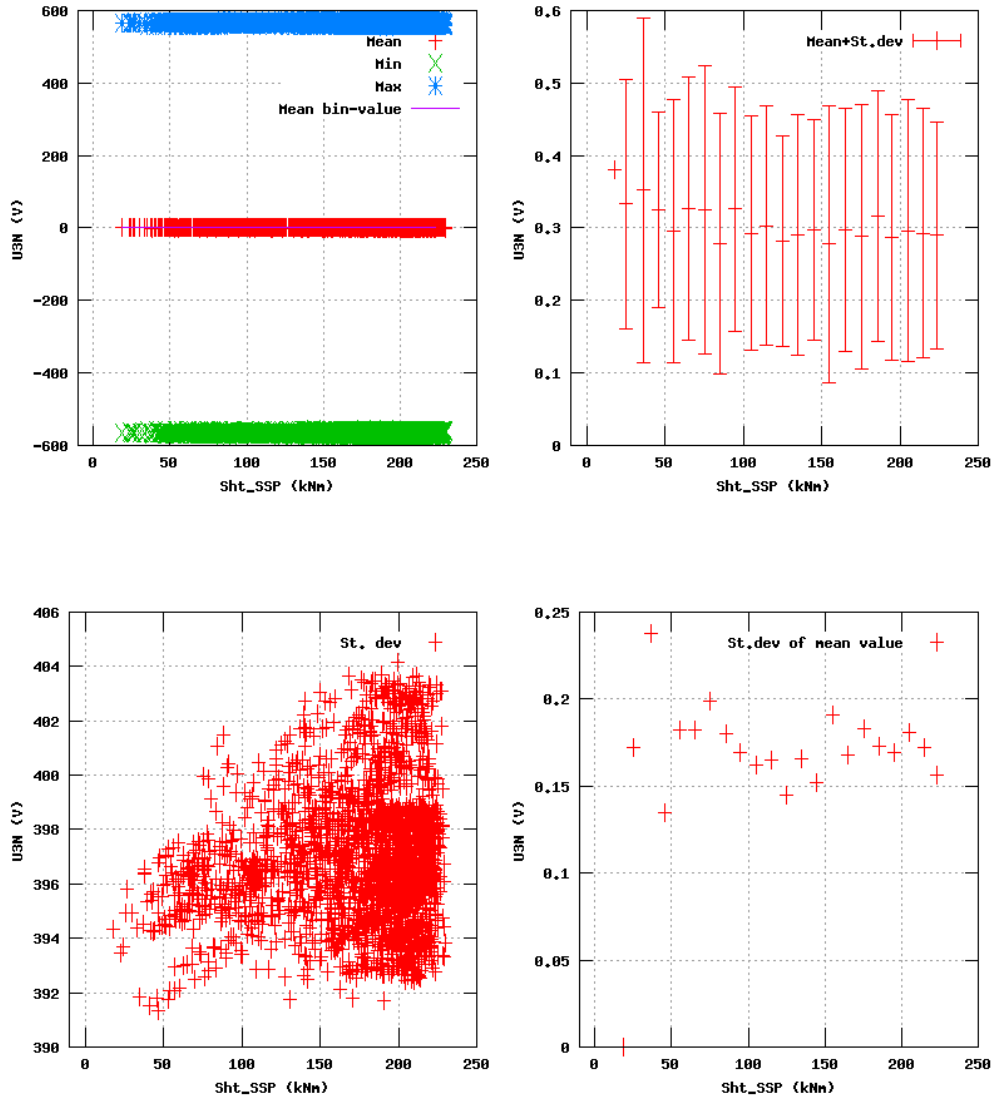
Figure 23a, Sensor 91: Phase Voltage versus mainshaft torsion 'Sht_SSP'
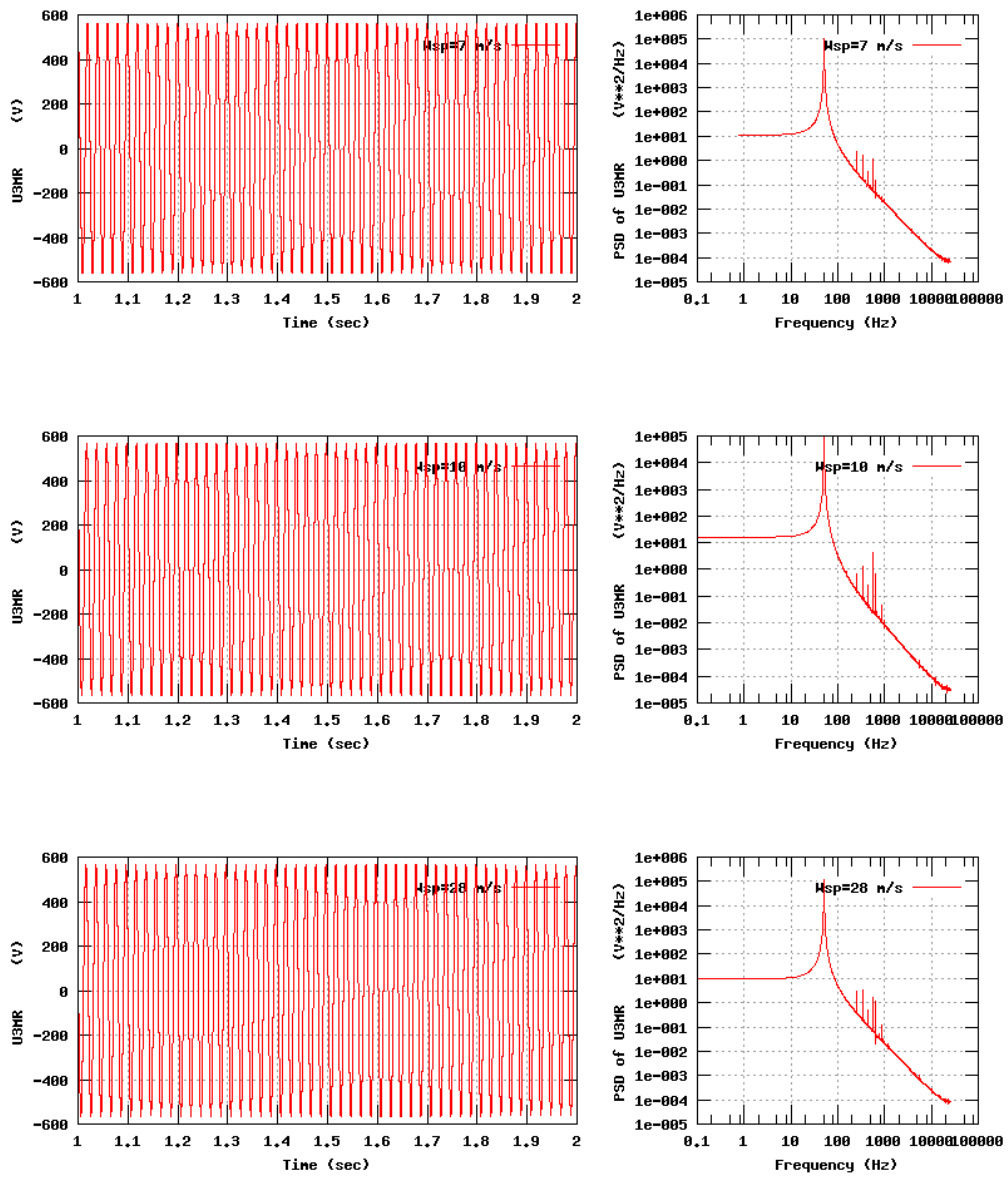Input files: NTK500fastres.dat, stat_91.dat
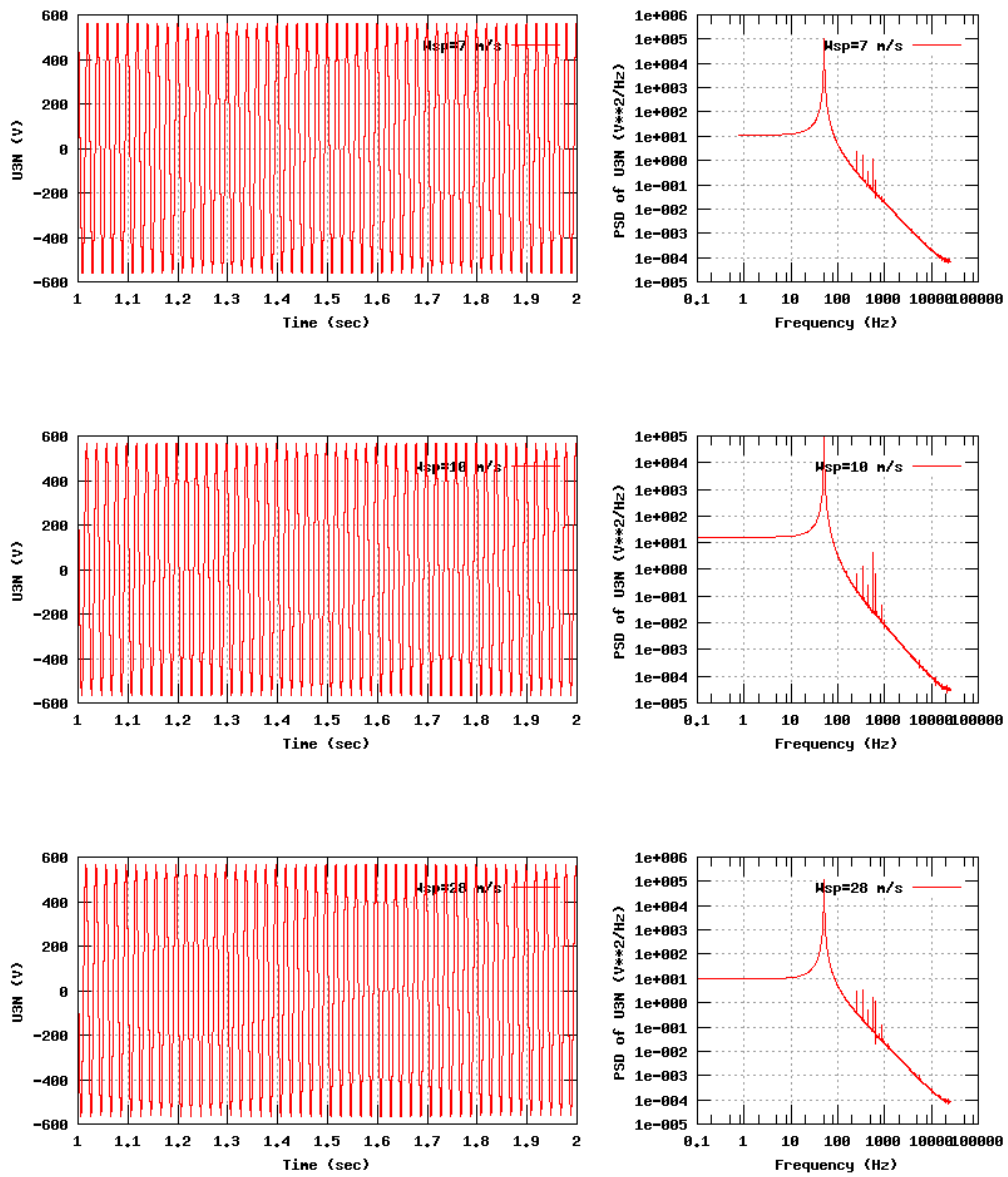
Figure 23b, Sensor 91: Phase Voltage versus time and frequency
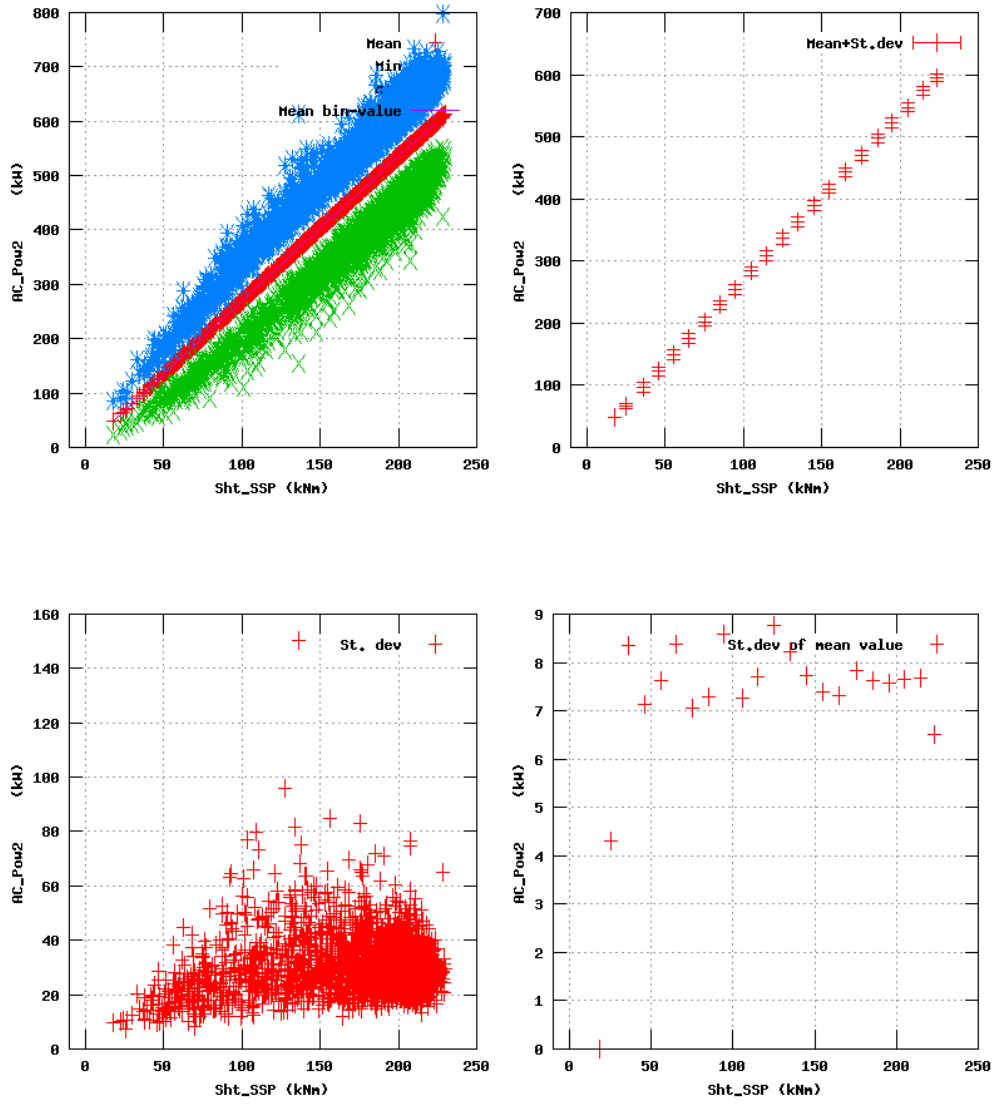Input files: m07.dat, m10.dat, m28.dat, m07.psd, m10.psd and m28.psd
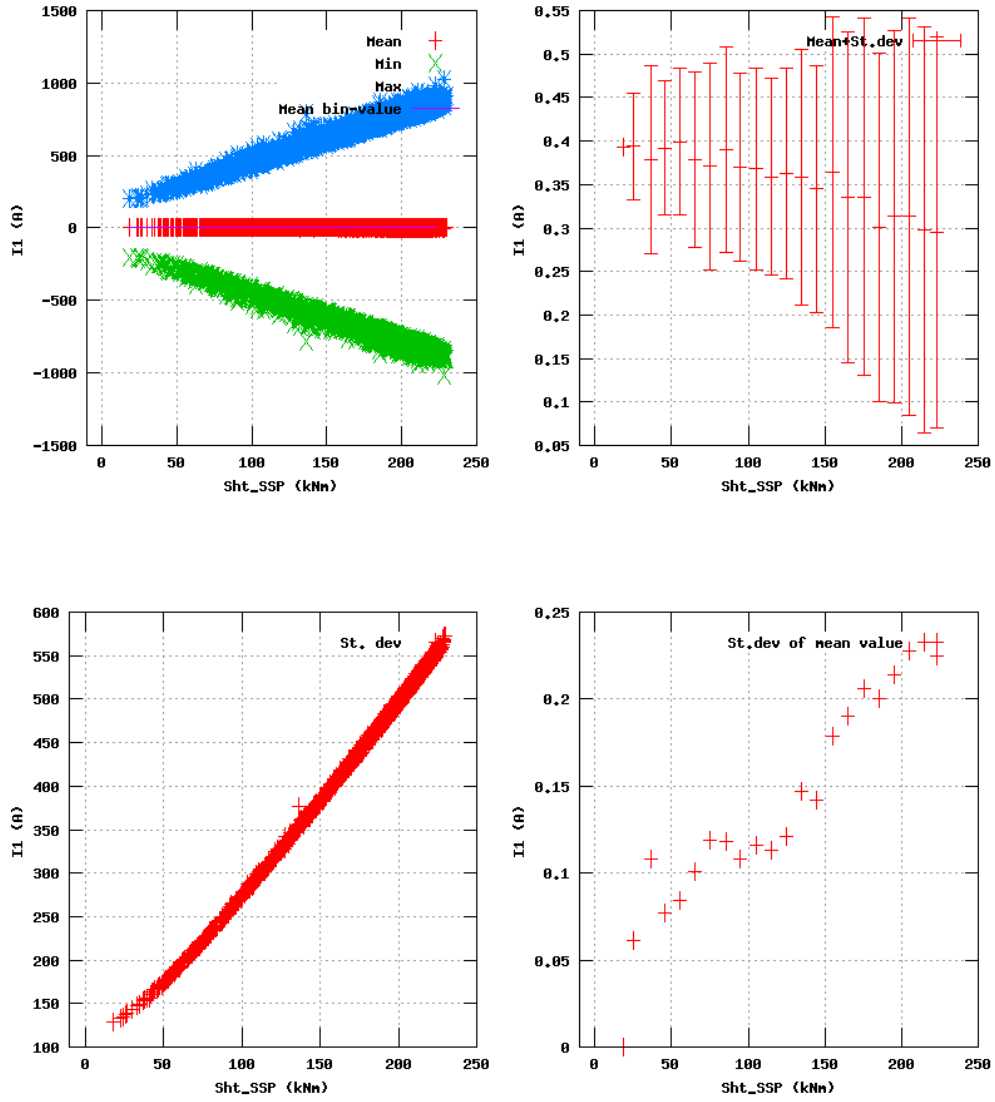
Figure 24a, Sensor 95: Phase Current versus mainshaft torsion 'Sht_SSP'
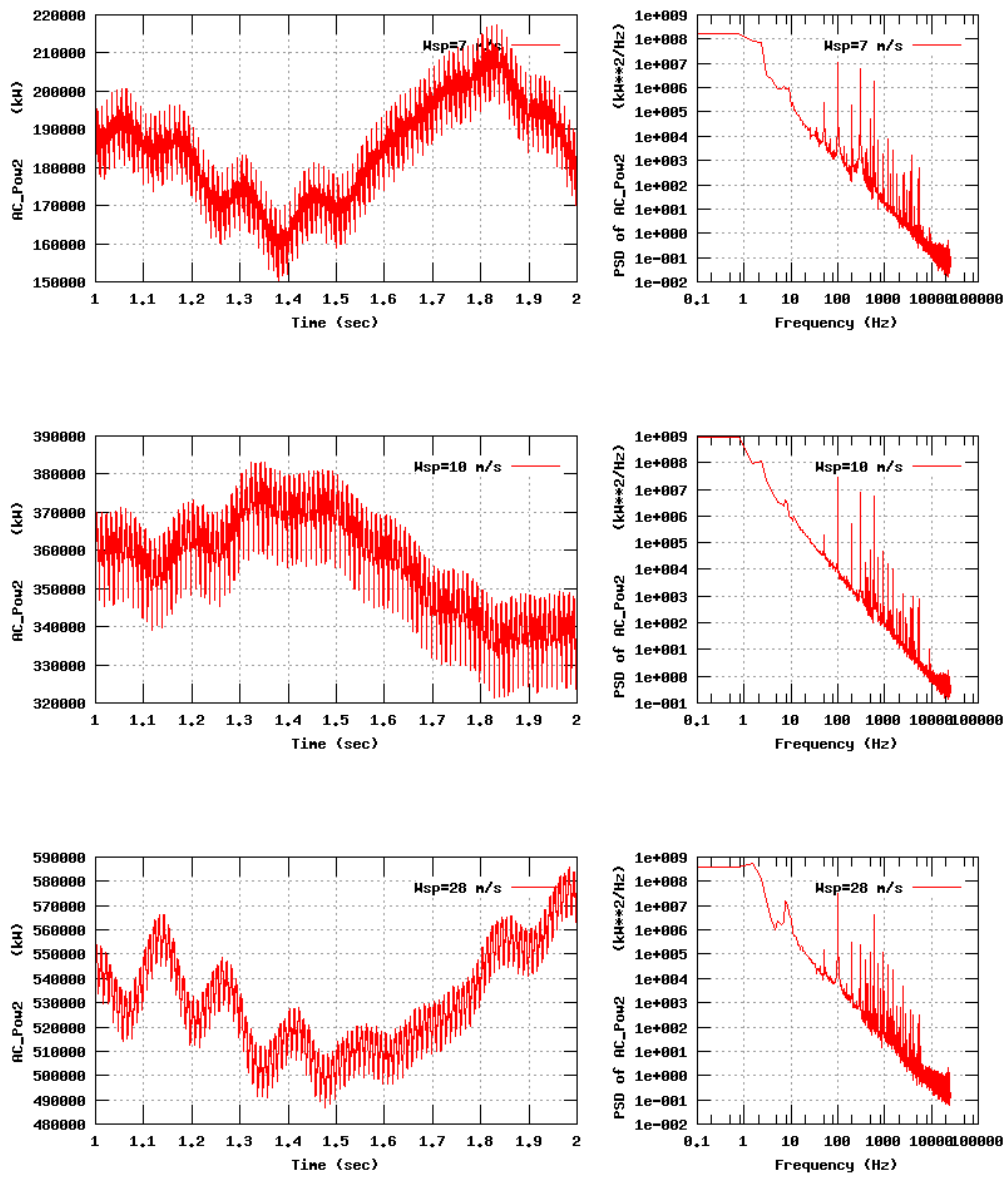Input files: NTK500fastres.dat, stat_95.dat
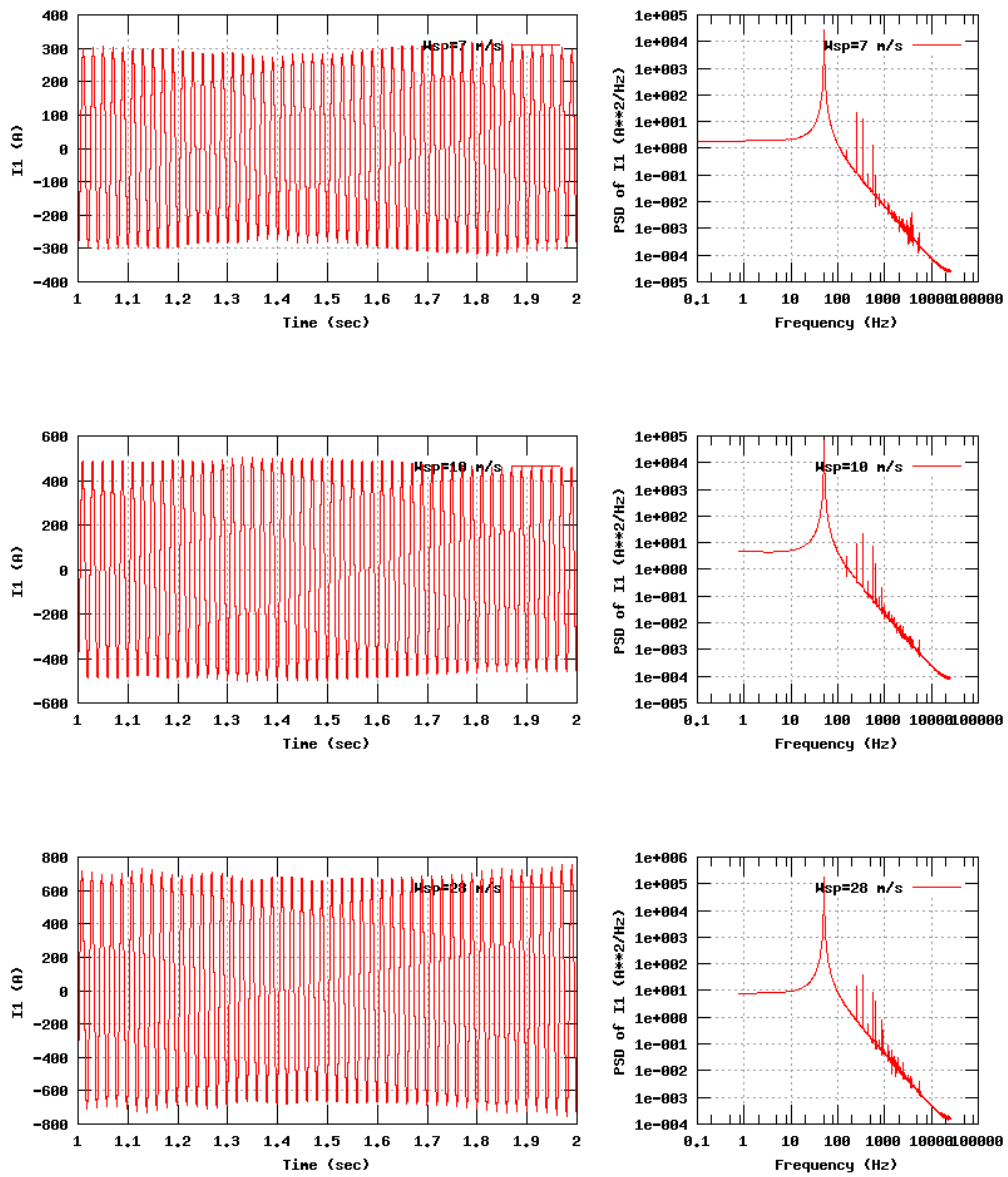
Figure 24b, Sensor 95: Phase Current versus time and frequency
Input files: m07.dat, m10.dat, m28.dat, m07.psd, m10.psd and m28.psd
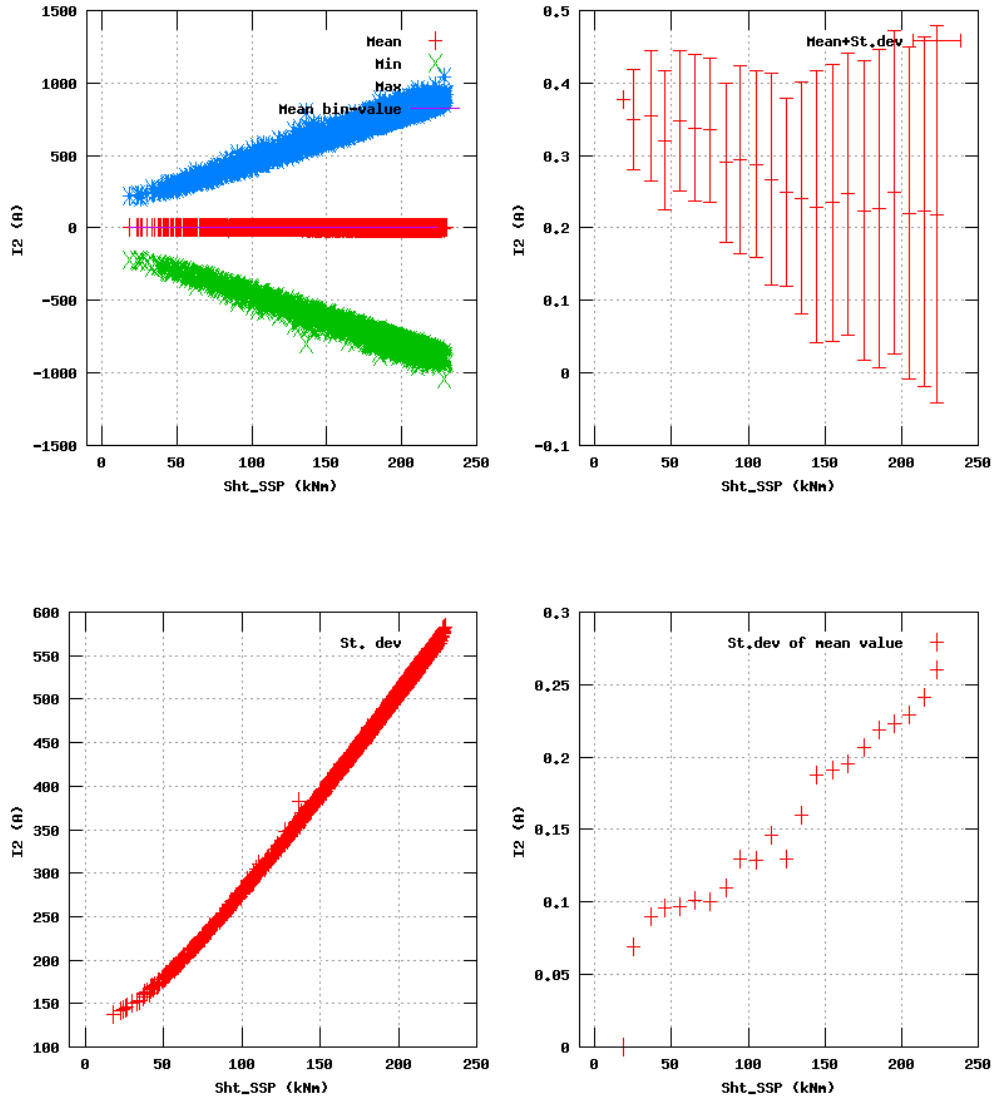
Figure 25a, Sensor 99: Phase Current versus mainshaft torsion 'Sht_SSP'
Input files: NTK500fastres.dat, stat_99.dat
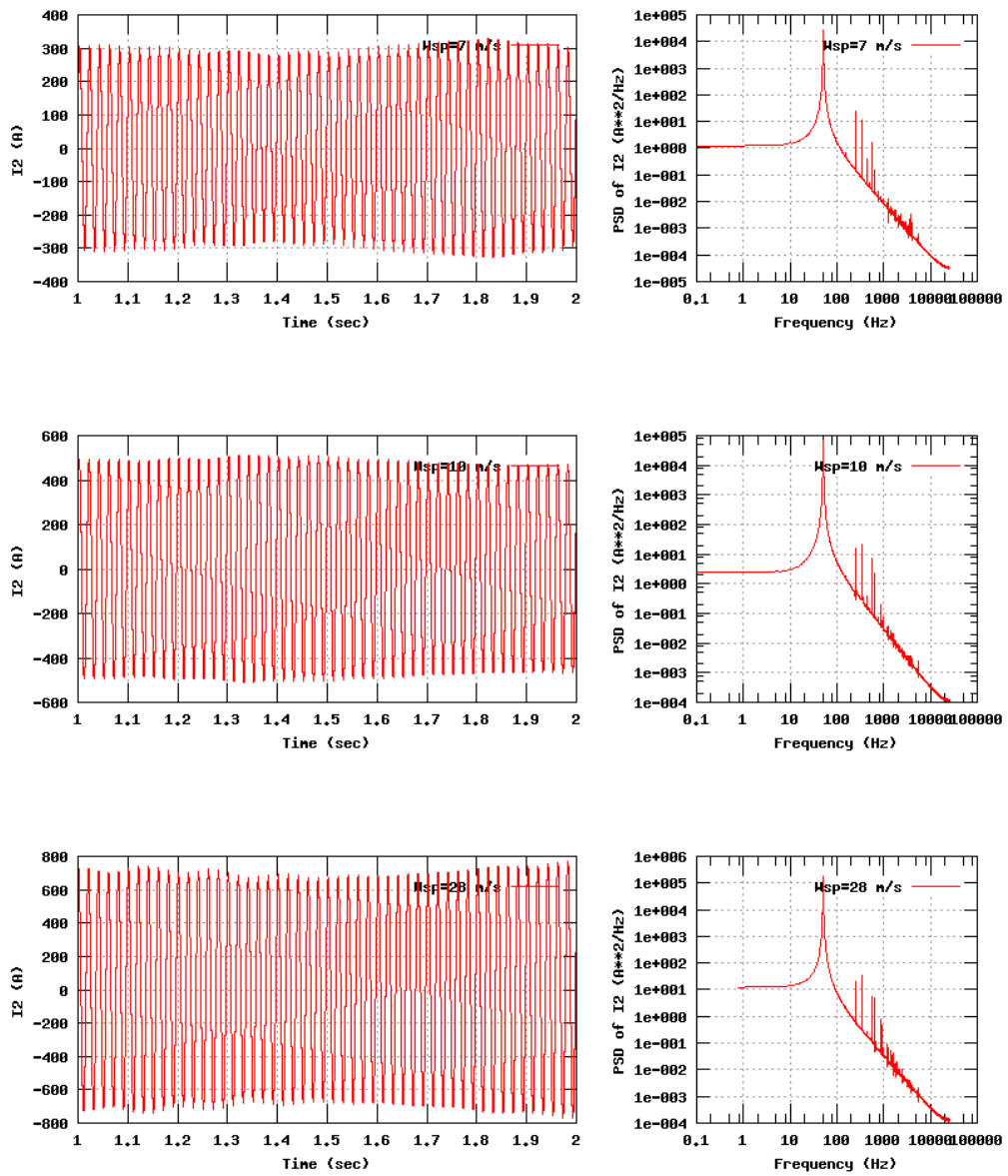
Figure 25b, Sensor 99: Phase Current versus time and frequency
Input files: m07.dat, m10.dat, m28.dat, m07.psd, m10.psd and m28.psd
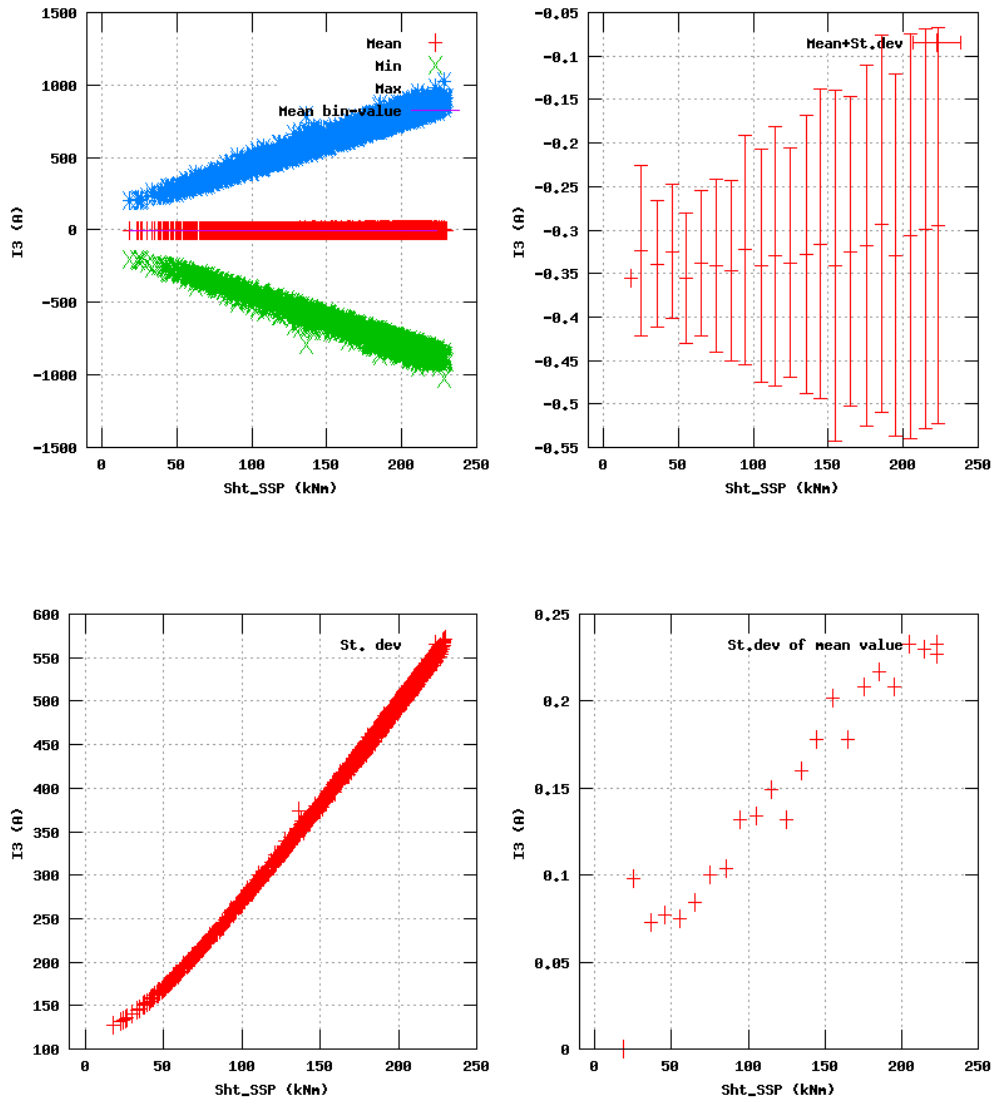
Figure 26a, Sensor 103: Phase Current versus mainshaft torsion 'Sht_SSP'
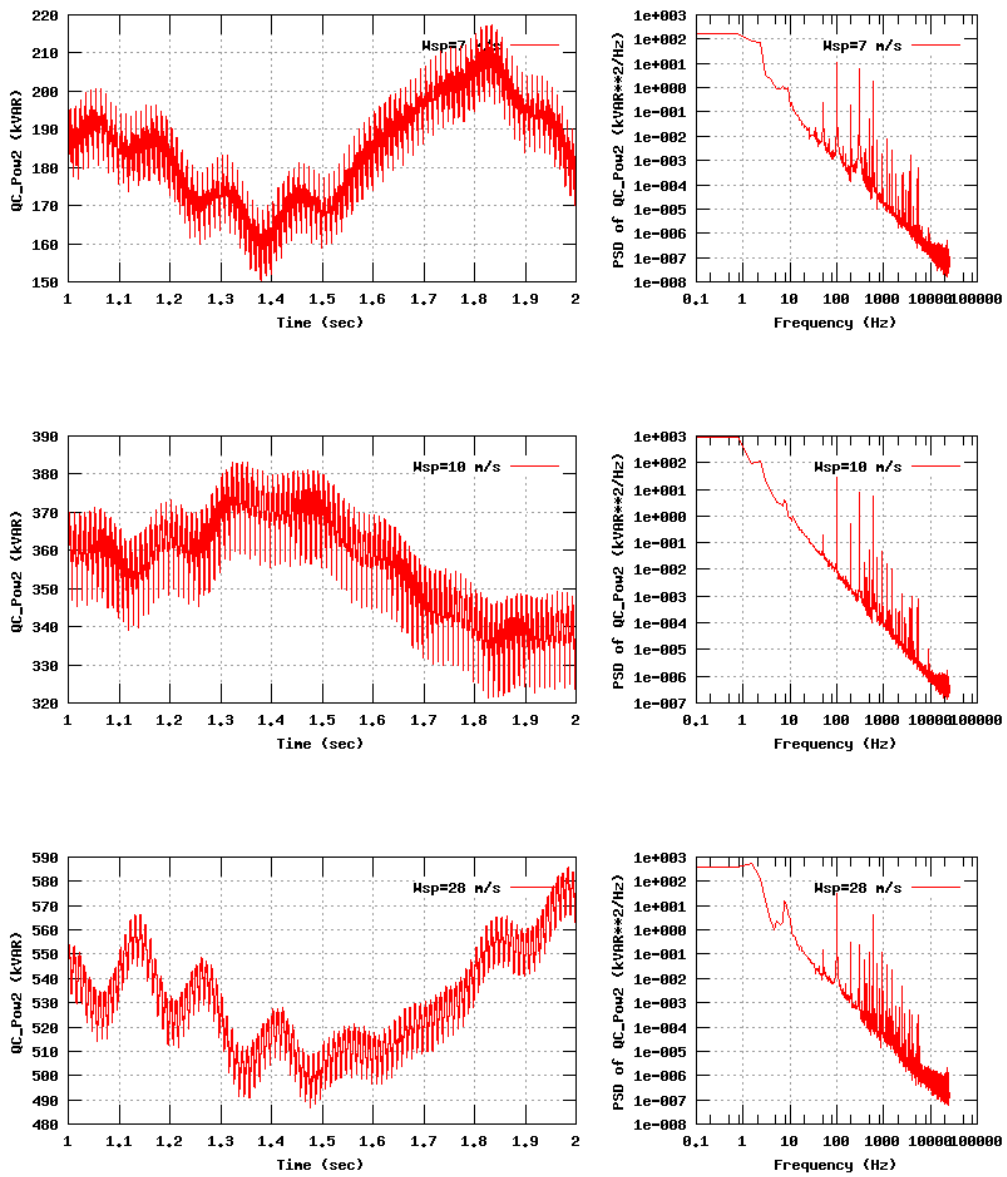Input files: NTK500fastres.dat, stat_103.dat
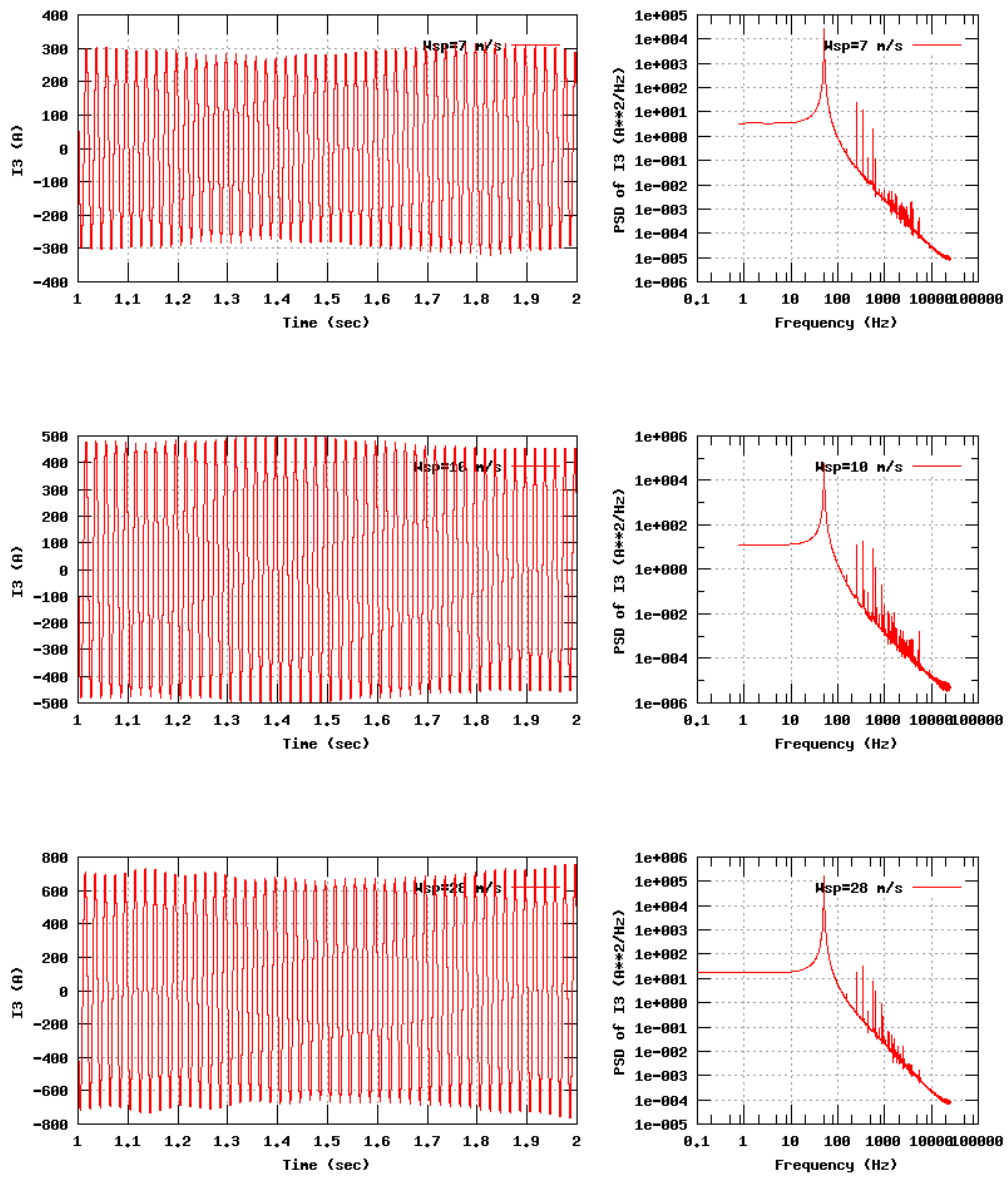
Figure 26b, Sensor 103: Phase Current versus time and frequency
Input files: m07.dat, m10.dat, m28.dat, m07.psd, m10.psd and m28.psd
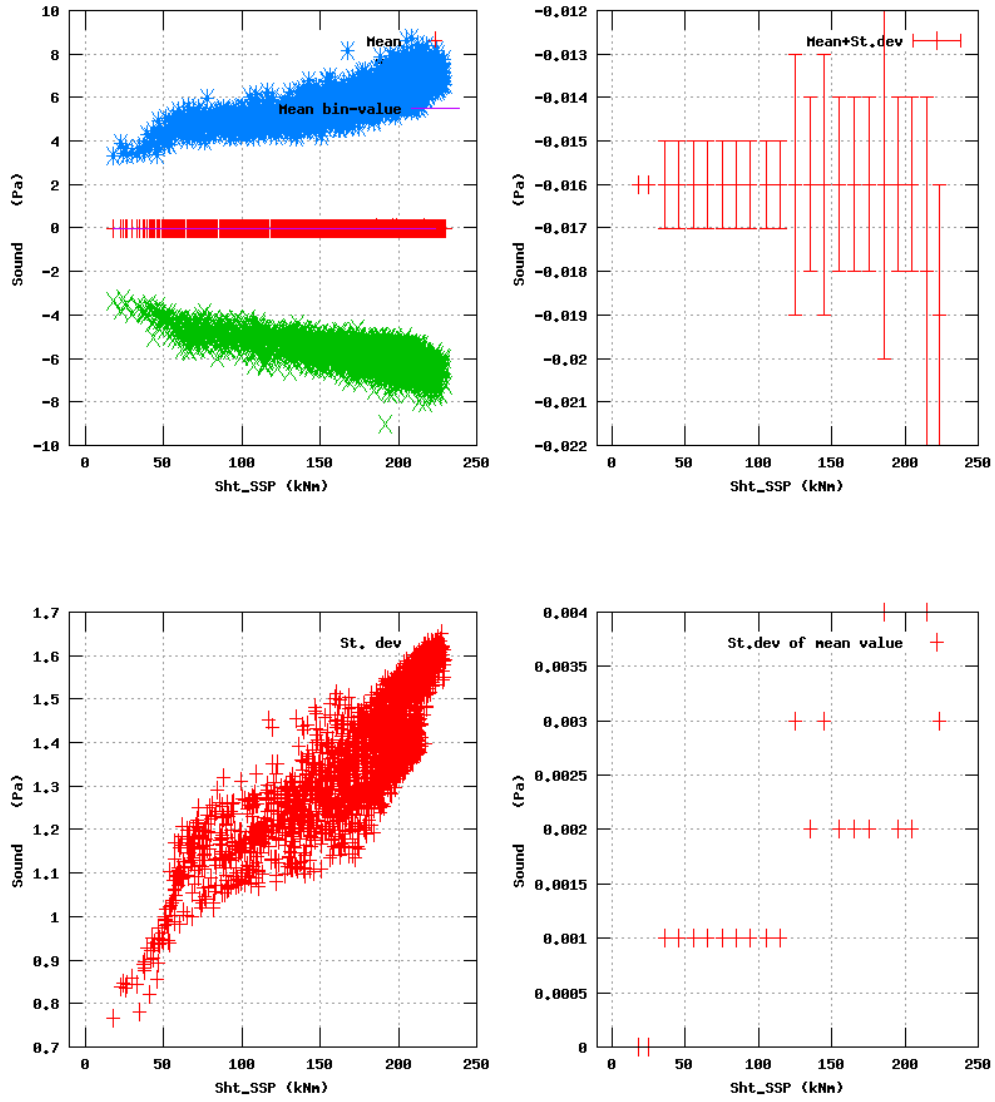
Figure 27a, Sensor 107: SoundPressure versus mainshaft torsion 'Sht_SSP'
Input files: NTK500fastres.dat, stat_107.dat
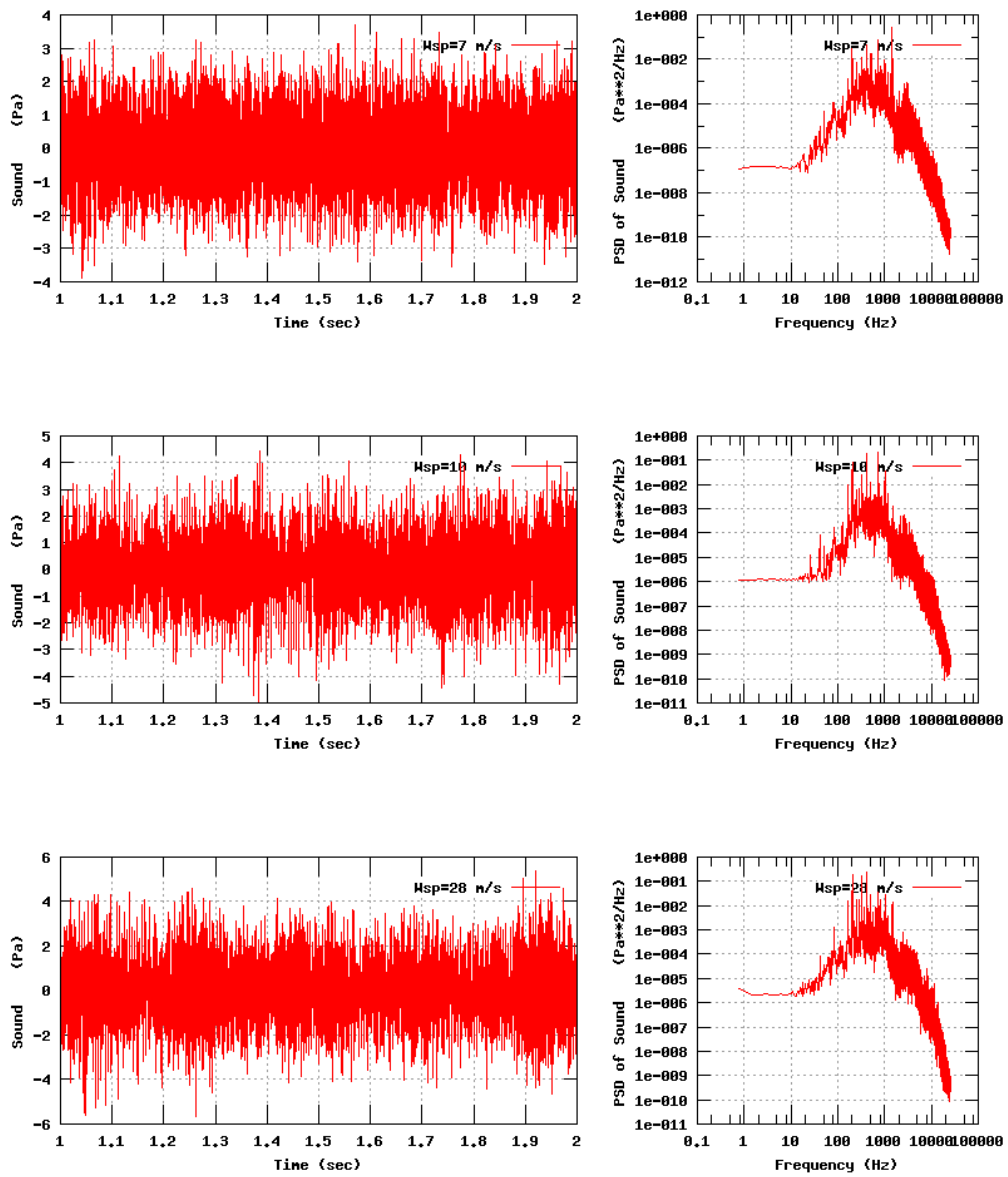
Figure 27b, Sensor 107: SoundPressure versus time and frequency
Input files: m07.dat, m10.dat, m28.dat, m07.psd, m10.psd and m28.psd
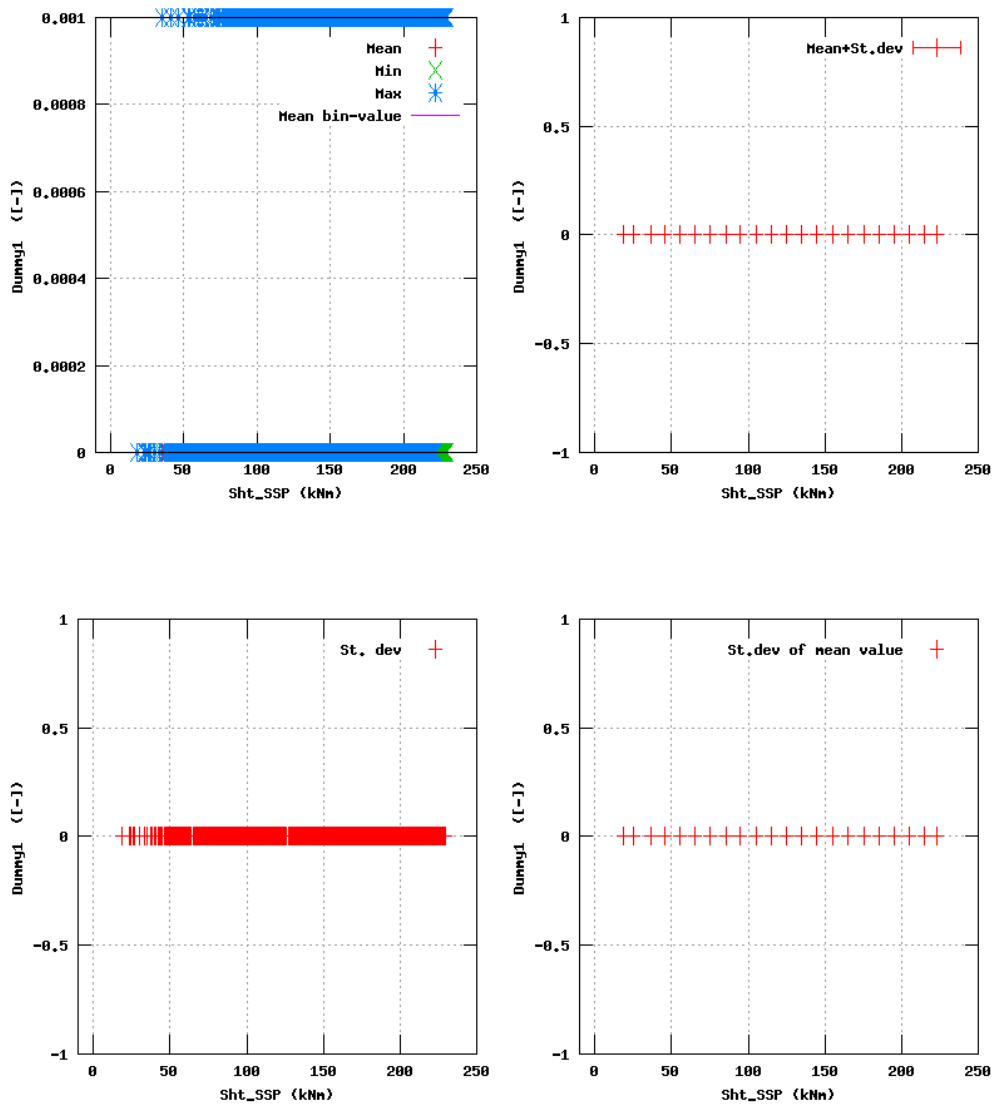
Figure 28a, Sensor 111: Dummy versus mainshaft torsion 'Sht_SSP'
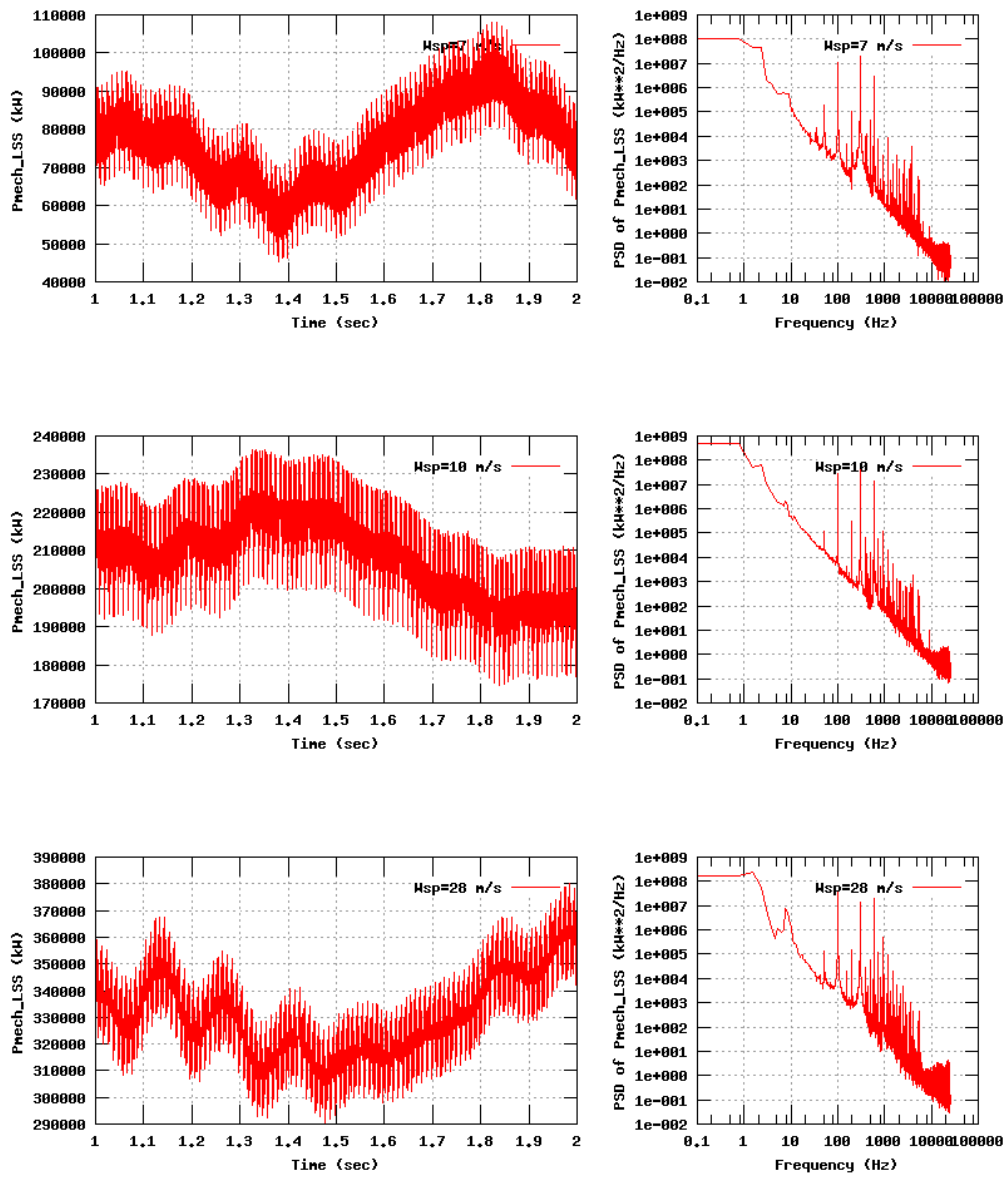Input files: NTK500fastres.dat, stat_111.dat
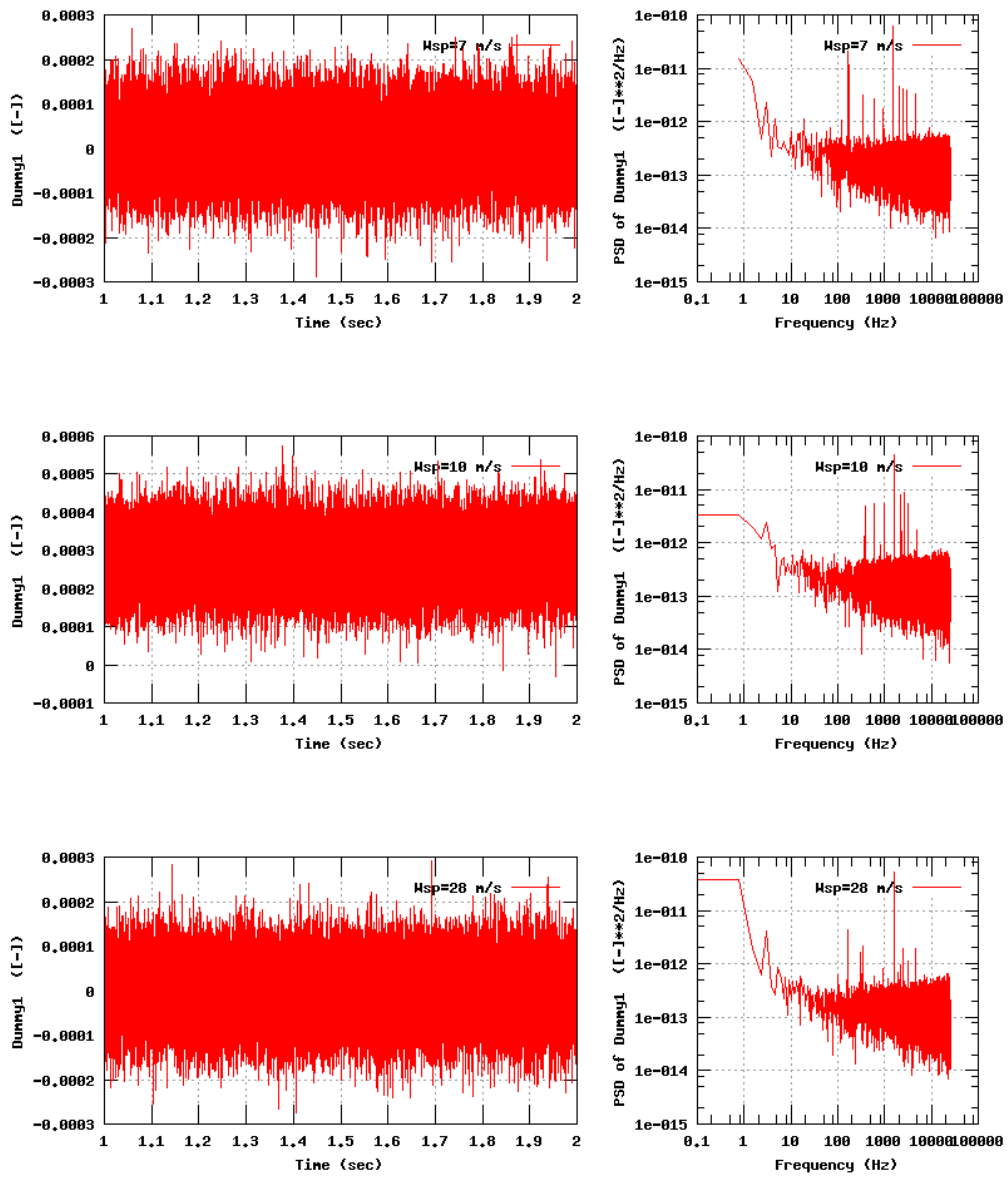
Figure 28b, Sensor 111: Dummy versus time and frequency
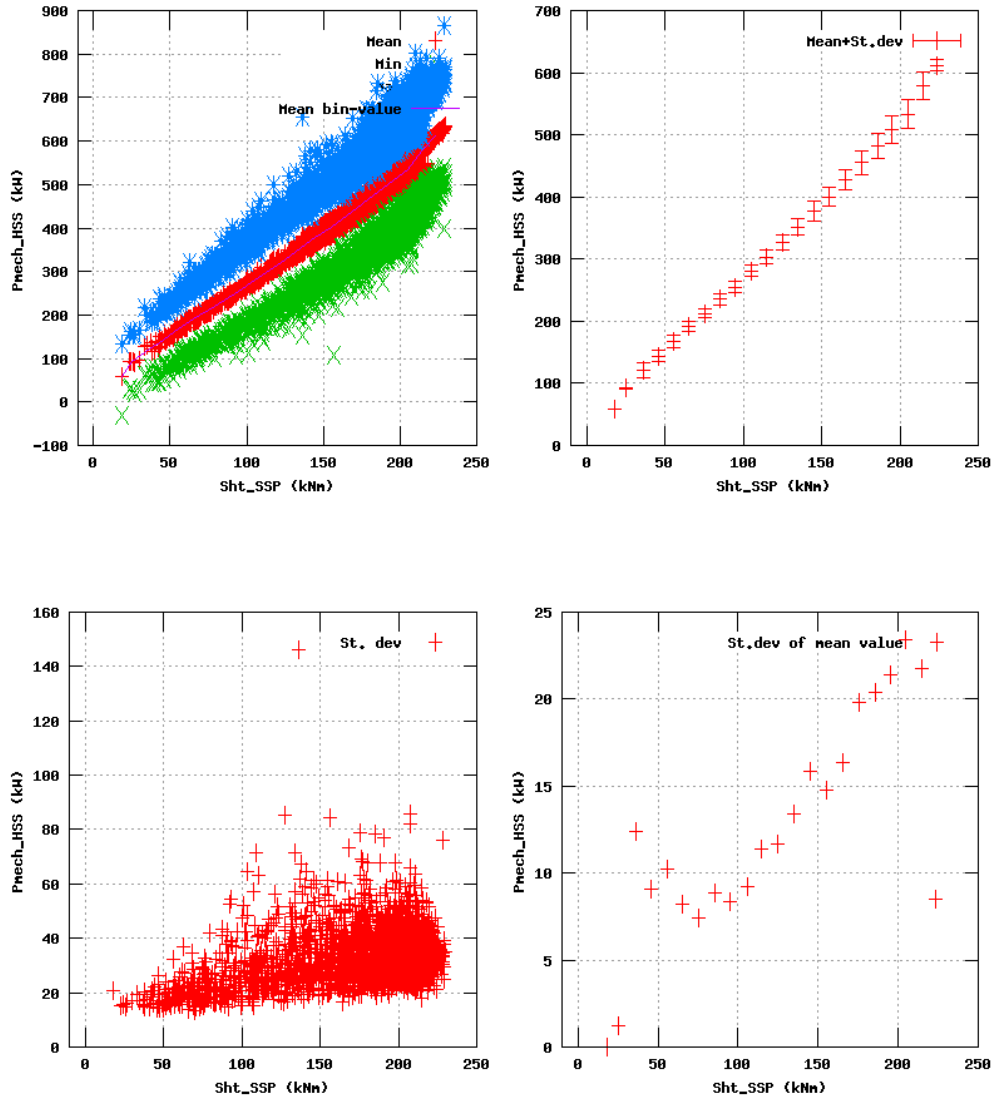Input files: m07.dat, m10.dat, m28.dat, m07.psd, m10.psd and m28.psd
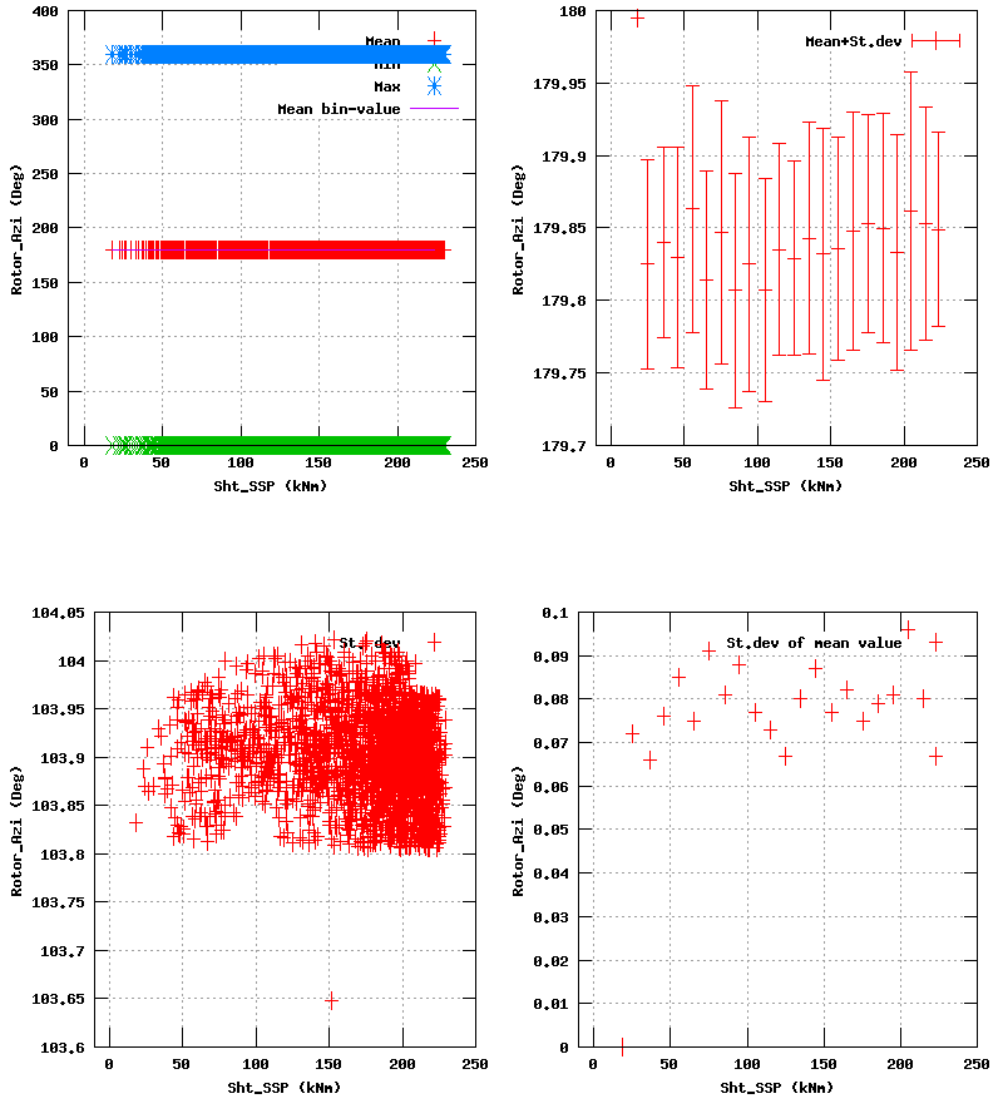
Figure 29a, Sensor 115: Angular_position versus mainshaft torsion 'Sht_SSP'
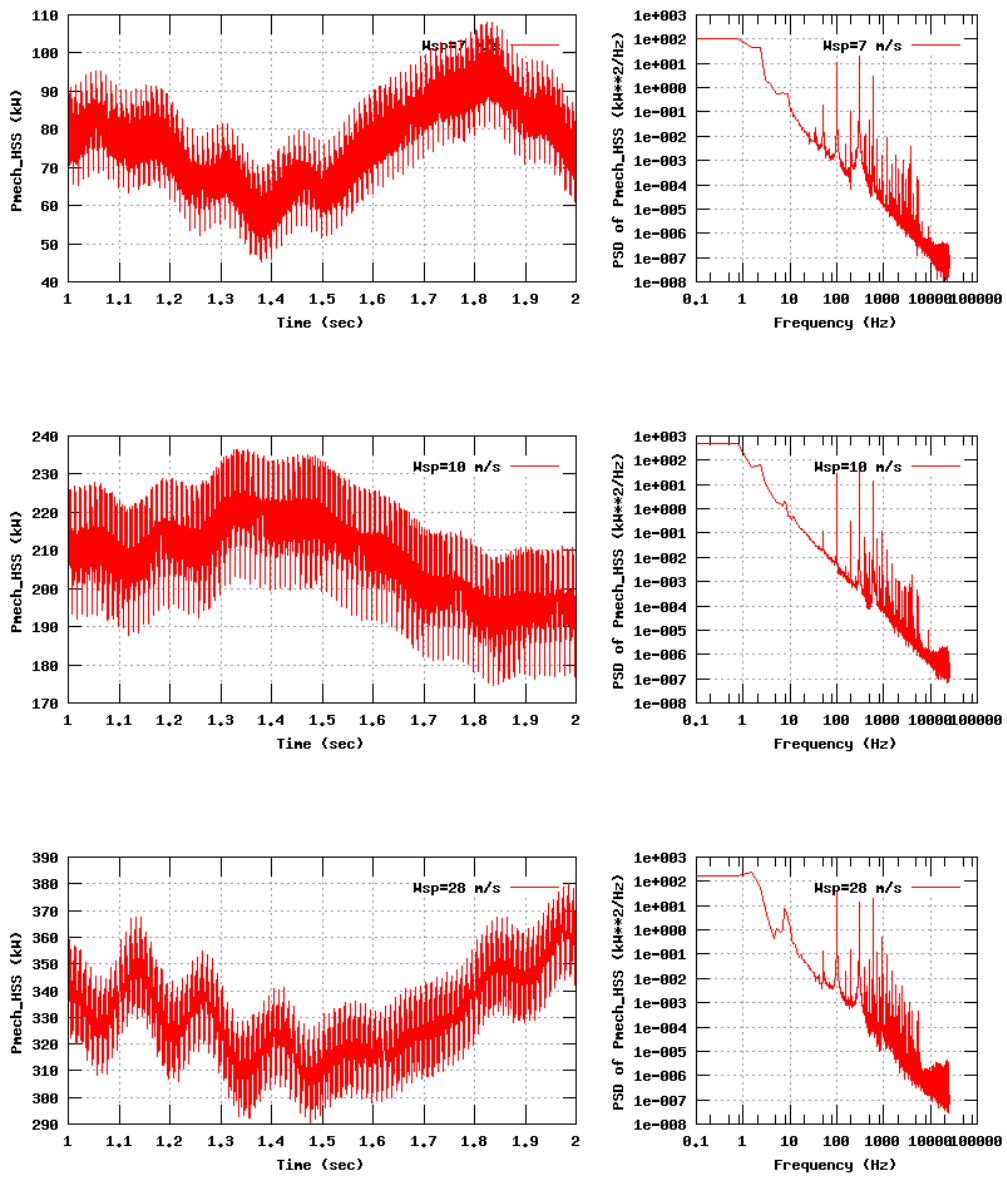Input files: NTK500fastres.dat, stat_115.dat

Figure 29b, Sensor 115: Angular_position versus time and frequency
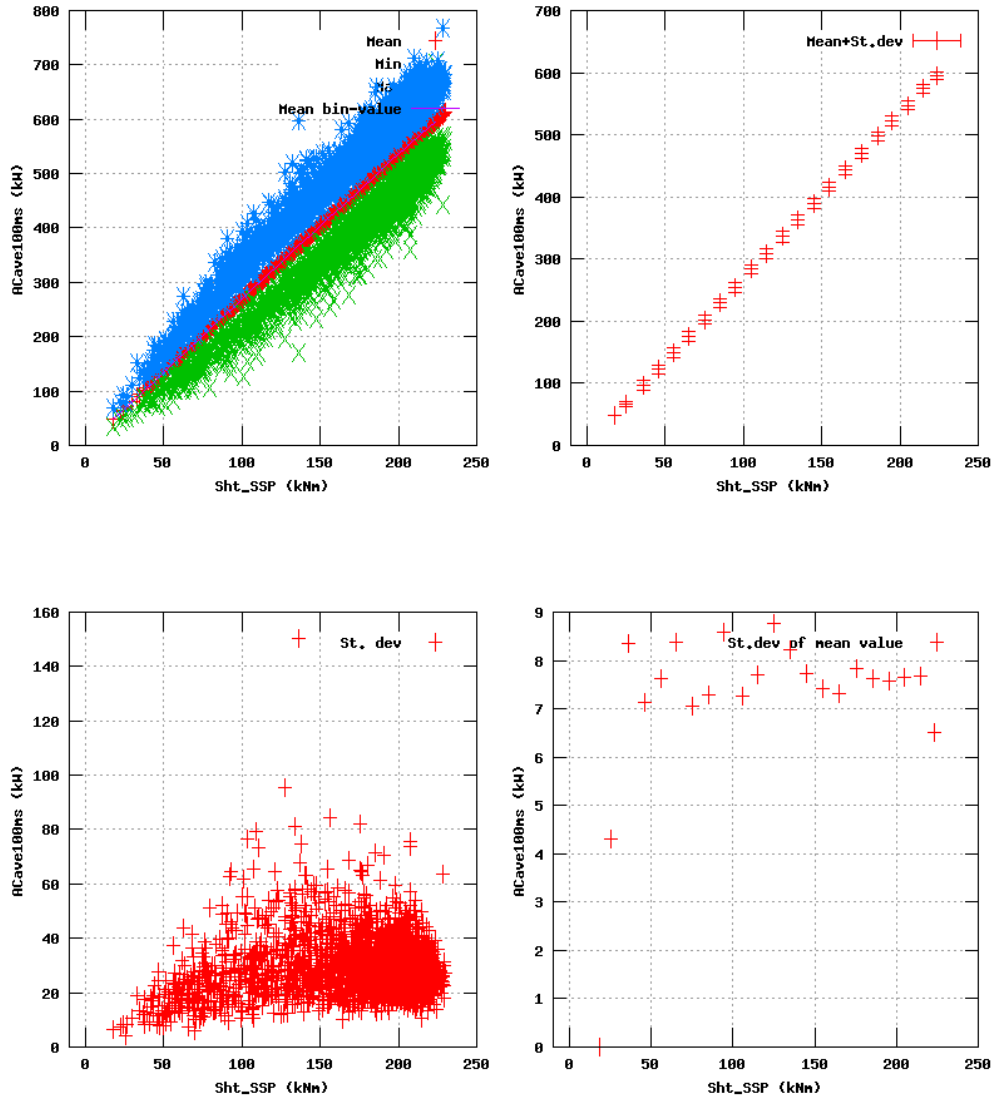Input files: m07.dat, m10.dat, m28.dat, m07.psd, m10.psd and m28.psd
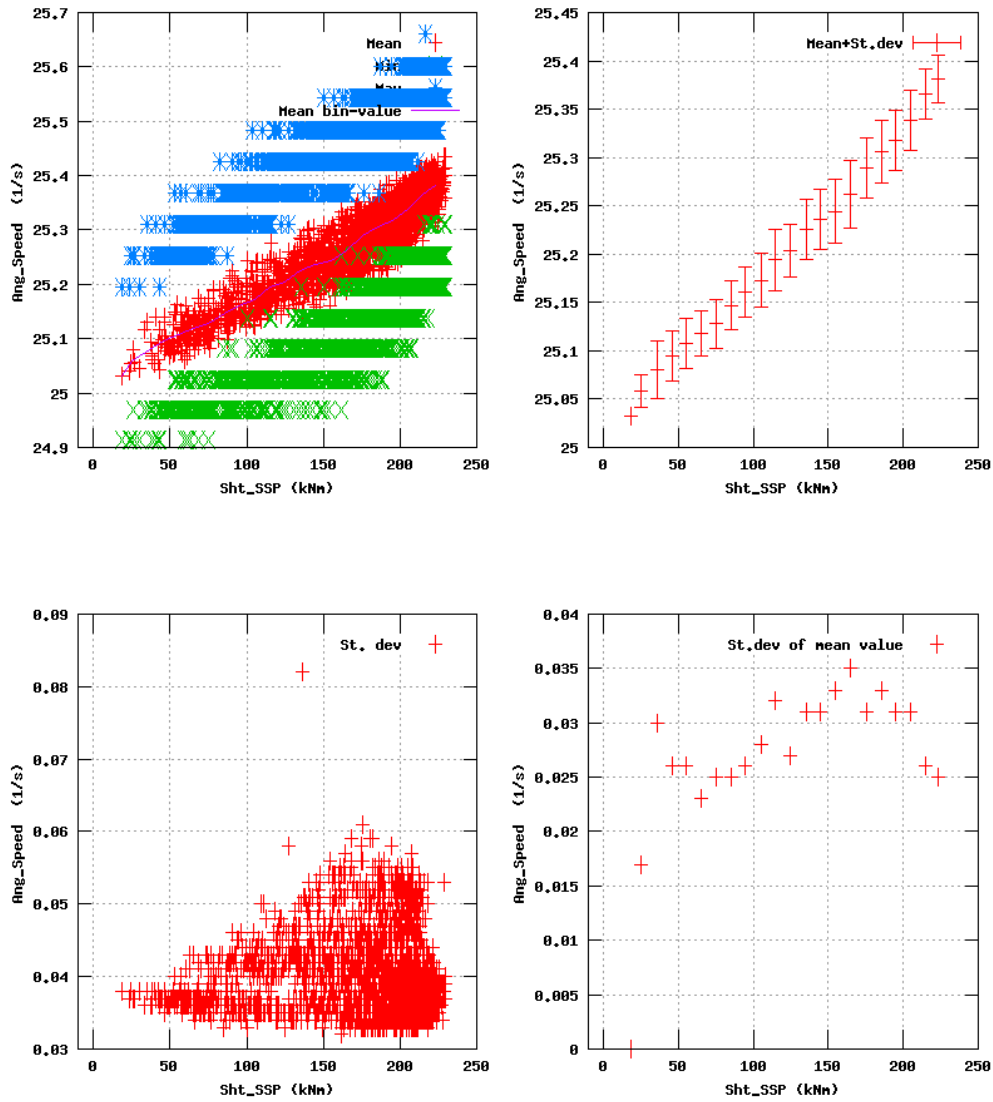
Figure 30a, Sensor 119: Angular_speed versus mainshaft torsion 'Sht_SSP'
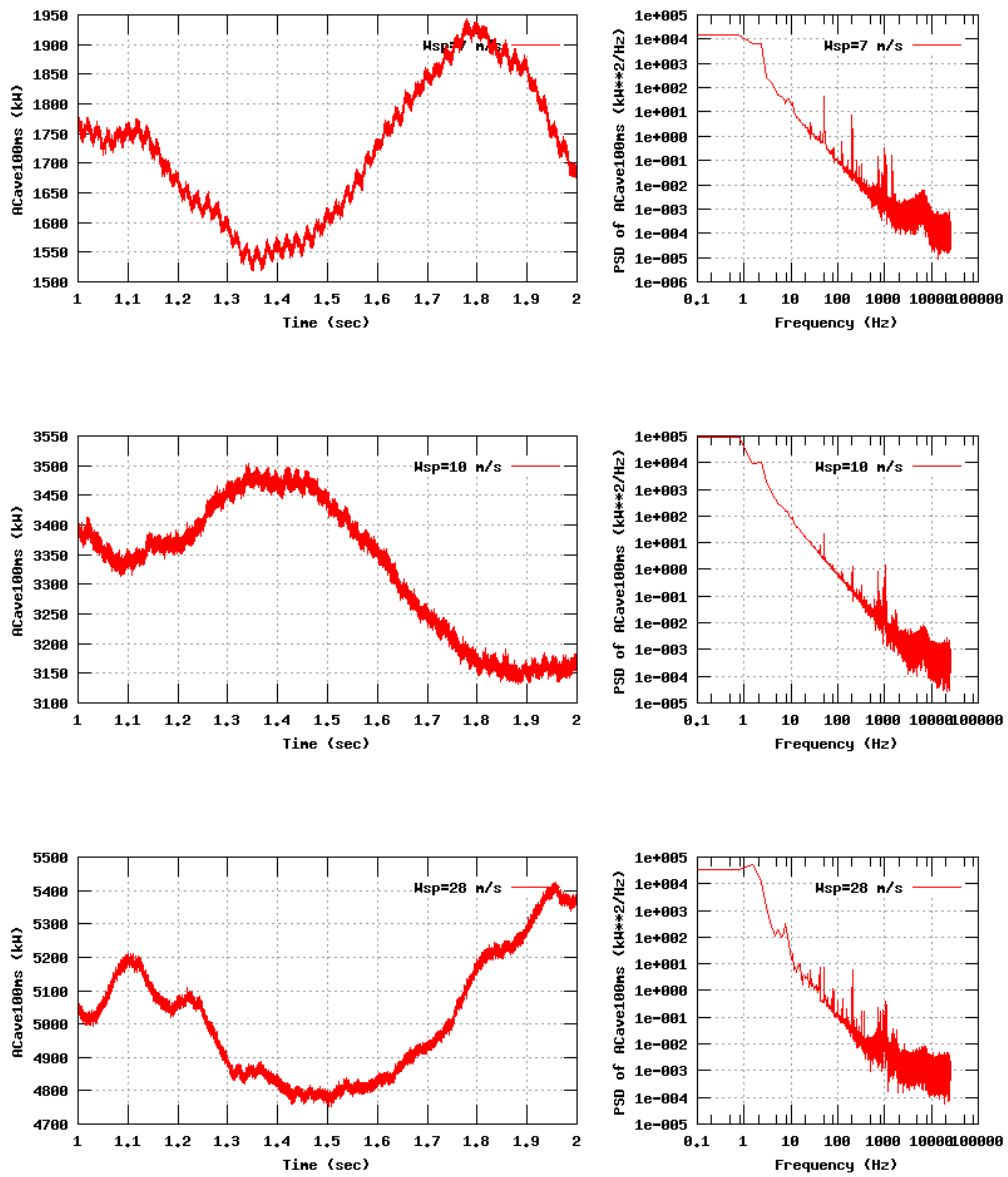Input files: NTK500fastres.dat, stat_119.dat

Figure 30b, Sensor 119: Angular_speed versus time and frequency
Input files: m07.dat, m10.dat, m28.dat, m07.psd, m10.psd and m28.psd
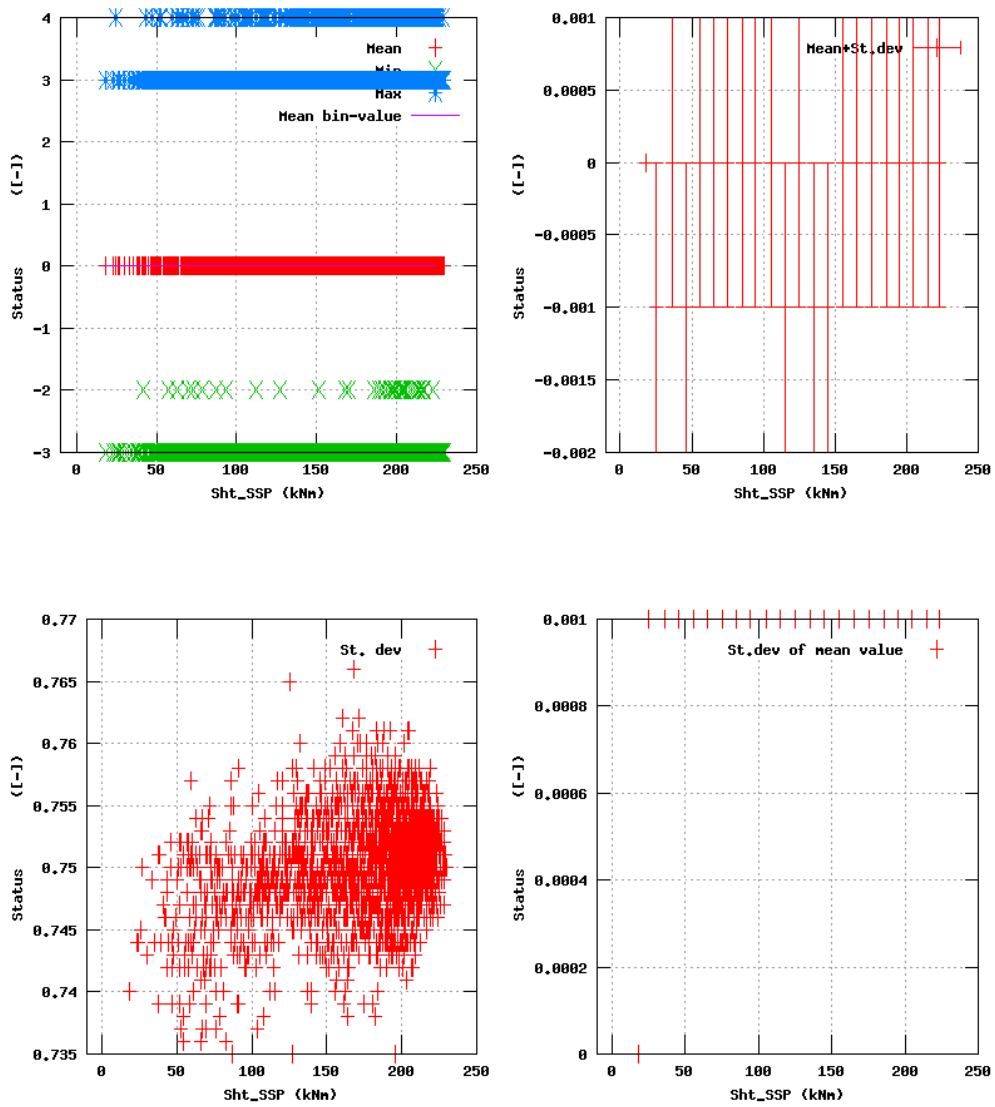
Figure 31a, Sensor 123: Status versus mainshaft torsion 'Sht_SSP'
Input files: NTK500fastres.dat, stat_123.dat

Figure 31b, Sensor 123: Status versus time and frequency
Input files: m07.dat, m10.dat, m28.dat, m07.psd, m10.psd and m28.psd

Figure 32a, Sensor 127: Dummy versus mainshaft torsion 'Sht_SSP'
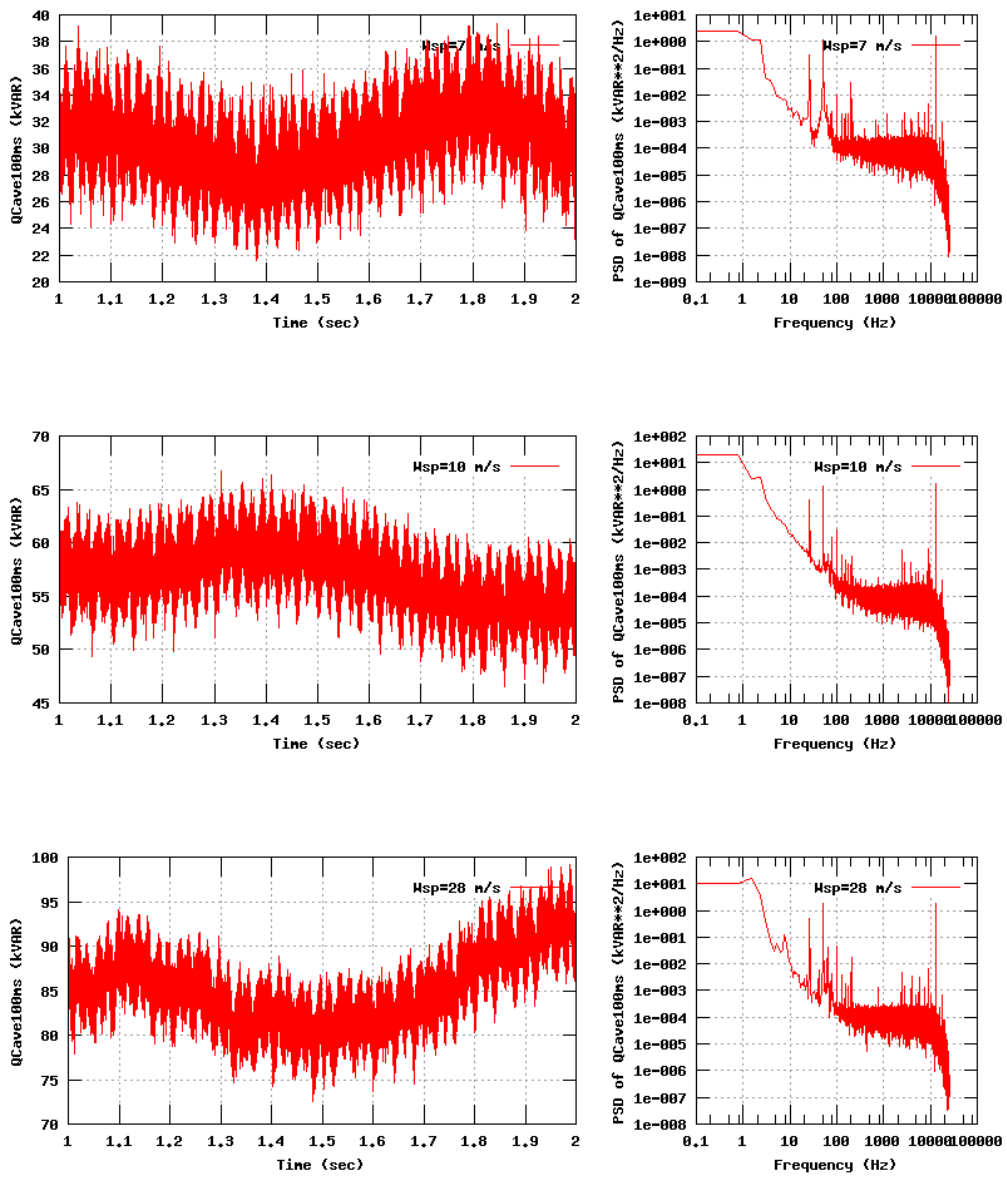Input files: NTK500fastres.dat, stat_127.dat
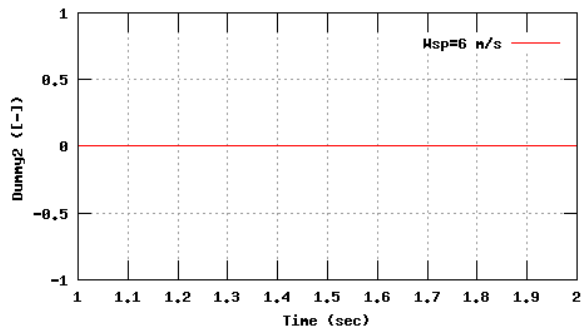
Figure 32b, Sensor 127: Dummy versus time and frequency
Input files: m06.dat, m16.dat, m22.dat, m06.psd, m16.psd and m22.psd
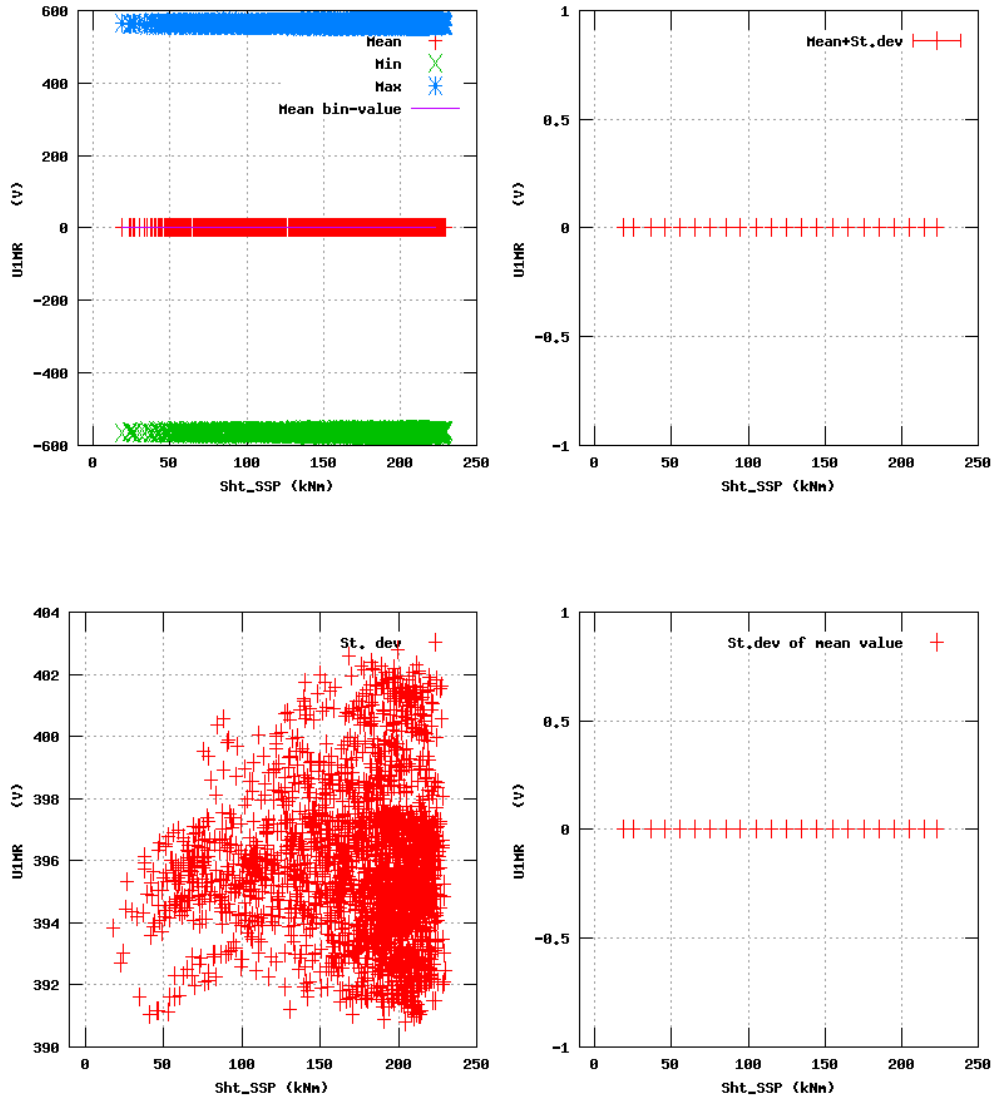
Figure 33a, Sensor 131: Phase Voltage versus mainshaft torsion 'Sht_SSP'
Input files: NTK500fastres.dat, stat_131.dat

Figure 33b, Sensor 131: Phase Voltage versus time and frequency
Input files: m07.dat, m10.dat, m28.dat, m07.psd, m10.psd and m28.psd

Figure 34a, Sensor 135: Phase Voltage versus mainshaft torsion 'Sht_SSP'
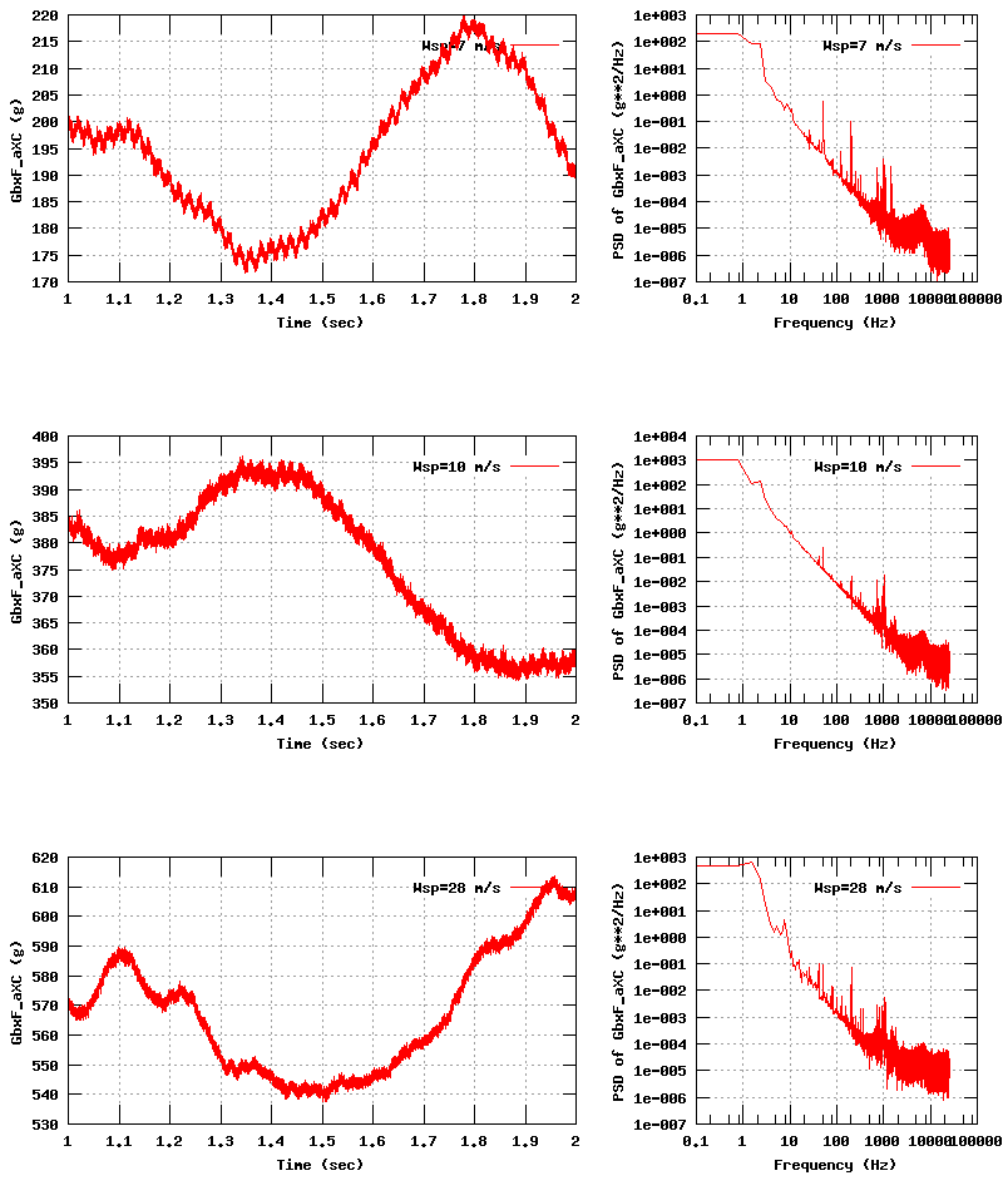Input files: NTK500fastres.dat, stat_135.dat

Figure 34b, Sensor 135: Phase Voltage versus time and frequency
Input files: m07.dat, m10.dat, m28.dat, m07.psd, m10.psd and m28.psd

Figure 35a, Sensor 139: Phase Voltage versus mainshaft torsion 'Sht_SSP'
Input files: NTK500fastres.dat, stat_139.dat

Figure 35b, Sensor 139: Phase Voltage versus time and frequency
Input files: m07.dat, m10.dat, m28.dat, m07.psd, m10.psd and m28.psd

Figure 36a, Sensor 143: AC_Power2 versus mainshaft torsion 'Sht_SSP'
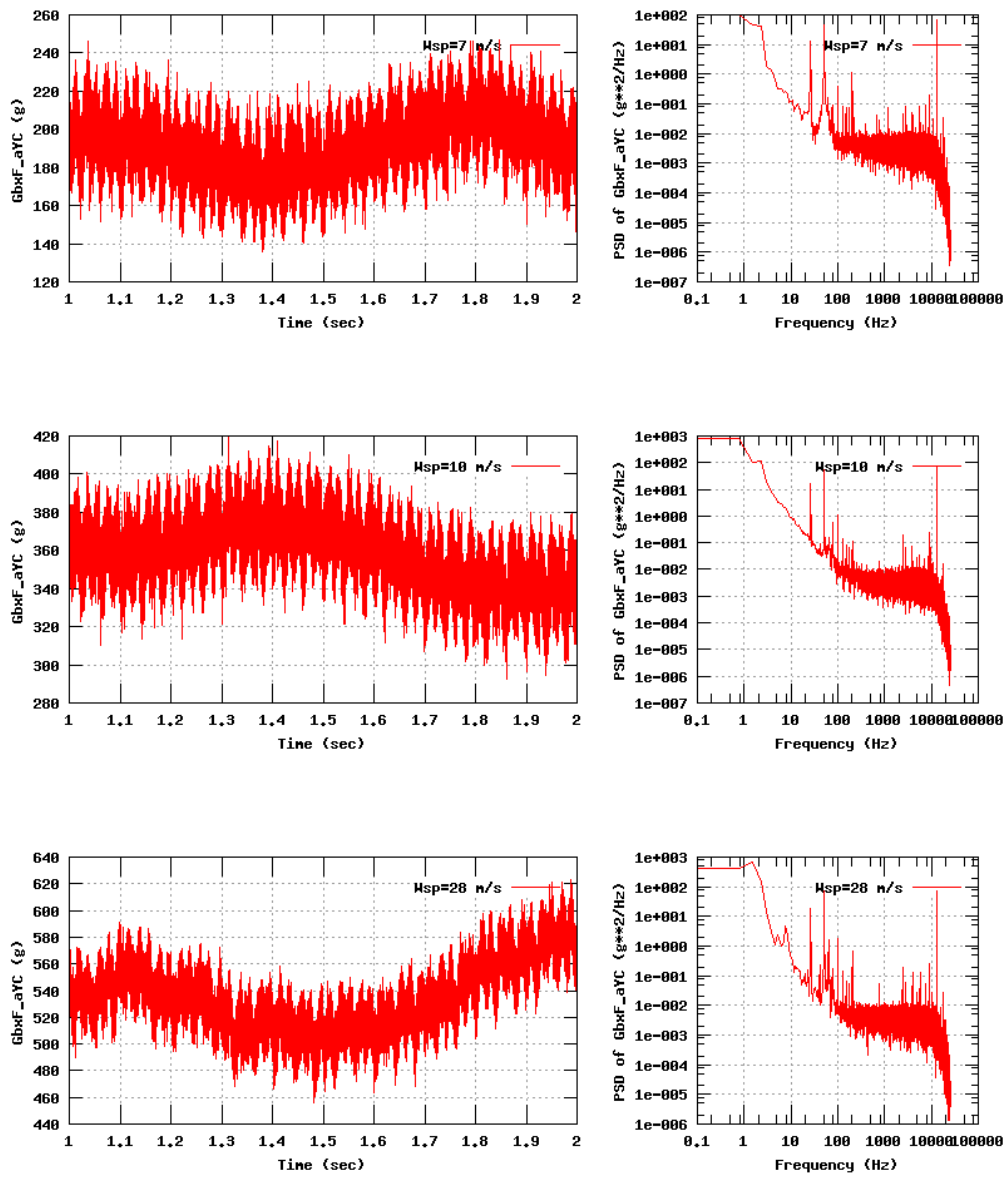Input files: NTK500fastres.dat, stat_143.dat

Figure 36b, Sensor 143: AC_Power2 versus time and frequency
Input files: m07.dat, m10.dat, m28.dat, m07.psd, m10.psd and m28.psd
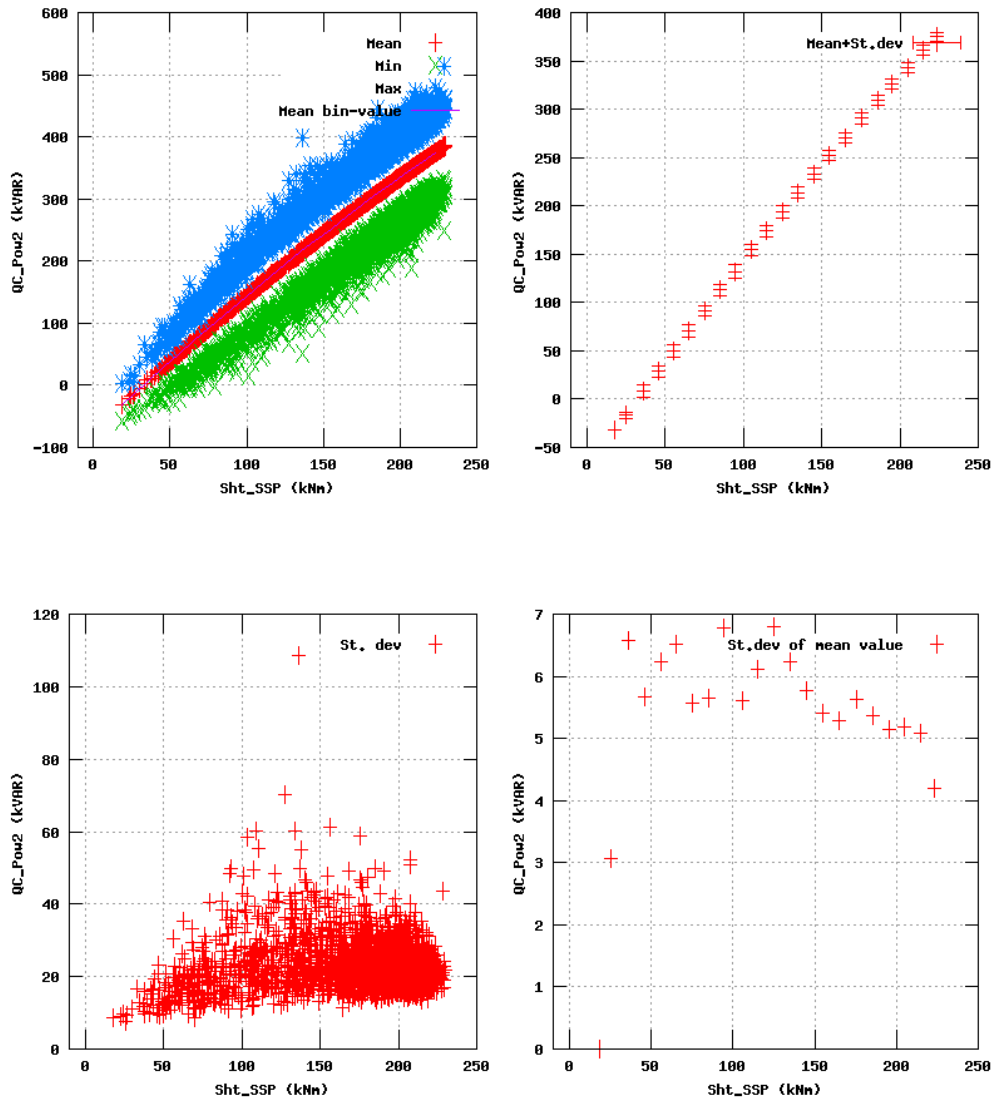
Figure 37a, Sensor 147: QC_power2 versus mainshaft torsion 'Sht_SSP'
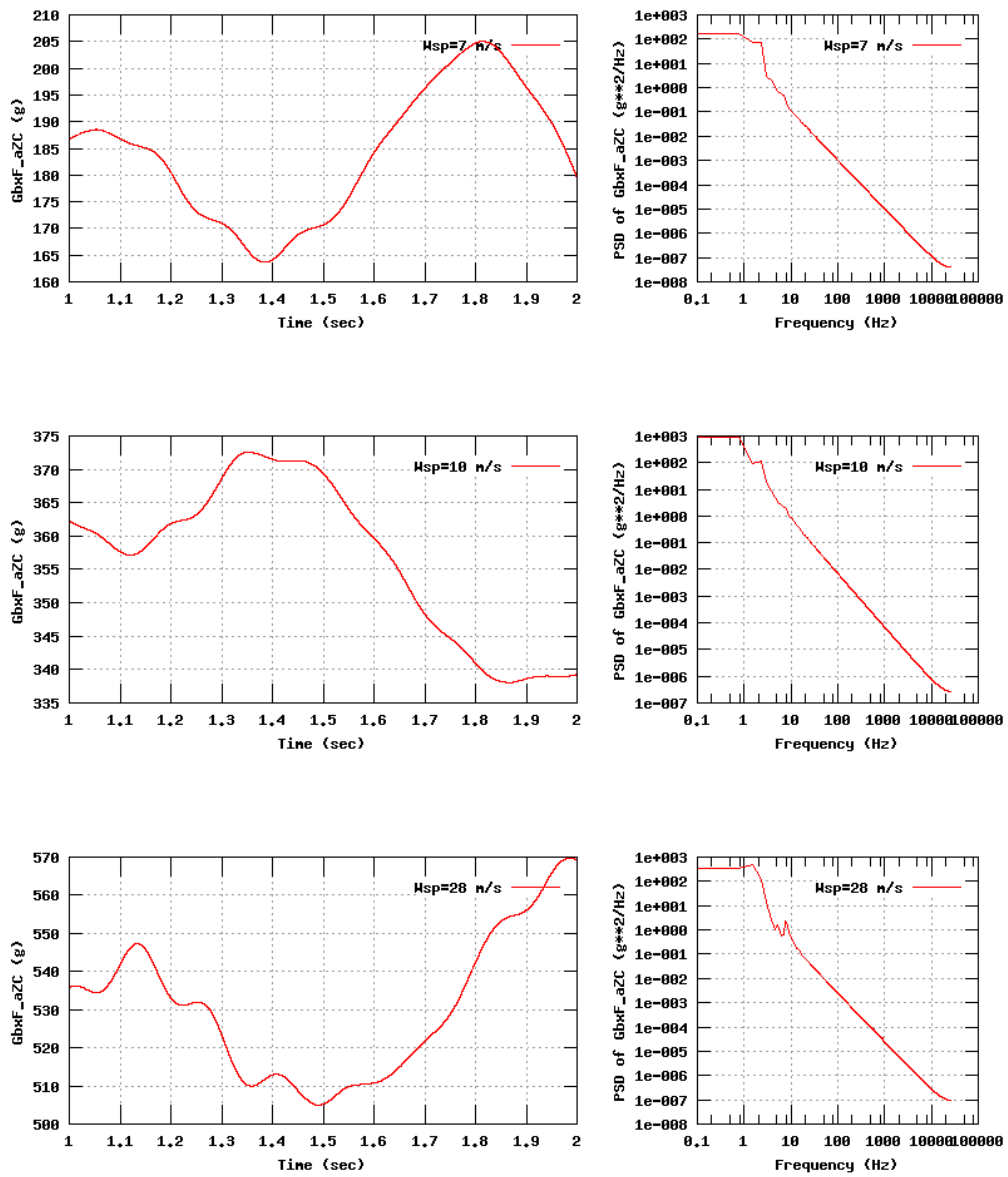Input files: NTK500fastres.dat, stat_147.dat

Figure 37b, Sensor 147: QC_power2 versus time and frequency
Input files: m07.dat, m10.dat, m28.dat, m07.psd, m10.psd and m28.psd
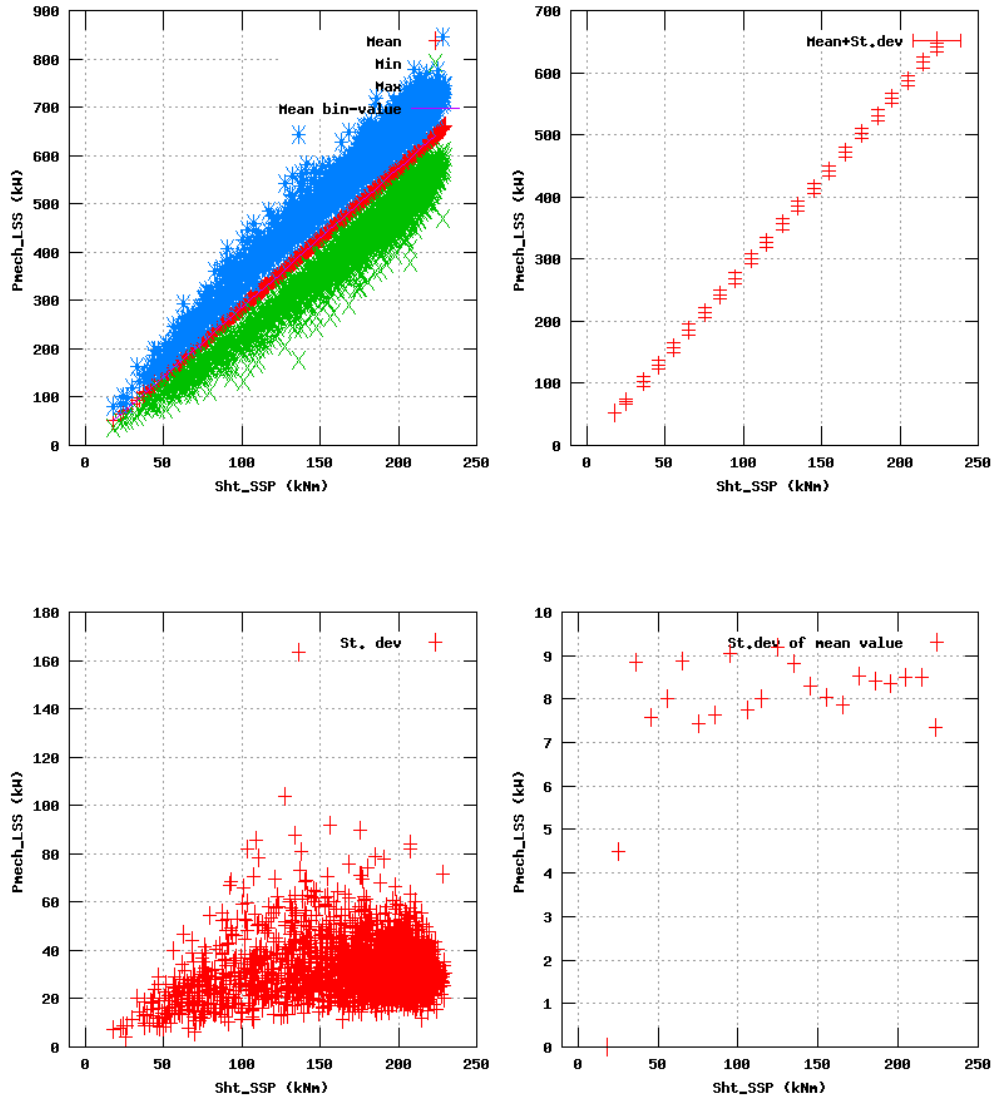
Figure 38a, Sensor 151: Pmech_LSS versus mainshaft torsion 'Sht_SSP'
Input files: NTK500fastres.dat, stat_151.dat

Figure 38b, Sensor 151: Pmech_LSS versus time and frequency
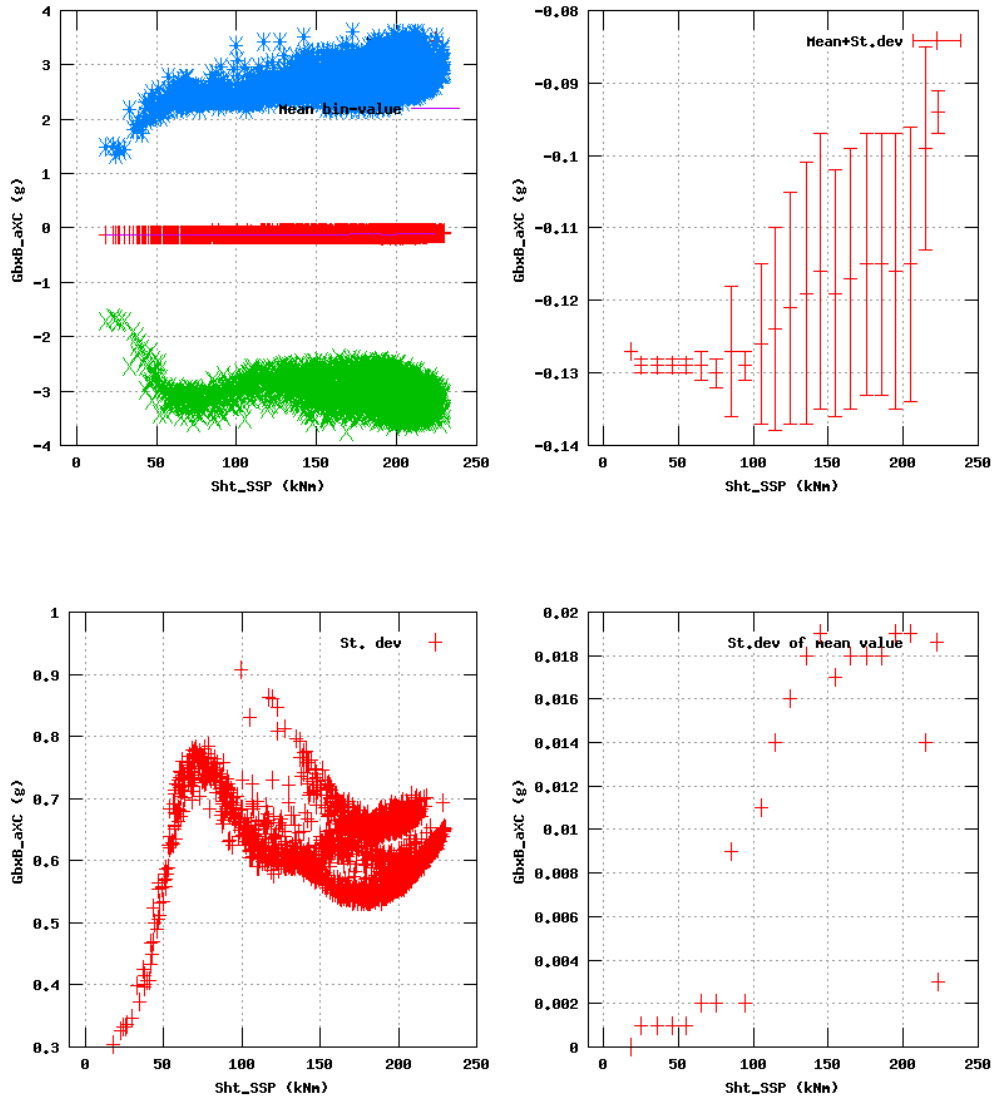Input files: m07.dat, m10.dat, m28.dat, m07.psd, m10.psd and m28.psd

Figure 39a, Sensor 155: Pmech_HSS versus mainshaft torsion 'Sht_SSP'
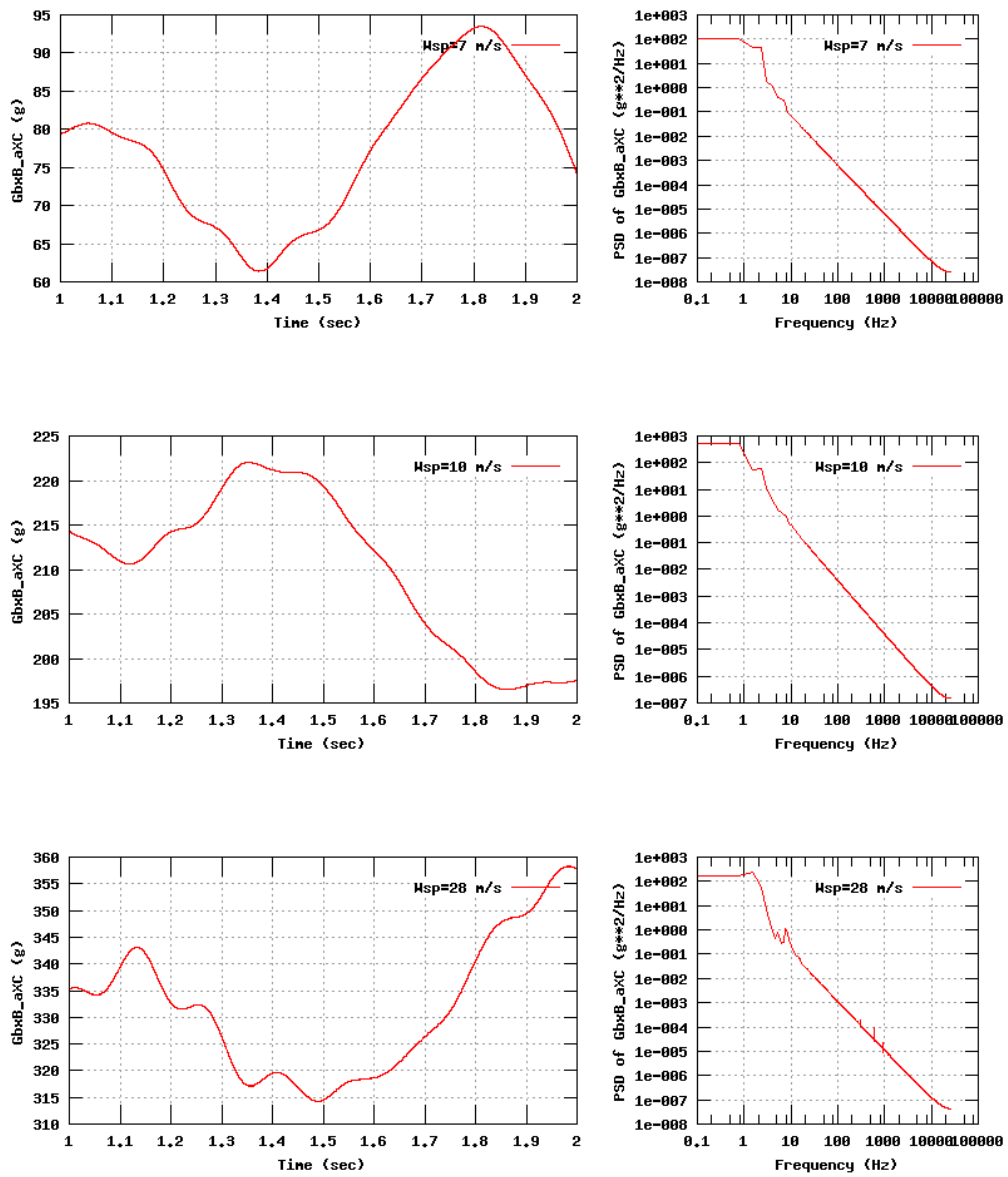Input files: NTK500fastres.dat, stat_155.dat

Figure 39b, Sensor 155: Pmech_HSS versus time and frequency
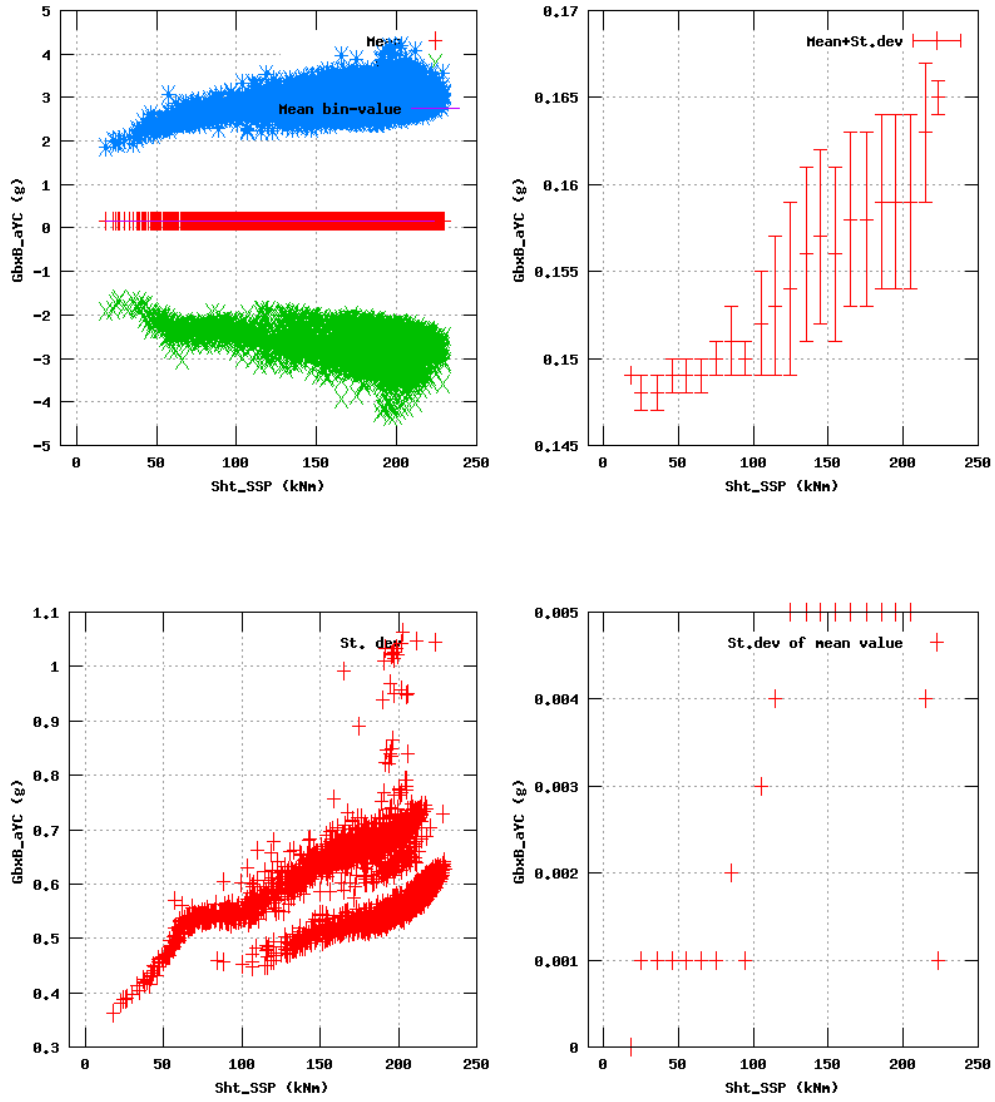Input files: m07.dat, m10.dat, m28.dat, m07.psd, m10.psd and m28.psd

Figure 40a, Sensor 159: AC_movav versus mainshaft torsion 'Sht_SSP'
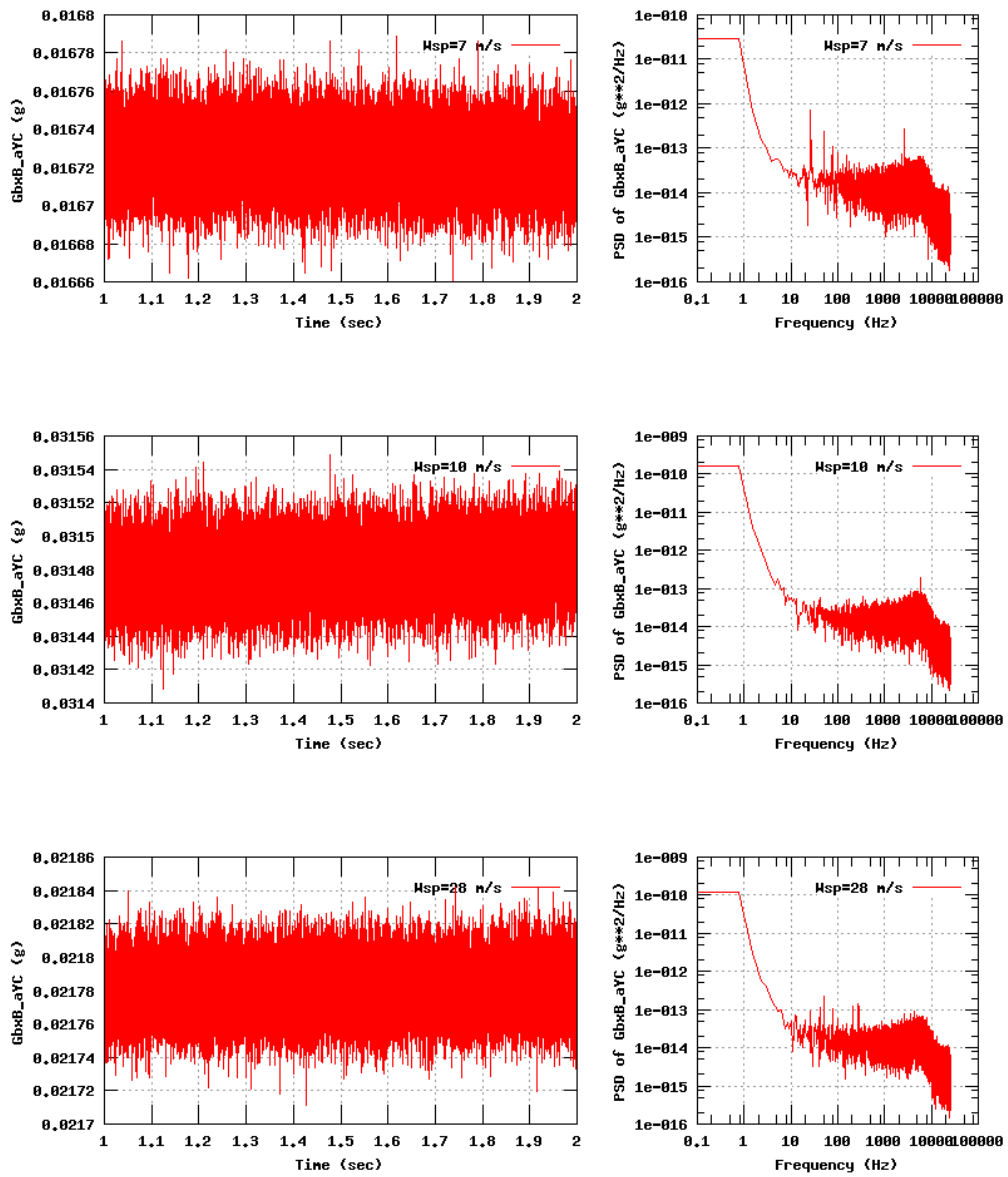Input files: NTK500fastres.dat, stat_159.dat

Figure 40b, Sensor 159: AC_movav versus time and frequency
Input files: m07.dat, m10.dat, m28.dat, m07.psd, m10.psd and m28.psd
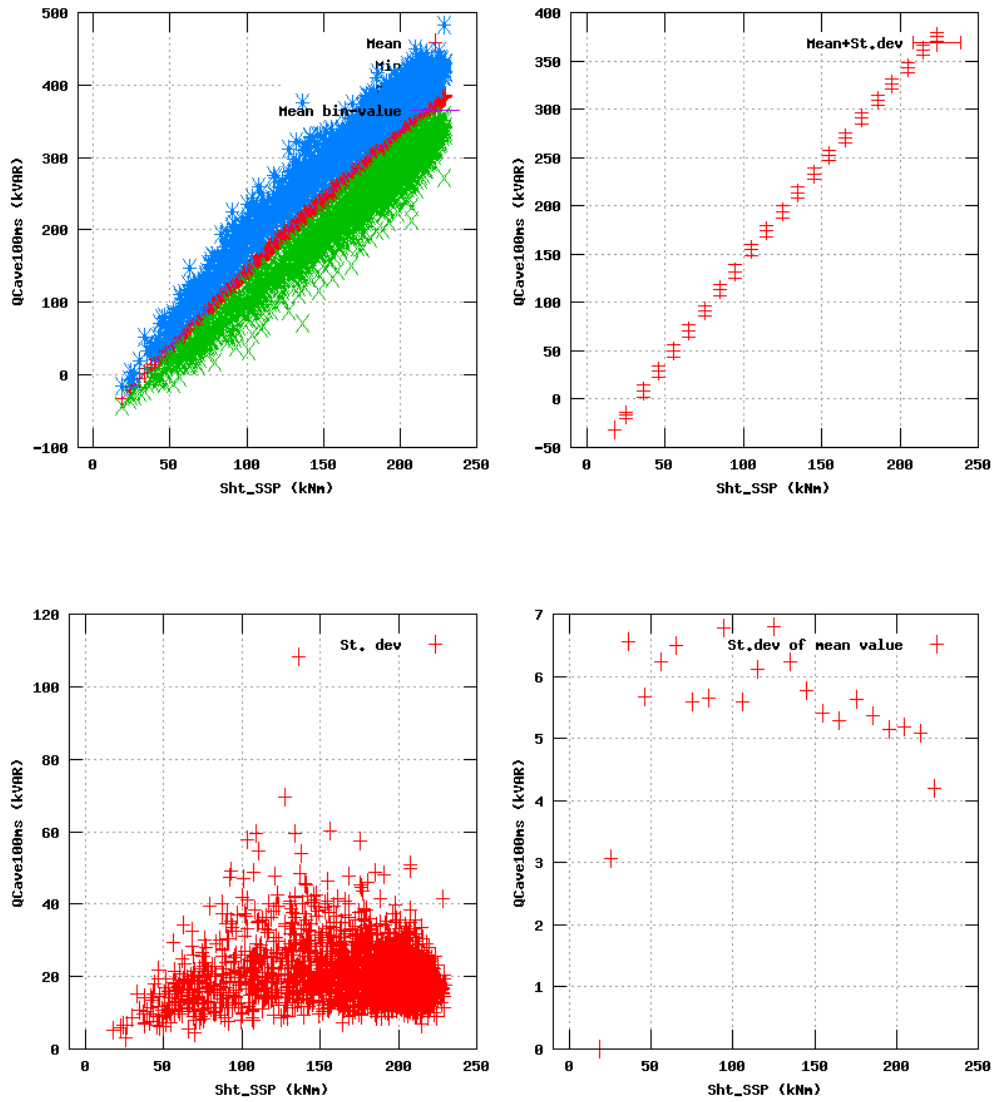
Figure 41a, Sensor 163: QC_movav versus mainshaft torsion 'Sht_SSP'
Input files: NTK500fastres.dat, stat_163.dat

Figure 41b, Sensor 163: QC_movav versus time and frequency
Input files: m07.dat, m10.dat, m28.dat, m07.psd, m10.psd and m28.psd
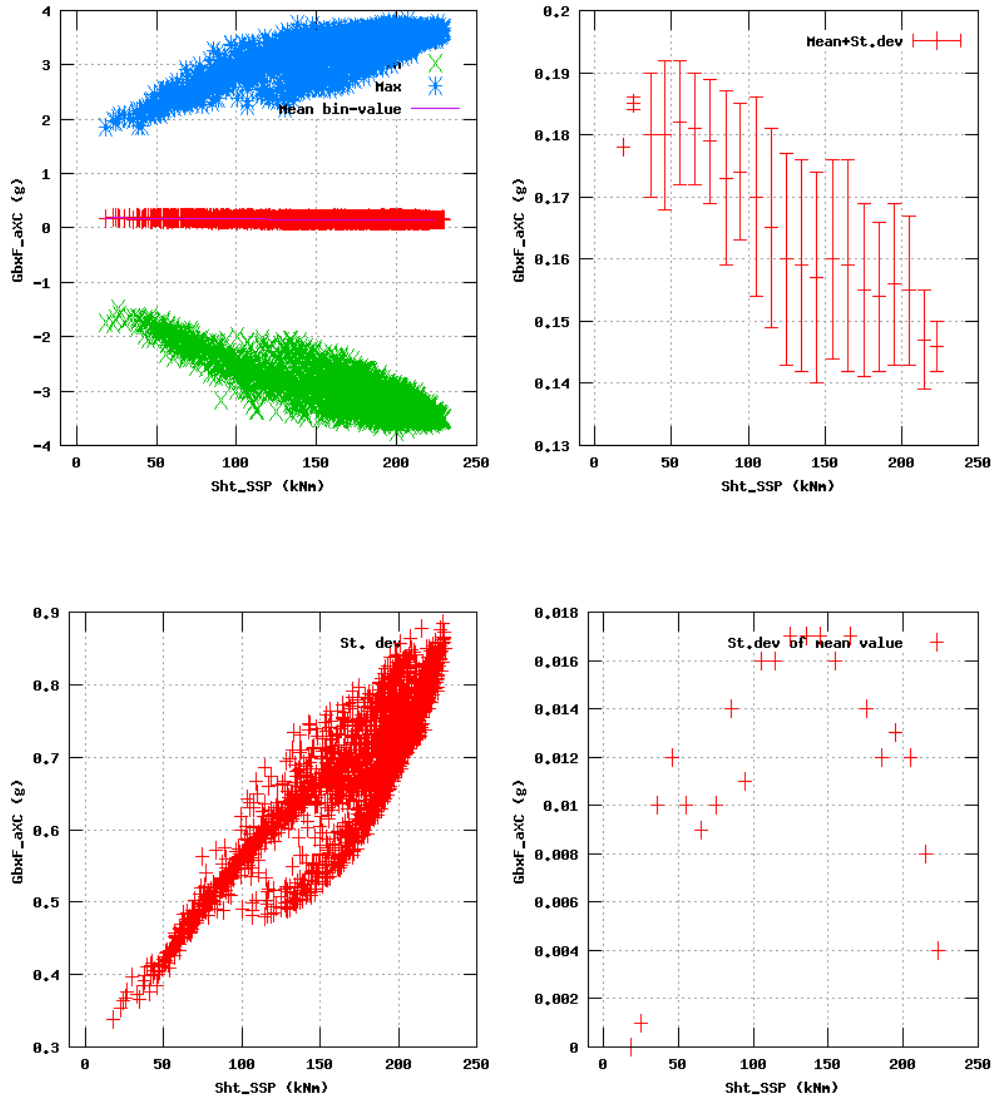
Figure 42a, Sensor 167: GearBoxF_aXC versus mainshaft torsion 'Sht_SSP'
Input files: NTK500fastres.dat, stat_167.dat

Figure 42b, Sensor 167: GearBoxF_aXC versus time and frequency
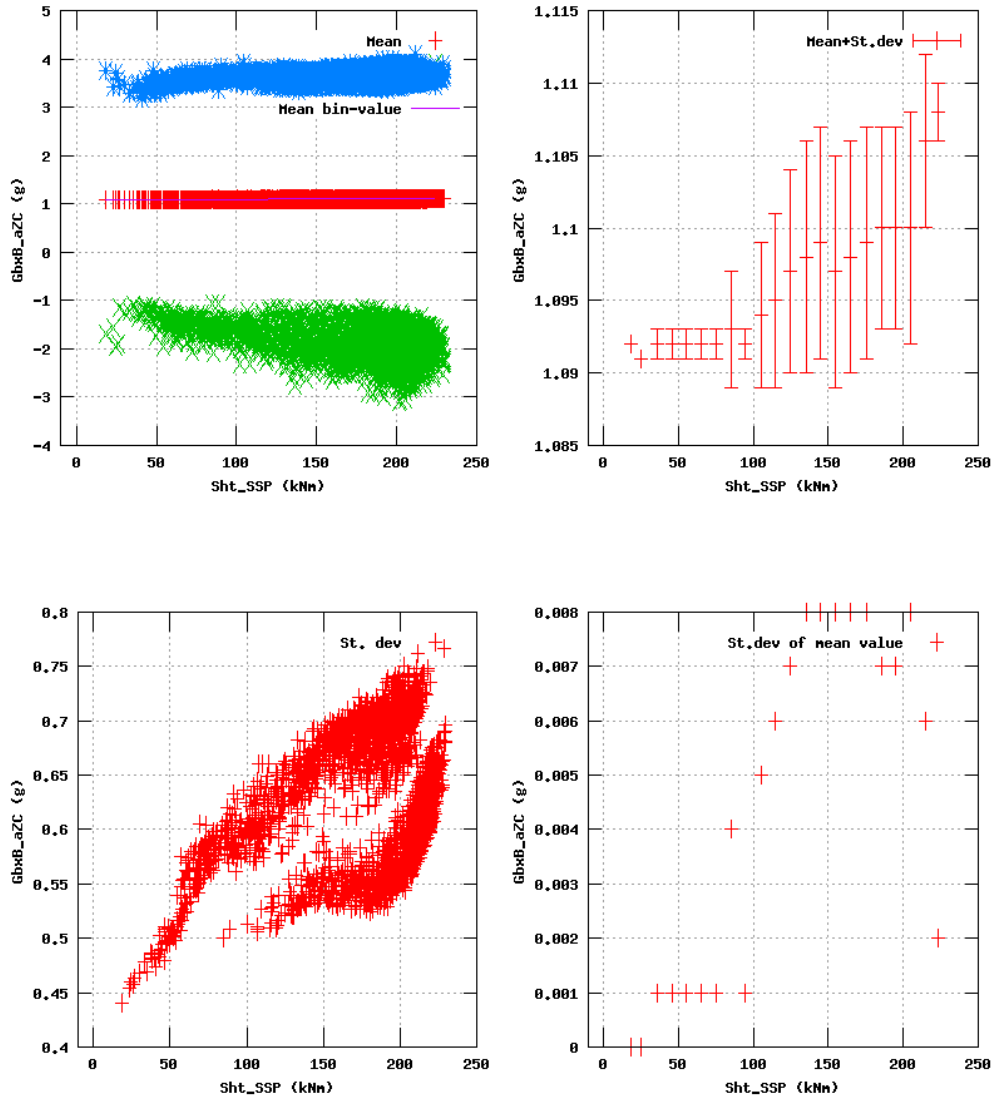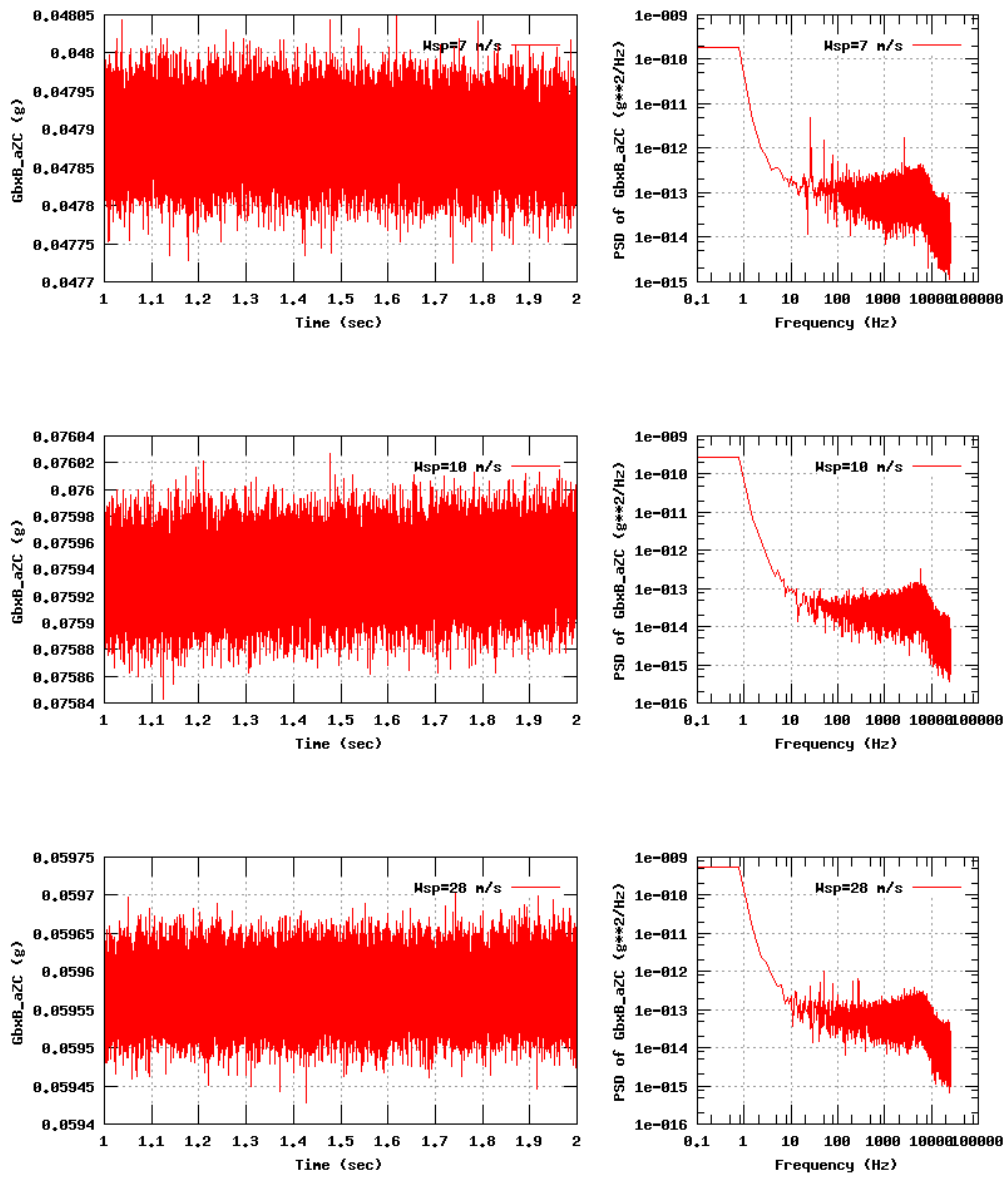Input files: m07.dat, m10.dat, m28.dat, m07.psd, m10.psd and m28.psd
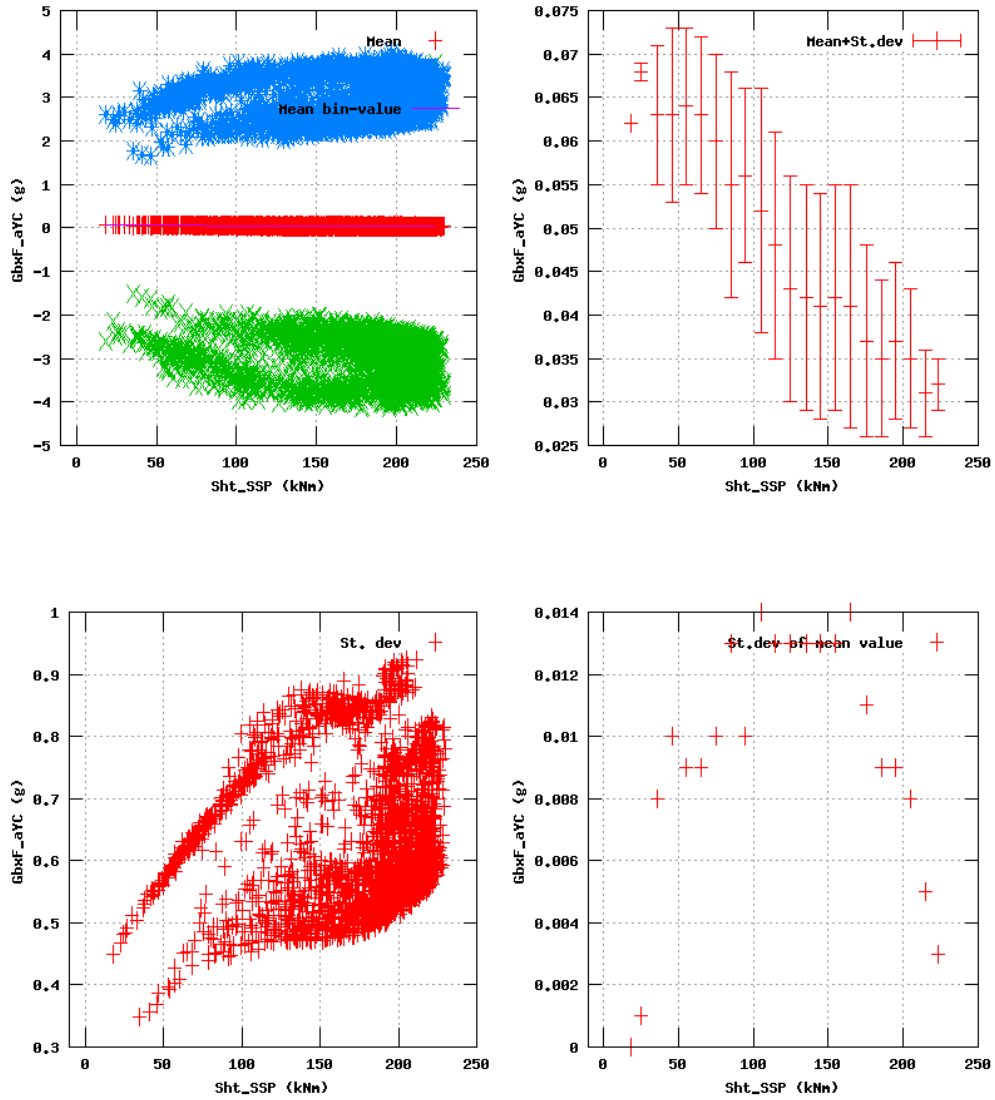
Figure 43a, Sensor 171: GearBoxF_aYC versus mainshaft torsion 'Sht_SSP'
Input files: NTK500fastres.dat, stat_171.dat

Figure 43b, Sensor 171: GearBoxF_aYC versus time and frequency
Input files: m07.dat, m10.dat, m28.dat, m07.psd, m10.psd and m28.psd
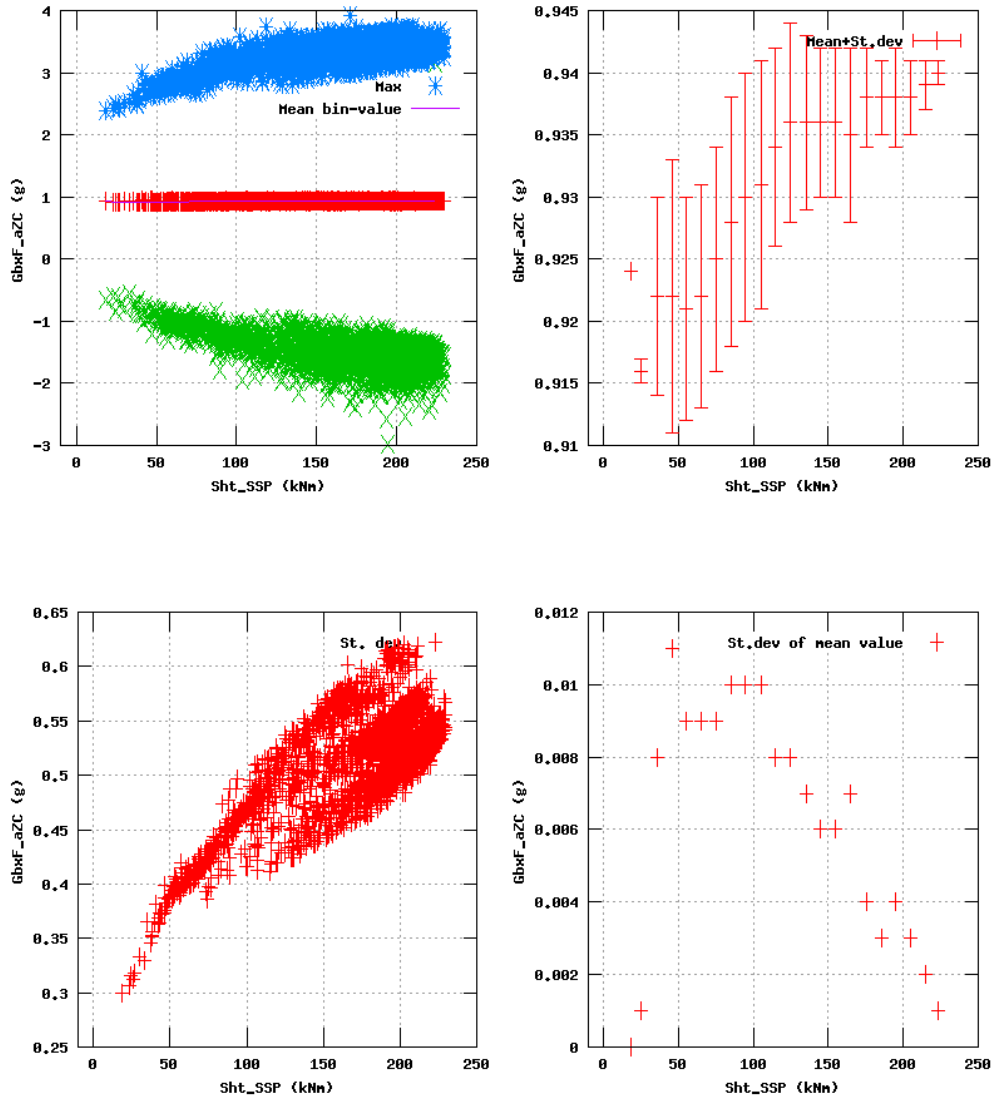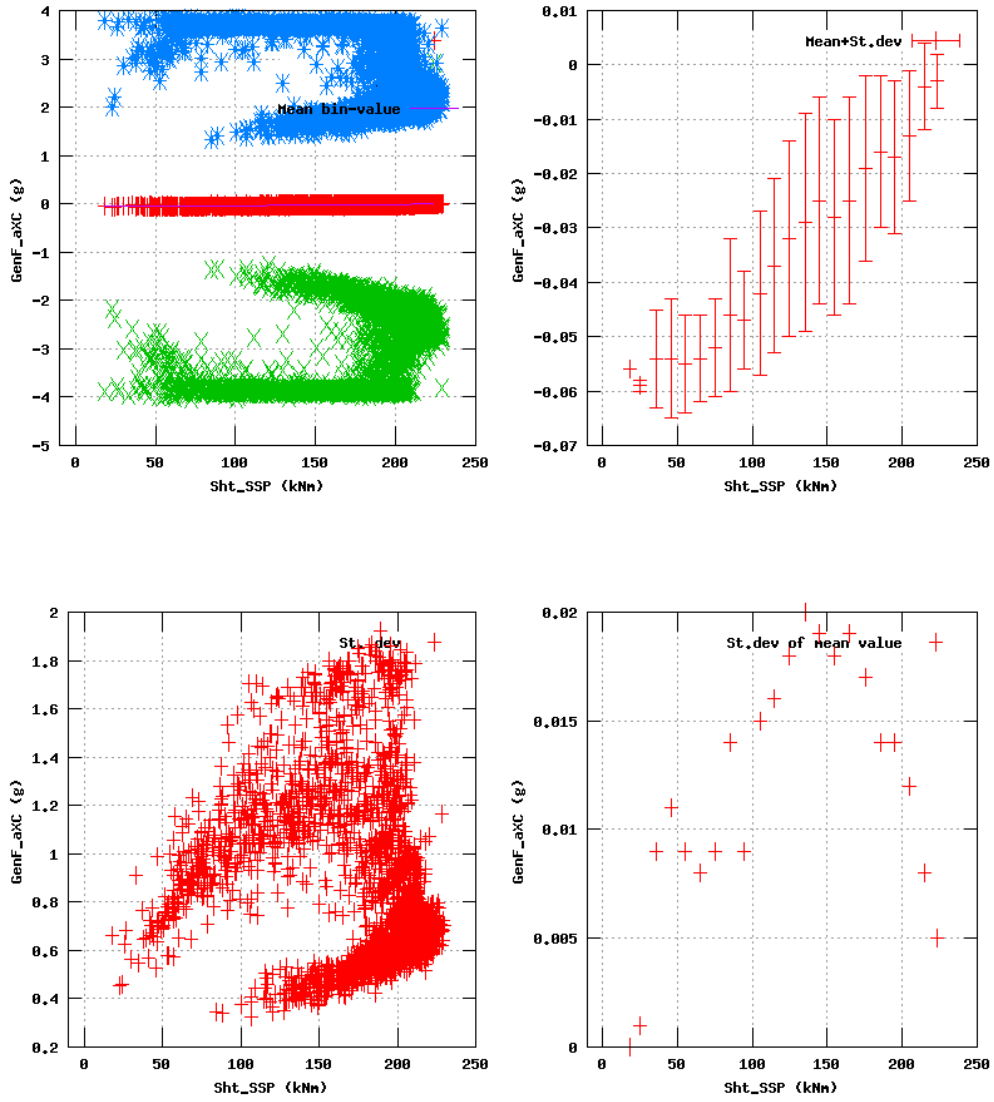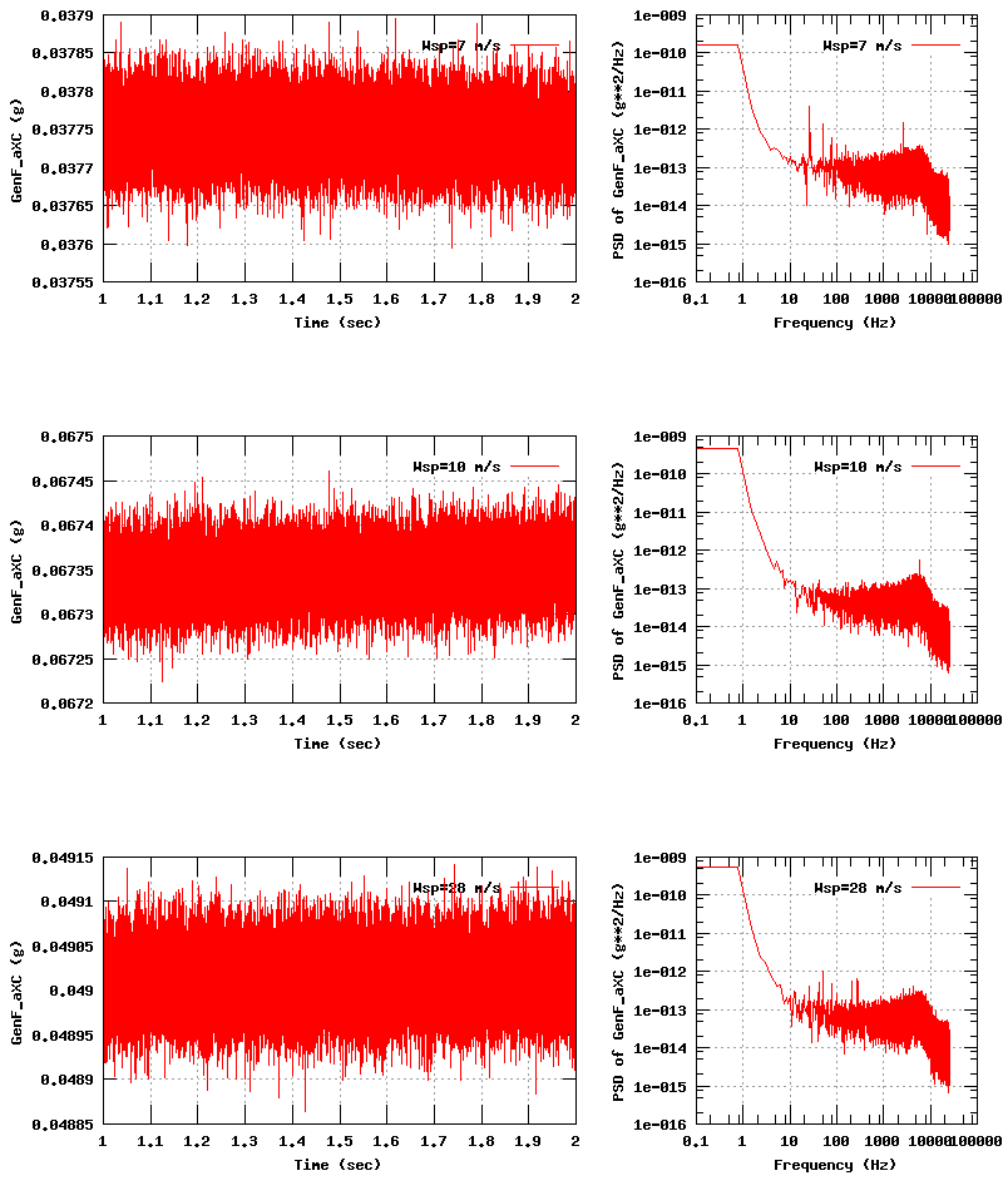
Figure 44a, Sensor 175: GearBoxF_aZC versus mainshaft torsion 'Sht_SSP'
Input files: NTK500fastres.dat, stat_175.dat

Figure 44b, Sensor 175: GearBoxF_aZC versus time and frequency
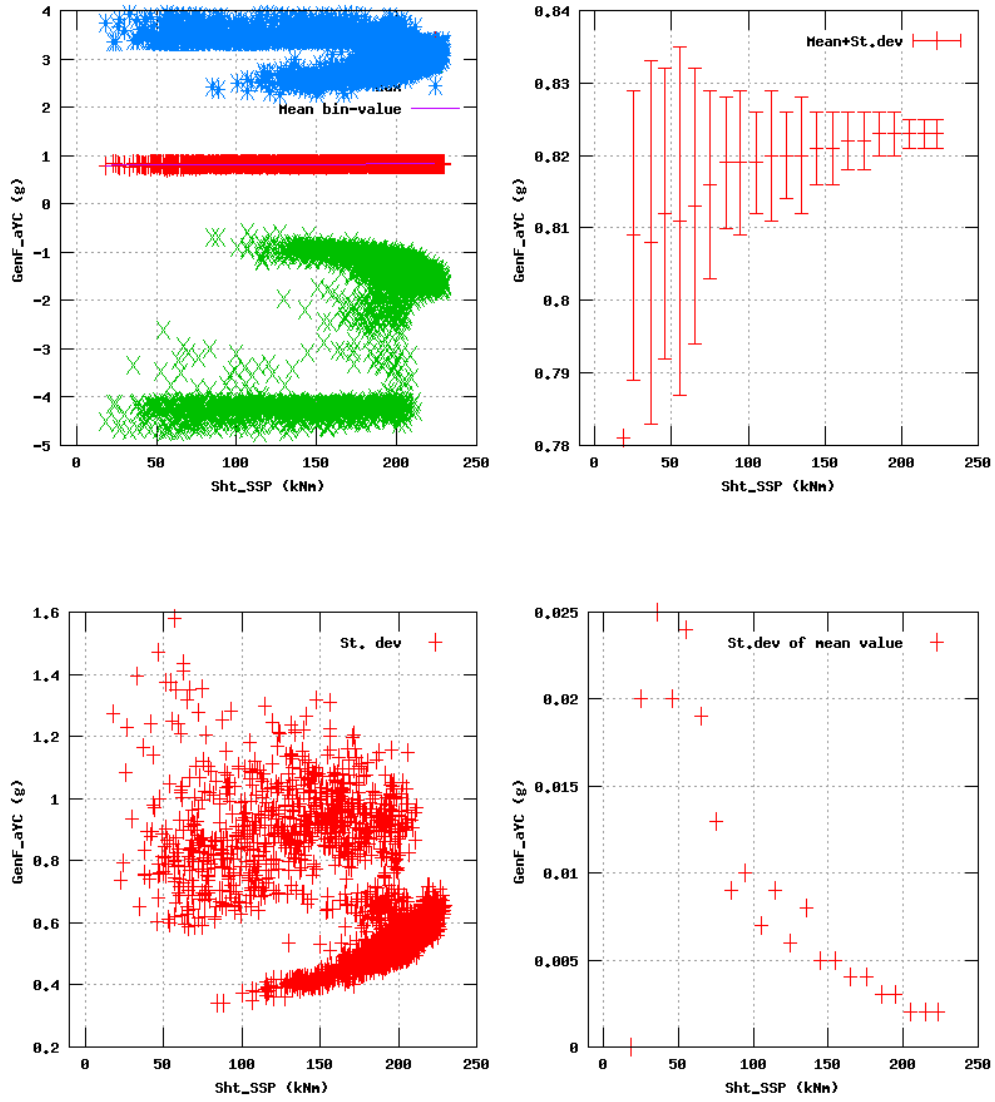Input files: m07.dat, m10.dat, m28.dat, m07.psd, m10.psd and m28.psd

Figure 45a, Sensor 179: GearBoxB_aXC versus mainshaft torsion 'Sht_SSP'
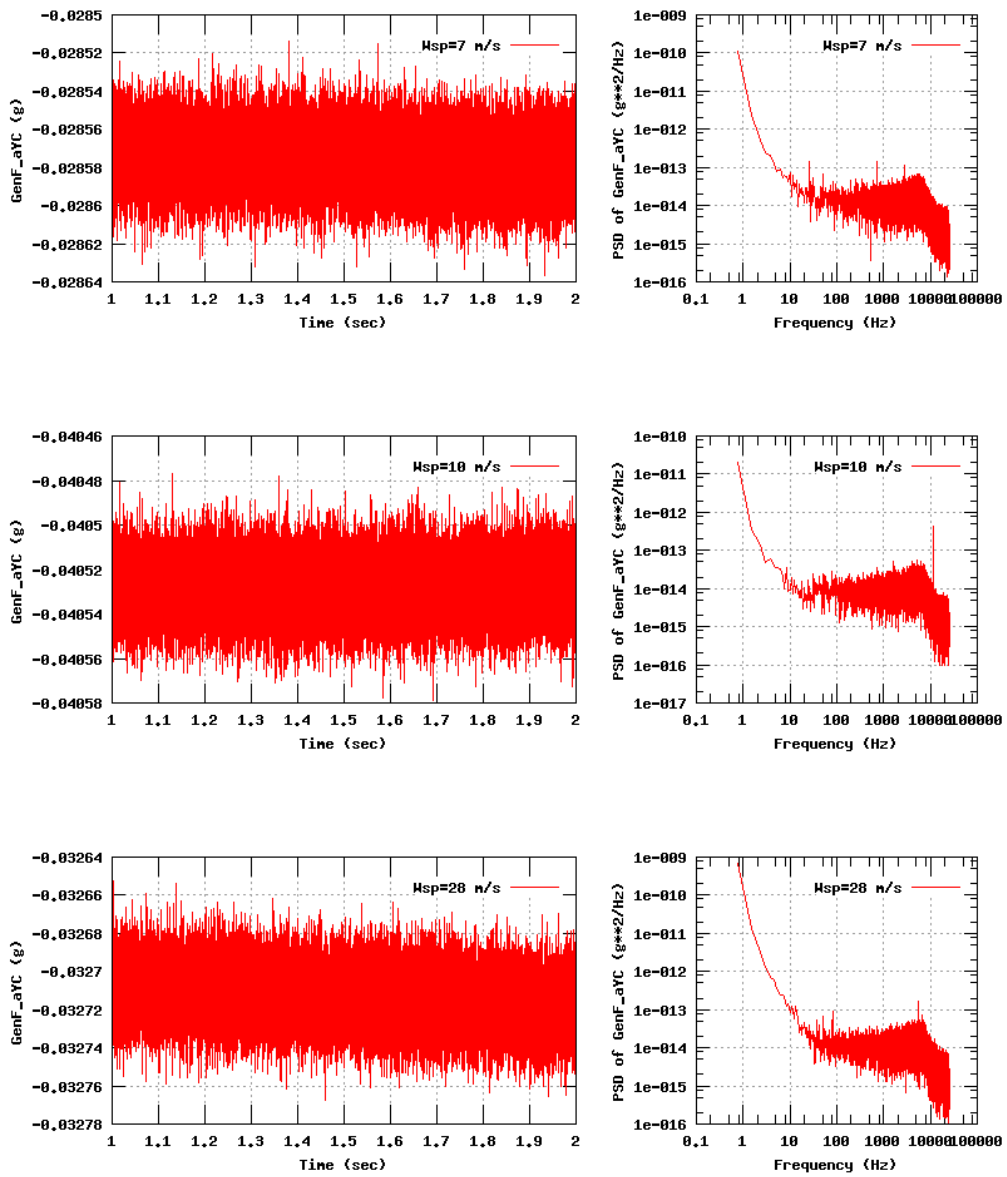Input files: NTK500fastres.dat, stat_179.dat

Figure 45b, Sensor 179: GearBoxB_aXC versus time and frequency
Input files: m07.dat, m10.dat, m28.dat, m07.psd, m10.psd and m28.psd

Figure 46a, Sensor 183: GearBoxB_aYC versus mainshaft torsion 'Sht_SSP'
Input files: NTK500fastres.dat, stat_183.dat

Figure 46b, Sensor 183: GearBoxB_aYC versus time and frequency
Input files: m07.dat, m10.dat, m28.dat, m07.psd, m10.psd and m28.psd

Figure 47a, Sensor 187: GearBoxB_aZC versus mainshaft torsion 'Sht_SSP'
Input files: NTK500fastres.dat, stat_187.dat

Figure 47b, Sensor 187: GearBoxB_aZC versus time and frequency
Input files: m07.dat, m10.dat, m28.dat, m07.psd, m10.psd and m28.psd

Figure 48a, Sensor 191: GeneratorF_aXC versus mainshaft torsion 'Sht_SSP'
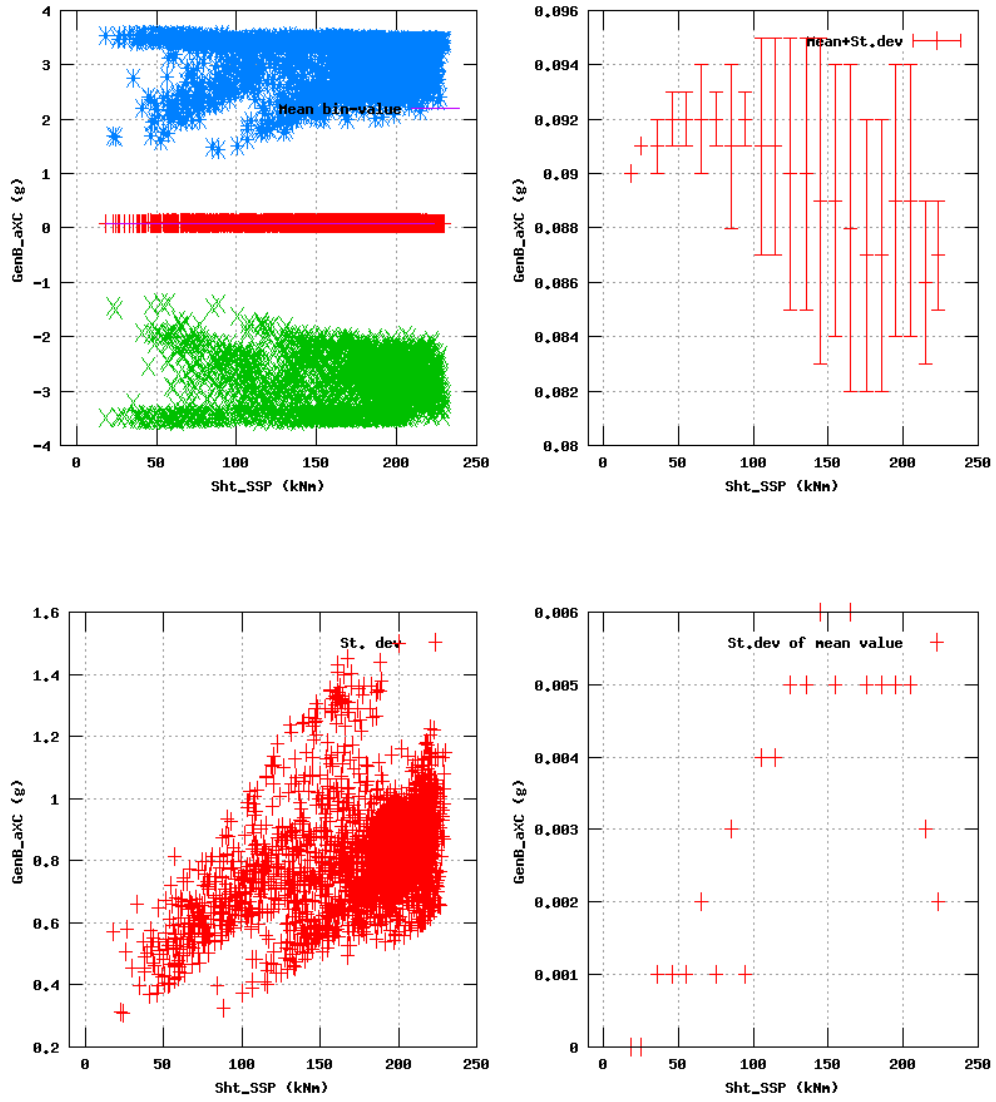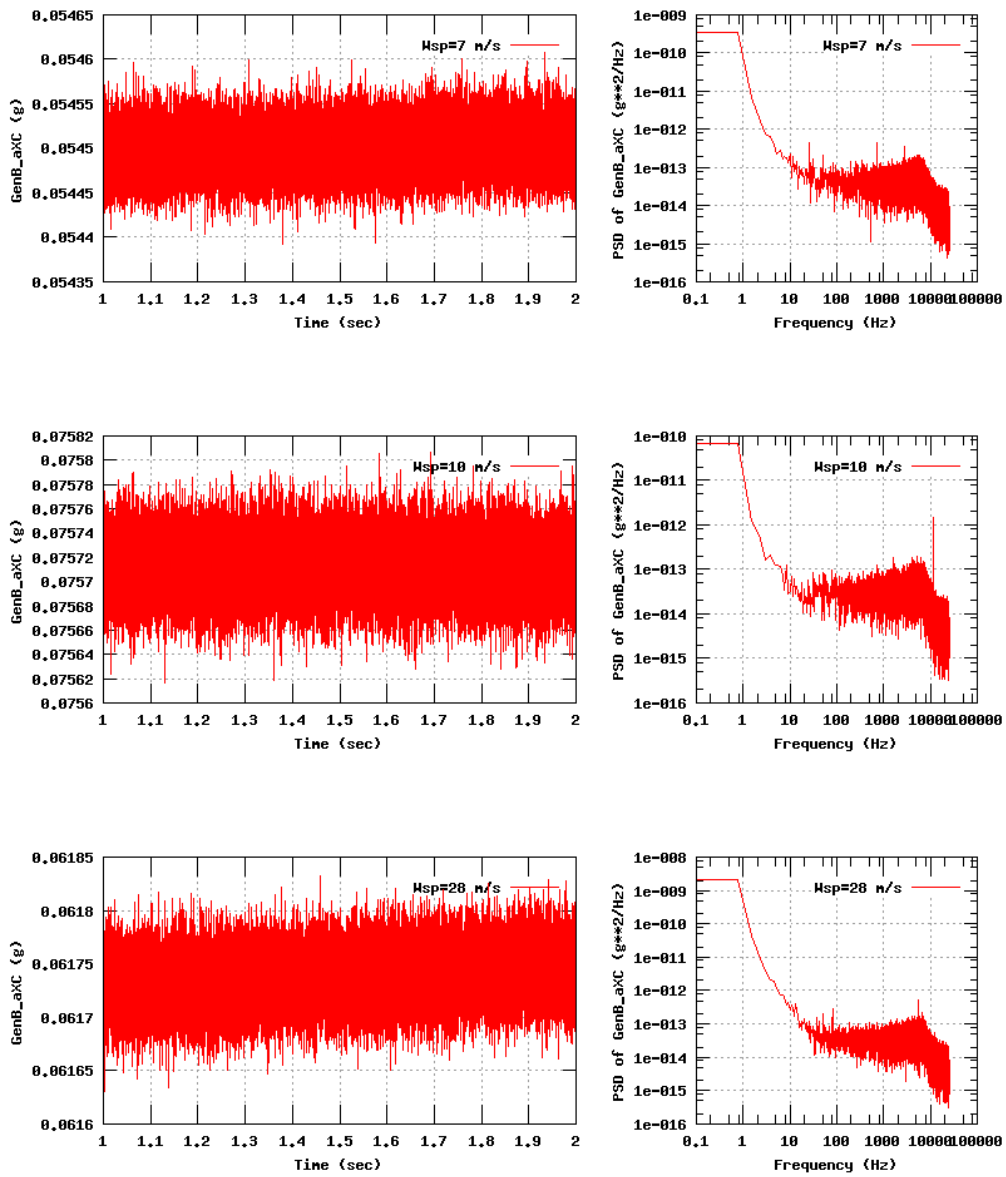Input files: NTK500fastres.dat, stat_191.dat

Figure 48b, Sensor 191: GeneratorF_aXC versus time and frequency
Input files: m07.dat, m10.dat, m28.dat, m07.psd, m10.psd and m28.psd

Figure 49a, Sensor 195: GeneratorF_aYC versus mainshaft torsion 'Sht_SSP'
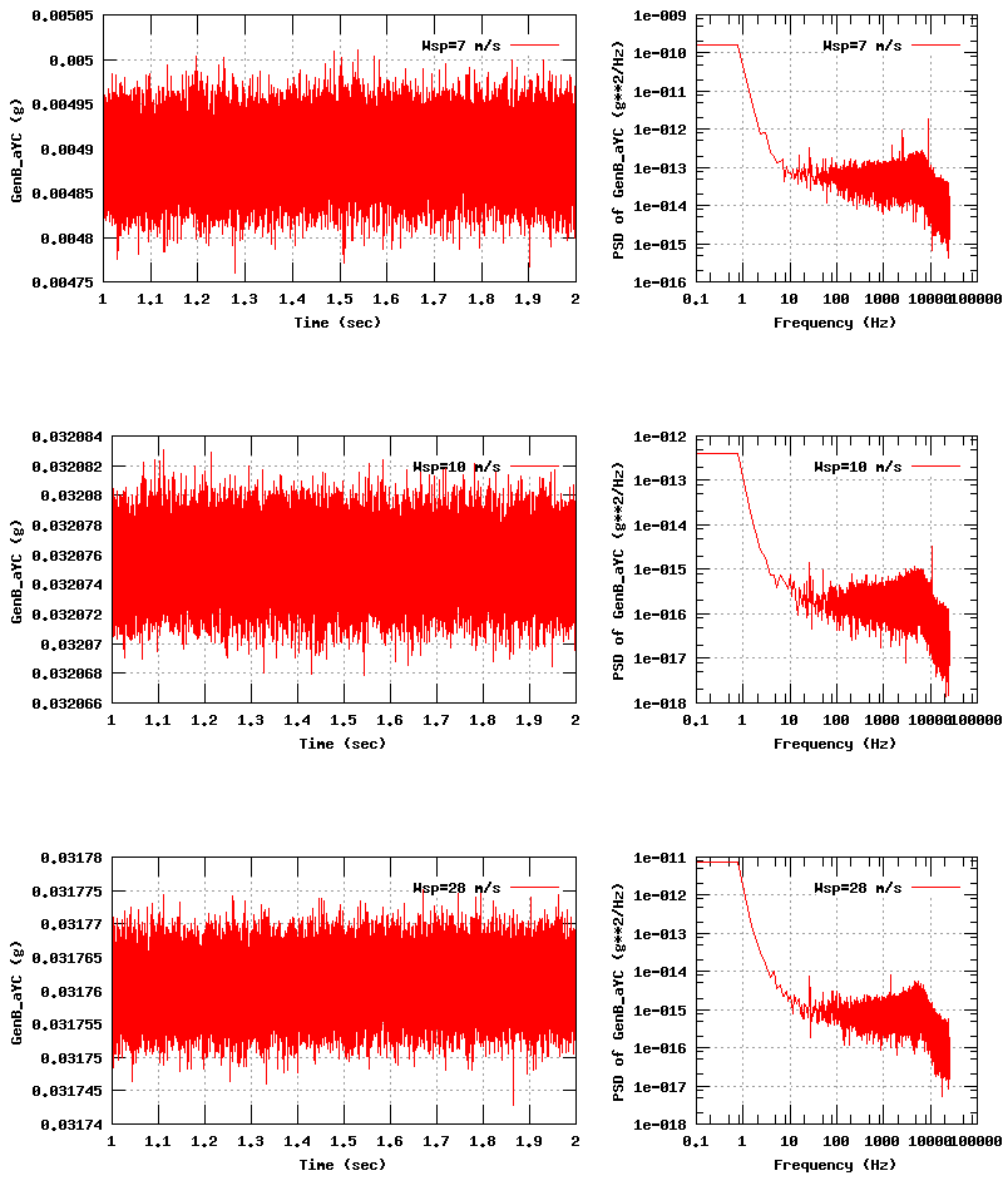Input files: NTK500fastres.dat, stat_195.dat

Figure 49b, Sensor 195: GeneratorF_aYC versus time and frequency
Input files: m07.dat, m10.dat, m28.dat, m07.psd, m10.psd and m28.psd
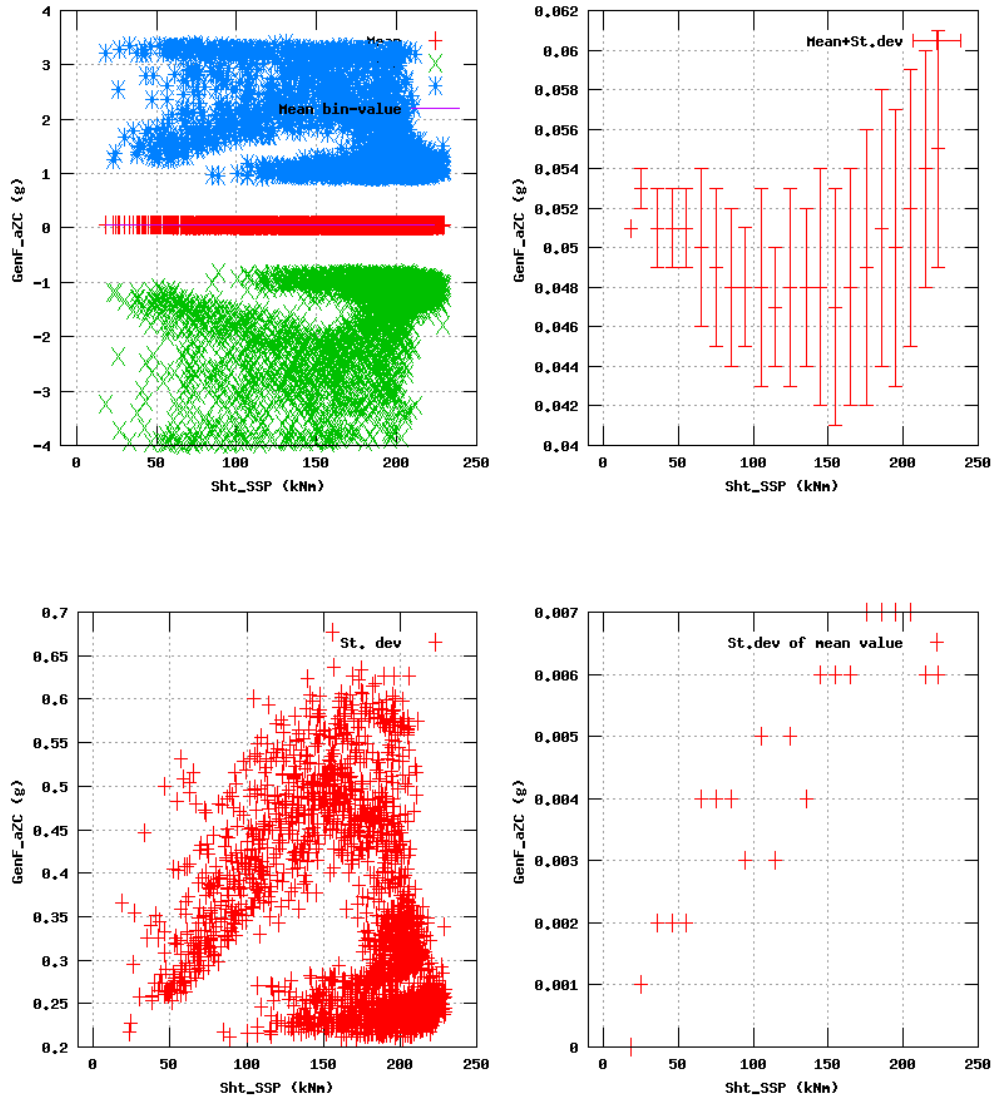
Figure 50a, Sensor 199: GeneratorF_aZC versus mainshaft torsion 'Sht_SSP'
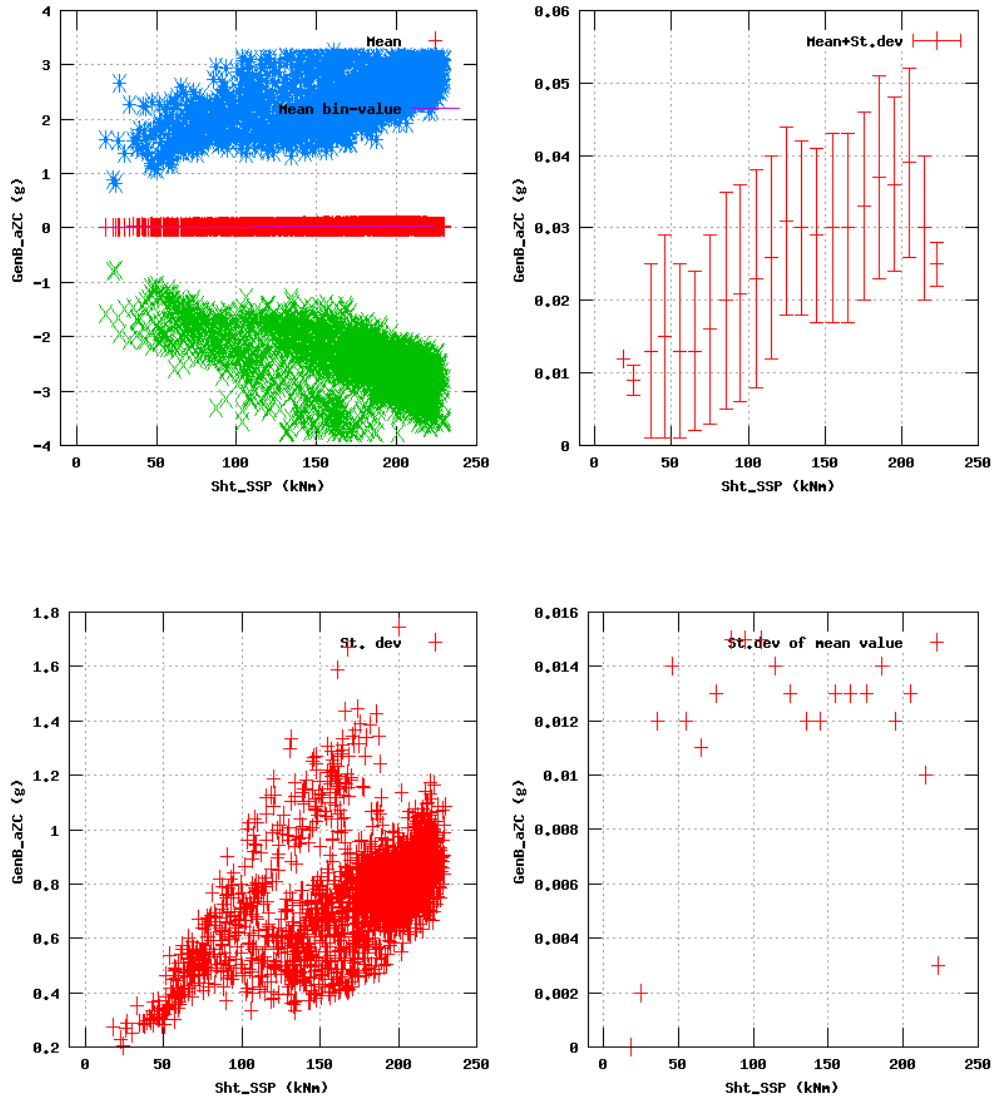Input files: NTK500fastres.dat, stat_199.dat

Figure 51a, Sensor 203: GeneratorB_aXC versus mainshaft torsion 'Sht_SSP'
Input files: NTK500fastres.dat, stat_203.dat

Figure 51b, Sensor 203: GeneratorB_aXC versus time and frequency
Input files: m07.dat, m10.dat, m28.dat, m07.psd, m10.psd and m28.psd
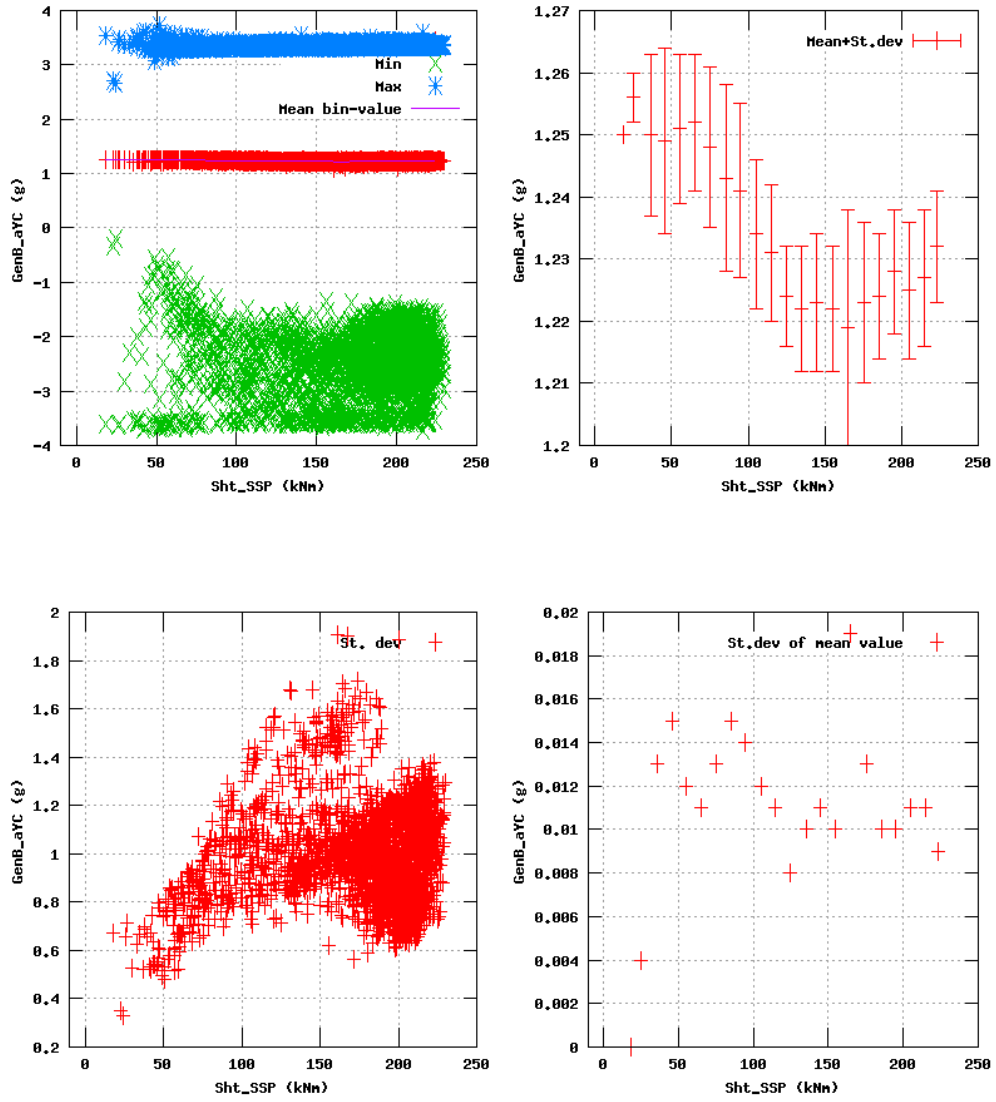
Figure 52a, Sensor 207: GeneratorB_aYC versus mainshaft torsion 'Sht_SSP'
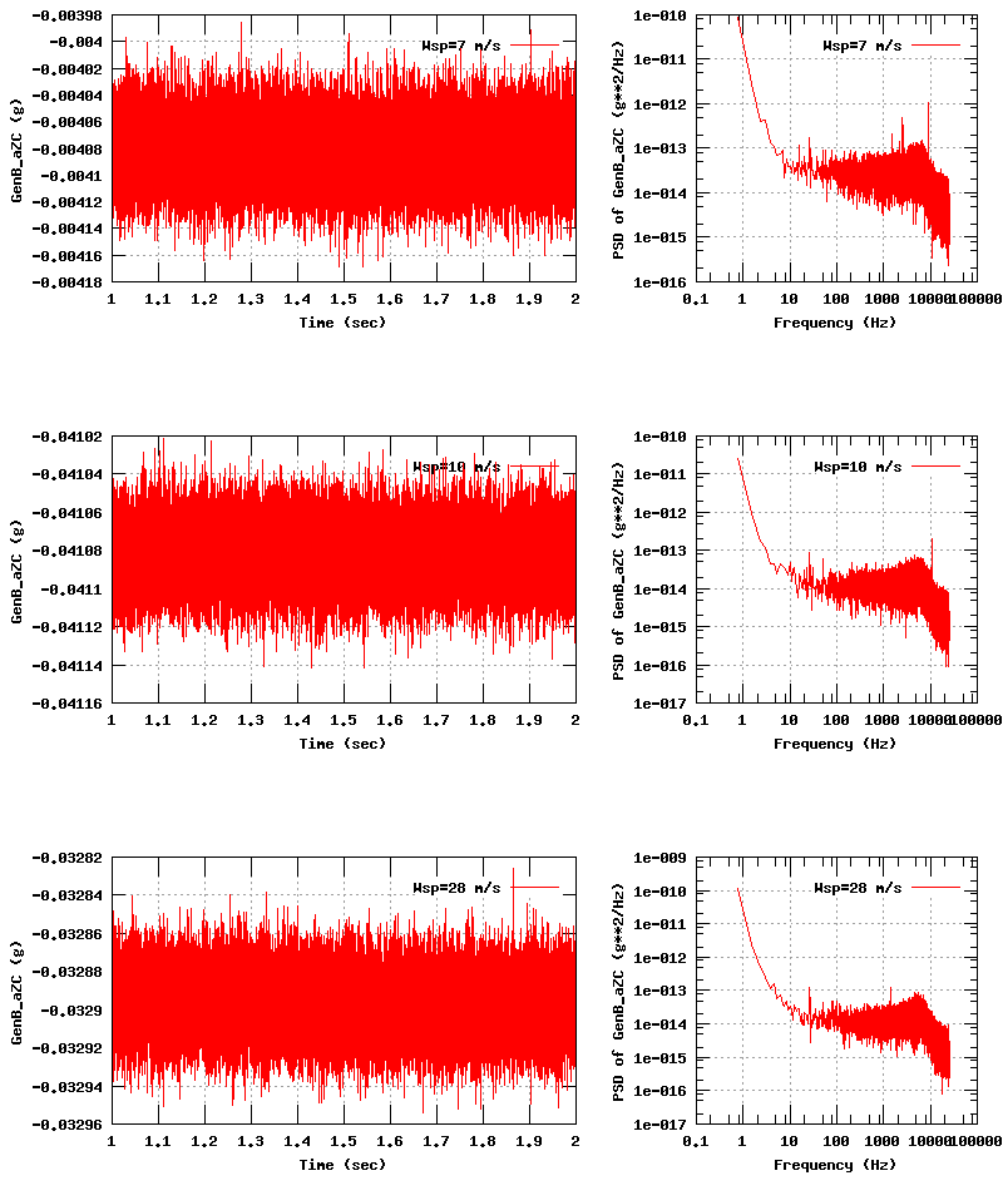Input files: NTK500fastres.dat, stat_207.dat

Figure 52b, Sensor 207: GeneratorB_aYC versus time and frequency
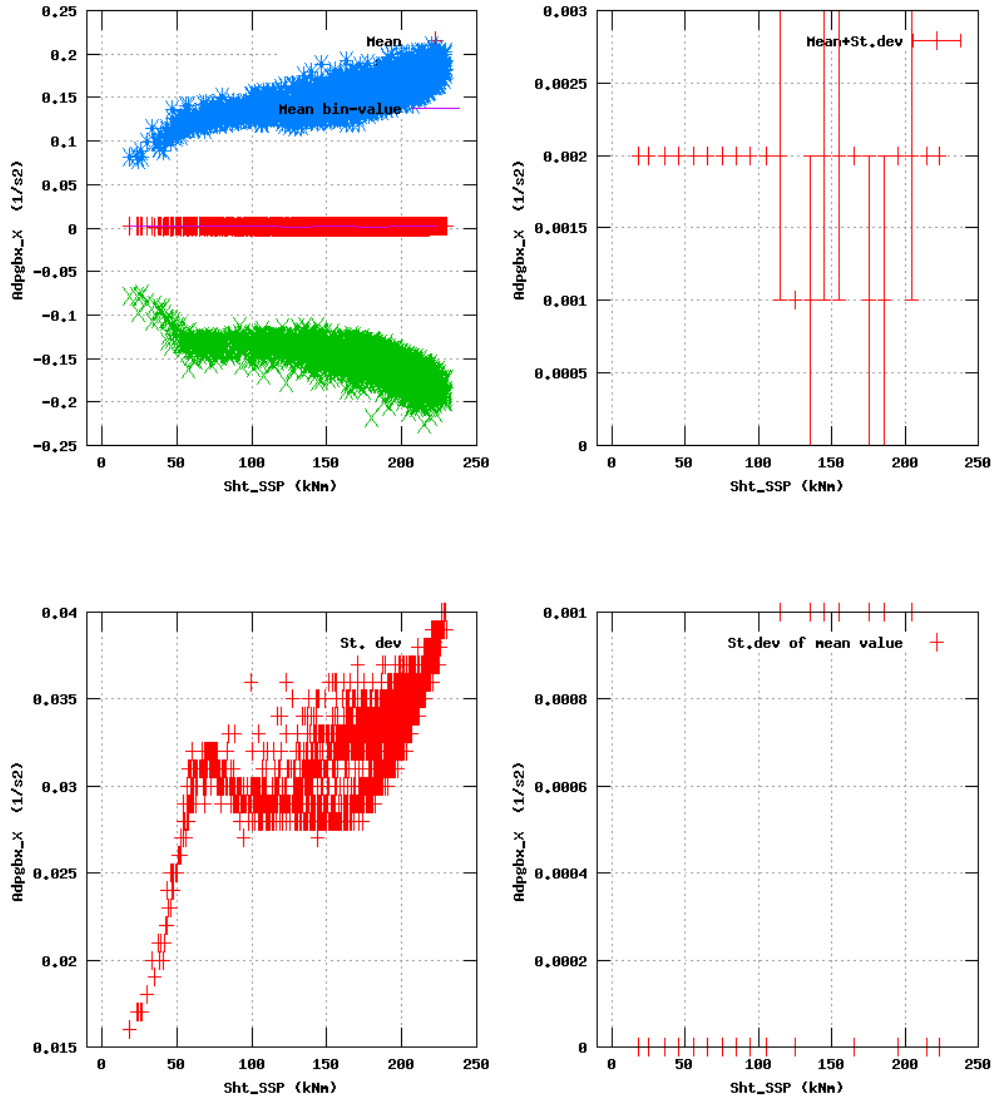Input files: m07.dat, m10.dat, m28.dat, m07.psd, m10.psd and m28.psd

Figure 53a, Sensor 211: GeneratorB_aZC versus mainshaft torsion 'Sht_SSP'
Input files: NTK500fastres.dat, stat_211.dat

Figure 53b, Sensor 211: GeneratorB_aZC versus time and frequency
Input files: m07.dat, m10.dat, m28.dat, m07.psd, m10.psd and m28.psd

Figure 54a, Sensor 215: Ang._displacement versus mainshaft torsion 'Sht_SSP'
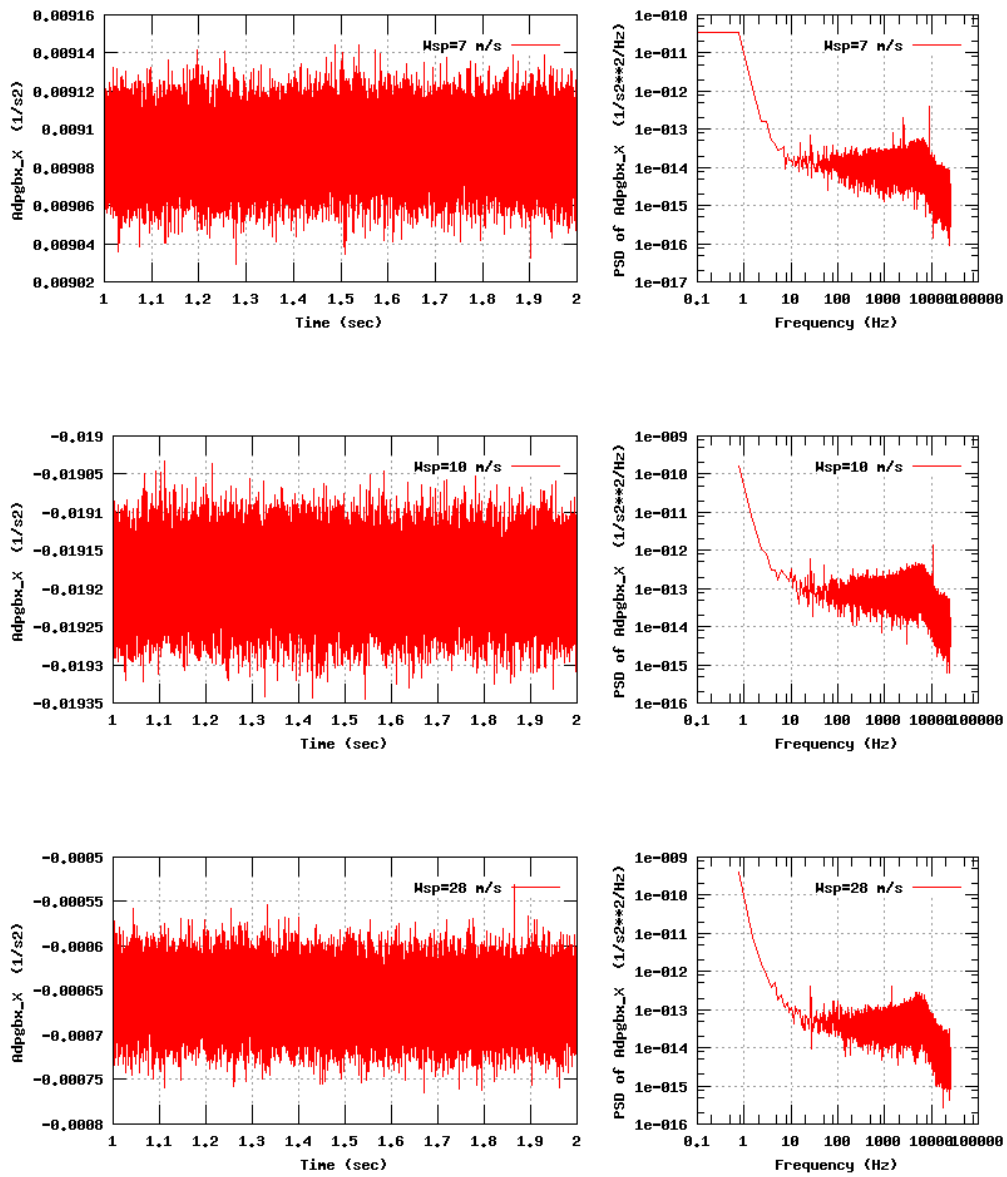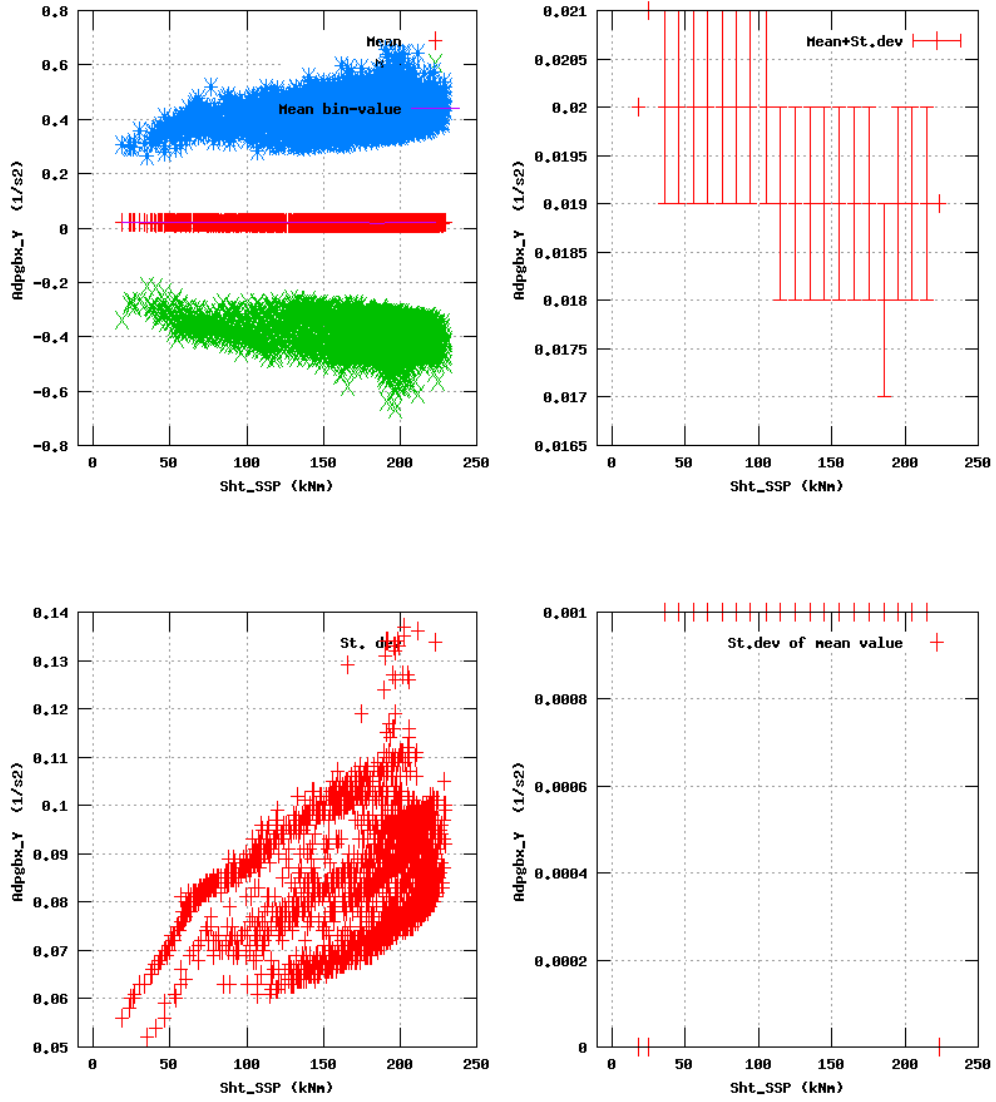Input files: NTK500fastres.dat, stat_215.dat

Figure 54b, Sensor 215: Ang. displacement versus time and frequency
Input files: m07.dat, m10.dat, m28.dat, m07.psd, m10.psd and m28.psd

Figure 55a, Sensor 219: Ang._displacement versus mainshaft torsion 'Sht_SSP'
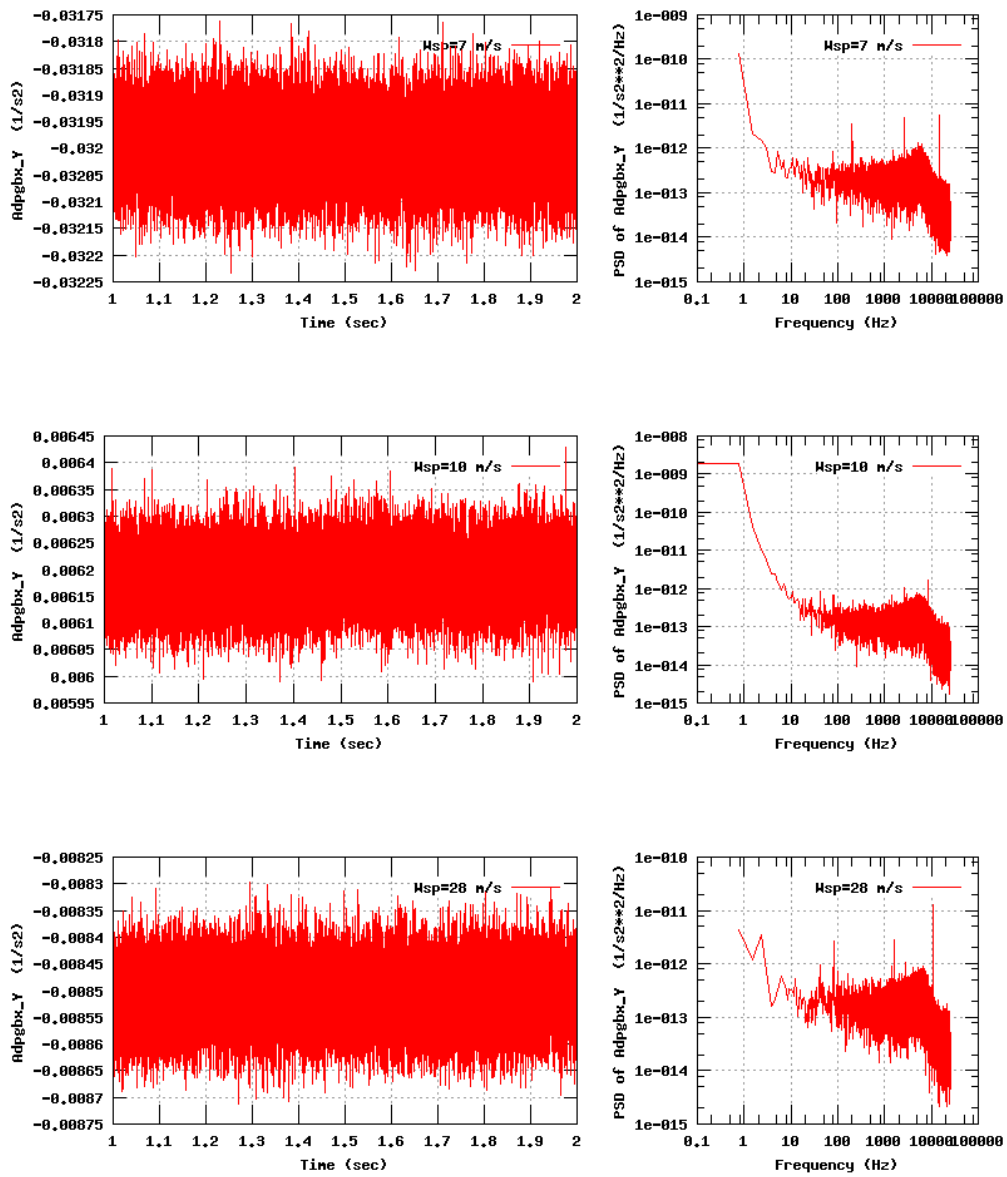Input files: NTK500fastres.dat, stat_219.dat

Figure 55b, Sensor 219: Ang._displacement versus time and frequency
Input files: m07.dat, m10.dat, m28.dat, m07.psd, m10.psd and m28.psd
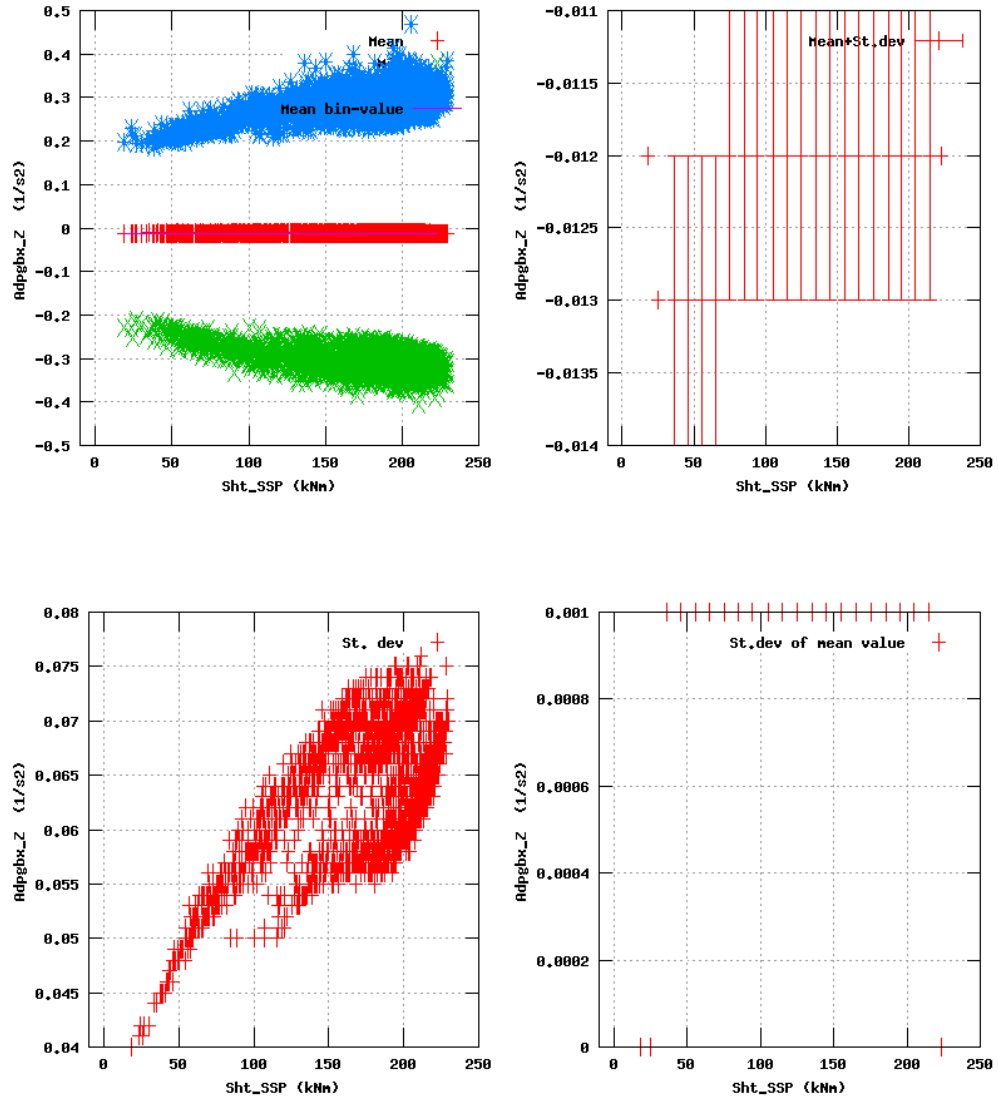
Figure 56a, Sensor 223: Ang._displacement versus mainshaft torsion 'Sht_SSP'
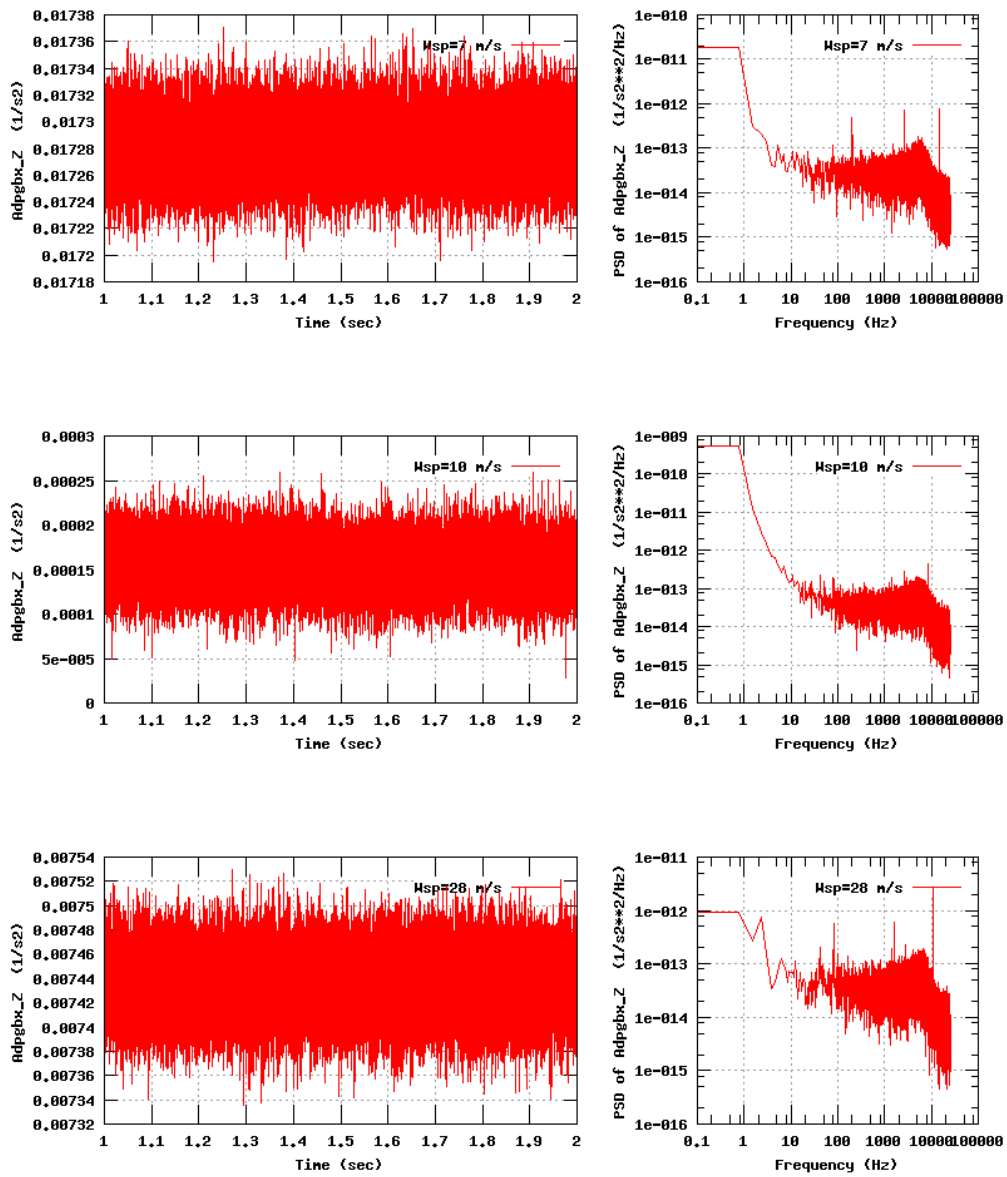Input files: NTK500fastres.dat, stat_223.dat

Figure 56b, Sensor 223: Ang._displacement versus time and frequency
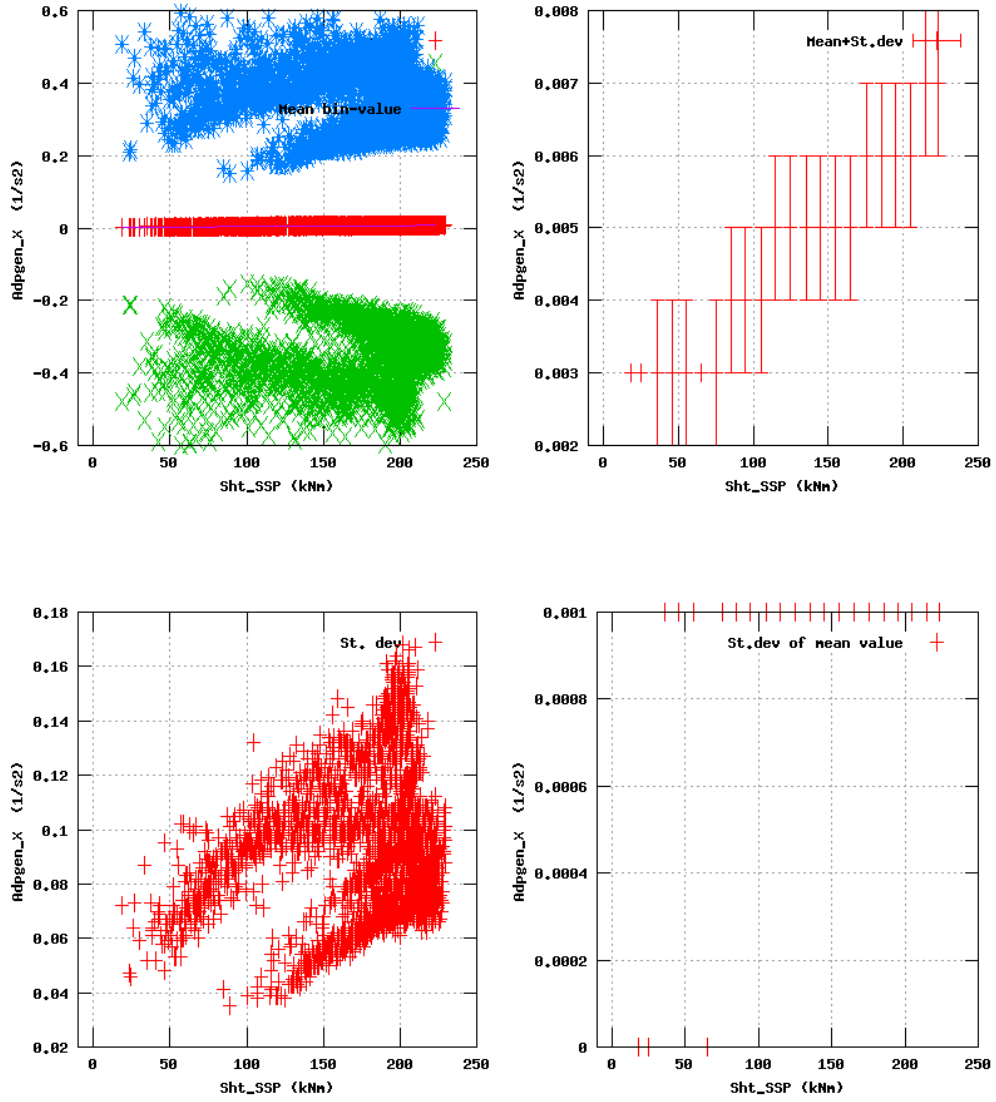Input files: m07.dat, m10.dat, m28.dat, m07.psd, m10.psd and m28.psd

Figure 57a, Sensor 227: Ang._displacement versus mainshaft torsion 'Sht_SSP'
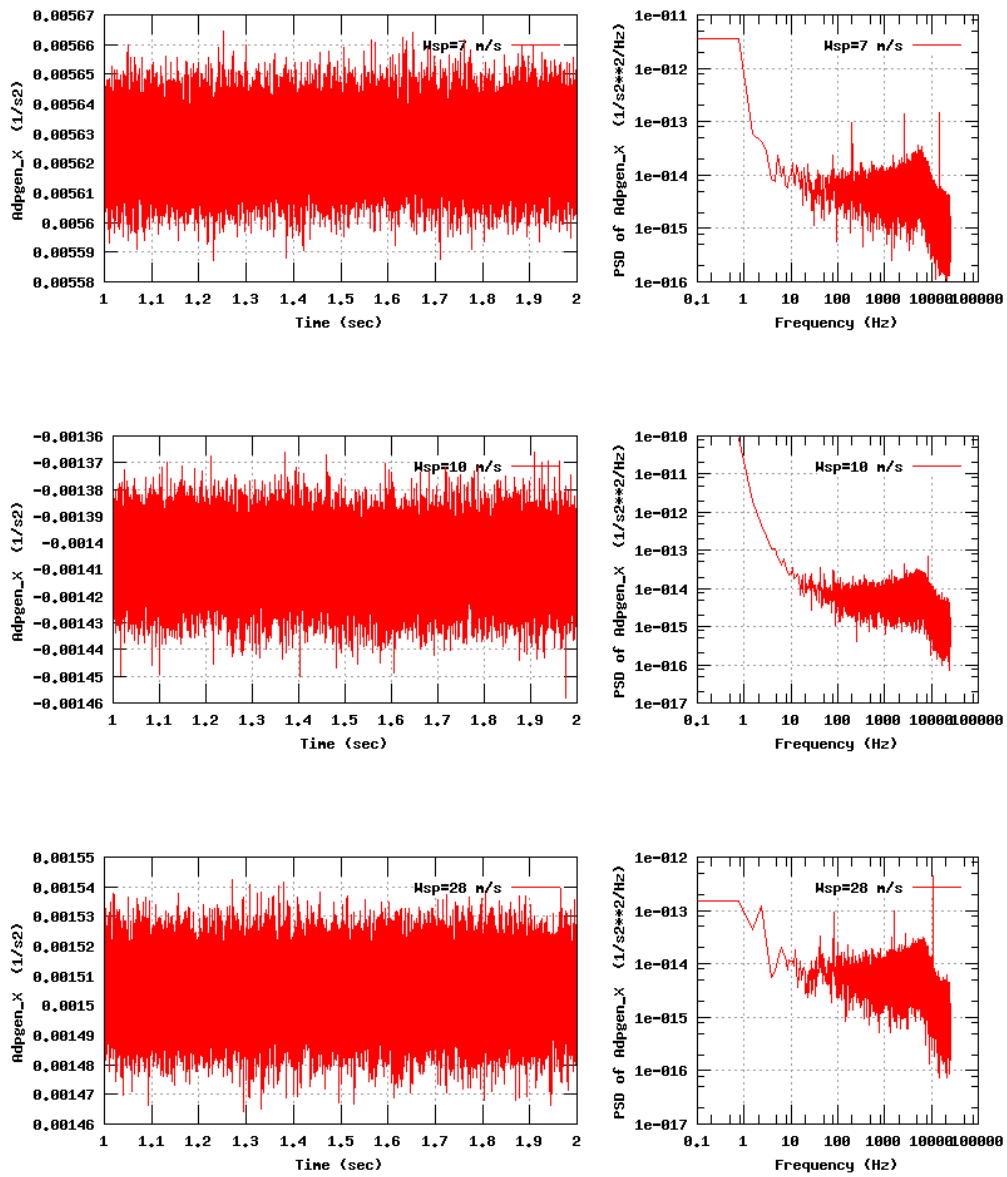Input files: NTK500fastres.dat, stat_227.dat

Figure 57b, Sensor 227: Ang._displacement versus time and frequency
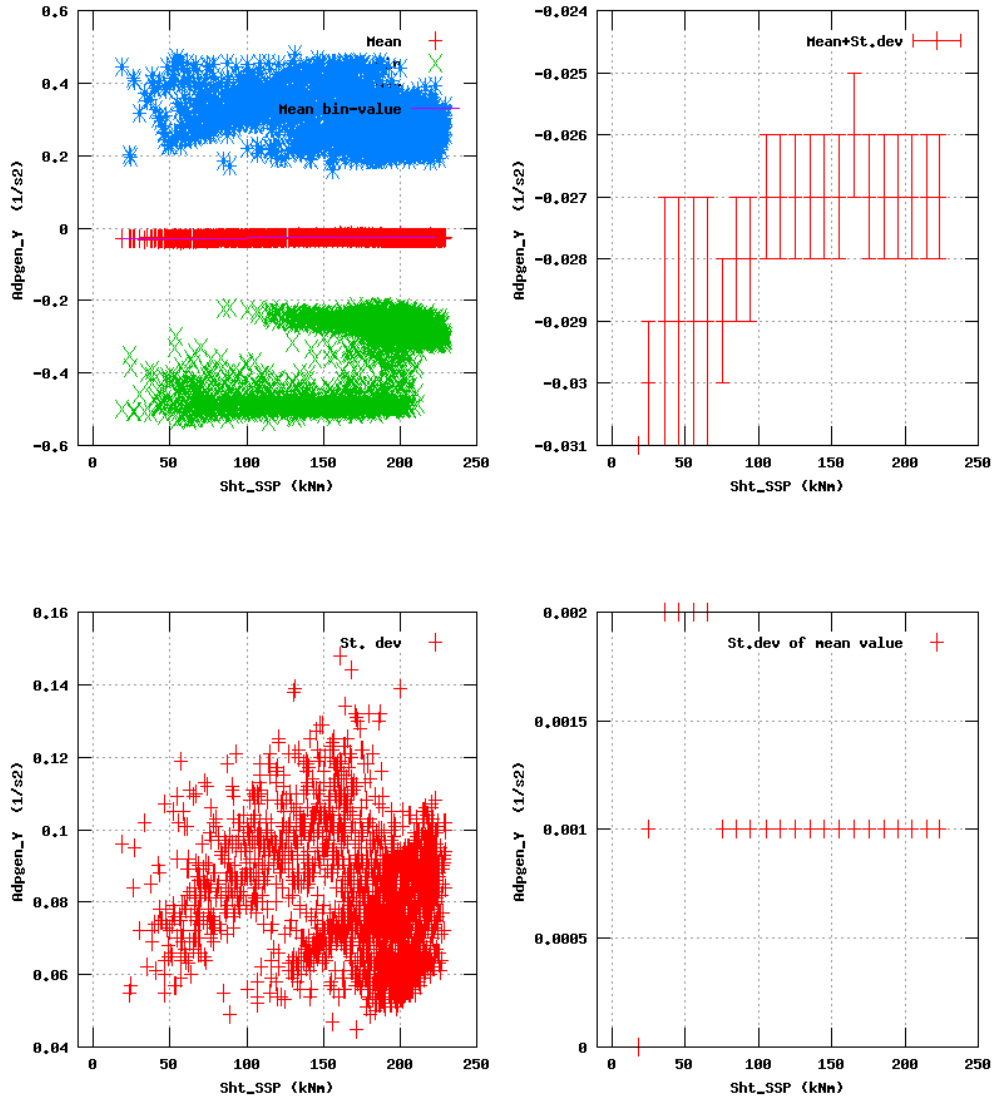Input files: m07.dat, m10.dat, m28.dat, m07.psd, m10.psd and m28.psd

Figure 58a, Sensor 231: Ang._displacement versus mainshaft torsion 'Sht_SSP'
Input files: NTK500fastres.dat, stat_231.dat

Figure 58b, Sensor 231: Ang. displacement versus time and frequency
Input files: m07.dat, m10.dat, m28.dat, m07.psd, m10.psd and m28.psd

Figure 59a, Sensor 235: Ang._displacement versus mainshaft torsion 'Sht_SSP'
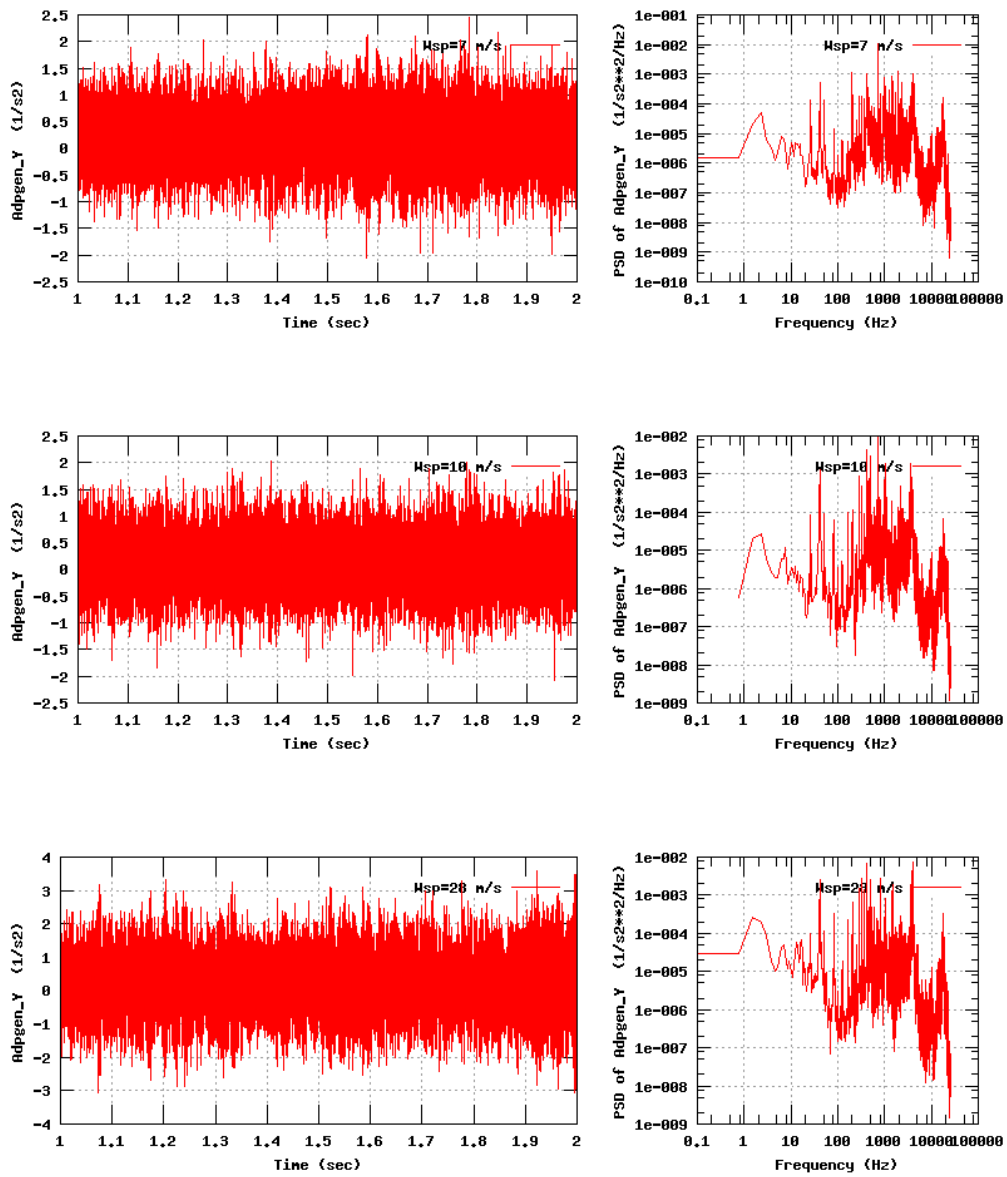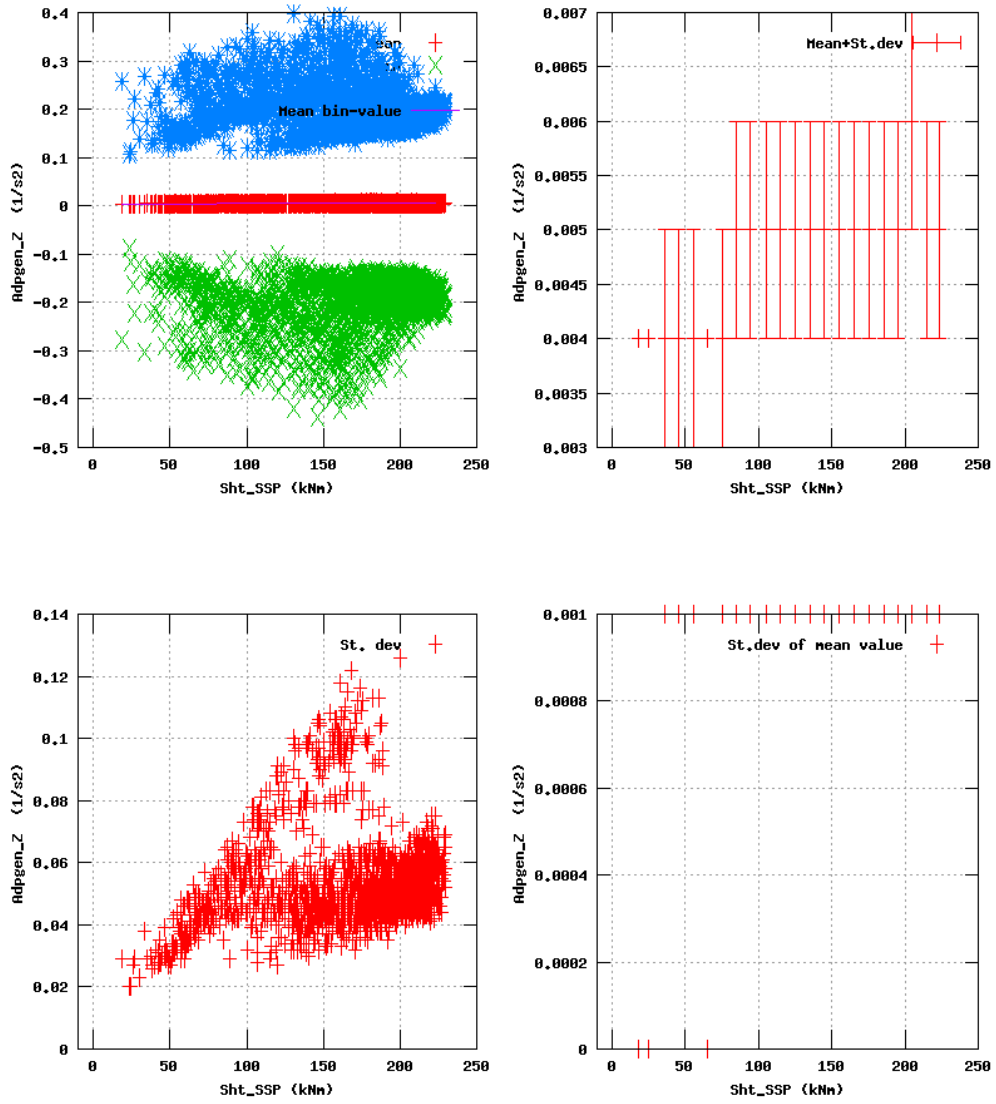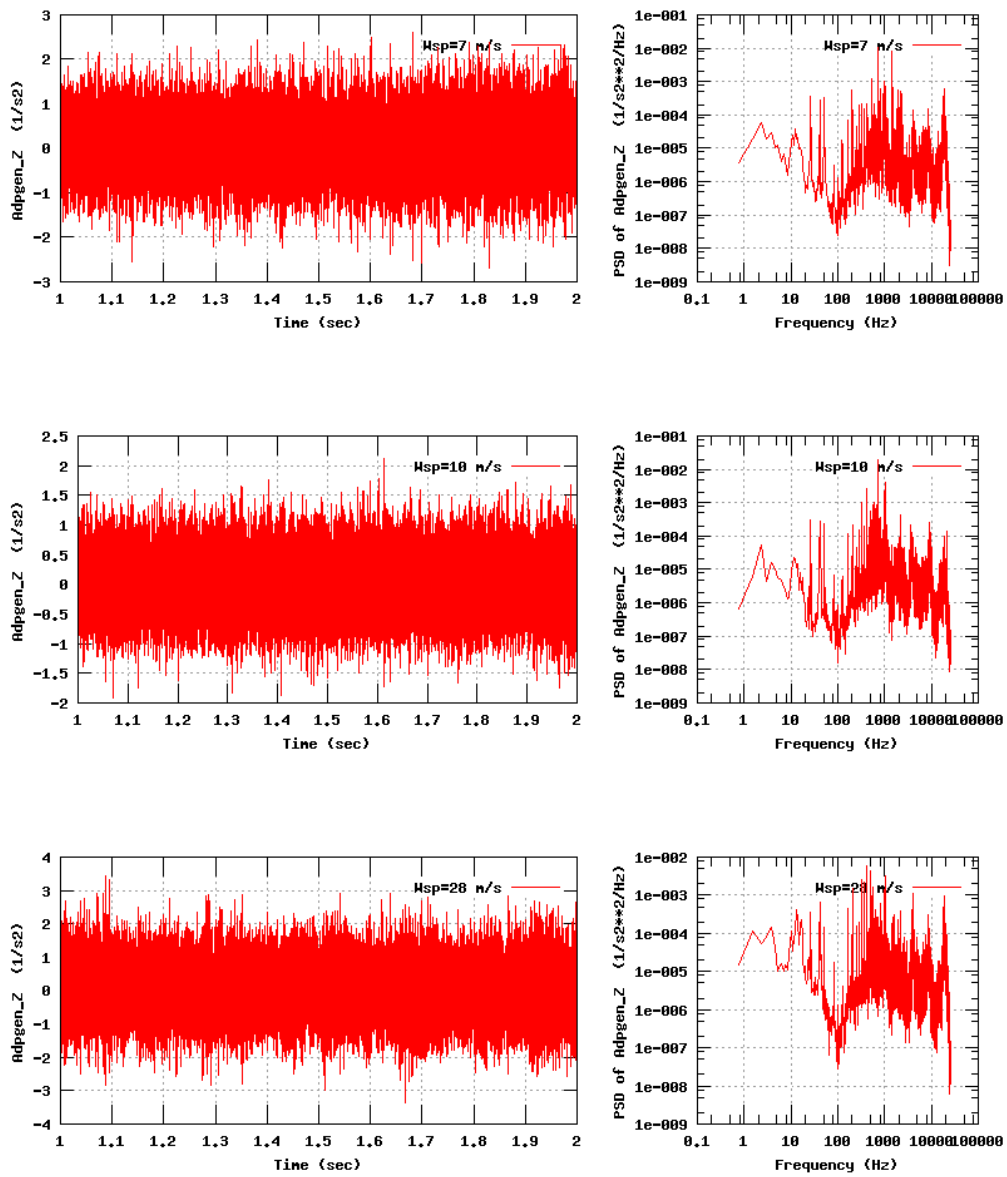Input files: NTK500fastres.dat, stat_235.dat

Figure 59b, Sensor 235: Ang. displacement versus time and frequency
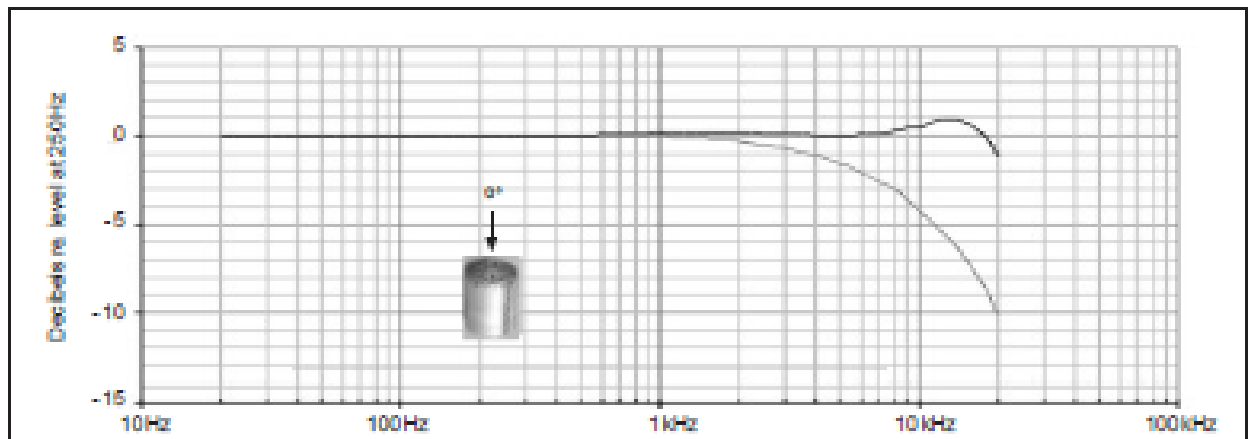Input files: m07.dat, m10.dat, m28.dat, m07.psd, m10.psd and m28.psd

Fig. 2   *Typical frequency response of Type 40AE. Upper curve shows free-field response for 0°, lower curve shows pressure response*

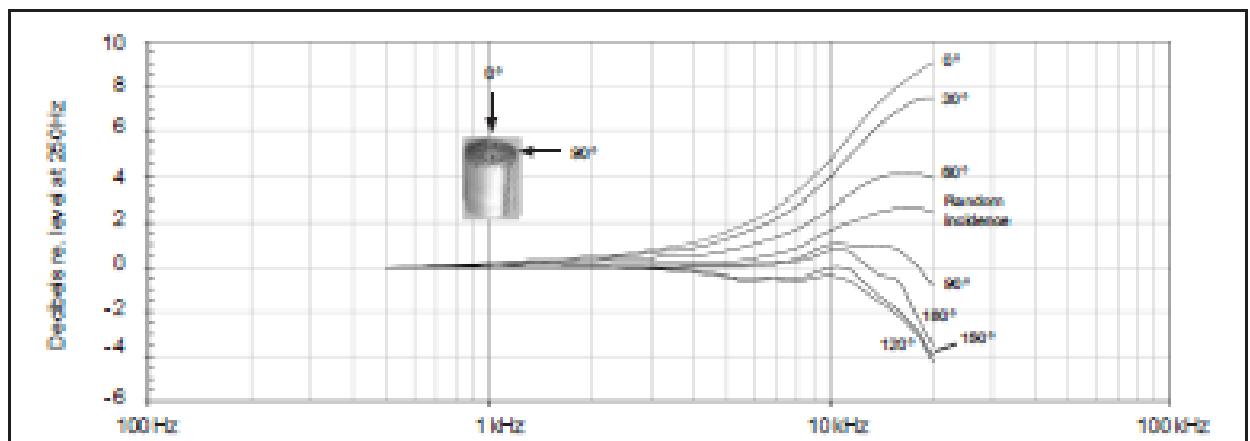Fig. 3   *Free-field corrections for various angles of incidence*

Specifications (continued)

Temperature coefficient (250 Hz):	**Dimensions (with protection grid):**	
-0.01 dB/°C	Length: . . . . 16.2 mm	
	Diameter: . . . . 13.2 mm	
Static-pressure coefficient:	**(without protection grid):**	
-0.014 dB/kPa	Length: . . . . 15.3 mm	
	Diameter: . . . . 12.7 mm	
Humidity range:	**Diameter (diaphragm ring):**	
0 - 100 % (non-condensing)	12.1 mm	
Influence of humidity (250 Hz):		
< 0.1 dB (0 - 100 % RH)	**Threads:**	
Influence of axial vibration, 1 m/s²:	Protection Grid: . . . . 12.7 mm - 60 UNS	
62 dB re. 20 µPa	Preamplifier Mounting: . . . . 11.7 mm - 60 UNS	
Venting:	**Weight:**	
Rear vented	6.5 g	
IEC 61094-4 designation:		
WS2F		

G.R.A.S. Sound & Vibration reserves the right to change specifications and accessories without notice

Risø DTU is the National Laboratory for Sustainable Energy. Our research focuses on development of energy technologies and systems with minimal effect on climate, and contributes to innovation, education and policy. Risø has large experimental facilities and interdisciplinary research environments, and includes the national centre for nuclear technologies.